

Tesi di dottorato in Ingegneria biomedica, di Alessio Gizzi,
discussa presso l'Università Campus Bio-Medico di Roma in data 20/03/2012.
La disseminazione e la riproduzione di questo documento sono consentite per scopi di didattica e ricerca,
a condizione che ne venga citata la fonte



“Campus Bio-Medico” University of Rome
Ph.D. in Biomedical Engineering

**SPATIO-TEMPORAL DYNAMICS OF
CARDIAC PHYSIOPATHOLOGY.
EXPERIMENTS, THEORY AND
SIMULATIONS**

Alessio Gizzi

Tesi di dottorato in Ingegneria biomedica, di Alessio Gizzi,
discussa presso l'Università Campus Bio-Medico di Roma in data 20/03/2012.
La disseminazione e la riproduzione di questo documento sono consentite per scopi di didattica e ricerca,
a condizione che ne venga citata la fonte

SPATIO-TEMPORAL DYNAMICS OF CARDIAC PHYSIOPATHOLOGY. EXPERIMENTS, THEORY AND SIMULATIONS

A thesis presented by

Alessio Gizzi

in partial fulfillment of the requirements for the degree of

Doctor of Philosophy

in Biomedical Engineering

“Campus Bio-Medico” University of Rome

XXIV ciclo

March, 2012

Tesi di dottorato in Ingegneria biomedica, di Alessio Gizzi,
discussa presso l'Università Campus Bio-Medico di Roma in data 20/03/2012.
La disseminazione e la riproduzione di questo documento sono consentite per scopi di didattica e ricerca,
a condizione che ne venga citata la fonte

© 2012

Alessio Gizzi

All Rights Reserved

Cover image by <http://www.unicampus.it>

Tesi di dottorato in Ingegneria biomedica, di Alessio Gizzi,
discussa presso l'Università Campus Bio-Medico di Roma in data 20/03/2012.
La disseminazione e la riproduzione di questo documento sono consentite per scopi di didattica e ricerca,
a condizione che ne venga citata la fonte

PH.D. COORDINATOR

Prof. Giulio Iannello

PH.D. ADVISOR

Prof. Simonetta Filippi

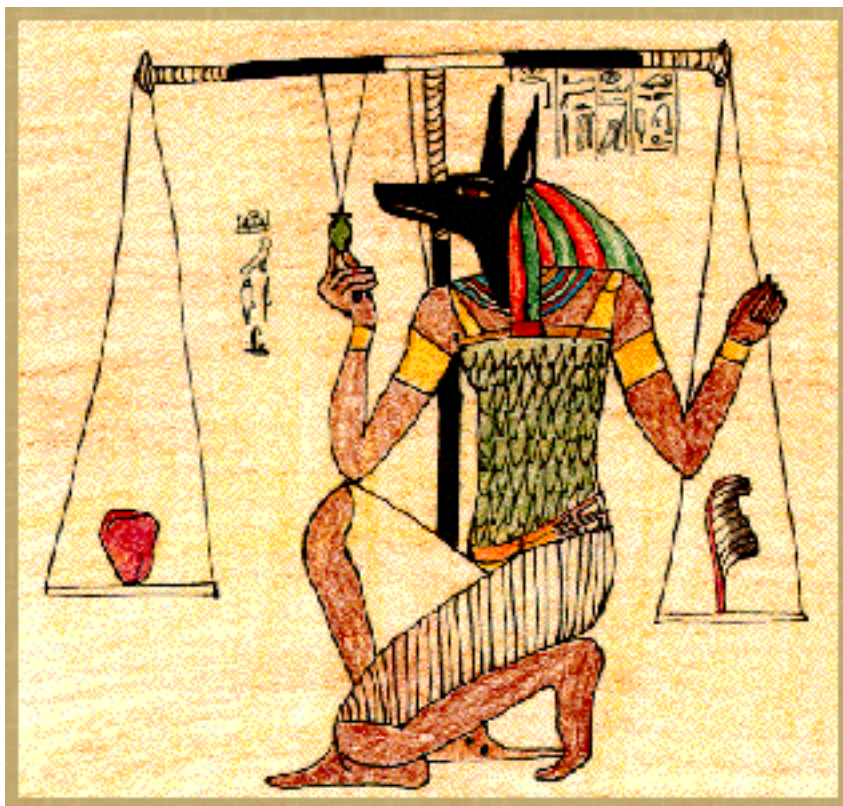
Tesi di dottorato in Ingegneria biomedica, di Alessio Gizzi,
discussa presso l'Università Campus Bio-Medico di Roma in data 20/03/2012.
La disseminazione e la riproduzione di questo documento sono consentite per scopi di didattica e ricerca,
a condizione che ne venga citata la fonte

*Dedicated to all the people who ...
believed in me, ...
supported me, ...
encouraged me, ...
loved me!*

Tesi di dottorato in Ingegneria biomedica, di Alessio Gizzi,
discussa presso l'Università Campus Bio-Medico di Roma in data 20/03/2012.
La disseminazione e la riproduzione di questo documento sono consentite per scopi di didattica e ricerca,
a condizione che ne venga citata la fonte

ANUBIS IN THE DESERTS WEST OF EGYPT 3RD MILLENNIUM BCE:

weighing the heart against the feather of Truth.



we are still trying...

A. T. WINFREE, PRINCETON GRADUATE SCHOOL CENTENNIAL, 2000.

Acknowledgments

The research work presented in this dissertation has been carried out thanks to the help of many people. I would like to thank all of them one by one.

First, special thanks to my research supervisor, Professor Simonetta Filippi, for her patience, time, encouragement and guidance throughout my studies. I am really indebted to Dr. Christian Cherubini, who always had time for answering, courage for correcting, interest in collaborating and joy in helping. These two people provided me all their expertise and understanding of the scientific and academic world.

Particular thanks to Dr. Donato Bini, who always had time for technical help and was full of effusive joy of life.

An honest thanks to Dr. Flavio H. Fenton, who introduced me to the experimental world, helped me in coding and was always busy but always willing.

I have to thank Professor Anna Pandolfi, for introducing me to the secrets of continuum mechanics, and training my research.

A collective thanks to all the friends and colleagues, both from Italy and US, who took part to my research work and academic life.

And finally, infinite thanks to my family, my parents, and especially my wife, for all the effort and support. They suffered most of my singularities, and for this I thank them once again.

Contents

1	Introduction to the Subject	1
1.1	Research Overview	2
1.2	Contributions & Limitations	2
1.3	Outline of the Dissertation	3
2	The Circulatory System: Risk Indicators	5
2.1	The Cardiovascular System	5
2.1.1	Blood Rheology	5
2.1.2	Cardiocirculatory Diseases	7
2.2	A Risk Indicator for the Cardiovascular System	9
2.3	Shear Stress on Vessel Walls	10
2.3.1	Basic Fluid Dynamics Definitions	10
2.3.2	The LESS Criterion	11
2.4	Three-Band Decomposition Analysis	12
2.5	A New Risk Indicator	14
2.6	Limitations and Future Perspectives	18
3	Anatomy and Physiology of the Heart	20
3.1	The Heart	20
3.1.1	Cardiac Anatomy & Functions	20
3.1.2	Biological Bases of Cardiac Cells	24
3.1.3	Cardiac Activation Network & Propagation	28
3.1.4	Excitation-Contraction Coupling	29
3.2	Cardiac Cycle	33
3.2.1	Controlling Cardiac Pumping	35
3.2.2	Muscular Energy Efficiency & Heart Failure	36
3.3	Mechanical Properties of Cardiac Tissue	38
3.3.1	Passive and Active Stress-Strain Relations	38
3.3.2	Uniaxial and Biaxial Passive Tests	39
3.4	Cardiac Arrhythmias	41
3.4.1	Arrhythmias: Definition & Classification	41
3.4.2	Anatomical and Functional Reentry	42
3.5	Clinical Treatments of Arrhythmias	43
3.5.1	Pharmacological Defibrillation and Cardioversion	44
3.5.2	Electrical Defibrillation and Cardioversion	44

<i>CONTENTS</i>	vii
3.5.3 Ablation	44
4 Cardiac Alternans	46
4.1 Microvolt T-Wave Alternans	47
4.2 Restitution Curves	47
4.2.1 Experiments vs Theory: Intrinsic Complexity	47
4.3 Conduction Blocks, Nodes & Nodal Lines	50
4.3.1 The Onset of Reentries	52
4.4 Nonlinear Dynamics of Alternans	54
4.4.1 Alternans Transitions in the Whole Heart	55
5 Complex Spatio-Temporal Patterns in Cardiac Tissue	56
5.1 Optical Mapping Recording of Cardiac Electrical Activity	56
5.2 Experiments Design and Implementation	59
5.2.1 Tissue Preparation	59
5.2.2 Optical Mapping Setup	59
5.2.3 Stimulation Protocol	63
5.3 Data Analysis	63
5.3.1 Ad Hoc Interactive Java Tools	63
5.4 Results & Statistics	70
5.5 Theoretical Assessment of Alternans Dynamics	77
5.5.1 Alternans & Higher-Order Rhythms	77
5.5.2 Period-Doubling Route to Chaos for VF	77
5.5.3 Initial Conditions and Multistability in Cardiac Tissue	79
5.6 Discussions	81
5.6.1 Limitations and Conclusions	81
6 Heart Modeling: Mathematical Review and Perspectives	83
6.1 Excitation Waves & Reaction-Diffusion Media	84
6.1.1 Spiral Waves in Natural Systems	85
6.2 Continuum Models of the Heart	87
6.2.1 Models of Cardiac Anatomy	87
6.2.2 Cell and Tissue Model Formulations	89
6.2.3 Computational Issues & Validation	95
6.3 Myocardial Mechanics Modeling	98
6.3.1 Material Properties, Cardiac Deformation and Strain	98
6.3.2 Constitutive Laws	99
6.4 Open Questions	101
6.5 Computer Models for Arrhythmogenesis	102
6.6 Computer Modeling of Atrial Fibrillation	102
6.6.1 Low-Energy Termination of Atrial Fibrillation	103
6.7 Models of Vortex Dynamics in Myocardium	104
6.7.1 Rotational Anisotropy, Tip Meandering and Curvature	105
6.7.2 Spiral Waves Breakup: Memory & Restitution Curves	106

<i>CONTENTS</i>	viii
7 Electro-Mechanics of the Heart	112
7.1 Introduction: Passive and Active Myocardium Modeling	112
7.2 A General Theory of Deformable Active Media	114
7.2.1 Formulation and General Statements	114
7.2.2 Electric Diffusion in a Moving Domain	115
7.2.3 Balance of Linear and Angular Momentum	116
7.2.4 Energy Balance and Dissipation Inequality	117
7.2.5 General Constitutive Theories	117
7.2.6 Helmholtz Potential for Electro-Mechanics	118
7.3 Numerical Tests	122
7.3.1 Uniaxial, Biaxial and Shear Tests	122
7.3.2 Passive and Active Mechanical Responses	124
7.4 Limitations and Future Perspectives	129
8 The Electro-Elastic Unpinning of Rotating Vortices	131
8.1 Minimal Electro-Elastic Cardiac Modeling	132
8.1.1 Theoretical Formulation & Numerical Implementation	132
8.1.2 Peculiar Spatial Distributions of the Model	136
8.1.3 Results: The Unpinning Band Measure	138
8.1.4 Discussion and Further Studies	141
9 Conclusions	142
9.1 Relevance of this Work	143
9.2 Validation	144
9.3 Future improvements and perspectives	144

Chapter 1

Introduction to the Subject

The synergic union of hypothesis and techniques from physics, mathematics, mechanics, biomedical engineering, cardiology, medicine and computer science in general represent a standard approach in the current high level scientific research and clinical practice. The increasing role of computer models as a complement of experimental and clinical studies is helping noticeably to elucidate the basic mechanisms hidden into biological systems at different scales, starting from gene expression up to tissue remodeling. Nonlinear dynamical theories and massive computational efforts are being applied in order to discover the emerging behavior from such a complexity and new theoretical assumptions, corrected on experimental basis, permit scientists to gain the building of multiscale whole tissue models, able to route new trends both in experiments and theories [129].

Models are, of course, approximations only of the actual physical system, and most of the scientists everyday using them, are well aware of this: if too simple, they fail to capture the salient behavior and have limited predictive ability; if too complex, they become computationally intractable. As in every engineering problem, the optimal choice of model structure and complexity depends on the questions to be addressed: nature of informations, time and space scales, computational demands, as an example.

The heart is a complex nonlinear system. It interacts both mechanically and chemically with different scales and levels of organization: from subcellular ionic kinetics to cellular propagating phenomena, reaching the emergent tissue electro-mechanic behavior of the overall coupling. In heart dynamics, most cardiac propagation models have been developed to understand the factors contributing to conduction failure or rhythm instability. To capture their essence, two fundamentally linked key parts have been considered: the description of the membrane ion kinetics and the representation of the electrical properties of the tissue (both starting from the work of Hodgkin and Huxley in the '50s [132]). When such a connection fails, the corresponding model can result in an inefficient or even wrong predictions for the clinical practice.

This work was initiated into the growing awareness of significant importance and beauty of cardiac tissue as excitable medium and complex dynamical system. The understanding of spatio-temporal cardiac behaviors, their relation with arrhythmogenesis and their connection with mechanical and control problems, will represent the leitmotiv of the present dissertation. Studying the heart from different perspectives, i.e. experimental, theoretical and computational, has therefore lead us to several parallel insights into such a system.

1.1 Research Overview

The main theme of this thesis is the study of cardiac spatio-temporal dynamics starting from experimental measurements, passing through the theoretical assessment of the data and ending with mathematical modeling formulations and numerical simulations.

The purpose of this procedure is to act both as a basic science, trying to understand and unveil some of the physiological and pathological mechanisms underlying cardiac arrhythmias, and as an applied science, identifying synthetic indicators for a theoretical-based clinical practice.

1.2 Contributions & Limitations

The duality of the proposed approach leads to several correlated adjoint topics, but necessary for the main theme. The contributions of this dissertation are multiple.

More specifically, the first contribution consists in the implementation of a Java open source tool for data analysis and visualization. The choice to adopt the Java Runtime Environment with a direct coding of the Java Virtual Machine was previously tested through a FORTRAN implementation. The flexibility of the resulting code, however, together with the direct access to reading and writing protocols, in union with open access interactive tools, made the software extremely useful not only for the purposes of this thesis, that is optical mapping data analysis, but also for several related projects started on its bases. The actual drawback of this tool consists in its memory requirement for large data analysis (> 4 Gbyte), which, however, would be easily corrected with specific reduced implementations.

The massive collected data (1362 recordings, 9 tissue preparations) and the full space-dependent analysis performed during this work through such a tool, highlighted several novel experimental results on cardiac alternans in accordance or not with the current literature. i) It was tested that as pacing cycle length is decreased, alternating dynamics predominantly develop first on the endocardial surface than on the epicardial one. ii) The postulated simple progression from normal rhythm (1:1) to concordant 2:2 to discordant 2:2 was not always observed; in some cases, concordant alternating rhythms may develop from discordant alternans as the pacing period is decreased. iii) In contrast to smaller tissue preparations, multiple stationary nodal lines, not alternating regions, may exist and need not to be perpendicular to the pacing site or to each other. iv) Alternans has fully three-dimensional dynamics: multiple nodal surfaces can be transmural or intramural and can form “islands”, and because of this, the epicardium and endocardium may have significantly different dynamics. In this case several examples of complex spatial discordant patterns were found. v) The complex spatio-temporal patterns observed during alternans are a function of both the direction of stimulation and the stimulation history in a non-trivial way. A drawback in this case may be seen in the necessity of other experimental campaign, specifically designed for testing the results obtained during this thesis.

From an applied engineering view, two main models were formulated and numerically implemented. (1) In relation with low-energy defibrillation protocols, in particular, an extended set (> 500 runs) of numerical simulations were conducted in order to identify an *effective unpinning band*, consisting in the right window of stimulation periods capable to unpin/defibrillate an anatomical reentry on a two-dimensional domain. The numerical analysis was carried on both a purely electric and an electro-mechanic cardiac medium, in which a phenomenological model [88] for cardiac action potential propagation was coupled with a minimal mechanical description comprising the active response of the medium in large deformations [45]. The theory was framed into the finite hyperelastic continuum mechanics material laws, assuming a multiplicative decomposition of the deformation tensor as the active component. Other

than structural simplifications, the main limitations of this approach are due to i) the necessity to test the same defibrillation protocol on three-dimensional geometries with fibers architecture, ii) the basic calcium-contraction modeling adopted, which should be upgraded to more biophysically-based kinetics.

(2) In relation with cardiovascular risk, moreover, a new risk indicator for shear stress effects was introduced, namely, the *three band decomposition* analysis (TBD). Simulating the Navier-Stokes equation in physiological and pathological domains, and comparing the standard indicators for wall shear stress (WSS), namely oscillation shear index (OSI) and mean WSS, the TBD indicator resulted to better enhance the risk induced by non-physiological WSS. In this case too, multiple tests of the proposed analysis on experimental and simulated signal are required in order to fully characterize TBD applicability.

From a more theoretical point of view, the general theory of deformable active soft media was explored and enriched with a specific constitutive law for cardiac tissue. A complete and detailed formulation resulted from an extended theoretical analysis, and at the same time, extremely handy from a numerical point of view. The resulting model was able to reproduce: i) passive tissue anisotropy; ii) nonlinear exponential stress-strain curves; iii) active electric nonlinear and anisotropic feedback. An accurate tuning of model parameters is still necessary for better reproduce cardiac electro-mechanics coupling, although its range of applicability is extremely vast.

1.3 Outline of the Dissertation

In this section, a brief outline of the content of the chapters is given.

Chapter 2. Introduction to the cardiovascular system and its related pathologies. Then, a first a computational fluid-dynamics model to study wall shear stress is presented. A new risk indicator is introduced in comparison with standard ones.

Chapter (3). Detailed description of cardiac anatomy and physiology, with specific insight into the mechanical properties of cardiac tissue. Then, the attention is focused on the pathologies that affect this organ, cardiac arrhythmias in particular, and the related clinical treatments.

Chapter 4. Discussion and description of cardiac arrhythmias from an experimental point of view. Then, the main mathematical and numerical tools through which arrhythmic phenomena are usually investigated are reviewed.

Chapter 5. Presentation of the experimental studies conducted on cardiac alternans and the novel results obtained. Characterization of the related theories and discussion of applications.

Chapter 6. General review of mathematical modeling of the heart, from different perspectives and with different methods. Specific description of the mathematical models for arrhythmogenesis.

Chapter 7. Presentation of a novel general energy-based theory for deformable active media. Characterization of the constitutive law for applications in cardiac tissue.

Chapter 8. Discussion of the extended simulation analysis performed for a novel study of the electro-elastic unpinning of rotating vortices.

Chapter 9. Conclusive remarks, limitations and future perspectives.

The dissertation is mainly based on the following publications:

- A. Gizzi, E. M. Cherry, R. F. Gilmour, Jr, S. Luther, S. Filippi, and F. H. Fenton. Spatio-temporal dynamics of alternans patterns in cardiac tissue. *In preparation for Circ. Res.*
- A. Gizzi, C. Cherubini, S. Filippi, and A. Pandolfi. Electromechanics of cardiac excitation. *In preparation for J. Biomech.*
- C. Cherubini, S. Filippi, and A. Gizzi. On the electro-elastic unpinning of rotating vortices in biological excitable media. *Accepted for publication Phys. Rev. E.* March 2012.
- A. Gizzi, C. Cherubini, S. Filippi, and A. Pandolfi. A coupled electromechanical material model for active tissues. Submitted to ECCOMAS, Vienna (AUS) 2012.
- M. Vasta, A. Pandolfi, and A. Gizzi. A fiber distributed model of biological tissue. Submitted to IUTAM symposium on Multiscale Problems in Stochastic Mechanics, Karlsruhe (D), 2012.
- A. Gizzi. Spatio-temporal dynamics of alternans patterns in cardiac tissue. 21st Annual Meeting UNYCES 2011, Syracuse (USA), invited talk.
- A. Gizzi. Complex dynamics of cardiac alternans. XXXI Dynamics Days Europe, Oldenburg (D) 2011.
- A. Pandolfi, C. Cherubini, S. Filippi, and A. Gizzi. Electro-mechanics of cardiac excitation. 2nd International Conference on Material Modeling, Paris (F) 2011.
- A. Gizzi, M. Bernaschi, D. Bini, C. Cherubini, S. Filippi, S. Melchionna, and S. Succi. Three-band decomposition analysis of wall shear stress in pulsatile flows. *Phys. Rev. E.* **83**:031902, 2011.
- D. Bini, C. Cherubini, S. Filippi, A. Gizzi, and P. E. Ricci. On spiral waves arising in natural systems. *Comm. Comput. Phys.* **8**:610-622, 2010.
- A. Gizzi, F. H. Fenton, E. M. Cherry, C. Cherubini, and S. Filippi. Thermo-electric cardiac modeling. 5th International Workshop on Cardiac Mechano-Electric Coupling and Arrhythmias, Oxford (ENG) 2010.
- C. Cherubini, S. Filippi, A. Gizzi, P. Nardinocchi, and L. Teresi. Mechano-electric coupling effects in reentrant arrhythmia. 5th International Workshop on Cardiac Mechano-Electric Coupling and Arrhythmias, Oxford (ENG) 2010.
- C. Cherubini, S. Filippi, and A. Gizzi. Thermal effects on cardiac tissue. SIAM, DSPDEs'10, Emerging Topics in Dynamical Systems and Partial Differential Equations, Barcelona (E) 2010.
- C. Cherubini, S. Filippi, and A. Gizzi. Modeling heat transfer in cardiac tissue. MPF2010, IV International Symposium on Modeling of Physiological Flows, Sardegna (IT) 2010.

Chapter 2

The Circulatory System: Risk Indicators

This chapter it's intended to give the reader a brief characterization of the anatomy and physiology of the cardiocirculatory system, introducing the specific medical and clinical topic of risk assessment for atherosclerotic diseases. Such an approach is not devoted to the precise and detailed description of the complexity of the cardiovascular system in toto, but it is meant to underline the main characters that are bear directly upon cardiac electro-mechanics. Therefore, following a multiscale zoom in, from cellular units to whole tissue, the vascular structure will be addressed and explored in relation to the wall shear stress analysis, both from a theoretical and numerical point of view. A discussion about clinical perspectives and applications will be then pursued.

2.1 The Cardiovascular System

The human circulatory system is in charge to carry oxygen and nutrients to tissues and organs as well as to remove carbon dioxide and catabolites from them. It can be considered both as a closed circulatory loop, from the mechanical point of view, or as a complex network, from the dynamical point of view: it is in charge to pump blood from the heart through large arteries, to the smaller arterioles, then through capillaries, where oxygen and nourishment release support cells and organs, then eventually, further down to the venules, where the blood is passed through veins back to the heart. This path thereby imposes a closed circular pattern though the whole body. In any case, the contribution of all parts of the system determine the “emerging” physiological behavior which comprises many sub-mechanisms. In Fig.(2.1.1) a schematic representation of the main constituents the cardiovascular system is depicted.

2.1.1 Blood Rheology

Rheology is defined as the science of deformation and flow of materials under controlled testing conditions; *haemorheology* is termed its application to blood. Through such a description, the basic concepts of kinematics and constitutive laws of blood and its former elements are introduced, thus the coupling between blood and vessels in living organisms. The interest in haemorheology is based on its primary importance as cause of many cardiovascular diseases when modifications from a physiological behavior arise.

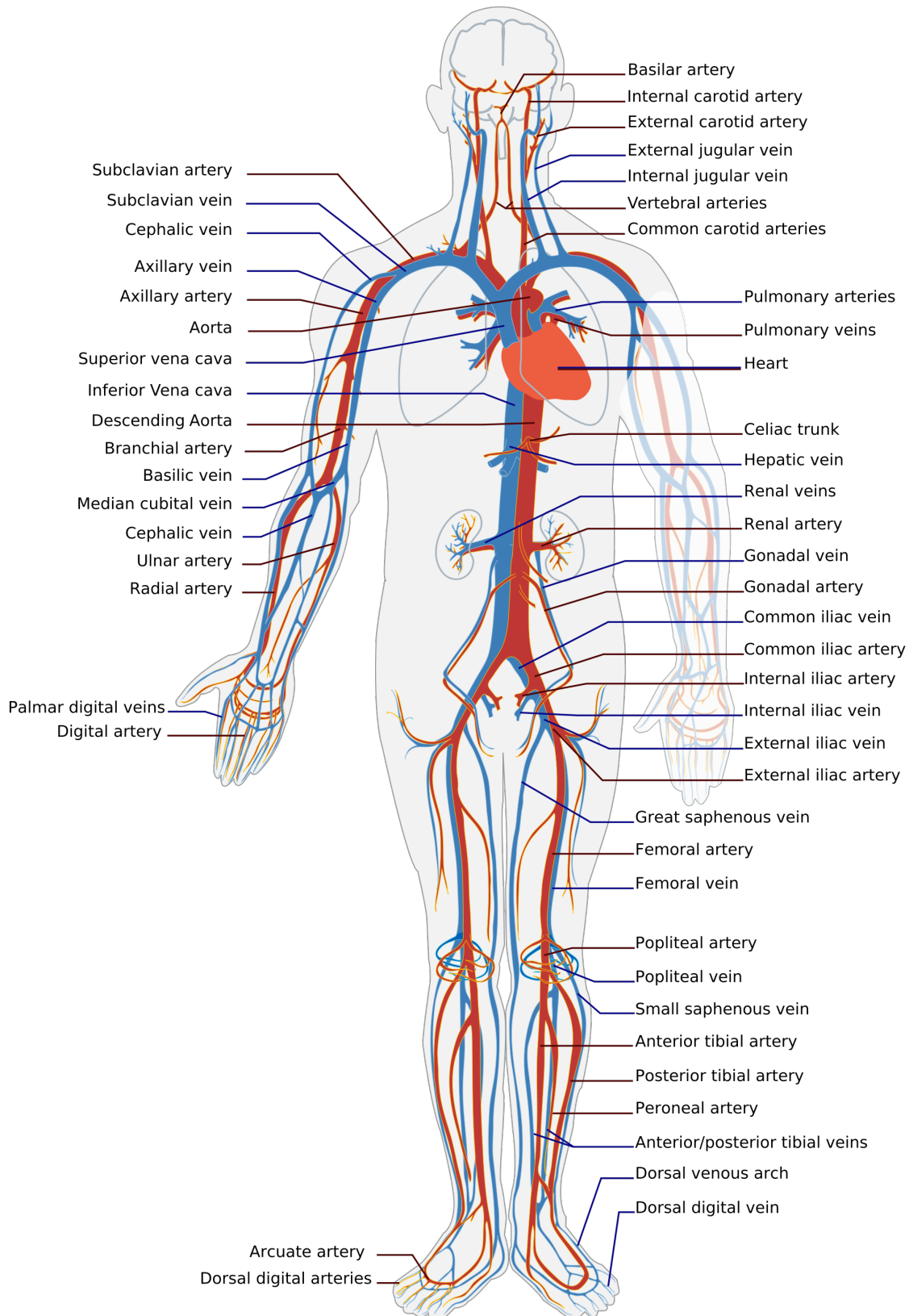


Figure 2.1.1: Simplified diagram of the human Circulatory system in anterior view [282].

Blood is a suspension of cellular elements (erythrocytes, leukocytes and thrombocytes) in an aqueous polymeric solution, *plasma*, containing electrolytes and organic molecules. The plasma, consisting of water for about the 90% of its mass, shows a nearly Newtonian response. The mechanical properties of blood, on the other side, are strongly influenced by the high concentration of red blood cells (RBCs), occupying about 45% of the total volume. The corresponding index defining the volumetric fraction of RBCs is called *haematocrit*. In fact, the global behavior of whole blood presents a non-Newtonian character, particularly at low shear rates, when RBCs tend to form a three-dimensional microstructure, while tend to deform and align with the flow field at high shear rates.

Two important indicators are often adopted to measure the flow state, i.e. the *Reynolds number* [231], Re , and the unsteady inertial effects to viscous phenomena, the *Womersley number* [307], α :

$$Re = \frac{\rho U D}{\mu}, \quad \alpha = \frac{1}{2} D \sqrt{\frac{\rho \omega}{\eta}} \quad (2.1.1)$$

where D is the vessel diameter, U the mean blood velocity, ω the angular frequency, $\rho \cong 1.06 \cdot 10^3 \text{ Kg} \cdot \text{m}^{-3}$ is the blood fluid density, and $\mu = 3.0 \div 5.5 \text{ mPa} \cdot \text{s}$ is its dynamics viscosity at 37°C . If blood viscoelasticity is considered, a dimensionless time scale, the *Deborah number* [230], can be introduced:

$$De = \lambda \omega \quad (2.1.2)$$

where λ is a characteristic time associated with the memory of the fluid. Several estimated and measured values for these numbers can be found in literature, see [98] as an example.

2.1.2 Cardiocirculatory Diseases

A partial list of the main diseases of the cardiocirculatory system will be given in this paragraph [213].

Diseases Related to the Blood Flow

Anaemia: a condition with an insufficient oxygen carrying capacity of the patients blood. It can be an anaemias with insufficient haemoglobin production or anaemias with waste of red cells.

Oedema: clinical state characterized by abnormal accumulation of interstitial or tissue fluid.

Hypocoagulability: condition with a prolonged coagulation time.

Haemolysis: disruption of the red cell membrane with liberation of the cellular content to the plasma of whole blood.

Thrombosis: formation of multiple thrombi or clots within the vascular system.

Embolism: process through which a thrombus is dislodged from its attachment and travels with the blood until it is lodged in a blood vessel too small to allow its passage.

Aneurysms: abnormal dilatations on a vessel typically due to degenerative processes in the wall: on brain or coronary arteries (leading to sudden death); aortic aneurysms (usually due to arteriosclerosis) with large atheromas in the wall; abdominal or thoracic aorta (requires immediate surgery); left ventricular aneurysm (complication to ischaemic heart disease); saccular aneurysms (on the circle of Willis and its adjacent branches).

Diseases Related to Heart Rhythm

Asystolia: refers to cardiac arrest.

Bradycardia: an unduly slow heart rate.

Sinus bradycardia: a sinus rhythm at rest below 60 beats per min (bpm) during the day or less than 50 at night.

Heart block: a blockage somewhere along the pathway for impulse conduction in the heart.

Atrial fibrillation: a continuous atrial activation with 400 or more contractions per min. Contractions spread through the atrial tissue almost without mechanical effect and only few electrical signals are conducted to the ventricles.

Atrial flutter: an atrial contraction rate around 300 per min, often with every second contraction conducted to the ventricles. Sawtooth-like flutter waves characterize the ECG.

Tachycardia: a cardiac rate above 100 bpm. Sinus tachycardia can be caused by anaemia, cardiac failure, catecholamines, emotion, exercise, fever, pregnancy, pulmonary embolism or thyrotoxicosis.

Ventricular tachycardia: defined as three or more ventricular beats occurring at a rate of 120 bpm or more.

Ventricular fibrillation: an extremely rapid ventricular activation without pumping effect.

Vulnerable period: a dangerous period in cardiac cycle just at the end of the contraction (simultaneous with the T-wave in the ECG). Refractory areas of cardiac muscle are spread among non-refractory areas.

Ectopic focus: a pacemaker focus located in other regions of the myocardium than the sinus node. Active ectopic foci cause abnormal contraction patterns in the related regions of the heart.

Diseases Related to Inflammation and Sudden Cardiac Death

Bathmotropic state: refers to the irritability of the myocardium.

Rheumatic Heart Disease: caused by repeated infections and mainly affects mitral and aortic valves.

Angina pectoris: (chest pains) pain felt beneath the sternum or in the precordial area. The hypoxic pains are typically provoked by exercise or cold and submitted by subendocardially situated nerve fibers.

Atherosclerosis: process of progressive lipid accumulation (atheromatosis) and calcification of the inner arterial walls in the abdominal aorta, lower extremities and the arteries of the heart, brain and kidneys.

Ischaemic heart disease: caused by reduced bloodflow to a region of the myocardium.

- Non-Q wave infarction occurs when only part of the wall is necrotic.
- Q-wave infarction presents a wide and deep Q wave in the ECG (a lesion wave), and the sign of transmural myocardial infarction with necrosis through the whole of the myocardial wall.

Cardiac failure (or cardiac insufficiency): heart cannot pump enough blood to satisfy the nutritive needs of the body.

- Cardiac oedema develops during congestive cardiac failure, because the kidneys retain NaCl and water. The accumulated fluid increases venous return, which in turn elevates the right atrial pressure. The rising atrial pressure elevates the venous and the capillary pressure. This causes loss of fluid into the interstitial fluid volume.
- Cardiogenic shock - terminal pump failure - is such a severe reduction of cardiac output that the peripheral tissues suffer seriously from lack of oxygen, the cells deteriorate and within hours or days the patient dies.

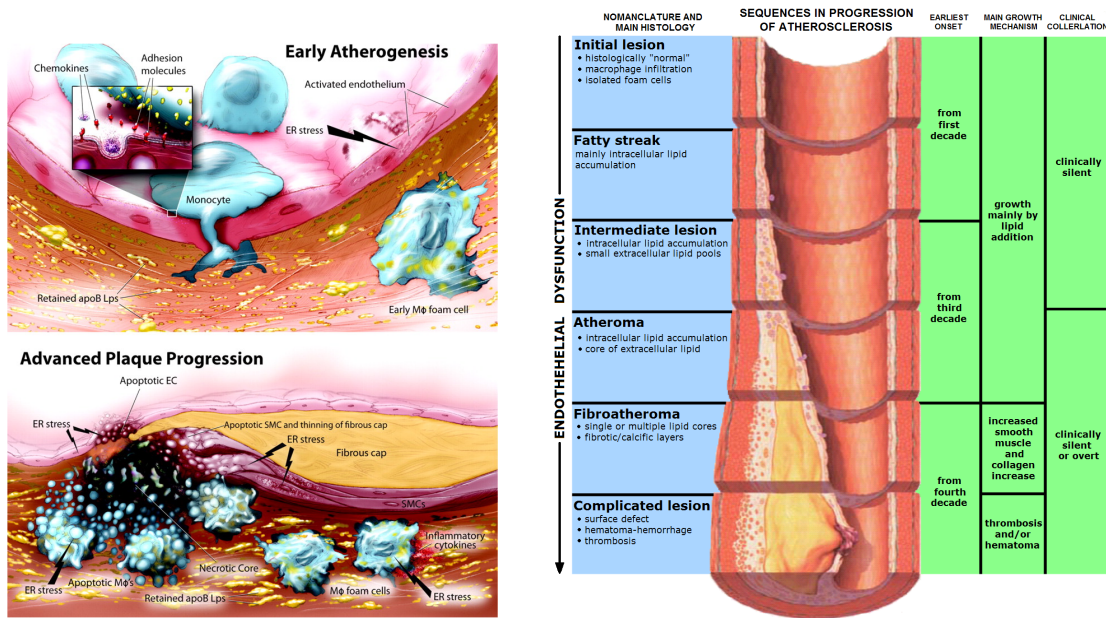


Figure 2.2.1: (LEFT) Possible roles of prolonged endoplasmatic reticulum stress in early atherogenesis and advanced plaque progression [262]. (RIGHT) Stages of endothelial dysfunction in atherosclerosis [49].

Acute myocardial infarction: due to a sudden coronary thrombosis from an atheromatous plaque causing cellular death (infarct) of a myocardial area.

2.2 A Risk Indicator for the Cardiovascular System

One of the major applications related to both the theoretical and experimental problems discussed in this dissertation, concerns the study of the physiopathology of the circulatory system through numerical simulation analysis. As described before, providing hundred millions heartbeats in a lifetime, such a complex network is ineluctably exposed to several risk factors. Among others, atherosclerosis is strongly related to sudden cardiac death [122, 170, 227, 229, 244, 280, 283, 300] and represents one the most common cardiovascular diseases [257, 284]. The early stage in atherosclerosis is often observed in coronary and peripheral arterial beds and prognosticated as endothelial dysfunction: an impairment of endothelium-dependent vasodilation with widespread abnormalities in endothelial integrity and homeostasis.

The progressive malfunctioning of the arterial blood vessels is due to the confluence of a variety of hemodynamic [3] and chemico-physical factors [262]. The development of atherosclerosis is highly sensitive to the presence of several systemic risk factors and comorbidities: high cholesterol, diabetes and high blood pressure, are only few examples. Even though, the clinical manifestations of the disease - heart attack, sudden coronary death and angina pectoris - appear to be focal, resulting from the accumulation of lipid molecules and inflammatory cells at specific locations within the wall of the coronary arteries (a sketch of such a progression is reported in Fig.(2.2.1)). Several studies have shown, both in vitro and in vivo, that the seed of atherosclerosis is mostly associated within regions of disturbed blood flow, in particular where the local Endothelial Shear Stress (ESS) assumes low values (< 0.5 Pa) or presents alternating directions [35]. Such a character induces a specific interest in the assessment of endothelial function as valuable and necessary research tool in applying vascular biology research to clinical practice through a deeper numerical analysis of ESS. A detailed description in this direction will be given.

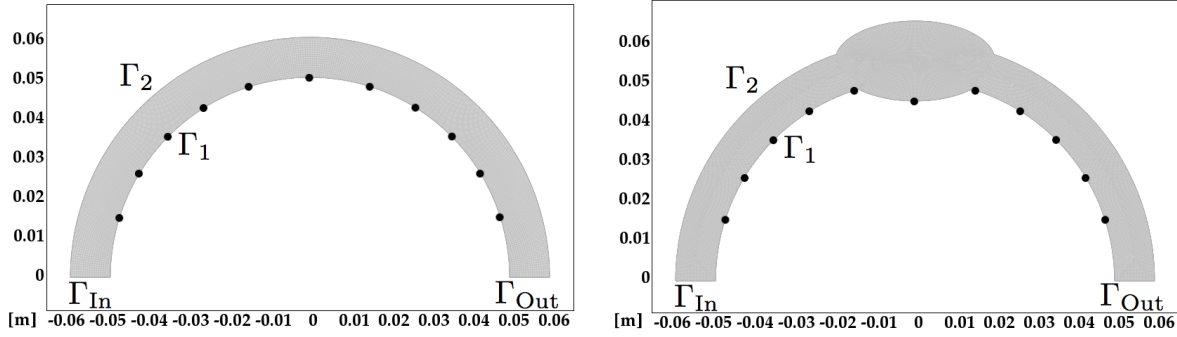


Figure 2.2.2: Semi-coronal flat simulation domain (units in meters) for a regular (**LEFT**) and aneurysm-like (**RIGHT**) domains. The fluid flows within the domain with rigid boundaries (Γ_1 , Γ_2) from left (Γ_{In}) to right (Γ_{Out}). Bullets denote the points at which the velocity field is analyzed below in terms of WSS map.

2.3 Shear Stress on Vessel Walls

2.3.1 Basic Fluid Dynamics Definitions

The Endothelial Shear Stress (ESS) is defined as the tangential stress stemming from the friction of the flowing blood on the endothelial surface of arterial walls. Considering two dimensional incompressible Navier-Stokes equations on a semi-coronal flat domain (see Fig. (2.2.2)), the following equations of motion can be derived:

$$\rho \frac{D\mathbf{u}}{dt} = -\nabla p + \mu \nabla^2 \mathbf{u}, \quad \text{div}(\mathbf{u}) = 0 \quad (2.3.1)$$

where ρ is the density of the fluid, p the pressure, μ the (constant) dynamic viscosity, ∇ the vector differential operator, and

$$\frac{D}{dt} = \partial_t + \mathbf{u} \cdot \nabla \quad (2.3.2)$$

denotes the Lagrangian derivative along the fluid flow. Indicating u and v as the Cartesian components of the velocity field, $\mathbf{u} = (u, v)$, we have $\partial_x u = -\partial_y v$ due to the incompressibility of the fluid and we define the shear tensor as $S_{ij} = (\partial_i u_j + \partial_j u_i)/2$, namely

$$S_{ij} = \begin{pmatrix} \partial_x u & \frac{1}{2} (\partial_x v + \partial_y u) \\ \frac{1}{2} (\partial_x v + \partial_y u) & \partial_y v \end{pmatrix}. \quad (2.3.3)$$

In particular, we are interested in the scalar invariants of the shear tensor along the radial and tangential directions \mathbf{n} and τ . The first one, i.e. its trace $I_1 = \text{Tr}(S_{ij}) = 0$, is trivially zero due to the fluid incompressibility, while the second one, i.e. the trace of its square, $I_2 = \frac{1}{2} \text{Tr}(S_{ij})^2 = -\det S_{ij}$ contains important information on the local flow topology and assumes the following explicit expression

$$S_{\tau n} = (-\partial_x u + \partial_y v) \frac{xy}{r^2} + \frac{(\partial_y u + \partial_x v)}{2} \frac{(x^2 - y^2)}{r^2}.$$

The following description focuses our analysis on the stress tensor σ , measured in Pa , and defined by the constitutive relation

$$\sigma = \mu \mathbf{S}, \quad (2.3.4)$$

where the fluid is regarded as Newtonian ($\mu = 3 \cdot 10^{-3} Pa \cdot s$) with $\rho = 10^3 Kg/m^3$ ($\nu = \mu/\rho = 3 \cdot 10^{-6} m^2/s$), a plausible approximation for large arteries.

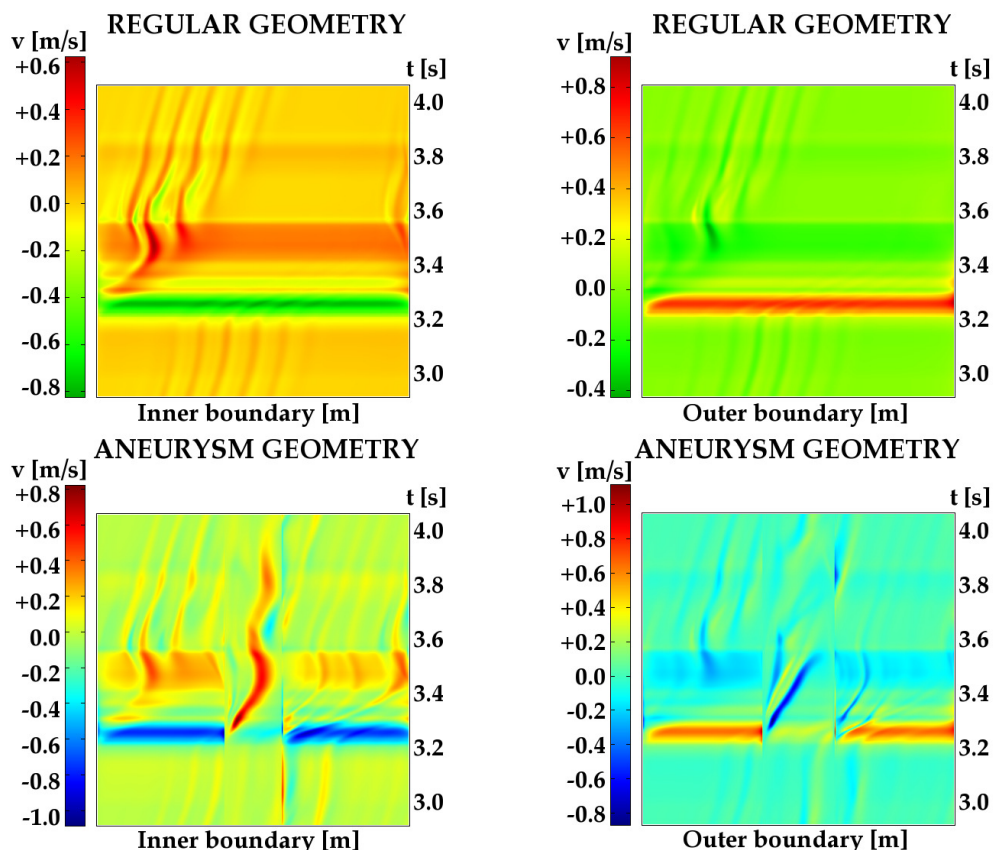


Figure 2.3.1: Space-time patterns of the inner and outer WSS, 10^{-3} s^{-1} , on the regular (TOP) and aneurysm-like geometry (BOTTOM). The aneurysm case shows strong inhomogeneities with respect to the regular case.

2.3.2 The LESS Criterion

A first qualitative picture indicates that under Low ESS (LESS) conditions ($< 0.5 \text{ Pa}$), endothelial cells present enhanced exposure to intramural penetration of micro and nanoscale biological bodies, such as B-cells and lipid molecules. Their subsequent accumulation in the underlying tissues may initiate apoptotic phenomena [30, 35, 248, 262, 285, 290].

A fully quantitative assessment of the actual risk map for each individual is beyond the current modeling capabilities, mostly on account of the extreme complexity of the coupling between biochemical mechanisms with their surrounding hemodynamic environment. Since geometry plays a driving role in establishing the local ESS patterns in human arteries, a growing body of computer simulations on relatively short biological time scales aimed at representing the global and local geometry in as much detail as affordable on present-day most powerful supercomputers, has been performed in the last decade [267, 112, 186, 10, 190, 102, 20]. Such leading-edge computational work is of primary importance to analyze the actual space-time configurations of hemodynamic flows to the highest possible degree of accuracy. A further innovative step in this direction is nowadays being realized throughout GPU's clusters [24, 85], which are able to significantly scale the computational time and effort opening new areas previously not accessible.

Even in relatively simple geometries, however, the ESS patterns can exhibit a very rich space-time structure (see Fig.(2.3.1)) [314], from which it is hard to extract synthetic indicators of clinical risk [273, 182]. At present, the most credited such indicators are the LESS, as defined above, and the Oscillatory

Shear Index (OSI), a measure of time-variability of the Wall Shear Stress (WSS) signal [35]:

$$\text{OSI} = \frac{\int_0^T |\gamma_w^*| dt}{\int_0^T |\gamma_w| dt}. \quad (2.3.5)$$

Here γ_w is the wall shear rate (WSR), and γ_w^* is the part of the WSR waveform in which the shear rate is in the opposite direction of the time averaged WSR.

In this work, a new set of indicators has been introduced, namely Three-Band-Diagrams (TBD), which provide a more accurate, and still handy, access to the additional information contained in the dynamic structure of the WSS signal as a function of the physiological risk threshold. Through such indicators, described in the following sections, it's intended to give a more quantitative and visually friendly assessment of the risk sensitivity to individual fluctuations of the physiological risk thresholds.

2.4 Three-Band Decomposition Analysis

In this section the TBD analysis is described considering a numerical analysis of incompressible fluid flow both in regular-physiological and irregular-pathological geometries, mimicking an aneurism-like endothelial deformation as described before.

It is commonly agreed [100] that “risky/unhealthy” WSS signals are characterized by a mean value, $\overline{\text{WSS}}$, below a given critical threshold and relatively high values of the OSI. Clearly, the specification of the solely pair $(\overline{\text{WSS}}, \text{OSI})$ cannot provide full information on the dynamical structure of the signal, so that different signals with different risk content may map into the same values of this pair. The information on the extra-risk not contained in the pair $(\overline{\text{WSS}}, \text{OSI})$ might be indeed of some value. For instance, short intervals carrying a negative signal, might not bear much physiological relevance (physiological damage is often associated with sufficient persistence of the WSS below the critical threshold) and should therefore be discounted from the OSI value.

Part of this information shall be regained by the three-band decomposition analysis here introduced: given a generic signed (both positive and negative) signal $S_{(\min)} \leq S(t) \leq S_{(\max)}$ and a control threshold $\sigma \geq 0$, we define the following triplet of “daughter” functions (three-band decomposition):

$$\begin{cases} S^+(t) \equiv S(t)H^+(\sigma) \\ S^-(t) \equiv S(t)H^-(\sigma) \\ S^0(t) \equiv S(t)H^0(\sigma) \end{cases} \quad (2.4.1)$$

where $H(S - \sigma)$ is the standard Heaviside step function by which we define

$$\begin{cases} H^-(\sigma) = 1, & \text{if } S < -\sigma \\ H^0(\sigma) = 1, & \text{if } -\sigma \leq S \leq \sigma \\ H^+(\sigma) = 1, & \text{if } S > \sigma \end{cases} \quad (2.4.2)$$

where $+, 0, -$ label the three bands. The support of these three functions, in the time interval $\Omega = [0, T]$,

is constituted by three series of discrete time-intervals, reading:

$$\begin{cases} \Omega^- = \cup_{j=1}^{N^-} [t_{2j}^-, t_{2j-1}^-] \\ \Omega^0 = \cup_{j=0}^{N^0} [t_{2j+1}^0, t_{2j}^0] \\ \Omega^+ = \cup_{j=1}^{N^+} [t_{2j}^+, t_{2j-1}^+] \end{cases} \quad (2.4.3)$$

Clearly $\cup_{s=0,\pm} \Omega^s = \Omega$, while the measures of the residency times of the signal in the corresponding bands are in general:

$$\begin{cases} T^- = \sum_{j=1}^{N^-} (t_{2j}^- - t_{2j-1}^-) \equiv \sum_{j=1}^{N^-} \Delta t_j^- \\ T^0 = \sum_{j=0}^{N^0} (t_{2j+1}^0 - t_{2j}^0) \equiv \sum_{j=0}^{N^0} \Delta t_j^0 \\ T^+ = \sum_{j=1}^{N^+} (t_{2j}^+ - t_{2j-1}^+) \equiv \sum_{j=1}^{N^+} \Delta t_j^+ \end{cases} \quad (2.4.4)$$

A schematic representation of such a decomposition is reported in Fig.(2.4.1) in order to visually identify the described subintervals.

The idea of the three-band analysis is to inspect the number of intervals and their individual extent $\Delta t_j^s = (t_{2j}^s - t_{2j-1}^s)$, as a function of the running threshold σ . More specifically, any generic signal $S(t)$ induces a partition of the time interval $\Omega = [0, T]$ into three mutually disjoint sets Ω^s , each consisting of N^s time intervals. The family of sets generated by letting the threshold parameter σ scan the entire range defines an ensemble of N^s trajectories, $\Delta t_j^s(\sigma)$ and a corresponding numerosity histogram, $N^s(\sigma)$.

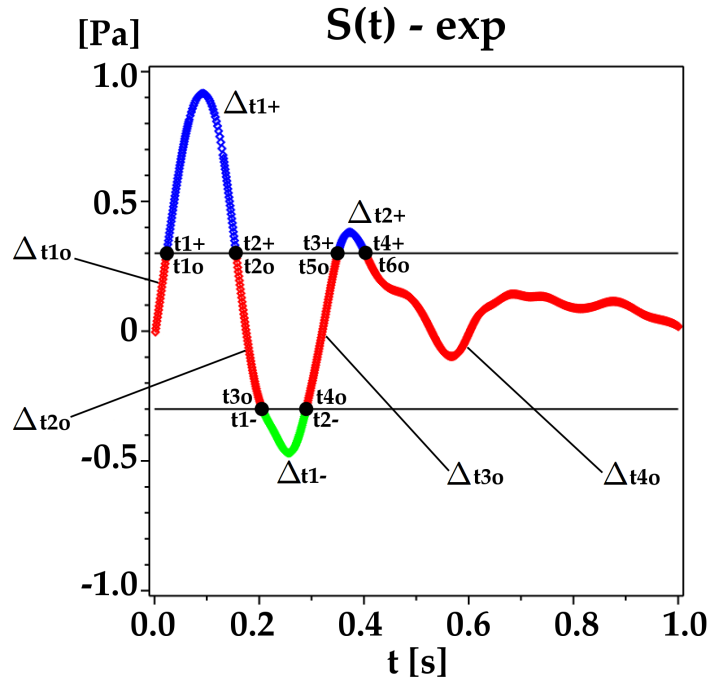


Figure 2.4.1: Three-band decomposition analysis applied to the flow rate signal measured by the time-of-flight probe, and reconstructed using the color and spectral Doppler methods [25]. Following the general formulation described in eq. (2.4.4), the color code is related to T^- (green), T^0 (red) and T^+ (blue) intervals and the identification of the time sequence Ω^s associated with the three bands, $s = -, 0, +$ and the corresponding residency times Δt_j^s , are explicitly shown.

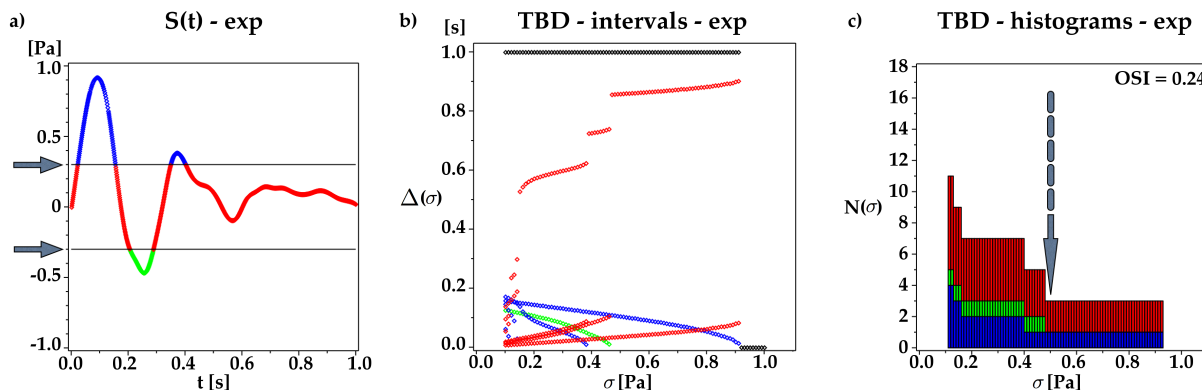


Figure 2.4.2: The three-banded (A) WSS signal from a healthy volunteer. The corresponding trajectories (B) and histogram (C) show a neat similarity with the healthy signals. Note that here the OSI index as well as the TBD analysis confirms the healthy nature of the signal.

2.5 A New Risk Indicator

The best way to extract synthetic indicators of clinical risk out of the rich and heterogeneous space-time structure of the wall shear stress (see Fig.(2.3.1)), is still an open question. For the sake of simplicity, following the standard risk indicators abbreviations \overline{WSS} and OSI, we denote the new set of trajectories and the corresponding histogram introduced as the *three-band diagram* (TBD) of the signal. Formally, TBD's are a family of *multi-functionals* mapping the signal $WSS(t)$ into a set of N intervals, for each value of the threshold σ :

$$\{WSS(t); \sigma\} \rightarrow \{\Delta t_j^s; N^s\}, \quad s = -, 0, +$$

Since t_j^\pm are the zeroes of the shifted signal, the sum $N = \sum_s N^s$ is generally much smaller than the number \mathcal{N} of discrete time samples of the discrete signal, $WSS_i \equiv WSS(t_i)$, $i = 1, \mathcal{N}$. In other words, while the standard indicators \overline{WSS} and OSI correspond to a strong $\mathcal{N} : 2$ compression of the signal, the TBD representation corresponds to a milder $\mathcal{N} : N$ compression. A basic advantage of scanning the structure of the signal with a running threshold is that the risk indicators become available for any value of the threshold, thereby conveying an idea of the risk sensitivity to fluctuations of the physiological threshold, as they may occur from individual to individual.

A key example for testing the new risk indicator is reported in Fig.(2.5.1), where a healthy (denoted by H) and unhealthy (denoted by U) simulated signals (namely the circular corona and the aneurysm-like geometry), are reported comparing the corresponding answers from both OSI and TBD analysis. As it is apparent from the original signals (H1, U1), the aneurysm signal is much flatter. The contrast between the two situations is further highlighted by the corresponding TBD's. In particular, for the case of the regular semi-corona, the TBD indicators point to a low-risk situation all along the spatial extension of the corona, while the aneurysm-like geometry is found to exhibit a highly heterogeneous, low-WSS distribution, eventually with sizable contrasts between nearby regions of the wall. In contrast, the corresponding OSI values are still high implying for both signals a risky situation. However, only one of them (unhealthy) corresponds to a risky behavior.

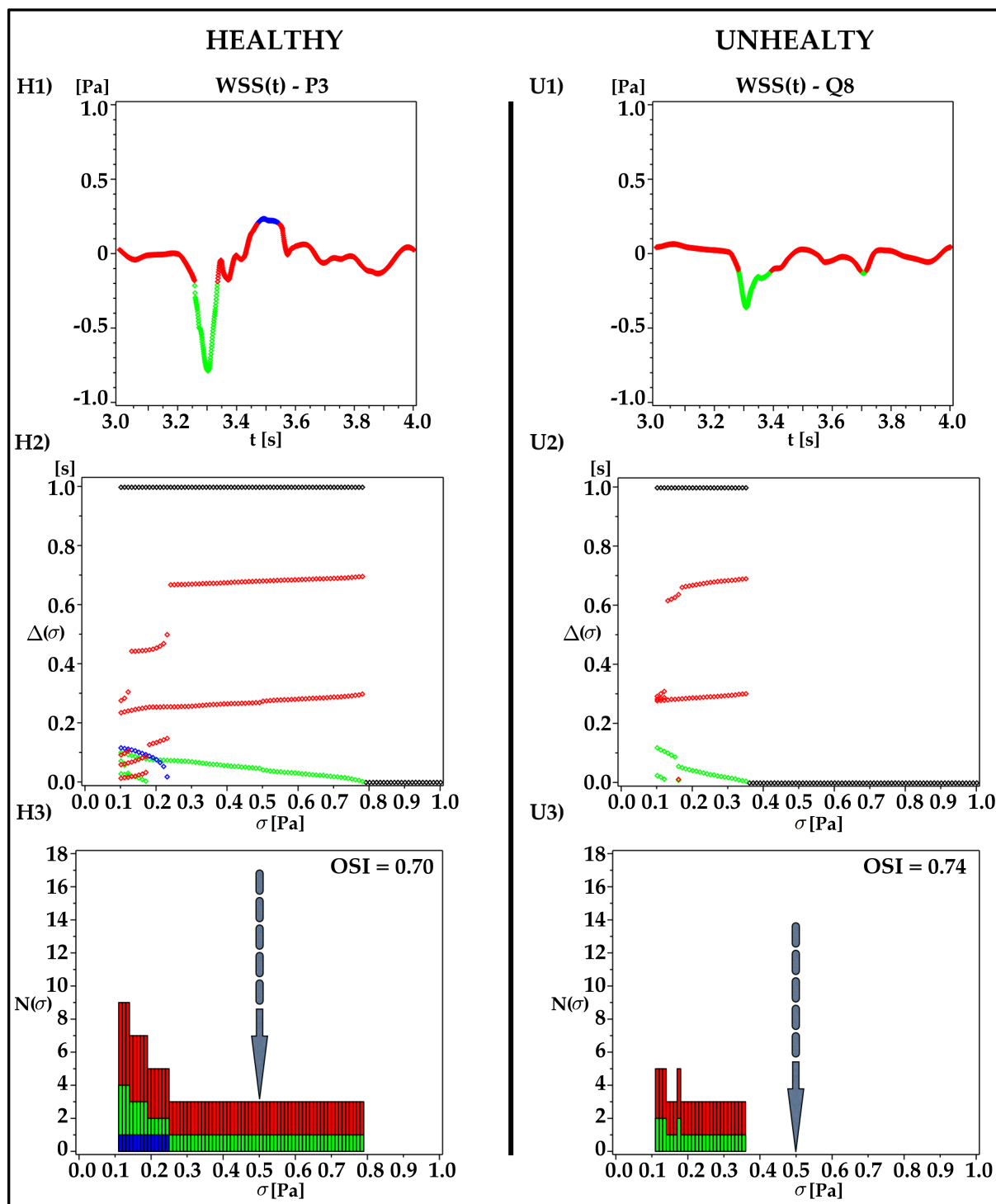


Figure 2.5.1: Three-band (TOP), trajectory (MIDDLE), and histogram (BOTTOM) for a healthy (left) and unhealthy (right) signal. The healthy signal, at point P3 in the circular corona, carries over the physiological threshold, while the unhealthy one, point Q8 does not. To be noted that the OSI index is very similar and pretty high in both cases, thus failing to highlight the absence of risk associated with the healthy signal.

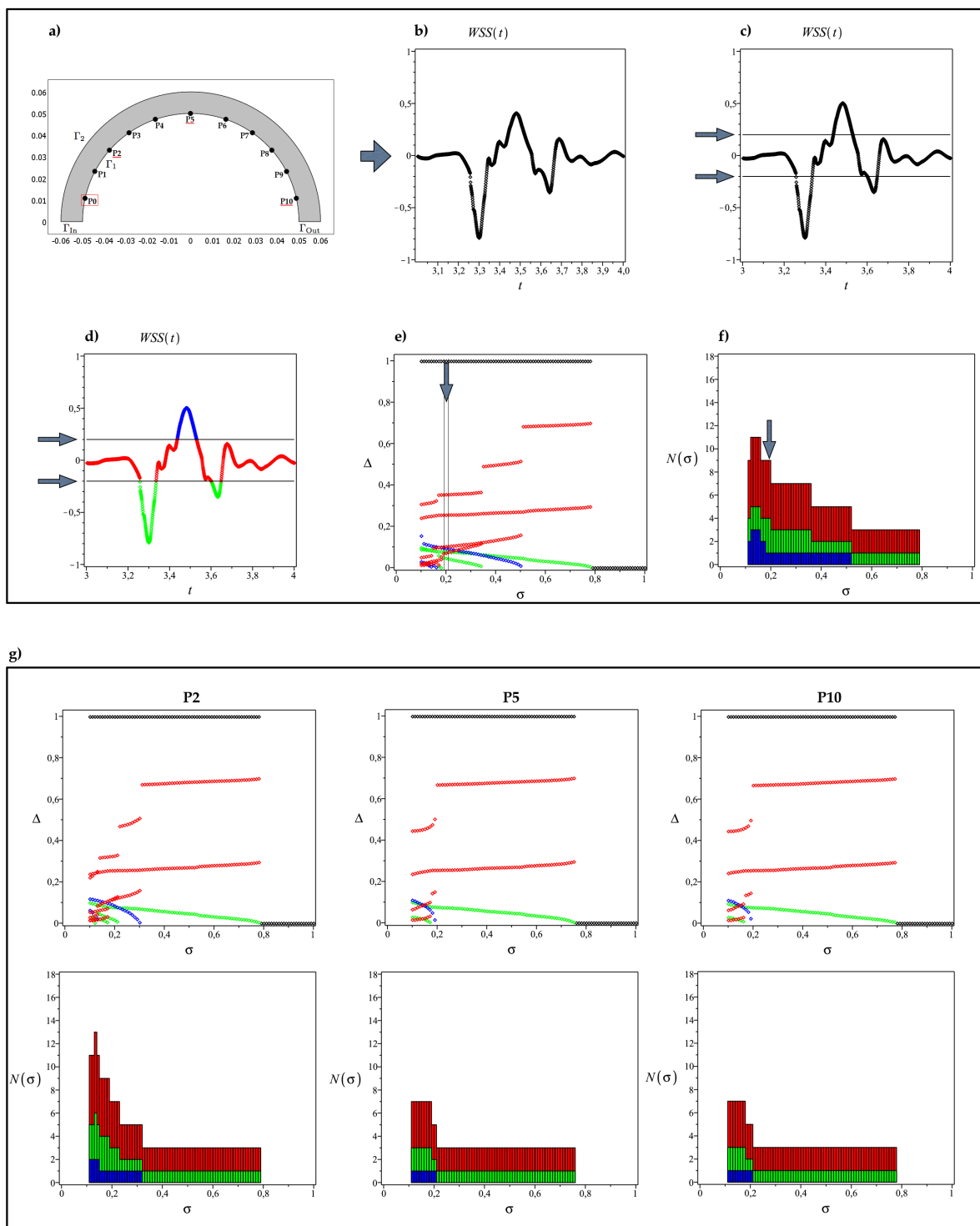


Figure 2.5.2: WSS signal in time, three-bands trajectories and histograms for the healthy case extracted from the position P0 (a-f). Extended TBD analysis at different locations (P2, P5, P10) along the inner boundary. It can be noted that in the healthy case all the TBD distributions on the inner boundary extend above the risky level of $0.5 Pa$.

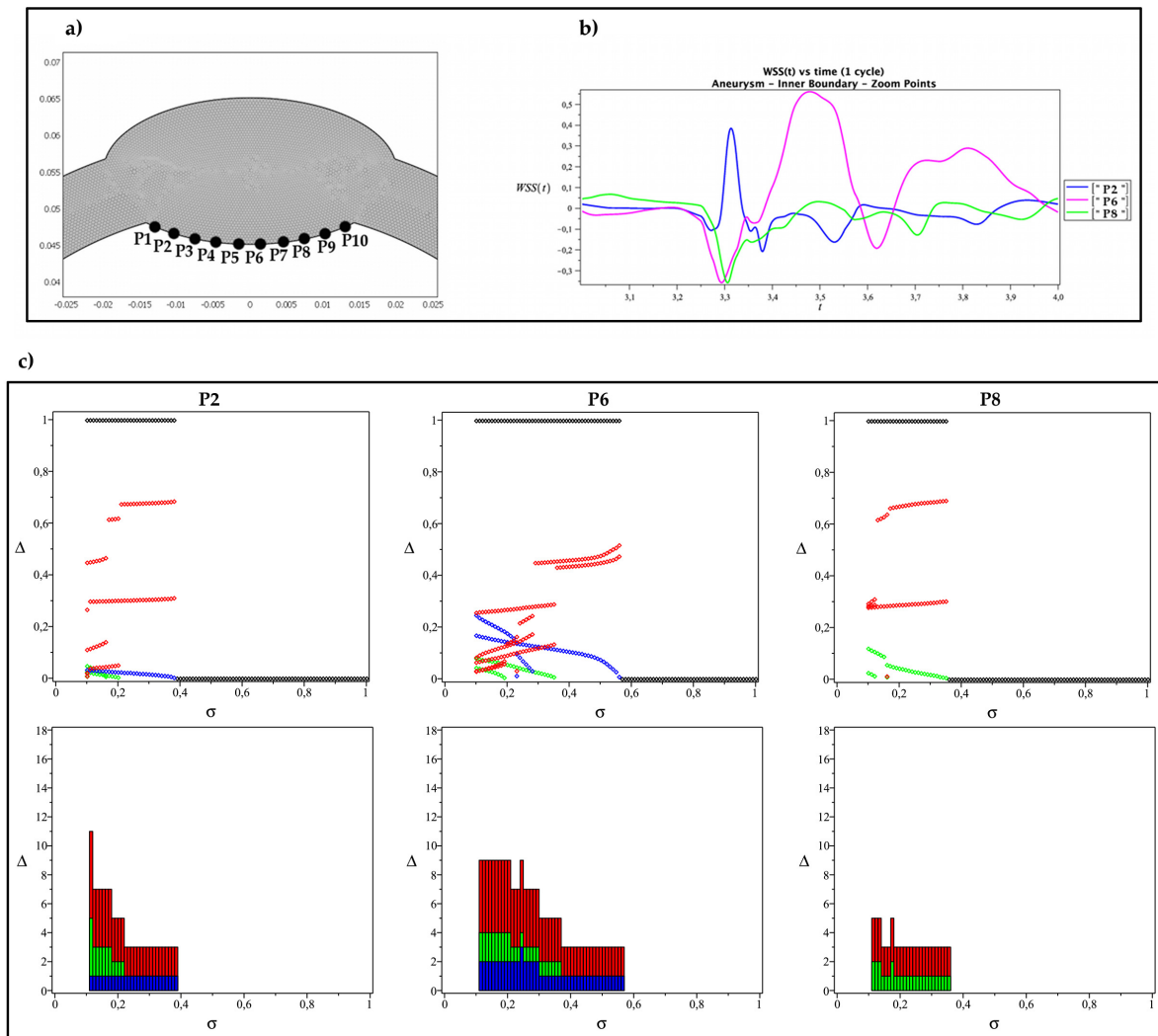


Figure 2.5.3: (a,b) WSS signals comparison between three different locations inside the internal aneurism boundary P2, P6, P8 and (c) corresponding three-bands trajectories and histograms.

TBD Applications

Several different analysis have been explored both in space and time in order to test the new TBD indicator, and the remarkable outcome can be stated as follows: two signals with essentially the same OSI value, may correspond to “healthy” and “unhealthy” situations.

As a further application, the TBD analysis has been applied to an experimental WSS signal (Fig.2.4.2 and suitably interpolated for our analysis), and found to yield the same conclusions resulting from the simulations, namely that healthy situations associate with a substantial homogeneous permanence of the WSS signal above the physiological risk threshold.

As compared to standard \overline{WSS} and OSI, TBD's provide a handy access to additional risk information contained in the dynamic structure of the signal as a function of the physiological risk threshold. This allows a quick visual assessment of the risk sensitivity to individual fluctuations of the physiological risk thresholds. Also to be noted, the TBD described in this work are as easily computed as the \overline{WSS} and OSI, and could therefore be automatized in connection with the analysis of any signal $S(t)$, be it of

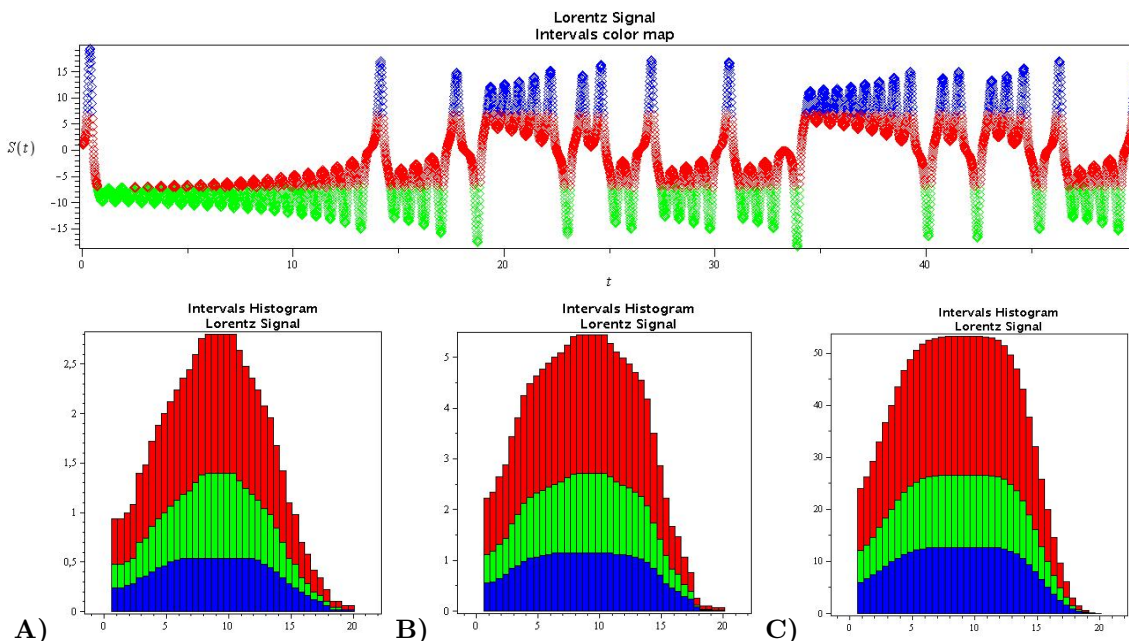


Figure 2.5.4: The three-banded applied to the Lorenz system as representative example of chaotic system. Time evolution of the signal (**TOP**) and corresponding numerosity diagram (**BOTTOM**). Shifted gaussian distributions arise depending on the time of application of the TBD analysis: **(A)** 50 time instants, **(B)** 100 time instants and **(C)** 200 time instants

experimental or synthetic nature.

We also built a three-dimensional version of the proposed $\Delta(\sigma)$ histograms, having as third dimension the spatial curvilinear variable of the boundary. In this case, however, the visualization is no more handily as the one shown in the point-wise cases in Fig.2.5.2 and 2.5.3.

Finally, applications of TBD analysis to chaotic-defined signals has been carried out. As shown in Fig.2.5.4, it can be noted an emerging regularity from chaos. In particular, analyzing the Lorenz system in the chaotic regime, shifted gaussian distributions arise depending on the time of observation. On this basis, TBD application, from a theoretical point of view, are just at the beginning. However, in the following section, specific feasible applications related with the cardiocirculatory system, in general, and with the heart, in particular, will be prospected.

2.6 Limitations and Future Perspectives

The investigation of space-time patterns of Wall Shear Stress (WSS) resulting from the numerical simulation of pulsating hemodynamic flows proposed in this work has still a major range of applications in three-dimensional realistic geometries. Several examples can be found in literature where both numerical and experimental signals are analyzed in terms of \overline{WSS} and OSI.

Systemic & Fluid-Structure Interaction Applications

With the purpose of extracting synthetic indicators of clinical risk from the space-time structure of wall shear stress, a new set of numerical and experimental analyses are required considering the more general framework of excitable deformable media with fluid-structure interaction. In fact, the mathematical tools here introduced, are not limited to hemodynamic studies, but readily extend to a broad class of

applications dealing with risk-assessment analysis.

- Soft tissue lesions induced by impulsive stresses or fatigue: flow-field data, flow streamlines, two-dimensional velocity profiles and mean wall shear stress as reported by Hoskins and Hardmant [140] within a carotid bifurcation with a moderate stenosis, or by Frydrychowicz et. al. [100] within an abdominal aortic aneurysm in association with incidence of proatherosclerotic low WSS and high OSI.
- Arrhythmic events due to non-physiological fluid dynamics and tissue heterogeneities.

In order to further motivate the necessary application of new risk indicators to the cardiovascular system behavior, it's important to note the occurrence of arrhythmic phenomena also in vessels tissues, i.e. pulmonary veins (PVs) [34, 40, 119, 239]. Still nowadays, after a large number of studies (at both the basic and clinical science levels) devoted to deciphering the mechanisms of PV arrhythmogenicity, atrial fibrillation therapy suffers from a limited mechanistic understanding of PV arrhythmogenicity, with the fact that electrophysiological properties of PVs may make them a site for reentry. Recent computational studies have addressed such a problem exploring the role of PV reentrant activity critically depending on vein size and coupling properties [40]. Such an approach, even tacking into account tissue anisotropy and heterogeneity, is still lacking of several coupled mechanisms connected with fluid-structure interaction phenomena. In fact, both tissue deformation and wall shear stress, would be of great importance in dealing with and understanding the complex (or chaotic) dynamics arising during cardiac arrhythmia.

Chapter 3

Anatomy and Physiology of the Heart

The cardiac muscle is part of the cardiovascular system and actively takes part to its main functions. In the following, a deserved description of the different aspects of heart tissue will be pursued.

3.1 The Heart

3.1.1 Cardiac Anatomy & Functions

The heart is one of the most vital muscular organs in the human body [263]. It is shaped like an inverted pyramid and is contained in the center of the rib cage. Located between the lungs and surrounding the diaphragm, it is separated by oesophagus and aorta from the vertebral column and it is protected by sternum and rib cartilages (see Fig.(3.0.1)). A double-walled sac, *pericardium*, with a superficial part, *fibrous pericardium*, envelops, lines and protects the whole contractile mass, *heart*, anchoring its surrounding structures, preventing excessive dilation and limiting ventricular filling. The pericardial cavity is filled with $10 \div 50 \text{ ml}$ of fluid [19], the *pericardial fluid*; this reduces the friction caused by the beating and moving of the heart.

The functional structure of the heart can be regarded as two parallel synchronized pumps separated

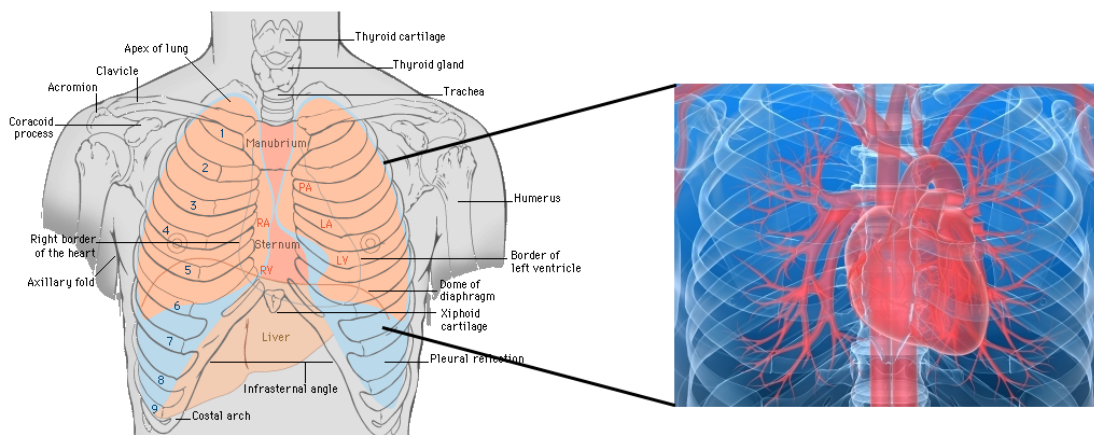


Figure 3.0.1: Gross anatomy of the heart, adapted from [124]: position of the cardiac muscle in the center of the rib.

by a *septum*: the right pair collects deoxygenated blood and perfuses lungs, while the left pair receives oxygenated blood and perfuses the rest of the body. Four communicating chambers, left (LA) and right (RA) atrium, collect blood from veins, and left (LV) and right (RV) ventricle, drive blood into systemic and pulmonary veins. The different contractile functions of the four chambers motivates the differences in their tissue properties, which assume a durable and thicker wall structure for ventricles than for atria.

Four valves ensure the selective and unidirectional flow between the atria and the corresponding ventricles: *mitral* and *tricuspid* valves control the atrioventricular (AV) communication, while *aortic* and *pulmonary* valves, semilunar (SL), regulate the outflow in the arteries leaving the heart. An active muscular structure, *papillary muscles*, together with chordae tendons synchronously act with fluid pressure as an external trigger in order to regulate the correct blood flow between the chambers. A particular view of these structures is shown in Fig.(3.1.2). The heart sounds that can be auscultated, commonly referred to as "lub-dub", are actually the sounds of the valves flapping closed. The AV valves close first and then the semilunar valves, during an heart cycle.

Cardiac wall tissue is composed of three layers: *epicardium*, the outer layer, *myocardium*, the middle

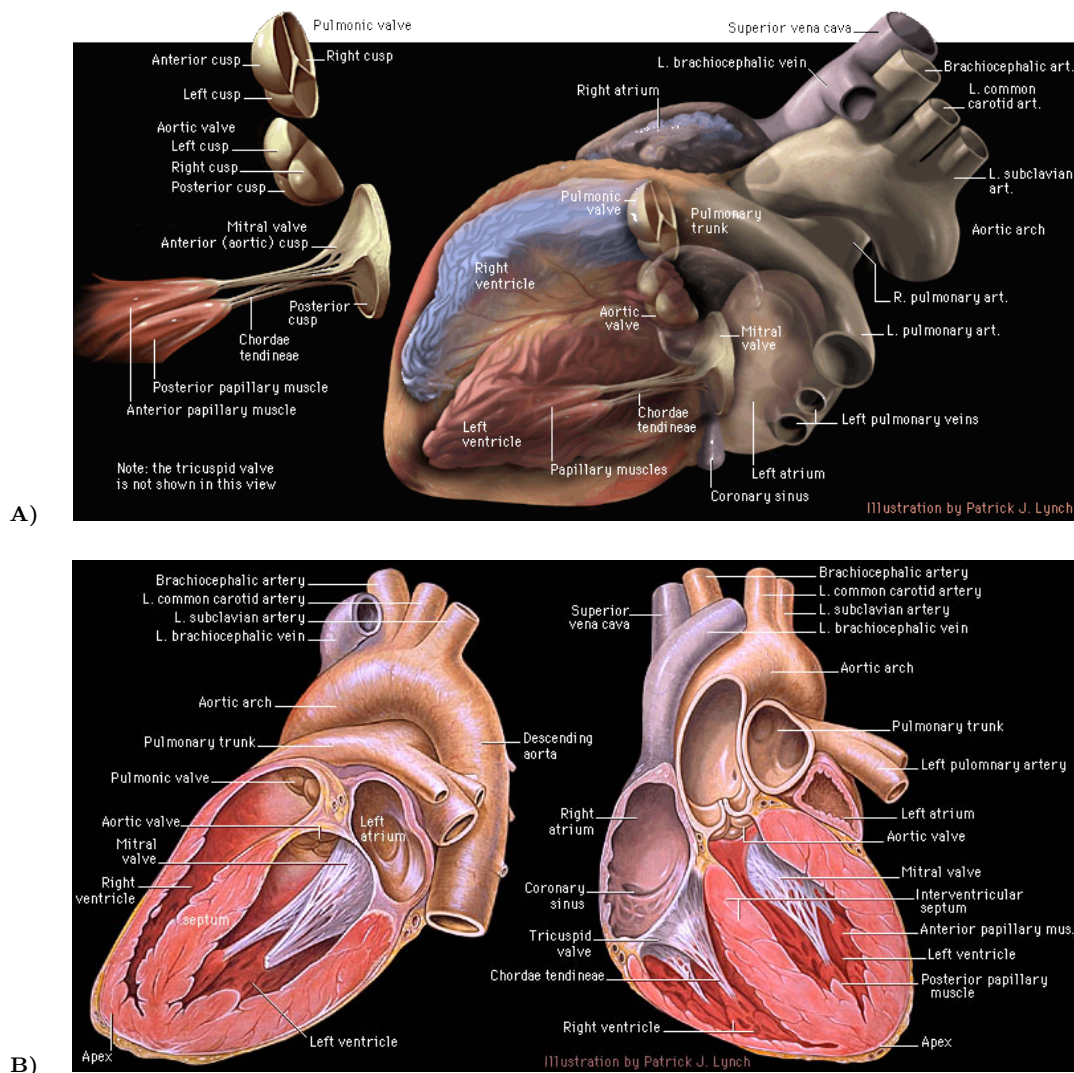


Figure 3.1.1: Gross anatomy of the heart [269]: (A) three-dimensional view of the internal structures, (B) sectional view from both left and right side.

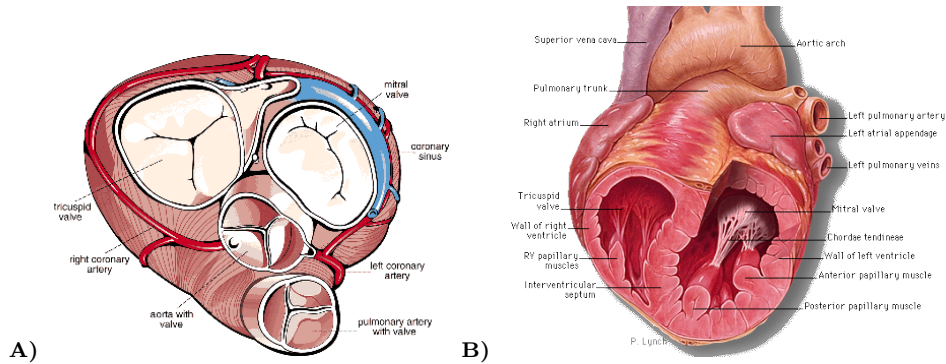


Figure 3.1.2: (A) Top-down sectional view of cardiac valves. (B) Low-sectional view of the internal structures of papillary muscles and chordae tendons[269].

layer, and *endocardium* (see Fig.(3.1.3)), the inner layer [73]. While endocardium is directly in contact with the blood that the heart pumps, myocardium is characterized by specialized muscle cells, *cardiomyocytes*, presenting lower contractibility and higher resistance to fatigue than the others [98].

The complexity of this organ is moreover enhanced by looking at the three-dimensional geometry of its microscopic structures. In fact, different components of the heart present structures that are fractal in nature: i.e. the network of blood vessels reported in Fig.(3.1.4)(A-B), has even led to the discovery of a power law in the vessel distribution [181]. Other examples of fractal geometry are the specialized cardiac conduction system, made up of Purkinje fibers (see Fig.(3.1.4)(C)) and described in the following.

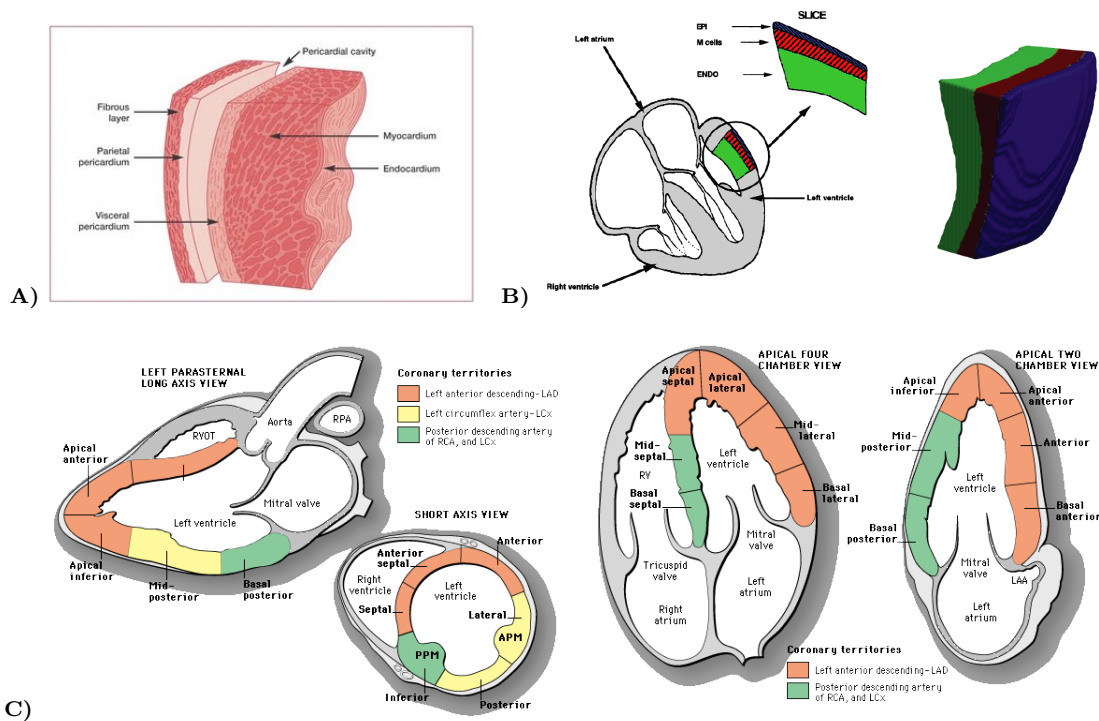


Figure 3.1.3: A) Pericardial layers and myocardial wall differentiation: fibrous layer, parietal pericardium and pericardial cavity; visceral pericardium, myocardium and endocardium. B) Reconstructed computer model of the myocardial wall layer [73]. C) Sectional and lateral views of left ventricle wall tissue composition. [84, 269] Color codes are referred to the different layers.

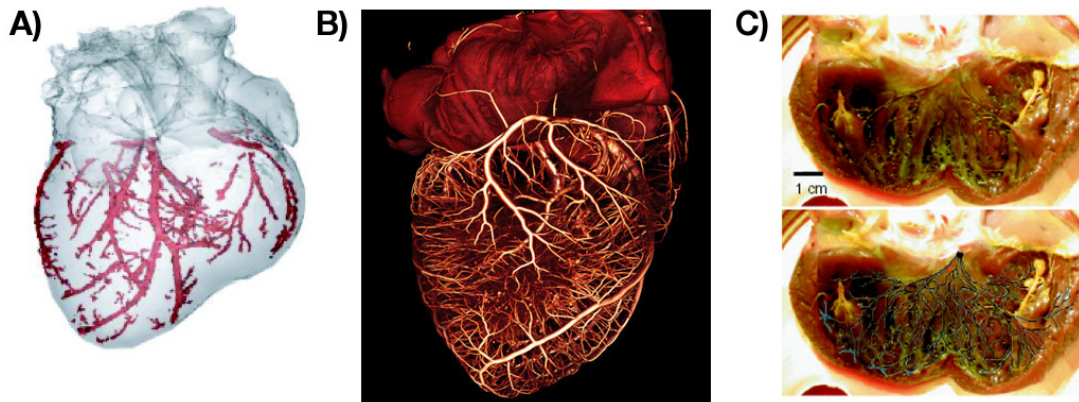


Figure 3.1.4: Fractal structures in the heart. (A) Blood vessels Reconstruction from MRI imaging [253]. (B) Whole heart micro-CT reconstruction [181]. (C) Purkinje system in right ventricular canine tissue (top) highlighted by Lugol's solution and (bottom) digitized to form a network [41].

Of course, the “fractal” geometric properties of biological structures, unlike a true mathematical fractal, terminate at a finite size of the order of a single cell.

Blood Flow Cycle

In physiological conditions the same amount of blood pumped from the right ventricle into the lungs is also pumped from the left ventricle out into the body. A concise description of the cycle is given.

1. Starting with the superior and inferior vena cava blood flows into the right atrium. (the force put on the atria to allow optimal atrial filling is referred to as *preload*).
2. After the right atrium is full of blood the tricuspid valve opens, allowing blood to flow freely into the right ventricle. The right atrium then contracts filling the ventricle even more (Starling's law [256]).
3. The right ventricle then contracts while the pulmonary semilunar valve is open and blood enters the pulmonary artery (the only non-oxygenated artery).
4. Blood flows from the pulmonary artery into the lungs. Blood fills the pulmonary capillaries which surround the alveoli of the lungs. After the blood becomes oxygenated it leaves the heart through the pulmonary veins (the only oxygenated veins).
5. The pulmonary vein dumps its volume into the left atrium using the residual pressure put on it by the right ventricle and pulmonary system (*preload*).
6. The left atrium sends blood through an open bicuspid/mitral valve similarly to the right side of the heart.
7. The oxygenated blood enters the left ventricle, ready to be sent to the rest of the body. The left ventricle then contracts and the blood passes through the aortic semilunar valve into the aorta (the force that the ventricles have to contract against is known as *afterload*).
8. After ventricular systole the aortic semilunar valve flaps closed and the blood passes over the aortic arch. Blood that doesn't make it over the arch falls back onto the closed aortic semilunar valve and

into the coronary arteries. The right and left coronary arteries are the first exits attached to the ascending aorta. They are used to perfuse the heart.

9. Most of the blood ejected from the left ventricle passes over the aortic arch and enters into the arteries of the body. From the arteries the blood enters into arterioles and then the systemic capillaries. The blood then needs to head back towards the lungs. The blood enters into venules and then veins. All the systemic veins eventually lead back to the vena cava.

3.1.2 Biological Bases of Cardiac Cells

Muscles

Muscles are effectors of mobility. From a mechanical point of view, they can be considered as structural elements capable of exerting force in contraction or flexion to respond to external and internal sensory information. The human body comprises three types of muscle:

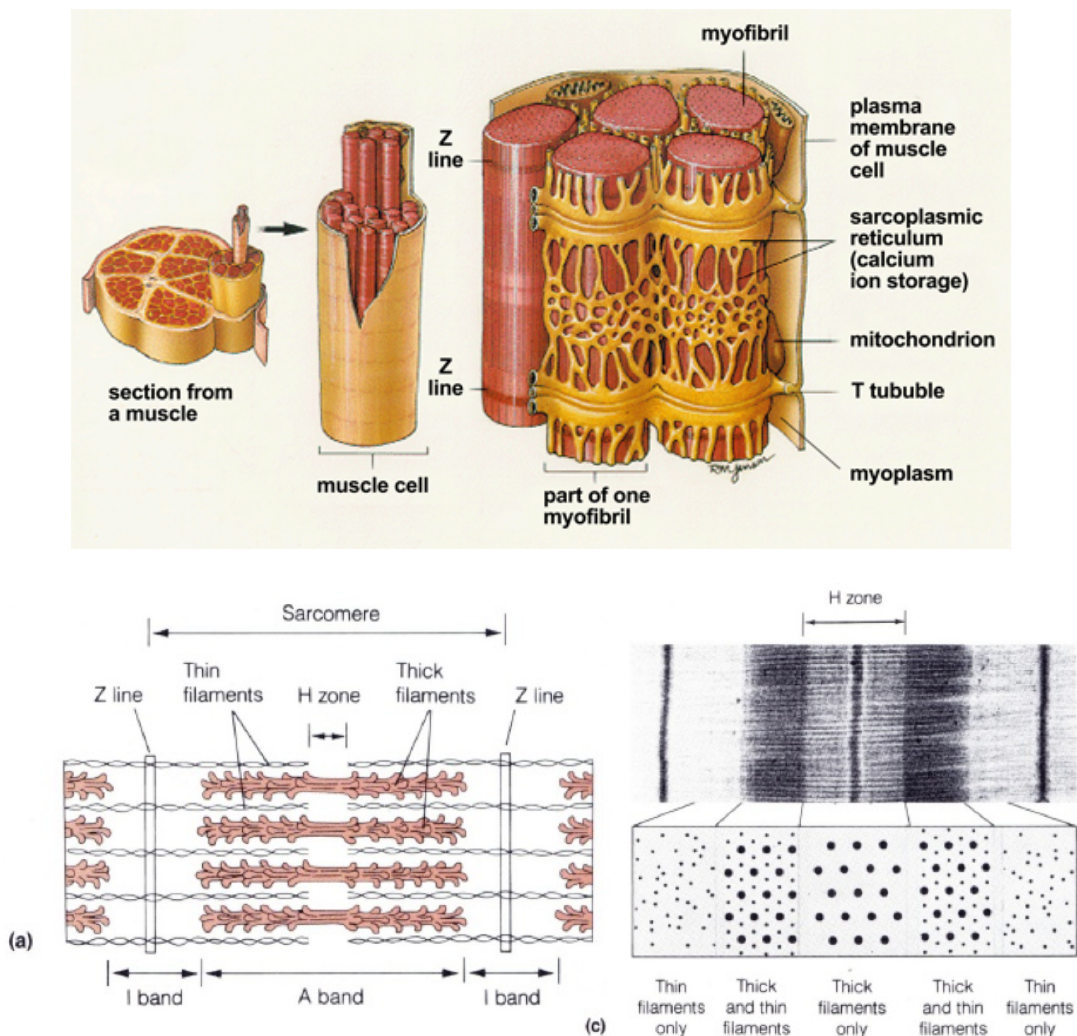


Figure 3.1.5: Multiscale muscular architecture. (TOP) Fiber sections, from muscle to myofibril. (BOTTOM) Sarcomere protein structure, protein filaments and connections [183].

- *smooth* muscle: surrounds internal organs, provides sustained slow contractions, which are not under voluntary control (blood vessels, intestines, and gallbladder).
- *striated* or skeletal muscle: about 40% of body weight (arms, legs, eyelids), makes possible rapid voluntary motions.
- *cardiac* muscle: specialized form of striated muscle evolved for the repetitive, rapid, involuntary contraction.

In Fig.(3.1.5) the multi-scale levels of organization in striated muscle and a zoom of the specific structure of a muscle cell are shown.

Cardiac Tissue

The cardiac muscle is usually termed a *syncytium*. It consists of densely packed cells, *cardiac myocytes*, organized in fiber-like arrays, *cardiac fibers* [254]. The single myocyte is roughly cylindrical in shape with typical dimensions of $30 \div 100 \mu\text{m}$ in length and $8 \div 20 \mu\text{m}$ in diameter. The boundary of each cell is defined through its double layered phospholipidic membrane, fundamental for the maintenance of its intracellular state. Even though, the full three-dimensional geometry, shown in Fig.(3.1.6), is more structured and complicated, due to the multiple columnar end processes [141].

Cardiac cells are immersed in the *interstitial* fluid and are generally separated with exception of the limited regions where two adjacent membranes are melted, the so called *gap junctions* (Fig.(3.1.6)). Such structures allow a single cell to be connected to as many as ten other cells, thus resulting into cardiac fibers. An important consequent property, related to these end processes, is the structural electrical anisotropy typical of cardiac cells and fibers: due to the low conductance of the membrane and the regional organization of the connexines in proximity to the ends of the cell, the ionic currents encounter an easier path in the longitudinal direction than orthogonal to the main axis of the cell. Therefore, the resulting mean electrical conductivity is much higher in the direction of the fiber [52].

Throughout the whole heart, the fibers usually form discrete layers or sheets radially oriented with respect to the ventricular surface (Fig.(3.1.7)). The rotational angle from epicardium to endocardium can reach 180° . Obviously, this is not generally true, in fact, in the subepicardial region this angle is $\sim 90^\circ$, in order to be tangent to the epicardial surface itself [205, 258], while into the ventricular wall it is $\sim 120^\circ$ with parallel sheets to both epicardium and endocardium surfaces. Such a complex structure induces a rotational propagation direction to the ionic current, as evidenced in the following.

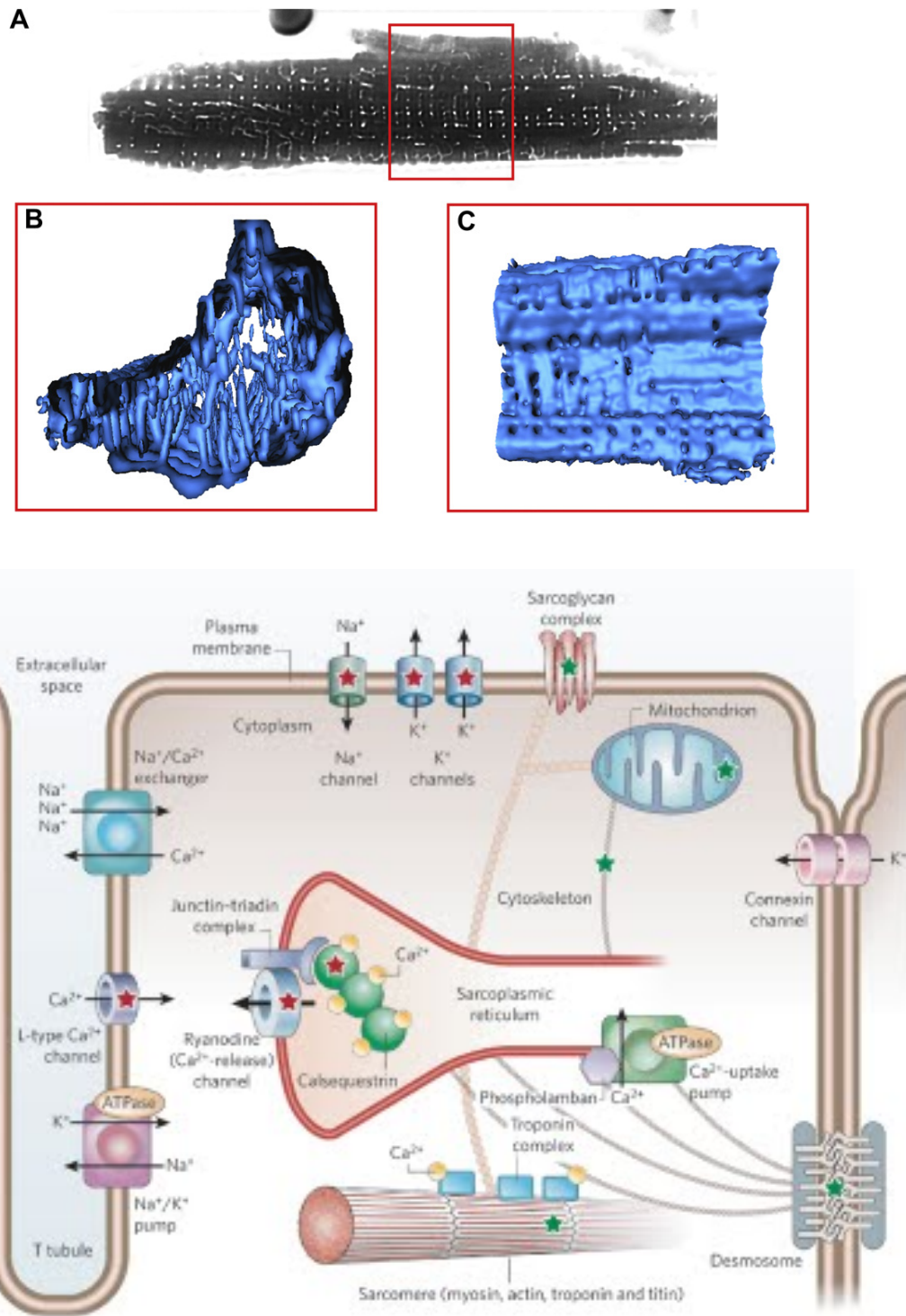


Figure 3.1.6: (TOP) Confocal microscopy of isolated living ventricular myocyte from rabbit: (A) transversal section, (B-C) three-dimensional segment of cell. The cell membrane includes deep invaginations, the transverse tubular system, into the cell interior [241]. (BOTTOM) Schematic representation of cardiac cell membrane protein structures and end processes (gap junctions) [51].

Muscular Units and Subunits

The basic muscular unit, as reported in the previous figures, is the sarcomere in which contraction and tension are provided by two protein content filaments, actin and myosin, while the elasticity properties are due to a different protein content molecule called titin. Under normal physiological conditions, actin exists as a long, helical polymer (*fibrous actin*, or F-actin) of a globular protein monomer (G-actin). G-actin is a two-domain asymmetric dumbbell-shaped molecule and can bind ADP and ATP¹. Asymmetry of G-actin determines directionally defined polymerization to F-actin via stacking of the dumbbell-shaped monomers and is favored by presence of Mg⁺. This process exhibit a preferred direction, especially in presence of ATP. The myosin molecule consists of six polypeptide chains: two large subunits (heavy chains) are connected by intertwining of two α -helices in the tail-like tail of the molecule. The globular headpieces carry two noncovalently bound light chains. Protruding arms and heads are called cross-bridges, which are flexible at two points (hinges), located at the base of the arm and base of the head; the head is an ATPase enzyme (see Fig.(3.1.5)).

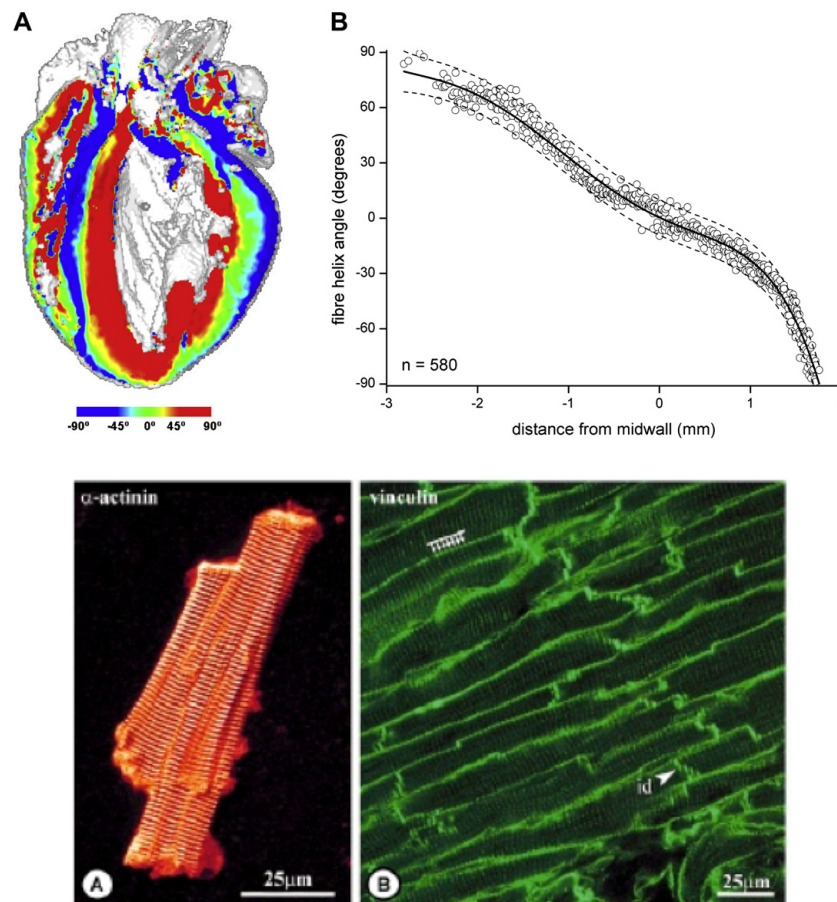


Figure 3.1.7: Fiber architecture in the heart. (TOP) (A) Reconstruction of fibre orientation in the rabbit heart using DT-MRI. Long-axis cross section through the heart showing fibre helix angle. (B) Transmural fibre helix angles extracted from a sector of the left ventricular mid free wall and fitted with a 5th order polynomial [51]. (BOTTOM) Representative picture of myocytes orientation [247].

3.1.3 Cardiac Activation Network & Propagation

At the macroscopic level, the spread and propagation of the electrical activation in the heart appears smooth, continuous and uniform. In Fig.(3.1.8) a schematic representation of the differentiated muscular cells for fast action potential conduction is shown. With the term *depolarization*, it is intended the firing of the cardiac cells, initiating or continuing an impulse. With the term *repolarization*, it is intended the regenerating of the cardiac cells, that is the cell is not firing, but building up the energy to depolarize again. In brief:

- The *sinoatrial* or *SA node*, located in the right atrium at the superior vena cava, consists of specialized self-excitatory muscle cells, *pacemaker cells*, generating an action potential at the rate of about $60 \div 100$ bpm. From the SA node, activation propagates throughout the atria reaching the beginning of the ventricles.
- The *atrioventricular node* or *AV node*, located at the boundary between the atria and ventricles just superior to the atrioventricular septum, is again self-excitatory at the rate of about $40 \div 60$ bpm, but, receiving the AV node activation, it follows this higher frequency. The AV node provides the only conducting path from the atria to the ventricles.
- The *bundle of His* is a specialized conduction system providing propagation from the AV node to the ventricles. Distally, it separates into two *bundle branches* propagating along each side of the septum. More distally the bundles ramify into the *Purkinje fibers* that diverge to the inner side of the ventricular wall and support an high propagation speed. These have an intrinsic rate of $20 \div 40$ bpm.
- From the inner side of the ventricular wall, the many activation sites cause the formation of a wavefront which propagates through the ventricular mass toward the outer wall. The duration of the action impulse is much shorter at the epicardium than at the endocardium, the termination of activity appears as if it were propagating from epicardium toward the endocardium.

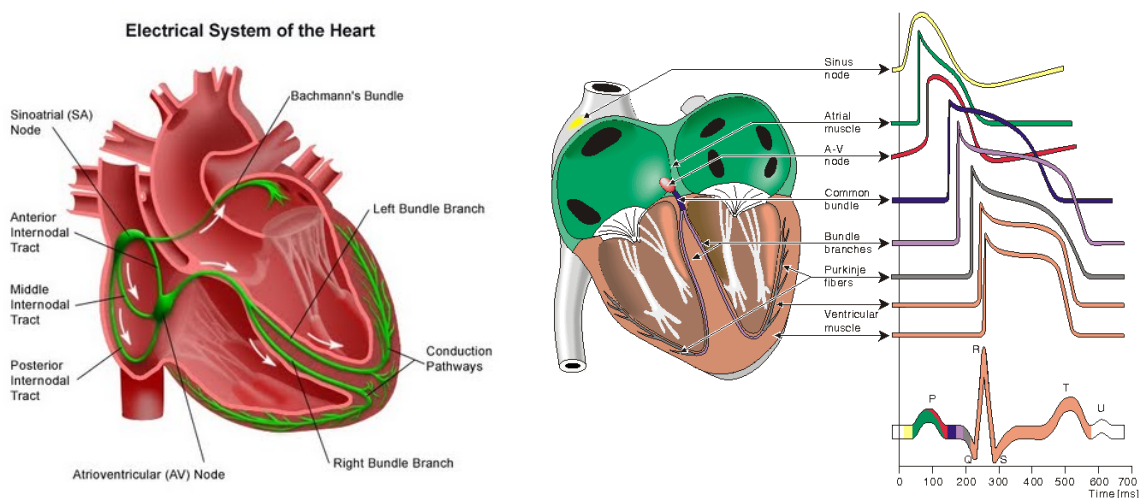


Figure 3.1.8: (LEFT) Cardiac activation network, pathways from atria to ventricles. (RIGHT) Action potentials morphology at the different levels of the activation network [18].

The electric events in the heart are summarized in Tab.(3.1). Because the intrinsic rate of the SA node is the greatest, it sets the activation frequency of the whole heart. If the connection from the atria to the AV node fails, the AV node adopts its intrinsic frequency. If the conduction system fails at the bundle of His, the ventricles will beat at the rate determined by their own region that has the highest intrinsic frequency.

However, at cellular level, this spread exhibits small delays on the gap junctions depending on the conditions surrounding the cell membrane [294]. In fact, the conductance of these junctions assumes a comparable value to that of the entire intracellular region within a cell [295]. The nonlinear emerging behavior from such a complex dynamical system is still being explored in order to better visualize and understand the different actors in the scene. As anticipated, the Purkinje specialized conduction system shows a fractal structure and it is able to conduct the action potential signal at speeds of meters per second. Such a prerogative allows a rapid excitation of the ventricles in a synchronized manner thus producing an effective contraction. This important role to coordinate ventricular contraction, is often involved in ventricular arrhythmias in various ways, as discussed later.

3.1.4 Excitation-Contraction Coupling

Across the ventricular cell membrane there is a steady potential difference of almost the same size as the equilibrium potential for potassium ions, K^+ ($-94 mV$), that is $-90 mV$ (see Fig.(3.1.9)). This negative potential is referred to as the *resting membrane potential* (RMP), because it represents the potential difference across the cell membrane (inside negative) at rest between successive action potentials.

The Action Potential Phases

Any process that depolarize the membrane tends to activate fast Na^+ -channels. Electrochemical forces favor the abrupt influx of Na^+ from neighboring regions. Hereby, the potential is further diminished and more and more Na^+ -channels are activated. The action potential, an all-or-none response, has a release threshold of about $25 mV$, from $-90 mV$, and can be divided into five phases:

Phase 0: the fast depolarization is shown by the abrupt upstroke, due to the rapid entry of Na^+ into the cell. Phase 0 stops at about $+30 mV$, because the fast Na^+ -channels become voltage-inactivated by closure of inactivation gates. The conduction velocity along the fast response fibre increases with the AP-amplitude and especially with the slope of phase 0.

Phase 1: is the early repolarization from the upstroke. This is related to K^+ -outflux.

Phase 2: is the plateau of the action potential, where the slow Ca^{2+} - Na^+ -channels remain open for a long period, up to $300 ms$. The net influx is almost balanced forming the plateau. Ca^{2+} activates the muscle contractile process. When the slow channels close at the end of the plateau, the voltage-gated K^+ -channels are activated, and the permeability for K^+ increases rapidly.

Phase 3: is the terminal repolarization. Large amounts of K^+ diffuse out of the ventricular fibre. The equilibrium potential is rapidly approached.

Phase 4: is recognized by a RMP of $-90 mV$. The Na^+ - K^+ pump restores ionic concentrations in a ratio of 3:2.

Phase 5: covers the relative refractory period, and the T-wave in the ECG. The long absolute refractory period of the ventricular cells covers the whole shortening phase of the contraction (blue curve). In

the relative refractory period, enough of the fast Na^+ -channels are recovered, so that a sufficiently large stimulus can break through and produce an action potential although smaller than normal. In the absolute refractory period all fast Na^+ -channels are voltage-inactivated and closed, which prevents sustained tetanus². As a consequence, no stimulus is sufficient to trigger contraction regardless of size. The long absolute refractory period protects the cardiac pump, as it is not possible to bring ventricles into smooth tetanus.

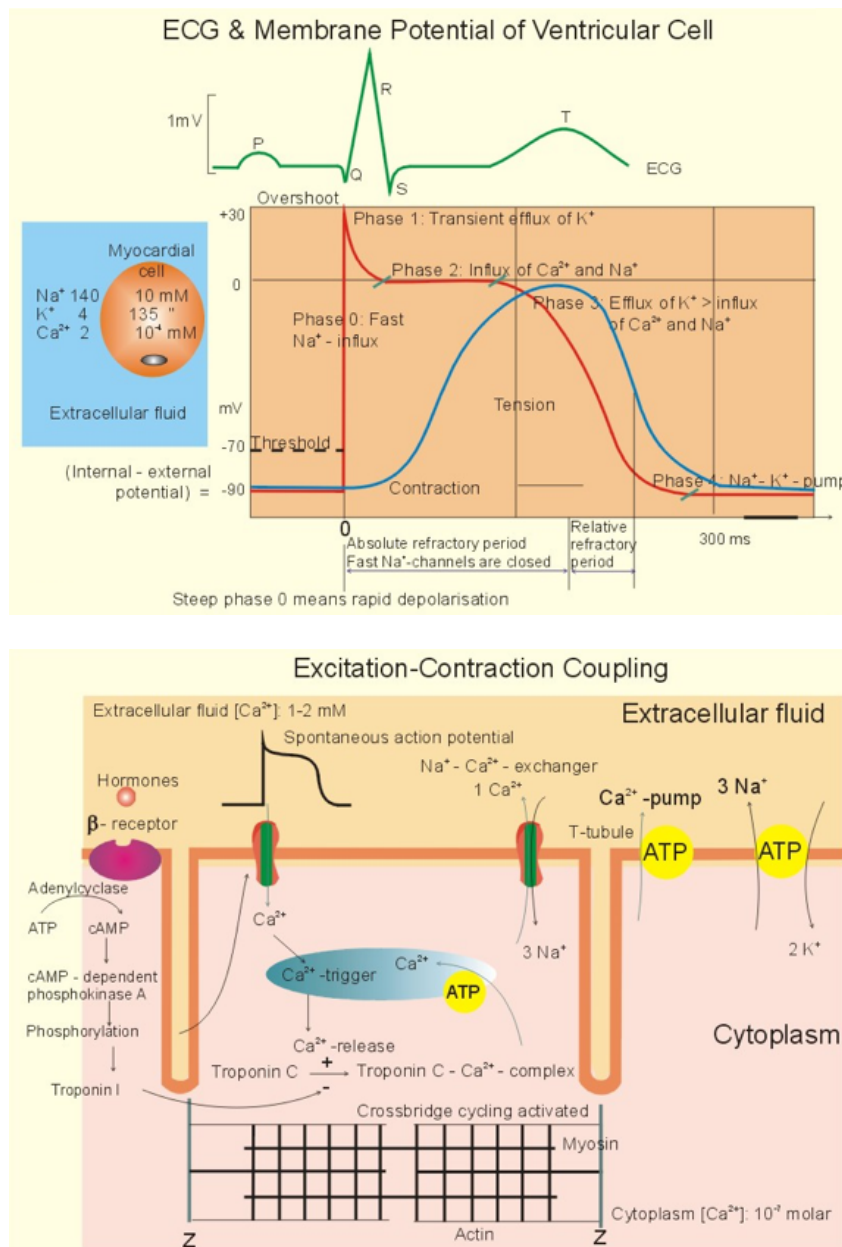


Figure 3.1.9: Excitation-contraction waves [213]. (TOP) Recordings of ECG (above), intracellular membrane potential (red curve) and contraction (blue curve) of one heart cycle in a ventricular fiber. Action potential phases description. (BOTTOM) Subcellular mechanisms of excitation-contraction coupling in a cardiac cell.

Table 3.1: Electric events in the heart for the activation and propagation network tissues: kind of activation, timing, electrocardiogram (ECG), and conduction velocity (CV). Abbreviations: SA, sinoatrial, RA, right atrium, LA left atrium, AV, atrioventricular, LV left ventricle, ENDO, endocardium, EPI, epicardium.

Tissue	Event	Time [ms]	ECG	CV [m/s]
SA node	pacemaker	0		0.05
RA	depolarization	5	P	0.8 ÷ 1.0
LA	depolarization	85	P	0.8 ÷ 1.0
AV node	arrival/departure	50/125	P-Q	0.02 ÷ 0.05
His's bundle	impulse	130		1.0 ÷ 1.5
Branches	activated	145		3.0 ÷ 3.5
Purkinje ENDO-LV	depolarization	175 ÷ 190	QRS	0.3 axial
Purkinje EPI-LV	depolarization	225 ÷ 250	QRS	0.8 transverse
Purkinje EPI-LV	repolarization	400	T	0.5
Purkinje ENDO-LV	repolarization	600	T	0.5

Subcellular Mechanisms: Calcium Cycle

The mechanism for muscle contraction is based on the so called *excitation-contraction coupling* (see Fig.(3.1.9)), which links electric action potential to muscular movement through subcellular triggering. In fact, the excitation reaches the interior of the cell through the large T-tubules filled with mucopolysaccharides. The levels set of such a feedback are mainly governed by calcium ions.

Intracellular Calcium ion (Ca) is the central regulator of cardiac contractility, and moreover critical in both the mechanical dysfunction and arrhythmogenesis associated with congestive heart failure [21]. A detailed control of calcium cycling requires an integrated approach in which several systems are considered [22, 82]. It is imperative, thus, the clear and quantitative understanding of calcium fluxes during the contraction-relaxation cycle:

1. An action potential travels along a motor nerve to its ending on muscle fibers.
2. The nerve secretes neurotransmitter *acetylcholine* (ACh).
3. ACh acts on acetylcholine-gated ion channels causing their opening, which allows influx of sodium ions: an action potential starts.
4. The action potential propagates along muscle fiber membrane, causing opening of internal stores of Ca ions, sarcoplasmic reticulum (SR), via the *Calcium Induced Calcium Release* (CICR) mechanism: this is the *systolic contraction activation mechanism*:
 - L-type Ca channels are activated during the cardiac action potential;
 - Ca enters the cell via calcium current, I_{Ca} , and Sodium-Calcium exchange (NCX);
 - calcium influx triggers Ca release (CICR) from the sarcoplasmic reticulum (SR) through maneuvers that modify the ryanodine receptor and directly contribute to activation of the myofilaments;
 - CICR raises cytosolic free Ca, causing calcium binding to multiple buffers, and mainly with the protein troponin C (TnC);
 - when Ca binds to TnC, it switches on the myofilaments in a cooperative manner activating contraction.

5. Calcium initiates attractive forces between the actin and myosin filaments, which is the contractile process.
6. Calcium ions are pumped back into the SR, causing muscle contraction to cease: this is the *diastolic contraction de-activation mechanism*:
 - 4 calcium transporters remove Ca from the cytosol: (1) SR Ca-ATPase, (2) sarcolemmal NCX, (3) sarcolemmal Ca-ATPase, and (4) mitochondrial Ca uniporter.

In Fig.(3.1.10) the cyclic process of crossbridge is depicted.

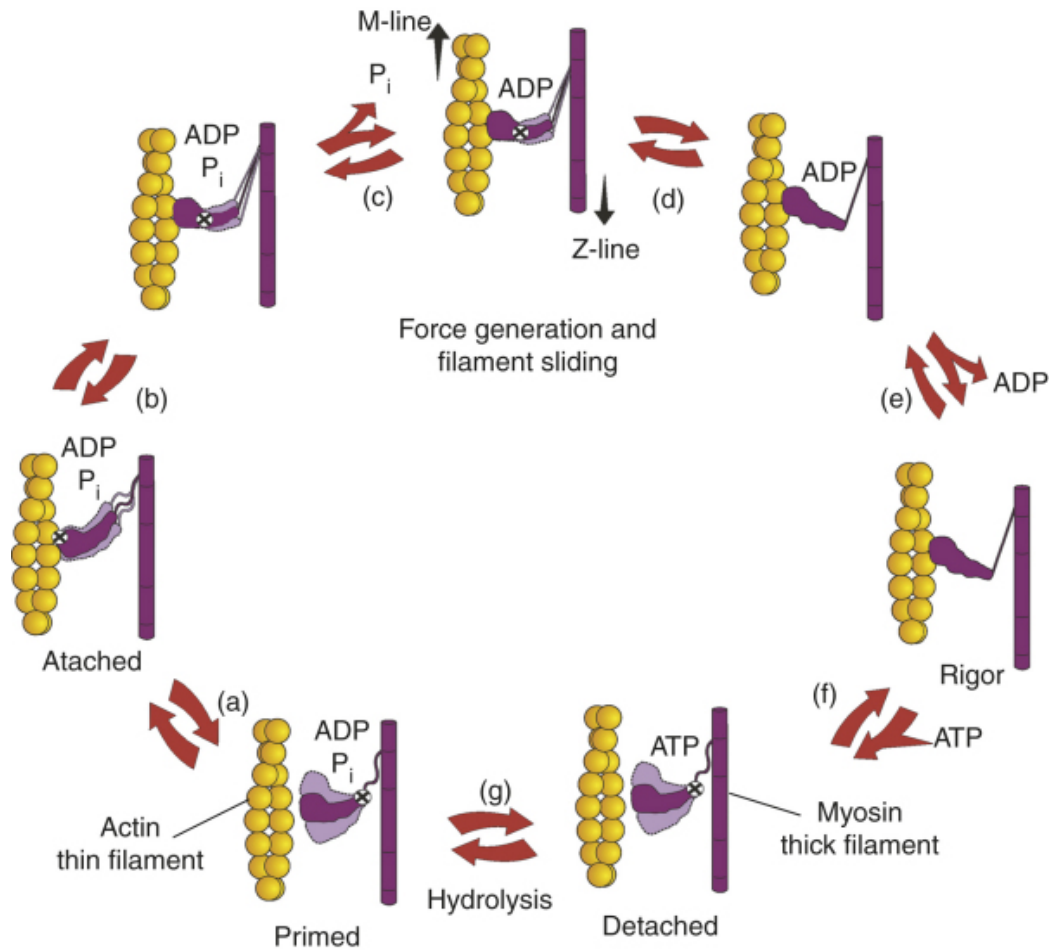


Figure 3.1.10: Thick and thin filaments. The cross bridge cycle and calcium excitation-contraction mechanisms [95].

3.2 Cardiac Cycle

The technology devoted to the measure and registration of the heart beat has been developed since the beginning of the 20th century (see Fig.(3.2.1)) [175, 176]. In those days, several kind of apparatus were invented, adapted and used in taking heart sounds records. More in detail, the curves of pressure in the carotid artery, aorta, left ventricle, right atrium and jugular vein were being collected and associated with echocardiogram (ECG) and phonogram of the human subject (see Fig.(3.2.2)).

Through these analyses, characteristic volumetric ranges of the healthy heart were standardized:

1. $110 \div 120$ mL of end-diastolic volume (EDV): is the volume of blood in the right and/or left ventricle at end load or filling in (diastole);
2. $40 \div 50$ mL of end-systolic volume (ESV): determines the stroke volume, or output of blood by the heart during a single phase of the cardiac cycle.
3. 70 mL for the stroke volume (SV): is the volume of blood pumped from one ventricle of the heart with each cardiac cycle.
4. 60% of ejection fraction (E_f): is the fraction of blood pumped out (forward) from the right ventricle of the heart to the pulmonary circulation (lungs) and left ventricle of the heart to the systemic circulation (brain and body) with each cardiac cycle.

On such bases, other indicators were introduced, i.e. the stroke work output (amount of energy converted to work during a heartbeat) as pressure difference between veins and arteries and kinetic energy of blood flow (see Fig.(3.2.2)B) the volume pressure diagram). This allows a direct visualization of the four phases as:

1. Period of filling.
2. Period of isovolumic (isometric) contraction.
3. Period of ejection.
4. Period of isovolumic relaxation.

In this way, the net external work output can be readily calculated, as well the degree of tension in the beginning of contraction (*preload*) and the arterial pressure (*afterload*).

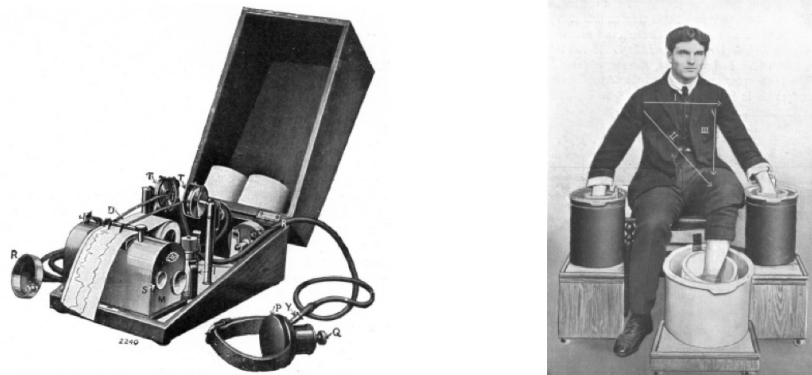


Figure 3.2.1: (LEFT) Representation of the first apparatus dedicated to cardiac flutter and fibrillation observation [176]. (RIGHT) Cambridge Scientific Instrument Co. First ECG Machine Type (1911) [151].

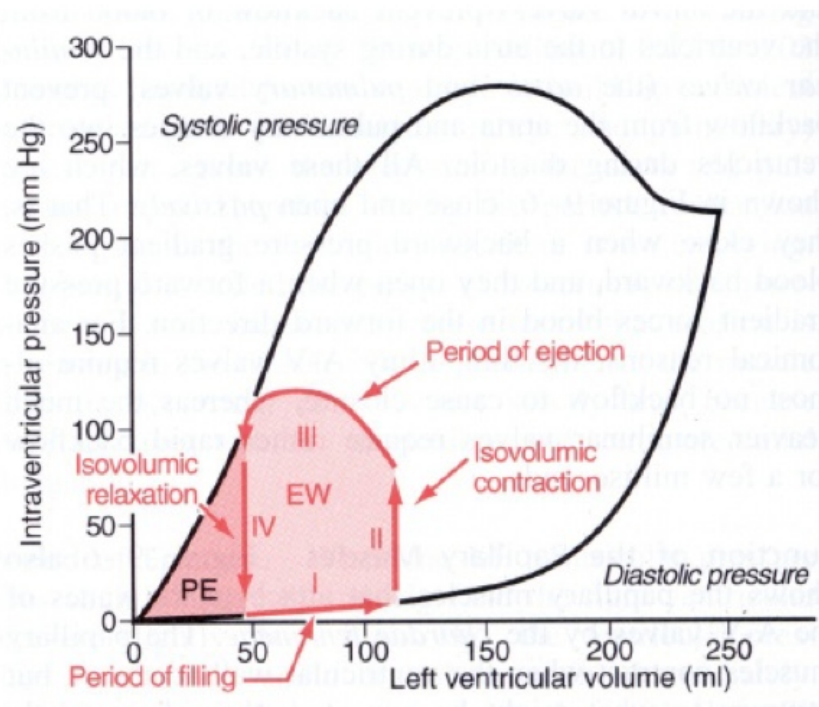
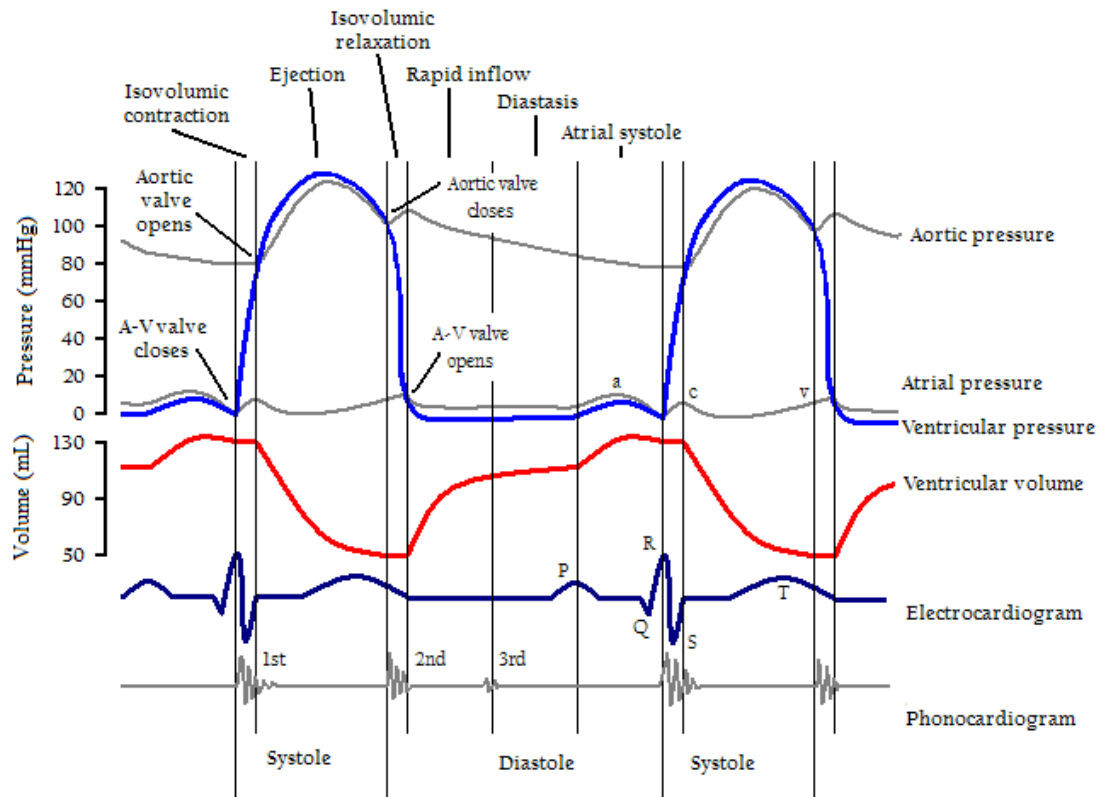


Figure 3.2.2: (TOP) Cardiac cycle curves of volume, pressure and ECG [84]. (BOTTOM) Volume-Pressure diagram of cardiac cycle with phase identification [213].

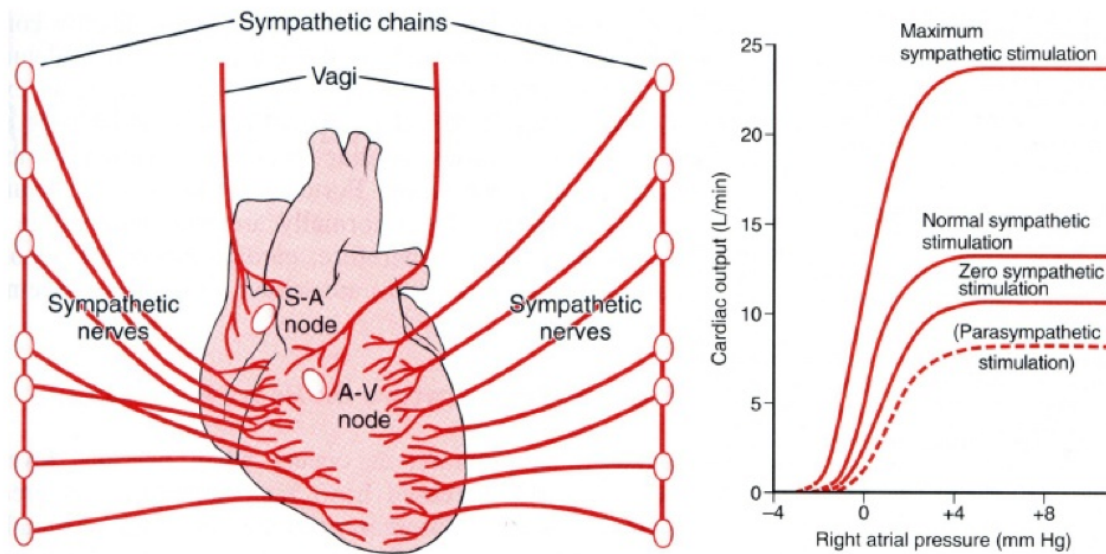


Figure 3.2.3: The neural control of the heart [213]. (LEFT) Sympathetic and parasympathetic networks. (RIGHT) Cardiac output vs neural stimulation curves.

3.2.1 Controlling Cardiac Pumping

One of the most used diagram in cardiac regulation of blood pumping is based on the Frank-Starling mechanism (see Fig.(3.2.2)). Within physiologic limits, the heart pumps all the blood that comes to it without allowing excessive damming of blood to veins. If veins return more blood to heart, heart volume is greater at end diastole and, therefore, heart pumps more vigorously on the next stroke to maintain the right ejection fraction. Such a mechanical controlling feedback may be, on the other hand, one of the side causes for dilated heart failures. In fact, as reported in Tab.(3.2), dilated ventricles present many altered values. A more specific control of heart rhythmicity and impulse conduction is performed by cardiac nerves, i.e. the sympathetic and parasympathetic network (see Fig.(3.2.3)).

The parasympathetic stimulation, usually called *vagal*, slows or even blocks cardiac rhythm and conduction causing ventricular escape (premature ventricular contraction). In particular, it slows the rate of rhythm of the sinus node and, at the same time, slows the conduction of the atrioventricular node through a precise biochemical mechanism: a release of acetylcholine increases the potassium permeability to the cell membrane; this in turn becomes hyperpolarized and decreases the excitability of the cell.

The sympathetic stimulation, on the other hand, increases the rate of cardiac rhythm and accelerates conduction. The underlying biochemical mechanism in this case necessitates of the release of norepinephrine which increases the permeability to sodium and calcium ions; the cell membrane thus becomes hyperdepolarized therefore increasing excitability and contractility of the cell.

In Fig.(3.2.3), the topology of such a network together with the dependence of cardiac output by the right atrial pressure is shown. Other regulation mechanisms of cardiac pumping can be identified into ionic concentrations and bath temperature. Specifically:

- high extracellular potassium $[K^+]_o$ decreases cardiac output;

- high intracellular calcium $[Ca^{2+}]_i$ increases cardiac output;
- high temperature temporarily increases cardiac output, but exhausts metabolic system.

Concluding, it's worth to mention that the heart is part of the circulatory system. A complete description of its control mechanisms should include also vasodilatation and vasoconstriction in vascular smooth muscles, as well as adrenergic and cholinergic stimulations. The main topics of this work are not closely related to these aspects, and their discussion is deferred to dedicated studies.

3.2.2 Muscular Energy Efficiency & Heart Failure

The main source of energy involved in muscular energy consumption comes from oxidative metabolism of fatty acids in addition with lactate and glucose. The main biochemical mechanisms are briefly summarized:

- cross-bridge cycling;
- pumping Calcium into the SR;
- pumping ions through the membrane ion exchangers;
- ATP (4 mMol/L, sufficient for $\sim 1 \div 2$ seconds);
- Phosphocreatine used for reconstitution of the ATP from ADP (20 mMol/L, sufficient for $\sim 5 \div 8$ seconds);
- Glycogen (glycolysis is fast in producing ATP, does not require oxygen, but produces large quantities of end products inhibiting itself, sufficient for ~ 1 minute);
- oxidative metabolism of food: carbohydrates, fats, and protein ($\sim 95\%$ of energy).

Even though, only $20 \div 25\%$ of the chemical energy goes to into work output. In fact $75 \div 80\%$ goes to heat.

Table 3.2: Ventricular dimensions comparison between normal and dilated ventricles [163].

Parameter	Normal	Dilated
AT START EJECTION		
Pressure (<i>mm Hg</i>)	100	100
Volume (cm^3)	92	380
Radius (<i>cm</i>)	2.8	4.5
Circumference (<i>cm</i>)	17.5	28
Wall tension (<i>dynes/cm</i>) $\times 10^5$	3.72	5.98
STROKE VOLUME (cm^3)	70	70
AT END OF EJECTION		
Pressure (<i>mm Hg</i>)	100	100
Volume (cm^3)	22	310
Radius (<i>cm</i>)	1.7	4.2
Circumference (<i>cm</i>)	11	26.5
Wall tension (<i>dynes/cm</i>) $\times 10^5$	2.26	5.59
EXTERNAL STROKE VOLUME (<i>dyne cm</i>) $\times 10^5$	9.3	9.3
CONDITIONS OF EXTERNAL WORK		
Average wall tension (<i>dyne/cm</i>) $\times 10^5$	2.99	5.79
Change in circumference (<i>cm</i>)	6.5	1.5
As % of end-diastolic circumference	-40	-5

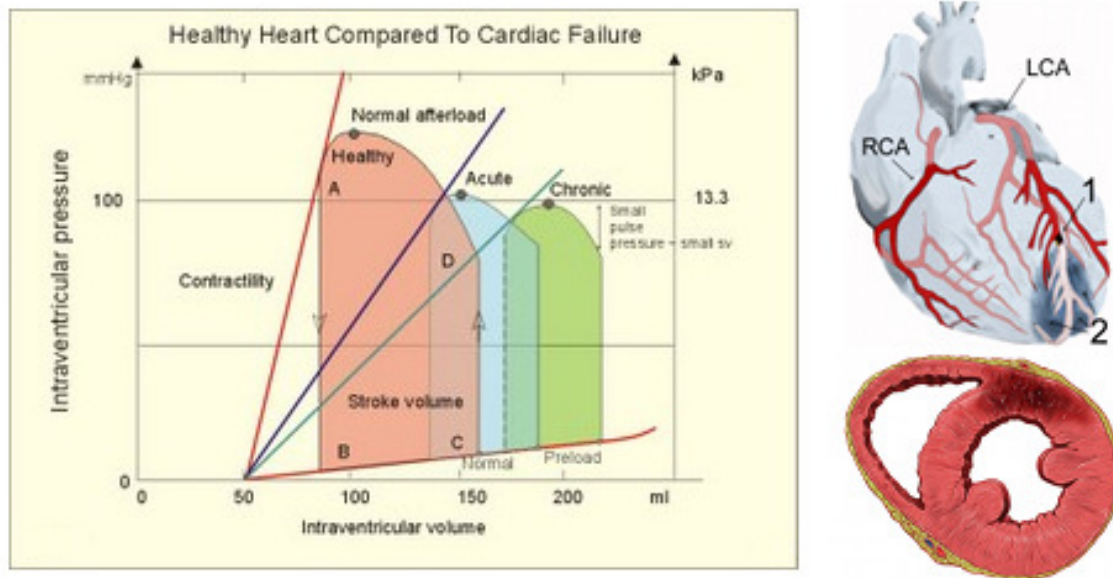


Figure 3.2.4: (LEFT) Left ventricular pressure-volume loops in a healthy person (red) and for persons with acute (blue area) or chronic, congestive (green area) cardiac failure. [213]. (RIGHT) Representation of tissue lesions in case of infarction.

Fatigue

With *muscular fatigue* is intended weakness and/or aches with consequent inability to exert force. In striated muscles, fatigue is primary due to depletion of energy supply by glycogen, inhibition of impulse transmission through the neuromuscular junction and hypoxia (limited oxygen supply). The cardiac muscle is very sensitive to such a process. In fact the *aerobic* production of ATP is strongly required for a muscle that must work continuously. Ischemia (reduced levels of oxygen) causes a decrease in ATP production. However, another *anaerobic* reaction can convert ADP to ATP using glycolysis without oxygen, but the counterpart of such a process is the glycolysis products (*lactic acid*) build up and stressing cells. For a healthy hear, the energy liberated is directly related to the oxygen consumption, about 4.8 kcal per liter of O_2 .

Heart Failure

Heart diseases in the industrialized countries comprise for the most: hypertension, coronary artery disease, myocardial infarction, angina pectoris, congestive heart failure, stroke, traumatic heart disease and congenital heart disorders. *Cardiac failure* is defined as the failure of the heart to pump enough blood to satisfy the needs of the body [50, 171]. Three types of mechanisms of cardiac failure can be identified:

1. Cardiomyopathy.
2. Pressure overload.
3. Volume overload.

In Fig.(3.2.4), examples of pressure load and overload are shown. In case of severe damage, no compensation by sympathetic stimulation or by fluid retention is sufficient to produce an adequate cardiac output. Because of renal function remains impaired, more and more fluid is retained. Therefore, severe edema

develops, resulting in death. In heart failure, efficiency of cardiac contraction is reduced as low as $5 \div 10\%$, although the source of energy is also altered to a greater degree to glucose.

3.3 Mechanical Properties of Cardiac Tissue

Different experimental tests can be carried out on myofilaments, bundles of fibers or complete muscles trying to estimate the stress induced in the muscle fiber. In Fig.(3.3.1) the two *isotonic* and *isometric* contraction experimental setup are reported. In the isotonic system, the muscular unit is electrically stimulated, loaded with a constant weight but left free to contract, while in the isometric system, the muscle is kept fixed at constant length and electrically stimulated.

3.3.1 Passive and Active Stress-Strain Relations

When mechanical tests are conducted on muscular tissue, the sarcomere length vs tension dependence relation can be extracted: the traditional expression for force is stress or tension, Newton per cross-sectional area of the muscle. Force is required to stretch a relaxed muscle, because muscle tissue is elastic, and the force increases with increasing muscle length. The *passive* blue curve in Fig.(3.3.2) (top) reflects the properties of the elastic, connective tissue, which becomes less compliant or stiffer with lengthening.

The length at which maximum active contractile force is developed is called L_o , corresponding to a sarcomere length of about 2 mm : L_o is the length of the muscle in the body when at rest. At this length there is a maximum number of active cross bridges. When an isolated muscle in isometric force or stress-meter is stimulated, the active muscle force decreases with the decrease in overlap between thin and thick filaments. The force is always proportional to the number of cycling cross-bridges interacting with the thin filament. Force also declines at muscle lengths less than L_o . Thin filaments overlapping, and thick filaments colliding against Z-discs cause this.

When the active muscle length is stretched beyond any overlapping between the thin and the thick filaments the muscle can only develop a force of zero. The lengths of the thick and thin filaments of human striated muscles are similar, they generate maximal tension forces at L_o , corresponding to about 300 kPa . Muscle mechanical properties can also be characterized with other curves, such as the force-velocity relationship derived from the Hill model [130] (see Fig.(3.3.2) (bottom)).

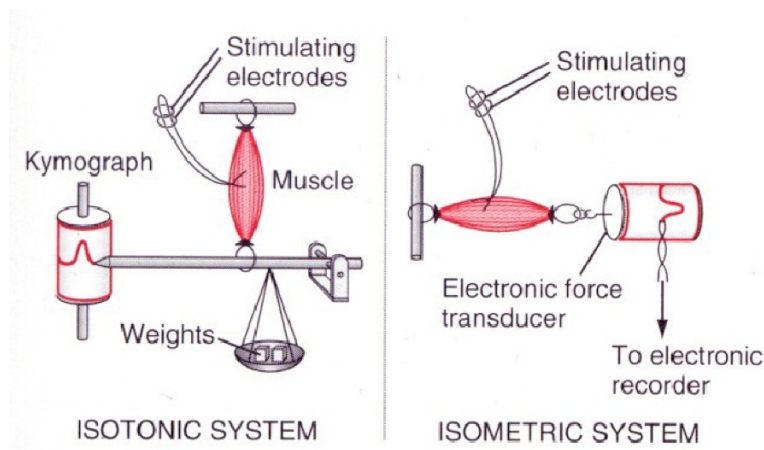


Figure 3.3.1: Classical experimental setup for testing muscular fibers [213].

3.3.2 Uniaxial and Biaxial Passive Tests

Biological media can be studied as passive tissues, from a mechanical point of view, via instrumentations like that reported in Fig.(3.3.3). The scope of these analysis is to obtain constitutive relationship between the normalized forces (stresses) and deformations (strain). Such a description is fundamental, because it is independent of geometry.

The usual tests conducted on myocardium consists in applying cyclic loading and unloading in the predominant fiber and cross-fiber directions to determine passive mechanical properties, Fig.(3.3.4). Myocardium under biaxial loading exhibits both nonlinear elasticity and viscoelasticity with some strain-rate dependence in the position of the stress-strain relations, but very little rate dependence in the area enclosed by the loading and unloading portions of the stress-strain loops. Fiber and cross-fiber directions demonstrate anisotropic behavior, with both the degree and direction of the anisotropy being dependent

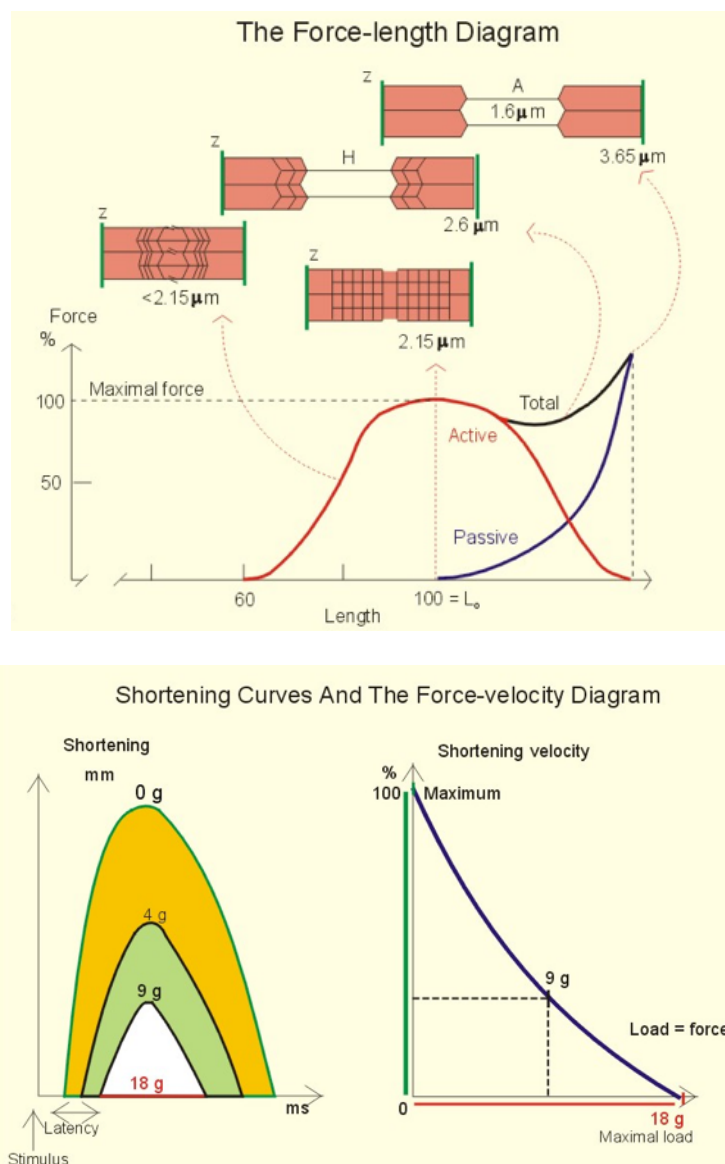


Figure 3.3.2: (TOP) Active and passive stress-strain relationship for muscular tissue. (BOTTOM) Hill's force-velocity diagrams (right) and related shortening curves (left) [213].

upon the region of the heart from which specimens are obtained. The biaxial test indicates no anisotropy whereas two successive uniaxial tests indicate the fibre direction to be stiffer than the cross-fiber direction. These tensile tests will be mathematically described later in the dissertation.

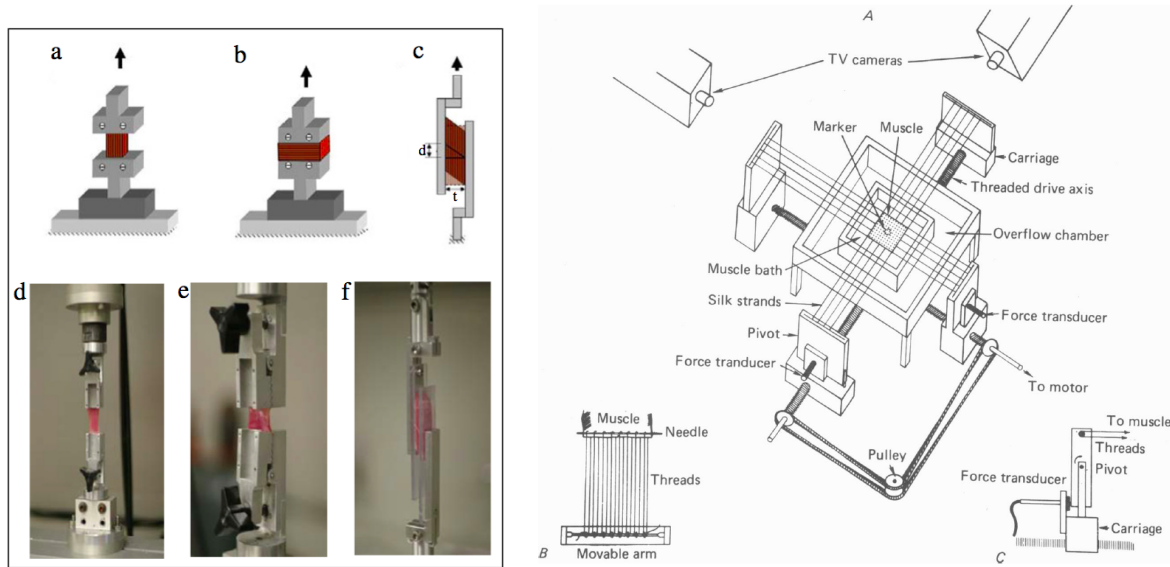


Figure 3.3.3: (LEFT) Uniaxial tensile test machine [233]. (RIGHT) Schematic illustration of the biaxial experimental apparatus viewed from above [67].

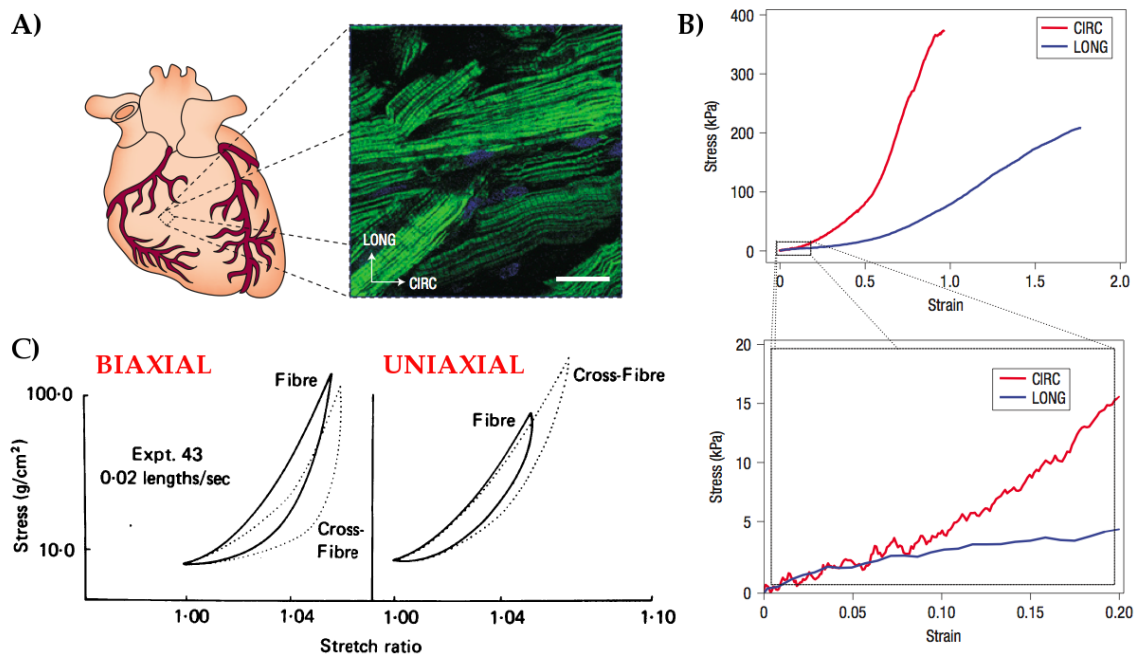


Figure 3.3.4: Structural and mechanical aspects of cardiac anisotropy [83]. (A) Schematic of a mammalian heart, and a full-thickness specimen of adult rat right ventricular myocardium showing preferentially oriented cardiac muscle fibre. (B) Representative uniaxial tensile stress-strain plots for circumferential and longitudinal specimens (physiologic regime below). (C) Comparison of anisotropy in the fiber with the cross-fiber directions in biaxial (left) and constrained uniaxial (right) tests [67].

3.4 Cardiac Arrhythmias

The leading causes of death in most developed countries are strongly related with cardiovascular diseases. In the last three decades, insights have been provided by experimental investigations of cardiac electrical activity into the mechanisms of arrhythmia formation and termination. The arrhythmogenesis processes have been analyzed following a reinforced multidisciplinary work, improving pharmacological and electrical therapies [129], thus discovering and creating new technologies and theories [181]. The difficulty or impossibility to measure all the quantities of interest *in vivo* is still an open problem. Therefore, the challenge is to relate *in vitro* measurements, performed on small tissue preparations or isolated cells, to the dynamics of the entire heart. Several mechanisms have been related to cardiovascular diseases and cardiac arrhythmias. In the following, a focus on the current knowledge of arrhythmias will be presented.

3.4.1 Arrhythmias: Definition & Classification

The term *arrhythmia*, also known as cardiac dysrhythmia, describes the wide set of conditions under which an abnormal electrical activity of the heart can be recorded: the rhythm may be faster or slower, and regular or irregular as well. The onset of cardiac arrhythmias was first associated with the concept of *reentry* by McWilliam at the end of the 19th century [189]: differences in action potential conduction in myocardial fibers can propagate unevenly waves which “reenter” inducing a re-excitation of previously excited tissue. Such a description has been found totally true, in fact the most dangerous cardiac arrhythmias are due to reentrant waves that recirculate through the tissue with a higher frequency than of the heart’s natural pacemaker. The corresponding physical literature targets this phenomenon as “rotating spiral waves” (discussed later).

An important source of arrhythmic pathologies [156] can be found in the wrong behavior of the Purkinje system that normally coordinates ventricular contraction. In fact, this network can act as a source of triggering activities [7, 26, 121] such as focal and post-shock activations [72], or as part of reentrant circuits [264]. Cardiac arrhythmias are divided into two main groups and classified as [213]:

1. *Pacemaker abnormalities* (disorders of rhythmogenesis):
 - (a) In the sinus node: sinus tachycardia (heart rate above 100 bpm), sinus bradycardia (heart rate below 60 bpm) or sinus arrhythmia (rise in heart rate during inspiration followed by a fall during expiration).
 - (b) Outside the node: ectopic beats (pacemaker cells outside the sinus node), tachycardia (paroxysms), and fibrillation (tumultuous twitching of ventricular muscle fibre) and shifting pacemaker (the impulse originates in shifting locations inside the SN, or the pacemaker shifts from the SN to the AV-node).
2. *Conduction abnormalities* (cardiac block):
 - (a) Sinoatrial block: long intervals between consecutive P-waves.
 - (b) Atrioventricular block: blockage of the conduction from the atria to the AV-node.
 - (c) Bundle branch block: block of the right or the left bundle branches.
 - (d) WPW-syndrome: *Wolf-Parkinson-White block* is not a direct block of the conduction through the Hiss bundle and branches, but is caused by a short cut through an extra conduction pathway from the atria to the ventricles.

- (e) Long QT-syndrome: frequently a genetic condition, where fast repolarised cells are re-stimulated by cells that have not repolarised.

3.4.2 Anatomical and Functional Reentry

A reentry can occur depending on both the topology and the local heterogeneity of the tissue (as in other chemical or physical excitable media, see Chap.(6) for details). In the medical literature, two kinds of reentry have been standardized: *anatomical reentry* (AR) and *functional reentry* (FR). The first occurs whenever an inexcitable obstacle, such as scar produced by an infarct, around which the electrical wave can rotate, or pin, is present into the tissue. The second case does not necessitate of such anatomical anchors, in fact the electric wave itself is responsible of a reduced excitability of the medium, thus creating a so called *functional block* around which the wave periodically rotates. Experimental and modeling examples of AR and FR are shown in Fig.(3.4.1)(A).

The geometric requirement for an AR is that the perimeter of such a feature is longer than the wavelength of the electric pulse. When this condition is not respected and the wavelength is comparable with the perimeter of the obstacle, more complex dynamics can occur, such as transient detachment and re-attachment or complicated alternans [42, 55, 109] (discussed later).

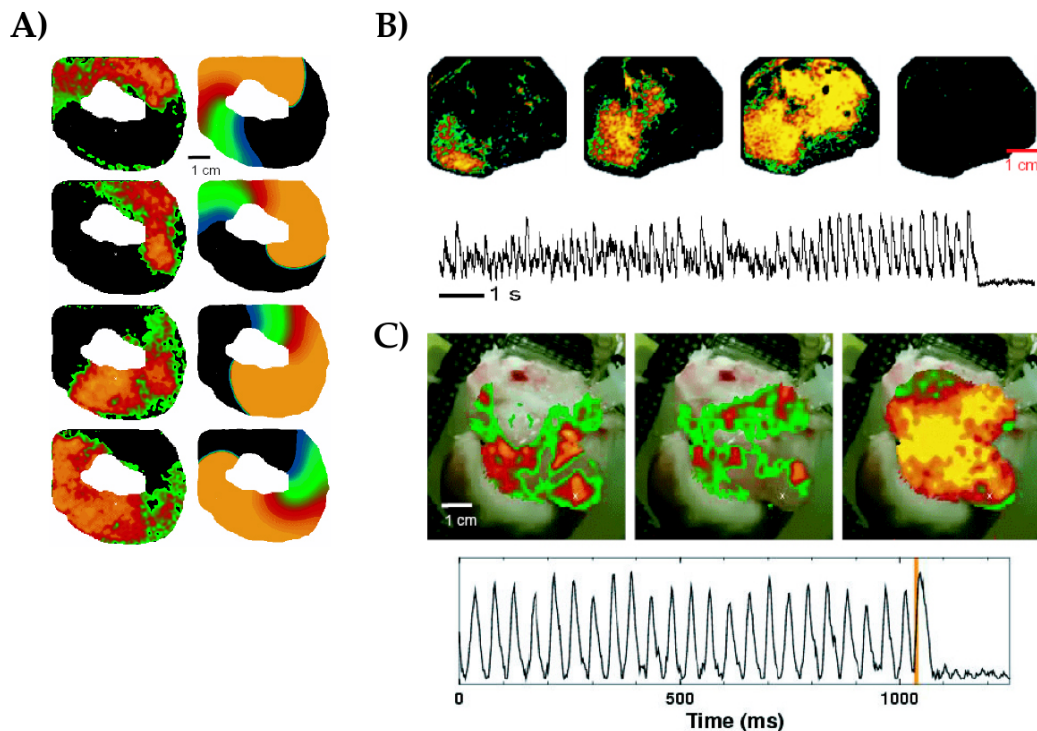


Figure 3.4.1: Reentry and termination of fibrillation [41]. (A) Experimental and simulated examples of an anatomical reentrant arrhythmia. On the left column: optical mapping recording of goat right ventricle preparation; the central region, serving as an obstacle, has been cryoablated. On the right column: two-dimensional representation of the experimental geometry through phenomenological numerical simulations of cardiac tissue. (B) Termination of equine AF by quinidine. AF induced in the presence of $4 \mu M$ acetylcholine is terminated by administration of $12 \mu M$ quinidine. Electrical activity during fibrillation (Top). Optical signal from one pixel showing AF termination (Bottom). (C) Example of defibrillation following application of a high-energy shock in canine atrium. Top: left and center frames show irregular activity characteristic of AF. Right frame shows near-simultaneous activation of almost the entire mapped region in response to the shock, after which quiescence ensues. Bottom: optical signal from a single pixel showing termination of fibrillation following the shock.

Anatomical reentry results particularly important in the atria and the corresponding pathology has been known clinically since 1920s as atrial flutter [175]. Atrial tissue encompasses abundant tissue boundaries, large blood vessels and valve annuli of different sizes. Each of these structures can act as an obstacle around which activation waves can strongly circulate. Nevertheless, functional reentry is even more dangerous because it can appear on healthy tissues too. The discovery of the dynamic process of changing excitability at the tip, due to both curvature and electrotonic effects, present during spiral wave reentry, was first demonstrated using cardiac models in 1991 [57, 133], and only subsequently experimentally shown in 1992 [65].

Under normal conditions, as often observed in vitro preparations, atrial arrhythmias do not occur spontaneously and usually self-terminate quickly if initiated. In ventricular tissue, however, reentrant waves can be initiated and sustained readily in large hearts. The physiological condition, however, is strongly altered in the presence of pharmacological agents or cardiovascular diseases. In these scenarios, self-sustained atrial arrhythmias (AF) can be induced and maintained, thus leading to ventricular tachyarrhythmias that can rapidly become a lethal ventricular fibrillation (VF). A mathematical-based description on these aspects will be given in Chap.(4).

3.5 Clinical Treatments of Arrhythmias

Ventricular fibrillation is a life-threatening arrhythmia. It must be terminated rapidly to prevent death and/or to minimize damage to cardiac tissue and other organs. In fact, the disorganized electrical activity associated with ventricular fibrillation prevents effective contraction and pumping of blood. Termination of ventricular arrhythmias is indicated in the medical literature as well as in the clinical practice as *defibrillation*.

Atrial arrhythmias in healthy atria, on the other hand, are an exception and atrial fibrillation is characteristic of diseased tissues. Although less immediately dangerous than ventricular fibrillation, such arrhythmias definitively increase the risk of other cardiac problems, including stroke and ventricular fibrillation itself. Termination of atrial arrhythmias is called *cardioversion*.

Arrhythmia termination generally is accomplished either through electrical stimulation, that act to reset electrical activity directly, or through pharmacological therapy, that affect the underlying dynamics modifying the electrophysiological properties of the tissue. In some cases, the use of *ablation* is adopted for arrhythmias termination, in which inexcitable lesions are created to disrupt reentrant circuits.



Figure 3.5.1: Evolution of the defibrillator apparatuses. From left to right, the defibrillator prototype [62], commercial defibrillator for workplace and public settings [127], and modern implantable pacemaker [23].

3.5.1 Pharmacological Defibrillation and Cardioversion

The market of anti-arrhythmic drugs has been increasing in the last decades. These pharmaceuticals are usually able to terminate arrhythmias (atrial) or to prevent their induction (atrial and ventricular) when diseases or pathologies are not compromised or fully developed yet. The precise mechanism by which such drugs work is not completely understood and one of their most critical aspect is related to the high variability of effectiveness seen in the clinical practice. As most of drugs, anti-arrhythmic too are strongly patient-dependent.

One of the most used agent is quinidine. Cardioversion for AF in equine tissue by quinidine is shown in Fig.(3.4.1)(B). Quinidine is believed to terminate atrial arrhythmias by increasing the effective refractory period and, at the same time, decreasing the frequency of the reentry until it can no longer be sustained. In highly sensitive situations, the most adopted therapy is however, electrical defibrillation, as described in the following section.

3.5.2 Electrical Defibrillation and Cardioversion

The most efficient treatment available for ventricular fibrillation consists in the delivering of therapeutic dose of electrical energy shocks to terminate arrhythmias. This method is mainly used because highly effective in a short period of time. Even if such a technique has been known since the end of the nineteenth century, and applied in the medical contest since 1947 [192], the fundamental achievement of the optimal shock strength is still debated [181]: weak shocks can be ineffective or re-initiate the arrhythmia [77, 78, 234], but strong shocks can damage the heart [288]. Electrical cardioversion also is able to disrupt atrial arrhythmias, although prolonged atrial fibrillation can induce tissue electrophysiological changes that allow AF to recur. Cardioversion for AF in canine tissue by electric shock is shown in Fig.(3.4.1)(C).

Although defibrillation can be highly effective, the actual mechanism by which it works is still not completely understood [150, 275]. Unless differences in size and materials, the goal of the first defibrillators has not been changed by the modern ones (see Fig.(3.5.1)): i.e. excite all remaining quiescent tissue, so that reentrant waves will be terminated. During the last decades, the idea that application of an external electric field can give rise to the formation of secondary sources has been explored both theoretically [78] and experimentally [86, 137, 217]. Such a phenomenon has been named *virtual electrode* effect, and prospects that new activations can arise at the interfaces between regions of different conductivity (heterogeneities such as collagen, blood vessels or other small-scale inexcitable regions). Recent studies have applied this methodology more in detail [181], giving rise to a new defibrillation technique, namely, LEAP: low-energy anti-fibrillation pacing. The basic idea does not necessitate high enough shocks in order to excite all remaining quiescent tissue, otherwise widely distributed heterogeneities are used as nucleation sites for the generation of intramural electrical waves in response to a pulsed electric field. Efficient termination of fibrillation is indeed reached thanks to a direct access to multiple vortex core, that result in a rapid synchronization of the whole tissue. An example of such a technique is shown in Fig.(3.5.2). Details will be discussed in Chap.(8).

3.5.3 Ablation

Alternative to both pharmacological and electrical therapies or interventions, ablation is an effective technique in terminating certain types of arrhythmias: some forms of ventricular tachycardia [64] and atrial fibrillation [155, 236], atrial flutter [173] and arrhythmias triggered from localized ectopic beats [120] (when lesions are positioned appropriately) are well suited for ablation. It consists in creating highly

localized lesions in the heart through the application of radio-frequency energy or cryoablation. In such a manner, all the possible sources of new irregular and high frequency activations are excluded, even if these new inexcitable regions can act as pinning areas as previously described.

This and other reasons force the clinical practice to often accompany a pharmacological anti-arrhythmic therapy in conjunction with an ablation intervention, or with a portable assistive pacemaker or defibrilating device in the worst cases.

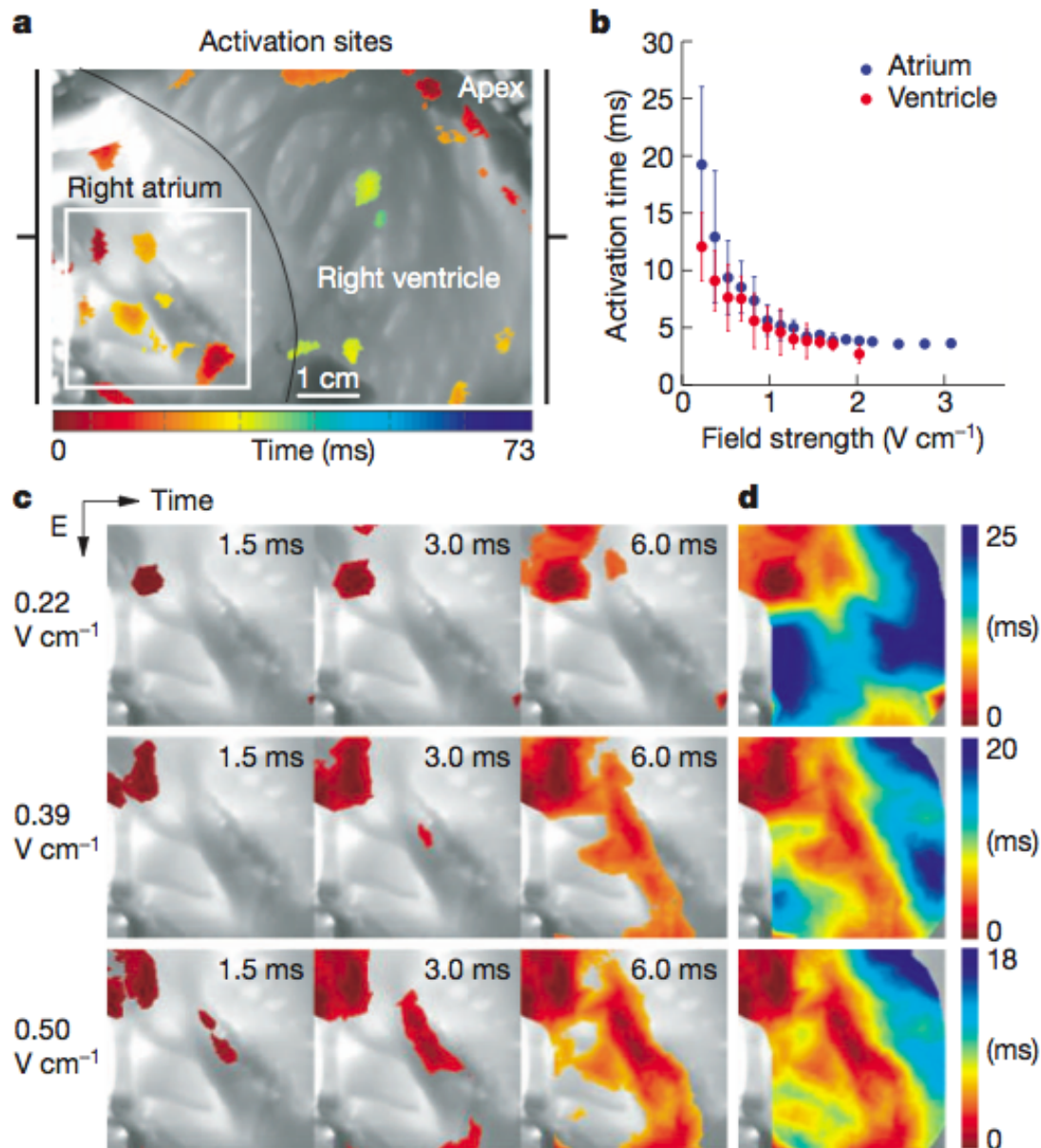


Figure 3.5.2: Sites of activation in a cardiac canine preparation via the LEAP method [181]. After an electric pulse was applied, the time of local activation observed with fluorescence imaging on the endocardium is reported in color indicates mean activation times for atria (blue circles) and ventricles (red circles). With increasing field strength, the number of activation sites increases and the time interval for total activation decreases.

Chapter 4

Cardiac Alternans

The phenomenon known as *alternans* is associated with cardiac tissue electrical activity, and defined as *a beat-to-beat variation in the cardiac action potential duration*. Intracellular calcium alternans events in myocytes have been identified and defined similarly. Cardiac alternans has been shown to be linked to ven-

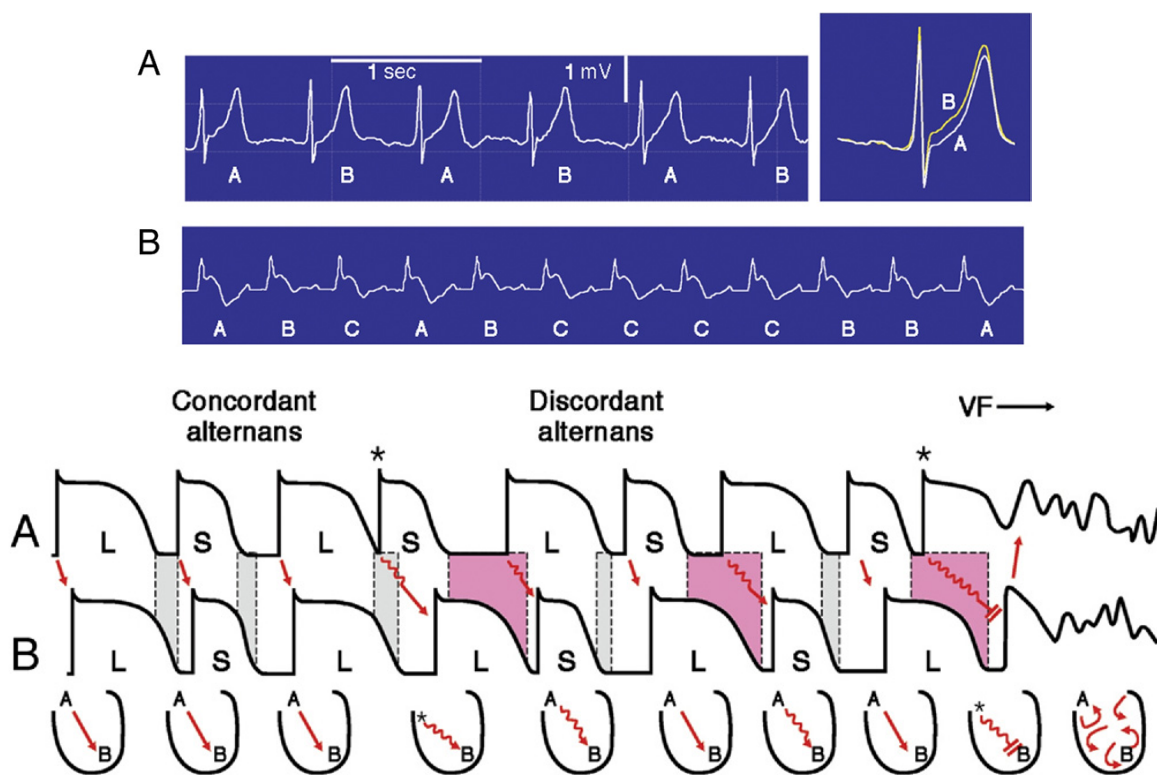


Figure 4.0.1: (TOP) TWA and nonalternating fluctuations [281]. (A) Precordial ECG rhythm strip (left) and high-resolution template of QRS-aligned complexes (right) during routine exercise testing from a patient with coronary artery disease. The template illustrates T-wave alternans (TWA) as a separation between ST-T segments in A and B beats. (B) Nonalternating fluctuations in T-wave amplitude after ajmaline administration in a Brugada syndrome patient. (BOTTOM) Discordant alternans leading to VF. Action potential propagation between two ventricular sites (A to B) is shown with transition from concordant to discordant alternans and development of ventricular fibrillation: shaded areas indicate dispersion of repolarization between sites; * for premature beats; L for long action potential duration; S for short action potential duration.

tricular fibrillation; in particular it desynchronizes depolarization, increases dispersion of refractoriness, and creates a substrate for reentry. Therefore, the ability to predict the onset of alternans could be clinically beneficial. In the following, the main theoretical and experimental procedures devoted to the study, analysis and prediction of cardiac alternans will be introduced. In Chap.(5) then, novel contributions in this direction will be presented.

4.1 Microvolt T-Wave Alternans

T-wave alternans (TWA) is defined as a repeating ABAB pattern in the morphology and amplitude of the ST-segment or T-wave ECG signal [281] (see Fig.(4.0.1) top), and usually named *microvolt* TWA in reason of the small measurable variations in such a pattern. It is recognized as a precursor of ventricular arrhythmias, and observed in a wide variety of clinical and experimental conditions. The primary cause of TWA has been identified in electrical alternans in single cells and small tissue preparations [214]. TWA is sensitive to perturbations in intracellular calcium handling and it is a mechanism of arrhythmogenesis by reflecting and amplifying spatiotemporal heterogeneity of repolarization.

The main character of TWA, and important for the purposes of this work, can be identified in its tight relation with “space”. In fact, TWA can be either spatially *concordant*, when action potentials in neighboring cell regions alternate in phase, or *discordant*, when they are out of phase (see Fig.(4.0.1) bottom). Several clinical and experimental studies have been carried out in order to categorize these properties, thus classify and test the resulting measurements [96]. Collective output, related to the survival curves for prospective TWA studies, are referred to Verrier et al. [281] and references therein.

4.2 Restitution Curves

It has been suggested that alternans onset in cardiac myocytes can be determined by analyzing their response to periodic stimulation, thus constructing a so called *APD-DI restitution curve* [58, 116, 232]. Such a diagram represents the nonlinear relationship between the action potential duration (APD) and the preceding diastolic interval (DI) recorded at a specific location in the tissue.

APD-DI is not the only restitution, in fact *CV restitution curves* are usually posed next to it, plotting the conduction velocity along the direction of propagation of an action potential with respect to the preceding DI. In this second case, spatial-dependent properties, wave-front and wave back velocities (*cm/s*) are extracted. Although the velocity of the wave back is a useful theoretical tool, its measurement is not straightforward. When the wave back velocity is measured in a short cable, electrotonic effects induced by the boundaries can change the curve substantially [44, 125]. Examples of restitution curves are shown in Fig.(4.1.1).

4.2.1 Experiments vs Theory: Intrinsic Complexity

Theoretically, it has been proposed that the slope of a restitution curve can predict the onset of alternans [207]. Experimentally, however, this hypothesis has not been consistently proven, mainly because of the intrinsic complexity of the dynamics of cardiac tissue. Short-term memory effects of cardiac myocytes, as an example, makes a certain APD dependent on the entire pacing history, not just the preceding DI [38, 108, 178]. As a consequence, the restitution curve will depend on the pacing protocol experimentally used to obtain it. The most commonly used ones are:

- *dynamic restitution*: the steady-state APD and DI are measured as the basic cycle length (CL) decreases;
- *S1-S2 restitution*: a premature stimulus (S2) is applied at various times relative to the end of a series of paced (S1) beats.

The restitution curves resulting from the different protocols, indeed, will be different and will present different slopes. Several experimental studies demonstrated the existence of alternans for a shallow restitution, or no alternans was observed for a steep one [123]. Hence, it is widely accepted that individual restitution curves fail to predict the onset of alternans correctly. A direct comparison of experimental and theoretical restitution curves is shown in Fig.(4.2.1).

A more theoretically-based determination of alternans onset has been proposed for periodically paced myocytes, the *downsweep* pacing protocol [274]: it consists of several restitution curves measured simultaneously at various basic cycle lengths, allowing the measure of the restitution portrait (see Fig.(4.2.2)). Quantification of restitution dispersion from the dynamic changes of the T-wave peak to end has been proposed too [221]. This alternative methodology combines ECG signal processing, computational modeling

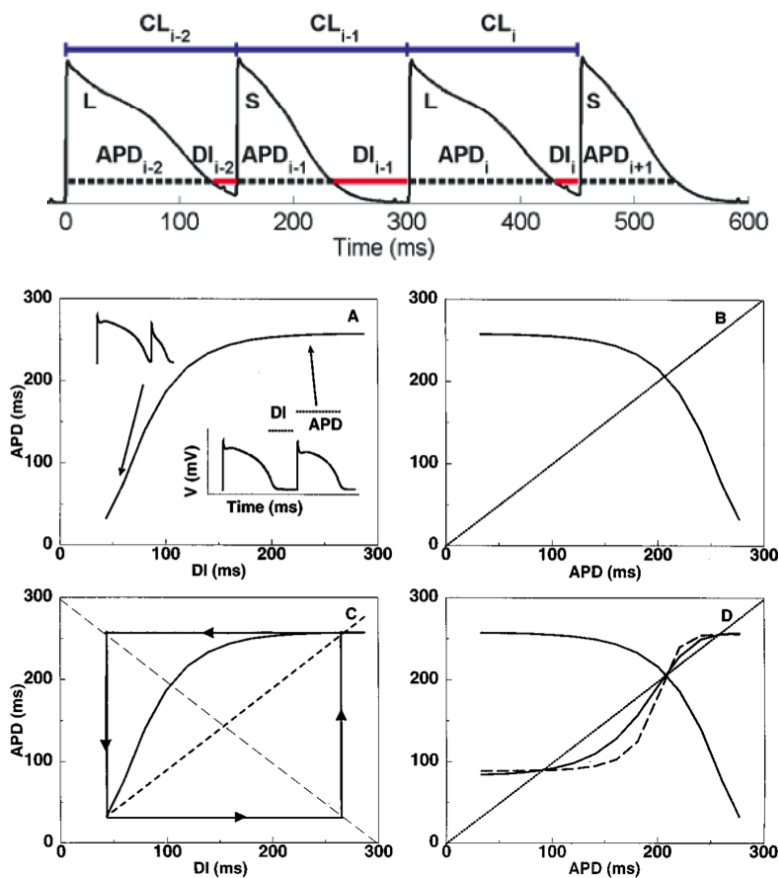


Figure 4.1.1: Constructing restitution curves. (TOP) Measuring of APD and DI from a sequence of action potentials paced at constant CL [42]. (BOTTOM) (A) Action potential duration restitution curve fitted to Beeler-Reuter kinetics, (B) The one-dimensional mapping (transition function) induced by this restitution curve. (C) Graphical construction of the minimum cycle length required for APD dynamics to be given by a one-dimensional map with one action potential per stimulus (no conduction block). (D) The transition function of CL and its twofold (solid sigmoidal curve) and fourfold (dashed sigmoidal) iterates [125].

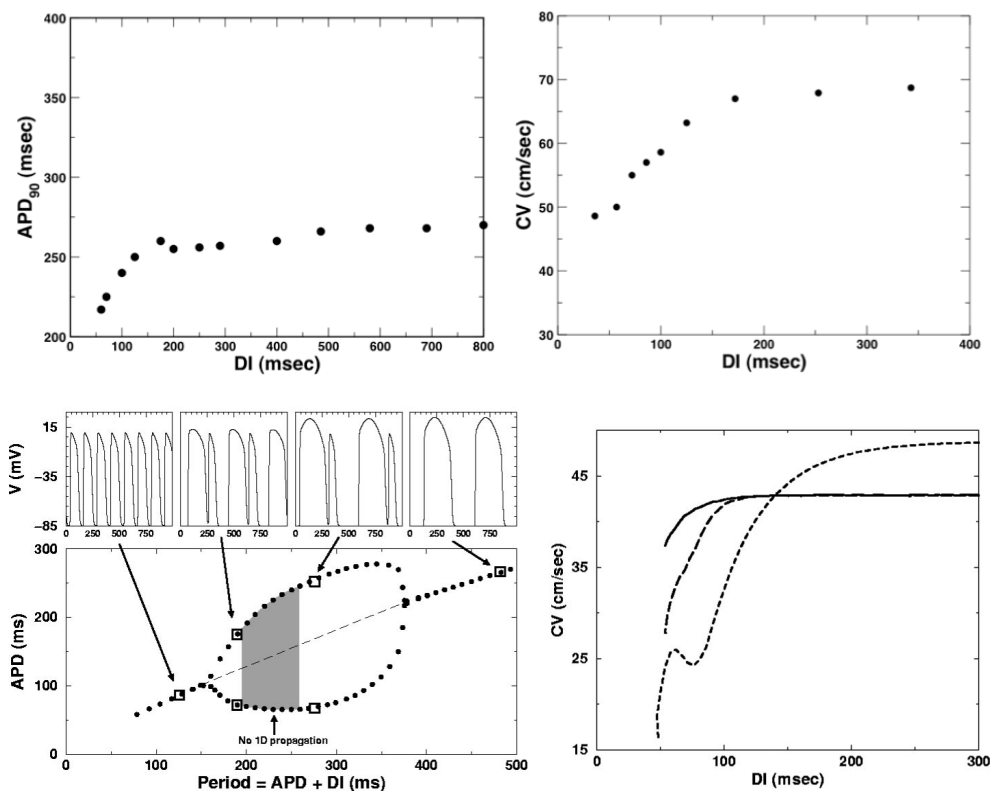


Figure 4.2.1: Experimental and modeling restitution curves in one-dimensional tissues. **(TOP)** Experimental APD-DI [195] and CV-DI [109] restitution curves. **(BOTTOM)** (Left) APD vs. CL with two regions with APD restitution curve slope less than one and consequently two Hopf bifurcations [259]. The inset on top shows the voltage as a function of time for the four cycle lengths indicated by the squares. Stable behavior is observed for the smallest and largest cycle lengths, while APD alternans occurs for the intermediate cycle lengths. The gray area indicates periods for which conduction block occurs in a 1D ring. The 1:1 solution branch (dashed line) exists in this region but is unstable. (Right) CV restitution curve for the wave front (solid line) and wave back (long dashes). At large DIs the slope is less than one, the front and back velocities are the same, but they diverge at small DIs corresponding to the region where the slope of the APD restitution curve is greater than one. The CV is measured at the center of a 1D cable 4 cm long [91].

and simulation. The underlying idea of this approach consists in non invasively quantify the dispersion of APD restitution curves at tissue level by making use of the surface ECG signal. In particular, the pseudo-ECG signal obtained from a two-dimensional ventricular model, is then compared with ECG recordings from control subjects undergoing a tilt test. Nevertheless, these alternative approaches still present several drawbacks which make their use very limitative.

Spatial Complexity

Although the more and more effort applied for the development of these indicators, the emerging dynamics of periodically paced whole hearts are still not completely captured [60]. The main reason can be associated with the intrinsic complexity of the spatial component, not full accessible via restitution curves. The emerging spatio-temporal dynamics, therefore, are still missing, even if they are essential for the study and the correct determination of alternans behavior. The next chapter will be devoted to the analysis and discussion of such a complexity from the experimental point of view, as one of the main topics of this thesis. A direct link between the onset and development of alternans in large mammal ventricles and local synthetic properties of the tissue will be then theoretically pursued.

4.3 Conduction Blocks, Nodes & Nodal Lines

Leaving the zero-dimensional frame, purely temporal, and entering the spatio-temporal one, more rich and complex behavior occur. The basic accepted mechanisms ruling alternans dynamics in space are: *conduction blocks*, *nodes* and *nodal lines*:

- A conduction block forms whenever a wave encounters tissue that is absolutely refractory and fails to propagate.
- A node is identified in one-dimensional domains, as that region in which two consecutive beats present the same APD (the node is not alternating). If a node is present in a 1D cable, then discordant alternans is present.
- A nodal line is identified in two-dimensional tissues, as that line separating regions alternating with opposite phase (discordant alternans as in the 1D case). Along this line the APD change is zero, that is there is no alternans on that line.

Obviously, such classification is not general, in fact, when three-dimensional structures are considered, not alternating regions still separate out-of-phase areas, but become, in this case, “nodal surfaces”. Experimental insight from this point of view will be given in Chap.5. Here, basic examples of discordant alternans structures and hysteresis are discussed.

Discordant Alternans. Spatially discordant alternans in the heart are thought to be formed via a dynamical pattern formation process which does not require tissue heterogeneity [126]. Even though, the high variability in the observed pattern makes mandatory to investigate the role of the substrate on which the pattern is formed or to analyze the dynamical properties of the system as a whole. In this direction, both experimental and numerical studies have been performed, but not complete understanding of the phenomenon has been reached yet [296]. Simulated and experimental examples are reported in Fig.(4.3.1).

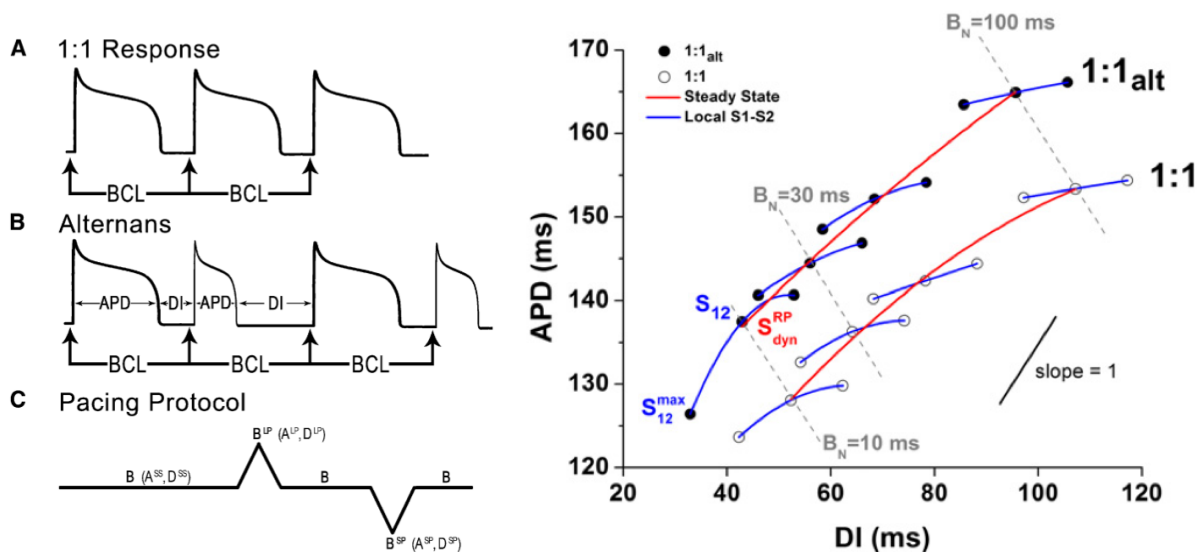


Figure 4.2.2: DownswEEP protocol and restitution portrait [60]. (LEFT) (A) Normal pacing response, (B) alternans response to periodic stimulation, (C) downswEEP protocol. (RIGHT) Representative examples of the restitution portraits constructed from the 1 : 1_{alt} (solid circles) and 1 : 1 (open circles) regions. Steady-state (red) and dynamic restitution curves (blue), over imposed.

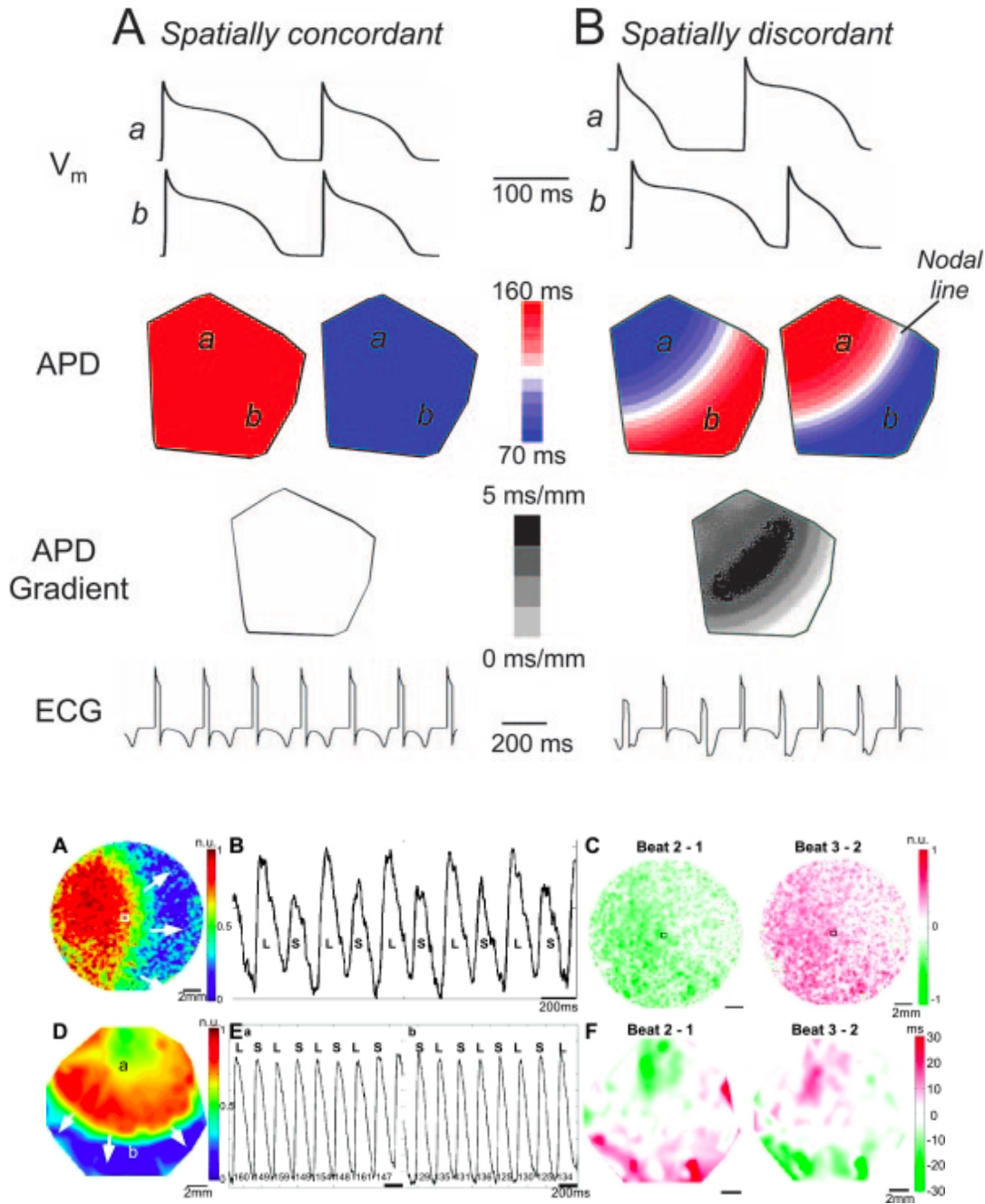


Figure 4.3.1: APD alternans in simulated 2D cardiac tissue [296]. (TOP) (A) Spatially concordant simulated action potentials from sites (a) and (b): both alternate in a long-short pattern. (Second panel) Spatial APD distribution is either long (blue) or short (red for each beat). (Third panel) APD dispersion (gray scale) is minimal. (Bottom panel) Simulated ECG with T wave alternans. (B) Simulated action potentials from site a alternate short-long, whereas at the same time, action potentials from site (b) alternate long-short. (Second panel) Spatial APD distribution, with a nodal line (white) with no APD alternation separating the out-of-phase top and bottom regions. (Third panel) APD dispersion markedly enhanced, with the steepest gradient (black) located at the nodal line. (Bottom panel) Simulated ECG, with both T wave and QRS alternans. (BOTTOM) Calcium and APD alternans [301]. (A) Ca map of paced propagation. (B) Representative Ca transient signal amplitudes. (C) Ca_i alternans map showing spatially concordant alternans. (D) Voltage map of paced propagation in a different monolayer. (E) Representative out-of-phase long-short alternations voltage traces. (F) APD alternans map showing spatially discordant alternans.

Hysteresis Effect. Cardiac alternans has been characterized in its spatial hysteresis effects [289]. Such a behavior is considered an intrinsic property of cardiac myocytes that is directly related to the mechanism for repolarization alternans. It occurs when heart rate exceeds the ability of the cell to effectively cycle calcium and it can be observed both in concordant and discordant regimes. In Fig.(4.3.2) experimental hysteresis effects both in single myocyte and isolated heart are shown. In particular, discordant alternans develops and persists for lower pacing rates.

4.3.1 The Onset of Reentries

Abnormal excitation-contraction coupling properties emerge at different scales in the heart. Beginning with the fundamental protein units, i.e. L-type Ca channels, where behaviors are dominated by randomness, several network of couplons lead to Ca alternans and Ca waves, promoting both reentrant and focal arrhythmias in the heart [297]. The transition from cell to tissue necessitates 1) to define the interaction between action potential and calcium transient at the cellular level, 2) the integration of the resulting coupling at the tissue level, 3) thus producing a new set of properties.

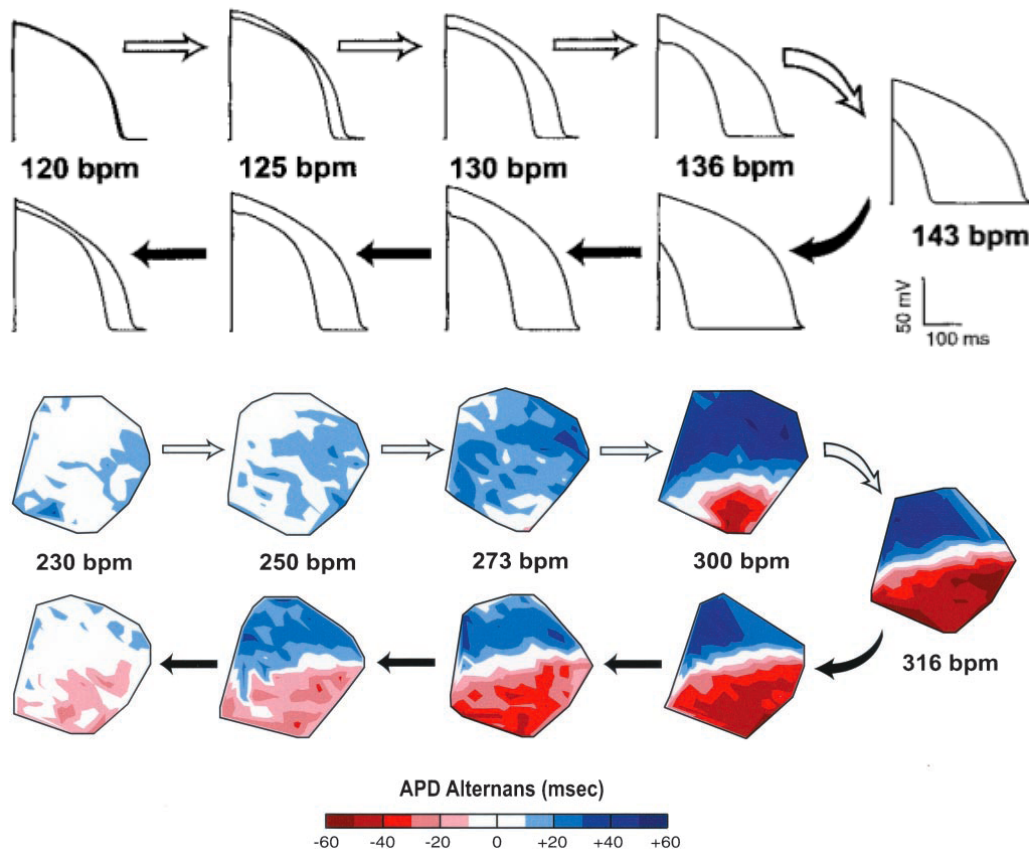


Figure 4.3.2: Alternans hysteresis effect [289]. (TOP) APs recordings from isolated myocyte. Signals from two consecutive beats are superimposed to illustrate APD alternans. During forward pacing (open arrows), alternans develops and increases with rate. When pacing is subsequently reversed (solid arrows), alternans persists at heart rates below those required for its induction. (BOTTOM) Hysteresis effect for discordant alternans. Contour maps showing magnitude of alternans across recording area in isolated guinea pig heart. Areas in blue are out of phase with areas in red (i.e., long-short versus short-long APD sequence). Alternans develops during forward pacing (open arrows). During reverse pacing (solid arrows) discordant alternans persists to rates below the previous onset.

Physiologically useful tissue properties, i.e. the electric wave propagation throughout the conduction system, may lead to undesirable emergent behavior, such as *reentry*: the most common mechanism of lethal cardiac arrhythmias. Electric reentry is not a property of either proteins or isolated cardiac cells; rather, it emerges only at the level of tissue, due to the interaction of cardiac cells with each other. The required factors to initiate a reentry can be summarized as:

1. Premature ventricular complex, i.e. a *trigger* [172].
2. Tissue vulnerability [293]:
 - (a) dispersion of refractoriness promotes unidirectional conduction block;
 - (b) slow conduction allows retrograde wave propagation.

These properties have been compared at the different levels of organization. Discordant alternans onset and development has been experimentally identified as the most dangerous precursor for the genesis of cardiac fibrillation [214] and related to the induction of reentry in simulated cardiac tissue [225] (see Fig.(4.3.3)).

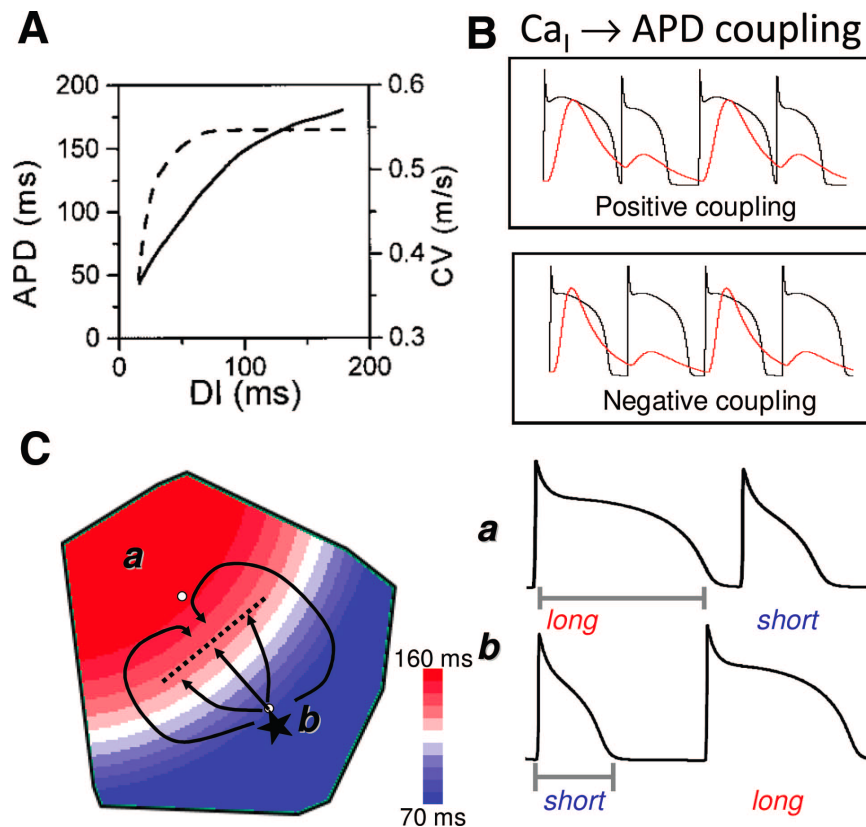


Figure 4.3.3: Electrical restitution, alternans and the initiation of a reentry [297]. (A) APD and CV restitution curves. (B) Coupling between calcium and action potential waves. (C) Discordant alternans and the induction of a reentry.

4.4 Nonlinear Dynamics of Alternans

Although anatomical factors can play a significant role in generating spatially discordant alternans, there is a critical role for instabilities that are dynamically generated [104]. The response of a nonlinear excitable medium, as the heart, to period excitation must be analyzed from different perspectives and scales in terms of alternans events. Briefly:

- APD cellular alternans [207];
- intracellular calcium alternans [69];
- positive or negative AP-Ca coupling [297];
- concordant and discordant alternans in tissue:

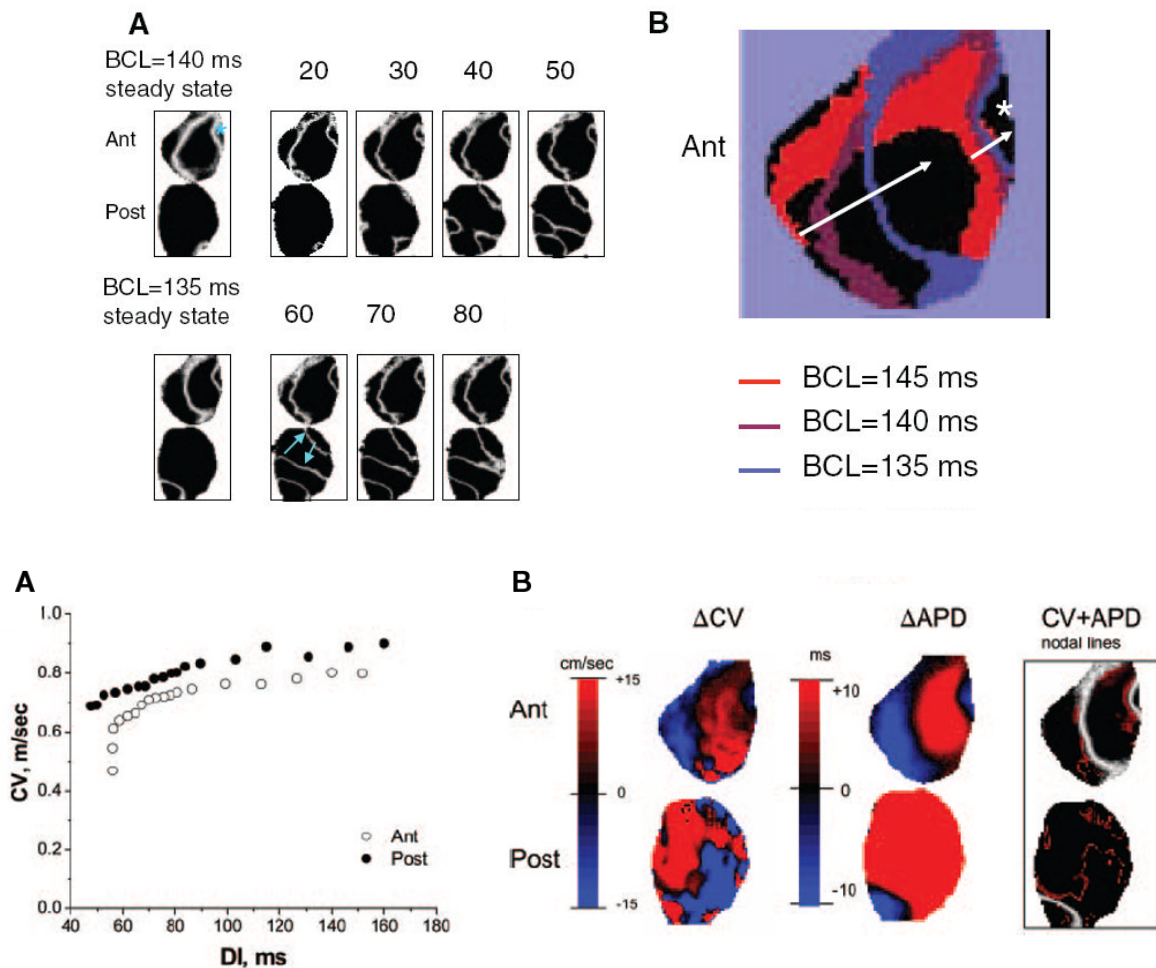


Figure 4.4.1: (TOP) Spatio-temporal evolution of nodal line in the whole heart (adapted from [193]). (A) Temporal evolution of the nodal lines on anterior (Ant) and posterior (Post) surfaces; blue arrows show the direction of nodal line drift as the stimulus number increases. (B) Superposition of the stable nodal lines at steady state for different values of BCLs. The white arrow shows that nodal lines drift toward the pacing site (white asterisk) as BCL decreases. (BOTTOM) CV restitution and alternans (adapted from [193]). (A) Mean CV restitution calculated for anterior (Ant) and posterior (Post). (B) Steady-state alternans maps for posterior and anterior surfaces showing alternans in CV (left), alternans in APD (middle), and superposition of their nodal lines (right). APD (red) and CV (white) nodal lines.

- TWA [281];
- CV restitution [29];
- dynamically generated nodal lines [76].

Although the vast literature, however, the proposed hypothesis and mechanisms have been derived from small tissue preparations. Even if partially confirmed from numerical simulations, such a “rules” do not seem to be still valid in larger mammal hearts, and in more realistic simulations neither. Novel results in this direction will be given in Chap.(5).

4.4.1 Alternans Transitions in the Whole Heart

The behavior of nodal lines has been shown to be crucial in determining the underlying mechanism of spatially discordant APD alternans [126] and thus in reentry initiation. Despite cultured cells or small tissue preparations, nodal line dynamics may present different scenarios in the same whole heart [193]:

1. Nodal lines can remain stationary during pacing at constant rate then move toward the pacing site as the rate increases (associated with a steep CV restitution).
2. Nodal line can be unstable and undergo spatio-temporal evolution, due to the spatial distribution of CV alternans and its strong correlation with APD alternans (associated with short-term memory).

In this condition, concordant and discordant alternans in space have been recognized to present the following characters:

- the onset of spatial alternans is a local phenomenon;
- the transition from spatially concordant to spatially discordant alternans is a time dependent process: after pacing CL variation, the transition does not always occur instantaneously;
- heterogeneity of APD does not correlate with the onset of alternans;
- short-term memory, i.e. dependence of APD on the entire pacing history, might be involved in spatially discordant alternans formation.

In Fig.(4.4.1), examples of whole heart experimental spatio-temporal alternans dynamics confirming the mechanisms are shown.

Chapter 5

Complex Spatio-Temporal Patterns in Cardiac Tissue

Despite the experimental and theoretical knowledge introduced in the preceding chapters, little is known about alternans dynamics in large mammalian hearts. Here, many complex spatio-temporal patterns not previously described in literature are discussed as part of the novel contributions of this dissertation. After a brief introduction about optical mapping techniques, a detailed description of the experimental setup will be given, focusing on the simultaneous recording of electrical activations from epicardial and endocardial surfaces. Then, ad hoc data analysis methods, devoted to optical mapping analysis and developed in collaboration with Prof. Flavio H. Fenton, will be provided. Finally, an extended discussion about the main results and application of the work will be given.

5.1 Optical Mapping Recording of Cardiac Electrical Activity

The concept of mapping rhythmic activation of the heart dates back to the beginning of the last century, to the first systematic mapping of sinus rhythm and then atrial flutter [13, 175]. Initial mapping was primarily performed using single probes to record activation in different regions of the heart. The 1960's and 70's saw the development of computerized mapping of the human heart, as well as a renewed and increasing interest in the usage of Langendorff preparations [75] (introduced in the late nineteen's century). In fact, most of the recent advances in cardiac mapping [226, 278] have focused on: i) improvements in multisite measurements on the surface of the heart, with the ability of synchronous recording electrical activation from several hundreds of locations; ii) calcium transients recordings [201, 169] via novel voltage sensitive protein dyes.

Micro-electrode vs Optical Mapping

Intracellular micro-electrode recordings are still considered the gold standard for action potential measurements. Micro-electrode techniques are limited however, by an inability to record action potentials from several sites simultaneously. Despite recent advances in optical mapping, technical problems are still associated with amplification, gains, sampling rates, signal-to-noise ratio, and the impossibility to see signals during high-voltage shocks [8]. However, in the last few years, the intrinsic limitation of mapping techniques, that is their inability to provide information about repolarization characteristics, thereby lim-

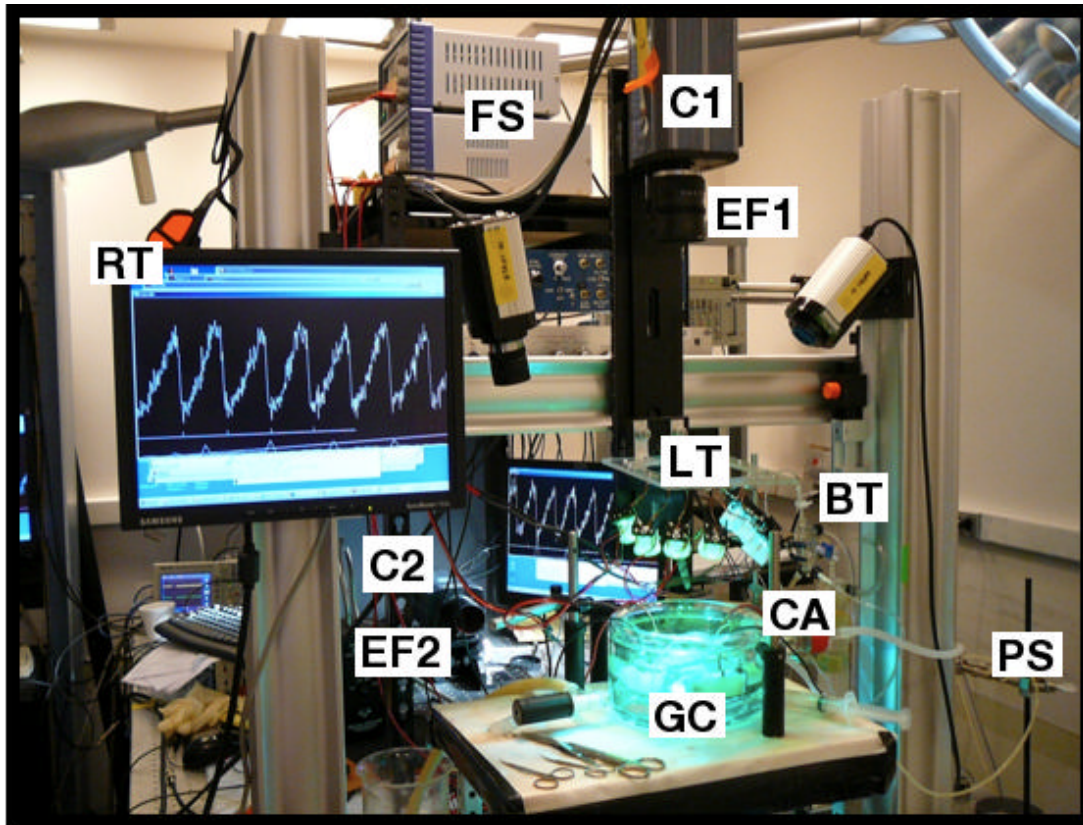


Figure 5.1.1: Optical mapping experimental setup. Cornell University, College of Veterinary Medicine, Gilmour Lab. The main components are labeled: C1, endocardial, C2, epicardial, cameras with emission filters, EF1, EF2, and LT, light lamps for tissue illumination; GC, water-jacketed glass chamber, BT, bubble trap and PS, perfusion system (partial view); RT, real-time monitor visualization of the acquired action potential fluorescence signals.

iting the analysis of entire action potentials, has been improved thanks to the development and use of voltage-sensitive dyes as a means to map not only activation, but repolarization as well. The optical signal allows the visualization of both activation and recovery processes in any region under view. This allows one to precisely evaluate the propagation of an excitation wave and to measure its wavelength visually.

Voltage-Sensitive Dyes and Photodetectors

Optical mapping techniques use imaging devices such as a photodiode array or a charge-coupled device (CCD) video camera with the heart being illuminated and either continuously or spatially scanned. The basis for these techniques is the use of voltage-sensitive dyes: molecules that bind to the cell membrane with high affinity. While bound to the cardiac cell membrane, the dye molecules fluorescence light in direct proportion to transmembrane voltage. Therefore, voltage-sensitive dyes become highly localized transducers, transforming a change of membrane potential into a change in fluorescence intensity. In fact, for any given constant excitation light intensity and wavelength, light is emitted over a range of wavelengths (emission spectra) that changes with membrane potential (see Fig.(5.1.2)A). A suitable filter then passes light only above a certain wavelength, and the precise shape of the emission spectra (and therefore the optical action potential) does not correspond to any absolute voltage (only a relative potential change is detected). The fractional change of the light collected in the camera is typically 2 – 6%.

The most common excitation light sources are tungsten-halogen lamps, mercury arc lamps and argon

ion lasers. The source of each optical action potential is derived from few to hundreds of cardiac cells, depending on the extent of optical magnification used. Therefore, a single optical action potential represents the average potential from a small aggregate of neighboring cells. High-quality images can be acquired with a microscope or with photographic lenses.

Photodiode arrays and charged coupled device (CCD) video cameras are the most widely used photodetectors: they transduce light energy into electricity via the photoelectric effect³. Photodiode arrays typically consist of several hundred individual photodiodes, and are configured to instantaneously convert photo-excited charge carriers to current flow (i.e. photocurrent). The magnitude of photocurrent is directly proportional to the light intensity falling on a single photodiode element, and is converted to a voltage signal using a current-to-voltage amplifier. A major advantage of a photodiode array is that it generates photocurrent in response to membrane potential changes continuously, allowing high sampling rates. The only drawback is the limited amount of photodetectors on the array, typically 256 or less. CCD camera can contain hundreds of thousands of pixels, permitting a greater spatial resolution between recording sites: photo-excited charge carriers are collected within a single pixel over a finite period of time (integration time), and are read off at regular time intervals (i.e. the frame rate). Readout time is a major factor that limits the sampling rate of CCD systems. However, because of a larger number of recording sites, CCD detectors are better suited for mapping larger preparations at low magnification.

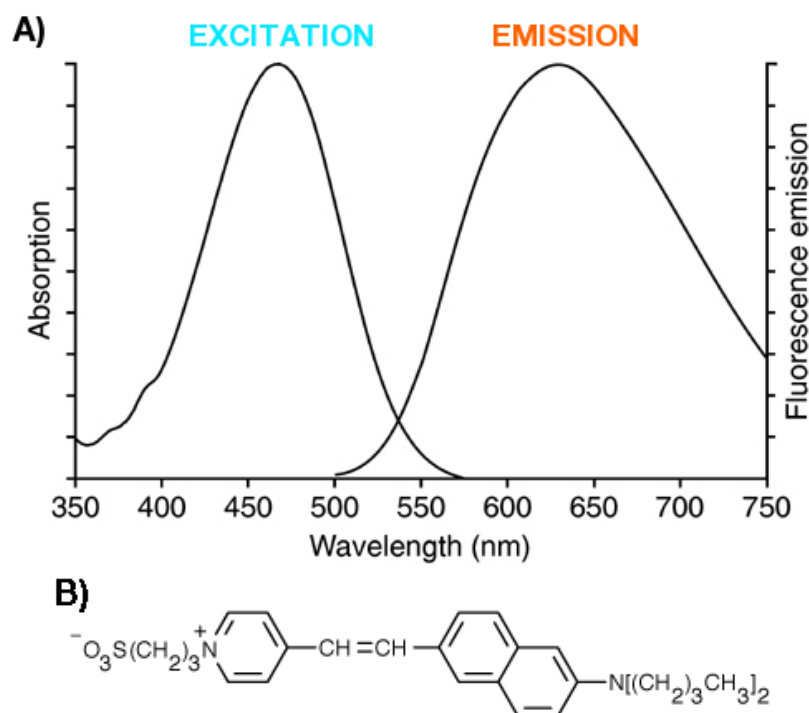


Figure 5.1.2: (A) Absorption and fluorescence emission spectra of ANEP bound to phospholipid bilayer membranes [152]. (B) Chemical structures of Di-4-ANEPPS, with molecular formula $C_{28}H_{36}N_2O_3S$, and molecular weight equals to 480.66. The CAS Name/Number is: Pyridinium, 4-(2-(6-(dibutylamino)-2-naphthalenyl)ethenyl)-1-(3-sulfopropyl)-, hydroxide, inner salt/ 90134-00-2.

5.2 Experiments Design and Implementation

A global view of the optical mapping laboratory adopted for the experimental recordings here discussed is shown in Fig.(5.1.1). The experimental apparatus, in toto, and the different setup, in particular, have been specifically designed and optimized for electrical activation waves recordings and alternans experiments.

5.2.1 Tissue Preparation

Tissue samples have been obtained from adult beagle dogs of either sex ($n = 9$), age 1–4 years. Animals were anesthetized with Fatal-Plus⁴, their hearts were rapidly excised via a left thoracotomy and placed in cold, aerated (95% O₂–5% CO₂) normal Tyrode solution⁵. In the following 20 minutes, three sequential operations were rapidly performed: 1) the right ventricular myocardium chamber was excised; 2) the right coronary artery was cannulated with polyethylene tubing; 3) the tissue was clamped opportunely in order to provide an optimal perfusion.

The preparation was then suspended in a heated transparent water-jacketed glass chamber. It was both perfused with a constant flow rate of 25 ml/min and super-fused with normal Tyrode solution by that artery. The choice of perfusing at constant flow rate is equivalent to a pressure control method, in the range of 50 ÷ 80 mm Hg, but allows a better timing of the overall experiment.

After 20 to 30 minutes of equilibration at physiological temperature ($37.0 \pm 0.5^\circ C$), the preparation was stained with the voltage-sensitive dye Di-4-ANEPPS (10 $\mu mol/L$ bolus). The choice of ANEP dyes⁶ as fluorescence molecules is due to their fast-response to a change in the surrounding electric field, with a 2 ÷ 10% fluorescence change per 100 mV, and a fluorescence excitation/emission maxima bound (for Di-4-ANEPPS) in the range 475 ÷ 617 nm (see Fig.(5.1.2)). Their optical response is sufficiently fast to detect transient (millisecond) potential changes; furthermore, these dyes display a potential-dependent shift in their excitation spectra, thus permitting the quantitation of membrane potential using excitation ratio measurements. Moreover, Di-4-ANEPPS is rapidly internalized in the cell ($\sim 15 min$), precluding its use in all but very short-term experiments.

Blebbistatin (10 $\mu mol/L$ constant infusion over 30 to 40 minutes) was added to prevent motion artifact [87]. All experimental procedures were approved by the Institutional Animal Care and Use Committee of the Center for Animal Resources and Education at Cornell University.

5.2.2 Optical Mapping Setup

A schematic flowchart of the main components of the optical mapping setup is shown in Fig.(5.2.1). The diagram indicates the tissue position and cannulation within the water-jacketed chamber. Both the perfusion system and the thermal bath are connected to an heater allowing an accurate temperature control of the overall apparatus (constant temperature monitoring was also performed in order to ensure an optimal thermalization). The illumination system, placed both on top and bottom of the tissue, together with the cameras alignment are specifically designed for synchronous recording of endocardial (top) and epicardial (bottom) surfaces. In particular, a first surface mirror is positioned below the tissue chamber and is directed towards the bottom camera. In Fig.(5.2.2), a sequence of pictures from the optical setup are shown illustrating the position and connection of the main components discussed.

Perfusion System. The perfusion system, Fig.(5.2.1) and (5.2.2)A-D, consists of a peristaltic pump directing the tyrode solution at constant flow rate towards the tissue via a heating coil and a bubble trap. This allows a continuous control of the delivered solution avoiding the presence of air bubbles, which would

lead to embolisms of the tissue. A heater is connected both to the bubble trap and the water-jacketed chamber in order to make a closed circulatory system, which allows the accurate temperature control of both the tissue and the perfusate.

Illumination-Recording System. The illumination system is shown in Fig.(5.2.1) and (5.2.2)E. Excitation light was provided by high-performance light-emitting diodes (Luxeon III star, LXHL-FM3C, wavelength 530 nm), nine for the top view and nine for the bottom view, driven by a low-noise constant-current source. The illumination efficiency was significantly enhanced by collimator lenses (Luxeon, LXHL-NX05). The epicardium and endocardium were imaged simultaneously using two synchronized cameras. The fluorescence emission light was collected for each camera by a Navitar lens (DO-2595, focal length 25 mm , $F\# 0.95$), passed through a long-pass filter ($< 610\text{ nm}$), and imaged by a 128×128 back-illuminated

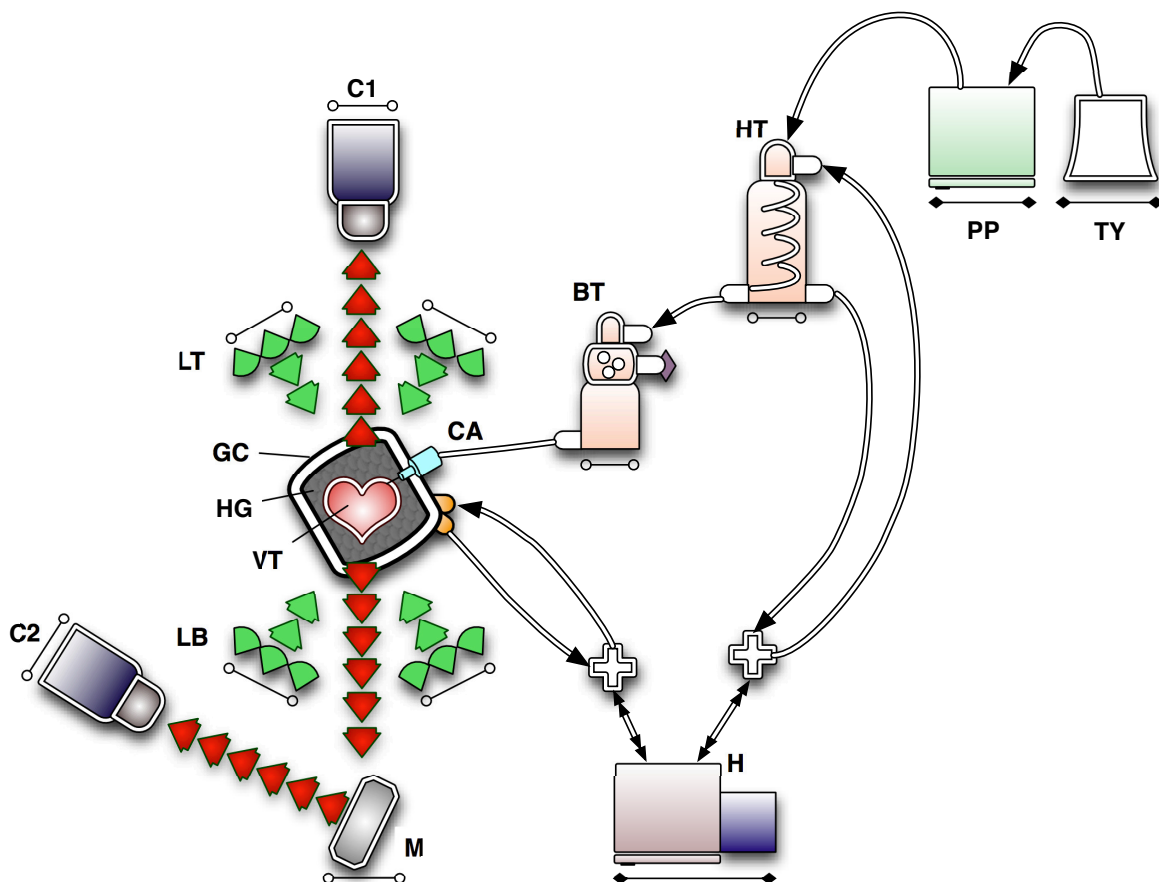


Figure 5.2.1: Schematic diagram of the optical mapping setup designed for alternans recordings. In the figure the main components are reported and specifically labeled. Ventricular tissue, **VT**, specimen is cannulated via the right coronary artery with a plexiglas syringe cannulation, **CA**, it is fixed through an holding grid, **HG**, and contained into a glass chamber, **GC**. The tissue is directly illuminated with selective light lamps from the top, **LT**, and the bottom, **LB**. The light emitted from the tissue is directly captured by a top camera, **C1**, for the endocardial surface, and via a directional mirror, **M**, by a bottom camera, **C2**, for the epicardial surface. The lenses of both cameras are equipped with an emission filter **EF1**, **EF2**. The perfusion system supplies the tissue with oxygenated tyrode solution, **TY**, using a peristaltic perfusion pump, **PP**. The tyrode is continuously dribbled in a bubble trap, **BT**, in order to avoid the presence of any gas bubbles which could lead to embolisms. Both the glass container and the cannulation are water jacketed for accurate temperature control using a heat bath, **H**.

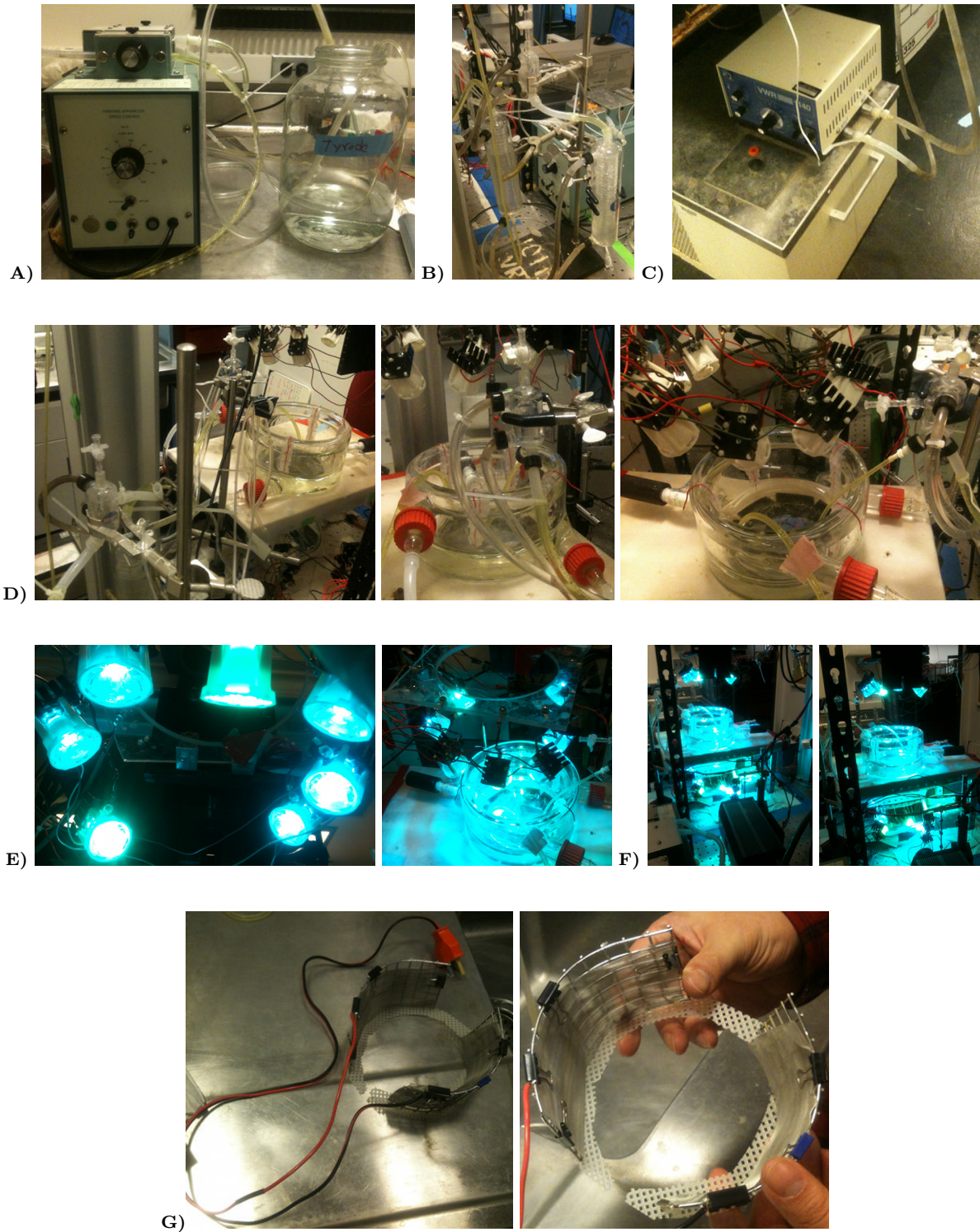


Figure 5.2.2: Pictures of the main components of the optical mapping setup. Cornell University, College of Veterinary Medicine, Gilmour Lab. (A) Oxygenated tyrode solution and the peristaltic pump. (B) Perfusion system with bubble trap. (C) Heat bath. (D) Water-jacketed tissue chamber from different perspectives, together with the multiple connections of the perfusion and heating system. (E) Light emitting diodes with collimating lenses providing the excitation light (from top and bottom). (F) Picture shows the alignment of cameras for epicardial (top) and endocardial (bottom) imaging. (G) Detail of the holding grid for tissue fixing and stimulation.

electron-multiplied charge-coupled device array (Photometrics Cascade 128+) with a high quantum efficiency (peak QE > 90%). The signal was digitized with a 16-bit analog/digital converter at a frame rate of 511 Hz (full frame, 128×128 pixels) with a spatial resolution of $600 \mu\text{m}$ per pixel for a grid size of $7.7 \text{ cm} \times 7.7 \text{ cm}$. The peripheral component interconnect interface provided high-bandwidth uninterrupted data transfer to the host computer. The instantaneous dominant frequency of an arrhythmia was obtained in real time by calculating the fast Fourier transform of the signal recorded from 1 pixel in the center of the preparation. The description of data analysis will be deferred to the following paragraphs describing a custom built Java program with interactive tools for visualization, segmentation, filtering and storage.

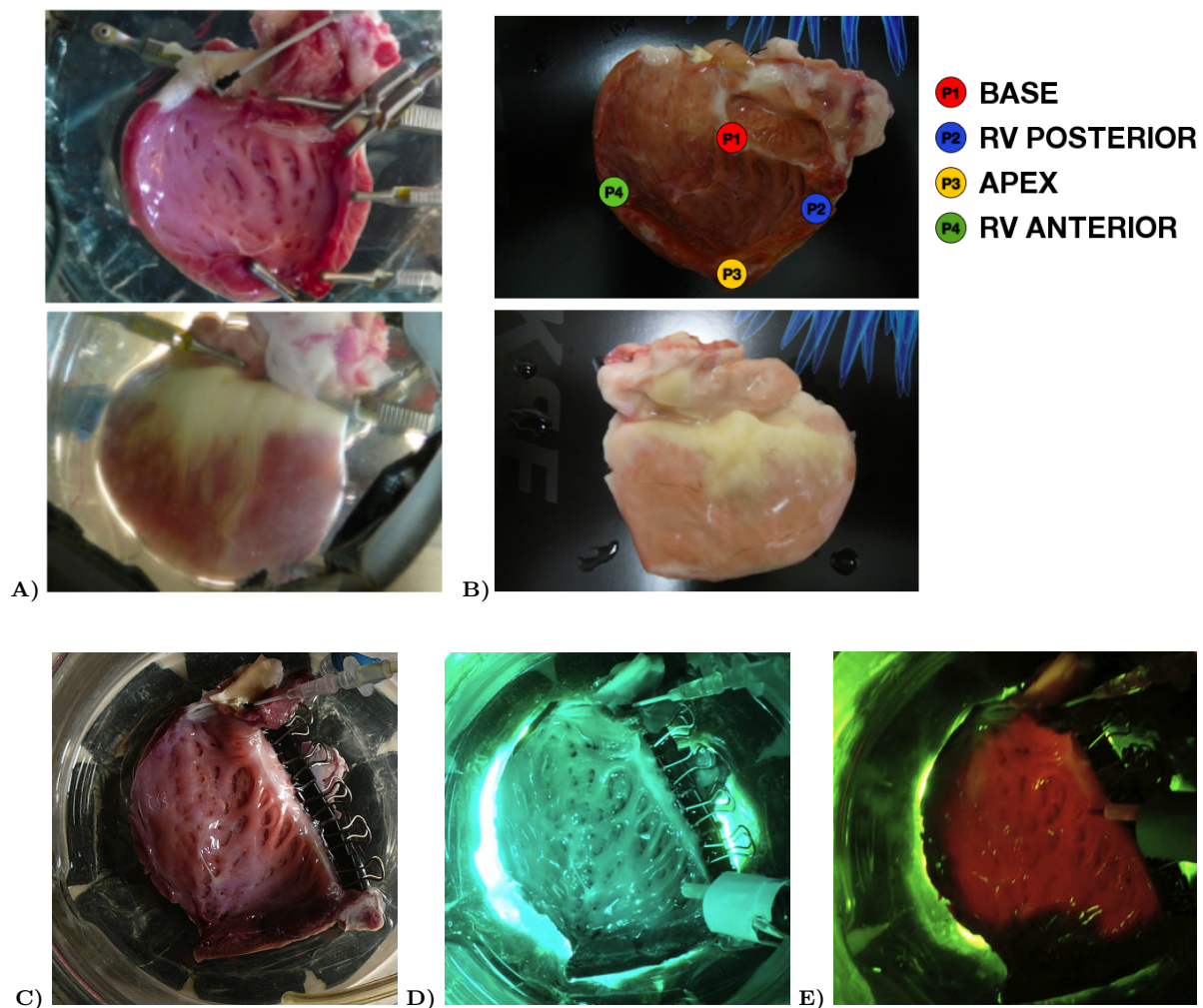


Figure 5.2.3: Representative example of tissue preparation: (A) canine right ventricle in the thermal bath with cannulation in endocardial (top) and epicardial (bottom) views; (B) frozen tissue with pacing sites locations on the endocardial surface: P1, base, P2, RV posterior, P3, apex, P4, RV anterior. Tissue illumination and emission: (C) natural light view; (D) illuminated tissue at 530 nm ; (E) infrared tissue light emission.

5.2.3 Stimulation Protocol

In Fig. (5.2.2)(G), the holding grid and the pacing electrode are shown. Platinum stimulating electrode has been used to pace the right ventricles from the endocardial surface. Data were recorded in episodes lasting between $6 \div 20$ s, always ensuring that stable propagating waves were been reached. Three different *temporal pacing protocols* were applied:

1. **Pacing-down (P) protocol.** Twice diastolic threshold current pulses were applied with the pacing cycle length (CL) starting from 550 ms and decreasing of 50 ms until reaching 250 ms after which the CL was shortened in 10 ms increments until capture was lost or VF was induced. At each CL, pacing was applied for $6 \div 15$ s.
2. **Quiescent (Q) protocol.** Twice diastolic threshold current pulses were applied at constant CLs of 220 , 200 , 160 , 150 , 110 and 100 ms for 20 s every 20 s of rest, in which the tissue has been left with no stimulation.
3. **Constant (C) protocol.** Twice diastolic threshold current pulses were applied at fixed CLs for 20 s, followed by cessation of pacing for 20 s during which the tissue returned to quiescence, thus repeating these two steps for about 20 min, for a total of about 30 repetitions.

Two different *spatial pacing protocols* were applied for each of the two temporal protocols. In one case the pacing electrode was fixed at the same anatomical position on the endocardium. In the second case the pacing electrode was posed in four orthogonal anatomical positions on the endocardium: base (P1), RV posterior (P2), apex (P3) and RV anterior (P4). A representative tissue preparation with pacing positions is shown in Fig.(5.2.3)B.

5.3 Data Analysis

The full experimental set of measurements comprised 1362 recordings (from 9 tissue preparations) and data analysis was performed through ad hoc interactive Java toolboxes. Such an amount of video data, consisting of several hundreds of Gbytes, would have not been analyzed in detail without the usage of a very flexible and interactive software, as the one described in detail in this paragraph. In particular, the main filtering algorithms and step analyses are discussed.

5.3.1 Ad Hoc Interactive Java Tools

One of the main result of this work consisted in implementing ad hoc codes for optical mapping data visualization and analysis. Starting from a FORTRAN implementation, the choice was finally directed towards the Java Runtime Environment with a direct coding of the Java Virtual Machine. The flexibility of the code, the direct access to reading and writing protocols, together with open access interactive tools, made the resulting software extremely useful not only for the purposes of this thesis, i.e. optical mapping data, but for a broader class of data analyses. Code architecture can be summarized as:

- 8 thousands lines code (50 buttons, 25 checkboxes, 50 text fields, 50 global matrices).
- 18 public subroutines: “static tools” for calculating properties, plotting, printing, saving, and “interactive tools” for dragging, scaling, zooming, moving.

- 28 internal subroutines: for signal drifting, normalization, time and space averages, identification of the region of interest as well as zooms, calculations of the local (APD, DI, averages, etc.) and global (CV, alternans percentage, mean values, etc.) properties of the tissue.

A screenshot of the running software interface is shown in Fig.(5.3.1). In Fig.(5.3.2), a flowchart diagram with the many different implemented actions is given. The most interesting characters of this software can be found in its extreme flexibility (visualized as shaded arrows in the scheme) and visualization tools:

- it is possible to load different kind of file types and video dimensions, i.e. there is no restriction about the space and time scales and durations;
- it allows to perform different operations several times, such as “time-average”, “space-average” or “signal drifting” as an examples, fine tuning the algorithm parameters, i.e. Gaussian variance, shifting frequency, etc.;
- it does not impose any fixed sequence of actions, allowing a tunable and personal analysis methodology depending on the data type;
- it allows the calculation of many different signal properties, as well as to save movies, images, phase patterns and APD-DI distribution at any time of the analysis;
- finally, its visualization tools allow to compare the signal analysis at different steps (thus maintaining in memory all the necessary information):
 - stop/resume forward/resume backward movies or APD spatial distribution sequences;
 - visualize APD-DI restitution distribution, mean values (also in case of alternating signals) and error bars;
 - zooming in and out on both the signal and the distributions;
 - plotting the single pixel time evolution during a movie and selecting in real time different kind of pixel or signals;
 - etc.

Methods of Analysis: Filtering and Removing Signal Drift. Starting from an initial display settings, the operator can choose which kind of data to study. If the signal has not been analyzed before, four automatic processes are performed. In particular:

1. the data type is converted in *short* format, described by 16 Bit and ranging over $-32.768 \div 32.767$, thus obtaining the “original” signal on which the analysis is applied (Fig.(5.3.3) A);
2. the casual saturation of the camera, due to the limited number of dedicated bytes (as stated before), is corrected recovering the right time sequence, thus “unwrapping” the signal as (Fig.(5.3.3) B):

```

if ((int)( Math.abs(max[i][j] - min[i][j]) ) > 30000 ){
    for (int k = 10; k < (ntimes - 10); k++) {
        u[i][j][k] = (short)(u[i][j][k] - 20000);
        unwrapped[i][j][k] = u[i][j][k];
    }
}

```

where “max” and “min” represent the maximum and minimum values of the signal in a given pixel, “u” is the matrix of the original signal and “unwrapped” the resulting unwrapped one. As it can be noted, if the saturation condition holds, the signal is subtracted of a fixed amount of 20.000 in order to recover the right sequence.

3. the unwrapped signal is averaged in time on a 7 pixel basis (3 forward and 3 backward) (Fig.(5.3.3) C);
4. the signal is conveniently normalized on a pixel-by-pixel basis in the range $0 \div 10.000$ (Fig.(5.3.3) D). This choice is suitable for subsequent calculation purposes, but it is important to note that the chosen normalization range does not affect the result, being a simple rescaling of the data.

The process of obtaining an optimal analysis can be then summarized in the following automatic, semi-automatic and interactive steps:

- The operator interactively defines the so called “mask”, i.e. the area imaged by the camera not part of the tissue, in order to avoid not useful and misleading calculations. In fact, any subsequent analysis is not performed for the selected pixels.
- The analysis continues with a symmetric weighted Gaussian space average. In particular the operator can choose the weighting coefficient, w^2 , in the range $4 \div 8$, representing the variance over the neighbor pixels:

$$G(x, y) = A \exp \left[\frac{-\left((x - x_0)^2 + (y - y_0)^2\right)}{2w^2} \right],$$

and $A = 9000$ has been held fixed.

- A major and well known problem in analyzing optical mapping data consists in removing the signal drift (see Fig.(5.3.4)). In the present code, a dedicate algorithm has been developed to perform such a task. In detail:
 1. the operator chooses a reference frequency, F ;
 2. the code evaluates the relative minima for each single range of the signal, $[n \cdot F; (n + 1) \cdot F]$, for $n \geq 0$;
 3. the code performs a linear interpolation of the relative minima building a piecewise “shifting” line;
 4. if the piecewise line is not well defined the operator can start back from point 1;
 5. if the piecewise line is well defined the code subtracts the piecewise line from the signal, thus removing the signal drift;
 6. if the signal drift is not appropriate the operator can start back from point 1.
- Finally, the operator interactively defines the time interval (indicated as ROI, region of interest) over which evaluates all the interesting signal properties.
- As represented by the shaded arrows in Fig.(5.3.2), any of the analysis step can be repeated several times or exchanged in the most suitable order which can lead to the best signal analysis.

Once the filtering has been correctly performed, signal properties can be extracted, visualized and saved. In particular, action potential durations and diastolic intervals, APD and DI, can be automatically evaluated choosing the appropriate threshold: a common choice is usually to take a threshold in the range $25 \div 30\%$ of the repolarization. This variability depends upon several factors related to the optical measurement (gain, illumination, frames, etc.), but also on the pacing cycle length. In fact, at high pacing frequencies, tissue repolarization can not be fully recovered, thus requiring a small increase in the threshold value.

This and several others not unexpected effects (i.e. motion artifacts), make the optical mapping analysis not fully automatable, requiring a careful inspection by the operator. This has been the main reason why the presented data analysis procedure has been implemented in the Java language, supplying several control tools and providing a user friendly and very flexible interface. In this regard, as stated before, the possibility to perform repetitive and not constraint actions helps the operator towards an optimal signal filtering.

Measuring Signal Properties: Alternans Phase Definition. To determine the temporal distribution of APD alternans across the mapped field, the difference between two consecutive APDs was computed as:

$$\Delta\text{APD}(x, y)_n = \text{APD}(x, y)_{n+1} - \text{APD}(x, y)_n \rightarrow \begin{cases} |\Delta\text{APD}(x, y)_n| > 2\text{ms} & \text{Alternans (RED - BLUE)} \\ |\Delta\text{APD}(x, y)_n| \leq 2\text{ms} & \text{Nodal line (WHITE)} \end{cases} \quad (5.3.1)$$

where n denotes the beat number, and $\text{APD}(x, y)$ is the duration of the action potential at a pixel in position (x, y) in the 2D mapped field. Due to our temporal resolution, 2ms , tissue has been defined as non-alternating when $\Delta\text{APD}(x, y)_n$ was less than -2 or greater than 2ms , and as alternating otherwise. Such a choice, considering a time interval double of the frame rate (4ms), induces an accurate distinction between alternating and non-alternating regions. Nevertheless, an interpolating procedure is further performed in order to select the correct threshold timing, thus leading to an even more robust and accurate definition. This methodology has been previously adopted by Fenton and Karma [88], and a representative case extracted from the Java interface is shown in Fig.(5.3.3).

The phase of alternans was defined negative for short-long APD sequences (blue scale) and positive for long-short APD sequences (red scale). Nodal lines were defined as areas separating out-of-phase regions of discordant alternans in which the amplitude of alternans was below the described threshold. Two-dimensional alternans maps were constructed to explore the spatial distribution of the amplitude and phase of the alternans. The onset of alternans (both concordant, CA, or discordant, DA) in tissue was defined separately between endocardial and epicardial surfaces, as the CL at which at least 5% of the surface pixels displayed APD alternans greater than 2ms . The local CV was only measured in the direction of the propagation wave through the distributions of activation times for spatial regions of 7×7 or 8×8 pixels and fitted with the plane.

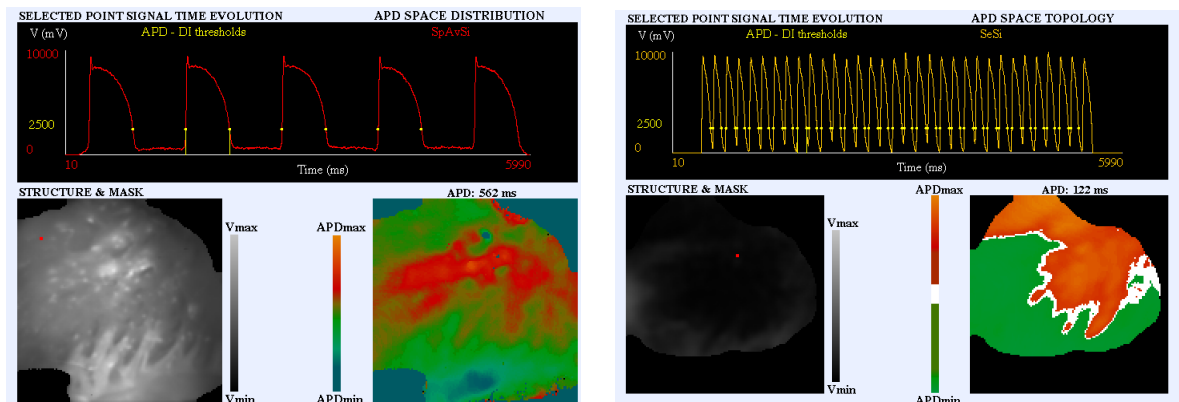
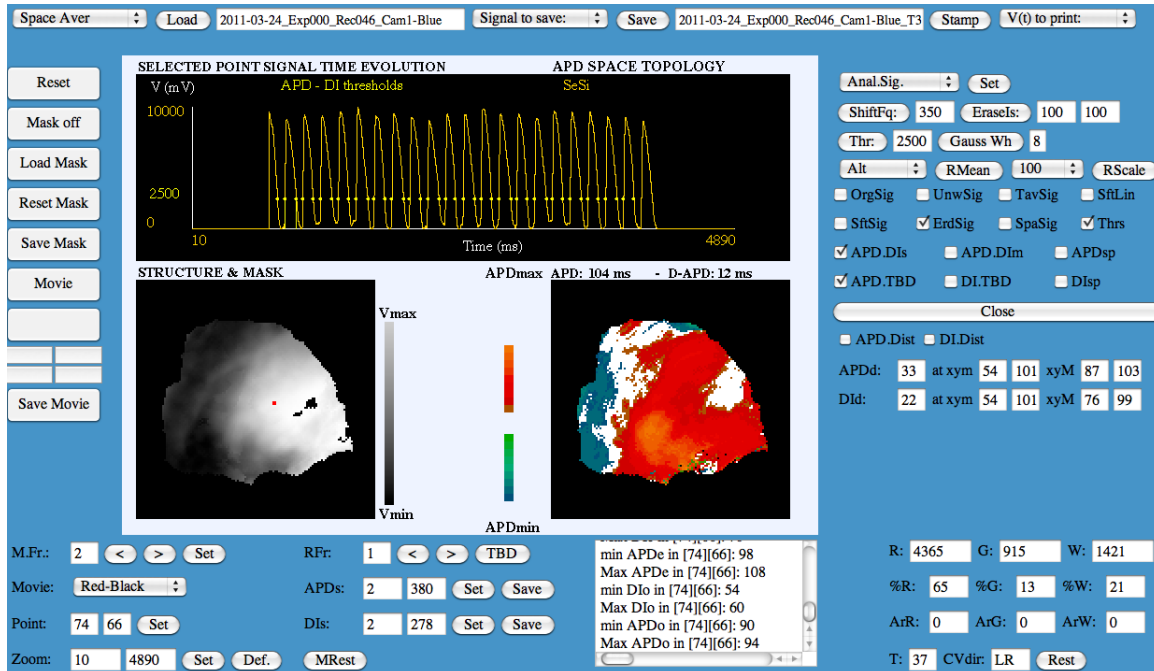


Figure 5.3.1: (TOP) Representative screenshot of the Java running software on a Mac OS X 10.7.2. Most of the buttons, text fields and text boxes are shown. The analyzed signal in time (top), the tissue structure (left) and the spatial pattern of alternans (right). In this case discordant alternans is present in the tissue: blue-scale short-long, red-scale long-short phases. (BOTTOM) Selected screenshot showing (left) a non-alternating regime with highly delineated action potential shapes, and (right) an alternating regime in which a nice spatial patterns can be seen.

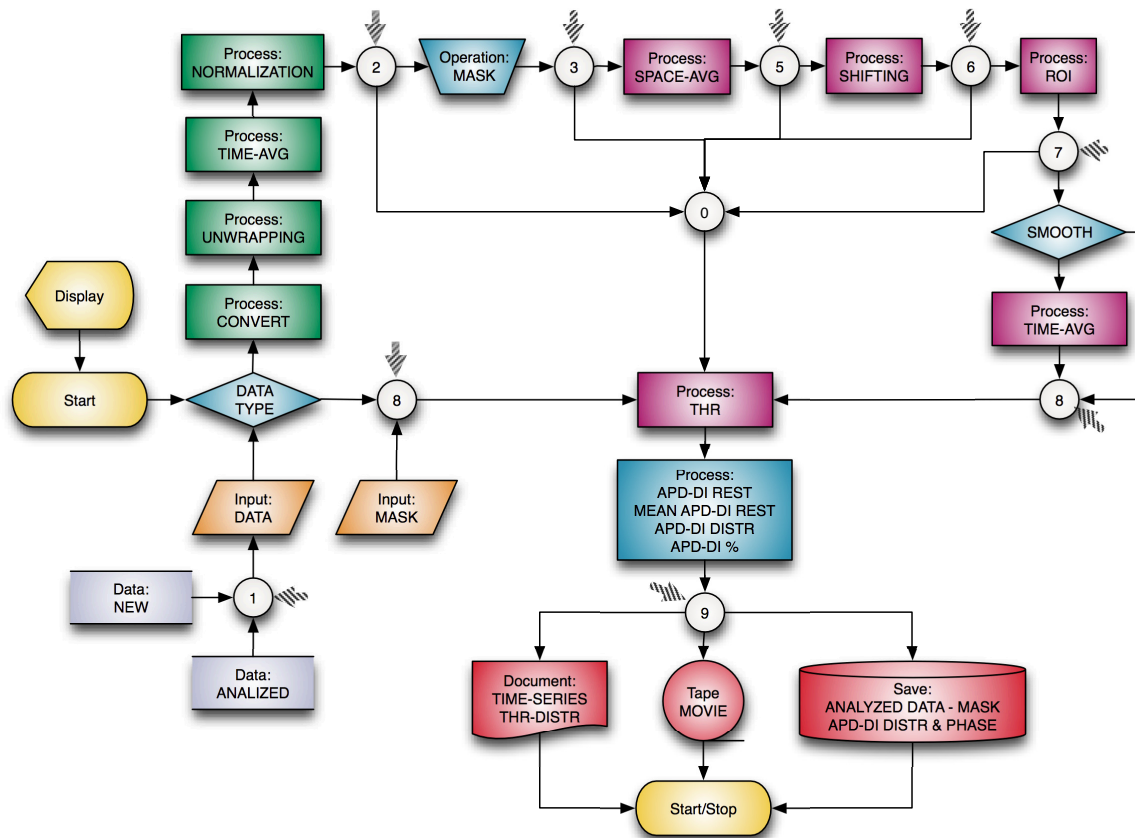


Figure 5.3.2: Flowchart of the developed Java software for optical mapping data analysis. The orange start/stop and display blocks enable display settings and analysis. Gray blocks for data loading allows two different routes depending on the data-type. Not analyzed data undergo four automatic operations: *i*) conversion of the data to *short-type* (CONVERT); *ii*) correction of camera saturations (UNWRAPPING); *iii*) time-averaging (TIME-AVG); *iv*) normalization (NORMALIZATION). The analysis process is then performed as: definition of the mask (interactive, MASK); tuning of the de-drifting parameters (SHIFTING); definition of the time range of interest (ROI). The process continues performing the space average of the signal (SPACE-AVG). At point 7 the signal can be used to evaluate the time-series of threshold (THR) at 25% of repolarization (or tunable), automatically calculating: *i*) restitution (APD-DI REST), *ii*) mean values (MEAN APD-DI REST); *iii*) distribution of APD, Δ APD, DI and Δ DI in space (APD-DI DISTR); *iv*) percentage of pixel in a certain state (APD-DI %). From point 8, the procedure is unique. Several different saving methods are implemented: printing the signal (Document: TIME-SERIES, THR-DISTR); displaying or saving movie (Tape MOVIE); saving analyzed data, mask, APD and DI distribution and alternans patterns (Save: ANALYZED DATA - MASK, APD-DI DISTR & PHASE). The dashed arrows indicate all the insertion points in which the operator can come back several times to the analysis. Similarly, the points 0, indicate the possibility to access the threshold evaluation at any time.

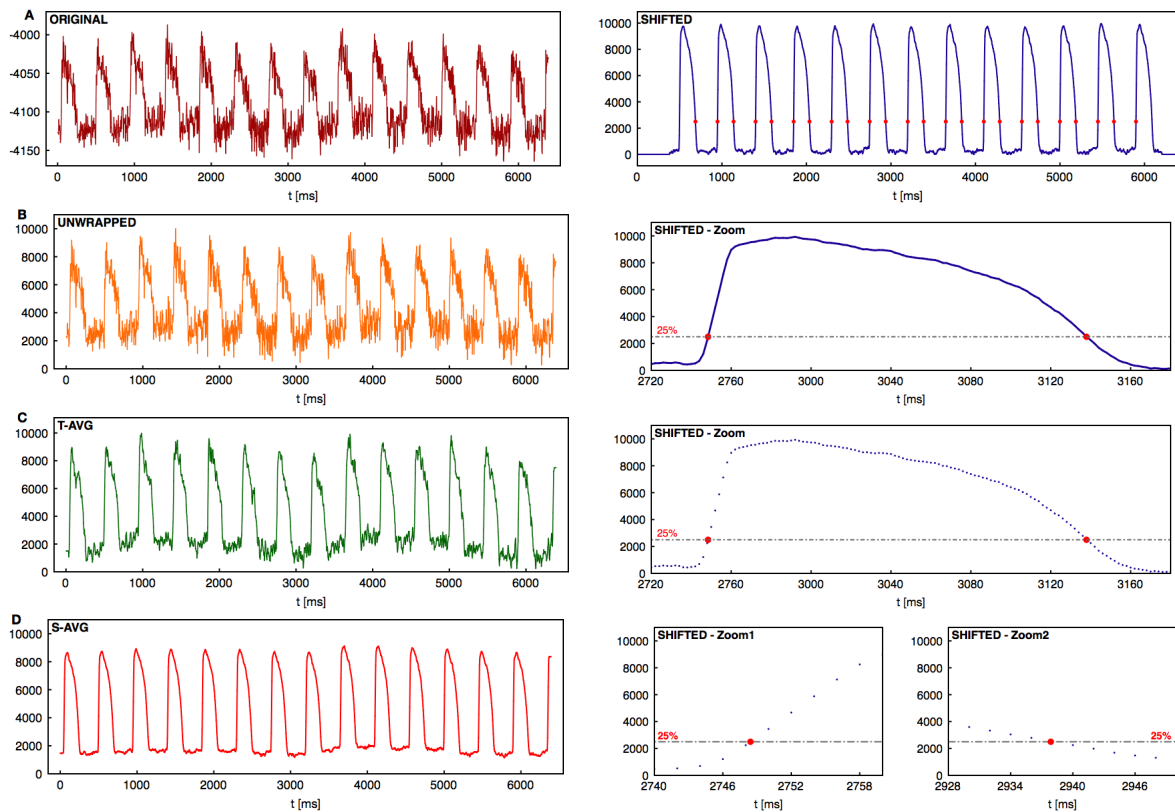


Figure 5.3.3: Representative signal examples of step analysis through Java toolboxes. **(LEFT)** From top to bottom, the sequence goes from the original red **(A)** to the unwrapped yellow **(B)** signal, then the resulting shape after the time-average green **(C)** and its space-average red **(D)**. **(RIGHT)** From top do bottom, signal 25% thresholding, zoomed action potential and interpolated thresholds (Zoom1, Zoom2).

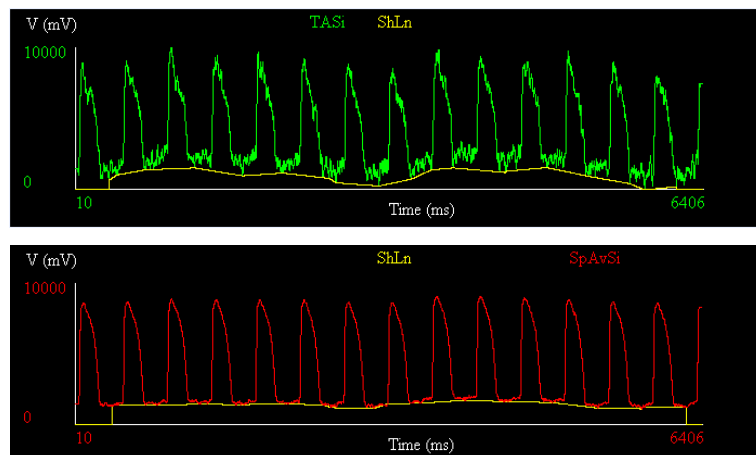


Figure 5.3.4: Representative snapshot examples of signal shifting performed through ad hoc Java toolboxes. The green line shows a time-averaged signal, while the red line corresponds to its space-average. In both cases, the yellow line represent the evaluated drift effect that will be subtracted to the signal.

5.4 Results & Statistics

This section is devoted to the description of the novel spatio-temporal dynamics highlighted during this work. The experimental set consisted of 9 right ventricle preparations, for a total amount of 1362 measurements. A detailed data analysis has been performed both for pacing-down, quiescent stimulation and constant protocols. The results here presented can be summarized into five main points.

1. As cycle length is decreased, alternans (2:2 rhythm) develops in about the 65% of the tested cases on the endocardium first, at $CL \simeq 400\text{ ms}$, and subsequently on the epicardium, at $CL \simeq 250\text{ ms}$ (see Fig.(5.4.1)).

To quantify regional differences in alternans properties, the cycle lengths for which alternans was present on the epicardial and endocardial surfaces have been compared in 14 different set of recordings (720 cases) taken from 6 canine RV preparations. A large range of cycle lengths spanning from 500 ms down to conduction block or VT initiation were used.

It is important to note that, even before alternans was detectable in the tissue, a noticeable spatial dispersion of APD was present on both surfaces, for cycle lengths greater than 500 ms . In particular, $\Delta APD \simeq 30 \div 40\text{ ms}$ was measured by the difference between the maximum and minimum APDs during steady state, as shown in Fig.(5.4.1)A-B. Moreover, once alternans appeared for lower CLs, the dispersion magnitude grew, but only an additional $10 \div 15\text{ ms}$.

As unexpected result found during cycle length decreasing, the dispersion magnitude decreased of about $10 \div 15\text{ ms}$ for both surfaces before increasing again when alternans was present. Therefore leading to a total dispersion increase of 20 ms on both endocardium and epicardium in the lower range of the tested CLs. Such a correlation can be seen in Fig.(5.4.1)C-D.

Another interesting result is related with alternans onset. In fact, the likelihood of developing concordant and discordant alternans at a given CL was different for the endocardium and epicardium. Fig.(5.4.1)E-F shows the percentage of experiments without (gray), with concordant alternans (red), and with discordant alternans (blue) for each CL. In particular, discordant alternans occurred in more than the 40% of the cases on the endocardium for CLs below 300 ms , and the probability reached more than the 80% for CLs below 240 ms . In contrast, discordant alternans occurred with less probability on the epicardium, in particular the 80% was mainly reached for CLs below 100 ms .

2. The experimental observed [66, 214, 235, 289, 293] and theoretical postulated [225, 291] simple progression from normal rhythm (1:1) to concordant 2:2 to discordant 2:2 alternans is not always observed. Our experimental analysis shows cases in which concordant alternans develops from discordant alternans as the pacing period is decreased (see Fig.(5.4.2)).

The case in which, decreasing the pacing cycle length, the occurrence of concordant alternans after a range of CLs where discordant alternans was present, is shown in Fig.(5.4.2)B. Such a transition will be named “extended” in the following, with respect to the “standard” one presented in Fig.(5.4.2)A.

The standard transitions are illustrated via alternans maps for selected CLs and displaying the three different behaviors: 1:1, no alternans, 2:2 CA, concordant alternans, and 2:2 DA, discordant alternans. The sequence ends before reaching conduction block or fibrillation. The corresponding histogram distribution represents the percentage of mapped pixels in the three states described (the cut-off has been fixed at 3%), and highlights the fact that alternans did not occur, in this case, until a CL of 300 ms , followed by the development of fully concordant alternans at 150 ms and discordant alternans between 110 and 70 ms .

The extended transition is shown in a similar way. It presents no alternans until 250 ms , then a short range of CLs, $250 \div 225\text{ ms}$, in which concordant alternans is present. From 225 to 180 ms a 2:2 discordant rhythm was present, then the range $170 \div 120\text{ ms}$ of 2:2 concordant alternans was followed by the last three tested CLs, $110 \div 90\text{ ms}$, in which 2:2 discordant alternans appeared again. Therefore, in this case both CA and DA occurred twice in a sequential manner.

3. In contrast to smaller tissue preparations, multiple stationary nodal lines may exist and need not be perpendicular to the pacing site or to each other (see Fig.(5.4.3)).

Canine RV preparations exhibit the same basic patterns of concordant and discordant alternans observed in other cardiac tissues. In our study, however, we found other types of patterns, not previously observed. In Fig.(5.4.3) different types of spatial alternans patterns are shown from selected examples of our experimental campaign. Panel A highlights that when concordant alternans develops, it does not always occupy the entire tissue at the same time. This means that in some cases only one region of the tissue alternates at 2:2 rhythm, while the rest is at 1:1. More specifically, in all the analyzed cases, we found such a behavior, leading to the interpretation of the alternating regime as a cooperative effect, which envelops little by little large tissue preparations, or as a tissue recruitment, which can be also interpreted as a phase transition. However, in other cases, Fig.(5.4.3)B, and usually at shorted CLs, the entire tissue may undergo alternating regimes.

Cardiac tissue also readily showed discordant alternans with one (panel C) or more nodal lines (panel D) where the APD remained constant on consecutive beats. In the last case, we can identify a more complicated pattern, in which three regions of alternans are separated by two nodal lines.

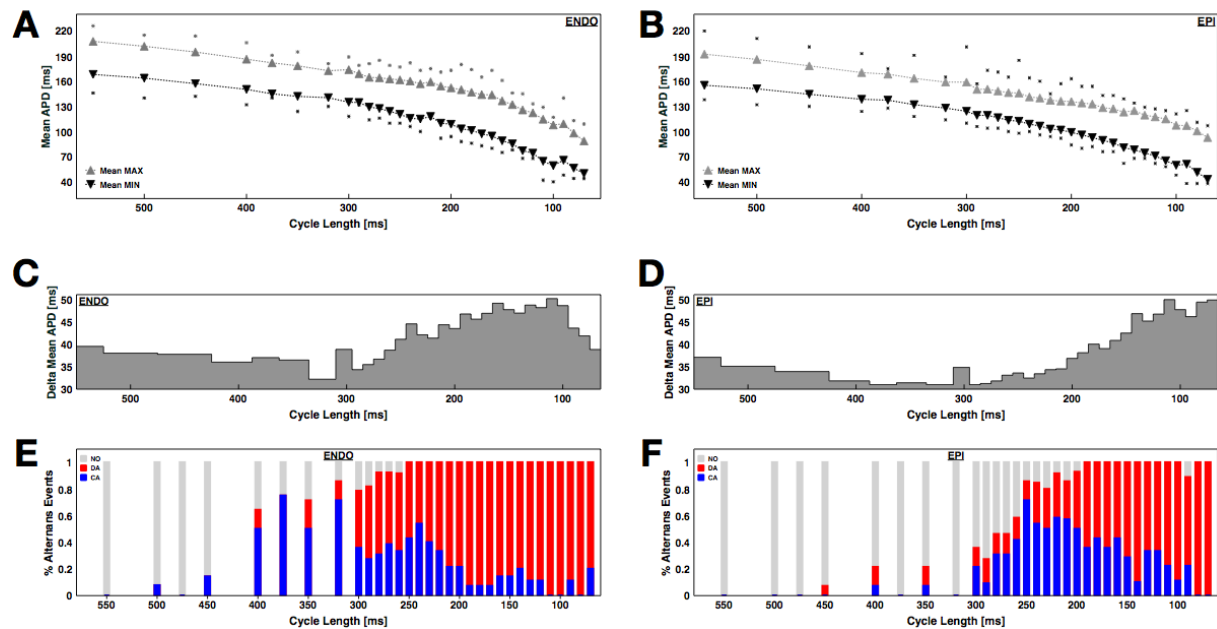


Figure 5.4.1: Statistics of dispersion and alternans development. Mean maximum APD (grey triangles) and mean minimum APD (black triangles) within the tissue for each CL for (A) endocardium and (B) epicardium. The squares indicate the maximum and minimum found from all preparations. Difference in maximum and minimum APDs as a function of CL for (C) endocardium and (D) epicardium. Percentage of cases found with no alternans (grey), concordant alternans (red) and discordant alternans (blue) as a function of CL for endocardium (E) and epicardium (F).

A representative line across the tissue is then used to plot two consecutive APDs clearly showing the large difference in alternans magnitudes and phases between alternans regions. The corresponding difference quantification is shown through the histograms below, reaching maximum alternans values of 30 ms. It is interesting to note, in addition, that even in more complicated scenarios, as the one reported in panel D, multiple nodal lines don't avoid the occurrence of high alternans magnitude in limited tissue areas.

4. Alternans has fully three-dimensional dynamics: multiple nodal surfaces can be transmural or intramural and can form islands, and because of this, the epicardium and endocardium may have significantly different dynamics (see Fig.(5.4.4)).

To further quantify transmural differences in alternans properties, steady-state simultaneous endocardial and epicardial alternans maps are compared: 834 surface recordings taken from 6 canine RV preparations

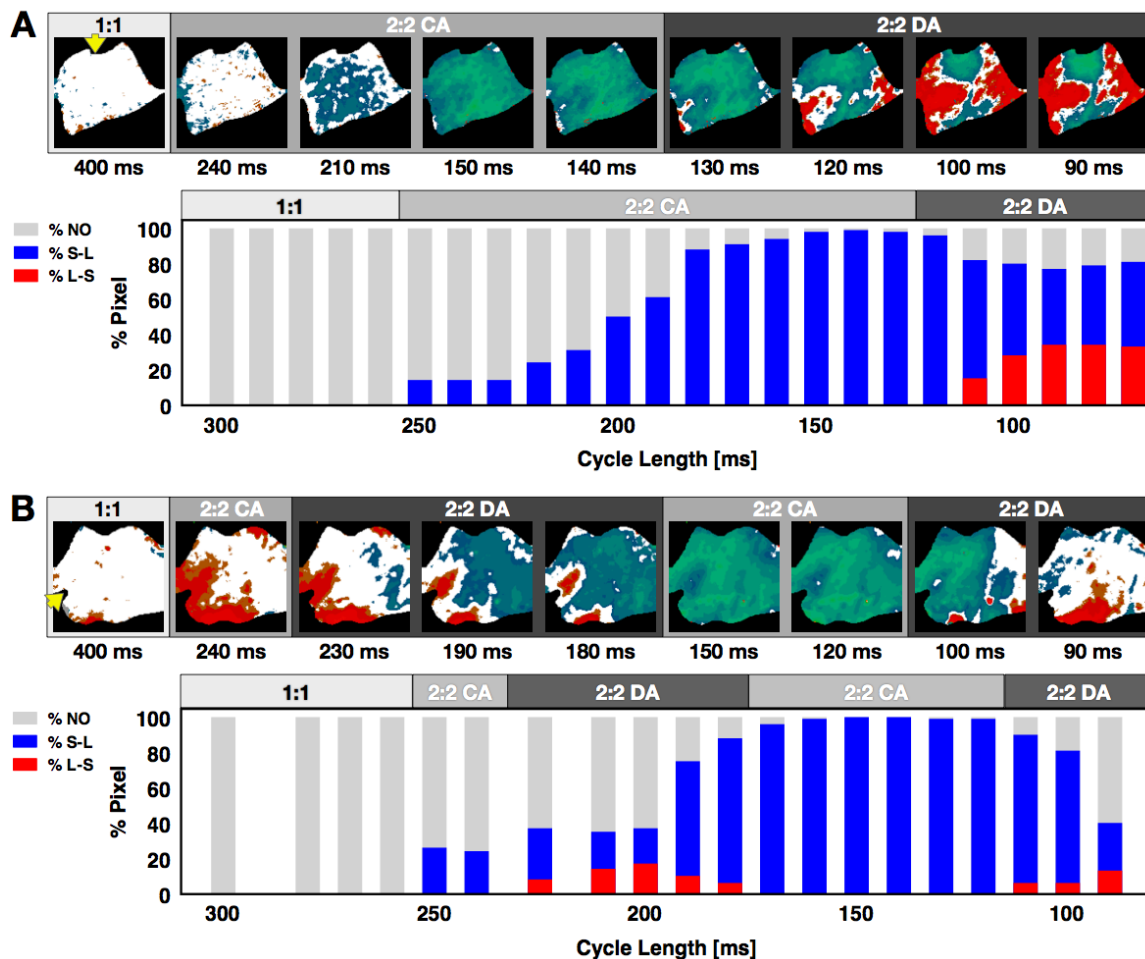


Figure 5.4.2: Representative examples of the standard and extended alternans transitions between concordant and discordant alternans as CL was decreased. (A) Standard transition from no alternans (1:1) to concordant alternans (2:2) to discordant alternans (2:2). Alternans maps for selected CLs are shown within each of the three regions. The lower plots shows the percentage of pixels in one of the three states at each CL. Gray represents pixels with no alternans, blue pixels alternating short-long, and red pixels in long-short phases; the presence of both red and blue colors indicates discordant alternans. (B) Extended transition from no alternans to concordant alternans to discordant alternans, then back to concordant alternans and discordant alternans. Yellow arrow indicates pacing site.

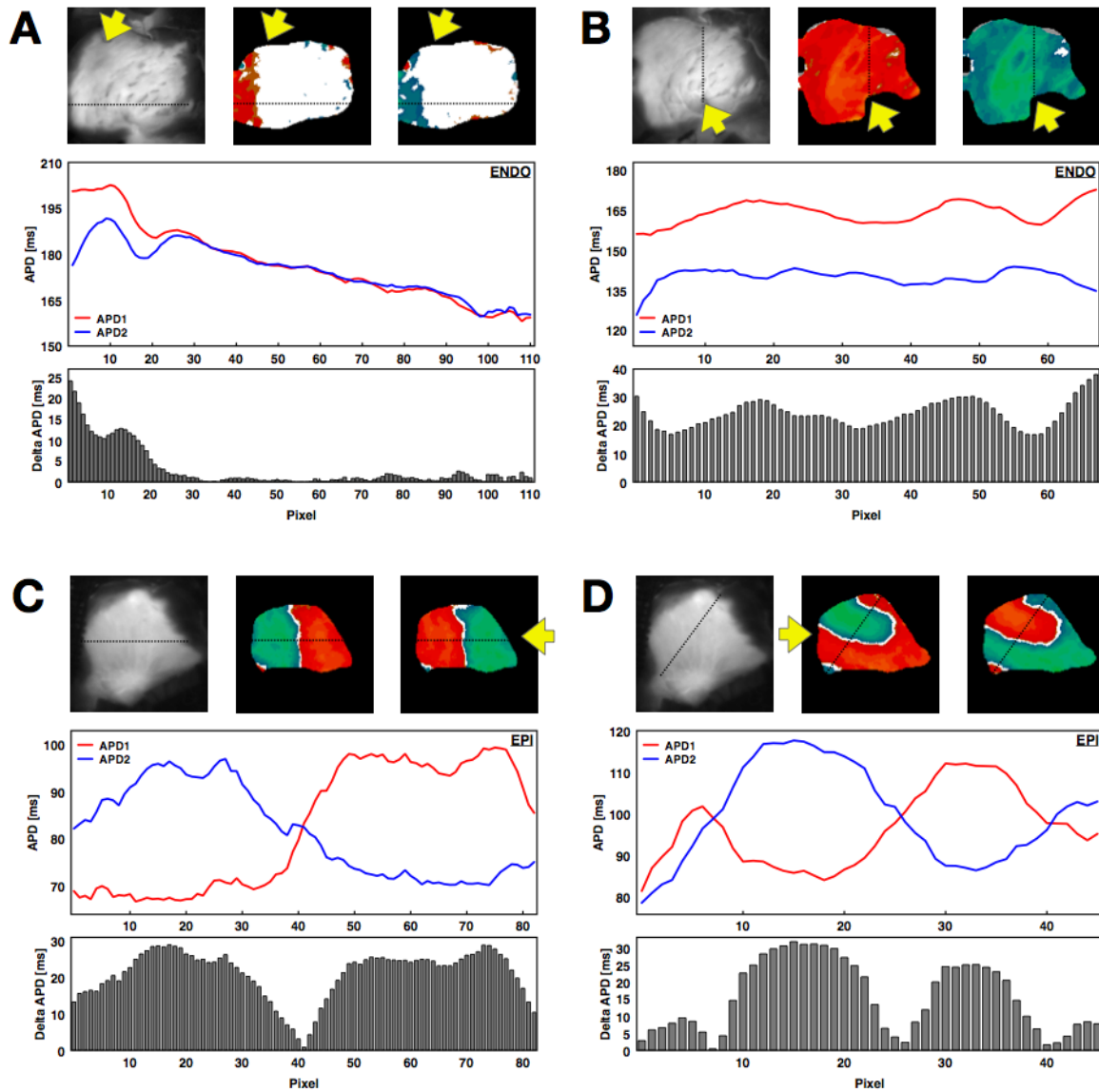


Figure 5.4.3: Concordant and discordant alternans in canine RV preparations. For all four panels a photograph of the corresponding RV structure is shown next to the spatial alternans maps for two consecutive beats after reaching steady state. The yellow arrow indicates the site of stimulation. In addition, the APDs calculated along the line indicated on the alternans maps are shown for two consecutive beats at steady state (red: first beat; blue: second beat), along with the magnitude of alternans (difference in consecutive APDs), and along the same lines a histogram for each pixel. (A) Regional concordant alternans ($CL = 400\text{ ms}$, endocardium), (B) global concordant alternans ($CL = 220\text{ ms}$, endocardium), (C) global discordant alternans with one node ($CL = 110\text{ ms}$, epicardium), (D) global discordant alternans with multiple (three) nodes ($CL = 150\text{ ms}$, epicardium).

were paced at cycle length ranging from 500 ms down to conduction block or fibrillation. By correlating the maps from the two surfaces, it is possible to gain information about the development and dynamics of alternans intramurally. In particular, three-dimensional nodal lines or nodal surfaces can be speculated.

One of the main result of the analysis, highlighted that nodal line patterns on the endocardium and epicardium usually differed greatly. Such a finding suggests that intramural nodal surfaces must have a complex topology.

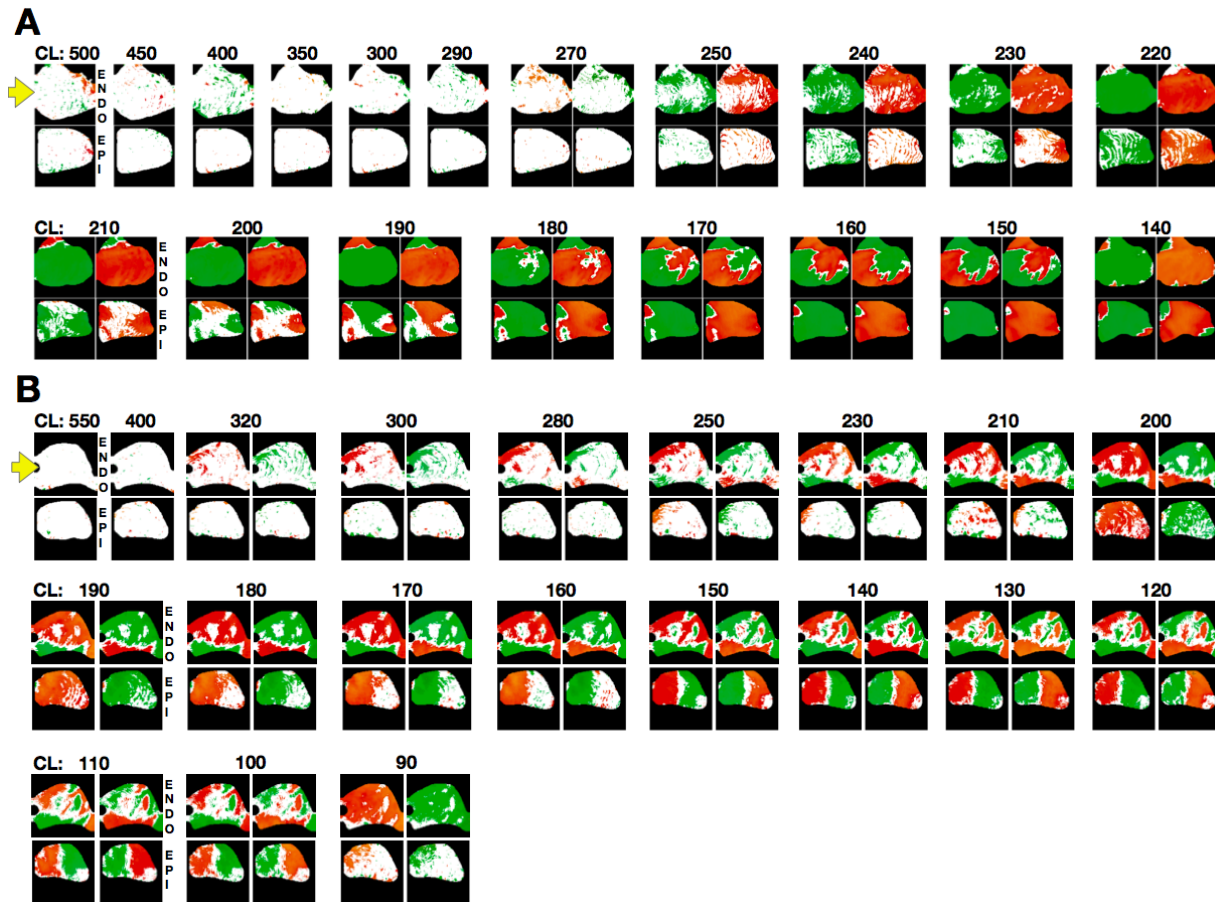


Figure 5.4.4: Steady-state spatial alternans patterns as a function of CL for endocardial (TOP) and epicardial (BOTTOM) RV preparations. Representative examples from two different preparations are shown in **A**) and **B**). Maps from two consecutive beats are shown for each case where alternans was present. Note that discordant alternans developed at longer CLs on the endocardium than the epicardium and that in most cases there was no apparent correlation between the two surfaces. Yellow arrow indicates pacing site. Steady state was reached for each CL by pacing for 60 seconds and recording for an additional 10-15 seconds.

The complete sequence of consecutive beats over the full range of cycle lengths is reported for two representative preparations in Fig.(5.4.4) to illustrate the complex evolution of nodal surfaces as the CL was decreased. Alternans developed at longer CLs for the endocardium than for the epicardium, and the alternans patterns often were more complicated for the endocardium. Interestingly, multiple and complex nodal lines led also to the formation of “alternating islands”, i.e. limited regions resulting from nodal lines forming a loop.

The direct comparison of endocardial and epicardial maps in panel A, for CLs around 190 *ms*, and in panel B, for CLs between 160 ÷ 120 *ms*, highlights that intramural nodal surfaces are not simply perpendicular to the thickness of the tissue, moreover they are quite complicated. On the other hand, panel A, for a CL of 140 *ms*, suggests that the intramural pattern could be perpendicular to the thickness. It is worth to mention that this last case was rarely observed.

5. The complex spatio-temporal patterns observed during alternans are a function of both the direction of stimulation and the stimulation history in a non-trivial way (see Fig.(5.4.5) and (5.4.6)).

The intrinsic tissue heterogeneity is one of the main effects on alternans behavior, and it becomes apparent by altering the location of the stimulus [66, 214, 313]. In order to investigate the effects of pacing site on alternans dynamics in canine right ventricle, a specific mapping measurement of alternans patterns has been performed, pacing from four different RV locations: apex (P1, blue), posterior free wall (P2, green), base (P3, yellow), and anterior free wall (P4, red) (see Fig.(5.2.3)A-B).

Interestingly, we observed that varying the pacing site can result in three main alternans differences: i) onset CLs, ii) amplitude, and iii) spatial patterns. A representative examples of how the alternans magnitude (difference between long and short APDs) increases on the epicardium and endocardium as CL is decreased for the four different and orthogonal pacing sites is shown in Fig.(5.4.5). The alternans magnitude depended strongly on the stimulus location: pacing from the posterior free wall produced the maximum alternans amplitude, and pacing from the opposite direction (anterior free wall) resulted in the smallest, whereas pacing from the base and the apex gave similar intermediate amplitudes. In this regard, it is worth to mention that, the discussed effects are not purely due to heterogeneity but also to tissue anisotropy. In fact, differences in propagation can arise from the spatial variation in fiber orientation, which is more symmetric between base and apex compared to the anterior and posterior free walls.

Another observed effect regards the growth in the dispersion magnitude as CL was decreased. In this case too there is a quantitative difference in the order of 150 ms between apex (blue) and posterior free wall (green). For both the endocardium and the epicardium, the alternans magnitude grew more rapidly

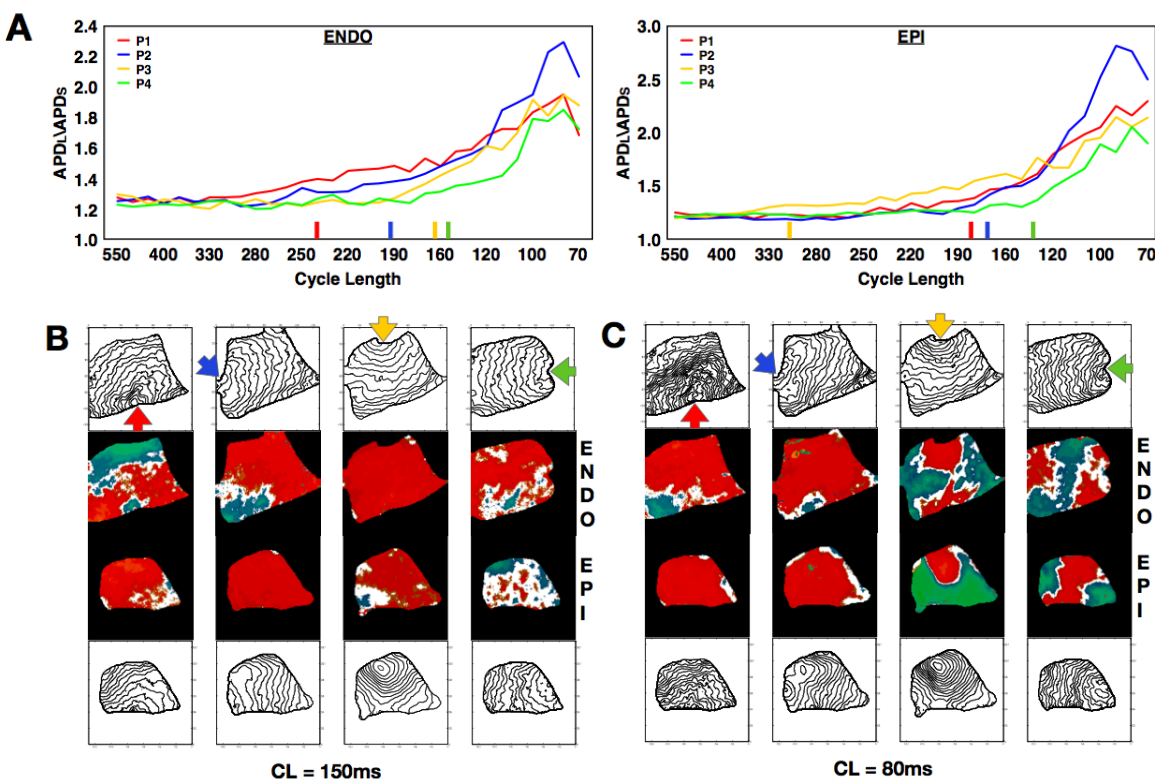


Figure 5.4.5: Effect of pacing site on the development of alternans. (A) Alternans magnitude for endocardium and epicardium from four different and orthogonal RV pacing sites: apex (P1, blue), posterior free wall (P2, green), base (P3, yellow) and anterior free wall (P4, red). Colored bars on the x-axes indicate the points at which each curve has grown more than 10% compared to its value at the longest CL. Alternans maps and activation contour maps at CLs of (B) 160 ms and (C) 80 ms for endocardium and epicardium showing the differences obtained by pacing from the four sites.

when pacing from the base than from any other location. The over imposed colored bars on the x -axes indicate the points at which each curve has grown more than 10% compared to its value at the longest CL.

In addition, different alternans patterns were obtained for each pacing. Panels B and C in Fig.(5.4.5) demonstrate these differences for two different CLs, i.e. 160 ms and 80 ms , in relation with activation isochrones in the contour plots. These graphs show that fiber orientation along the LV tissue affected the pattern of activation and the conduction velocity depending on the pacing site, thus altering the emerging discordant alternans patterns.

Pacing history and the dynamical state of the tissue before pacing can significantly affect how alternans develops [193, 313]. To quantify this phenomenon alternans maps obtained in the same tissue preparations (3 RV, 524 recordings) for the same CL using two different protocols are shown in Fig.(5.4.6): 1) a pace-down (P protocol), where the tissue was paced initially at $CL = 550\text{ ms}$ and slowly decreased, and 2) a quiescent (Q protocol), by pacing at the given CL directly following quiescence. In both cases measurements were performed following steady state tissue assessment.

Panels A and B show simultaneous steady state, endocardial (top) and epicardial (bottom), recordings obtained using the two protocols and for the same CL. In the former case the pacing site is the same, while the second row presents three different pacing sites. A direct comparison can be made via $CL = 100\text{ ms}$, in which the difference in pacing site affects the spatial patterns produced although the tissue preparation is the same.

The main finding of such analysis is that the dynamical state of the tissue before pacing can significantly affect how alternans develops. We found that during the P protocol, more nodal lines appear with respect to the Q one. In addition, alternans often appeared at a longer CL from the quiescent protocol.

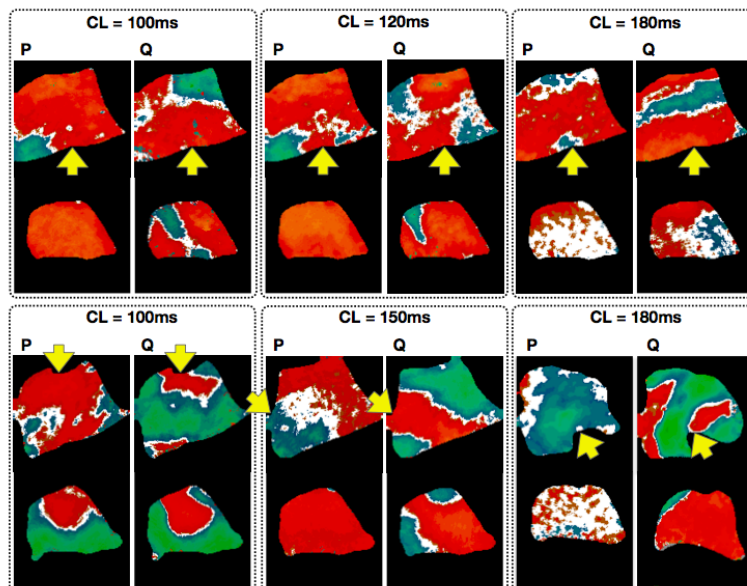


Figure 5.4.6: Effect of pacing history on the development of alternans. Each panel shows the endocardial (TOP) and epicardial (BOTTOM) patterns obtained via a CL pace-down (P) and directly from quiescence (Q). Arrows indicate pacing site. The top panels show alternans patterns in a single preparation for three CLs (100, 120, and 180 ms). The bottom panels are taken from different preparations and show the patterns resulting from different pacing sites for three different CLs (100, 150, and 180 ms). Note that for the two $CL = 100\text{ ms}$ cases, the difference in pacing site affects the resulting spatial pattern although the tissue preparation is the same.

5.5 Theoretical Assessment of Alternans Dynamics

5.5.1 Alternans & Higher-Order Rhythms

Although most often during rapid pacing-induced alternans a period-two (2:2) response is observed, in some cases higher-order periodicities can be seen [232]. For example, a long-short-long-short pattern in which two distinct long and two distinct short APDs occur before the sequence repeats is observed occasionally and constitutes a stable 4:4 pattern.

The experiments conducted during this work, revealed cases during DA patterns in which higher-order rhythms beyond 2:2 were present. Figure (5.5.1)(A) shows a series of higher-order rhythms observed in individual pixels, beginning with a standard 2:2 rhythm in the first panel. Three examples of a 4:4 rhythm are shown as well, and the last panel includes an example of an 8:8 rhythm, which was observed considerably less frequently. These rhythms can occur globally throughout the whole tissue, as shown in the top upper panel of Fig.(5.5.1)(B) for a 4:4 case, but more commonly they occurred only in local regions of the tissue while the rest of the tissue followed a standard 2:2 rhythm. The lower panel of Fig.(5.5.1)(B) shows an example of this regional variation in rhythm, where a 4:4 rhythm occurred in the upper part of the tissue, and the lower portion followed a standard 2:2 rhythm. Plotting the APD as a function of DI for a single pixel over time provides an alternative means for visualizing higher-order rhythms. Figure (5.5.1)(C) shows representative plots of APD as a function of DI for a 2:2 case and two 4:4 cases. Although the central plot appears to indicate a 3:3 rhythm, such rhythms do not occur as part of a period-doubling cascade, and a careful analysis shows that this scenario is a degenerate case of a 4:4 rhythm in which the two short APDs are nearly identical.

5.5.2 Period-Doubling Route to Chaos for VF

Although multiple routes to chaos exist, the most commonly observed route in dynamical systems is a period-doubling cascade [6, 125]. Considering APD dynamics as a function of the stimulation pacing, as the cycle length decreases a period doubling appears because of the restitution slope (greater than 1). This is followed by a 2:1 conduction block, thus followed by subsequent period doubling, chaos, higher-order blocks etc. For cardiac tissue, however, the type of bifurcation that leads to complex dynamics still has not been well characterized. This is not only because multiple mechanisms can lead to fibrillation, but because even considering rapid pacing to be the underlying mechanism, different bifurcation routes have been implicated in the transition from period 1 to period 2 (alternans) and to higher-order rhythms [48, 107].

The first transition (1:1 to 2:2) as the pacing period is decreased, was originally described experimentally and numerically as a supercritical period-doubling bifurcation [47, 99, 115, 117]; however, later studies suggested that a Hopf bifurcation can develop when considering other effects such as memory, spatial coupling and calcium dynamics in the analysis [249]. Similarly, the transition from 2:2 to higher-order rhythms could have multiple sources. Transitions to 2:1, 3:2 and other Wenckebach rhythms [309], which are not typical of many other dynamical systems, are present in cardiac dynamics as a result of the discontinuity in the response due to refractoriness and conduction blocks [117], which is equivalent to a discontinuity in any m -dimensional map reproducing the dynamics. In space these $m : n$ transitions, where $m > n$ far from the pacing site and $m = n$ at or near the pacing site, can lead to the development of alternans that is different from the alternans described in this manuscript. In those cases a “pseudo-alternans” is created at the border between the $m = n$ and $m > n$ regions, which it will be referred to here as *Gaskell-alternans* [5], as he was the first to suggest that mechanical alternans could be the

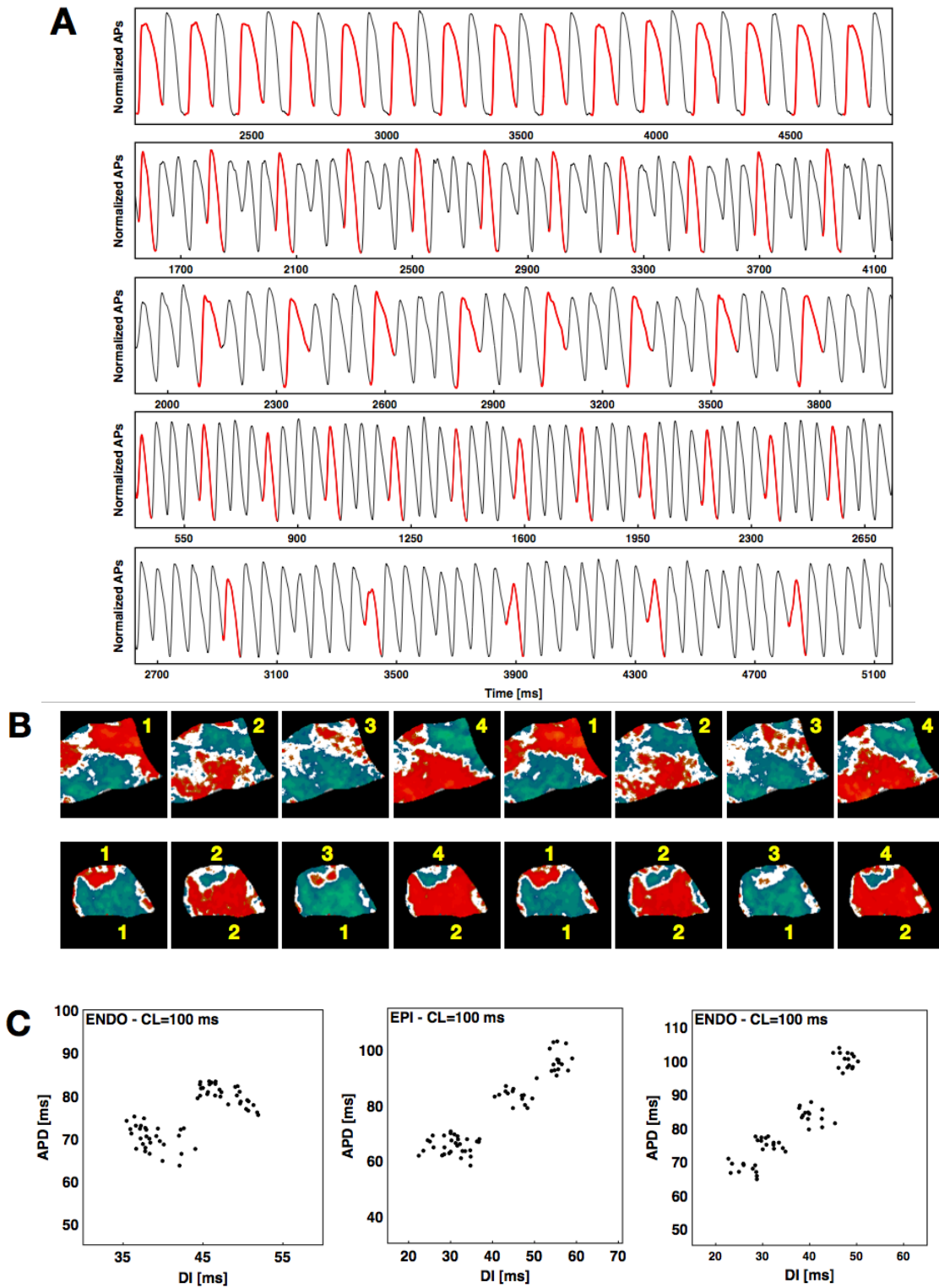


Figure 5.5.1: Examples of higher-order rhythms. (A) From top to bottom 2:2, 4:4, 4:4, 4:4, and 8:8 rhythms. The first AP of each rhythm is shown in red. (B) Top: alternans map of an endocardial preparation with a 4:4 sequence; bottom: alternans map of an epicardial preparation with mixed rhythms (4:4 at the top and 2:2 at the bottom). Two consecutive sequences are shown for both cases. (C) Plots of APDs vs. DIs showing an example of 2:2 rhythm and two examples of 4:4 rhythm, with the middle 4:4 a degenerate case.

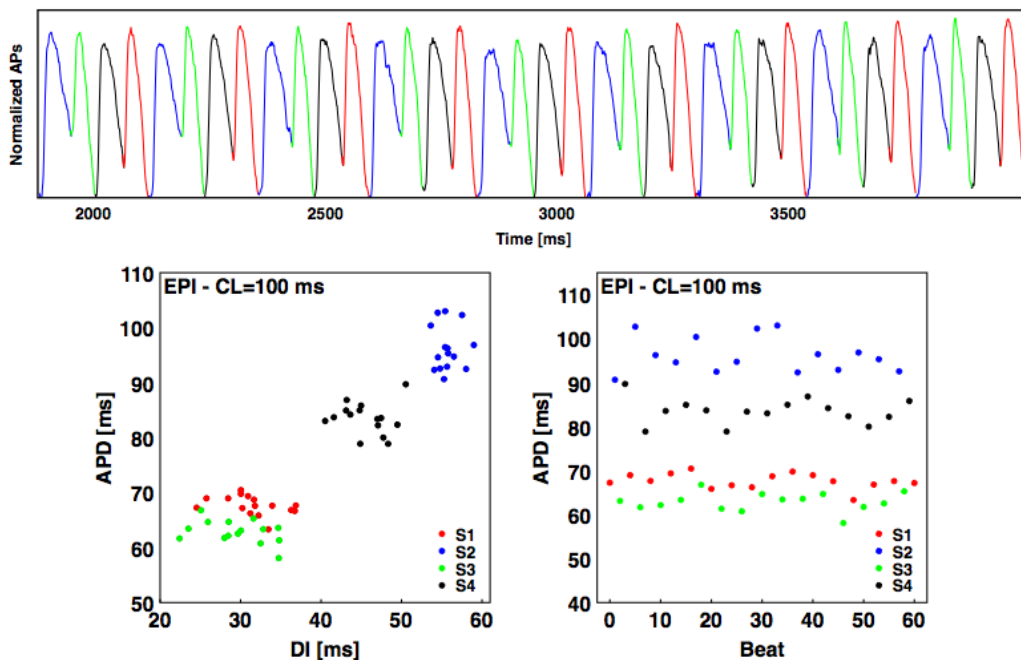


Figure 5.5.2: Examples of higher-order rhythms with the a 4:4 degenerate case. Color code associates each action potential with the corresponding APD-DI (left) and APD-CL (right) representations.

result of a 2:1 subregion in 1:1 domain. It is possible that Gaskell-alternans is the type of alternans most commonly observed during ischemia. Although 2:2 rhythms most commonly are followed by Wenckebach rhythms, higher-order rhythms periods of 4:4 and 8:8 (see Fig.(5.5.1)), have been observed in other cardiac preparations, such as bullfrog and sheep fetal ventricular tissue, and up to 16:16 in canine Purkinje fibers.

Because the range of CLs over which a given period doubling can be observed decreases exponentially with increasing periodicity, it is not surprising that higher-order rhythms (4:4, 8:8 and 16:16) are not often recorded, but the fact that they have been observed suggest that in some cases the transition to fibrillation may be the a result of a period doubling bifurcation. However, because other higher-order rhythms such as 3:3, and 3:1 have been also observed, it is possible that other attractors can co-exist and other type of bifurcations such as intermittency, supercritical and subcritical Hopf bifurcations, and other complex dynamics due to biphasic APD restitution or supernormal CV restitution may contribute as well.

Mass reduction has been shown to decrease the dynamical complexity of VF as measured by Kolmogorov entropy and Poincaré plots [164]. In particular, a decrease in the number of wave fronts in ventricular fibrillation by tissue mass reduction causes a transition from chaotic to periodic dynamics via the quasi-periodic route.

5.5.3 Initial Conditions and Multistability in Cardiac Tissue

The discussed experimental and theoretical findings characterize differences in alternans patterns depending on several effects: pacing site, stimulation protocol and initial conditions. In this regard, the present study was also dedicated to the experimental analysis of alternans patterns to pacing history from a more general point of view. Specifically, we evaluated the effects of similar initial conditions on pattern formation by pacing three different RV preparations and performing 126 recordings with similar initial

conditions and constant CL. As described in Chap.(5.2.3), a constant (C) stimulation protocol was applied, pacing the tissue at a fixed CL for 20 s then leaving the tissue recovering quiescence and repeating these two step for a total of about 30 repetitions. The first 10 s of each episode were recorded and the steady state alternans maps, always reached within $10 \div 15$ beats, were constructed.

The main result found consists in significant variations in the alternans patterns over different repetitions. Fig.(5.5.3) shows selected examples of such a variety for $CL = 150\text{ ms}$. Panels A, B, and C are referred to different pacing sites, and differences in the number recording (on top) and nodal lines shapes can be observed. Interestingly, the overall state of the tissue, i.e. concordant vs. discordant alternans, resulted different. In addition, the pattern observed for a given repetition showed no obvious correlation with the patterns resulting from the immediately previous and following repetitions.

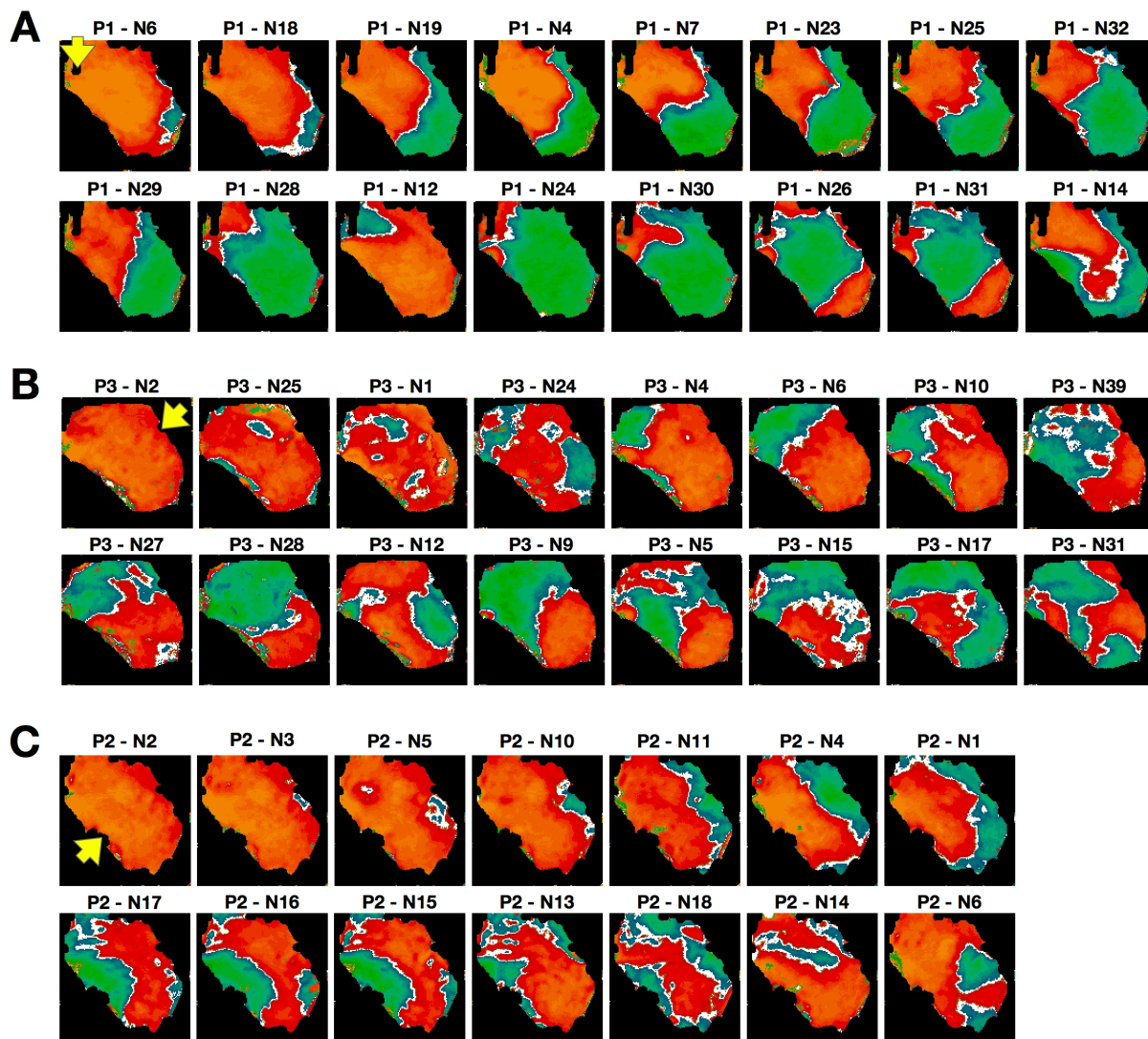


Figure 5.5.3: Representative examples of alternans patterns obtained in a given preparation over a 20 min interval at a single CL of 150 ms. The patterns are arranged in order of similarity, even if their appearance is not in chronological order (the experiment number is indicated on top of each panel). Pacing sites are indicated by the arrows.

5.6 Discussions

Electrical alternans has been amply correlated experimentally and numerically with the onset of arrhythmias, and it is considered a well-known marker for electrical instabilities in cardiac tissue. Even though, most studies of spatially extended alternans have been performed in monolayers or small mammalian hearts and often at low temperatures where the alternans magnitude more easily visible. Only a small number of studies of alternans have been conducted in larger mammalian hearts such as dogs and pigs, but in general these have been performed in the context of ischemia and without optical mapping. Very few exceptions can be found in literature about short-term memory effects in left ventricular canine wedges [311] or equine atrial fibrillation [92]. Therefore, very little is actually known about the spatio-temporal properties of alternans in ventricles of large mammals at physiological temperatures.

In this chapter, it has been presented and discussed the full analysis of 1362 different experiments involving dual synchronous mapping of the epicardial and endocardial surfaces, for 9 canine right ventricular preparations. Several experimental findings were found in accord with monolayers, smaller hearts, and numerical studies. In particular alternans develops as the pacing cycle length decreases, and concordant and discordant alternans patterns are present and can lead to fibrillation. However, we found many different, much richer and complicated scenarios though a careful and dedicated analysis, thus emerging from the larger canine preparations at normal physiological temperature.

In this regard, a dedicated Java software for data analysis and visualization has been developed providing a manageable tool for more than 1300 measurements. Flexibility and generality are the main characters of the software: it does not present any kind of constraint in the data analysis methodology (the operator can decide which strategy is more suited for the data at hand), and it can be used on every operating system. Furthermore, several interactive visualization tools have been implemented in order to highlight at the best the important properties of the experimental signals.

Thanks to the usage of such a supporting tool, we were able to identify several interesting and not previous observed phenomena summarized in the following. (i) Both concordant and discordant alternans are readily observed at physiological temperature. (ii) As the pacing cycle length is decreased, alternans predominantly develops sooner on the endocardium than on the epicardium. (iii) The transition from normal rhythm to concordant alternans to discordant alternans and finally to fibrillation or conduction block, as CL is decreased, may be extended by the appearance of second regions of concordant and discordant alternans. (iv) Multiple stationary nodal lines can exist and need not be perpendicular to the pacing site or to each other. (v) The presence of higher rhythms, such as 4:4, 8:8 and 16:16 in cardiac tissue suggests that in some cases the transition to fibrillation may arise from a period-doubling bifurcation. (vi) Alternans has fully three-dimensional dynamics with nodal surfaces and may form islands of alternans as a result of differences in behavior between the endocardial and the epicardial surfaces. (vii) The complex spatio-temporal patterns observed during alternans are a function of both the site of stimulation and the stimulation history in a non-trivial way.

5.6.1 Limitations and Conclusions

In this study, only canine right ventricles from a single species (beagles) were used, and thus our results may not extend to the left ventricle or the whole heart. Choosing to perform the pacing on the endocardium may be a driving effect because alternans generally developed sooner on the endocardium. However, because the RV is relatively thin and contour lines on the epicardium showed that the activation quickly reached the other side essentially as a point stimulus, we believe that our results would not change with

an opposite stimulation site.

From a subcellular point of view, the intracellular calcium concentration was not optically recorded, but this information would help to clarify the complex patterns observed, and specifically to elucidate how islands and nodal surfaces form.

Concluding, based on our result, the prediction of alternans pattern formation may not be a trivial task because of the high sensitivity to initial conditions, which may indicate some underlying chaotic predisposition. Therefore, efforts that focus not on how to predict the patterns but rather on ways to avoid reaching the arrhythmic substrates or to find methods to make these substrates less sensitive to initial conditions may be more useful and successful.

Chapter 6

Heart Modeling: Mathematical Review and Perspectives

Providing a current and complete overview of the state of the heart in cardiac modeling it's hard for several reasons: first, heart tissue is still an open problem in understanding its emerging behavior from subcellular to tissue level; second, more basic mechanisms of physiological function, including metabolic and signal transduction pathways, need to be included before significant progress can be made in understanding many disease processes.

In this chapter, a brief overview of the general theory of reaction diffusion media, in which cardiac tissue belongs, will be given. In this perspective, a novel mathematical description of spiral waves will be presented.

Computational models of the electrical and mechanical function of the heart will be reviewed as well. The purpose of describing the different mathematical approaches to subcellular, cellular and tissue mechanisms are devoted to the extended theory of coupled electro-mechanic formulations discussed in the following.



Figure 6.0.1: Spiraling bark, Rome 2009 (C. Cherubini).

6.1 Excitation Waves & Reaction-Diffusion Media

In an assemblage of particles, the individual motion is usually totally irregular and random [215]. When this microscopic movement results in some macroscopic regular motion of the group then a *diffusion* process can be defined [80]. If such a process is “simple” or “classical” it is said *Fickian diffusion* [94]. When interaction between particles occurs or the environment gives some bias, then the gross movement is not simple diffusion but is generally defined a *reaction-diffusion* process [277]. To derive reaction-diffusion equations, is necessary to identify a continuum model system for the global behavior in terms of a particle density or concentration.

Considering a diffusion process in three space dimensions, let S be an arbitrary surface enclosing a volume V , and \mathbf{x} the spatial coordinate vector, i.e. $\mathbf{x} = (x_1, x_2, x_3) \equiv (x, y, z)$ in Cartesian coordinates. The general conservation equations reads as: the rate of change of the amount of material in V is equal to the rate of flow of material across S into V plus the material created in V . Thus

$$\frac{\partial}{\partial t} \int_V c(\mathbf{x}, t) dv = - \int_S \mathbf{J} \cdot d\mathbf{s} + \int_V F(c, \mathbf{x}, t) dv \quad (6.1.1)$$

where $c(\mathbf{x}, t)$ is the concentration of the species, \mathbf{J} is the flux of material, $d\mathbf{s}$ the oriented area element, (\cdot) indicates the scalar or inner product, and $F(c, \mathbf{x}, t)$ represents the source of material, a function of c , \mathbf{x} and t in general. Applying the divergence theorem to the surface integral, assuming $c(\mathbf{x}, t)$ is continuous and for the arbitrary of the volume V , the local *conservation equation* for c derives

$$\frac{\partial c}{\partial t} = -\nabla \cdot \mathbf{J} + F(c, \mathbf{x}, t), \quad (6.1.2)$$

where ∇ is the standard differential operator vector. This equation hold for a general flux transport \mathbf{J} , whether by diffusion or some other process. In particular, the specification of \mathbf{J} gives a constitutive prescription to the diffusion process itself.

If classical diffusion is the chosen process, i.e. $\mathbf{J} = -\mathbf{D}\nabla c$, then Eq.(6.1.2) becomes the so called *diffusion equation* [113]:

$$\frac{\partial c}{\partial t} = \nabla \cdot (\mathbf{D}(c, \mathbf{x}, t) \nabla c) + F(c, \mathbf{x}, t) \quad (6.1.3)$$

where $\mathbf{D}(c, \mathbf{x}, t)$ is the diffusion tensor or diffusivity, which may be a function of both the variable concentration itself, the spatial position and time, as F in general. Situations where \mathbf{D} is space-dependent are arising in more and more modeling situations of biomedical importance. In the following, the specific case of cardiac dynamics will be discussed, but such a formulation is generally applicable from the diffusion of generically engineered organisms in heterogeneous environments to medical imaging or tumor growth and spread, and so on [196].

The nonlinear part of these equations is usually described by the source term F . Many different expression have been proposed for such a function: in an ecological context, for example, F could represent the birth-death process and c the population density. In this case, the famous *logistic* growth law, known as the *Fisher-Kolmogoroff equation*, has been introduced and studied both analytically and numerically.

A further generalization of Eq.(6.1.3) can be done towards the situation in which there are, for example, several interacting diffusive species or chemicals [46]. In this case, a vector $\mathbf{u} = u_i(\mathbf{x}, t)$, $i = 1, \dots, m$ of densities or concentrations can be defined. Each of these terms diffuses with its own diffusion tensor \mathbf{D}_i and interacting according to the vector source term $\mathbf{F} = F_i$. Then, Eq.(6.1.3) becomes a *reaction-diffusion*

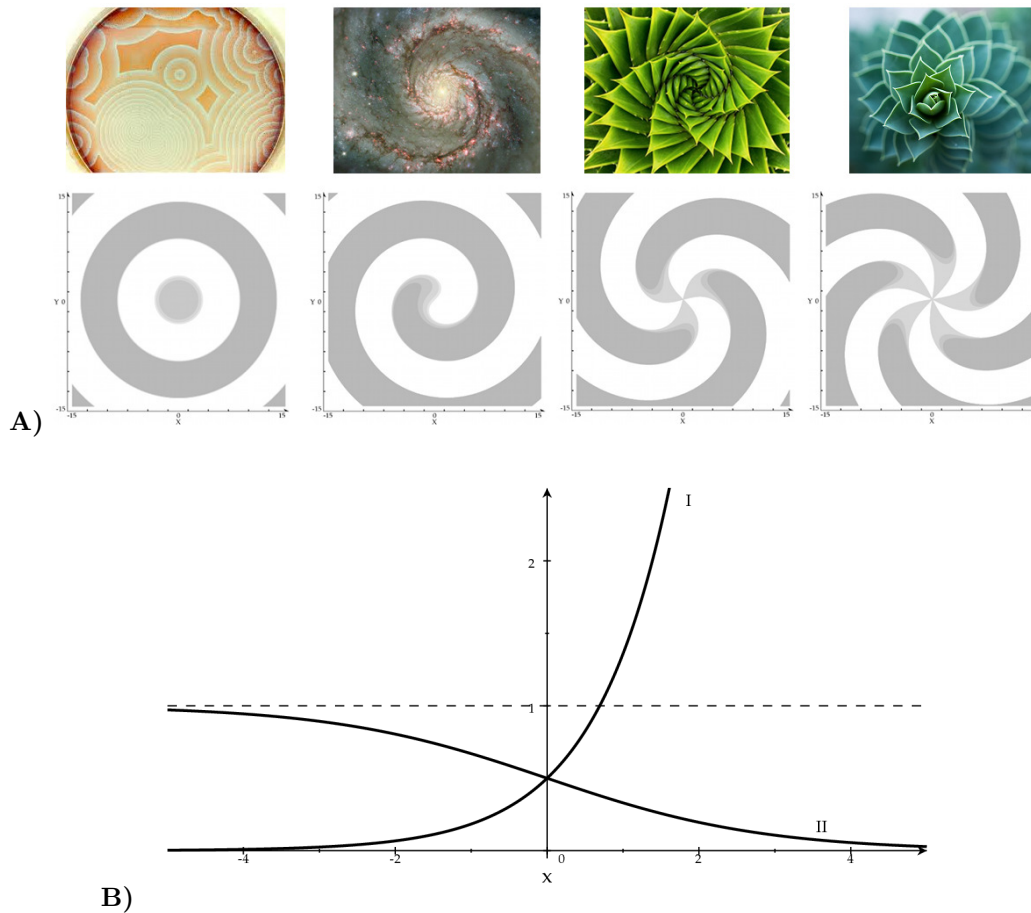


Figure 6.1.1: (A) From target pattern to multi-armed spiral waves. (TOP) Examples in nature: chemical reaction, galaxy, flowers and plants. (BOTTOM) Analytical solution of the diffusion equation in terms of integer Bessel functions of complex argument: target pattern, single spiral, three-armed spiral, five-armed spiral. (B) Graphics of the two Bessel solutions in space: I linear case, II nonlinear case, $C_1 = 0$ and $C_2 = 1$.

system:

$$\frac{\partial \mathbf{u}}{\partial t} = \nabla \cdot (\mathbb{D} \nabla \mathbf{u}) + \mathbf{F} \quad (6.1.4)$$

where now \mathbb{D} is a matrix of the diffusivities which, if there is no cross diffusion among species, has a diagonal structure.

Reaction-diffusion systems present much more reach phenomena, dynamics and spatial patterns as well. Cross-diffusion, among other, does not arise often in genuinely practical models and can pose mathematical difficulties regarding well-posed equations [46]. Such a mechanism was proposed as a model for the chemical basis of morphogenesis by Turing [277] in one of the most important papers in theoretical biology of the last century. The complete mathematical review of reaction-diffusion systems is deferred to Crank [61] and Murray [196]. In the following, specific aspects related to spatial patterns arising from these systems will be discussed.

6.1.1 Spiral Waves in Natural Systems

The mathematical form of reaction-diffusion processes belongs to the theory of nonlinear parabolic partial differential equations. The study of these systems has been carried out since more than one century ago

[63, 298], but it is still full of interest and applications. One of the most intriguing aspect for the aims of this work, is related to the fascinating patterns arising from their mathematical structure: spiral waves.

Spiral waves appear in many different natural contexts, both as single or many-armed configurations: excitable biological tissues, fungi and amoebae colonies, chemical reactions, growing crystals, fluids and gas eddies as well as galaxies. Moreover, such phenomenologies develop in time with different time scales and they all manifest wave behaviors. A partial sequence of these structures is shown in Fig.(6.1.1)A and compared with numerical solution performed in this work (see Bini et. a. 2010).

Although dynamical and mathematical complexities, self-sustained spiral wave regime is already present in the linear heat operator, in terms of integer Bessel functions of complex argument, that is

$$P = a_1 J_m(z) + a_2 Y_m(z) \quad (6.1.5)$$

where a_1 and a_2 are generic constants, z enters the definition of a rescaled dimensionless radius in cylindrical coordinates, and J_m and Y_m are the Bessel functions. The corresponding solution of the dimensionless real diffusion equation becomes

$$c = (\text{Re}[J_m(z)] + i\text{Im}[J_m(z)]) e^{i\omega T + ikZ + im\phi} \equiv \text{Re}[c] + i\text{Im}[c] \quad (6.1.6)$$

Such solutions (see Fig.(6.1.1)B) play a central role in the understanding of the universality of spiral process. In particular, in nonlinear reaction-diffusion models the linear part of the equations determines the wave front appearance while nonlinearities are mandatory to cancel out the blowup of solutions. Even though, the spiral wave pattern still requires at least two cross-reacting species to be physically realized.

These mathematical bases suggest that the diffusion process must be seen as a theoretical model of possible discrete complex systems whose dynamics can be described in a first approximation with a non-linear continuum field theory. Cardiac tissue, in fact, like any other chemical or physical excitable media, can exhibits reentrant waves. Spiral waves can occur on their own, in pairs, or as multiple waves. Their variability depends on tissue size, morphology, electrophysiological properties, and initial conditions. The size requirement is related to the critical mass hypothesis, first described by Garrey [105], which postulates a minimum mass necessary for fibrillation. Analogously, for scroll waves to exist, there is a minimum size and thickness requirement [2, 7, 164, 303, 304], and this size is related to the wavelength [279] of the propagating wave. Such nonlinear dynamics have been recognized in close association with pathological situations, i.e. arrhythmia and fibrillation, leading to non-physiological states that compromise the heart's ability to contract and pump blood efficiently.

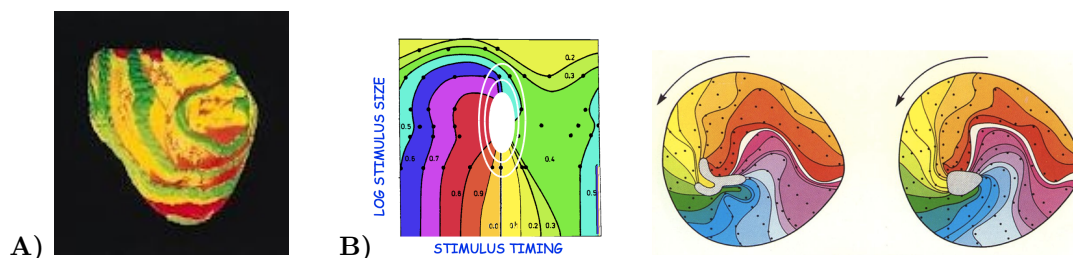


Figure 6.1.2: (A) The last wave from the dying heart assume a spiraling shape [134]. (B) Time patterns of cardiac activation [305].

6.2 Continuum Models of the Heart

Cardiac tissue is usually described as a syncytium. Its complex microstructure comprises coupled cells, enveloped by an interstitial made up of blood vessels, connective tissue, and fluid. Such a medium presents several interesting aspects, either in understanding the tissue as an electrical medium [128], or as a soft hyperelastic material or as an active electro-mechanic biological pump as well.

Linking molecular and cellular events with physiological function must deal with wide ranges of length and time scales. Mathematical and computer models attempt to give an integrated overview, covering several aspects at different levels: atrial and ventricular anatomy, structure and material properties, membrane ion channels and calcium handling, myofilament mechanics of cardiac myocytes, etc. The resulting computational framework, therefore, necessitates a hierarchy of models as shown in Fig.(6.2.1). Different types of model are appropriate to each level, and relationships must be established between models at one level and the more detailed, but spatially or temporally limited, models at the level below.

6.2.1 Models of Cardiac Anatomy

Most continuum models of cardiac function require detailed information about the three-dimensional geometry and structural organization of the heart. They are, therefore, complex boundary value problems requiring numerical solutions [147, 174]. The most used approach for a geometrical identification consists in formulating a finite element model (FEM) of heart anatomy. This requires the definition of a reference mesh that matches the geometry of the cardiac chambers. As usual for FEM applications, each element identify the unitary cell which represent the geometrical framework where field variables are approximated by interpolation of values associated with each of the element nodes. Several interpolating methods can be adopted, from Linear Lagrange to higher order polynomials, such as cubic Hermite basis functions [312]. Ventricular surface geometry can be identified adopting different measure techniques: fixing the

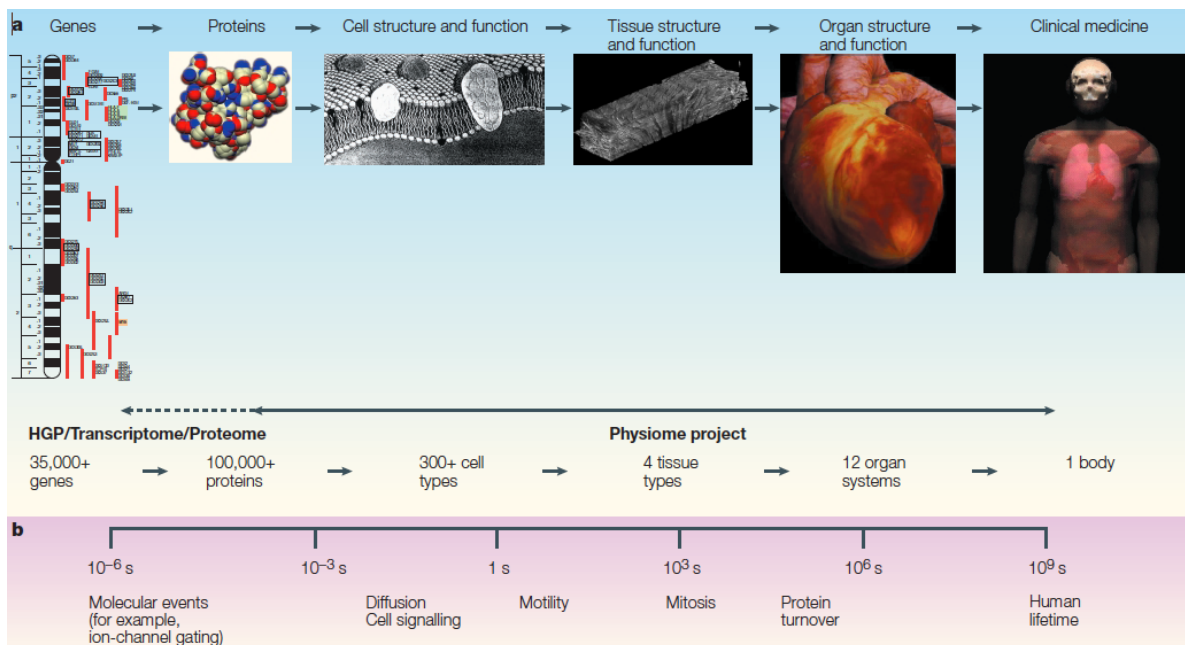


Figure 6.2.1: Levels of biological organization from genes to proteins, cells, tissues, organs and finally the whole organism. The spatial scales range from 1 nm for proteins to 1 m for the whole body [146].

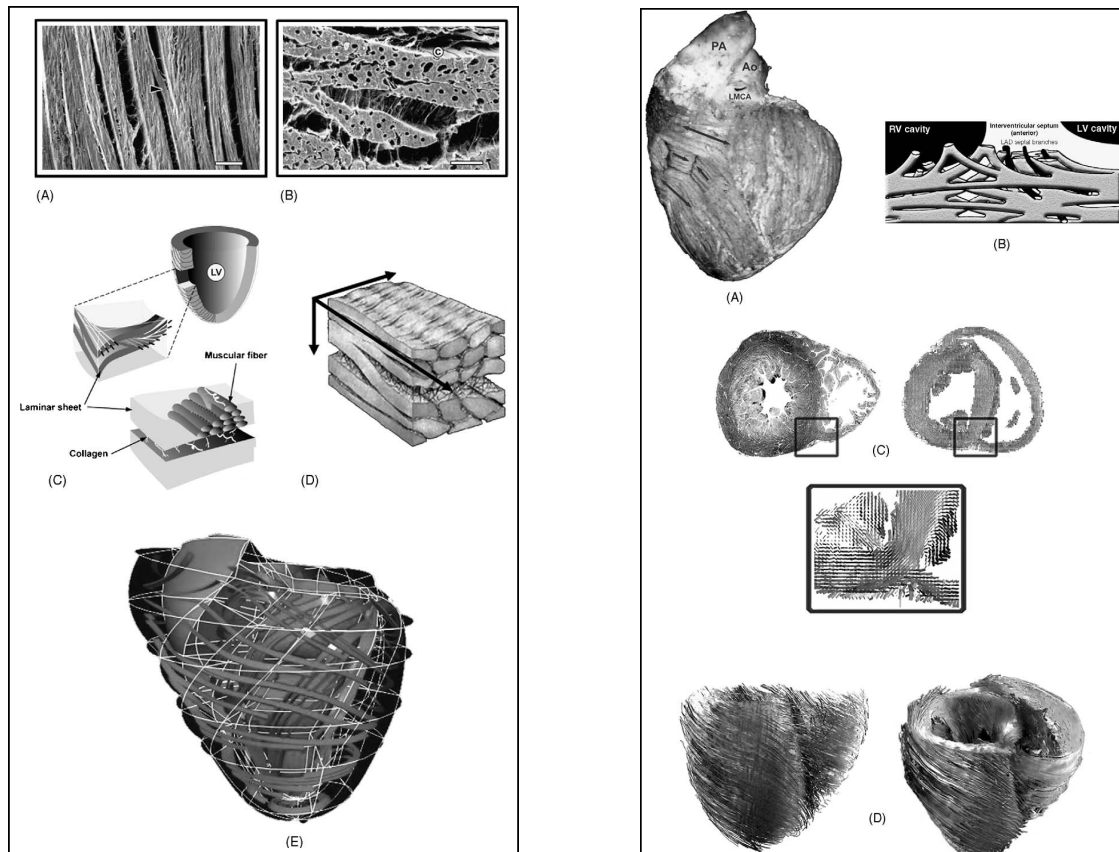


Figure 6.2.2: Heart structures [167]. **(LEFT)** The laminar sheet computer model of ventricular mass microstructure of human heart. **(A)** layered organization of myocytes, branching of layers (arrow), and collagen fibers between adjacent sheets. **(B)** Perimysial connective tissue weave surrounding myocardial sheets and covering surface capillaries. **(C)** Schematic of cardiac microstructure. **(D)** Orientations of the principal muscle fiber axes. **(E)** Rectangular tubes track along the fiber direction with the major flat dimension lying in the sheet plane. **(RIGHT)** Fiber disarray in the anterior and the posterior inter-ventricular grooves. **(A)** Aberrant fibers of the ascendant segment bridging the anterior inter-ventricular sulcus (bovine heart). **(B)** Cartoon depicting anterior inter-ventricular fiber disarray. **(C)** Histological and diffusion tensor MRI visualization. **(D)** Reconstruction of the posterior inter-ventricular fibers.

area, for a passive reference state, or imaging modalities, providing information about the static and dynamic surface geometry [310, 12, 147]. Several coordinate systems have been adopted for an efficient characterization of such complex geometries, the prolate spheroid at most, but resulting less accurate for the atrioventricular ring and apex modeling. More accurate and flexible resulted, however, a rectangular Cartesian coordinate system with full cubic Hermite polynomial interpolation.

Another fundamental character of muscular architecture is its anisotropy, and specifically the transmural variation of myocyte orientation [167] (see Fig.(6.2.2) and (6.2.3)). This aspect results crucial for the determination of the right function of the heart model: in most continuum models of the heart, in fact, it has been assumed that the material properties are transversely isotropic with respect to the myofiber axis, ventricular myocardium is certainly structurally orthotropic, with myocytes arranged in layers that are typically four cells thick [138]. Adjacent layers are separated by cleavage planes. Combination of intramural electrical mapping, and experiment-specific computer modeling, demonstrates that left ventricular myocardium has unique bulk conductivities associated with three microstructurally-defined axes. The voltage fields induced by intramural current injection are influenced by not only myofiber direction,

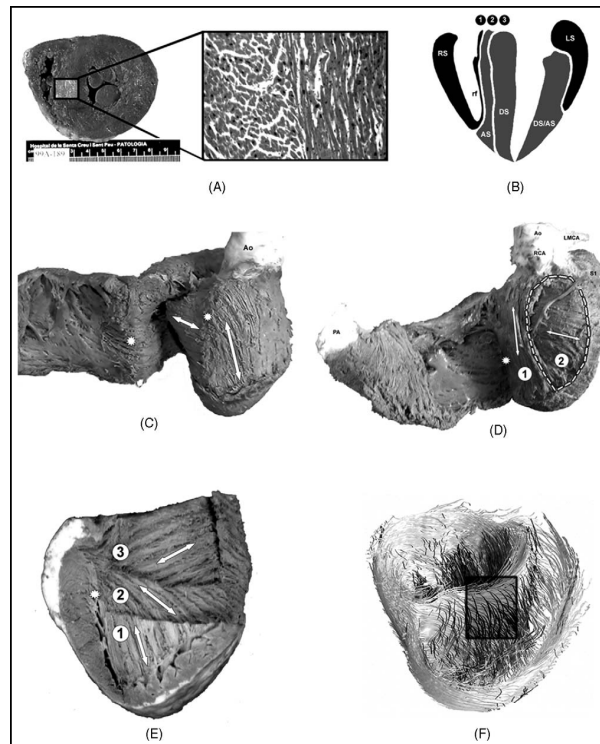


Figure 6.2.3: Inter-ventricular septum [167]. **(A)** Histological evidence (human heart) of septal fiber crossing. **(B)** Cartoon of the cleavage plans (longitudinal section). **(C)** Septal disarray (crossing). **(D)** Septal crossing at the level of the anterior inter-ventricular sulcus. **(E)** Special dissection of the inter-ventricular septum (bovine heart). **(F)** Reconstruction of the septal fibers.

but also the transmural arrangement of muscle layers or myolaminae. Such a character can, therefore, be incorporated in a continuous representation of the local structures defining three structurally based material axes: i) in the fiber direction, ii) perpendicular to the fiber direction within a muscle layer, iii) normal to the muscle layer. Computer models best matched recorded voltages with conductivities in the myofiber direction, and parallel and normal to myolaminae, set in the ratio 4:2:1, respectively. These findings redefine cardiac tissue as an electrically orthotropic substrate. Among others, the Purkinje conduction system still remain the most hard to identify, both for its morphologic variability that for its identification through medical imaging.

6.2.2 Cell and Tissue Model Formulations

The goal of integrative modeling of the electrical activity of the heart is to understand the genesis of the myocardial activation sequence, using models of cellular ion currents and tissue conductivity, and studying how current flow into the torso generates the body surface potentials. These quantities in turn generate the source for the dipole model of Einthoven [81], which was used to explain the electrocardiogram (ECG), still the most widely used noninvasive cardiac diagnostic tool. Modeling electrical activation, therefore, offers the only rational approach to understanding the highly complex events underlying reentrant arrhythmias and fibrillation.

Cell Models

Cellular electrical activity is involved in all large scale models of the heart. Electrical cell models date back to the Hodgkin-Huxley formulation of the squid axon [132], describing the flow of ions across the cell membrane through time-dependent gates of first-order kinetics and voltage-dependent rate constants. It consists of 3 currents (I_{Na} , I_K , I_L) and 3 gating variables (m , n , h).

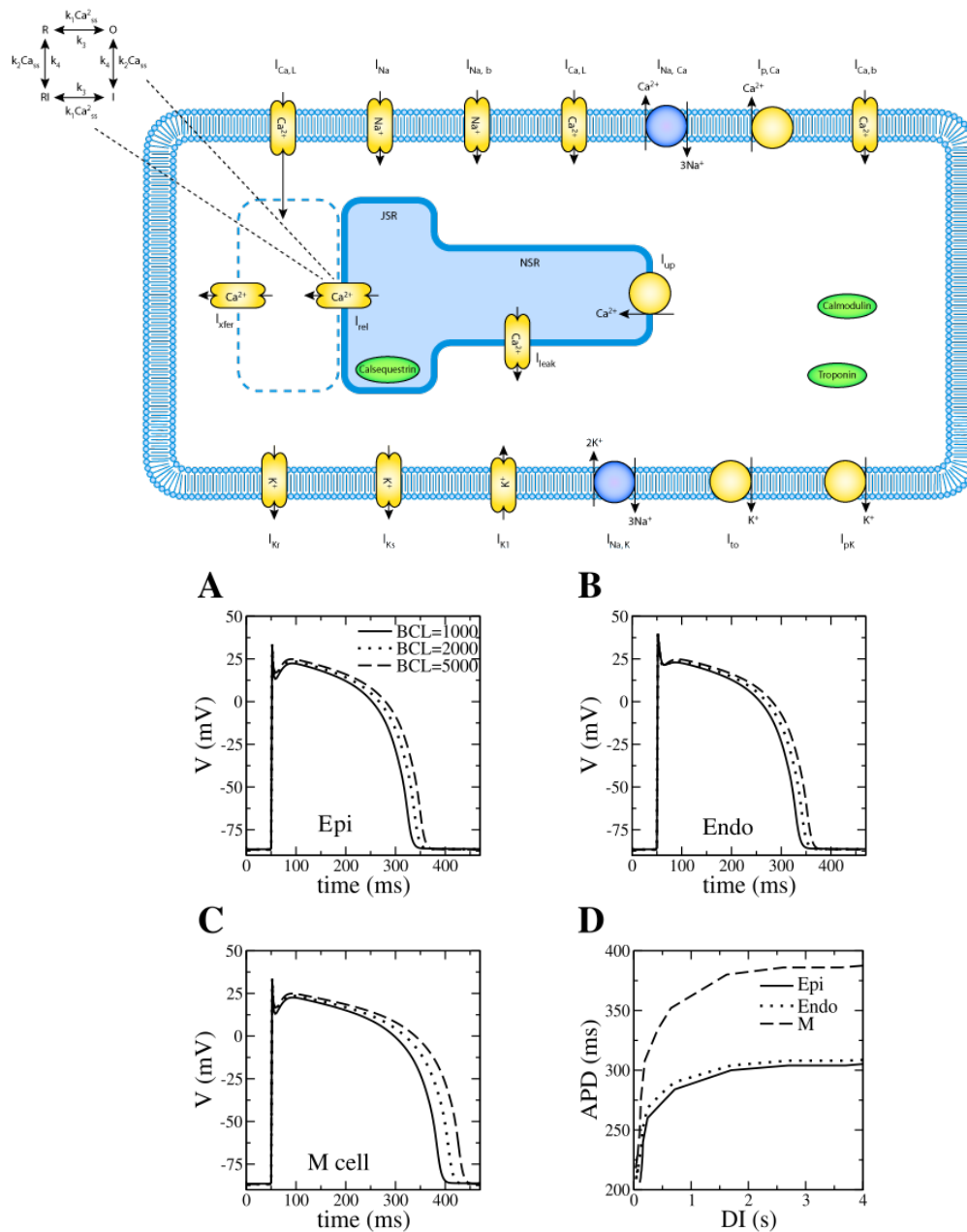


Figure 6.2.4: (LEFT) A schematic diagram describing the ionic currents, pumps, and exchangers that are captured in the ten Tusscher model of human ventricular action potential [31]. The intracellular compartment is the sarcoplasmic reticulum (SR), which comprises the network SR (NSR) and the junctional SR (JSR). Calcium buffers are present in both the cytoplasm and the JSR. (RIGHT) Steady-state action potential shapes simulated using the ten Tusscher model for the three cardiac layers [270]. (A) epicardium (Epi), (B) endocardium (Endo), and (C) mid-myocardium (M cell). Basic cycle length of 1000, 2000, and 5000 ms. (D) APD restitution curves of the three layers with the dynamic restitution protocol.

The subsequent increase in the knowledge of subcellular mechanisms has rapidly led to many different and incredibly complicated cell models. Highlighting such a trend, the better-known for cardiac cells are:

- DiFrancesco-Noble model of the Purkinje fiber cell [70]: consists of 12 currents and 7 gating variables.
- Beeler-Reuter model of the ventricular cell [17]: consists of 4 currents and 6 gating variables.
- Luo-Rudy model of the mammalian ventricular cell [179, 180]: consists of 14 currents, 4 fluxes and 11 gating variables.
- Nobel model of the guinea pig ventricular cell [206]: consists of 18 currents and 22 variables.
- Priebe-Beuckelmann model for human ventricular action potential [219]: it consists of 22 variables and represent the behavior of epicardial cells only.
- Tusscher-Noble-Noble-Panfilov model for human ventricular action potential [270]: consists of 17 variables and addresses epicardial, endocardial and mid-myocardial cells.
- Iyer-Marhari-Winslow model for human ventricular action potential [154]: consists of 67 variables and describes epicardial cells only.

In Fig.(6.2.4), a schematic representation of the ionic currents, pumps and exchanger considered in the ten Tusscher model is shown, and the corresponding simulated action potential shapes for endocardium, epicardium and mid-myocardium compared.

Tissue Models

Cell models can be incorporated into large-scale models, either as discrete, bundles or continuum. In the first case, a cellular automata or complex network is created [237]. However, the approach that

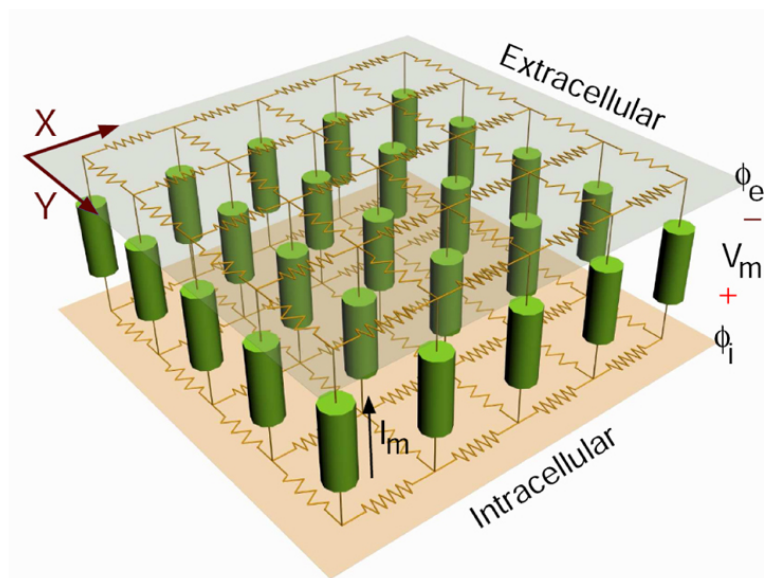


Figure 6.2.5: Representation of the bidomain scheme [32]. Two parallel plates of interconnected resistors, i.e. the intracellular and extracellular domains, are schematically connected via nonlinear elements. The membrane voltage is defined as $V_m = \phi_i - \phi_e$.

has gained considerable favor considers the tissue as two coupled, continuous domains representing a syncytium: one for the intracellular space and the other for the interstitial space (see Fig.(6.2.5)). The structure is partially preserved by assigning a conductivity tensor at each point. One advantage of using this space-averaged model is that the governing equations for the electric fields can be described by partial differential equations, resembling the structure of reaction-diffusion systems, that on occasion lead to analytical solutions. This formal treatment of cardiac tissue is referred to as the *bidomain model*.

The choice of size scale is fundamental to the formulation of a bidomain other than a monodomain approach. The bidomain formulation requires the identification of a length scale over which the behavior of interest can be averaged without a significative loss of information. If such a scale spans over the dimensions of several cells, then the discrete cellular structure can be replaced with a uniform and continuum domain.

The bidomain approach was first proposed in cardiac electric field in the late 1960s [242] and then mathematically formulated [276]. It is usually addressed by distinguishing cardiac tissue in three passive conducting regions, i.e. *intracellular*, *interstitial* and *extracellular space* (the region inside and between cells, and the bath surrounding the tissue, respectively). Adopting the usual homogeneizing technique of syncytial tissues [204] and because of the vast interconnection of cells, cardiac tissue can be regarded as a single intracellular continuous region separated from the outside interstitial by a membrane: the so called *giant effective cell*. Therefore, the bidomain model characterizes the intracellular and interstitial spaces as two uniformly continuous domains, and three key elements for cardiac tissue modeling can be identified [128]:

1. Current flow as a generalized Ohm's law.
2. Distribution of electrical potential.
3. Conservation of charge and current.

The description of each domain is based on a generalized version of Ohm's law, that for the intracellular and extracellular spaces assume the form:

$$\begin{cases} \mathbf{J}_i = \mathbf{G}_i \mathbf{E}_i = -\mathbf{G}_i \nabla \phi_i, & \mathbf{E}_i = -\nabla \phi_i \\ \mathbf{J}_e = \mathbf{G}_e \mathbf{E}_e = -\mathbf{G}_e \nabla \phi_e, & \mathbf{E}_e = -\nabla \phi_e \end{cases} \quad (6.2.1)$$

thus defining the relationship between the electric field \mathbf{E} (V/m), or the electric potential ϕ (V), the current density \mathbf{J} [A/m^2], and the conductivity tensor \mathbf{G} [S/m].

Considering the transmembrane current per unit volume, I_m [A/m^3], as

$$I_m = A_m \left(C_m \frac{\partial V_m}{\partial t} + I_{ion} \right), \quad (6.2.2)$$

the conservation of current and charge results in:

$$\begin{cases} \nabla \cdot \mathbf{J}_i = -I_m \\ \nabla \cdot \mathbf{J}_e = I_m \\ \nabla \cdot (\mathbf{J}_i + \mathbf{J}_e) = 0. \end{cases} \quad (6.2.3)$$

Here, A_m [m^{-1}] is the surface to volume ratio of the cell membrane, C_m [F/m^2] is the membrane capacitance per unit area, and I_{ion} [A/m^2] is the ionic component resulting from current flow through

ion channels, pumps and exchangers in the cell membrane. The transmembrane voltage, V_m , is given by:

$$V_m = \phi_i - \phi_e. \quad (6.2.4)$$

Bidomain model equations are finally given by combining Eq.(6.2.1), (6.2.2), (6.2.3) and (6.2.4) result in:

$$\begin{cases} \nabla \cdot [(\mathbf{G}_i + \mathbf{G}_e) \nabla \phi_e] = -\nabla \cdot (\mathbf{G}_i \nabla V_m) + I_{s1} \\ \nabla \cdot (\mathbf{G}_i \nabla V_m) + \nabla \cdot (\mathbf{G}_i \nabla \phi_e) = A_m \left(C_m \frac{\partial V_m}{\partial t} + I_{ion} \right) - I_{s2} \end{cases} \quad (6.2.5)$$

where I_{s1} and I_{s2} are external stimuli applied to either the extracellular or intracellular spaces. It's important to stress that any kind on subcellular mechanism, from the simplest FitzHugh-Nagumo-like to the more articulated one, can be easily incorporated in such a formalism through the I_{ion} term.

Assuming that the extracellular space is bounded and there is no electric current flowing from the extracellular space to adjacent spaces, homogeneous Neumann (zero-flux) boundary conditions can be implemented at the boundary Ω of outward normal \mathbf{n} , as:

$$\begin{cases} \mathbf{n} \cdot (\mathbf{G}_i \nabla \phi_i) = \mathbf{n} \cdot (\mathbf{G}_i \nabla (V_m + \phi_e)) = 0 \\ \mathbf{n} \cdot (\mathbf{G}_e \nabla \phi_e) = 0. \end{cases} \quad (6.2.6)$$

The local anisotropic properties and the effects of geometric heterogeneities are taken into account by assigning a local effective conductivity tensor for each domain, i.e. \mathbf{G}_i and \mathbf{G}_e . This is a fully orthotropic in the fiber/sheet/cross-sheet anatomical coordinate description, although typically treated as transversely isotropic to the fiber direction (see Eq.(6.2.12)). Even if in the actual tissue, ionic currents can pass only from one region into the other through the cellular membrane, mathematical and computational reasons necessitate to associate averaged properties to the intracellular and interstitial spaces defined over the entire tissue volume. For this reason, the transmembrane current too is volume averaged and is defined at each point of the bidomain model.

Monodomain Model

A simplified version of the bidomain equations (6.2.5), assumes an infinitely conducting extracellular field (or the two domains to be equally anisotropic), that is:

$$\mathbf{G}_e = \lambda \mathbf{G}_i \quad (6.2.7)$$

where λ is the scalar anisotropy ratio. This assumption leads to the removal of the first equation in (6.2.5) (always respected), namely the *monodomain model* [222], and resulting in:

$$\nabla \cdot (\mathbf{G} \nabla V_m) = A_m \left(C_m \frac{\partial V_m}{\partial t} + I_{ion} \right) - I_s, \quad (6.2.8)$$

and corresponding boundary

$$\mathbf{n} \cdot (\mathbf{G} \nabla V_m) = 0. \quad (6.2.9)$$

Here an average conductance, \mathbf{G} , has been introduced, readily:

$$\mathbf{G} = \frac{\lambda}{1 + \lambda} \mathbf{G}_i. \quad (6.2.10)$$

The proposed monodomain equation, also called *cable equation*, is usually expressed in terms of diffusivity as:

$$\frac{\partial V_m}{\partial t} = \nabla \cdot \mathbf{D} \nabla V_m - \frac{I_{ion}}{C_m} + I_s. \quad (6.2.11)$$

This writing is only true assuming the membrane capacitance with a constant value, otherwise the divergence operation would be not respected. In the case, the emerging diffusion tensor \mathbf{D} (m^2/s) can be defined depending of tissue properties:

- *axially symmetric anisotropy*: diffusion in all directions orthogonal to the fiber direction is assumed to be the same; propagation is described by two values of the diffusion coefficient, D_1 and D_2 .

$$\mathbf{D} = D_2 \mathbf{I} + (D_1 - D_2) \mathbf{f} \mathbf{f}^T \rightarrow D_{ij} = \begin{cases} D_2 + (D_1 - D_2) f_i f_j, & i = j \\ (D_1 - D_2) f_i f_j & i \neq j \end{cases} \quad (6.2.12)$$

where \mathbf{I} is the identity matrix, \mathbf{f} is the fiber direction vector and \mathbf{f}^T its transpose; D_1 acts longitudinally, and D_2 acts transversally.

- *orthotropic anisotropy*: principal directions longitudinal to fibers in the sheet plane (\mathbf{f}), normal to fibers in the sheet plane (\mathbf{s}), and normal to the sheet plane (\mathbf{n}); propagation is described by three values of the diffusion coefficient, D_1 , D_2 and D_3 .

$$\mathbf{D} = D_1 \mathbf{f} \mathbf{f}^T + D_2 \mathbf{s} \mathbf{s}^T + D_3 \mathbf{n} \mathbf{n}^T \quad (6.2.13)$$

with the orthonormal condition

$$\mathbf{f} \mathbf{f}^T + \mathbf{s} \mathbf{s}^T + \mathbf{n} \mathbf{n}^T = \mathbf{I} \quad (6.2.14)$$

and the simplified expression for \mathbf{D} as:

$$\mathbf{D} = D_2 \mathbf{I} + (D_1 - D_2) \mathbf{f} \mathbf{f}^T + (D_3 - D_2) \mathbf{n} \mathbf{n}^T. \quad (6.2.15)$$

However, most complex cardiac electric phenomena, i.e. fibrillation and defibrillation, multiple reentry and spiral breakup, require knowledge of the extracellular field [181]. The main reason is due to the practical possibility to deliver shocks only in the extracellular medium. Increasingly, therefore, the monodomain modeling approach is being phased out and the bidomain formulation adopted.

Eikonal Modeling

An alternative modeling approach, developed for large-scale simulations [54], assumes that the upstroke of the action potential is sufficiently quick with short temporal and spatial durations that it can be modeled as a step jump (see Fig.(6.2.6)). Of course, such models cannot capture the details inherent in the different cellular models and are not appropriate for modeling repolarization or reentrant phenomena.

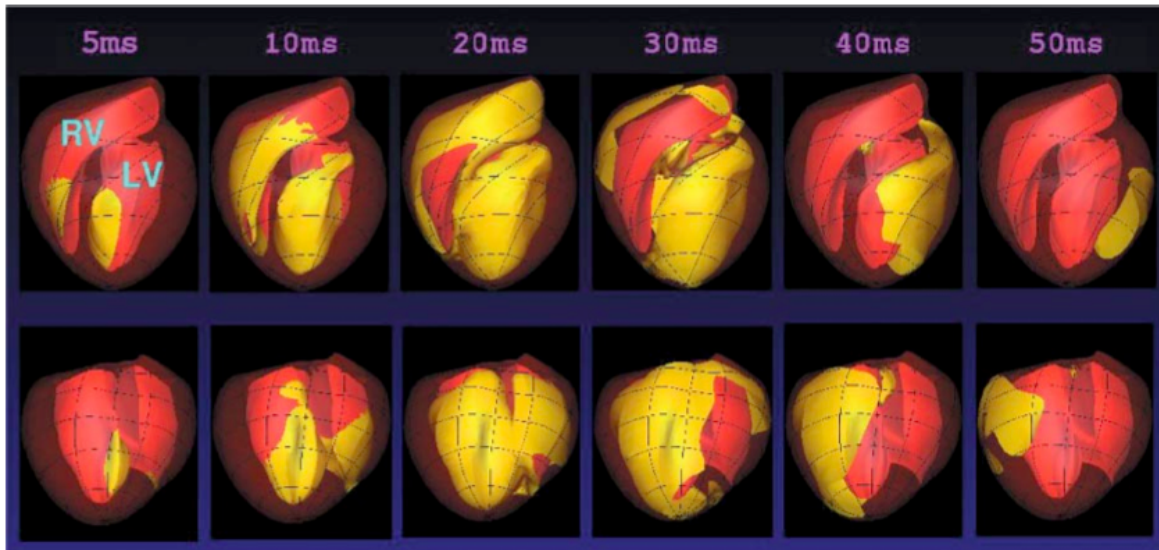


Figure 6.2.6: Integrative computer model of human heart, based on a FEM reconstruction of the geometry and fibrous-sheet structure of myocardial tissue. Simulated wavefront locations using an eikonal equation [146].

6.2.3 Computational Issues & Validation

Computer Models

The usual method to solve bidomain equations are finite differences, finite elements and finite volumes. The most challenging aspect, from a numerical point of view, is due to the sharp rise in the action potential (upstroke): converged implementations require time steps close to 0.01 ms and spatial step of about 0.2 mm [260]. Detailed simulation of an average heart, $\sim 250\text{ cm}^3$, performing this level of time and space discretization require several days on high-performance computers: about 30 million grid points, 5×10^4 time steps for a single heart beat of 0.5 s , tens of gigabytes of storage. Most of the time, however, such a complexity is not necessary. In fact, advanced numerical techniques can significantly reduce both spatial and time demands. A specific example is the space-time-adaptive time-integration algorithm [36] (see Fig.(6.2.7)A-B), which can achieve a factor of 5 reduction in computational effort and memory when compared to an algorithm using a uniform space-time mesh at the finest resolution. Other techniques are based on spectral smoothed boundary methods [27] (see Fig.(6.2.7)C) and similar. Unfortunately, this is not the case for arrhythmic behavior, such as ventricular tachycardias. When multiple reentrant wave fronts are present, the high-resolution mesh is required everywhere. Parallel procedures on CPU cluster machines have been implemented, even if the actual solution seems to be in favor of GPU clusters. As recently shown by Bartocci et al. [16], model-specific optimization of GPU implementations for 2D and 3D cardiac models is leading to detailed and realistic simulations close to real time using a desktop computer (see Fig.6.2.8 and Tab.(6.1)).

Integration of cell and tissue models

If the computational issues seem to have new open routes, the measurement of material properties and model validation remain the most difficult aspects. The scientific community is still facing the correct characterization of conductivity tensors for the normal heart. Of equal uncertainty are many of the values required in the cellular models.

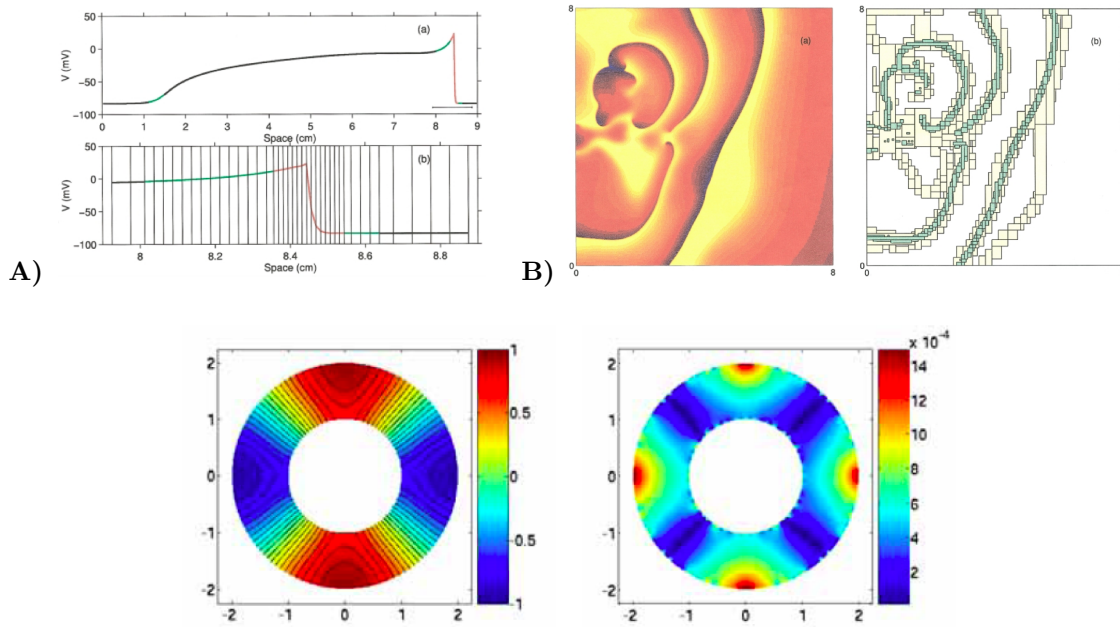


Figure 6.2.7: (TOP) Space-time adaptive meshing method example [36]. (A) 1D refinement of the spatial profile of an action potential propagating wave. (B) 2D rotating waves and hierarchical Cartesian meshes refinement. (BOTTOM) Spectral smoothed boundary method example [27], solution and error.

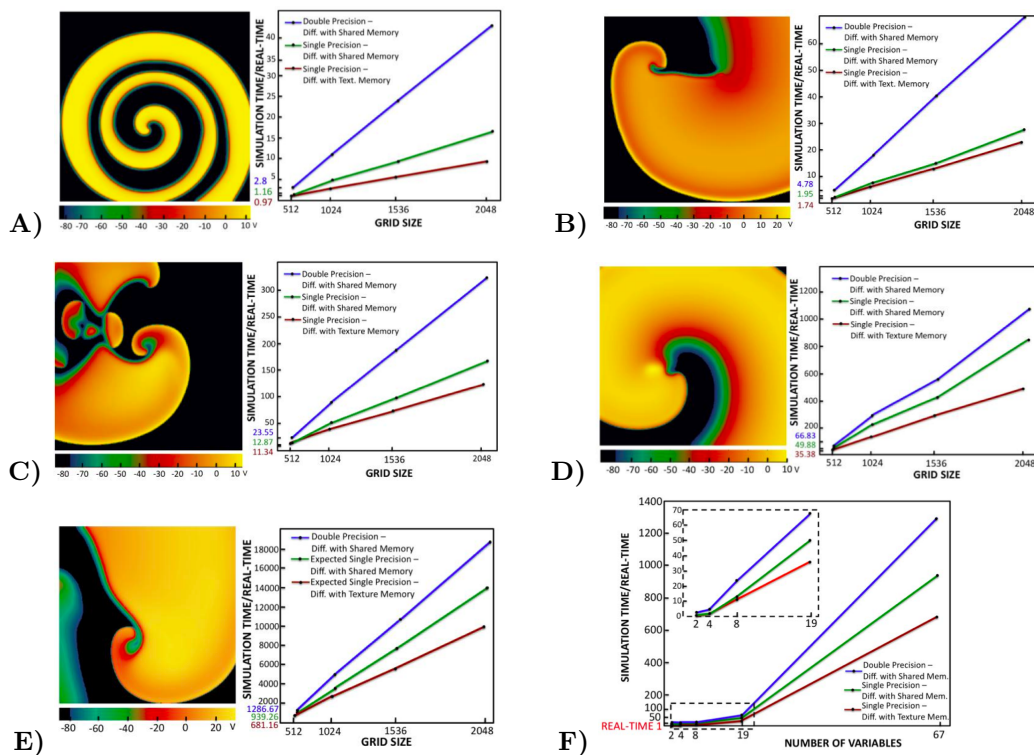


Figure 6.2.8: Spiral wave simulations of action potential models in a 512×512 grid tissue, and corresponding simulation times normalized to real time for computing 1 s using different grid sizes. (A) Karma model. (B) Minimal model. (C) Beeler-Reuter model. (D) Ten Tusscher model. (E) Iyer model. (F) Simulation time normalized to real time as a function of the number of model variables.

Therefore, both computational and experimental limitations, are inducing more and more convergence towards “synthetic indicators” able to integrate local cell properties into space dependent tissue behavior. In a short list can be cited:

- *Liminal length*: minimum length below which no combination of stimulus strength and duration can produce a propagating wave.
- *Minimum cycle length for propagation*: minimum cycle length that can be used to achieve successful wave propagation, or effective refractory period.
- *Conduction velocity*: related to the strength of cell-to-cell coupling, and scales as the square root of the diffusion coefficient

In Tab.(6.2) a direct comparison of maximum conduction velocity, maximum upstroke and maximum conductance sodium current in tissue for different models is reported. Other effects that have to be considered in integrating cell and tissue models are due to electrotonic current-mediated dynamics. The flow of current within the tissue resulting from regional differences in potential can have an important influence on local dynamics and excitation. The two most important ones can be recognized in decreased action potential amplitude and shape, and changes in restitution, alternans, and memory [51].

Table 6.1: Computational complexity comparison related to monodomain and bidomain cardiac model formulations.

DOMAIN	MODEL	PDE	ODE	COMPLEXITY
Bidomain	Luo-Rudy I	2	7	200
Bidomain	FitzHugh-Nagumo	2	1	3
Monodomain	Luo-Rudy	1	7	60
Monodomain	FitzHugh-Nagumo	1	1	1
Monodomain	Aliev-Panfilov	1	1	1

Table 6.2: Maximum conduction velocity (CV), maximum upstroke velocity (dv/dt), and maximum conductance sodium current (g_{Na}) in tissue for different models [51].

MODEL	CV	dv/dt	g_{Na}
Lou-Rudy I	64.7	275	23
Shannon	61.8	263	16
Iyer	60.1	266	56.32
Faber-Rudy	59.4	246	16
ten Tusscher	59.4	227	14.838
Priebe-Beuckelmann	58.7	247	16
Mahajan	52.2	173	12
Fox	51.3	196	12.8
Courtemanche	50.4	127	7.8
Beeler-Reuter	47.6	110	4
Hund-Rudy	47.3	133	8.25
Pandit	45.1	103	8
Nygren	39.5	83	n/a
Bondarenko	39.1	94	13

6.3 Myocardial Mechanics Modeling

The mechanical behavior of uniaxial cardiac structures has been studied extensively [271], and a sophisticated understanding of the mechanisms that underlay mechanical function at cellular and subcellular levels has been reached. However, while heart wall motion and local myocardial deformation and strain can nowadays be estimated with high precision, regional stress cannot be measured. Mathematical models based on established continuum mechanics principles tried to bridge such a gap.

The usual starting point in muscle modeling is the famous Hill's three element model for tetanized muscle contraction [101, 130] (see Fig.(6.3.1)): a passive spring (1), representing the titin molecule, is connected in series with two parallel elements, one elastic spring (2), representing the passive stiffness of the actin-myosin filaments, and a contractile element (3), representing muscle activation. Even if this classic approach has been specifically though for smooth muscles, it has been later modified for striated tissues.

Continuum models of cardiac mechanics have two fundamental requirements:

1. an appropriate representation of the three-dimensional geometry and muscular architecture of the heart (as described before);
2. an accurate description of the time-varying contracting and non-contracting tissue in different regions of the heart.

On this basis, it is possible to solve governing physical laws:

- Conservation of mass.
- Conservation of momentum.
- Conservation of energy.

It is worth to note that the solution of these equations requires appropriate pressure and displacement boundary conditions. Moreover, two major limitations can be identified in model validation:

1. the only physical comparison is limited to displacement and strain fields;
2. the incomplete knowledge of the constitute relations governing the three-dimensional mechanical behavior of myocardium.

6.3.1 Material Properties, Cardiac Deformation and Strain

Information about tissue motion, deformation, and strain can be collected with the use of different techniques: X-ray with embedded radio-opaque markers; cardiac magnetic resonance tissue tagging; uniaxial,

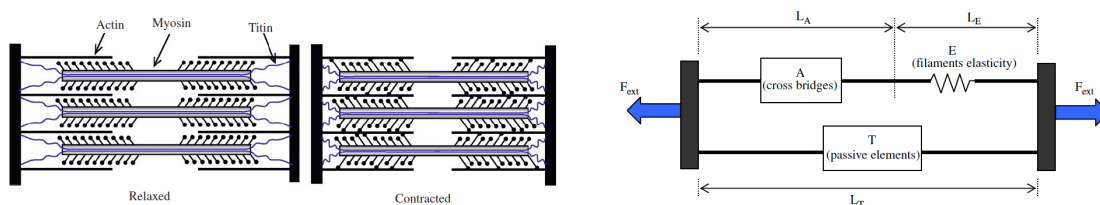


Figure 6.3.1: (LEFT) Schematic illustration of a single sarcomere. Contraction occurs due to relative sliding between the thin (actin) and thick (myosin) filaments, and force is generated by myosin heads that bind to the thin filaments and form cross-bridges [110]. (RIGHT) A lumped model of a single sarcomere [68].

biaxial and shear tests on passive tissues, etc. The main observations aimed through these measurements are [147]:

- transmural strain gradients in both systole and diastole;
- torsional deformation during systole;
- large deformations of the inner wall during ejection.

Gaining 3D information starting from local measurements has been shown to be unrealistic [255], in fact, the resulting changes are much greater than what can be accounted for by myocyte shortening. The reason for such a misleading is due to the altered myocyte arrangement in the inner wall, revealing substantial shearing between adjacent layers [266].

Characterization of the material properties of myocardium, therefore, requires detailed information about multi-axial relationship between force and length. The only possible measurements for understanding constitutive relations are based on in vitro specimens, as discussed in Chap.(2). Uniaxial, biaxial and shear tensile testing have been extensively applied [67, 272], revealing the highly nonlinear, viscoelastic, anisotropic response with greater stiffness in the fiber direction then transverse to it. Triaxial devices, moreover, have recently been developed [71] to control compressive and shear deformations while measuring the resulting orthogonal forces.

These tests does not depict significant differences between different tissues, however, the material properties of collagen are qualitatively different, influencing the passive mechanical behavior. Novel techniques capable to unveil the remaining mysteries are only appearing in these years. Ultrasound imaging to map propagating action potential waves in the moving tissue has been recently adopted [210] (see Fig.(6.3.2)) in order to obtain image of action potential propagation deep within the walls of the heart.

Calcium Levels for Muscle Contraction

Calcium cycling has been described in Chap.(2). An important property for mathematical modeling is the minimum quantity of calcium required to activate the myofilaments and produce contraction. Such amount has been quantified in $\sim 600 \text{ nmol/L}$. Moreover, Ca dependence on force is crucial too. The Hill coefficient for contraction initiation has been quantified as ≥ 4.6 , indeed, increased myofilament Ca sensitivity at longer sarcomere lengths is crucial in Starling's law of the heart. However, these measurements are indicative and change from laboratory to laboratory [21].

6.3.2 Constitutive Laws

For modeling purposes, taking into account the material properties of passive myocardium, it is necessary to formulate constitutive laws that provide an accurate representation of the material responses. This paragraph will briefly introduce the problem, while a more detailed description will be given in Chap.(7).

Incompressible elastic media are usually the starting point for soft biological tissue modeling. In this case, the second Piola-Kirchhoff stress tensor, T_{ij} , assumes the following form:

$$T_{ij} = \frac{\partial W}{\partial E_{ij}} - pC_{ij}^{-1}, \quad (6.3.1)$$

where W is the strain energy density function, E_{ij} is the Green deformation strain tensor, C_{ij} is the right Cauchy-Green strain tensor, and p is a Lagrange multiplier, accounting for a hydrostatic pressure.

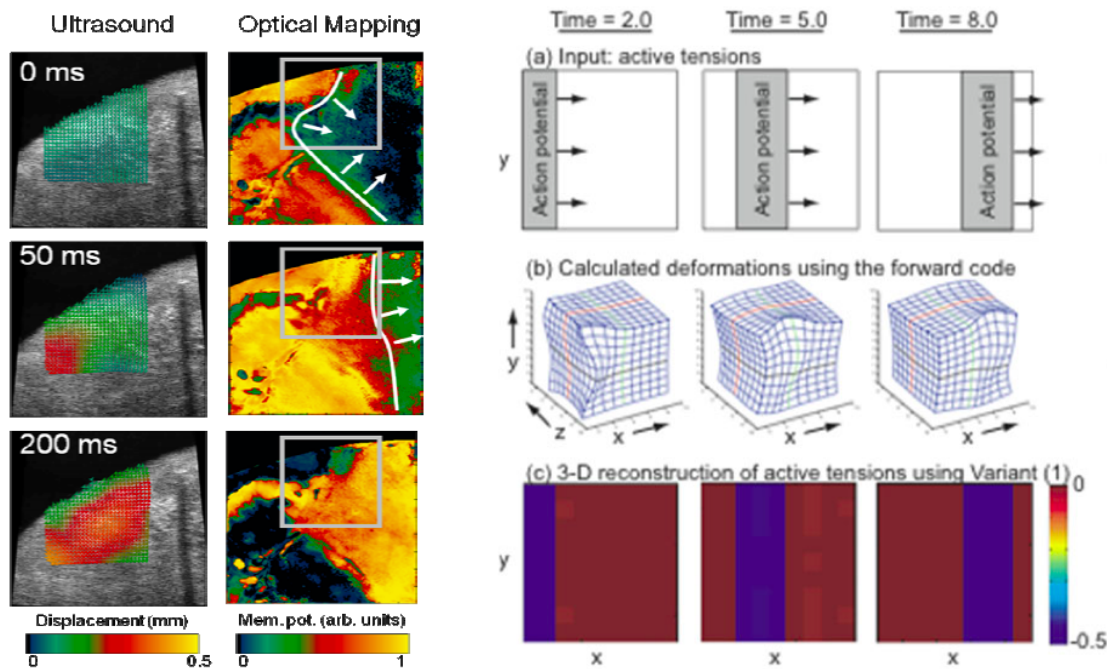


Figure 6.3.2: (LEFT) A series of three ultrasound images and calculated tissue displacements (top panels) and three optical mapping images (bottom panels) of approximately the same region during the passage of the same action potential. Red and yellow correspond to depolarization. (RIGHT) (A) Applied active tension in the local fiber direction as a function of time and space. (B) Resulting deformations of the cubically shaped tissue system. (C) Reconstruction of the active tensions in the local fiber direction (adapted from [210]).

The last term does not contribute to the deformation but it is necessary to respect the incompressibility constraint.

The functional form of the strain energy function can be inferred from experimental data, and the material parameters may then be estimated using fitting techniques. One of the most successfully used form has been the exponential strain energy function, in general given by:

$$W = \frac{1}{2} C_{ij} (e^{Q_{ij}} - 1) ,$$

Q_{ij} is a function in which the strain components E_{ij} are referred to local structure-based coordinates, and its form determines whether the strain energy function is transversely isotropic or orthotropic. Generalization of such a formulation have been recently proposed [79, 153]. In this contest, it is important to enhance that, through these constitutive formulations, a single material parameter is associated with each of the strain components. This allows a direct and easy fit of the model with experimental data.

Forces developed during contraction have been usually assumed to act only in the fiber direction, then active stress added to the passive one, and associated with the tissue deformation thus producing a composite constitutive law:

- Time-varying elastance active stress [114]: simplest threshold induced active state.
- Fading memory active stress [145]: realistic length and velocity dependence, calcium binding and cross-bridge kinetics.
- Active stress superposition [199]: subcellular kinetic mechanisms for excitation-contraction coupling

are modeled as an adjoint stress.

- Active multiplicative decomposition [45, 198]: fiber activation via calcium cycling is modeled modifying the geometrical representation of the domain, i.e. deformation gradient tensor.

Further steps have been done in order to get robust structure-based constitutive laws that accurately represent the mechanical properties of both passive and active myocardium in different regions. In Chap.(7) different models available in the literature will be reviewed and a new general formulation proposed.

6.4 Open Questions

When a modeling approach is initiated, in general, it requires assumptions and simplifications. From this point of view, cardiac electrophysiology has not stated a generally accepted framework for choosing an appropriate combination of cellular electrophysiological model, tissue model, geometrical model, and numerical model. Even though, there are several evidences [51] of the high sensitivity of cardiac model behavior to such assumptions. Here, the open questions arising from such a lack of uniformity are listed:

- Choice of tissue model: monodomain versus bidomain formulation and the role of boundary conditions.
- Numerical approach: irregular and hybrid meshes for complex emergent behaviors.
- Benchmarks for numerical methods: comparison of different tissue models and numerical approaches with respect to a set of example problems.
- Parameters and parameter sensitivity: discordance in the correct value of tissue conductivities.
- Methods for detailed tissue microstructure: the role played by subcellular structures remain unexplored in detail.
- Representation of pathological structure and function: lack of robust methods and parameters to represent pathological conditions.
- Validation against experimental data: difficulty in verifying the modeling criteria.

Throughout this dissertation, the underlying leitmotif consisted in approaching both theory and simulations from a basic point of view. Even though, the minimal modeling assumptions done led to interesting results, both from a basic and an applied science point of view. In this regard, the final chapters will be devoted to an extended description of all the essential steps through which novel results were obtained.

6.5 Computer Models for Arrhythmogenesis

Computer models can help in understanding the complex phenomenology of arrhythmia initiation and evolution, as well as tissue remodeling during fibrillation events. Many experimental studies have shown the presence of scroll waves of electrical activation, rotating at higher frequencies than the heart's natural pacemaker (100 – 200 *ms*), thus preventing normal function. On the other hand, many numerical and computer models have explored the complex dynamics of existing scroll waves, as well as their breakup and the new waves formation phenomena. These findings are mainly based on *cell models*, thus including membrane potential, transmembrane ionic currents and ion concentrations, and *tissue models*, describing the overall geometric structure of the tissue as well as cells interconnection.

Two main usage of computer models can be identified: 1) performing *ad hoc* in silico experiments, in which exactly one parameter of interest is varied, an impossible task to pursue in experiments; 2) complementing experimental and clinical works, guiding *in vivo* and *in vitro* tests, thus investigating and explaining experimental and clinical observations. The continual feedback between simulation and experiments, therefore, is mandatory in order to reduce both economic and time investments on animal experiments, and at the same time to generate a valuable information about human arrhythmias while avoiding issues of patient safety. In this perspective, a novel numerical study will be presented in Chap.8.

This section is devoted to the description of new mathematical investigative tools in the analysis of cardiac arrhythmias.

6.6 Computer Modeling of Atrial Fibrillation

The shape of the atrial cellular action potential is essentially different from that of the ventricular cell, in particular, outward potassium currents create a variety of atrial AP morphologies. To be cited:

- Nygren model of human atrial myocytes [208]: consists of 29 variables, 12 transmembrane currents, a two-compartment sarcoplasmic reticulum and restricted subsarcolemmal space for calcium handling.
- Courtemanche model of human atrial myocytes [59]: consists of 21 variables, 12 transmembrane currents, and intracellular calcium handling with a two-compartment sarcoplasmic reticulum and buffering.

Each of these models was developed using Hodgkin-Huxley-style gating variables, detailed intracellular calcium handling and transmembrane currents. The most noticeably differences between the two are present in their action potential morphologies, the Nygren model has a triangular shape at all cycle lengths, while the Courtemanche one has a spike-and-dome morphology at long CLs that become triangular at shorter ones. Some of these characters are summarized in Fig.(6.5.1)(left) together with restitution curves, where short-term memory properties characteristic of Hodgkin-Huxley-like formulations are enhanced, comparing steady-state with S1-S2 restitution protocols.

Anatomically, the atria are complex structures, containing nonconductive regions like blood vessels and valves as well as slow-conducting and anisotropic fast-conducting regions. Small models focusing on a single complex structure within the atria have provided valuable information about that structure contributions during arrhythmia initiation and maintenance [37]. Nevertheless, in pathologic cases, the already complex geometry of the atria often is quite different from structures considered normal, and different diseases may cause different morphological changes [200]. From a modeling point of view, several currents can be varied to simulate electrophysiological changes that take place as a result of sustained

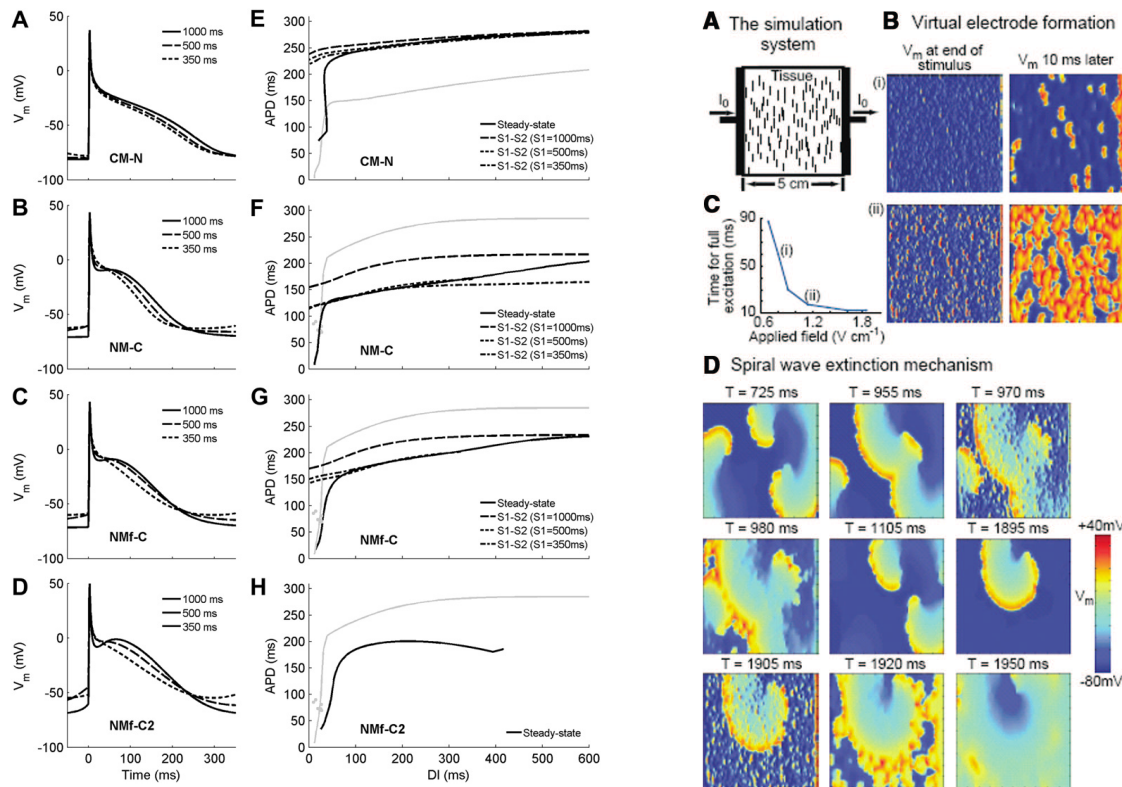


Figure 6.5.1: **(LEFT)** Action potentials and restitution curves for shape and morphology comparison between the Nygren and Courtemanche models [42]. Action potentials after 30 s of pacing at CLs of 1000, 500, and 350 ms. Restitution curves obtained using steady-state and S1-S2 protocols. **(RIGHT)** Schematic description of the far field method and numerical simulation of virtual electrode formation and termination of reentry in tissue with multiple small conductivity discontinuities [93, 181].

atrial fibrillation [59]. In this scenario, APs are triangular in morphology at all CLs and are shorter in duration.

6.6.1 Low-Energy Termination of Atrial Fibrillation

The *far-field antifibrillation pacing* method has been recently introduced in addition to antitachycardia pacing and cardioversion electrical based therapies [93]. Such a methodology, delivers a short train of low-intensity electric pulses at the frequency of antitachycardia pacing but from field electrodes, and it is mathematically based on the virtual electrode theory (see Chap.2). In particular, it takes advantage of the fact that new activations, *secondary sources*, arise at interfaces separating regions with different conductivities, depending on the extent of the conductivity discontinuity and the electric field strength. The corresponding mathematical description is based on the bidomain equations reported in Eq.(6.2.5), and the corresponding secondary sources simulations are shown in Fig.(6.5.1)(right). Current injected by the positive electrode produces regions of opposite polarization, which in turn create new activation waves and finally terminate the reentry.

In Tab.(6.3) a direct comparison of electrically based therapies in terms of delivered energy is reported. It's worth to mention that the far field pacing technique necessitates of several orders of magnitude less than the standard ones.

Table 6.3: Electrically based therapies: amount of delivered energy. Comparison of the different protocols.

Therapy	Stimulations	Results & Drawback
Cardioversion	1 pulse $> 5 V/cm$	Reset all the electrical activity in the atria but produces pain, trauma, myocardial damage, reduced battery life in implanted devices
Antitachycardia Pacing	$8 \div 10$ low-energy pulses at $50 Hz$	Suppresses paroxysmal AF but it is not effective for converting AF
Far-Field Pacing	5 pulses at $0.9 \div 1.4 V/cm$	Delivered energy, $0.074 \div 0.81 J$, below the energy at which sedation is necessary ($0.5 \div 1 J$)

6.7 Models of Vortex Dynamics in Myocardium

Ventricular fibrillation (VF) is characterized by electrical vortices of action potential (spiral and scroll waves), topologically analogs of the hydrodynamic point and filament vortices in a turbulent fluid. Such propagating dynamics are further complicated by the rotational anisotropy of the intramural ventricular wall [88, 89], producing twists and breakups, and causing the transition to wave turbulence similarly to solitons along hydrodynamic vortex lines. The complexity of these dynamics, and the computational efforts necessary to numerically solve long run simulations, has led to the rise of simplified phenomenological models. Starting from simplified versions of Hodgkin-Huxley formulation [160, 259], their primary character consists in variables reduction and mathematical simplification.

- Barkley model [14, 15] (2 variable): qualitative model in pattern forming systems. The model consists of 2 variables, a fast variable, and a slow gate variable, following a FitzHugh-Nagumo or Van Der Pol like formulation [160, 259].
- Karma model [158] (2 variable): based on an analysis of the Noble model [70, 206] where the fast gate variables have been eliminated adiabatically. The model consists of 2 variables, a fast variable related to the membrane voltage and a slow gate variable.
- Fenton-Karma model [88] (3 variable): known as the 3V-model, is a three-variable model of the cardiac action potential. The model consists of 3 transmembrane currents, a fast inward and two slow outward. Along with the voltage, 2 gating variables regulate inactivation of these currents.
- Simitev-Biktashev model [250] (3 variables): reduction of the Courtemanche et al. human atrial model [59] to describe excitation fronts. The model consists of 1 transmembrane current for the sodium. Along with the voltage, 2 gating variables regulate inactivation of this current.
- Cherry-Ehrlich-Nattel-Fenton model [39] (4 variables): based on the Fenton-Karma model [88], it follows a similar formulation. An additional variable accurately describes action potential shape and includes separate parameter sets to represent canine left atrial and pulmonary vein action potentials.
- Minimal model [28] (4 variable): representing human ventricular cells, separate parameter sets describe epicardial, endocardial, and mid-myocardial cells action potential shapes and morphologies. The model consists of 3 transmembrane currents, a fast inward and two slow outward. Along with the voltage, 3 gating variables regulate inactivation of these currents.

6.7.1 Rotational Anisotropy, Tip Meandering and Curvature

Isocrones

The spread of an excitation wavefront in bulk myocardial tissue has been studied extensively: wavefronts spread essentially according to Huygen's principle up to small curvature corrections to the conduction velocity [159]. If no fiber rotation is considered, isochrones (lines of constant arrival times of the wavefront) would appear as simple striding ellipses [303] (see Fig.(6.7.1) left). Differently, if fiber rotation is considered, the isochrone lines twist in time and change shape [88] (see Fig.(6.7.1) right). The overall phenomenon is even more complicated in higher dimensions, because of the electric coupling between the different anisotropic planes. In this case the excitation can spread back to the epicardium/endocardium from deeper layers [89], and alternative visualization tools are necessary.

Spiral Meandering and Scroll Waves

When a single spiral wave is present in the tissue (a rare situation in healthy tissues), then its continuous movement, called *meandering*, can be studied. Several numerical analysis have shown that spiral meander markedly changes depending on tissue properties [303]. The usual way to visualize these dynamics, consists in "follow" the trajectory of the *tip wave* over time, and the resulting trajectory generally depends on the way the wave tip is defined (Fig.(6.7.2)). A practical way to identify the spiral wave tip in two-dimensions is to arbitrarily choose a single isopotential line of constant membrane potential, i.e. a threshold reference value,

$$V(\mathbf{r}, t) = V_{\text{iso}}, \quad (6.7.1)$$

where $\mathbf{r} = x\mathbf{x} + y\mathbf{y}$ is the position vector, in order to represent the boundary between depolarized and repolarized regions of the tissue. The wave tip can then be defined as the point where the excitation wavefront meets the repolarization waveback of the action potential. In other words, it is the point of zero normal velocity along this boundary. It may be mathematically identified as the intersection point of the lines $V = V_{\text{iso}}$ and $\partial_t V = 0$, defined by the coordinates $(x_{\text{tip}}, y_{\text{tip}})$ of the vector $\mathbf{R} = x_{\text{tip}}\mathbf{x} + y_{\text{tip}}\mathbf{y}$,

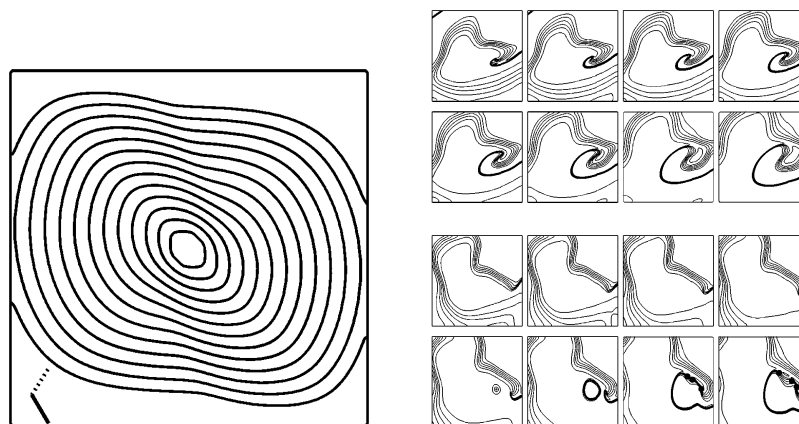


Figure 6.7.1: Contour plots of simulated membrane potential via the three-variable Fenton-Karma model [88]. **(LEFT)** Isochrone lines spaced every 5 ms in time showing the spread of excitation on the homogeneous epicardium in response to a point stimulus at the center of the epicardium. **(RIGHT)** Isochrone lines spaced at intervals of 20 mV on the epicardium (a) and endocardium (b).

that satisfy:

$$V(\mathbf{R}, t) - V_{\text{iso}} = \partial_t V(\mathbf{R}, t) = 0. \quad (6.7.2)$$

Such a mathematical prescription, moreover, is applicable to higher spatial dimensions or more complex models, although not the unique way. In fact, Eq. (6.7.2) defines the *instantaneous* vortex line in three-dimensions as the intersection of two surfaces:

$$\mathbf{R}(s, t) = x(s, t)\mathbf{x} + y(s, t)\mathbf{y} + z(s, t)\mathbf{z}, \quad (6.7.3)$$

where s is the arc length along the line. The filament curvature, k , and the torsion, ν , are defined by the Frenet-Serret equation relating the unit vector locally tangent to the filament, \mathbf{t} , the normal direction to the filament, \mathbf{n} , and the binormal direction to the filament, \mathbf{b} :

$$\begin{cases} \partial_s \mathbf{t} = k\mathbf{n} \\ \partial_s \mathbf{n} = -k\mathbf{t} + \nu\mathbf{b} \end{cases} . \quad (6.7.4)$$

Finally, in order to calculate the *twist*, it is useful to define the vector field

$$\mathbf{N} = \left[\frac{\nabla V}{|\nabla V|} \right]_{\mathbf{r}=\mathbf{R}},$$

which in two dimensions coincides with the unit vector perpendicular to the wave tip trajectory, while in three dimensions $\mathbf{N}(s, t)$ becomes a vector field along the vortex line, locally perpendicular to the tangent $\mathbf{t}(s, t)$. In this case, it is possible to identify the quantity twist, $W(s, t)$, distinct from the torsion, and defined as the scalar field

$$W(s, t) = [\partial_s \mathbf{N}(s, t) \times \mathbf{N}(s, t)] \cdot \mathbf{t}(s, t). \quad (6.7.5)$$

This field measures the rate at which \mathbf{N} rotates in the plane perpendicular to $\mathbf{t}(s, t)$ as one moves along the filament [302]. In Fig.(6.7.3) representative examples of cardiac simulated dynamics are shown in terms of simulated scroll waves and of vortex lines.

6.7.2 Spiral Waves Breakup: Memory & Restitution Curves

Multiple mechanisms underlying spiral dynamics have been identified and categorized. The breakup of spiral waves has been known to occur since the early numerical experiments of Wiener and Rosenbluth [299] and Moe [194]. In many cases, existing scroll waves break and form new waves, which in turn yield further breakup and more waves.

These scenarios present faster heart rates than normal, and the relative durations of systole and diastole are adjusted to ensure an efficient pumping activity. If a second action potential is initiated soon after the first, when not all ionic processes have been recovered fully to their rest states, the duration of the second AP is shorter than the first because the transmembrane current is reduced. It follows that an action potential duration is a function of both the previous APDs (memory effect) and the time between excitations (diastolic interval). Building such restitution curves, as described in Chap.(4), has led to many insight into the theory of complex dynamics of cardiac arrhythmias and spiral breakup.

Similarly to the APD-DI restitution curves, a second fundamental mesoscopic property of excitable media is the restitution of conduction velocity (CV). When a sequence of propagating pulses is produced (plane waves), the influence of the preceding pulse on the subsequent one (memory effect) is reflected not

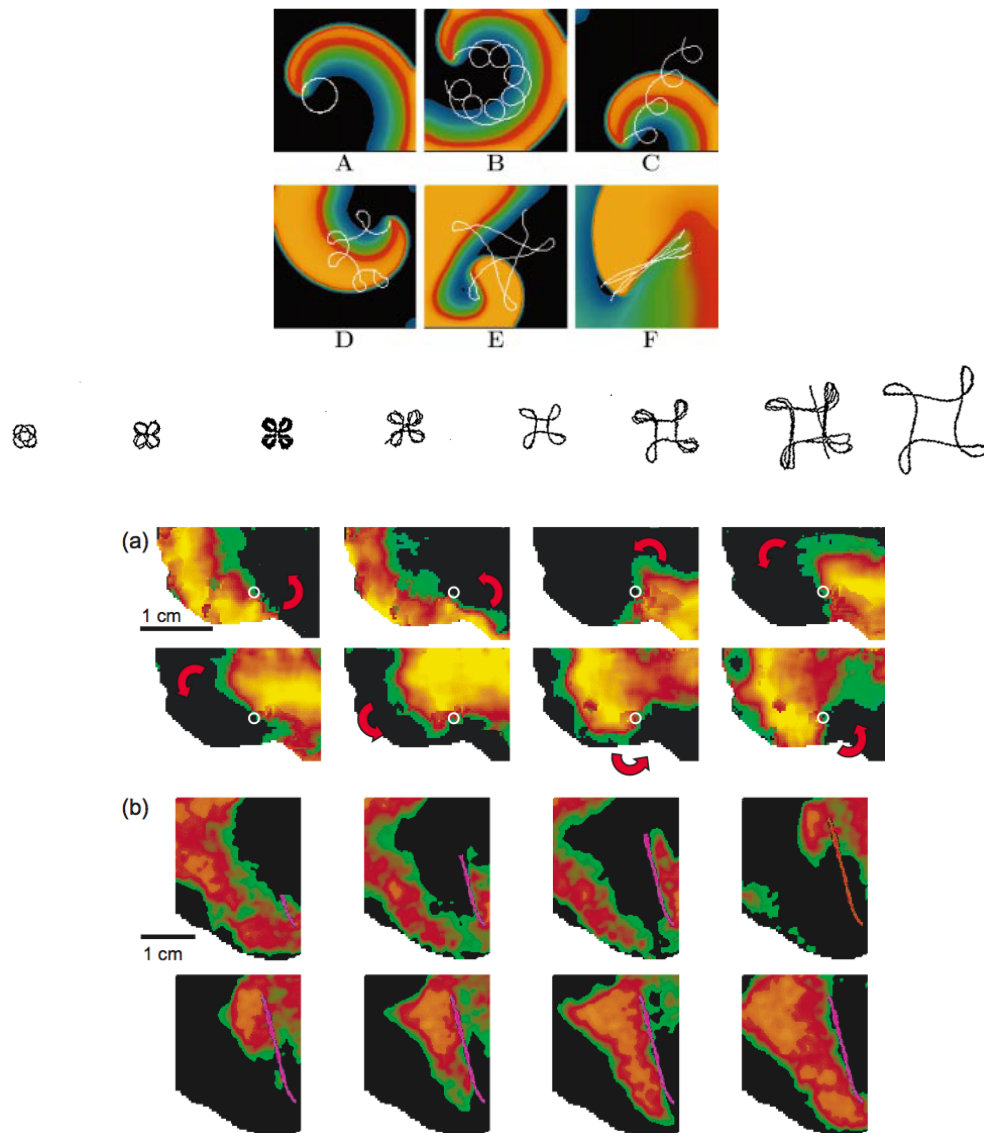


Figure 6.7.2: (TOP) Varieties of spiral wave tip trajectories[88]: (A) circular, (B) epicycloidal, (C) cycloidal, (D) hypocycloidal, (E) hyper-meandering, and (F) linear trajectories. (CENTER) Tip meandering during electrical turbulence in three-dimensional heart muscle [303]. (BOTTOM) (A) Reentrant wave trajectories in canine atrium preparations. (B) Linear trajectory in canine ventricle [41].

only in its APD but also in its propagation speed. Such curves, therefore, relates the speed of a pulse (CV) at a given site to the recovery time at that site (DI). Although CV depends on the orientation of the wave front with respect to the fiber axis of the cells, in continuum tissue models its characterization can be easily obtained.

These phenomena, i.e. memory via restitution, are strongly related to the transition from a single spiral wave to multiple waves. Such evolution is accomplished via wave break, which are usually due to conduction blocks. However, breakup processes are more complex than this, and depend both on electrophysiological-based and structural-based tissue properties [91]. The analysis and classification of spiral waves breakup has been extensively studied, and several mechanisms can be identified. Here, a synthetic graphical overview of such a phenomena will be given, therefore following a 5-points short list.

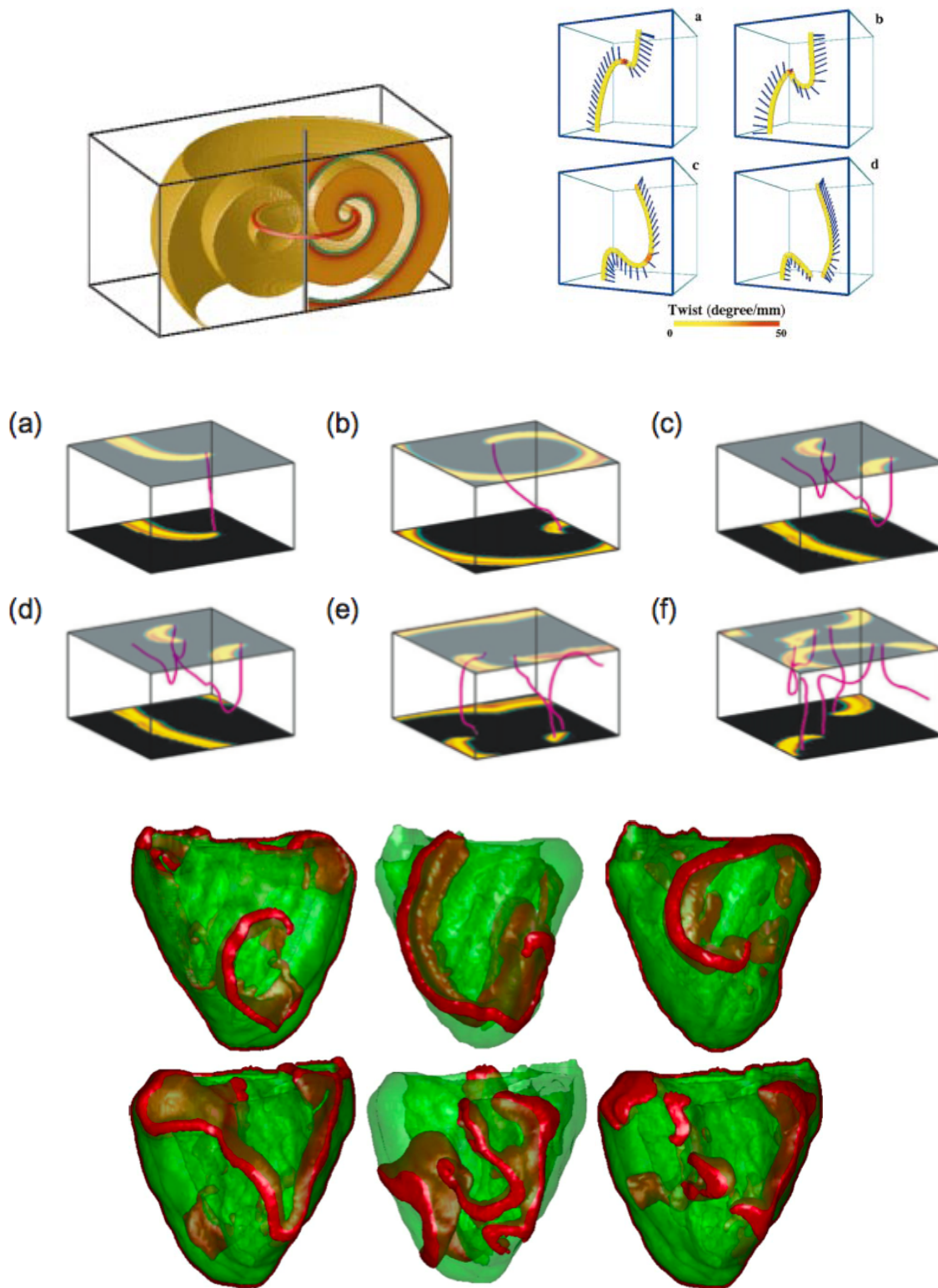


Figure 6.7.3: Visualization of scroll waves. **(TOP)** (Left) Three-dimensional scroll wave [41, 91] and (Right) intramural twist and vortex elongation. **(CENTER)** Breakup of scroll waves in a simulated 3D tissue slab [41]. **(BOTTOM)** Visualization of scroll waves in simulated reconstructed hearts [161].

I. APD and CV restitution curves:

- slope greater than one (see Fig.(6.7.4)): breakup close to or far from the tip trajectory.
- bifurcations (see Fig.(6.7.5)): alternating regimes due to the presence of Hopf bifurcations [259].

II. Tissue excitability:

- discordant alternans due to biphasic restitution curves (see Fig.(6.7.6)): APD decreasing and out-of-phase irregular oscillation development.

III. Spiral period and tip trajectory:

- Doppler shift and supernormal conduction velocity (see Fig.(6.7.7)): drifting of the spiral tip meandering.

IV. Initial conditions:

- APD variations due to pacing cycle length belongs to bistability and hysteresis effects.
- conduction blocks (2:1 response): the longer APD occurs only for every two pacing beats.

V. Tissue heterogeneity:

- local space-dependent properties (see Fig.(6.7.8)): coexistence of stable rotors with fibrillatory conduction and breakup.

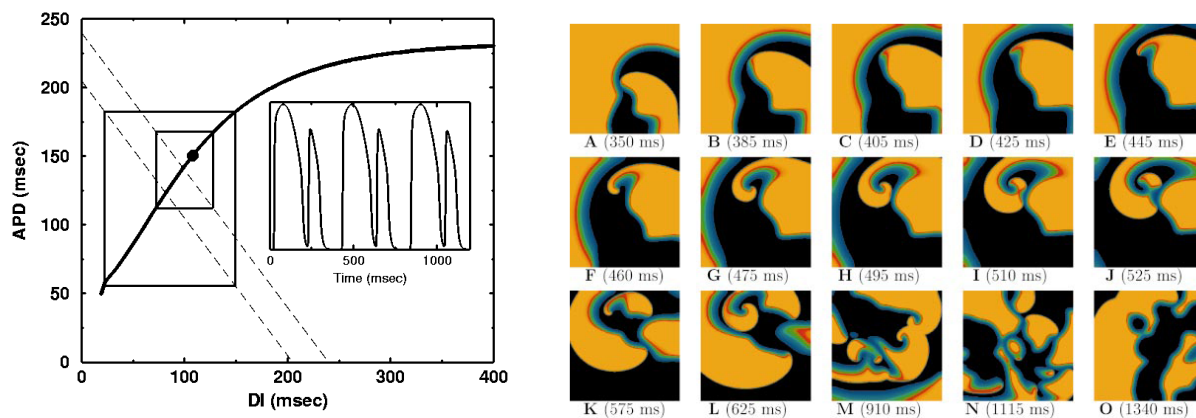


Figure 6.7.4: Alternans development and spiral breakup [91] (LEFT) APD restitution curve with slope greater than one, allowing alternans to develop over a wide range of periods before reaching conduction block. Periods below 260 ms display alternans. (RIGHT) Evolution of breakup close to the tip due to steep APD restitution with wave fronts were blocked by refractory regions resulting in a transient breakup.

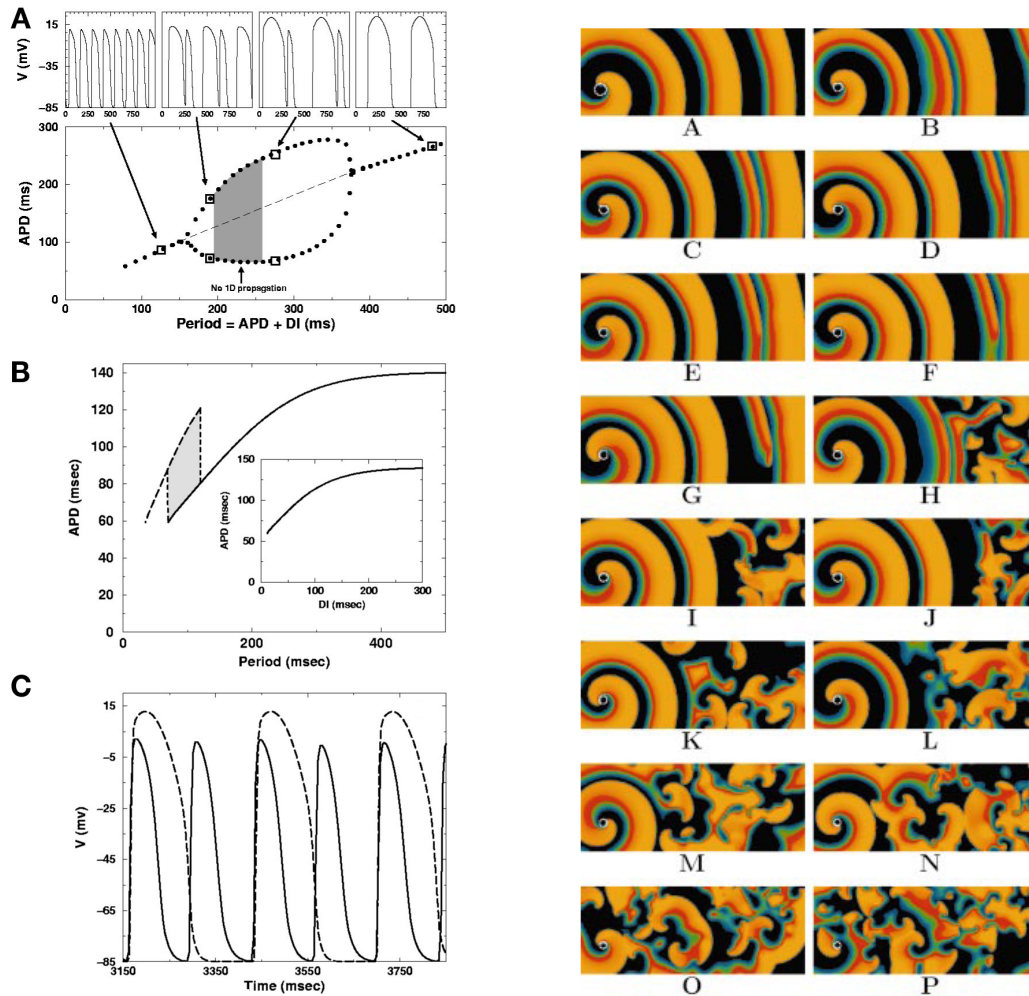


Figure 6.7.5: Restitution bifurcation and spatial alternans (adapted from [91]). (LEFT) APD restitution curve showing two Hopf bifurcations (A) and bistability and hysteresis (B-C). (RIGHT) Discordant alternans-induced breakup far from the tip. After decreasing the period APD oscillations developed and grew over several seconds.

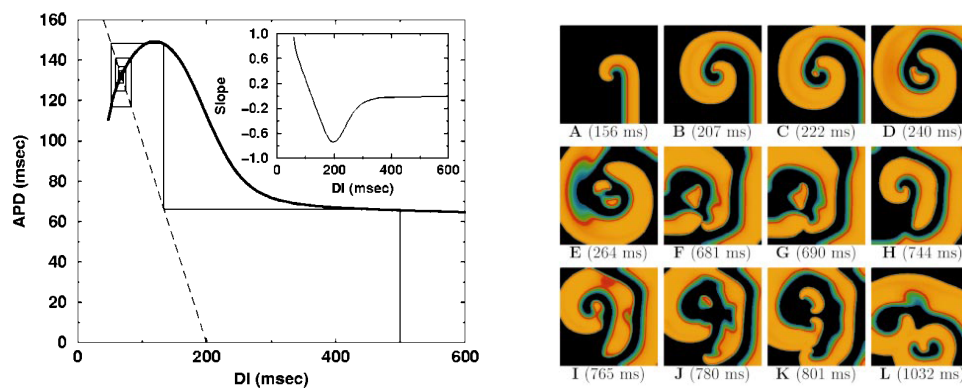


Figure 6.7.6: Bifasic restitution effects (adapted from [91]). (LEFT) Oscillations due to a biphasic APD restitution curve. Even when the slope of the restitution curve never exceeds one in magnitude conduction block can form and lead to breakup. (RIGHT) Spiral wave breakup due to a biphasic APD restitution curve (A-L) via conduction block formation.

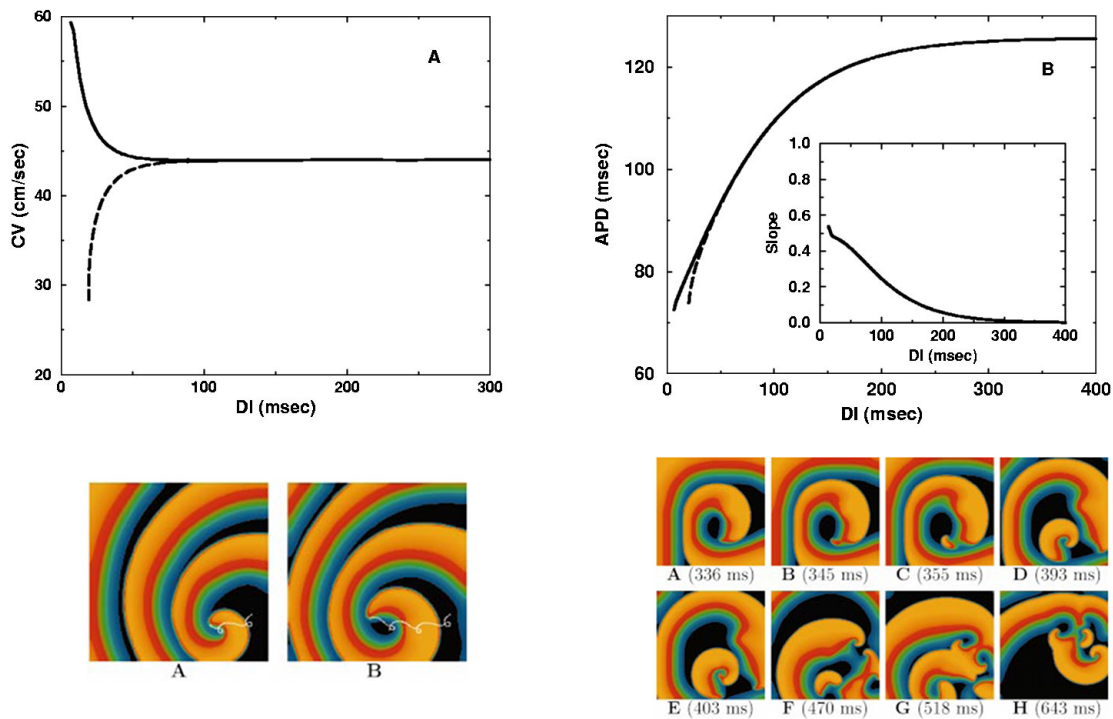


Figure 6.7.7: (TOP) CV (A) and APD (B) restitution curves producing supernormal conduction velocity (solid line) while the dashed lines are associated with a more usual CV restitution curve [88]. (BOTTOM) (Left) Stable spiral wave with cycloidal trajectory. The wave fronts became more closely packed on the left-hand side of the domain because the spiral was moving in that direction. The Doppler shift in frequency also decreased the period of waves to the left. (RIGHT) Breakup of a spiral wave whose tip followed a hypocycloidal trajectory. The Doppler shift induced by the meandering tip caused the period to fall below the minimum period for propagation, causing 2:1 block and wave break.

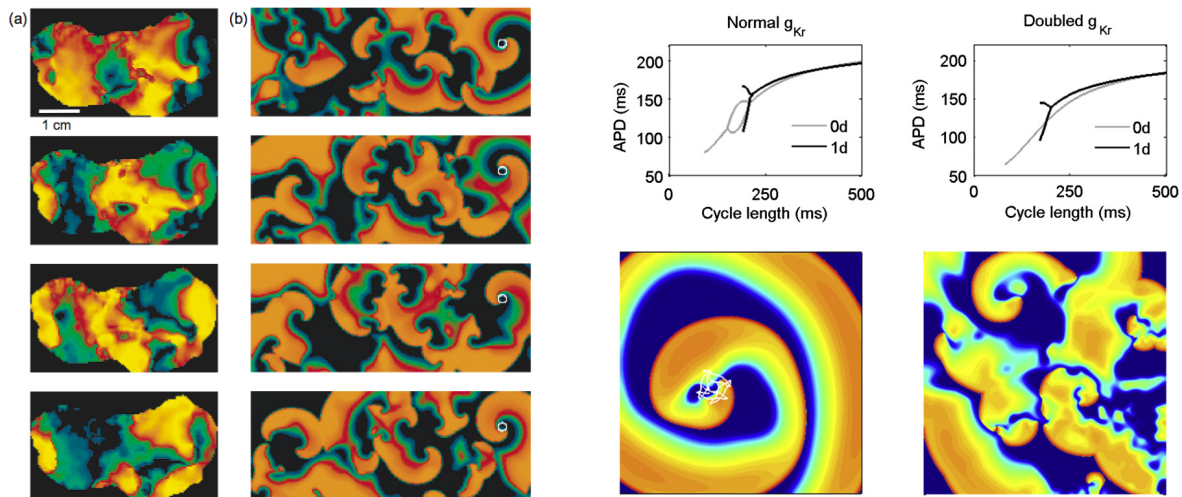


Figure 6.7.8: Rotors with fibrillatory conduction and breakup [41]. (LEFT) Breakup and stable spiral coexistence. (A) Experimental example in canine atrium: a stable rotor remaining on the right side of the domain despite irregular activity on the left. (B) Example in simulated cardiac tissue. (RIGHT) Differences in simulated dynamics with modification of a single parameter (conductance g_{Kr}). With the modification, alternans is eliminated in a single cell (0-D) but reappears in tissue (1-D), and a spiral wave initiated in two-dimensional tissue experiences sustained breakup.

Chapter 7

Electro-Mechanics of the Heart

Electro-mechanical processes of heart contraction are discussed in this chapter. General constitutive hypothesis for deformable active media will be exposed, balance equations and measurable quantities will be derived in the framework of finite theory of continuum mechanics. It will be expose then, calculations and numerical results for energy functions which are able to mimic cardiac behavior.

In the following it will be refer both to the “matrix notation”, i.e. *lower-case bold* letters to indicate vectors and *upper-case bold* letters for tensors (unless specified), and to “indicial notation”, i.e. Einstein convention, giving, when necessary, both representations.

7.1 Introduction: Passive and Active Myocardium Modeling

Cardiac electro-mechanic coupling is based on the connection between structural large-scale mechanical properties [315] with the underlying subcellular dynamics [144]. The current state of the art employs passive hyperelastic compressible and incompressible material modeling, in combination with basic active stress formulations which encompasses all aspects of the electrophysiological coupled dynamics, i.e. calcium inward and outward from the myocyte for the corresponding activation and de-activation of actin and myosin[118].

Constitutive Models of Passive Myocardium

There are several models of the elasticity of the myocardium available in the literature [136], including isotropic models, transversely isotropic models and, more recently, orthotropic models. In a short and partial list can be cited:

1. *Transversely isotropic* models:
 - (a) Humphrey-Yin model [142]: strain energy function as sum of exponentials, based on right Cauchy–Green tensor invariants, I_1 and I_4 ; contains 4 material parameters; incompressible.
 - (b) Humphrey et al. model [143]: polynomial strain energy function, based on right Cauchy–Green tensor invariants, I_1 and I_4 ; contains 5 material parameters; incompressible.
 - (c) Kerckhoffs et al. model [162]: polynomial strain energy function with sum of exponentials, based on Green-Lagrange strain invariants in the fiber direction, \hat{I}_1 and \hat{I}_2 ; contains 6 material parameters; compressible.

- (d) Horowitz et al. model [139]: exponential invariant-based strain energy function.
- (e) Huyghe et al. model [149]: strain energy function accounting for passive viscoelastic response of the myocardium.

2. *orthotropic* models:

- (a) Costa et al. model [56]: Fung-type exponential strain energy function; 7 material parameters.
- (b) Schmid et al. model [252]: Fung-type decoupled exponential strain energy function; 12 material parameters.
- (c) Hunter et al. [144]: pole-zero strain energy function; 18 material parameters.
- (d) Holzapfel-Ogden [136]: exponential invariant-based strain energy function; 8 material parameters.
- (e) Itskov-Ehret [153]: polyconvex invariant-based strain-energy functions; 3 material parameters.

Constitutive Models of Active Myocardium

The last decade has been characterized by the onset of several model for the active behavior of soft biological tissues. In particular, muscle fibers have been studied in their response to the activation-contraction coupling previously described.

From a continuum point of view, the internal actin–myosin binding can be considered as a microstructural alteration of the internal kinematic state of the muscle fibre properties, which leads to changes in the macroscopic behavior. Since the sliding of the filaments occurs parallel to the fibre axis, the binding between actin and myosin filaments has been usually associated to a change of longitudinal fibre properties, assuming that the cross-sectional properties remain unchanged.

Following such assumptions, Ehret et al. [79] proposed a constitutive law for active muscle behavior based on polyconvex strain-energy functions and described through generalized invariants. In particular, they assumed that the influence of the muscle fibre properties on the material behavior was controlled by a weight factor w_p . Activation was then included by increasing this parameter by an additional value $w_a \geq 0$, so that the generalized invariant \tilde{I} associated with longitudinal properties could be defined as

$$\tilde{I} = \frac{w_0}{3} \text{tr}(\mathbf{C}) + (w_p + w_a) \text{tr}(\mathbf{CM}) , \quad (7.1.1)$$

where \mathbf{C} is the right Cauchy-Green strain tensor and $\mathbf{M} = \mathbf{m} \otimes \mathbf{m}$ is the structural tensor. Therefore, the resulting second Piola-Kirchhoff stress tensor for the activated muscle was able to include the passive stress as a special case when $w_a = 0$. In such a way, their formulation did not express an additive decomposition of the stress into passive and active parts.

However, the two approaches gaining major success in the literature can be identified in:

1. Nash-Panfilov model [199]: following a superposition principle, an active stress component was added to the passive one:

$$\mathbf{T} = \frac{1}{2} \left(\frac{\partial W}{\partial \mathbf{E}} + \frac{\partial W}{\partial \mathbf{E}} \right) + \mathbf{T}_a \mathbf{C} , \quad (7.1.2)$$

where \mathbf{C} are components of the metric tensor. In this case, the active stress is assumed following a dynamic evolution voltage dependent

$$\frac{\partial \mathbf{T}_a}{\partial t} = \epsilon (V_m) (k_{T_a} V - \mathbf{T}_a) \quad (7.1.3)$$

with k_{T_a} controlling the amplitude of the active stress twitch and the function $\epsilon(V)$ controls the delay in the development and recovery of active stress with respect to the action potential, and it is defined by

$$\epsilon(V) = \begin{cases} \epsilon_0 & \text{for } V_m < 0.05 \\ 10\epsilon_0 & \text{for } V_m \geq 0.05 \end{cases} \quad (7.1.4)$$

with $\epsilon_0 = 1$.

In this formulation both capacitive and ionic dependencies on contraction were neglected.

2. Cherubini et al. [45, 198]: based on “kinematic” contraction (opposite to that of “tension”), the multiplicative decomposition of the gradient deformation tensor, \mathbf{F} , was assumed:

$$\mathbf{F} = \mathbf{F}_e \mathbf{F}_o, \quad (7.1.5)$$

where \mathbf{F}_e is the elastic component, accounting for constraints, and \mathbf{F}_o is the active one, measuring the change of length of the tissue due to the muscle contraction. In this case, \mathbf{F} is a function of the subcellular calcium dynamics, as discussed in Chap.6, and the resulting stress tensor derives from kinematic assumptions and reads as:

$$\mathbf{T} = 2\mathbf{F}\mathbf{F}_o^{-1} \frac{\partial \psi}{\partial \mathbf{C}_e} \mathbf{F}_o^{-1} \mathbf{F}^T - p\mathbf{I}$$

with the usual meaning of the symbols.

In this formulation only capacitive dependencies on contraction were neglected, while stretch activated currents were considered.

7.2 A General Theory of Deformable Active Media

Cardiac cells change length by up to 20% during a normal heart beat. Such a characters, frames the electromechanical analysis into finite deformation elasticity theory [187, 209, 233, 261], and a detailed description of the novel theory proposed in this work is reported.

7.2.1 Formulation and General Statements

We refer to a continuous body of mass density per unit undeformed volume ρ_0 undergoing a motion $\varphi(\mathbf{X}, t)$ described in the reference configuration through the coordinates $\mathbf{X} = X_I$ and in the spatial configuration by the coordinates $\mathbf{x} = x_i$. The corresponding deformation gradient is $\mathbf{F} = \nabla_{\mathbf{X}}\varphi = F_{iJ}$. The material velocity is denoted by \mathbf{V} and the spatial velocity by \mathbf{v} . The mass density per unit deformed volume is ρ , and the volume change is measured by $\det \mathbf{F} = J = \rho_0/\rho$.

By definition, the spatial gradient of the electric potential is the electric field in the spatial configuration, i.e. $\mathbf{e} = -\nabla_{\mathbf{x}}\phi$. The electric field induces a dielectric displacement of the charge that in the spatial description is denoted with \mathbf{d} . Here, the electric field and the dielectric displacement must satisfy the Maxwell equations

$$\nabla_{\mathbf{x}} \times \mathbf{e} = 0, \quad \nabla_{\mathbf{x}} \cdot \mathbf{d} = 0 \quad (7.2.1)$$

where $(\nabla_{\mathbf{x}} \times)$ denotes the curl operator and $(\nabla_{\mathbf{x}} \cdot)$ denotes the divergence operator. The material counterpart of these equations is

$$\nabla_{\mathbf{x}} \times \mathbf{E} = 0, \quad \nabla_{\mathbf{x}} \cdot \mathbf{D} = 0 \quad (7.2.2)$$

In the material configuration, the electric field is denoted with \mathbf{E} and the dielectric displacement with \mathbf{D} . The electric field \mathbf{e} transforms through a pull-back operation as $\mathbf{E} = -\nabla_{\mathbf{x}}\phi = \mathbf{F}^T \mathbf{e}$. The relation can be proved through the definition of spatial and material gradient:

$$\nabla_{\mathbf{x}}\phi = \phi_{,i} = \frac{\partial\phi}{\partial x_i} = \frac{\partial\phi}{\partial X_J} \frac{\partial X_J}{\partial x_i} = F_{Ji}^{-1} \phi_{,J} = \mathbf{F}^{-T} \nabla_{\mathbf{X}}\phi, \quad \mathbf{E} = \mathbf{F}^T \mathbf{e}. \quad (7.2.3)$$

The dielectric displacement transforms from spatial to material description in the standard way, through the deformation gradient, i.e., $\mathbf{D} = \mathbf{F}^{-1} \mathbf{d}$ or $D_J = F_{Ji}^{-1} d_i$.

7.2.2 Electric Diffusion in a Moving Domain

The propagation of an electric wave within the cardiac tissue obeys the standard diffusion equation, which in spatial description reads:

$$C_m \frac{\partial\phi}{\partial t} = \nabla_{\mathbf{x}} \cdot \mathbf{h} + I_m, \quad C_m \frac{\partial\phi}{\partial t} = h_{i,j} + I_m, \quad (7.2.4)$$

where $C_m = C_m(\mathbf{F})$ is the membrane capacitance; $\mathbf{h}(\nabla_{\mathbf{x}}\phi)$ is the flux of electric charges, and $I_m(\mathbf{F})$ is the total ionic transmembrane current. The symbol $\partial/\partial t$ denotes the time derivative in the spatial configuration. Equation (7.2.4) holds in the domain B of boundary ∂B and outward normal \mathbf{n} , with the following boundary conditions:

$$[\mathbf{h}] \cdot \mathbf{n} = \omega, \quad [h_i] n_i = \omega, \quad (7.2.5)$$

where ω is the charge density on the boundary in the spatial configuration and $[a]$ denotes the jump of a across the boundary. The material form of (7.2.4) is:

$$C_m \frac{d\phi}{dt} = \frac{1}{J} \nabla_{\mathbf{X}} \cdot (J\mathbf{H}) + I_m, \quad C_m \frac{d\phi}{dt} = \frac{1}{J} (JH_I)_{,I} + I_m \quad (7.2.6)$$

where the material electric flux derives as $\mathbf{H} = \mathbf{F}^{-1} \mathbf{h}$, or $H_I = F_{Ii}^{-1} h_i$ and the material time derivative is denoted as d/dt . The corresponding boundary conditions are:

$$J [\mathbf{H}] \cdot \mathbf{N} = \Omega, \quad J [H_I] N_I = \Omega \quad (7.2.7)$$

where \mathbf{N} is the outward normal to the boundary and Ω denotes the surface charge density in the material configuration.

The weak form of (7.2.4) is:

$$\int_B C_m \frac{\partial\phi}{\partial t} \eta dv + \int_B h_i \eta_{,i} dv = \int_{\partial B} \omega \eta ds + \int_B I_m \eta dv \quad (7.2.8)$$

or

$$\int_B C_m \frac{\partial\phi}{\partial t} \eta dv + \int_B \mathbf{h} \cdot \nabla_{\mathbf{x}} \eta dv = \int_{\partial B} \omega \eta ds + \int_B I_m \eta dv \quad (7.2.9)$$

where the spatial test function η has been introduced.

The weak form of (7.2.6) is instead:

$$\int_{B_0} JC_m \frac{\partial \phi}{\partial t} \eta dV + \int_{B_0} JH_I \eta_{,I} dV = \int_{\partial B_0} \Omega \eta dS + \int_{B_0} JI_m \eta dV \quad (7.2.10)$$

or

$$\int_{B_0} JC_m \frac{\partial \phi}{\partial t} \eta dV + \int_{B_0} J\mathbf{H} \cdot \nabla_{\mathbf{x}} \eta dV = \int_{\partial B_0} \Omega \eta dS + \int_{B_0} JI_m \eta dV \quad (7.2.11)$$

where the Nanson's relation [135] has been used:

$$\mathbf{n} ds = J\mathbf{F}^{-T} \cdot \mathbf{N} dS, \quad n_i ds = JF_{Ii}^{-1} N_I dS. \quad (7.2.12)$$

A very common expression for the electric flux \mathbf{h} accounts linearly for the gradient of the electric potential through a spatial second-order tensor of conductivities $\mathbf{k} = \mathbf{k}(\mathbf{F})$:

$$\mathbf{h} = \mathbf{k}(\mathbf{F}) \nabla_{\mathbf{x}} \phi, \quad h_i = k_{ij} (F_{hk}) \phi_j, \quad (7.2.13)$$

and the corresponding expression for the electric flux \mathbf{H} in the material form through a Lagrangian second-order tensor of conductivities $\mathbf{K} = \mathbf{F}^{-1} \mathbf{k} \mathbf{F}^{-T}$, or $K_{IJ} = F_{Ii}^{-1} k_{ij} F_{Jj}^{-1}$:

$$\mathbf{H} = \mathbf{K} \nabla_{\mathbf{X}} \phi, \quad H_I = K_{IJ} \phi_{,J}. \quad (7.2.14)$$

The proper definition will derive from the constitutive behavior, left for the next section.

7.2.3 Balance of Linear and Angular Momentum

The local form of the balance of mass reads:

$$\dot{\rho}_0 = 0. \quad (7.2.15)$$

The local forms of the linear momentum is:

$$\rho_0 \frac{d\mathbf{V}}{dt} = \nabla_{\mathbf{x}} \cdot \mathbf{P} + \rho_0 \mathbf{B}, \quad \rho_0 \frac{dV_i}{dt} = \frac{\partial P_{iJ}}{\partial X_J} + \rho_0 B_i \quad (7.2.16)$$

where \mathbf{B} are the body forces per unit of mass (\mathbf{T} the surface tractions), and \mathbf{P} denotes the first Piola-Kirchhoff stress tensor. The angular momentum balance is satisfied by the symmetry of the product:

$$\mathbf{P}\mathbf{F}^T = \mathbf{F}\mathbf{P}^T, \quad P_{iJ} F_{iK} = F_{iJ} P_{iK}. \quad (7.2.17)$$

The balance on the traction boundary is expressed through the Cauchy's relation:

$$\mathbf{T} = \mathbf{P}\mathbf{N}, \quad T_i = P_{iJ} N_J. \quad (7.2.18)$$

The weak form of the linear momentum in the material configuration is [188, 218]

$$\int_{B_0} \frac{dV_i}{dt} \tilde{\eta}_i dV + \int_{B_0} P_{iJ} \tilde{\eta}_{i,J} dV = \int_{B_0} T_i \tilde{\eta}_i dS + \int_{B_0} B_i \tilde{\eta}_i dV. \quad (7.2.19)$$

7.2.4 Energy Balance and Dissipation Inequality

For any portion of body, the total energy increase is given by: i) the rate of internal energy, ii) the rate of kinetic energy, and iii) the rate of electric energy, done by the electric field on the electric displacement \mathbf{D} , equals the sum of the corresponding work rate done on the body and the heat added to the body through a volume heat source Q and a boundary heat flux \mathbf{H} . Accounting for the linear momentum balance (7.2.16) and the mass balance (7.2.15), the energy balance equation in local form reads as:

$$\dot{E} = \mathbf{P} : \dot{\mathbf{F}} + \mathbf{D} \cdot \dot{\mathbf{E}} + \rho_0 Q - \nabla_{\mathbf{x}} \cdot \mathbf{H}, \quad \dot{E} = P_{iJ} \frac{\partial V_i}{\partial X_J} + D_J \dot{E}_J + \rho_0 Q - \frac{\partial H_I}{\partial X_I} \quad (7.2.20)$$

The second law of thermodynamics states the non negativeness of the entropy production $\dot{\Gamma}$, in local form:

$$T\dot{\Gamma} = T\dot{N} - \rho_0 Q + \nabla_{\mathbf{x}} \cdot \mathbf{H} - \frac{1}{T} \mathbf{H} \cdot \nabla_{\mathbf{x}} T \geq 0. \quad (7.2.21)$$

Relation (7.2.21) allows for the description of dissipative phenomena, such as heat flow and the development of irreversible deformations. Accounting for the energy balance (7.2.20), Eq.(7.2.21) can also be written as:

$$T\dot{\Gamma} = T\dot{N} - E + \mathbf{P} : \dot{\mathbf{F}} + \mathbf{D} \cdot \dot{\mathbf{E}} - \frac{1}{T} \mathbf{H} \cdot \nabla_{\mathbf{x}} T \geq 0. \quad (7.2.22)$$

It is interesting to note the analogy with the heat equation, which is formally the same expression and deals with heat fluxes and temperature gradients.

7.2.5 General Constitutive Theories

In order to provide constitutive equations, we introduce the thermodynamical potential in a suitable form. Following the framework proposed in [53, 308], the local thermodynamic state of an infinitesimal neighborhood of the body B is fully defined by the deformation gradient \mathbf{F} , the entropy density N , and the electric displacement \mathbf{D} . The equation of state, describing the internal energy E , and the temperature function, describing the absolute temperature T , are functions of the local state only, i.e:

$$E = E(\mathbf{F}, N, \mathbf{D}), \quad T = T(\mathbf{F}, N, \mathbf{D}) \quad (7.2.23)$$

The local absolute temperature $T > 0$ and the electric potential are intensive thermodynamic variables. Extensive thermodynamic variables are the internal energy, E , per unit of volume and the local entropy, N , density per unit of mass.

In this derivation, it is useful to make use of an alternative equation of state, \tilde{E} , defined as so as to drop the dependence on the dielectric displacement \mathbf{D} and assume the dependence on the electric field $\mathbf{E} = -\nabla_{\mathbf{x}} \phi$ only:

$$E \equiv \tilde{E}(\mathbf{F}, N, \mathbf{E}) = \inf_{\mathbf{D}} \{E(\mathbf{F}, N, \mathbf{D}) - \mathbf{D} \cdot \mathbf{E}\} \quad (7.2.24)$$

In the following we will always refer to the alternative internal energy, and we will use E to denote \tilde{E} . By definition, the elastic stresses is the partial derivative of the internal energy:

$$\mathbf{P}^e \equiv \partial_{\mathbf{F}} E(\mathbf{F}, N, \mathbf{E}). \quad (7.2.25)$$

It follows that the equilibrium stress tensor \mathbf{P} , entering in the balance equations, is the sum of two terms, one of which \mathbf{P}^e is called elastic and depends on \mathbf{F} and N only; the other \mathbf{P}^i is called inelastic and may

depend also on \mathbf{E} :

$$\mathbf{P}^i \equiv \mathbf{P} - \mathbf{P}^e \quad (7.2.26)$$

Taking the differential of (7.2.23)₁ one obtains:

$$\dot{E} = \frac{\partial E}{\partial \mathbf{F}} : \dot{\mathbf{F}} + \frac{\partial E}{\partial N} \dot{N} + \frac{\partial E}{\partial \mathbf{E}} \cdot \dot{\mathbf{E}} \quad (7.2.27)$$

Replacing (7.2.27) into (7.2.22) and considering (7.2.25):

$$T\dot{\Gamma} = \left(T - \frac{\partial E}{\partial N} \right) \dot{N} + (\mathbf{P} - \mathbf{P}^e) : \dot{\mathbf{F}} + \left(\mathbf{D} + c \frac{\partial E}{\partial \mathbf{E}} \right) \cdot \dot{\mathbf{E}} - \frac{1}{T} \mathbf{H} \cdot \text{Grad}T \geq 0 \quad (7.2.28)$$

Inequality (7.2.28) must hold for any admissible process. Let us consider an isothermal case. It follows that the temperature T , in the case $\dot{\mathbf{F}} = \mathbf{0}$ and $\dot{\mathbf{E}} = \mathbf{0}$, and the electric displacement \mathbf{D} , in the case $\dot{\mathbf{F}} = \mathbf{0}$ and $\dot{N} = 0$, must be necessarily of the form:

$$T = \partial_N E(\mathbf{F}, N, \mathbf{E}), \quad \mathbf{D} = \partial_{\mathbf{E}} E(\mathbf{F}, N, \mathbf{E}) \quad (7.2.29)$$

The energy balance equation (7.2.20) can be written in the entropy form by using (7.2.25), in order to highlight the contribution of dissipative terms:

$$T\dot{N} = \mathbf{P}^i : \dot{\mathbf{F}} + \rho_0 Q - \nabla_{\mathbf{x}} \cdot \mathbf{H} \quad (7.2.30)$$

Also the dissipation inequality (7.2.28) can be rendered in the operative form:

$$T\dot{\Gamma} = \mathbf{P}^i : \dot{\mathbf{F}} - \frac{1}{T} \mathbf{H} \cdot \nabla_{\mathbf{x}} T \geq 0 \quad (7.2.31)$$

particularly suitable for the definition of constitutive relationships.

The Helmholtz free energy A , alternative thermodynamic potential especially advantageous in constitutive theories, is obtained by applying the Legendre transform to the free energy E :

$$A(\mathbf{F}, T, \mathbf{E}) = \inf_N \{ E(\mathbf{F}, T, \mathbf{E}) - TN \} \quad (7.2.32)$$

The associated equilibrium equations are:

$$\mathbf{P}^e = \partial_{\mathbf{F}} A(\mathbf{F}, T, \mathbf{E}), \quad N = \partial_T A(\mathbf{F}, T, \mathbf{E}), \quad \mathbf{D} = \partial_{\mathbf{E}} A(\mathbf{F}, T, \mathbf{E}). \quad (7.2.33)$$

7.2.6 Helmholtz Potential for Electro-Mechanics

Assume a non dissipative process, and assume a multiplicative decomposition of the deformation gradient into an elastic part, related to the sole passive response of the material, and an inelastic part, defining the geometrical changes of the initial configuration induced by other phenomena [198, 45]:

$$\mathbf{F} = \mathbf{F}^e \mathbf{F}^i, \quad \mathbf{F}^e = \mathbf{F} \mathbf{F}^{i-1}.$$

The underlying idea is to assume the existence of an ideal intermediate configuration where all the inelastic phenomena take place without activating stresses, but where compatibility conditions are violated in general [177]. The compatibility requirement will move the body from such intermediate configuration to

the deformed configuration, where all the equilibrium and compatibility conditions are satisfied.

We are searching a particular form of the Helmholtz free energy able to provide the constitutive relations for the electromechanical problem at the hand. A good choice is to assume the additive decomposition of the free energy density in two distinct contributions:

$$A(\mathbf{F}, T, \mathbf{E}) = A^e(\mathbf{F}, T) + A^i(\mathbf{F}, T, \mathbf{E}) \quad (7.2.34)$$

The first contribution, A^e , can be seen as the classical strain energy density of any hyperelastic material. The second contribution, A^i , is a term that accounts for any sort of inelasticity that induce deformations of the materials. It includes an electric field, temperature, and eventually also chemical contributions. It follows that the stress is the sum of two terms:

$$\mathbf{P} = \mathbf{P}^p + \mathbf{P}^a, \quad \mathbf{P}^p = \mathbf{P}^e \mathbf{F}^{i-T}, \quad \mathbf{P}^a = \frac{\partial A^i(\mathbf{F}, T, \mathbf{E})}{\partial \mathbf{F}}. \quad (7.2.35)$$

The first term, \mathbf{P}^p , defines the passive stress typical of any hyperelastic tissue. It is related to the elastic strain energy density A^e , which determines a stress \mathbf{P}^e in the traditional sense, by the action of the elastic part of the deformation gradient \mathbf{F}^e :

$$\mathbf{P}^e = \frac{\partial A^e(\mathbf{F}^e, T)}{\partial \mathbf{F}^e} \quad (7.2.36)$$

The elastic stress \mathbf{P}^e is then pulled-back onto the undeformed configuration through the inverse of the inelastic deformation gradient.

The second term, \mathbf{P}^a , corresponds to the active stress typical of a biological active tissue, and it originates from the inelastic part of the free energy density A^i .

The expression of the consistent tangent stiffness is:

$$\mathbb{D} = \frac{\partial \mathbf{P}^p}{\partial \mathbf{F}} + \frac{\partial \mathbf{P}^a}{\partial \mathbf{F}} = \mathbb{D}^p + \mathbb{D}^a, \quad \mathbb{D}^p = \mathbf{F}^{i-1} \frac{\partial \mathbf{P}^e}{\partial \mathbf{F}^e} \mathbf{F}^{i-T}, \quad \mathbb{D}^a = \frac{\partial^2 A^i}{\partial \mathbf{F} \partial \mathbf{F}}. \quad (7.2.37)$$

The form of the inelastic deformation must reflect the material structure. It has to be intended as the effect of an electric field on an unconfined portion of the material. In the case of isotropic material, the inelastic deformation can be modeled as a stretch in the direction of the electric field:

$$\mathbf{F}^i = \gamma_{\text{vol}}(E) \mathbf{I} + \gamma_{\text{dev}}(E) \mathbf{E} \otimes \mathbf{E} = \gamma_{\text{vol}}(E) \delta_{IJ} + \gamma_{\text{dev}}(E), \quad (7.2.38)$$

where $\gamma_{\text{vol}}, \gamma_{\text{dev}}$ are two parameters with dimensions of the square of the inverse of E , possibly dependent on the intensity E of the electric field. In simple cases, they can be assumed as constants. For anisotropic materials, the expression of \mathbf{F}^i is obviously more general, and it can be described as:

$$\mathbf{F}^i = \mathbf{F}^i(E, \gamma^{(k)}, \mathbf{E} \otimes \mathbf{E}) \quad (7.2.39)$$

where (k) spans over the anisotropy directions. When referred to the three principal anisotropy directions $\mathbf{n}^{(k)}$, it can be described as:

$$\mathbf{F}^i(E, \gamma^{(k)}, \mathbf{E} \otimes \mathbf{E}) = \mathbb{F}(E, \gamma^{(k)}) \mathbf{E} \otimes \mathbf{E} \quad (7.2.40)$$

where, for example, we can set:

$$\begin{cases} \mathbb{F}(E, \gamma^{(k)}) = \sum_{(k)} \left[\gamma_{\text{vol}}^{(k)}(E) \mathbb{I} + \gamma_{\text{dev}}^{(k)}(E) (\mathbb{N}^{(k)} - \mathbb{I}) \right], \\ \mathbb{N}^{(k)} = \mathbf{n}^{(k)} \otimes \mathbf{n}^{(k)} \otimes \mathbf{n}^{(k)} \otimes \mathbf{n}^{(k)}. \end{cases} \quad (7.2.41)$$

The above expression specializes for transversally isotropic material with the unique preferential direction \mathbf{n} as:

$$\mathbb{F}(E, \gamma^{(k)}) = \left[\gamma_{\text{vol}}^{(k)}(E) + \gamma_{\text{dev}}^{(k)}(E) \right] \mathbb{I} + \gamma_{\text{dev}}^{(k)}(E) \mathbf{n}^{(k)} \otimes \mathbf{n}^{(k)} \otimes \mathbf{n}^{(k)} \otimes \mathbf{n}^{(k)}. \quad (7.2.42)$$

For the latter expression, in components \mathbf{F}^i becomes:

$$F_{IJ}^i = \left[\gamma_{\text{vol}}^{(k)}(E) + \gamma_{\text{dev}}^{(k)}(E) \right] E^2 \delta_{IJ} + \gamma_{\text{dev}}^{(k)}(E) (\mathbf{E} \cdot \mathbf{n})^2 n_I n_J. \quad (7.2.43)$$

Special Cases

It make sense that the exact dependence of such contribution on \mathbf{F} should be stated in terms of \mathbf{F}^i , so that it follows:

$$\mathbf{P} = \frac{\partial A^i(\mathbf{F}^i, T, \mathbf{E})}{\partial \mathbf{F}^i} \mathbf{F}^{e-T}, \quad (7.2.44)$$

For analogy, the electric displacement derives as:

$$\mathbf{D} = \frac{\partial A^i(\mathbf{F}^i, T, \mathbf{E})}{\partial \mathbf{E}}, \quad (7.2.45)$$

As example of application, let us assume \mathbf{F}^i and A of the particular forms:

$$\mathbf{F}^i = \mathbf{F}^i(\mathbf{E}), \quad A(\mathbf{F}, T, \mathbf{E}) = A^e(\mathbf{F}^e, T) + A^i(\mathbf{F}^i, T, \mathbf{E}) \quad (7.2.46)$$

Thus:

$$\mathbf{P} = \frac{\partial A^e(\mathbf{F}^e, T)}{\partial \mathbf{F}^e} \mathbf{F}^{i-T} + \frac{\partial A^i(\mathbf{F}^i, T, \mathbf{E})}{\partial \mathbf{F}^i} \mathbf{F}^{e-T}, \quad (7.2.47)$$

Also the electric displacement splits in two terms:

$$\mathbf{D} = \frac{\partial A^i(\mathbf{F}^i, T, \mathbf{E})}{\partial \mathbf{F}^i} \frac{\partial \mathbf{F}^i}{\partial \mathbf{E}} + \frac{\partial A^e(\mathbf{F}^e, T)}{\partial \mathbf{E}}, \quad (7.2.48)$$

The second term in (7.2.48) accounts for the effects of the electric field on the charges in the vacuum, while the first term accounts for the presence of the material.

We would like to include also anisotropy [79, 153] through structure invariants.

A Particular Helmholtz Potential Expression for General Electro-Active Anisotropic Tissues

Assumptions:

1. We drop the dependence on the temperature.
2. We include anisotropy through structure invariants, i.e. the tensor \mathbf{G} in the case of a preferential direction \mathbf{n} defined by a set of fibers, $\mathbf{G} = \mathbf{n} \otimes \mathbf{n}$.
3. In analogy with well settled theories of materials, the elastic part of A depends only on \mathbf{F}^e .
4. To satisfy material frame indifference, the dependence from \mathbf{F}^e is through $\mathbf{C}^e = \mathbf{F}^{eT} \mathbf{F}^e$.

5. We will use the following definitions:

$$J^e = \det \mathbf{F}^e, \quad \bar{I}_1^e = \text{tr} \bar{\mathbf{C}}^e, \quad \bar{I}_2^e = \frac{1}{2} \left[\text{tr} \left(\bar{\mathbf{C}}^{e2} \right) - \text{tr}^2 \bar{\mathbf{C}}^e \right]. \quad (7.2.49)$$

We can write the expressions by referring to a Mooney-Rivlin like material with additional preferential orientation:

$$A(\mathbf{C}, \mathbf{E}, \mathbf{G}) = A^e(\mathbf{C}^e, \mathbf{G}) + A^i(\mathbf{C}, \mathbf{E}, \mathbf{G}) \quad (7.2.50)$$

The elastic part of the Helmholtz energy is taken as:

$$A^e(\mathbf{C}^e, \mathbf{G}) = W_{\text{vol}}(J^e) + W_{\text{iso}}(\bar{I}_1^e, \bar{I}_2^e) + W_{\text{aniso}}(\bar{\mathbf{C}}^e, \mathbf{G}) \quad (7.2.51)$$

where

$$W_{\text{vol}}(J^e) = \frac{1}{2} \lambda \log^2 J^e - \mu \log J^e; \quad (7.2.52)$$

$$W_{\text{iso}}(\bar{I}_1^e, \bar{I}_2^e) = \mu_1 \bar{I}_1^e + \mu_2 \bar{I}_2^e, \quad \mu_1 + \mu_2 = \mu; \quad (7.2.53)$$

$$W_{\text{aniso}}(\bar{\mathbf{C}}^e, \mathbf{G}) = \frac{K_g}{2k} \left[\exp \left(k(\bar{I}_4^e - 1) \right) - 1 \right]. \quad (7.2.54)$$

The inelastic part of the Helmholtz energy is:

$$A^i(\mathbf{C}, \mathbf{E}, \mathbf{G}) = \frac{1}{2} \mathbf{E} \cdot \varepsilon_0 [\mathbf{I} + \chi(\mathbf{C}, \mathbf{G})] \mathbf{E} \quad (7.2.55)$$

where the expression of the tensor χ is assumed to be:

$$\chi(\mathbf{C}, \mathbf{G}) = \chi_0(\mathbf{G}) + \mathbb{H} : (\mathbf{C} - \mathbf{I}) \quad (7.2.56)$$

Let us assume a particular form of Eq.(7.2.56), where we describe the rank-two tensor χ_0 and the rank-4 tensor \mathbb{H} in terms of only four constants $\chi_{\text{iso}}, \chi_{\text{aniso}}, \chi_{\text{iso}}^{\mathbf{C}}$ and $\chi_{\text{aniso}}^{\mathbf{C}}$

$$\chi_0(\mathbf{G}) = \chi_{\text{iso}} \mathbf{I} + \chi_{\text{aniso}} \mathbf{G}, \quad \mathbb{H}(\mathbf{G}) = \chi_{\text{iso}}^{\mathbf{C}} \mathbf{I} \otimes \mathbf{I} + \chi_{\text{aniso}}^{\mathbf{C}} \mathbf{G} \otimes \mathbf{G} \quad (7.2.57)$$

This allows to write the χ tensor as:

$$\chi(\mathbf{C}, \mathbf{G}) = (\chi_{\text{iso}} + \chi_{\text{iso}}^{\mathbf{C}}) \mathbf{I} + (\chi_{\text{aniso}} + \chi_{\text{aniso}}^{\mathbf{C}}) \mathbf{G} + \mathbb{H}(\mathbf{G}) : \mathbf{C}. \quad (7.2.58)$$

which can be also written as:

$$\chi(\mathbf{C}, \mathbf{G}) = [\chi_{\text{iso}} + \chi_{\text{iso}}^{\mathbf{C}} (I_1 - 3)] + [\chi_{\text{aniso}} + \chi_{\text{aniso}}^{\mathbf{C}} (I_4 - 1)] \quad (7.2.59)$$

and account for the deformability through the two invariants of the right Cauchy-Green deformation tensor \mathbf{C} :

$$I_1 = \mathbf{C} : \mathbf{I}, \quad I_4 = \mathbf{C} : \mathbf{G} \quad (7.2.60)$$

In the proposed model, we introduce 11 material constants: $\lambda, \mu, \mu_1, K_g, k, \chi_{\text{iso}}, \chi_{\text{aniso}}, \chi_{\text{iso}}^{\mathbf{C}}, \chi_{\text{aniso}}^{\mathbf{C}}, \gamma_{\text{vol}}$, and γ_{dev} as reported in Tab.(7.1).

The expression of the inelastic (active) stress tensor reads:

$$\mathbf{P}^a = \frac{\partial A^i}{\partial \mathbf{F}} = \left(\frac{\partial A^i}{\partial I_1} \frac{\partial I_1}{\partial \mathbf{C}} + \frac{\partial A^i}{\partial I_4} \frac{\partial I_4}{\partial \mathbf{C}} \right) \frac{\partial \mathbf{C}}{\partial \mathbf{F}} \quad (7.2.61)$$

leading to

$$\mathbf{P}^a = \varepsilon_0 \chi_{\text{iso}}^{\mathbf{C}} E^2 \mathbf{F} + \varepsilon \chi_{\text{aniso}} (\mathbf{E} \cdot \mathbf{n})^2 \mathbf{G} \mathbf{F}^T \quad (7.2.62)$$

or in components

$$P_{iK}^i = \varepsilon_0 \chi_{\text{iso}}^{\mathbf{C}} E^2 F_{iK} + \varepsilon_0 \chi_{\text{aniso}}^{\mathbf{C}} (E_I n_I)^2 n_K n_J F_{iJ}. \quad (7.2.63)$$

The expression of the inelastic (active) tangent stiffness is then

$$\mathbb{D} = \frac{\partial^2 A^i}{\partial \mathbf{F} \partial \mathbf{F}} = \varepsilon_0 \chi_{\text{iso}}^{\mathbf{C}} E^2 \mathbb{I} + \varepsilon_0 \chi_{\text{aniso}}^{\mathbf{C}} (\mathbf{E} \cdot \mathbf{n})^2 \mathbf{G} \mathbb{I}^T \quad (7.2.64)$$

where

$$\frac{\partial \mathbf{F}}{\partial \mathbf{F}} = \mathbb{I}, \quad \left(\frac{\partial \mathbf{F}}{\partial \mathbf{F}} \right)_{iKjH} = \frac{\partial F_{iK}}{\partial F_{jH}} = \delta_{ij} \delta_{KH} = (\mathbb{I})_{iKjH} \quad (7.2.65)$$

$$\frac{\partial \mathbf{F}^T}{\partial \mathbf{F}} = \mathbb{I}^T, \quad \left(\frac{\partial \mathbf{F}^T}{\partial \mathbf{F}} \right)_{JijH} = \frac{\partial F_{iJ}}{\partial F_{jH}} = \delta_{ij} \delta_{JH} = (\mathbb{I}^T)_{JijH}. \quad (7.2.66)$$

or in components

$$\mathbb{D}_{iKjH}^a = \varepsilon_0 \chi_{\text{iso}}^{\mathbf{C}} E^2 \delta_{ij} \delta_{HK} + \varepsilon_0 \chi_{\text{aniso}}^{\mathbf{C}} (\mathbf{E} \cdot \mathbf{n}) n_K n_H \delta_{ij}. \quad (7.2.67)$$

7.3 Numerical Tests

In this section, examples of uniaxial, biaxial and shear tests are reported, depending on 5 fiber orientations and electric field. The numerical solution of the nonlinear electro-mechanic model has been obtained through ad hoc Matlab routines, implementing all the tensorial quantities involved into the discussed formulation. The first and second derivatives of the proposed free energy function, Eq.(7.2.34), (7.2.51) and (7.2.55), have been evaluated as theoretically described in the previous section, with no usage of any internal Matlab subroutine. This implementation has led to a fine control of each sequential step necessary for the evaluation of the error during the iterative procedures. Ad hoc routines for stress correction have been implemented too as described in the following.

7.3.1 Uniaxial, Biaxial and Shear Tests

A schematic representation of testing loads and fiber orientations is shown in Fig.(7.3.1). Pictures are referred to the reference control volume (A), with a single fiber family among five different orientations. The mechanical tests depicted in both three-dimensional (B) and two-dimensional (C) views correspond to the following physical interpretation.

Table 7.1: Electro-mechanical model parameters used in the numerical tests with applications of the electro active feedback.

λ [MPa]	μ [MPa]	μ_1 [MPa]	K_g [MPa]	k -	ε_0	χ_{iso}	χ_{aniso}	$\chi_{\text{iso}}^{\mathbf{C}}$	$\chi_{\text{aniso}}^{\mathbf{C}}$	γ_{vol}	γ_{dev}
5	0.06	0.1	0.05	200	$8 \cdot 10^{-12}$	1	5	3	12	$-1.35 \cdot 10^{-4}$	$-0.95 \cdot 10^{-4}$

Uniaxial test Fig.(7.3.1)(Un): tissue is constrained on a surface and stretched on the opposite side, or equivalently it is stretched in only one direction. In this case the total gradient deformation tensor assumes the matrix description

$$F_{ij} = \begin{bmatrix} 1+i & 0 & 0 \\ 0 & a & 0 \\ 0 & 0 & a \end{bmatrix}$$

where i indicates the imposed load increment acting on the first strain direction, F_{11} . The other two principal directions, F_{22} and F_{33} , assume an identical value, $a \neq 1$, in order to induce a free stress state. Therefore, the only measurable stress in the uniaxial test corresponds to the stress in the direction of the loading. The ad hoc implemented subroutine for stress correction has been calibrated for a numerical tolerance of 10^{-10} and, with a corresponding meaning of the symbols previously described, in this case assumes the following form:

```
% Correction: UNIAXIAL & ACTIVE CONSTRAINT tests (P22 = 0, P33 = 0)
corrTol = 1e-10;
den = D(2,2,2,2)*D(3,3,3,3) - D(2,2,3,3)*D(3,3,2,2);
num1 = P(2,2)*D(3,3,3,3) - P(3,3)*D(2,2,3,3);
num2 = P(3,3)*D(2,2,2,2) - P(2,2)*D(3,3,2,2);
% To set P22 to zero
if abs(num1/den) > corrTol
    F(2,2) = F(2,2) - num1/den;
    iterate1 = 1;
else
    iterate1 = 0;
end
% To set P33 to zero
if abs(num2/den) > corrTol
    F(3,3) = F(3,3) - num2/den;
    iterate2 = 1;
else
    iterate2 = 0;
end
```

Biaxial tests Fig.(7.3.1)(Bx): tissue is stretched on two orthogonal directions. In this case the total gradient deformation tensor assumes one of the following matrix descriptions:

$$F_{ij} = \begin{bmatrix} 1+i & 0 & 0 \\ 0 & 1+i & 0 \\ 0 & 0 & a \end{bmatrix}, F_{ij} = \begin{bmatrix} 1+i & 0 & 0 \\ 0 & a & 0 \\ 0 & 0 & 1+i \end{bmatrix}, F_{ij} = \begin{bmatrix} a & 0 & 0 \\ 0 & 1+i & 0 \\ 0 & 0 & 1+i \end{bmatrix}$$

where i indicates the imposed load increment. Considering the first case, the increment acts on the first and second strain directions, F_{11} and F_{22} , respectively. The remaining principal direction, F_{33} , assumes a value, $a \neq 1$, inducing a free stress state in that direction. In this case several stretch combinations and stress measures are feasible. The ad hoc implemented subroutine for stress correction in the first case assumes the following form:

```

% Correction: BIAxIAL – SHEAR & ACTIVE CONSTRAINT tests (P33 = 0)
corrTol = 1e-10;
% To set P33 to zero
if abs(P(3,3)/D(3,3,3,3)) > corrTol
    F(3,3) = F(3,3) - P(3,3)/D(3,3,3,3);
    iterate = 1;
else
    iterate = 0;
end

```

Shear tests Fig.(7.3.1)(Sh): tissue is stretched on two orthogonal directions. In this case the total gradient deformation tensor assumes one of the following matrix descriptions:

$$F_{ij} = \begin{bmatrix} 1 & i & 0 \\ 0 & 1 & 0 \\ 0 & 0 & a \end{bmatrix}, F_{ij} = \begin{bmatrix} 1 & 0 & 0 \\ i & 1 & 0 \\ 0 & 0 & a \end{bmatrix}, F_{ij} = \begin{bmatrix} a & 0 & 0 \\ 0 & 1 & i \\ 0 & 0 & 1 \end{bmatrix}, F_{ij} = \begin{bmatrix} a & 0 & 0 \\ 0 & 1 & 0 \\ 0 & i & 1 \end{bmatrix},$$

where i indicates the load increment which is no more imposed on a diagonal component. In this case two principal direction are constrained, while the third one assumes a value, $a \neq 1$, in order to induce a free stress state in that direction. Similarly to the biaxial case, several stretch combinations and stress measures are feasible and the subroutine for stress correction assumes the same form as in the biaxial case.

7.3.2 Passive and Active Mechanical Responses

Considering the model parameters set reported in Tab.(7.1), the mechanical response of the proposed model is significantly affected by the implemented active feedback.

Passive Response. We began our analysis by tuning the purely passive behavior of the proposed hyperelastic material model under stretch tests, by observing the uniaxial, biaxial and shear response. In Fig.(7.3.2), a comprehensive overview of the three different scenarios discussed is shown. From top to bottom, uniaxial, biaxial and shear stress-strain curves are compared for five different fiber orientations with respect to the loading direction. The coordinate axes represent the total Cauchy stress components, σ_{ij} [MPa], vs. the Hencky strain, e_{ij} , respectively:

$$\sigma_{ij} = J^{-1} P_{iJ} F_{Jj}, \quad e_{ij} = \frac{1}{5} \log C_{ij}.$$

The right column, in particular, highlights a detail of the graphs reported on the left column in order to better appreciate the behavior of the material model for very low stress values. To be noted that the vertical stress-scale is two order of magnitude less than the corresponding full range. It is important to underline the strong nonlinear response arising from the model with the concave shapes for low stress values tending to a stress free state:

- for uniaxial case, the response weakens with fiber inclination, and it drops to zero when the fibers are orthogonal to the loading;

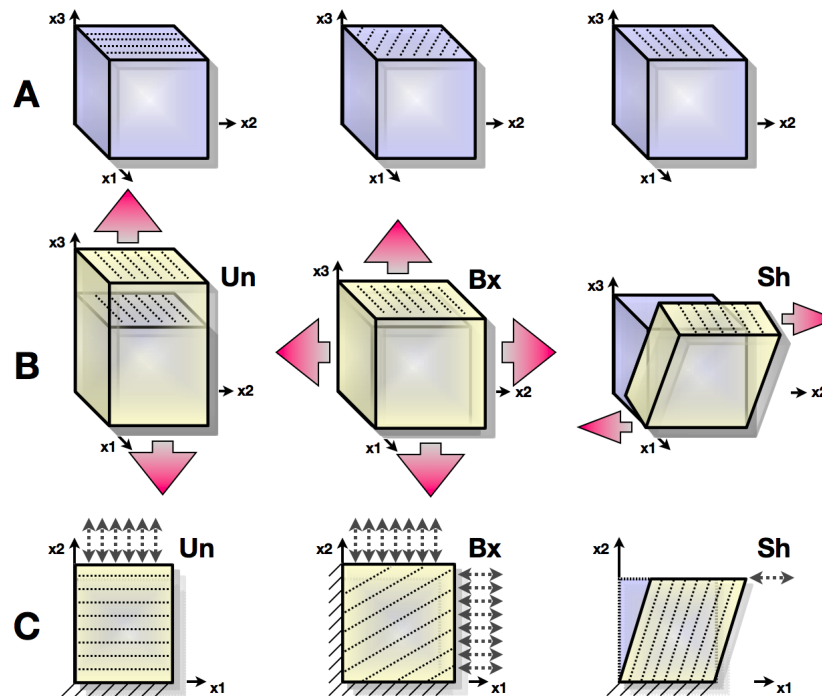


Figure 7.3.1: Schematic representation of the stretch tests implemented into ad hoc Matlab routines. (A) Reference control volume with a single fiber family (dashed lines) and oriented in one of the five tested orientations with respect to the loading direction, $n_1 = 0^\circ$, $n_2 = 30^\circ$, $n_3 = 60^\circ$, $n_4 = 90^\circ$, and $n_5 = \perp$. (B) Three-dimensional and (C) two-dimensional views of the three tension tests: uniaxial (Un), biaxial (Bx) and shear (Sh). Arrows indicate the loading direction which can be applied both in traction and compression.

- the biaxial transversal response in the direction of the constraint (biaxial 1) is softer, and shows a non significant response for both parallel and orthogonal fiber orientation;
- for biaxial loading and response in the direction of the applied stretch (biaxial 2), both cases with fiber parallel and orthogonal to the loading show no differences with respect to the uniaxial case;
- for shear loading, both cases with fibers parallel and orthogonal to the loading are characterized by a non significant response, since both configurations are not prone to activate the fiber reinforcement. The case with fiber inclination 60° , n_3 , shows a stiffer response with respect to the case with fiber inclination 30° , n_2 , due to the particular shear deformation applied. Moreover, the former case is characterized by a stiffening and then a reduction of the stiffness, while the one of fiber with 30° inclination is characterized by a monotonous stiffening.

A complete sensitivity analysis of the mechanical response under stretch tests to the fiber related material parameters is shown in Fig.(7.3.3). Representative examples of stress-strain curves for parameter varying are described. Color codes correspond to two parameter values, λ and K_g , for uniaxial and biaxial cases. the model is characterized by a low sensitivity to the fiber stiffness K_g and more sensitivity to the fiber rigidity k .

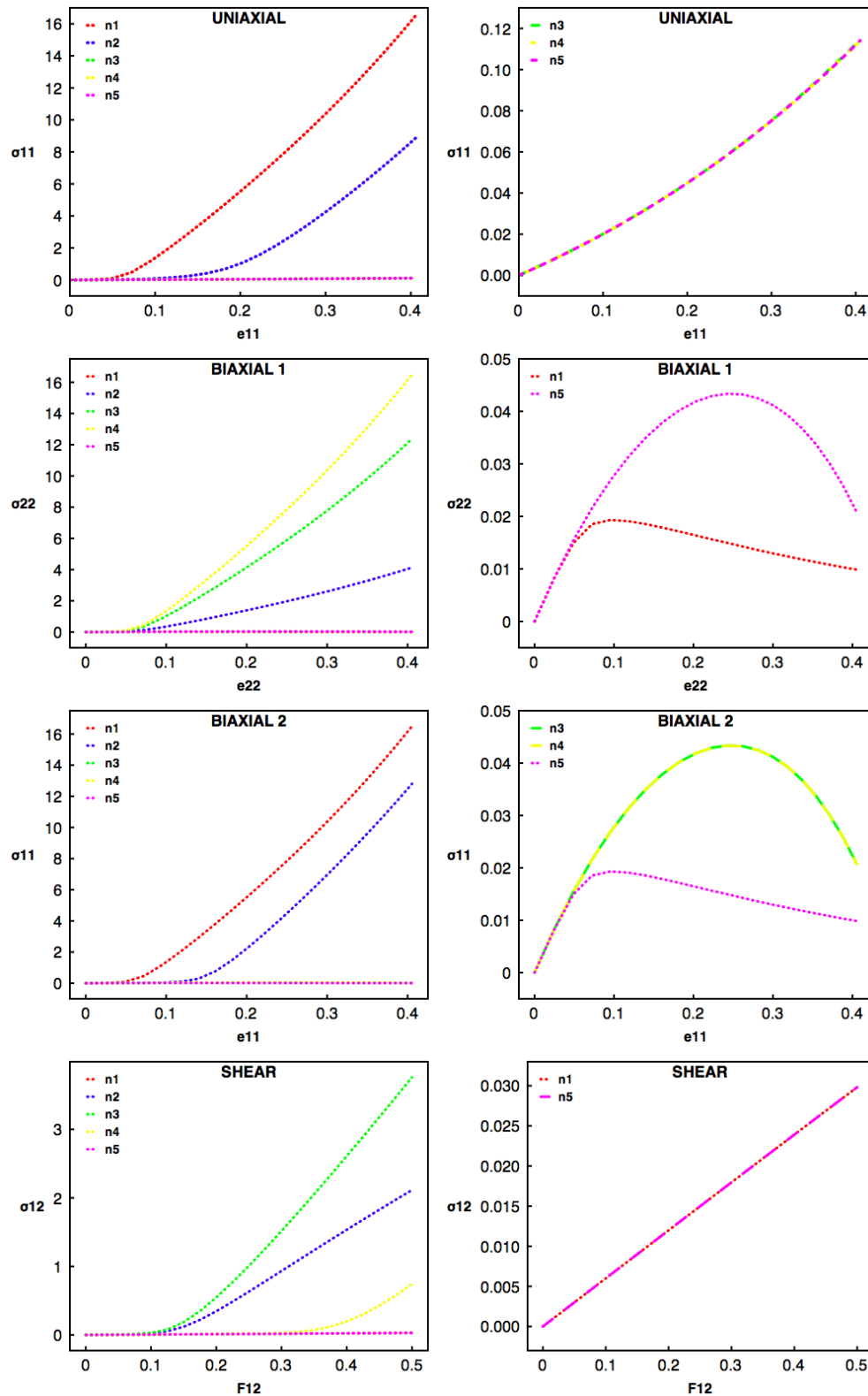


Figure 7.3.2: Mechanical response (total Cauchy stress, σ_{ij} [MPa], versus the total Hencky strain, e_{ij}) of the proposed model for uniaxial, biaxial and shear tension tests under five different fiber orientations with respect to the loading direction: $n_1 = 0^\circ$, $n_2 = 30^\circ$, $n_3 = 60^\circ$, $n_4 = 90^\circ$, and $n_5 = \perp$.

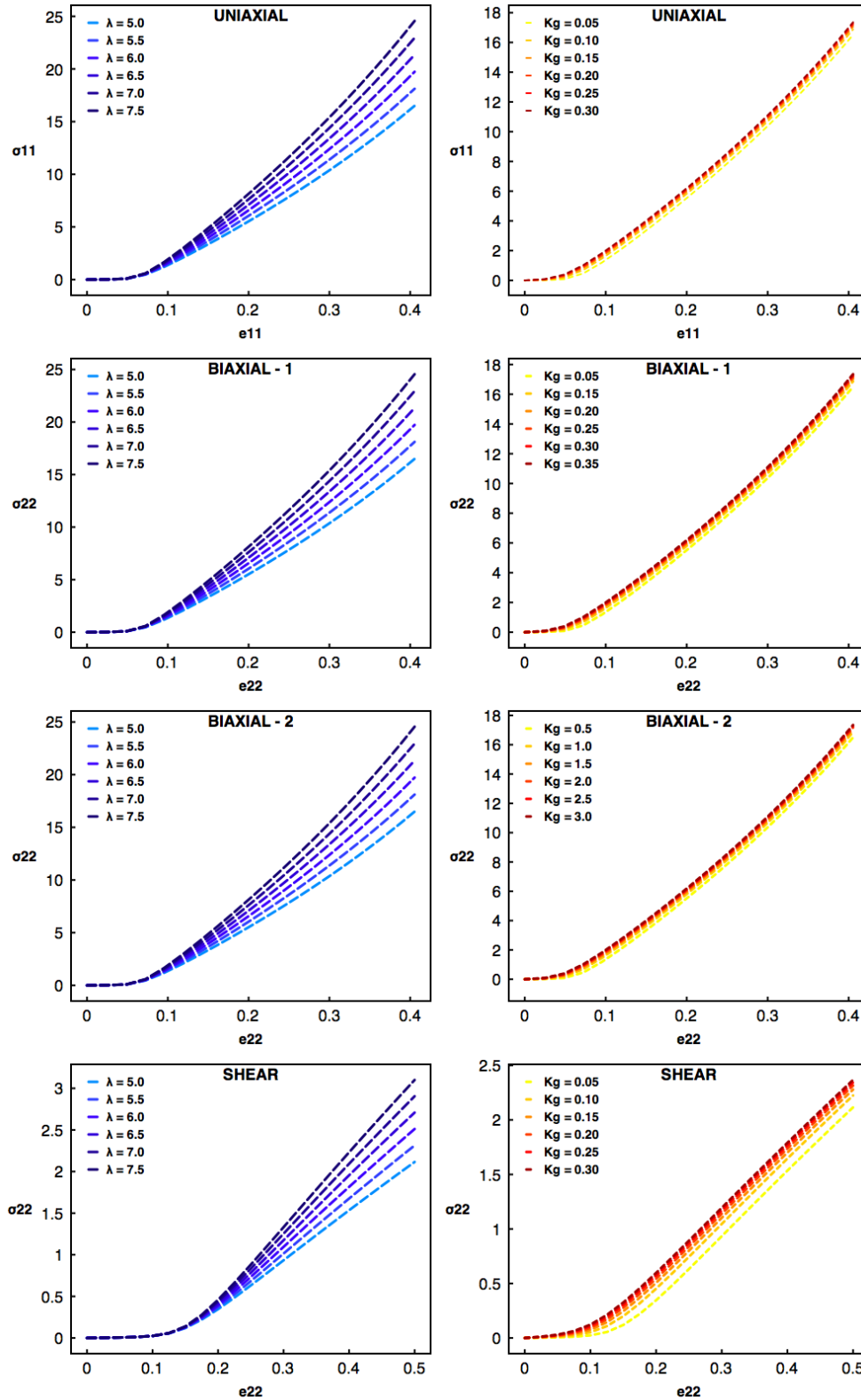


Figure 7.3.3: Mechanical response (total Cauchy stress, σ_{ij} , versus the total Hencky strain, e_{ij}) for uniaxial, biaxial and shear tests, varying two model parameters, λ and K_g measured in $[MPa]$. The uniaxial and biaxial 2 tests are referred to fiber orientation, $n_1 = 0^\circ$, biaxial 1 test is referred to $n_4 = 90^\circ$, and shear test is referred to $n_2 = 30^\circ$, with respect to the load direction.

Active Response. It is important to highlight that a fine and experimental-based parameter tuning is fundamental for a correct and meaningful interpretation of the numerical results obtained from nonlinear material models, as the one here proposed.

In this regard, we corroborated the passive stretch tests just described with the analysis of a “tetanized”-like tissue state under uniaxial test. In other words, we considered a fixed amount of electric field, E_i , whose presence induced a non-zero stress state in the material model, then we applied the usual stretch tests as previously discussed. The resulting stress-strain relationships are shown in Fig.(7.4.1) for two different order of magnitude of the electric field, $E = 1 V/m$ and $E = 20 V/m$. The corresponding electric field E_i assumes an anisotropic distribution due to the presence of the fibers as described by Eq.(7.2.43).

Several interesting behaviours were observed:

1. Different non-zero stress states (zero stretch) were found depending on both the electric field value and the fiber orientation. In particular, a higher stress state has been obtained for the higher value of E_i and for the stretch in the direction of the fiber (red curves).
2. The stress scale induced by the presence of an active electric field is five times higher than the one obtained in the passive regime. Such a result corroborates the proposed material model, because this is a well-known phenomenon greatly studied in skeletal muscles behavior: the tetanized state represent the maximal stimulated state for which the highest possible stress can be reached.
3. The overall material response is totally changed by the presence of an active part. The nonlinear interaction between the constitutive active free energy with the purely elastic one makes the resulting material model not a priori predictable.

In order to further validate the proposed electro-active mechanical model, ad hoc tests were implemented in which the driving variable was identified in the electric field. In this case, an external electric field was applied in the range $0 \div 20 V/m$ with a step increment of $0.5 V/m$. The maximum value reached is motivated by the action potential shape morphology in cardiac tissue. More precisely, we simulated a realistic action potential propagating wave (Beeler-Reuter [17]) in a one-dimensional cable and we considered its negative spatial gradient, $-\partial V/\partial x$, in order to recover the standard definition of the electric field (see Sec.(7.2.1)). The maximum value of the gradient, reached upon the upstroke of the traveling wave, ranges between $15 \div 20 V/m$, so we considered as highest biophysical-base value the proposed $20 V/m$.

In Fig.(7.4.2) the stress response is shown for five fiber orientations with respect to the imposed electric field. The main and unexpected result consists in the high response variability depending on the fiber orientation. In particular, four different scenarios can be identified in the case of biaxial constraint (bottom panel):

1. muscular fiber orthogonal to the electric plane (n_5 , pink): the stress induced grows mimicking the corresponding passive behavior;
2. muscular fiber oriented at 30° into the electric plane (n_2 , blue): the stress induced decreases and becomes strongly negative;
3. muscular fiber oriented at 0° into the electric plane (n_1 , red): the stress induced is small, positive and tends to a free-stress state;
4. muscular fiber oriented at 60° , 90° into the electric plane (n_3 , green, n_4 , yellow): the stress induced is small, positive and tends to grow but with a very smooth slope.

7.4 Limitations and Future Perspectives

The overall formulation described in this chapter is one of the major results of this thesis. Even if a better parameter tuning is still necessary upon experimental data, the proposed theoretical approach encompasses all the different aspects necessary for a complete mechanic formulation and characterization of soft electro-active biological excitable media. Other general approaches can be found in the literature, in particular the Lagrangian-based work of Maugin and Epstein [184], or the more recent work of McMeeking and Landis [187]. However, an extended review related to the state of the art of muscle modeling turn out in a complete and detailed formulation reported in this dissertation, which resulted also extremely handy from a numerical point of view.

Concluding, it is worth to mention that the strong nonlinear nature of the mechanical material response, both in the passive and active regimes, requires ad hoc numerical implementations. Several iterative tools are necessary in order to obtain the stress free state in the unconstraint directions. In this regard, the proposed constitutive law has a direct implementation into three-dimensional realistic heart geometries. In fact, it already comprises anisotropy as a single fiber family and can be easily extended to two fiber families or general distributed fiber orientation material models [211]. Its implementation into dynamical time-varying problems would be then the final step towards complete cardiac tissue characterization. Coupling cardiac electrical dynamics for studying reentry onset and evolution, as well as alternans patterns in large tissue models will give a further understanding of the underlying behaviors of this complex organ.

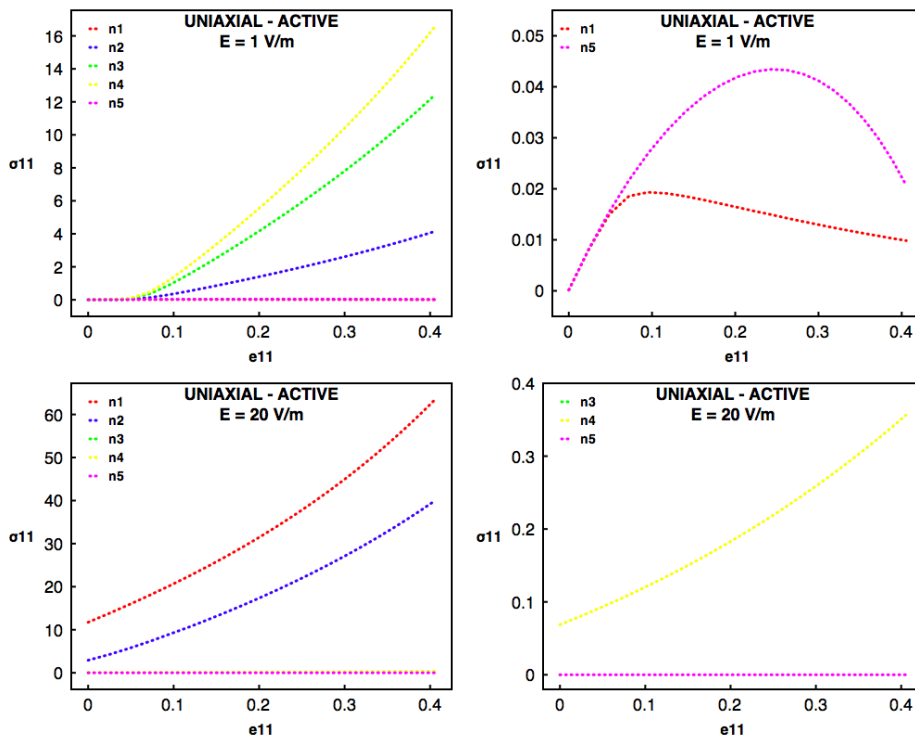


Figure 7.4.1: Mechanical response (total Cauchy stress, σ_{ij} , versus the total Hencky strain, e_{ij}) for active uniaxial test for five fiber orientations, $n_1 = 0^\circ$, $n_2 = 30^\circ$, $n_3 = 60^\circ$, $n_4 = 90^\circ$, and $n_5 = \perp$, and two constant electric fields equals to $E = 1 \text{ V/m}$ and $E = 20 \text{ V/m}$

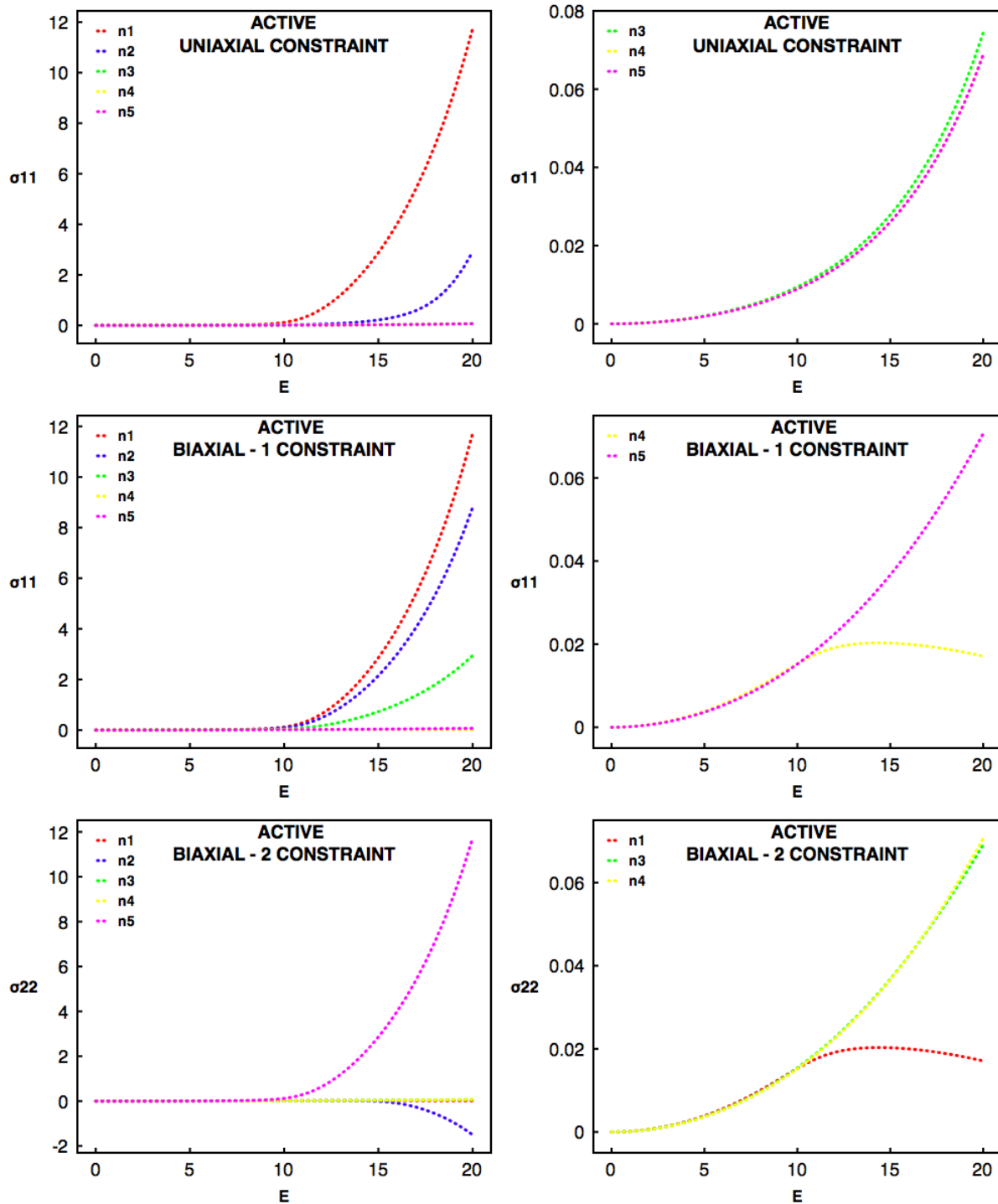


Figure 7.4.2: Mechanical response (total Cauchy stress, σ_{ij} , versus the electric field, E) for purely active tests. Five fiber orientations are tested $n_1 = 0^\circ$, $n_2 = 30^\circ$, $n_3 = 60^\circ$, $n_4 = 90^\circ$, and $n_5 = \perp$. The electric field is varied in the range $E \in [0; 20]$ V/m, with an incremental step of 0.5 V/m. Uniaxial constraint is reported in the top row, while biaxial cases are reported in the middle and bottom rows.

Chapter 8

The Electro-Elastic Unpinning of Rotating Vortices

The merging of knowledges, hypotheses and techniques from different scientific fields is helping computer models to complement experimental data and clinical studies. The final target seeks to elucidate the mechanisms of arrhythmogenesis in order to improve pharmacological and electrical therapies. Atrial fibrillation (AF), the most common sustained cardiac arrhythmia worldwide [287], and ventricular fibrillation (VF), the most dangerous life-threatening arrhythmia, represent an intrinsic three-dimensional problem. Despite this, current experimental technologies don't provide three-dimensional imaging capabilities for synchronous voltage and calcium measurements. Therefore, the need for combining experimental and numerical techniques, as the overarching theme of this thesis, requires a modeling approach which is able to take into account the role of specialized anatomical structures during arrhythmic states.

Although the advent of implantable devices and anti-arrhythmic drugs has yielded much success in avoiding arrhythmic episodes, these combined therapies are not always successful. In some cases, in fact, drug use increases mortality or defibrillating protocols are not effective, underlining our lack of knowledge with respect to the basic fibrillation mechanisms. In this perspective, a novel numerical study will be presented in this chapter together with a detailed description of its main clinical applications.

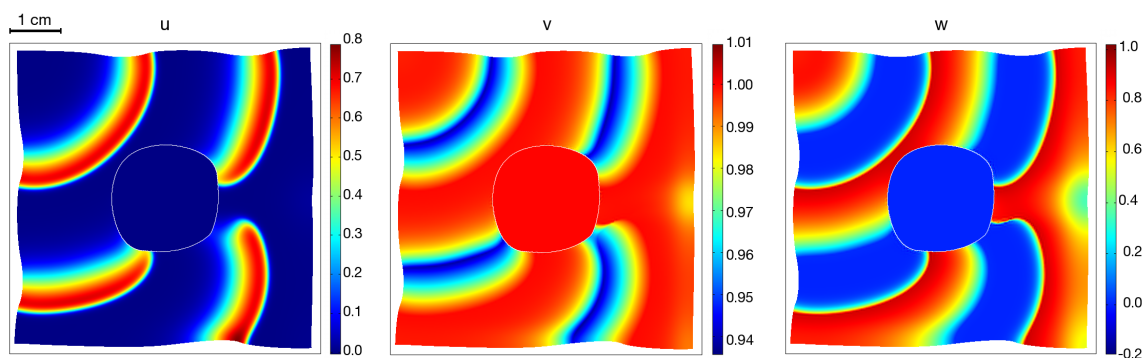


Figure 8.0.1: Representative example of the anatomical reentry unpinning protocol implemented on a two-dimensional electro-elastic domain: $L = 6 \text{ cm}$, $R_{ob} = 1.1 \text{ cm}$, $t = 1000 \text{ ms}$. From left to right, the spatial distribution of the three variables of the Fenton-Karma model [88], u , v and w respectively. For each of three fields the corresponding color scale is reported.

8.1 Minimal Electro-Elastic Cardiac Modeling

The strong nonlinear interaction of excitation waves in a heterogeneous anatomical substrate, as shown in the previous chapters, makes the control of life-threatening cardiac arrhythmias extremely difficult. Moreover, in recent years, new experimental techniques have been validated in order to establish theoretically-based relationship between the response of the tissue to low-energy electric fields and its rapid synchronization towards an efficient termination of fibrillation [181].

Nevertheless, schemes for alternans and spiral wave control have not yet performed at the level required for clinical implementation yet. In particular, most of these models are purely electric-based and do not take into account the deformation of the medium [106].

In this section, an electro-elastic low-energy defibrillation/unpinning model-protocol is presented [111, 166, 223, 224]. In particular, implementing a minimal electro-mechanical model, a pinned spiral in the heart is considered, i.e. an anatomical reentry, and a train of weak electric pulses is delivered at the boundary of the obstacle. A representative case of successful simulated unpinning protocol is shown in Fig.(8.0.1) via the two-dimensional spatial distributions of the three electrophysiological variables of the adopted model (discussed later). The model is fine tuned to qualitatively fit electro-physiological experiments, and belongs to the general theory presented in Chap.7.

8.1.1 Theoretical Formulation & Numerical Implementation

As briefly anticipated in Chap.(6), mechano-electric feedback can be modeled by assuming that, when cardiac muscle fibers are stimulated, these generate contractile forces which, at the macroscopic scale of the tissue, are mathematically described by an active stress tensor. Complete agreement about the characterization of such a *projector* within the scientific community is not present yet, even though, it is constitutively related to the tissue's electro-physiological activity, and specifically, to the subcellular calcium dynamics.

Electro-physiologic Equations

Assuming the three-variable phenomenological model [88] for action potential propagation and a basic non-diffusive kinetic equation for calcium dynamics, the electric part of the model is described by the following equations:

$$\begin{cases} \frac{\partial u}{\partial t} = \frac{1}{J} \frac{\partial}{\partial X_J} \left(J D_{IJ} \frac{\partial u}{\partial X_I} \right) + I_{\text{ion}} \\ \frac{\partial v}{\partial t} = \theta_c \left(\frac{1-v}{\tau_v^-} \right) - (1 - \theta_c) \frac{v}{\tau_v^+} \\ \frac{\partial w}{\partial t} = \theta_c \left(\frac{1-w}{\tau_w^-} \right) - (1 - \theta_c) \frac{w}{\tau_w^+} \end{cases} \quad (8.1.1)$$

where ion currents and time constants are given by:

$$I_{\text{ion}} = I_{\text{fi}} + I_{\text{so}} + I_{\text{si}}$$

$$\begin{cases} I_{\text{fi}} = -\frac{v}{\tau_d} \theta_c (1 - u) (u - u_c) \\ I_{\text{so}} = \frac{u}{\tau_o} (1 - \theta_c) + \frac{1}{\tau_r} \theta_c \\ I_{\text{si}} = -\frac{w}{2\tau_{si}} \left(1 + \tanh [k (u - u_c^{si})] \right) \end{cases} \quad (8.1.2)$$

$$\tau_v^-(u) = \theta_v \tau_{v1}^- + (1 - \theta_v) \tau_{v2}$$

while calcium kinetic is:

$$\frac{\partial c}{\partial t} = q_{ca}(u + V_{ca}) - k_{ca}c. \quad (8.1.3)$$

Here, u is the membrane potential, v and w are the fast and slow gates, c is the scalar calcium concentration field, θ_c is the Heaviside step function and I_{ion} is the total transmembrane current. The diffusion tensor, D_{IJ} , is expressed in the reference coordinates and mapped via the deformation gradient tensor, F_{iJ} , (pull back, with $J = \rho_o/\rho$ the volume change during motion [135]) from its current representation, D_{ij} , following the geometric transformation $D_{IJ} = F_{jJ}^{-1}D_{ij}F_{Ii}^{-1}$. For simulation purposes, tissue isotropy is considered, therefore the diffusion tensor assumes the diagonal form $D_{ij} = d_o I_{ij}$, with I_{ij} the unit tensor and d_o being the constant intensity in the three orthogonal directions.

Active Mechanic Equations and Coupling

The mechanical part of the model belongs to the framework of hyperelastic continuum mechanics material laws, and presents the multiplicative decomposition of the deformation tensor, in order to introduce the active component:

$$F_{iJ} = F_{iK}^e F_{KJ}^a.$$

Specifically, adopting a neo-Hookean incompressible representation, the elastic strain energy, ψ , depends only on the first invariant of the right Cauchy-Green elastic strain tensor, $I_1 = \text{tr}(C_{IJ}^e)$, readily:

$$\psi(I_1) = \frac{\alpha_1}{2}(I_1 - 3), \quad (8.1.4)$$

where α_1 is the elastic modulus. Simplifying tissue architecture in a planar, isotropic muscular fiber distribution, h_I , at the macroscopic scale the activation of the muscle fibers is prescribed by the active deformation field expressed as

$$F_{IJ}^a = \gamma_o(c)(\delta_{IJ} - h_I h_J). \quad (8.1.5)$$

The active stretch $\gamma_o(c)$ measures the amount of active contraction of any fiber and accounts for the relation between calcium dynamics and deformation:

$$\begin{cases} \gamma_o(c) = \frac{\lambda_{ca}}{1+f_{ca}(c)(\lambda_{ca}-1)}\gamma_o^{\max} \\ \lambda_{ca} = \frac{f_{ca}(c^*)-1}{f_{ca}(c^*)-\gamma_o^{\max}} \\ f_{ca}(ca) = \frac{1}{2} + \frac{1}{\pi} \arctan\left(\beta_c \log \frac{c}{c_o}\right) \end{cases} \quad (8.1.6)$$

where λ_{ca} and f_{ca} are ad hoc functions necessary to induce the muscular active excitation-contraction scheme.

Boundary Conditions and Numerical Implementation

The electric and kinetic boundary conditions of the model have been implemented with standard Neumann zero flux. However, the mechanical counterpart has been constitutively characterized in order to mimic the tissue surrounding the patch, i.e.

$$t_I = -k^b \delta_{IJ} U_J. \quad (8.1.7)$$

In other words, the reference traction density, t_I , has been constrained to depend linearly on the boundary displacement U_J via an isotropic stiffness tensor $K_{IJ} = k^b \delta_{IJ}$, where k^b is a dimensionless parameter fine tuned to mimic myocardial stiffness.

The fully coupled model has been implemented into different squared shaped domains, side lengths $L = 5, 6, 7 \text{ cm}$, in which a circular obstacle of variable radius, $0.35 \text{ cm} \leq R_{ob} \leq 1.4 \text{ cm}$, has been considered. Such heterogeneity has been modeled as a non-excitabile circular obstacle with altered mechanical properties:

- no action potential can generate or propagate: no diffusion, static ion dynamics;
- increased stiffness than the surrounding tissue: the Young modulus has been lowered of the 90%.

Tissue stimulation has been electrically induced as a circular electrode centered on the upper-left corner of the domain of radius $R_p = 0.4 \text{ cm}$. The stimulation protocol consisted in delivering regular sequences of squared waves with a pulse duration $\tau = 2 \text{ ms}$. For each tested radius, the stimulation period has been increased by 2 ms , and starting from the same initial conditions.

Fine tuning of the mesh grid size, as well as of the maximum time stepping has been performed upon several different simulation protocols. The mesh size has been explored both for the purely electric or rigid (RIG) and coupled electro-mechanical (ELA) models as shown in Fig.(8.1.1). The procedure consisted in evaluating the conduction velocity of action potential (AP) and elastic (EL) waves, as well as calcium (Ca) (kinematic waves) for different regular squared meshes adopting Lagrange quadratic elements, until stable flat curves were reached. The electric problem resulted mesh independent for mesh sizes $dx \leq 0.07 \text{ cm}$, both in 1D and 2D. In order to evaluate the minimal electro-mechanical mesh size,

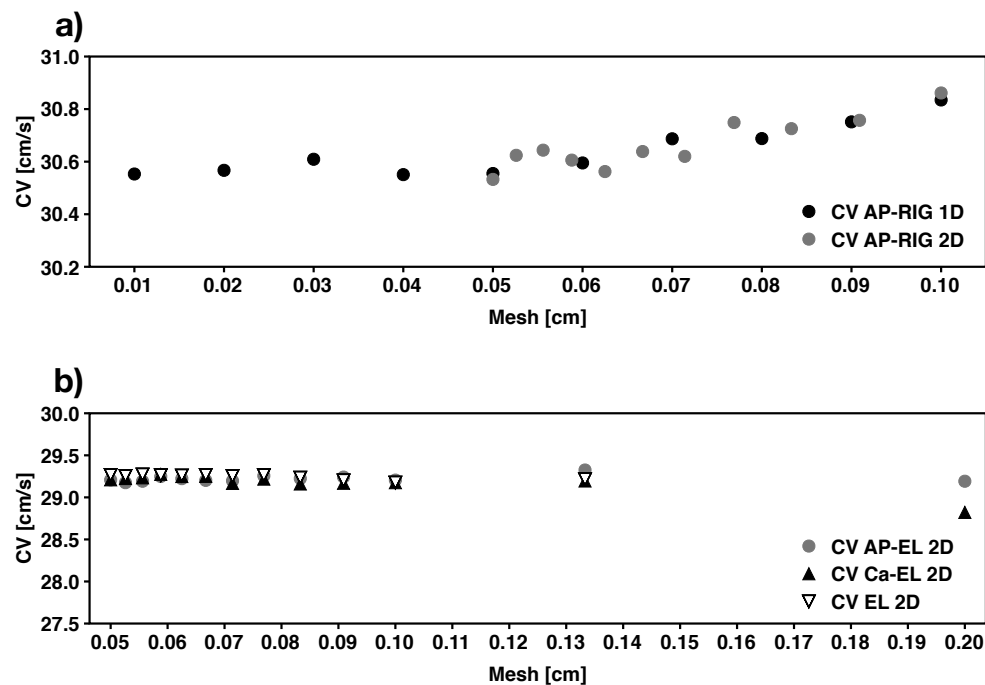


Figure 8.1.1: Conduction velocity (CV) versus mesh size restitution graphs. Action potential (AP), elastic (EL) and calcium (Ca) (kinematic) waves are compared to set the right mesh size for numerical solution purposes. The plane wave traveling front timing has been taken at the 35% of its upstroke at two consecutive mesh positions nodes in order to evaluate the resulting velocity (several mesh nodes sequences have been tested). (A) Purely electric AP conduction velocities are compared between 1D (black) and 2D (gray) simulation domains. (B) AP (gray circle), Ca (black triangle) and EL (gray triangle) conduction velocities are compared for a 2D simulation domain where the electric mesh has been kept fixed at $dx = 0.5 \text{ cm}$. In both cases a good agreement between the estimated velocities can be observed for mesh sizes lower than $dx = 0.1 \text{ cm}$.

the 2D coupled problems were solved adopting different grids for AP and Ca-EL respectively: for a fixed AP grid, $dx = 0.05 \text{ cm}$, flat Ca-EL conduction velocities resulted for a mesh size $dx \leq 0.1 \text{ cm}$. On these basis, the final choice was a unique mesh size, $dx = 0.067 \text{ cm}$, for the complete coupled model, further subdivided into triangles in order to increase the accuracy and convergence of the numerical solution. The main results of this article (i.e. the unpinning band) are insensitive to the mesh size then.

Each simulation has been run for $T = 3000 \text{ ms}$ of physical time. The complete set of simulations consisted of more than 500 distinct runs, for a computational time of several months on a multiprocessor machine.

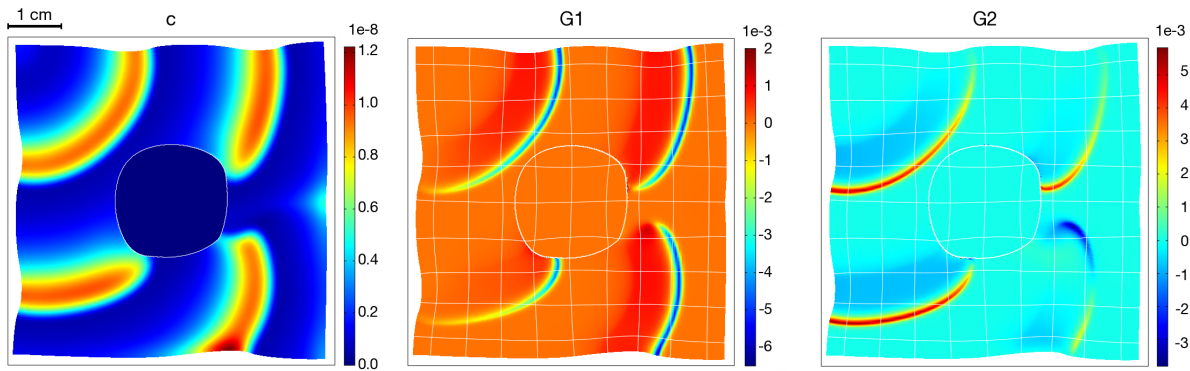


Figure 8.1.2: Spatial distribution of peculiar values with reference to the representative condition reported in Fig.(8.0.1). **(LEFT)** Non-diffusive variable, c , representing calcium dynamics for mechanical contraction. Modified diffusion coefficients, G_1 **(CENTER)** and G_2 **(RIGHT)** due to tissue deformation with the highest values on the wave front/back where the curvature is maximum. For each field the corresponding color scale is reported.

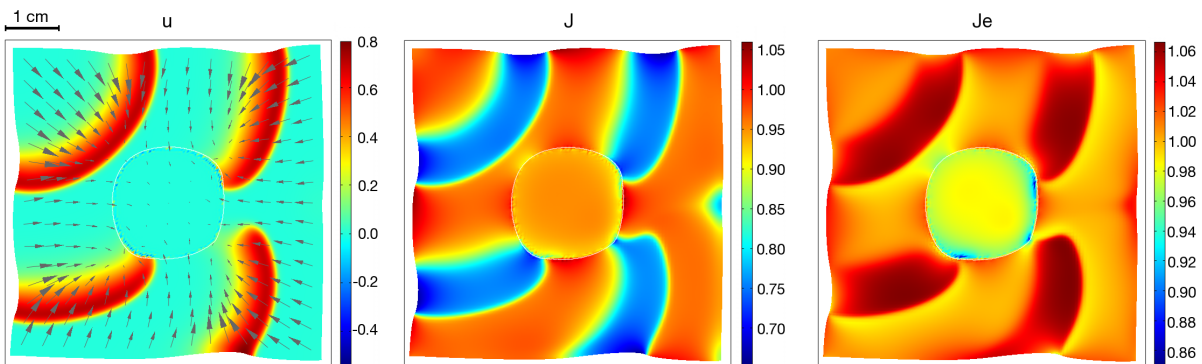


Figure 8.1.3: Spatial distribution of peculiar values with reference to the representative condition reported in Fig.(8.0.1). **(LEFT)** Arrow plot of the deformation field over imposed to the non-dimensional action potential distribution. Determinant of the total deformation gradient, $J = \det(F_{iJ})$ **(CENTER)**, and of the purely elastic one, $J_e = \det(F_{iJ}^e)$ **(RIGHT)**. For each field the corresponding color scale is reported.

8.1.2 Peculiar Spatial Distributions of the Model

In this paragraph, a description of peculiar spatial distributions of the different fields calculated during the simulation is reported.

- Fig.(8.1.2): the non-diffusive calcium dynamics, c , is shown, noting the close similarity with the action potential distribution reported in Fig.(8.0.1). The next two panels, G_1 and G_2 , enhance the modified diffusion coefficient due to tissue deformation:

$$\begin{cases} G_1 = \frac{d_o}{J} \left(C_{22} \frac{\partial u}{\partial x} - C_{12} \frac{\partial u}{\partial y} \right) \\ G_2 = \frac{d_o}{J} \left(-C_{12} \frac{\partial u}{\partial x} + C_{11} \frac{\partial u}{\partial y} \right), \end{cases}$$

where C_{ij} are the components of the Cauchy-Green strain tensor. In particular, it can be noted that the highest values are obtained in correspondence to the front/back of the action potential propagating wave, which are the spatial locations with maximum curvature.

- Fig.(8.1.3): the arrow deformation field, u , is over imposed to the action potential distribution, enhancing the global directions of the field and how important is the obstacle for the overall phenomenon. The next two panels report the spatial distribution of the determinant of the total and elastic deformation gradient tensors, J and J_e , respectively:

$$\begin{cases} J = \det(F_{iJ}) \\ J_e = \det(F_{iJ}^e) \\ F_{iJ} = F_{iK}^e F_{KJ}^a. \end{cases}$$

In this case the spatial pattern is very similar although the variability ranges are different.

- Fig.(8.1.4): the three independent (symmetric) components of the right Cauchy-Green deformation tensor, C_{IJ} , (top row), are compared with its three principal invariants (bottom row):

$$\begin{cases} I = \text{tr} C_{IJ} \\ II = \frac{1}{2} \left[(\text{tr} C_{IJ})^2 - \text{tr} (C_{IJ})^2 \right] \\ III = \det C_{IJ}. \end{cases}$$

It is interesting to note the high variability of the components, which maximize the deformation field on the discontinuity border of the central obstacle, while its three invariant assume the spatial distribution resembling the action potential spatial pattern.

- Fig.(8.1.5): this panel reports the three components of the second Piola-Kirchhoff stress tensor, S_{IJ} ,

$$S_{IJ} = F_{iJ}^{-1} P_{iI} = J F_{iI}^{-1} \sigma_{ij} F_{jJ}^{-1},$$

directly related to the first Piola-Kirchhoff stress tensor, P_{iJ} , and to the true Cauchy stress tensor, σ_{ij} . In this case, the tensor is not symmetric and the difference between the two non-diagonal components is reported in the last picture, enhancing the location of nonlinear interaction between the electric and the mechanical model which lead to a non-symmetric stress concentration.

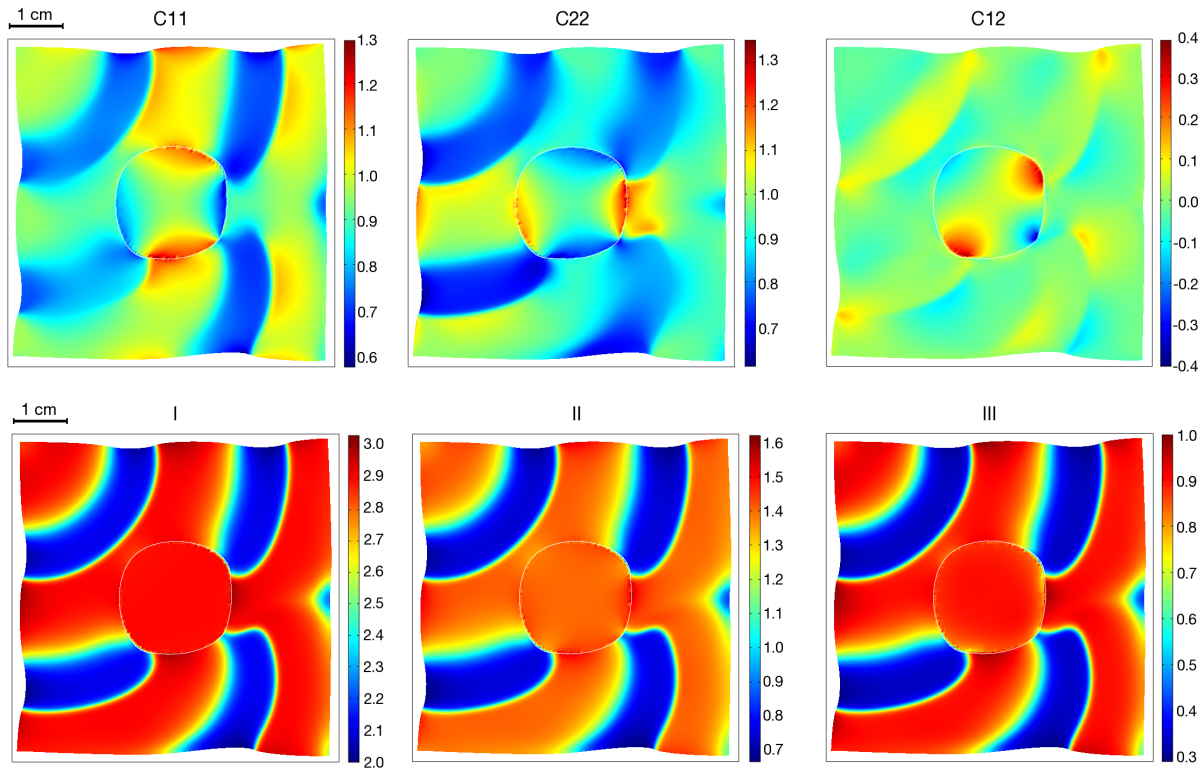


Figure 8.1.4: Spatial distribution of peculiar values with reference to the representative condition reported in Fig.(8.0.1). (TOP) From left to right, the independent components of the right Cauchy-Green deformation tensor, C_{IJ} are shown. (BOTTOM) From left to right, the first, I , second, II , and third, III , invariant of C_{IJ} . It can be noted that the non-diagonal component of the tensor (which is symmetric) induces deformation measures which are not deductible from the other two components due to the nonlinearity of the theory, however, the spatial distribution of the three invariants resemble the action potential waves shape. For each field the corresponding color scale is reported.

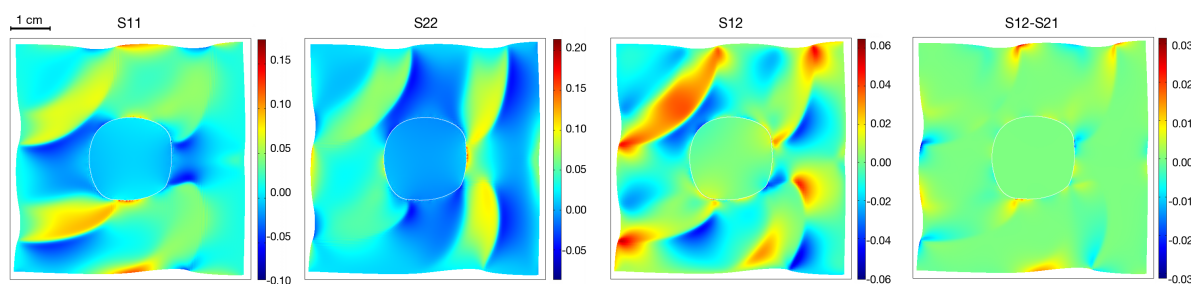


Figure 8.1.5: Spatial distribution of peculiar values with reference to the representative condition reported in Fig.(8.0.1). From left to right, the diagonal, S_{11} and S_{22} , and non diagonal, S_{12} , components of the second Piola-Kirchhoff stress tensor, S_{IJ} . The last panel on the right represents the difference between the non-diagonal components of the tensor, $S_{12} - S_{21}$, which is non-symmetric. For each field the corresponding color scale is reported.

8.1.3 Results: The Unpinning Band Measure

Several interesting results have been obtained from such an extended simulation campaign (> 500 runs), with measurable differences between the rigid purely electric (RIG) and deformable electro-mechanic (ELA) model.

1. Spiraling periods around the heterogeneity separate following an almost linear interpolated trend as the obstacle radius increases:
 - Fig.(8.1.6)(A) shows the overall results from the explored simulations set. In particular, the spiral rotational period is compared for the purely electric or rigid (RIG), gray, and electro-mechanic or elastic (EL), black, simulations versus the radius of the obstacle. The superimposed histogram reports the difference between the two cases showing as the divergence trend reaches its maximum value, 34 ms , for the higher radii analyzed.
2. An *unpinning band* can be identified in both cases (RIG and ELA), defined as the range of unpinning pacing periods which lead to the detachment of an action potential wave rotating in a persisting manner around a circular heterogeneity of the medium:
 - Fig.(8.1.6)(B) shows the upper and lower limits of the unpinning bands (stimulation periods for which the unpinning has been reached) comparing the purely electric (gray) and the electro-mechanic (black) cases (on vertical axis the lowest and highest successful stimulation periods expressed in ms). The explored pacing periods range in $90 \div 120\text{ ms}$ with a finite time-step of variation of 2 ms . The horizontal axis reports the discrete simulated obstacle radii ranging between 3.5 cm and 1.4 cm with a spatial step of 1 cm . The intermedium case, $R_{ob} = 0.75\text{ cm}$, has been tested in order to verify the resulting interpolating trend. The superimposed histogram reports the absolute difference of the two bands obtained. Both the trends are highly nonlinear and reach their minimum for the largest obstacle radii analyzed.
3. The simulation domain has been varied in order to quantify the effects of boundary conditions [44] and to change the relative distance between the pacing electrode and the central obstacle:
 - Fig.(8.1.7)(A): changing in size of the simulation domain does not affect the spiraling rotation periods as further highlighted in Fig.(8.1.8)(A).
 - Fig.(8.1.7)(B-C): the unpinning bands are affected by the domain size in a different way: the rigid case, in particular, reduces the successful unpinning periods as the ratio between the obstacle radius and the domain size increases, and specifically when $R_{ob}/L \geq 0.2$. Such a result seems to be in agreement with the recent work of Cherry and Fenton on boundary conditions effects [44].
4. Fig.(8.1.7)(C): although measurable differences can be extracted from the numerical analysis, rigid and elastic unpinning band trends result very similar both in shape and periods. Moreover, it can be noted that both trends tend to shrink and reduce for higher obstacle radii, therefore confirming previous works on the theme [224], where a maximum unpinning obstacle size is reached, meaning that, after a certain value of the obstacle size, unpinning by simple electric pacing is no more feasible.
5. Fig.8.1.8(A): the observed dynamics seem to be indifferent to changes of the pacing position, both for the rigid and elastic cases.

6. Fig.8.1.8(B): the large strain regime addressed by the model induces visible deformations of the obstacle leading to a strong nonlinear interaction between the electric and the mechanical quantities (in particular on the discontinuity border).
7. Fig.8.1.9: a comparative sequence of the unpinning protocol with and without deformation is reported, enhancing a measurable time shifting between the two cases for a successful unpinning.

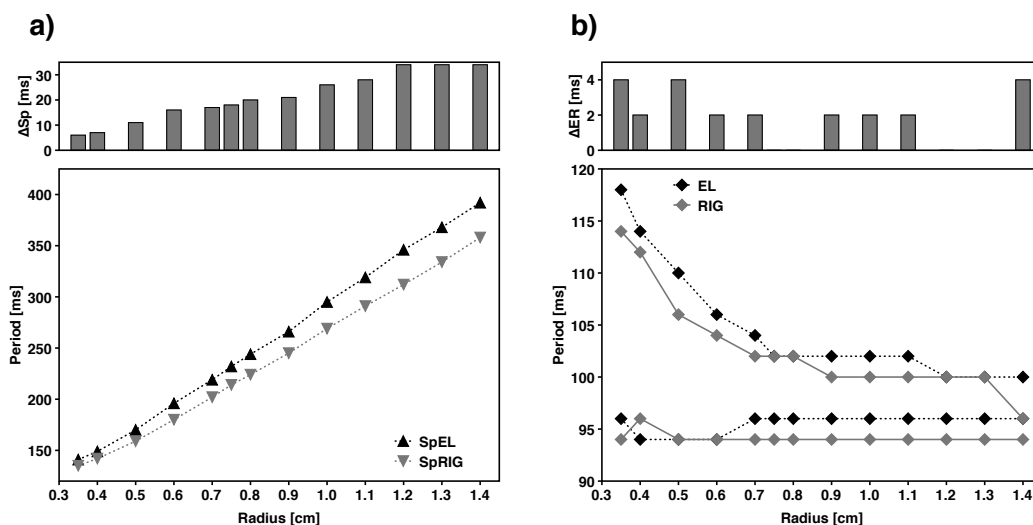


Figure 8.1.6: Overall results from the explored simulations set. **(A)** Spiral rotational period compared for purely electric or rigid (RIG), gray, and electro-mechanic or elastic (EL), black, simulations versus obstacle radius. The superimposed histogram reports the difference between the two cases. **(B)** Comparison of the unpinning bands (upper and lower defibrillation limits) for the purely electric (gray) and the electro-mechanic (black) cases. The vertical axis reports the lowest and highest successful stimulation periods (ms), i.e. the ones for which the unpinning has been reached. The horizontal axis reports the discrete simulated obstacle radii. The superimposed histogram reports the absolute difference of the band ranges between the two modeling.

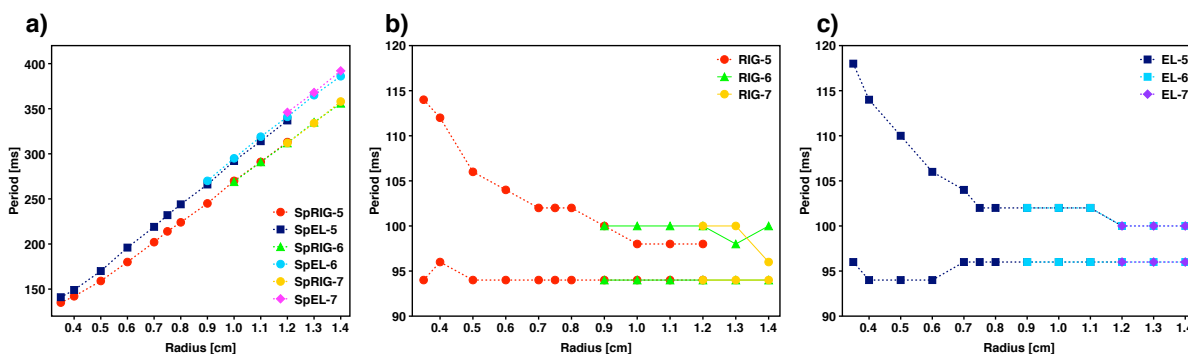


Figure 8.1.7: Comparison of the spiral rotation and successful defibrillation periods for three different domain sizes, $L = 5, 6, 7$ cm, for both rigid (RIG) and elastic (EL) modeling, versus obstacle radius. The spiral rotational periods **(A)** seem to be unaffected by changing the domain size, following the same behavior as reported in the previous case. In the purely electric case **(B)** the boundary effects induce a reduction of the unpinning band when the ratio $R_{ob}/L \geq 0.2$, while the electro-elastic model **(C)** shows a better robustness to this effect.

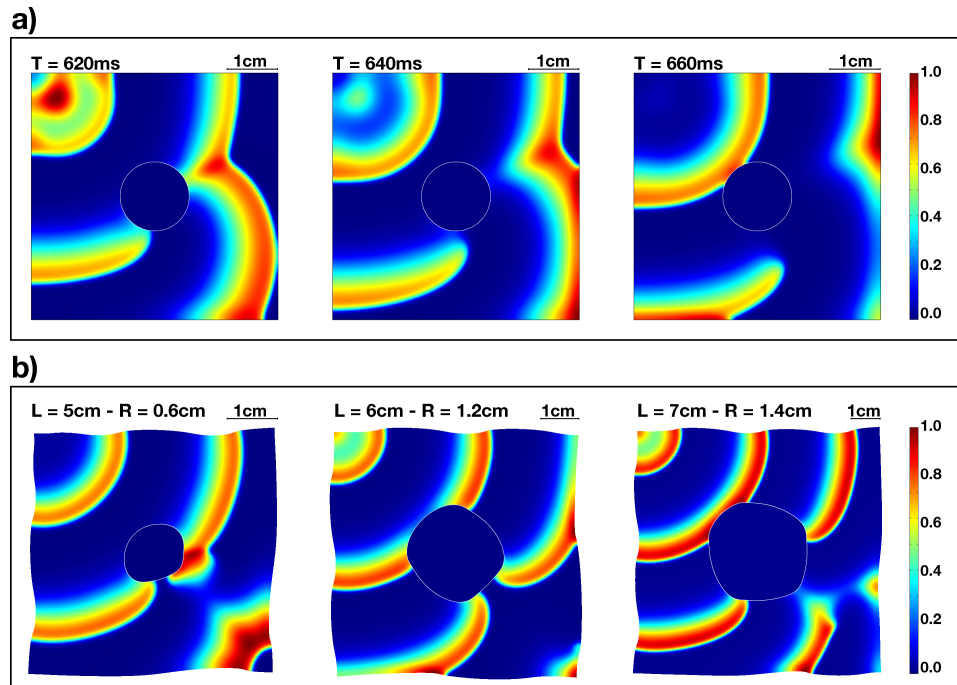


Figure 8.1.8: Differences induced by pacing site and elasticity. (A) Defibrillation sequence in the case of the pacing electrode inside the tissue (top left), confirming that the unpinning dynamics are similar to those observed with the pacing at the corner of the domain ($L = 5\text{ cm}$, $T = 98\text{ cm}$). (B) Three different domain sizes ($L = 5, 6, 7\text{ cm}$) with different obstacle sizes ($R_{ob} = 0.6, 1, 2, 1.4\text{ cm}$) reporting an example of the distorted obstacle shapes varying in time due to the presence of elastic effects. The color map is referred to the normalized action potential of the Fenton-Karma model [88].

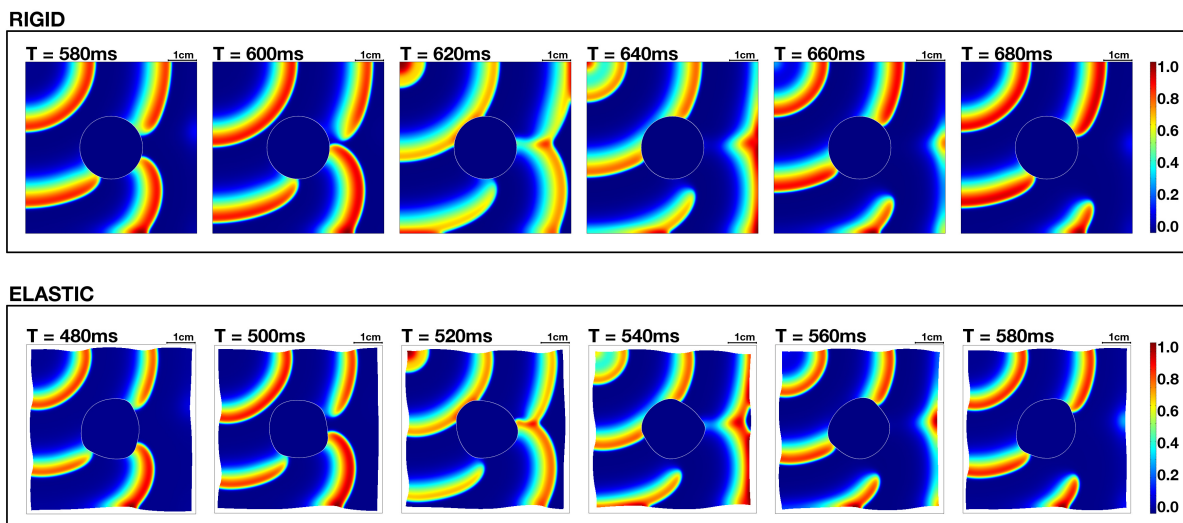


Figure 8.1.9: Sequences of unpinning scenarios with no elasticity (TOP, RIGID) and contraction activated (BOTTOM, ELASTIC). Both sequences are referred to a domain size $L = 6\text{ cm}$, an obstacle radius $R_{ob} = 1.2\text{ cm}$ and a stimulation period $T = 100\text{ ms}$. The timing reported in the panels shows a noticeable shifting in the unpinning event between the two cases. The color map is referred to the normalized action potential of the Fenton-Karma model [88].

8.1.4 Discussion and Further Studies

The importance of theoretical and numerical studies has relevance for the clinical necessity of obtaining the highest efficiency for low-energy implantable defibrillation devices. The problem to identify the correct periods of the electrical stimuli necessary to detach and remove the electrical reentries, should take into account the electro-mechanical properties of a real pulsing heart. In particular, lower pacing rates and delivered energy would save the tissue from a further induction of arrhythmia and would save the mean life of the implantable device itself.

The analysis here proposed is based on a minimal electro-mechanic model: in a first approximation, the numerical study has been limited to a simple mechano-electric electro-physiological modeling, considering a two-dimensional heterogeneous and isotropic medium. The heterogeneity has been implemented as a circular obstacle in the center of the domain, and modeled as a non-excitable area, capable to attach action potential waves in a persisting manner. The same stimulation protocol has been then compared both for the rigid and electro-mechanic cases.

Even provided these simplifying assumptions however, the presence of an active stress tensor, coming from a multiplicative decomposition procedure, has made the modeling non trivial both from the theoretical and numerical points of view. Several interesting results, in fact, can be observed: separating spiral rotational periods for increasing obstacle radii and similarity of unpinning bands. Moreover, these results appear to be insensitive to the location of the pacing stimulus.

It is important to stress that, for this specific situation studied at least, elasticity does not seem to play a major role in the pinning/unpinning dynamics. The nature of the involved nonlinearities, however, does not mean that in other different and more realistic scenarios, like studies of free spiral dynamics on large domains, the role of the elastic coupling could be small. In fact, a more biologically accurate contractile heart modeling could better reveal these differences in comparison with the non elastic case.

To this aim it is necessary to extend in a near future the proposed model to imported three-dimensional cardiac domains (reconstructed from Nuclear Magnetic Resonance), where tissue heterogeneity and fiber anisotropy could reveal more complex dynamics, in analogy with already existing purely electrical studies. This aspect, in fact, plays a key role to further increase of the mentioned defibrillation efficiency, although starting from simplified theoretical analysis at first.

The final target of this work, therefore, can be identified, by taking into account the complete phenomenology of the tissue, as the increase the existing data on defibrillation efficiency by reducing the energy dispersion in the tissue. In this regard, the evidence of a remarkable electro-mechanic role in pinning phenomena, suggests the necessity to plan more advanced experiments, to be performed in order to fine-tune the electro-physiological and bio-mechanical experimental data of the nonlinear cardiac tissue dynamics.

In the spirit of the comprehensive view of the topics presented in the thesis, this model belongs to the general theory of deformable active media presented in Chap.7. Therefore, other than the experimental-based quantities necessary to further advanced numerical studies, as discussed, a necessary generalization of the theoretical formulation, considering both the frameworks of continuum mechanics and excitable media, is mandatory. Such a theoretical assessment, is strongly requested for an appropriate reformulation of the problem, trying to make the numerical calculations as handle as possible, thus reducing the computational time and effort in order to performed more advanced and extended simulation campaigns.

Chapter 9

Conclusions

Cardiovascular diseases represent the main cause of death worldwide, as reported by the latest World Health Organization Statistics Report [306]. A considerable challenge, in the modern era, is represented by realistic simulation of whole heart functions and pathologies. Mathematical models of cardiac cells electrophysiology have advanced considerably since the first model consisting of four differential equations and published in the 1960s [203]. The description of Purkinje cell transmembrane currents, as an example, heralded the beginning of a new era. Since then, a large number of complicated models, up to nearly 100 differential equations, have been developed in order to catch the fine details of many more currents and ion concentrations, to represent different types of cells and to incorporate increasingly complex intracellular calcium dynamics [43].

However, the nature of action potential propagation deep within myocardial tissue is still unclear. As a result, a complete understanding of cardiac dynamics remains elusive, especially for life-threatening phenomena like ventricular fibrillation. Controlling the complex spatio-temporal dynamics underlying cardiac arrhythmias is thus extremely challenging and demanding. The nonlinear interaction of excitation waves in a heterogeneous anatomical substrate together with large deformations of the tissue, makes theory and simulations still far from reality. The systemic integration of experimental data into numerical models is mandatory then, and the development of parameter estimation and model evaluation/validation methods represents one of the major topics of the current scientific research.

The methodological approach that combines experiments with numerical simulations and theory, as pursued in this thesis, is a significant step towards this goal. The object of this dissertation was to study cardiac spatio-temporal dynamics starting from experimental measurements, passing through theoretical assessment and synthetic indicators, thus concluding with mathematical modeling and simulations of cardiac electro-mechanics. The massive experimental campaign (1362 recordings) performed on canine right ventricles (9 tissue preparations) and measuring the electrical activity of both the endocardial and epicardial surfaces, necessitated the development of novel data analysis algorithms within an interactive framework. To this aim, a Java software was developed in collaboration with Dr. Flavio Fenton, leading to a very flexible, user friendly and performing tool for data analysis and visualization.

The resulting properties from this extended analysis were further studied and manipulated in order to enhance novel behaviors not previously observed in cardiac alternans on large mammalian hearts. We found that spatial patterns of concordant and discordant alternans on both endocardium and epicardium present complex morphologies of nodal lines and surfaces (cases of alternating islands and multiple nodal lines were not rare). In this regard, several cooperating effects were identified as stimulation cycle length,

anatomical location of the pacing electrode and pacing history more generally. In addition, considering different initial conditions of action potential duration, tissue heterogeneity and fiber anisotropy, we found uncorrelated patterns between endocardium and epicardium via synchronous recordings of the two electrical activities. This finding means that complicated nodal lines and surfaces are also present transmurally in the tissue wall, although the thickness of right ventricles is small (~ 1.5 cm) in comparison with the right ventricle surface ($\sim 7 \times 7$ cm²).

From a more general point of view, we found that the onset and developing of alternans patterns varying the pacing cycle length does not always follows the well-known standard transition from concordant (CA) to discordant (DA) alternans. In fact, examples in which concordant and discordant patterns follow an extended non-standard sequence, i.e. CA-DA-CA-DA, were presented and discussed in details, and further corroborated by quantitative evaluations of optical pixel percentages measuring the amount of tissue in alternating or non-alternating states. Moreover, alternans onset does not involve the whole tissue at the same time, but gradually recruits more and more areas.

The theoretical assessment of the overall study was framed into the general theory of electro-mechanical active media subjected to large deformations. A new constitutive law for cardiac tissue was introduced and derived from the most general energy statements. It comprises passive and active tissue anisotropy with electro-mechanic excitation-contraction coupling. Ad hoc numerical routines were developed in order to test the material model under both standard and novel strain tests. In particular, the effect of the electric field was explored by evaluating the stress induced into the constraint material and depending on muscular fiber orientation and electric field intensity.

Advanced and extended numerical simulations of cardiac low-energy defibrillation protocols were also performed on both rigid and deformable domains, i.e. unpinning of an anatomical reentry attached to a circular non-excitabile obstacle. The finding resulted from a broad number of runs (more than 500 simulations), permitted to quantify the successful unpinning windows (unpinning bands) comparing a standard electric model with an electro-mechanic one undergoing large deformations. The final comparison revealed that, although strong differences are present in the rotation period, the resulting unpinning bands were very similar in both shape and intervals. In addition, we analyzed several effects in terms of stimulation pacing periods and positions, ratio between size of the domain and the anatomical obstacle. From this analysis we were able to further characterize the effects of the boundary conditions on the resulting dynamics, more evident in the rigid case, quantifying in the ratio size of $R_{ob}/L \geq 0.2$ (obstacle radius on domain size) as the threshold value below which boundary effects are negligible.

Finally, aortic fluid dynamics simulations were performed in order to characterize a new risk indicator for the wall shear stress. The proposed three-band decomposition technique, providing a novel signal analysis tool, revealed that the standard oscillation shear indicator (OSI) is not always accurate in the risk prediction. This adjoint validation methodology, therefore, with an easy and general implementation on every operating system, could help the clinical practice towards more accurate and patient-specific diagnosis.

9.1 Relevance of this Work

The emphasis of this work will be put on unveiling some of the hidden behavior of cardiac arrhythmias in terms of alternating spatio-temporal patterns. The main goal is to provide cardiologists with supporting tools for clinical practice and to predict the onset of particular diseases or disorders, thus plan preventive therapies. The predictive medicine approach can be therefore framed inside the theoretical assessment

performed in this work as a general formulation of deformable excitable media, with new constitutive prescriptions for cardiac electro-mechanics, and the numerical study of efficient defibrillation techniques. These findings, therefore, may be helpful to improve design and performance of the actual devices and drug therapies as well.

9.2 Validation

The experimental work is validated by Cornell University, Department of Biomedical Sciences, Gilmour Lab., whose scientists guided the study on cardiac alternans, provided tissue preparations and experimental setup, helped in interpretation of results, giving a significant contribution to the main experimental findings.

The theoretical work is validated by Politecnico di Milano University, Department of Structures, that guided the theoretical formulation and numerical implementation of the mechanical tests.

The simulation work is validated by Campus Bio-Medico University, Engineering Faculty, Nonlinear Physics and Mathematical Modeling Lab, that supervised the mathematical modeling and the numerical implementation, provided workstations for simulations, and helped in interpretation of the overall results presented in this dissertation.

9.3 Future improvements and perspectives

The different aspects presented in this dissertation constitute the starting point for more advanced and complex studies relating cardiac alternans with electro-mechanics large deformations. Each of the topics here discussed is producing new interesting research works and international collaborations. The most direct improvement consists in applying the theoretical framework proposed for excitation-contraction coupling on realistic three-dimensional geometries together with fluid-structure interaction. Testing both the defibrillating protocols of cardiac reentries and the new risk indicator for cardiovascular diseases on realistic numerical simulations, could be applied for specific clinical therapies. Finally, it would be useful to carry out a detailed experimental study of cardiac alternans onset and evolution in order to point out its relations with mechanic and haemodynamic parameters.

Bibliography

- [1] R. R. Aliev, and A. V. Panfilov. A simple two variable model of cardiac excitation. *Chaos*. **7**:293-301, 1996.
- [2] M. A. Allesie, M. J. Schlij, C. J. Kirchhof, L. Boersma, M. Huybers, and J. Hollen. Experimental electrophysiology and arrhythmogenicity. Anisotropy and ventricular tachycardia. *Eur. Heart J.* **10**:E2-E8, 1989.
- [3] J. Ando, and K. Yamamoto. Effects of shear stress and stretch on endothelial function. *Antioxid. Redox. Signal.* **15**:1389-1403, 2011.
- [4] H. Aravelo, B. Rodriguez, and N. Trayanova. Arrhythmogenesis in the heart: multiscale modeling of the effects of defibrillation shocks and the role of electrophysiological heterogeneity. *Chaos*. **17**:015103, 2007.
- [5] H. Arce, A. Xu, M. R. Guevara, and H. González. Issue Alternans and higher-order rhythms in an ionic model of a sheet of ischemic ventricular muscle. *Chaos*. **10**:411-426, 2000.
- [6] J. L. Aron, and I. B. Schwartz. Seasonality and period-doubling bifurcations in an epidemic model. *J. Theor. Biol.* **110**:665-679, 1984.
- [7] D. O. Arnar, and J. B. Martins. Purkinje involvement in arrhythmias after coronary artery reperfusion. *Am. J. Physiol. Heart Circ. Physiol.* **282**:H1189-H1196, 2002.
- [8] R. Arora, M. K. Das, D. P. Zipes, and J. Wu. Optical mapping of cardiac arrhythmias. *J. Pac. Electrophysiol.* **3**:187-196, 2003.
- [9] S. Arrhenius, *On the reaction velocity of the inversion of cane sugar by acids*, Zeitschrift fur physikalische Chemie, 1889.
- [10] A. Artoli, A. Hoekstra, and P. Sloat. Mesoscopic simulations of systolic flow in the Human abdominal aorta. *J. Biomech.* **39**, 873, 2006.
- [11] T. Ashihara, and N. Trayanova. Cell and tissue responses to electric shocks. *Europace*. **7**:155-165, 2005.
- [12] K. F. Augustein, E. R. McVeigh, and A. A. Young. Magnetic resonance imaging and ventricular mechanics. *Phil. Trans. R. Soc. London A.* **359**:1263-1276, 2001.
- [13] P. S. Barker, and J. Alexander. The excitatory process observed in the exposed human heart. *Am. Heart J.* **5**:720-742, 1930.
- [14] D. Barkley, M. Kness, and L. S. Tuckerman. Spiral wave dynamics in a simple model of excitable media: the transition from simple to compound rotation. *Phys. Rev. A* **42**:2489-2492, 1990.
- [15] D. Barkley. A model for fast computer simulation of waves in excitable media. *Physica D.* **49**:61-70, 1991.
- [16] E. Bartocci, E. M. Cherry, J. Glimm, R. Grosu, S. A. Smolka, and F. H. Fenton. Toward real-time simulation of cardiac dynamics proceedings of the 9th *ACM International Conference*, CMSB, 2011.
- [17] G. W. Beeler, and H. Reuter. Reconstruction of the action potential of ventricular myocardial fibres. *J. Physiol.* **268**:177-210, 1977.
- [18] <http://www.bem.fi>.
- [19] S. Ben-Horin, A. Shinfeld, E. Kachel, A. Chetrit, and A. Livneh. The composition of normal pericardial fluid and its implications for diagnosing pericardial effusions. *Am. J. Med.* **118**:636-40, 2005.
- [20] M. Bernaschi, S. Melchionna, S. Succi, M. Fyta, E. Kaxiras, and J. K. Sircar. MUPHY: A parallel MUlti PHYsics/scale code for high performance bio-fluidic simulations. *Comp. Phys. Comm.* **180**, 1495, 2009.
- [21] D. M. Bers. Calcium Fluxes Involved in Control of Cardiac Myocyte Contraction. *Circ. Res.* **87**:275-281, 2000.

- [22] M. J. Berridge, M. D. Bootman, and H. L. Roderick. Calcium signalling: dynamics, homeostasis and remodelling. *Nature Rev.* **4**:517-529, 2003.
- [23] www.biotronik.com.
- [24] M. Bisson, M. Bernaschi, S. Melchionna, S. Succi, and E. Kaxiras. Multiscale Hemodynamics Using GPU Clusters. *Comm. Comput. Phys.* doi:10.4208/cicp.210910.250311a, 2011
- [25] J. R. Blake, S. Meacher, K. H. Fraser, W. Easson, and P. R. Hoskinsa. A method to estimate wass whear rate with a clinical ultrasound scanner. *Ultrasound Med. Bio.* **34**:760-774, 2008.
- [26] F. Bogun, E. Good, S. Reich, D. Elmouchi, P. Igc, D. Tschopp, S. Dey, A. Wimmer, K. Jongnarangsin, H. Oral, A. Chugh, and F. Pelosi, F. Morady. Role of Purkinje fibers in post-infarction ventricular tachycardia. *J. Am. Coll. Cardiol.* **48**:2500-2507, 2006.
- [27] A. Bueno-Orovio, V. M. Perez-Garcia, and F. H. Fenton. Spectral methods for partial differential equations in irregular domains: the spectral smoother boundary method. *SIAM J. Sci. Comput.* **28**:886-900, 2006.
- [28] A. Bueno-Orovio, E. M. Cherry, F. H. Fenton. Minimal model for human ventricular action potentials in tissue. *J. Theor. Biol.* **253**:544-560, 2008.
- [29] J. M. Cao, Z. Qu, Y. H. Kim, T. J. Wu, A. Garfinkel, J. N. Weiss, H. S. Karagueuzian, and P. S. Chen. Spatiotemporal heterogeneity in the induction of ventricular fibrillation by rapid pacing: importance of cardiac restitution properties. *Circ. Res.* **84**:1318-1331, 1999.
- [30] C. Caro, J. Fitzgerald, and R. Schroter. Arterial wall shear and distribution of early atheroma in man. *Nature.* **223**:1159-1160, 1969.
- [31] www.cellML.org.
- [32] carp.meduni-graz.at.
- [33] A. Chakraborty, S. Chakraborty, V. R. Jala, B. Haribabu, M. K. Sharp, and R. E. Berson. Effects of biaxial oscillatory shear stress on endothelial cell proliferation and morphology. *Biotechnol. Bioeng.* doi.10.1002/bit.24352, 2011.
- [34] M. Chard, and R. Tabrizchi. The role of pulmonary veins in atrial fibrillation: a complex yet simple story. *Pharmacol. Ther.* **124**:207-218, 2009.
- [35] Y. S. Chatzizisis, M. Jonas, A. U. Coskun, R. Beigel, B. V. Stone, C. Maynard, R. G. Gerrity, W. Daley, C. Rogers, E. R. Edelman, C. L. Feldman, and P. H. Stone. Prediction of the localization of high-risk coronary atherosclerotic plaques on the basis of low endothelial shear stress. An intravascular ultrasound and histopathology natural history study. *Circ.* **117**: 993-1002, 2008.
- [36] E. M. Cherry, H. S. Greenside, and C. S. Henriquez. A space-time adaptive method for simulating complex cardiac dynamics. *Phys. Rev. Lett.* **84**:1343-1346, 2000.
- [37] E. M. Cherry, F. Xie, Z. Feliciano, and A. Garfinkel. Computer modeling of atrial fibrillation. *Card. Electrophysiol. Rev.* **5**:271-276, 2001.
- [38] E. M. Cherry, and F. H. Fenton. Suppression of alternans and conduction blocks despite steep APD restitution: electrotonic, memory, and conduction velocity restitution effects. *Am. J. Physiol. Heart. Circ. Physiol.* **286**:H2332-H2341, 2004.
- [39] E. M. Cherry, and F. H. Fenton. A tale of two dogs: analyzing two models of canine ventricular electrophysiology. *Am. J. Physiol. Heart Circ. Physiol.* **292**: H43-H55, 2007.
- [40] E. M. Cherry, J. R. Ehrlich, S. Nattel, and F. H. Fenton. Pulmonary vein reentry - Properties and size matter: Insights from a computational analysis. *Heart Rhythm.* **4**:1553-1562, 2007.
- [41] E. M. Cherry, and F. H. Fenton. Visualization of spiral and scroll waves in simulated and experimental cardiac tissue. *New J. Phys.* **10**:125016, 2008.
- [42] E. M. Cherry, and S. J. Evans. Dynamics of human atrial cell models in tissue: restitution, memory, propagation, and reentry. *Prog. Biophys. Mol. Biol.* **98**:24-37, 2008.
- [43] E. M. Cherry, and F. H. Fenton. Realistic cardiac electrophysiology modelling: are we just a heartbeat away? *J. Physiol.* **588**:2689, 2010.
- [44] E. M. Cherry, and F. H. Fenton. Effects of boundaries and geometry on the spatial distribution of action potential duration in cardiac tissue *J. Theor. Biol.* **285**:164-176, 2011.
- [45] C. Cherubini, S. Filippi, P. Nardinocchi, and L. Teresi. An electromechanical model of cardiac tissue: Constitutive issue and electrophysiological effects. *Prog. Biophys. Mol. Biol.* **97**:562-573, 2008.

- [46] C. Cherubini, and S. Filippi. Lagrangian field theory of reaction-diffusion. *Phys. Rev. E*. **80**:046117, 2009.
- [47] D. R. Chialvo, and J. Jalife. Non-linear dynamics of cardiac excitation and impulse propagation. *Nature*. **330**:749-752, 1987.
- [48] D. R. Chialvo, R. F. Gilmour, Jr., and J. Jalife. Low dimensional chaos in cardiac tissue. *Nature, London* **343**:653-657, 1990.
- [49] G. Child, wikipedia, 2006.
- [50] M. Cikes, G. R. Sutherland, L. J. Anderson, and B. H. Bijmens. The role of echocardiographic deformation imaging in hypertrophic myopathies. *Nat. Rev. Cardiol.* **7**:384-396, 2010.
- [51] R. H. Clayton, O. Bernus, E. M. Cherry, H. Dierck, F. H. Fenton, L. Mirabella, A. V. Panfilov, F. B. Sachse, G. Seemann, and H. Zhang. Models of cardiac tissue electrophysiology: Progress, challenges and open questions. *Prog. Biophys. Mol. Biol.* **104**:22-48, 2011.
- [52] L. Clerc. Directional differences of impulse spread in trabecular muscle from mammalian heart. *J. Physiol.* **25**:335-346, 1976.
- [53] B. D. Coleman, and W. Noll. The thermodynamics of elastic materials with heat conduction and viscosity. *Arch. Rat. Mech. Anal.* **13**:167-178, 1963.
- [54] P. Colli-Franzone, L. Guerri, M. Pennacchio, and B. Taccardi. Spread of excitation in 3-D models of the anisotropic cardiac tissue. Effects of fiber architecture and ventricular geometry. *Math. Biosci.* **147**:131-171, 1998.
- [55] P. Comtois, and A. Vinet. Multistability of reentrant rhythms in an ionic model of a two-dimensional annulus of cardiac tissue. *Phys. Rev. E*. **72**:051927, 2005.
- [56] K. D. Costa, J. W. Holmes, and A. D. McCulloch. Modeling cardiac mechanical properties in three dimensions. *Phil. Trans. R. Soc. Lond. A*. **359**:1233-1250, 2001.
- [57] M. Courtemanche, and A. T. Winfree. Re-entrant rotating waves in a Beeler-Reuter based model of two-dimensional cardiac electrical activity. *Int. J. Bifurc. Chaos*. **1**:431-444, 1991.
- [58] M. Courtemanche. Complex spiral wave dynamics in a spatially distributed ionic model of cardiac electrical activity. *Chaos*. **6**:579-600, 1996.
- [59] M. Courtemanche, R. J. Ramirez, and S. Nattel. Ionic mechanisms underlying human atrial action potential properties: insights from a mathematical model. *Am. J. Physiol.* **275**:H301-H321, 1998.
- [60] A. R. Cram, H. M. Rao, and E. G. Tolkacheva. Toward prediction of the local onset of alternans in the heart. *Biophys. J.* **100**:868-874, 2011.
- [61] J. Crank. *The Mathematics of Diffusion*, 2nd ed., Oxford University Press, 1975.
- [62] www.cwru.edu.
- [63] W. T. D'Arcy. *On Growth and Form*. Cambridge University Press, 1992.
- [64] M. K. Das, G. Dandamudi, and H. Steiner. Role of ablation therapy in ventricular arrhythmias. *Cardiol. Clin.* **26**:459-479, 2008.
- [65] J. M. Davidenko, A. V. Pertsov, R. Salomonsz, W. Baxter, and J. Jalife. Stationary and drifting spiral waves of excitation in isolated cardiac muscle. *Nature*. **355**:349-351, 1992.
- [66] C. de Diego, R. K. Pai, A. S. Dave, A. Lynch, M. Thu, F. Chen, L.-H. Xie, J. N. Weiss, and M. Valderrábano. Spatially discordant alternans in cardiomyocyte monolayers. *Am. J. Physiol. - Heart Circ. Physiol.* **294**:H1417-H1425, 2008.
- [67] L. L. Demer, and F. C. P. Yin. Passive biaxial mechanical properties of isolated canine myocardium. *J. Physiol.* **339**:615-630, 1983.
- [68] J. Denoth, E. Stussi, G. Csucs, and G. Danuser. Single muscle fiber contraction is dictated by inter-sarcomere dynamics. *J. Theor. Biol.* **216**:101-122, 2002.
- [69] M. E. Diaz, S. C. O'Neill, D. A. Eisner. Sarcoplasmic reticulum calcium content fluctuation is the key to cardiac alternans. *Circ. Res.* **94**:650-656, 2004.
- [70] D. DiFrancesco, and D. Noble. A model of cardiac electrical activity incorporating ionic pumps and concentration changes. *Phil. Trans. R. Soc. Lond. B*. **307**:353-398, 1985.
- [71] S. Dokos, A. A. Young, B. H. Smaill, and I. J. LeGrice. A triaxial-measurement shear-test device for soft biological tissues. *ASME J. Biomech. Eng.* **122**:471-478, 2000.

- [72] D. J. Dossdall, K. A. Cheng, J. Huang, J. S. Allison, J. D. Allred, W. M. Smith, and R. E. Ideker. Transmural and endocardial Purkinje activation in pigs before local myocardial activation after defibrillation shocks. *Heart Rhythm*. **4**:758-765, 2007.
- [73] E. Drouin, F. Charpentier, C. Gauthier, K. Laurent, and H. Le Marec. Electrophysiologic characteristics of cells spanning the left ventricular wall of human heart: evidence for presence of M cells. *JACC*. **26**:185-192, 1995.
- [74] T. J. DuBose. *Fetal Sonography*. W. B. Saunders Co., 1996.
- [75] D. Durrer, R. TH. Van Dam, G. E. Freud, M. J. Janse, F. L. Meijler, R. C. Arzbaecher. Total excitation of the isolated human heart. *Circulation*. **41**:899-912, 1970.
- [76] B. Echebarria, A. Karma. Instability and spatiotemporal dynamics of alternans in paced cardiac tissue. *Phys. Rev. Lett*. **88**:208101, 2002.
- [77] I. R. Efimov, Y. Cheng, D. R. van Wagoner, T. Mazgalev, and P. J. Tchou. Virtual electrode-induced phase singularity: a basic mechanism of defibrillation failure. *Circ. Res*. **82**:918-925, 1998.
- [78] I. R. Efimov, R. A. Gray, and B. J. Roth. Virtual electrodes and deexcitation: new insights into fibrillation induction and defibrillation. *J. Cardiovasc. Electrophysiol*. **11**:339-353, 2000.
- [79] A. E. Ehret and M. Itskov. A continuum constitutive model for the active behavior of skeletal muscle. *J. Mech. Phys. Sol*. **59**:625-636, 2011.
- [80] A. Einstein. *Autobiographical notes* in Albert Einstein, PhilosopherScientist, ed. Paul Schilpp Library of Living Philosophers. Evanston, 1949.
- [81] W. Einthoven. Die galvanometrische registrering des menschlichen elektrokardiogramms, zugleich eine beurtheilung der anwendung des capilar-elektrometers in der physiologie. *Pfluegers Arch*. **99**:472-480, 1903.
- [82] D. A. Eisner, H. S. Choi, M. E. Díaz, S. C. O'Neill, and A. W. Trafford. Integrative analysis of calcium cycling in cardiac muscle. *Circ Res*. **87**:1087-1094, 2000.
- [83] G. C. Engelmayr, M. Cheng, C. J. Bettinger, J. T. Borenstein, R. Langer, and L. E. Freed. Accordion-like honeycombs for tissue engineering of cardiac anisotropy. *Nature Mat*. **7**:1003-1010, 2008.
- [84] <http://en.wikipedia.org>.
- [85] Z. Fan, F. Qiu, A. Kaufman, and Y. S. Stover. GPU cluster for high performance computing. *Supercomputing, 2004*. Proceedings of the ACM/IEEE SC2004 Conference.
- [86] V. G. Fast, S. Rohr, A. M. Gillis, and A. G. Kléber. Activation of cardiac tissue by extracellular electrical shocks: formation of 'secondary sources' at intercellular clefts in monolayers of cultured myocytes. *Circ. Res*. **82**:375-385, 1998.
- [87] V. V. Fedorov, I. T. Lozinsky, E. A. Sosunov, E. P. Anyukhovskiy, M. R. Rosen, C. W. Balke, and I. R. Efimov. Application of blebbistatin as an excitation-contraction uncoupler for electrophysiologic study of rat and rabbit hearts. *Heart Rhythm*. **4**:619-626, 2007.
- [88] F. H. Fenton, and A. Karma. Vortex dynamics in three-dimensional continuous myocardium with fiber rotation: filament instability and fibrillation. *Chaos*. **8**:S1054-S1500, 1998.
- [89] F. H. Fenton, and A. Karma. Fiber-rotation-induced vortex turbulence in thick myocardium. *Phys. Rev. Lett*. **81**:481-484, 1998.
- [90] F. H. Fenton, S. J. Evans, and H. M. Hastings. Memory in an excitable medium: a mechanism for spiral wave breakup in the low-excitability limit. *Phys. Rev. Lett*. **83**:3964-3967, 1999.
- [91] F. H. Fenton, and E. M. Cherry. Multiple mechanisms of spiral wave breakup in a model of cardiac electrical activity. *Chaos*, **12**:852-892, 2002.
- [92] F. H. Fenton, E. M. Cherry, and B. G. Kornreich. Termination of equine atrial fibrillation by quinidine: an optical mapping study. *J. Veter. Cardiol*. **10**:87-102, 2008.
- [93] F. H. Fenton, S. Luther, E. M. Cherry, N. F. Otani, V. Krinsky, A. Pumar, E. Bodenschatz, and R. F. Gilmour, Jr. Termination of atrial fibrillation using pulsed low-energy far-field stimulation. *Circ*. **120**:467-476, 2009.
- [94] A. Fick. On liquid diffusion. *Phil. Mag. and Jour. Sci*. **10**:31-39, 1855.
- [95] G. S. Firestein, W. N. Kelley, R. C. Budd, and E. D. Harris. Kelley's textbook of rheumatology. Saunders, 2008.

- [96] G. I. Fishman, S. S. Chugh, J. P. DiMarco, C. M. Albert, M. E. Anderson, R. O. Bonow, A. E. Buxton, P. S. Chen, M. Estes, X. Jouven, R. Kwong, D. A. Lathrop, A. M. Mascette, J. M. Nerbonne, B. O'Rourke, R. L. Page, D. M. Roden, D. S. Rosenbaum, N. Sotoodehnia, N. A. Trayanova, and Z. J. Zheng. Sudden cardiac death prediction and prevention report from a national heart, lung, and blood. Institute and Heart Rhythm Society Workshop. *Circ.* **122**:2335-2348, 2010.
- [97] R. FitzHugh. Mathematical models of threshold phenomena in the nerve membran. *Bull. Math. Biophys.* **17**:257-278, 1955.
- [98] L. Formaggia, A. Quarteroni, and A. Veneziani. *Cardiovascular Mathematics. Modeling and Simulation of the Circulatory System*. Springer Series, 2009.
- [99] J. J. Fox, E. Bodenschatz, and R. F. Gilmour, Jr. Period-doubling instability and memory in cardiac tissue. *Phys. Rev. Lett.* **89**:138101, 2002.
- [100] A. Frydrychowicz, A. F. Stalder, M. F. Russe, J. Bock, S. Bauer, A. Harloff, A. Berger, M. Langer, J. Hennig, and M. Markl. Three-dimensional analysis of segmental wall shear stress in the aorta by flow-sensitive four-dimensional-MRI. *J. Mag. Res. Imag.* **30**:77-84, 2009.
- [101] Y. C. Fung. *Biomechanics: Mechanical Properties of Living Tissues*. New York, Springer-Verlag. 1993.
- [102] M. Fyta, S. Melchionna, E. Kaxiras, and S. Succi. Multiscale coupling of molecular dynamics and hydrodynamics: application to DNA translocation through a nanopore. *Multiscale Model. Sim.* **5**, 1156-1173, 2006.
- [103] R. Garcia. Ventricular fibrillation in artificial hypothermia *J. Thoracic. Surg.* **31**:635, 1955.
- [104] A. Garfinkel. Eight (or more) kinds of alternans. *J. Electrocardiol.* **40**:S70-S74, 2007.
- [105] W. E. Garrey. Nature of fibrillary contraction of the heart: its relation to tissue mass and form. *Am. J. Physiol.* **33**:397-414, 1914.
- [106] A. Garzón, R. O. Grigoriev, and F. H. Fenton. Model-based control of cardiac alternans on a ring. *Phys. Rev. E.* **80**:021932, 2009.
- [107] M. Giglio, S. Musazzi, and U. Perini. Transition to chaotic behavior via a reproducible sequence of period-doubling bifurcations. *Phys. Rev. Lett.* **47**:243-246, 1981.
- [108] R. F. Gilmour, Jr. Electrical restitution and ventricular fibrillation: negotiating a slippery slope. *J. Cardiovasc. Electrophysiol.* **13**:1150-1151, 2002.
- [109] S. D. Girouard, J. M. Pastore, K. R. Laurita, K. W. Gregory, and D. S. Rosenbaum. Optical mapping in a new guinea pig model of ventricular tachycardia reveals mechanisms for multiple wavelengths in a single reentrant circuit. *Circ.* **93**:603-613, 1996.
- [110] S. Givli, and K. Bhattacharya. A coarse-grained model of the myofibril: overall dynamics and the evolution of sarcomere non-uniformities. *J. Mech. Phys. Sol.* **57**:221-243, 2009.
- [111] L. Glass, and M. E. Josephson. Resetting and annihilation of reentrant abnormally rapid heartbeat. *Phys. Rev. Lett.* **75**:2059, 1995.
- [112] L. Grinberg, and G. Karniadakis. Outflow boundary conditions for arterial networks with multiple outlets. *Ann. Biomed. Eng.* **36**, 1496, 2008.
- [113] Grindrod P. *The theory and applications of reaction-diffusion equations: patterns and waves*. Oxford Applied Mathematics and Computing Science Series. Oxford University Press, New York, 1996.
- [114] J. M. Guccione, L. K. Waldman, and A. D. McCulloch. Mechanics of active contraction in cardiac muscle. Cylindrical models of the systolic left ventricle. *ASME J. Biomech. Eng.* **115**:82-90, 1993.
- [115] M. R. Guevara, L. Glass, and A. Shrier. Phase locking, period-doubling bifurcations, and irregular dynamics in periodically stimulated cardiac cells. *Science.* **214**:1350-1353, 1981.
- [116] M. R. Guevara, G. Ward, and L. Glass. Electrical alternans and period-doubling bifurcations. *Comput. Cardiol.* 167-170, 1984.
- [117] M. R. Guevara, and L. Glass. Phase locking, period doubling bifurcations and chaos in a mathematical model of a periodically driven oscillator: a theory for the entrainment of biological oscillators and the generation of cardiac dysrhythmias. *J. Math. Biol.* **14**:1-23, 1987.
- [118] Z. Y. Guo, X. Q. Peng, and B. Moran. A composites-based hyperelastic constitutive model for soft tissue with application to the human annulus fibrosus. *J. Mech. Sol. Phys.* **54**:1952-1971, 2006.
- [119] M. Haïssaguerre, P. Jais, D. C. Shah, A. Takahashi, M. Hocini, G. Quiniou, S. Garrigue, A. Le Mouroux, O. Le Metayer, and J. Clementy. Spontaneous initiation of atrial fibrillation by ectopic beats originating from the pulmonary veins. *N. Engl. J. Med.* **339**:659-666, 1998.

- [120] M. Haïssaguerre, P. Jaïs, D. C. Shah, S. Garrigue, A. Takahashi, T. Laverigne, M. Hocini, J. T. Peng, R. Roudaut, and J. Clémenty. Electrophysiological end point for catheter ablation of atrial fibrillation initiated from multiple pulmonary venous foci. *Circulation*. **101**:1409–1417, 2000.
- [121] M. Haïssaguerre, D. C. Shah, P. Jaïs, M. Shoda, J. Kautzner, T. Arentz, D. Kalushe, A. Kadish, M. Griffith, F. Gaïta, T. Yamane, S. Garrigue, M. Hocini, and J. Clémenty. Role of Purkinje conducting system in triggering of idiopathic ventricular fibrillation. *Lancet*. **359**:677-678, 2002.
- [122] J. P. J. Halcox, W. H. Schenke, G. Zalos, R. Mincemoyer, A. Prasad, M. A. Waclawiw, K. R. A. Nour, and A. A. Quyyumi. Prognostic value of coronary vascular endothelial dysfunction. *Circ*. **106**:653-658, 2002.
- [123] G. M. Hall, S. Bahar, and D. J. Gauthier. Prevalence of rate-dependent behaviors in cardiac muscle. *Phys. Rev. Lett*. **82**:2995-2998, 1999.
- [124] Heart diagram. www.omnimedicalsearch.com.
- [125] H. M. Hastings, F. H. Fenton, S. J. Evans, O. Hotomaroglu, J. Geetha, K. Gittelsohn, J. Nilson, and A. Garfinkel. Alternans and the onset of ventricular fibrillation. *Phys. Rev. E*. **62**:4043-4048.
- [126] H. Hayashi, Y. Shiferaw, D. sato, M. Nihei, S. F. Lin, S. F. Chen, A. Garfinkel, J. N. Weiss, and Z. Qu. Dynamic origin of spatially discordant alternans in cardiac tissue. *Biophys. J*. **92**:448-460, 2008.
- [127] www.healthcare.philips.com.
- [128] C. S. Henriquez. Simulating the electrical behavior of cardiac tissue using the bidomain model. *Crit. Rev. Biomed. Eng*. **21**:1-77, 1993.
- [129] C. S. Henriquez, and A. A. Papazoglu. Using computer models to understand the roles of tissue structure and membrane dynamics in arrhythmogenesis. *Proceed. IEEE*, **84**:334-354, 1996.
- [130] A. V. Hill. The heat of shortening and dynamics constants of muscles. *Proc. R. Soc. Lond. B*. **126**:136-195, 1938.
- [131] A. L. Hodgkin, and W. A. H. Rushton. The electrical constants of crustacean nerve fiber. *Proc. R. Soc. London Ser. B*. **133**:444, 1946.
- [132] A. Hodgkin, and A. Huxley. A quantitative description of membrane current and its application to conduction and excitation in nerve. *J. Physiol*. **117**:500-544, 1952.
- [133] A. V. Holden, and A. V. Panfilov. Spatiotemporal chaos in a model of cardiac electrical activity. *Int. J. Bifurc. Chaos*. **1**:219-225, 1991.
- [134] A. V. Holden. Cardiac physiology: A last wave from the dying heart. *Nature*. **392**:20-21, 1998.
- [135] G. A. Holzapfel. *Nonlinear Solid Mechanics. A Continuum Approach for Engineering*. John Wiley & Sons, 2000.
- [136] G. A. Holzapfel, and R. W. Ogden. Constitutive modelling of passive myocardium: a structurally based framework for material characterization. *Phil. Trans. R. Soc. A* **367**:3445-3475, 2009.
- [137] D. A. Hooks, K. A. Tomlinson, S. G. Marsden, I. J. LeGrice, B. H. Smaill, A. J. Pullan, and P. J. Hunter. Cardiac microstructure: implications for electrical propagation and defibrillation in the heart. *Circ. Res*. **91**:331-338, 2002.
- [138] D. A. Hooks, M. L. Trew, B. J. Caldwell, G. B. Sands, I. J. LeGrice, and B. H. Smaill. Laminar arrangement of ventricular myocytes influences electrical behavior of the heart. *Circ Res*. **101**:e103-e112, 2007.
- [139] Horowitz, A., Lanir, Y., Yin, F. C. P., Perl, M., Sheinman, I. & Strumpf, R. K. 1988 Structural three-dimensional constitutive law for the passive myocardium. *J. Biomech. Eng*. **110**, 200–207.
- [140] P. R. Hoskins, and D. Hardmunt. Three-dimensional imaging and computational modelling for estimation of wall stresses in arteries. *Br. J. Radiol*. **82**:S3-S17, 2009.
- [141] R. H. Hoyt, M. L. Cohen and J. E. Saffitz. Distribution and three-dimensional structure of intercellular junctions in canine myocardium. *Circ. Res*. **64**:563-574, 1989.
- [142] J. D. Humphrey, and F. C. P. Yin. On constitutive relations and finite deformations of passive cardiac tissue. Part I. A pseudo-strain energy function. *J. Biomech. Eng*. **109**:298-304, 1987.
- [143] J. D. Humphrey, R. K. Strumpf, and F. C. P. Yin. Determination of constitutive relation for passive myocardium. I. A new functional form. *J. Biomech. Eng*. **112**:333-339, 1990.
- [144] P. J. Hunter, M. P. Nash, and G. B. Sands. Computational electromechanics of the heart, in *Computational biology of the heart*. Wiley, London, 1997.
- [145] P. J. Hunter, A. D. McCulloch, H. E. D. J. ter Keurs. Modeling the mechanical properties of cardiac muscle. *Prog. Biophys. Mol. Biol*. **69**:289-331, 1998.

- [146] P. J. Hunter, and T. K. Borg. Integration from proteins to organs: the physiome project. *Nat. Rev. Mol. Cell. Biol.* **4**:237-243, 2003.
- [147] P. J. Hunter, A. J. Pullan, and B. H. Smaill. Modeling total heart function. *Annu. Rev. Biomed. Eng.* **5**:147-177, 2003.
- [148] E. Husfeldt, and O. Secher. Ventricular fibrillation during hypothermia successfully treated by rewarming and electroshock. *Thorax.* **11**:67, 1956.
- [149] J. M. Huyghe, D. H. van Campen, T. Arts, and R. M. Heethaar. The constitutive behavior of passive heart muscle tissue. A quasi-linear viscoelastic formulation. *J. Biomech.* **24**, 841-849, 1991.
- [150] R. E. Ideker, T. N. Chattipakorn, and R. A. Gray. Defibrillation mechanisms: the parable of the blind men and the elephant. *J. Cardiovasc. Electrophysiol.* **11**:1008-1013, 2000.
- [151] www.ineedmd.com
- [152] <http://invitrogen.com>.
- [153] M. Itskov, and A. E. Ehret. A universal model for the elastic, inelastic and active behavior of soft biological tissues. *GAMM-Mitteilungen*, **2**:221-236, 2009.
- [154] V. Iyer, R. Mazhari and R. L. Winslow. A computational model of the human left-ventricular epicardial myocyte. *Biophys. J.* **87**:1507-1525, 2004.
- [155] P. Jaïs, R. Weerasooriya, D. C. Shah, M. Hocini, L. Macle, K. J. Choi, C. Scavee, M. Haïssaguerre, and J. Clémenty. Ablation therapy for atrial fibrillation (AF): past, present and future. *Cardiovasc. Res.* **54**:337-346, 2002.
- [156] M. J. Janse, F. J. Wilms-Schopman, and R. Coronel. Ventricular fibrillation is not always due to multiple wavelet reentry. *J. Cardiovasc. Electrophysiol.* **6**:512-521, 1995.
- [157] Z. Jian, H. Bien, and E. Entcheva. Detecting space-time alternanting biological signals close to the bifurcation point. *IEEE Trans. Biomed. Eng.* **57**:316-324, 2010.
- [158] A. Karma. Spiral breakup in model equations of action potential propagation in cardiac tissue. *Phys. Rev. Lett.* **71**:1103-1106, 1993.
- [159] J. Keener. An eikonal-curvature equation for action potential propagation in myocardium. *J. Math. Biol.* **29**:629-651, 1991.
- [160] J. Keener, and J. Sneyd. *Mathematical Physiology*, Springer, 1998.
- [161] R. H. Keldermann, M. P. Nash, and A. V. Panfilov. Modeling cardiac mechano-electrical feedback using reaction-diffusion-mechanics systems. *Physica D*, **238**:1000-1007, 2009.
- [162] R. C. P. Kerckhoffs, P. H. M. Bovendeerd, J. C. S. Kotte, F. W. Prinzen, K. Smits, and T. Arts. Homogeneity of cardiac contraction despite physiological asynchrony of depolarization: a model study. *Ann. Biomed. Eng.* **31**:536-547, 2003.
- [163] A. M. Katz. *Physiology of the Heart*, 2nd ed. Lippincott Williams & Wilkins, 1992.
- [164] Y. H. Kim, A. Garfinkel, T. Ikeda, T. J. Wu, C. A. Athill, J. N. Weiss, H. S. Karagueuzian, and P. S. Chen. Spatiotemporal complexity of ventricular fibrillation revealed by tissue mass reduction in isolated swine right ventricle. Further evidence for the quasiperiodic route to chaos hypothesis. *J. Clin. Invest.* **100**:2486-2500, 1997.
- [165] S. B. Knisley, R. K. Justice, W. Kong, and P. L. Johnson. Ratiometry of transmembrane voltage-sensitive fluorescent dye emission in hearts. *Am. J. Physiol. Heart. Circ. Physiol.* **279**:H1421-H1433, 2000.
- [166] V. I. Krinsky, V. N. Biktashev, and A. M. Pertsov. Autowave approaches to cessation of reentrant arrhythmias. *Ann. N. Y. Acad. Sci.* **591**:232-246, 1990.
- [167] M. J. Kocica, A. F. Corno, F. Carreras-Costa, M. Ballester-Rodes, M. C. Moghbel, C. N. C. Cueva, V. Lackovic, V. I. Kanjuh, and F. Torrent-Guasp. The helical ventricular myocardial band: global, three-dimensional, functional architecture of the ventricular myocardium *Eur. J. Cardiothorac. Surg.* **29**:21-40, 2006.
- [168] C. Koch. *Biophysics of Computation: information processing in single neurons*, Oxford University Press, 1999.
- [169] D. Lang, M. Sulkin, Q. Lou, and I. R. Efimov. Optical mapping of action potentials and calcium transients in the mouse heart. *J. Vis. Exp.* **55**:e3275, DOI: 10.3791/3275, 2011.
- [170] U. Landmesser, B. Hornig, and H. Drexler. Endothelial function a critical determinant in atherosclerosis? *Circ.* **109**:27-3, 2004.
- [171] S. Large. Surgery for heart failure. *Heart.* **93**:392-402, 2007.

- [172] K. R. Laurita, S. D. Girouard, F. G. Akar, and D. S. Rosenbaum. Modulated dispersion explains changes in arrhythmia vulnerability during premature stimulation of the heart. *Circ.* **98**:2774-2780, 1998.
- [173] K. W. Lee, Y. Yang, and M. M. Scheinman. Atrial flutter: a review of its history, mechanisms, clinical features, and current therapy. *Curr. Probl. Cardiol.* **30**:121-167, 2005.
- [174] I. LeGrice, P. J. Hunter, A. Young, and B. H. Smaill. The architecture of the heart: a data-based model. *Philos. Trans. R. Soc. London A.* **359**:1217-1232, 2001.
- [175] T. Lewis, H. Feil, and W. Stroud. Observations upon flutter and fibrillation ii. Nature of auricular flutter. *Heart.* **7**:127, 191-244, 1920.
- [176] T. Lewis. *The mechanism and graphic registration of the heart beat*. 3rded. Shaw & Sons Ltd., London, 1925.
- [177] V. A. Lubarda. Constitutive theories based on the multiplicative decomposition of deformation gradient: thermoelasticity, elastoplasticity, and biomechanics. *Appl. Mech. Rev.* **57**:95-108, 2004.
- [178] Q. Lou, and I. R. Efimov. Enhanced susceptibility to alternans in a rabbit model of chronic myocardial infarction. *Conf. Proc. IEEE Eng. Med. Biol. Soc.* 4527-4530, 2009.
- [179] C. Luo, and Y. Rudy. A model of the ventricular cardiac action potential: depolarization, repolarization and their interaction. *Circ. Res.* **68**:1501-1526, 1991.
- [180] C. Luo, and Y. Rudy. A dynamic model of the cardiac ventricular action potential: I. Simulations of ionic currents and concentration changes. *Circ. Res.* **74**:1071-1096, 1994.
- [181] S. Luther, F. H. Fenton, B. G. Kornreich, A. Squires, P. Bittihn, D. Hornung, M. Zabel, J. Flanders, A. Gladuli, L. Campoy, E. M. Cherry, G. Luther, G. Hasenfuss, V. I. Krinsky, A. Pumir, R. F. Gilmour Jr, and E. Bodenschatz. Low-energy control of electrical turbulence in the heart. *Nature.* **475**:235-241, 2011.
- [182] J. M. Mari, M. Khoo, C. Riga, G. Coppola, C. Bicknell, and C. G. Caro. Index proposal and basic estimator study for quantification of oscillation of the secondary flow pattern in tortuous vessels. *Ultrasonics.* **52**:294-305, 2012.
- [183] C. K. Mathews, and K. E. Van Holde. *Biochemistry*. Prentice Hall, 1995.
- [184] G. A. Maugin, and M. Epstein. The electroelastic energy-momentum tensor. *Proc. R. Soc. Lond. A.* **433**:299-312, 1991.
- [185] G. A. Maugin. On canonical equations of continuum thermomechanics. *Mech. Res. Comm.* **33**:705-710, 2006.
- [186] M. D. Mazzeo, and P. V. Coveney. HemeLB: a high performance parallel lattice-Boltzmann code for large scale uid ow in complex geometries. *Comp. Phys. Comm.* **178**, 894, 2008.
- [187] R. M. McMeeking, and C. M. Landis. Electrostatic forces and stored energy for deformable dielectric materials. *J. Appl. Mech.* **72**:581-590, 2005.
- [188] R. M. McMeeking, C. M. Landis, and M. A. Jimenez. A principle of virtual work for combined electrostatic and mechanical loading of materials. *Int. J. Nonlin. Mech.* **42**:831-838, 2007.
- [189] J. A. McWilliam. Fibrillar contraction of the heart. *J. Physiol.* **8**:296-310, 1887.
- [190] S. Melchionna, M. Bernaschi, S. Succi, E. Kaxiras, F. J. Rybicki, D. Mitsouras, A. U. Coskun, and C. L. Feldman. Hydrokinetic approach to large-scale cardiovascular blood flow. *Comp. Phys. Comm.* **181**, 462, 2010.
- [191] L. Mesin, and D. Ambrosi. Spiral waves on a contractile tissue. *Eur. Phys. J. Plus.* **126**:21, 2011.
- [192] J. A. Meyer. Claude Beck and cardiac resuscitation. *Ann Thorac Surg.* **45**:103-105, 1988.
- [193] S. Mironov, J. Jalife, and E. G. Tolkacheva. Role of conduction velocity restitution and short-term memory in the development of action potential duration alternans in isolated rabbit hearts. *Circ.* **1**:17-25, 2008.
- [194] G. K. Moe. On the multiple wavelet hypothesis of atrial fibrillation. *Arch. Int. Pharmacodyn Ther.* **140**:183-188, 1962.
- [195] J. M. Morgan, D. Cunningham, and E. Rowland. Dispersion of monophasic action potential duration: demonstrable in humans after premature ventricular extrastimulation but not in steady state. *J. Am. Coll. Cardiol.* **19**:1244-1253, 1992.
- [196] J. D. Murray. *Mathematical Biology*. 3rd ed., Springer, 2000.
- [197] A. Murthy, E. Bartocci, F. H. Fenton, J. Glimm, R. Gray, S. A. Smolka, and R. Grosu. Curvature analysis of cardiac excitation wavefronts. *Proceedings of the 9th ACM International Conference, CMSB*, 2011.
- [198] P. Nardinocchi, and L. Teresi. On the active response of soft living tissues. *J. Elasticity.* **88**:27-39, 2007.

- [199] M. P. Nash, and A. V. Panfilov. Electromechanical model of excitable tissue to study reentrant cardiac arrhythmias. *Prog. Biophys. Mol. Biol.* **85**:501-522, 2004.
- [200] S. Nattel, D. Li, and L. Yue. Basic mechanisms of atrial fibrillation - Very new insights into very old ideas. *Ann. Rev. Physiol.* **62**:51-77, 2000.
- [201] J. Nemeç, J. J. Kim, B. Gabris, and G. Salama. Calcium oscillations and T-wave lability precede ventricular arrhythmias in acquired long QT type 2. *Heart Rhythm.* **7**:1686-1694, 2010.
- [202] B. Nielsen, T. Ruud, G. Lines, and A. Tveito. Optimal monodomain approximations of the bidomain equations. *Appl. Math. Comput.* **184**:276-290, 2007.
- [203] D. Noble. A modification of the Hodgkin-Huxley equations applicable to Purkinje fibre action and pacemaker potentials. *J. Physiol.* **160**:317-352, 1962.
- [204] J. C. Neu, and W. Krassowska. Homogenization of syncytial tissues. *Crit. Rev. Biomed. Eng.* **21**:137-99, 1993.
- [205] P. M. F. Nielsen, I. J. Le Grice, B. H. Smaill, and P. J. Hunter. Mathematical model of geometry and fibrous structure of the heart. *Amer. J. Physiol.* **29**:H1365-H1378, 1991.
- [206] D. Noble, A. Varghese, P. Kohl, and P. Noble. Improved guinea-pig ventricular cell model incorporating a diadic space, i_{Kr} and i_{Ks} , and length-tension-dependent processes. *Can. J. Cardiol.* **14**:123-134, 1998.
- [207] J. N. Nolasco, and R. W. Dahlen. A graphic method for the study of alternation in cardiac action potentials. *J. Appl. Physiol.* **25**:191-196, 1968.
- [208] A. Nygren, C. Fiset, L. Firek, J. W. Clark, D. S. Lindblad, R. B. Clark, and W. R. Giles. Mathematical model of an adult human atrial cell: the role of K^+ currents in repolarization. *Circ. Res.* **82**:63-81, 1998.
- [209] G. M. Odegard, T. L. Haut Donahue, D. A. Morrow, and K. R. Kaufman. Constitutive modelling of skeletal muscle tissue with an explicit strain-energy function. *J Biomech. Eng.* **130**:061017, 2008.
- [210] N. F. Otani, R. Singh, F. H. Fenton, J. Butcher, D. W. Infanger, A. Neumann, S. Luther, R. L. Davisson, and R. F. Gilmour. Use of ultrasound imaging to map propagating action potential waves in the heart. *Comp. Cardiol.* **36**:617-620, 2009.
- [211] A. Pandolfi, G. A. Holzapfel. Three-dimensional modeling and computational analysis of the human cornea considering distributed collagen fibril orientations. *J. Biomech. Eng.* **130**:061006, 2008.
- [212] A. V. Panfilov, R. H. Keldermann, and M. P. Nash. Self-organized pacemakers in a coupled reaction-diffusion-mechanics system. *Phys. Rev. Lett.* **95**:258104, 2005.
- [213] P. E. Paulev, and G. C. Zubietta. *Textbook in Medical Physiology And Pathophysiology Essentials and clinical problems*. 2nd Edition, Copenhagen, Denmark, 2000.
- [214] J. M. Pastore, S. D. Girouard, K. R. Laurita, F. G. Akar, and D. S. Rosenbaum. Mechanism linking T-wave alternans to the genesis of cardiac fibrillation. *Circ.* **99**:1385-1394, 1999.
- [215] J. Perrin. Le Mouvement Brownien et la Réalité Moléculaire. *Ann. Chim. Phys.* **18**:5-114, 1909.
- [216] P. J. Podrid. Aggravation of arrhythmia: a complication of antiarrhythmic drugs. *J. Cardiovasc. Electrophysiol.* **4**:311-319, 1993.
- [217] R. Plonsey. The nature of sources of bioelectric and biomagnetic fields. *Biophys. J.* **39**:309-312, 1982.
- [218] P. Podio-Guidugli. A virtual power format for thermomechanics. *Cont. Mech. Thermodyn.* **20**:479-487, 2009.
- [219] L. Priebe, and D. J. Beuckelmann. Simulation study of cellular electric properties in heart failure. *Circ. Res.* **2**:1206-1223, 1998.
- [220] M. Prinzmetal. Mechanism of spontaneous auricular flutter and fibrillation in man. *Circ.* **7**:607, 1953.
- [221] A. M. E. Pueyo, J. F. Rodriguez, E. Zacur, M. Doblare, and P. Laguna. Quantification of restitution dispersion from the dynamic changes of the T-Wave peak to end, measured at the surface ECG. *IEEE Trans. Biomed. Eng.* **58**:1172-1182, 2011.
- [222] A. J. Pullan. *Mathematically Modeling the Electrical Activity of the Heart: From Cell to Body Surface and Back*. World Scientific Publishing Company, 2005.
- [223] A. Pumir, V. Nikolski, M. Horning, A. Isomura, K. Agladze, K. Yoshikawa, R. Gilmour, E. Bodenschatz, and V. Krinsky. Wave Emission from Heterogeneities Opens a Way to Controlling Chaos in the Heart. *Phys. Rev. Lett.* **99**:208101, 2007.
- [224] A. Pumir, S. Sinha, S. Sridhar, M. Argentina, M. Horning, S. Filippi, C. Cherubini, S. Luther, and V. Krinsky. Wave-train-induced termination of weakly anchored vortices in excitable media. *Phys. Rev. E.* **81**:010901, 2010.

- [225] Z. Qu, A. Garfinkel, P. S. Chen, and J. N. Weiss. Mechanisms of discordant alternans and induction of reentry in simulated cardiac tissue. *Circ.* **102**:1664-1670, 2000.
- [226] F. Qu, C. M. Ripplinger, V. P. Nikolski, C. Grimm, and I. R. Efimov. Three-dimensional panoramic imaging of cardiac arrhythmias in rabbit heart. *J. Biomed. Opt.* **12**:044019, 2007.
- [227] A. A. Quyyumi. Prognostic value of endothelial function. *Am. J. Cardiol.* **91**:H19-H24, 2003.
- [228] W. J. Rappel, F. H. Fenton, and A. Karma. Spatiotemporal control of wave instabilities in cardiac tissue. *Phys. Rev. Lett.* **83**:456-459, 1999.
- [229] K. G. Reddy, R. N. Nair, H. M. Sheehan, and J. McB. Hodgson. Evidence that selective endothelial dysfunction may occur in the absence of angiographic or ultrasound atherosclerosis in patients with risk factors for atherosclerosis. *JACC.* **23**:533-543, 1994.
- [230] M. Reiner. The Deborah Number. *Physics Today.* **17**: 62, 1964.
- [231] O. Reynolds. An experimental investigation of the circumstances which determine whether the motion of water shall be direct or sinuous, and of the law of resistance in parallel channels. *Philos. Trans. R. Soc.* **174**:935-982, 1883.
- [232] M. L. Riccio, M. L. Koller, and R. F. Gilmour, Jr. Electrical restitution and spatiotemporal organization during ventricular fibrillation. *Circ. Res.* **84**:955-963, 1999.
- [233] A. W. Richards, and G. M. Odegard. Constitutive modelling of electrostrictive polymers using a hyperelasticity-based approach. *J. Appl. Mech.* **77**:014502, 2010.
- [234] B. Rodriguez, J. Eason, and N. Trayanova. Differences between left and right ventricular anatomy determine the types of reentrant circuits induced by an external electric shock: a rabbit heart simulation study. *Prog. Biophys. Mol. Biol.* **90**:399-413, 2006.
- [235] D. S. Rosenbaum, L. E. Jackson, J. M. Smith, H. Garan, J. N. Ruskin, and R. J. Cohen. Electrical alternans and vulnerability to ventricular arrhythmias. *N. Engl. J. Med.* **330**:235-241, 1994.
- [236] P. Ruchat, N. Virag, L. Dang, J. Schlaepfer, E. Pruvot, and L. Kappenberger. A biophysical model of atrial fibrillation ablation: what can a surgeon learn from a computer model? *Europace.* **9**:71-76, 2007.
- [237] Y. Rudy. From genome to physiome: integrative models of cardiac excitation. *Ann. Biomed. Eng.* **28**:945-950, 2000.
- [238] F. Sachse, C. Riedel, G. Seemann, C. Werner, and O. Dossel. Simulation the excitation propagation in mechano-electrical models myocardial cells. *Comp. Cardiol.* **5**:247-250, 2000.
- [239] K. Satomi, D. Bänsch, R. Tilz, J. Chun, S. Ernst, M. Antz, H. Greten, K. H. Kuck, and F. Ouyang. Left atrial and pulmonary vein macroreentrant tachycardia associated with double conduction gaps: a novel type of man-made tachycardia after circumferential pulmonary vein isolation. *Heart Rhythm.* **5**:43-51, 2008.
- [240] G. V. Savino, L. Romanelli, D. L. Gonzalez, O. Piro, and M. E. Valentinuzzi. Evidence for chaotic behavior in driven ventricles. *Biophys. J.* **56**:273-280, 1989.
- [241] E. Savio-Galimberti, J. Frank, M. Inoue, J. I. Goldhaber, M. B. Cannell, J. H. Bridge, and F. B. Sachse. Novel features of the rabbit transverse tubular system revealed by quantitative analysis of three-dimensional reconstructions from confocal images. *Biophys. J.* **95**:2053-2062, 2008.
- [242] O. H. Schmitt. Biological information processing using the concept of interpenetrating domains. In *Information Processing in the Nervous System*, ed. KN Leibovic, New York, Springer-Verlag, 1969.
- [243] H. Schmid, Y. K. Wang, J. Ashton, A. E. Ehret, S. B. S. Krittian, M. P. Nash, and P. J. Hunter. Myocardial material parameter estimation: a comparison of invariant based orthotropic constitutive equations. *Comp. Meth. Biomech. Biomed. Eng.* **12**:283-295, 2009.
- [244] R. E. Schmieder, and H. P. Schobel. Is endothelial dysfunction reversible. *Am. J. Cardiol.* **76**:A117-A121, 1995.
- [245] D. C. Schwartz, X. Li, L. I. Hernandez, S. P. Ramnarain, E. J. Huff, and Y. K. Wang. Ordered Restriction Maps of *Saccharomyces Cerevisiae* Chromosomes Constructed by Optical Mapping. *Science.* **262**:110-114, 1993.
- [246] N. G. Sepulveda, B. J. Roth, J. P. Wikswo. Current injection into a two-dimensional anisotropic bidomain. *Biophys. J.* **55**:987-999, 1989.
- [247] N. J. Severs. The cardiac muscle cell. *Bioessays.* **22**:188-199, 2000.
- [248] A. M. Shaaban, and A. J. Duerinckx. Wall shear stress and early atherosclerosis: a review. *AJR Am. J. Roent.* **174**:1657-1665, 2000.
- [249] Y. Shiferaw, D. Sato, and A. Karma. Coupled dynamics of voltage and calcium in paced cardiac cells. *Phy. Rev. E.* **71**:2, 2005.

- [250] R. D. Simitev, and V. N. Biktashev. Conditions for propagation and block of excitation in an asymptotic model of atrial tissue. *Biophys J.* **90**:2258-2269, 2006.
- [251] B. Skallerud, V. Prot, I. S. Nordrum. Modeling active muscle contraction in mitral valve leaflets during systole: a first approach. *Biomech. Model. Mechanobiol.* **10**:11–26, 2011.
- [252] H. Schmid, M. P. Nash, A. A. Young, and P. J. Hunter. Myocardial material parameter estimation - a comparative study for simple shear. *J. Biomech. Eng.* **128**:742–750, 2006.
- [253] R. M. Smith, A. Matiukas, C. W. Zemlin, and A. M. Pertsov. Nondestructive optical determination of fiber organization in intact myocardial wall. *Microsc. Res. Tech.* **71**:510-516, 2008.
- [254] J. R. Sommer, and B. Scherer. Geometry of cell and bundle appositions in cardiac muscle: light microscopy. *Amer. J. Physiol.*, **248**:H792-H803, 1985.
- [255] H. M. Spotnitz, W. D. Spotnitz, T. S. Cottrell, D. Spiro, and E. H. Sonnenblick. Cellular basis for volume related wall thickness changes in the rat left ventricle. *J. Mol. Cell. Cardiol.* **6**:317–331, 1974.
- [256] E. H. Starling, and M. B. Visscher. The regulation of the energy output of the heart. *J. Physiol.* **62**:243261, 1926.
- [257] J. Steffel, and T. F. Lüscher. Predicting the development of atherosclerosis. *Circ.* **119**:919-921, 2009.
- [258] D. Streeter. *Gross morphology and fiber geometry of the heart*, in Handbook of Physiology: *The Cardiovascular System*, S. R. Geiger, Ed. Bethesda.
- [259] S. H. Strogatz, *Nonlinear dynamics and Chaos: with application in physics, biology, chemistry, and engineering*, Perseus Books Publishing, 1994.
- [260] J. Sundnes, G. T. Lines, and A. Tveito. Efficient solution of ordinary differential equations modeling electrical activity in cardiac cells. *Math. Biosci.* **172**:55-72, 2001.
- [261] Z. Suo, X. Zhao, and W. H. Greene. A nonlinear field theory of deformable dielectrics. *J. Mech. Phys. Sol.* **56**:467-486, 2008.
- [262] I. Tabas. The role of endoplasmic reticulum stress in the progression of atherosclerosis. *Circ. Res.* **107**:839-850, 2010.
- [263] C. W. Taber, and D. Venes. *Taber's cyclopedic medical dictionary*. Donald Venes, 2009.
- [264] P. B. Taberoux, G. P. Walcott, J. M. Rogers, J. Kim, D. J. Dossall, P. G. Robertson, C. R. Killingsworth, W. M. Smith, and R. E. Ideker. Activation patterns of Purkinje fibers during long-duration ventricular fibrillation in an isolated canine heart model. *Circ.* **116**:1113-1119, 2007.
- [265] A. Tagagi, A. Pumir, D. Pazò, I. Efimov, V. Nikolaski, and V. Krinsky. A physical approach to remove anatomical reentries: a bidomain study. *J. Theor. Biol.* **230**:489-497, 2004.
- [266] Y. Takayama, K. D. Costa, and J. W. Covell. Contribution of laminar myofiber architecture to load-dependent changes in mechanics of LV myocardium. *Am. J. Physiol. Heart Circ. Physiol.* **282**:H1510-H1520, 2001.
- [267] C. A. Taylor, and M. T. Draney. Experimental and Computational Methods in Cardiovascular Fluid Mechanics. *Ann. Rev. Fluid Mech.* **36**:197-231, 2004.
- [268] Theoretical and Computational Bio-physics Group. www.ks.uiuc.edu.
- [269] Thoracic landmarks. www.yale.edu.
- [270] K. H. W. J. ten Tusscher, D. Noble, P. J. Noble, and A.V. Panfilov. A model for human ventricular tissue. *Am. J. Physiol.* **286**:H1573-H1589, 2004.
- [271] H. E. D. J. ter Keurs, W. H. Rijnsburger, R. Van Heuningen, and M. J. Nagelsmit. Tension development and sarcomere length in rat cardiac trabeculae: evidence for length-dependent activation. *Circ. Res.* **46**:703-714, 1980.
- [272] H. ter Keurs. Sarcomere function and crossbridge cycling. *Adv. Exp. Med. Biol.* **382**:125-135, 1995.
- [273] A. Thury, J. J. Wentzel, R. V. H. Vinke, F. J. H. Gijssen, J. C. H. Schuurbiens, R. Krams, P. J. de Feyter, P. W. Serruys, and C. J. Slager. Focal in-stent restenosis near step-up roles of low and oscillating shear stress? *Circ.* **105**:e185-e187, 2002.
- [274] E. G. Tolkacheva, D. G. Schaeffer, D. J. Gauthier, and W. Krassowska. Condition for alternans and stability of the 1:1 response pattern in a “memory” model of paced cardiac dynamics. *Phys. Rev. E.* **67**:031904, 2003.
- [275] N. A. Trayanova. Are we closer to understanding defibrillation in the whole heart? *J. Cardiovasc. Electrophysiol.* **13**:1128–1130, 2002.
- [276] L. Tung. *A bidomain model for describing ischemic myocardial D-C potentials*. M.I.T. Cambridge, Mass., Ph.D. thesis, 1978.

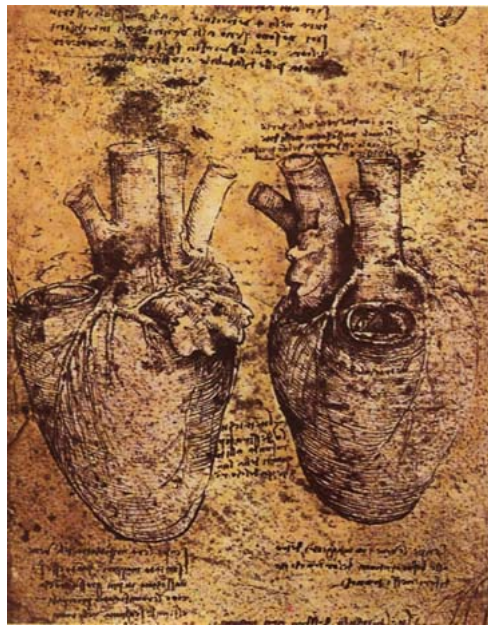
- [277] A. M. Turing. The Chemical Basis of Morphogenesis. *Philosophical Transactions of the Royal Society of London. B.* **237**:37-72, 1952.
- [278] K. Umapathy, K. Nair, S. Masse, S. Krishnan, J. Rogers, M. P. Nash, and K. Nanthakumar. Phase Mapping of Cardiac Fibrillation. *Cir. Arrhy. Electrophys.* **3**:105-114, 2010.
- [279] D. Vaidya, G. E. Morley, F. H. Samie, and J. Jalife. Reentry and fibrillation in the mouse heart. A challenge to the critical mass hypothesis. *Circ. Res.* **85**:174-181, 1999.
- [280] P. M. Vanhoutte. Endothelial dysfunction and atherosclerosis. *Europ. Heart J.* **18**:E19-E29, 1997.
- [281] R. L. Verrier, T. Klingenheben, M. Malik, N. El-Sherif, D. V. Exner, S. H. Hohnloser, T. Ikeda, J. P. Martinez, S. M. Narayan, T. Nieminen, D. S. Rosenbaum. Microvolt T-Wave alternans physiological basis, methods of measurement, and clinical utility - consensus guideline by international society for holter and noninvasive electrocardiology. *J. Am. Coll. Cardiol.* **58**:1309-1324, 2011.
- [282] M. R. Villarreal. *Circulatory System*, <http://en.wikipedia.org>, 2009.
- [283] J. A. Vita, and J. F. Keaney, Jr. Endothelial function: a barometer for cardiovascular risk? *Circ.* **106**:640-642, 2002.
- [284] J. A. Vita. Endothelial function. *Circ.* **124**:e906-e912, 2011.
- [285] D. A. Vorp, D. A. Steinman, and C. R. Ethier. Computational modeling of arterial biomechanics. *Comput. Sci. Eng.* **51**:64, 2001.
- [286] E. Votta, E. Caiani, F. Veronesi, M. Soncini, F. V. Montecchi, A. Redaelli. Mitral valve finite element modelling from ultrasound data: a pilot study for a new approach to understand mitral function and clinical scenarios. *Phil. Trans. R. Soc. A.* **366**:3411-3434, 2008.
- [287] J. E. Waktare. Cardiology patient page: atrial fibrillation. *Circ.* **106**:14-16, 2002.
- [288] G. P. Walcott, C. R. Killingsworth, and R. E. Ideker. Do clinically relevant transthoracic defibrillation energies cause myocardial damage and dysfunction? *Resuscitation.* **59**:59-70, 2003.
- [289] M. L. Walker, X. Wan, G. E. Kirsch, and D. S. Rosenbaum. Hysteresis effect imparts calcium cycling as a mechanism of repolarization alternans. *Circ.* **108**:2704-2709, 2003.
- [290] Y. Wang, and P. Dimitrakopoulos. Normal force exerted on vascular endothelial cells. *Phys. Rev. Lett.* **96**:028106, 2006.
- [291] M. A. Watanabe, F. H. Fenton, S. J. Evans, H. M. Hastings, and A. Karma. Mechanisms for discordant alternans. *J. Cardiovasc. Electrophysiol.* **12**:196-206, 2001.
- [292] S. Weidmann. The electrical constants of Purkinje fibers. *J. Physiol.* **188**:348-360, 1952.
- [293] S. Weinberg, N. Malhotra, and L. Tung. Vulnerable windows define susceptibility to alternans and spatial discordance. *Am. J. Physiol. - Heart Cir. Physiol.* **298**:H1727-H1737, 2010.
- [294] R. Weingart, and P. Maurer. Action potential transfer in cell pairs isolated from adult rat and guinea pig ventricles. *Circ. Res.* **63**:72, 1988.
- [295] R. Weingart. Electrical properties of the nexal membrane studied in rat ventricular pairs. *J. Physiol. (London).* **370**:267, 1986.
- [296] J. N. Weiss, A. Karma, Y. Shiferaw, P. S. Chen, A. Garfinkel, and A. Qu. From pulsus to pulseless: the saga of cardiac alternans. *Circ. Res.* **98**:1244-1253, 2006.
- [297] J. N. Weiss, M. Nivala, A. Garfinkel, and Z. Qu. Alternans and arrhythmias from cell to heart. *Circ. Res.* **108**:98-112, 2011.
- [298] H. Weyl. *Symmetry*. Princeton University Press, 1952.
- [299] N. Wiener, and A. Rosenblueth. The mathematical formulation of the problem of conduction of impulses in a network of connected excitable elements, specifically in cardiac muscle. *Arch. Inst. Cardiol. Mex.* **16**:205-265, 1946.
- [300] M. E. Widlansky, N. Gokce, J. F. Keaney, JR, and J. A. Vita. The clinical implications of endothelial dysfunction. *JACC.* **42**:1149-1160, 2003.
- [301] S. Winberg, N. Malhotra, L. Tung. Vulnerable windows define susceptibility to alternans and spatial discordance. *Am. J. Physiol. Heart. Circ. Physiol.* **298**:H1727-H1737, 2010.
- [302] A. T. Winfree. Stable particle-like solutions to the nonlinear wave equations of three-dimensional excitable media. *SIAM Soc. Ind. Appl. Math. Rev.* **32**:1-53, 1990.
- [303] A. T. Winfree. Electrical turbulence in three-dimensional heart muscle. *Science.* **266**:1003-1006, 1994.

BIBLIOGRAPHY

157

- [304] A. T. Winfree. Rotors, fibrillation and dimensionality. *Computational Biology of the Heart*, ed. Chichester: Wiley, 1997.
- [305] A.T. Winfree. *The Geometry of Biological Time*, 2nd ed., Springer, New York, 2001.
- [306] www.who.int.
- [307] J. R. Womersley. Method for the calculation of velocity, rate of flow and viscous drag in arteries when the pressure gradient is known. *J. Physiol.* **127**: 553-563, 1955.
- [308] Q. Yang, L. Stainier, and M. Ortiz. A variational formulation of the coupled thermo-mechanical boundary-value problem for general dissipative solids. *J. Mech. Phys. Sol.* **54**:401-424, 2006.
- [309] A. R. Yehia, A. Shrire, K. C. L. Lo, and M. R. Guevara. Transient outward current contributes to Wenckebach-like rhythms in isolated rabbit ventricular cells. *Am. J. Physiol.* **273**:H1-H11, 1997.
- [310] A. A. Young, R. Orr, B. H. Smaill, and L. J. Dell'Italia. Three dimensional changes in left and right ventricular geometry in chronic mitral regurgitation. *Am. J. Physiol. Heart Circ. Physiol.* **271**:H2689-H2700, 1996.
- [311] H. Zhang, T. Ueyama, J. Wang, R.-J. Wu, and S.-F. Lin. Short-term memory and electrical restitution in the canine transmural ventricle. *Physiol. Meas.* **32**:207-222, 2011.
- [312] O. C. Zienkiewicz. *The Finite Elements Method*. McGraw-Hill, London, 1994.
- [313] O. Ziv, E. Morales, Y. K. Song, X. Peng, K. E. Odening, A. E. Buxton, A. Karma, G. Koren, and B. R. Choi. Origin of complex behavior of spatially discordant alternans in a transgenic rabbit model of type 2 long QT syndrome. *J. Physiol.* **587**:4661-4680, 2009.
- [314] C. Zhang, S. Xie, S. Li, F. Pu, X. Deng, Y. Fan, and D. Li. Flow patterns and wall shear stress distribution in human internal carotid arteries: the geometric effect on the risk for stenoses. *J. Biomech.* **45**:83-89, 2012.
- [315] M. A. Zulliger, A. Rachev, and N. Stergiopoulos. A constitutive formulation of arterial mechanics including vascular smooth muscle tone. *Am. J. Physiol. Heart Circ.* **287**:H1335-H1343, 2004.

“Anatomia del cuore”



LEONARDO DA VINCI, 16TH CENTURY
BIBLIOTECA AMBROSIANA, MILANO

On the Electro-Elastic unpinning of rotating vortices in biological excitable media

C. Cherubini^{a,b}, S. Filippi^{a,b} and A. Gizzi^{a,c}

^a *Nonlinear Physics and Mathematical Modeling Lab,
University Campus Bio-Medico, I-00128 Rome, Italy*

^b *ICRA, University of Rome "La Sapienza,"
I-00185 Rome, Italy*

^c *Alberto Sordi Foundation - Research Institute on Aging, Rome, Italy*

(Dated: March 12, 2012)

Spiral waves in excitable biological media are associated with pathological situations. In the heart, an action potential vortex pinned by an obstacle has to be removed through defibrillation protocols fine-tuned theoretically by using electro-physiological nonlinear mathematical models. Cardiac tissue however is an electro-elastic medium whose electrical properties are strongly affected by large deformations. In this paper we specifically investigate the *electro-elastic pinning/unpinning* mechanism in order to include cardiac contraction in the preexisting theoretically modelled defibrillation scenarios. Based on a two-dimensional minimal electro-mechanical model, we show numerically the existence of an *unpinning band* characterized by the size of the obstacle, the pacing site and frequency. Similar numerical simulations, performed in the absence of elastic coupling, show small differences in comparison with the electro-elastic studies, suggesting for this specific scenario of pinning/unpinning dynamics, a non prominent role of elasticity.

PACS numbers: 87.19.Hh,05.45.-a,87.10.Pq,46.25.Hf,87.10.Kn

I. INTRODUCTION

A wide range of spiral waves behavior can be recognized in many different natural systems [1–7]. Such a phenomenology has relevance in particular in heart dynamics in association with dangerous and even lethal pathologies [8–10]. Spiral control is mandatory then, but while such an action can easily be achieved in homogeneous active media (cell cultures typically [11–13]), it becomes an extremely complicated problem in heterogeneous systems. The so called “pinning regions” (scar in heart tissue or large vessels for example) in fact, represent spatial obstacles, characterized by altered electro-physiological properties, which tend to attach a propagating spiral wave in a persistent manner.

A pinned spiral in the heart muscle can be removed by a weak electric pulse delivered at the boundary of the obstacle [14–16]. Advanced techniques have been proposed however, in order to use wave trains for sudden termination of pinned systems [5, 17–19]. The low energy defibrillation procedures proposed to remove spiral reentries both in vitro and in vivo appear to be even more complicated [20]. Many of these studies adopt mathematical models fine tuned with experiments in order to give new predictions for applications. Most of these analyses, however, neglect mechanical deformations induced by electrical activity. The main reason for this is that 1) continuum mechanics is a complicated nonlinear physical theory and 2) there is little experimental data in comparison with the cases (non-deformable) in which contraction is blocked through calcium or gating blockers [21, 22]. While in excitable media such as nerves, elastic deformations due to voltage passage are very small [23, 24], cardiac tissue undergoes very large deformations (a myocyte can change its elongation up to 20% of its rest length [25–30]), requiring finite elasticity theory.

The heart is an electrically driven mechanical pump. Studies on isolated tissues and whole hearts have shown that mechanical stimuli can affect both cardiac electrical excitation and wave spread due to the presence of mechano-sensitive ion channels. Such a behavior has been specifically termed Mechano-Electric Feedback [31–33], and its effects range from physiological heart rate modulation to the mechanical induction of heart rhythm disturbances or to their mechanical termination (see [34, 35] and references therein). The necessity to include and understand the effects of mechanical deformations on the delicate problem of spiral wave pinning/unpinning thus appears to be mandatory.

This point is discussed theoretically in this article using a minimal mechanical model which has been fine tuned to qualitatively fit electro-physiological experiments. The main reason for this choice is the exiguity of mechano-electrical experimental studies in comparison with the very large amount of electro-physiological ones. The main outcome of the present analysis, in particular, consists in exploring the role of elasticity during electrical defibrillation of a pathologic portion of cardiac tissue. An important point addressed here, relevant both for experimental and clinical arrhythmia studies [35, 36], is the theoretical existence of an *unpinning band*; i.e. the full range of defibrillation pacing periods which enable the detachment (unpinning) of an action potential wave (pinned spiral) rotating in a persistent manner around a circular heterogeneity of the medium (obstacle). This mathematical tool can be defined both in the presence and absence of elastic coupling. In both of these cases, this band has been quantified in its variability with respect to the size of the obstacle, the pacing period and position of external stimulation current on the lines of the purely

electrical (i.e. rigid) analysis reported in [17]. The main outcome of the analyses here performed is the fact that the presence of elastic coupling does not seem to change the pinning/unpinning dynamics dramatically in comparison with non elastic situations. This is somewhat an unexpected result, due to the strong nonlinear nature of all the physical equations involved, although electro-elastic coupling may in any case still play an important role in other situations as free spiral dynamics in large domains and generation of turbulent cardiac regimes. The article is organized as follows: after the introduction, in section II we describe the conventions adopted to build up the model, reporting the continuum mechanics balance equations with associated constitutive prescriptions for both the passive and active deformation schemes [37]. We then present the three-variable phenomenological Fenton-Karma model of cardiac action potential [38], here coupled with an additional basic non-diffusive calcium dynamics and finite elasticity equations on the lines of Ref. [39, 40]. In section III we discuss a set of numerical simulations reporting the electrical successful defibrillation events on a two dimensional electro-elastic medium, in which an action potential spiral wave is pinned by a circular non-excitabile portion of tissue located at the center of the domain. In section IV we finally analyze the physical implications of our study and the possible future extensions of our work.

II. THE MODEL

Mechano-Electric Feedback can be modelled by assuming that when cardiac muscle fibers are stimulated, these generate contractile forces which, at the macroscopic scale of the tissue, are described by an active stress tensor constitutively related to the tissue's electro-physiological activity. The overall stress in the tissue is then recovered by adding a passive one to the active stress, depending on the mechanical properties of the myocardium [41–44]. While the distribution of muscle fibers influences the active response of the tissue, the spatial variation in collagen distribution is related to the material constitutive parameters and determines the nonlinear anisotropic passive response of the tissue. Here, we adopt the point of view presented in [37] which introduces the notion of active deformation as alternative to that of active stress motivated by the wide range of constitutive theories based on this approach [45]. We assume that, at the macroscopic scale, the activation of a cardiac muscle fiber is described by the change in its rest length; then, the stress state in the activated tissue is due to the difference between its actual configuration and its rest state. The active deformation is in turn related to the electro-physiological activity of the tissue. As suggested by many experiments, calcium concentration is the main factor driving the variation in the rest length of muscles. In this study the electro-mechanical model of myocardium proposed in [39] has been generalized adopting the three-variable electro-physiological model by Fenton and Karma [38]. The high degree of deformability of the medium makes it mandatory to set the diffusion process in a moving deformable domain, thereby producing a direct influence of the deformation on the electrical activity. We now give the various ingredients of the model just described.

a. Conventions. The model equations are defined using a general curvilinear coordinate system relating a reference (material or undeformed) domain with a current (spatial or deformed) one. From standard continuum mechanics we denote X_I ($I = 1, 2, 3$) as the coordinates in the reference domain B with boundary ∂B , and x_i ($i = 1, 2, 3$) as the coordinates in the current domain B_0 with boundary ∂B_0 . We assume that uppercase subscription refers to the reference configuration while lowercase refers to the current one. The relation between the two coordinate systems is geometrically defined by the deformation gradient tensor $F_{iJ} = (\partial x_i / \partial X_J)$ from which $J = \det(F_{iJ}) = (\rho_o / \rho)$ can be defined, representing the volume change (density ratio) during motion [46].

We assume a multiplicative decomposition [32] of the deformation gradient tensor into a passive and an active part, $F_{iJ} = F_{iK}^e F_{KJ}^a$, leading to the implicit definition of the elastic deformation tensor $F_{iK}^e = F_{iJ}(F_{JK}^a)^{-1}$. Such assumption splits the elastic and active responses on F_{iJ}^e and F_{iJ}^a , respectively. We assume the right Cauchy-Green strain tensor, $C_{IJ}^e = F_{kI}^e F_{kJ}^e$, as the elastic deformation measure of the body. In our modeling the medium is treated as incompressible in only the elastic (passive) behavior, with the corresponding incompressibility kinematic constraint given by $\det(C_{IJ}^e) = 1$.

Taking the strain energy function $\psi = \psi(C_{IJ}^e)$, and applying the standard variational method [47] with respect to the elastic measure of deformation, C_{IJ}^e , we define the second Piola-Kirchhoff stress tensor, S_{IJ} , as

$$S_{IJ} = 2 \frac{\partial \psi}{\partial C_{IJ}^e} - p C_{IJ}^{e-1} \quad (1)$$

In this relation p represents the hydrostatic pressure (a Lagrange multiplier) necessary to satisfy the incompressibility constraint. In order to adopt the balance equation, we then introduce the first Piola-Kirchoof stress tensor, $P_{iJ} = F_{iK} S_{KJ}$.

b. Continuum mechanics balance equations. Imposing the conservation of linear momentum in the reference configuration, and neglecting inertial terms, we get Eq. (2) in the reference domain B and Eq. (3) on its boundary

∂B .

$$0 = \frac{\partial}{\partial X_I} (P_{IJ}), \quad \text{in } B \quad (2)$$

$$t_I = N_J P_{IJ}. \quad \text{on } \partial B \quad (3)$$

Equation (3) introduces the normal, N_J , in the reference domain, which can be derived from its current (deformed) representation using the Nanson's formula relating the surface area elements between the two configurations ($n_i ds = J F_{Ii}^{-1} N_I dS$, [47]).

c. Constitutive prescriptions. The nature of cardiac tissue is extremely complex in the passive mechanical response [48]. Here we focus mainly on the coupling between mechanical deformation and electro-physiological aspects, treating the myocardium as a homogeneous, elastic, isotropic and incompressible tissue. Adopting a neo-Hookean incompressible material representation (with all the mechanical quantities normalized by the elastic modulus α_1 , see [40] for details), the elastic strain energy, ψ , depends only on the first invariant of the right Cauchy-Green elastic strain tensor, $I_1 = \text{tr}(C_{IJ}^e)$, so that we can write:

$$\psi(I_1) = \frac{\alpha_1}{2} (I_1 - 3) \quad (4)$$

This is a classical choice because C_{IJ}^e collects the complete information on the stretches experienced in any of the three orthogonal directions.

In our minimal model we assume a planar, isotropic muscle fiber distribution defined by the unit vector h_I . At the macroscopic scale the activation of the muscle fibers is prescribed by the active deformation field expressed by

$$F_{IJ}^a = \gamma_o(c) (\delta_{IJ} - h_I h_J) \quad (5)$$

The active stretch $\gamma_o(c)$ measures the amount of active contraction of any fiber and accounts for the relation between calcium, c , dynamics and deformation.

The constitutive characterization of the boundaries aims to mimic the tissue surrounding the patch, i.e.

$$t_I = -k^b \delta_{IJ} U_J. \quad (6)$$

We assume that the reference traction density t_I depends linearly on the boundary displacement U_J through an isotropic stiffness tensor $K_{IJ} = k^b \delta_{IJ}$, where k^b is a dimensionless parameter mimicking the stiffness of the surrounding tissue.

d. Electro-physiological equations. The adopted nondimensional model of cardiac action potential (AP) propagation [38] in the reference configuration assumes the following form:

$$\frac{\partial u}{\partial t} = \frac{1}{J} \frac{\partial}{\partial X_J} \left(J D_{IJ} \frac{\partial u}{\partial X_I} \right) + I_{ion} \quad (7)$$

$$\frac{\partial v}{\partial t} = \theta_c \left(\frac{1-v}{\tau_v^-} \right) - (1-\theta_c) \frac{v}{\tau_v^+} \quad (8)$$

$$\frac{\partial w}{\partial t} = \theta_c \left(\frac{1-w}{\tau_w^-} \right) - (1-\theta_c) \frac{w}{\tau_w^+}. \quad (9)$$

It consists of three variables: the membrane potential u plus a fast and a slow transmembrane ionic gate, v and w respectively; $\theta_c = \theta_c(u - u_c)$ is the standard Heaviside function; D_{IJ} is the diffusion tensor expressed in the reference coordinates and mapped via F_{iJ} (pull back) from its current representation, D_{ij} , following the geometric transformation $D_{IJ} = F_{jJ}^{-1} D_{ij} F_{Ii}^{-1}$. Assuming tissue isotropy we have $D_{ij} = d_o I_{ij}$ with I_{ij} the unit tensor and d_o being the constant intensity in the three orthogonal directions; $I_{ion} = I_{fi} + I_{so} + I_{si}$ is the total transmembrane density current, sum of a fast inward inactivation current, I_{fi} , a slow, time-independent rectifying outward current, I_{so} , and a slow inward inactivation current, I_{si} . Their expressions are given by:

$$I_{fi} = -\frac{v}{\tau_d} \theta_c (1-u) (u - u_c) \quad (10)$$

$$I_{so} = \frac{u}{\tau_o} (1-\theta_c) + \frac{1}{\tau_r} \theta_c \quad (11)$$

$$I_{si} = -\frac{w}{2\tau_{si}} (1 + \tanh [k(u - u_c^{si})]). \quad (12)$$

The time constant governing the reactivation of the fast inward current is given by

$$\tau_v^-(u) = \theta_v \tau_{v1}^- + (1 - \theta_v) \tau_{v2}^- \quad (13)$$

and is defined over two voltage ranges ($u_v < u < u_c$ and $u < u_v$) ruled by the Heaviside function θ_v .

We have adopted a parametric setup fitted for a modified version of the Beeler-Reuter model, giving a circular meandering for a free spiral on a homogeneous and isotropic domain. Equations (7-9) describe a normalized dimensionless membrane potential, ranging from 0 to 1, while the mapping $u = (V_m - V_o) / (V_{fi} - V_o)$ shall recover the physical quantity measured in mV (see [38] for details): here V_m stands for transmembrane potential, V_o as the resting membrane potential and V_{fi} as the Nernst potential of the fast inward current (model parameters are reported in Table I).

e. Electro-mechanical coupling. Here we assume the role of free Ca^{2+} ions in the activation mechanism of the contraction process as well as the sensitivity of cardiac tissue to Ca^{2+} modeled by

$$\frac{\partial c}{\partial t} = q_{ca}(u + V_{ca}) - k_{ca}c \quad (14)$$

where c is the scalar field describing calcium concentration. A linear coupling is assumed between membrane voltage, u , and calcium concentration, c . The proposed mass balance equation is a non-diffusive version of more general reaction-diffusion systems needed for a realistic handling of calcium dynamics [49, 50]. This minimal choice has been motivated by the main aim of this article, which is to explore the most basic nature of the anatomic reentry defibrillation scheme on a deformable isotropic excitable medium.

The remaining expressions for electro-mechanical coupling are the following:

$$\gamma_o(c) = \frac{\lambda_{ca}}{1 + f_{ca}(c)(\lambda_{ca} - 1)} \gamma_o^{max} \quad (15)$$

$$\lambda_{ca} = \frac{f_{ca}(c^*) - 1}{f_{ca}(c^*) - \gamma_o^{max}} \quad (16)$$

$$f_{ca}(c) = \frac{1}{2} + \frac{1}{\pi} \arctan\left(\beta_c \log \frac{c}{c_o}\right) \quad (17)$$

on the lines of [39]. Here $\gamma_o(c)$ rules the active deformation scheme entering the definition of F_{IJ}^a , Eq. (5), while λ_{ca} and f_{ca} are ad hoc functions necessary to induce the active contraction following calcium variations.

III. RESULTS

The electro-mechanical model equations (7)-(17), have been numerically integrated through a direct PARDISO finite element method scheme [51, 52] with a nested dissection pre-ordering algorithm on the COMSOL Multiphysics 3.5a software [53]. Different squared-shaped areas (side lengths $L = 5, 6, 7 \text{ cm}$) have been adopted as the simulation domain. Each simulation has been run for $T = 3000 \text{ ms}$ of model time. An adaptive time stepping procedure with tolerance of 10^{-5} has been adopted, limiting the maximum time step to 0.2 ms . The complete set of simulations consisted of more than 500 distinct runs for a computational time of several months on a multiprocessor machine.

The numerics has been fine tuned upon several different simulation protocols. The mesh size has been explored both for the purely electric or rigid (RIG) and coupled electro-mechanical (ELA) models, as reported in Fig.1. The procedure consisted in evaluating the conduction velocity of action potential (AP) and elastic (EL) waves, as well as calcium (Ca) (kinematic waves [54]), for different regular squared meshes adopting Lagrange quadratic elements, until we reached stable flat curves. The electric problem results mesh independent for mesh sizes $dx \leq 0.07 \text{ cm}$ both in 1D and 2D (Fig.1(a)). In order to evaluate the minimal electro-mechanical mesh size we solved the 2D coupled problem adopting different grids for AP and Ca-EL respectively: for a fixed AP grid, $dx = 0.05 \text{ cm}$, we got flat Ca-EL conduction velocities for a mesh size $dx \leq 0.1 \text{ cm}$. On this basis, we finally chose a unique mesh size, $dx = 0.067 \text{ cm}$, for the complete coupled model; we further subdivided each squared mesh element into triangles in order to increase the accuracy and convergence of the numerical solution. The main results of this article (i.e. the unpinning band) are thus insensitive to the mesh size.

Zero flux boundary conditions on the current (deformed) border have been imposed for AP variables while the mechanical boundaries, as anticipated, have been modeled as springs dynamics (in analogy with rubber samples experiments [55]).

Tissue heterogeneity has been introduced in the center of the domain and modeled as a non-excitabile circular obstacle with altered mechanical properties. Therein, no action potential can generate or propagate, i.e. no diffusion,

$d_o = 0 \text{ cm}^2/\text{ms}$, static ion dynamics, and the patch is considered stiffer than the surrounding tissue, i.e. the Young modulus has been lowered to 10%. The obstacle radius ranges in $0.35 \text{ cm} \leq R_{ob} \leq 1.4 \text{ cm}$, in which discrete values have been selected with a finite step of 1.0 cm . An intermediate radius, $R_{ob} = 0.75 \text{ cm}$, has been tested too, in order to verify the resulting trend. The lower limit, $R_{ob} = 0.35 \text{ cm}$, is forced by the choice of electric parameters whereby spiral pinning is no more possible for smaller obstacles. The upper limit, $R_{ob} = 1.4 \text{ cm}$, is forced both by the domain size (which has to fit the anatomy of large mammals ventricle as pig, dog or human) and the unpinning trend band, (discussed in the following), which tends to shrink, meaning that a purely electrical defibrillation is no more possible at any stimulation period. This result is in accordance with the non-deformable numerical simulations reported in [17].

Tissue stimulation has been electrically induced as a circular electrode centered on the upper-left corner of the domain and characterized by a radius $R_p = 0.4 \text{ cm}$. The pulse duration has been fixed at $\tau = 2 \text{ ms}$ with a dimensionless amplitude of 1.5. The stimulation protocol consisted in delivering regular sequences of squared waves, at constant periods and for 3000 ms of simulation time or until spiral unpinning occurs. For each tested obstacle radius and starting from the same initial conditions, the stimulation period has been varied in the range $90 \div 120 \text{ ms}$ with a finite time-step of 2 ms , for a total amount of 15 simulations.

Our numerical results show that the electro-elastic medium is characterized by small differences with respect to the rigid one. Fig.2(a) shows the spiraling period around the circular obstacle comparing the rigid with the elastic cases. The two periods are separated following an almost linear interpolated trend and reaching the largest difference of 34 ms for the largest obstacle radius we analyzed, $R = 1.4 \text{ cm}$. The superimposed histogram enhances this difference plotting $\Delta Sp = SpE - SpR$, where SpE and SpR are the spiral rotational periods in the elastic and rigid case respectively.

Despite such an elastic separation effect, the resulting unpinning trends are very similar both in shape and periods as reported in Fig.2(b), even if they present a strong nonlinearity, and become almost flat for larger obstacles. The graph indicates on the vertical axis the lowest and highest stimulation periods, respectively, which are able to detach the rotating spiral away from the obstacle. The horizontal axis shows the discrete radius values tested. The superimposed curves (black for elastic, gray for rigid) reveal that the elastic case can be defibrillated for stimulation periods greater (or at least equal) than the rigid one. The matching of the two lines can be motivated by the changes of rate adopted to increase the stimulation period, i.e. 2 ms (which gives the graph resolution on the y -axis). The over imposed histogram shows the difference between the two modeling bands as $\Delta ER = (T_{max}^{ELA} - T_{min}^{ELA}) - (T_{max}^{RIG} - T_{min}^{RIG})$, where the T are the maximum and minimum successful stimulation unpinning periods. This result reveals that major differences can be found for the smaller as well as for the higher radii analyzed. In these extreme cases the explanation can be found respectively in weak attaching of the AP waves for small obstacles and in boundary effects for larger ones. Our results seem to confirm the work presented in [17] where a maximum obstacle size for unpinning is reached depending on the spiral meandering radius (R_s). In fact, as reported in Fig.2(b), we find a minimum band amplitude at $R = 1.4 \text{ cm}$. Our choice of parameters gives a free rigid spiral meandering with rotation period $T_s^R = 147 \text{ ms}$ and radius $R_s^R \sim 0.35 \text{ cm}$ while for the elastic one $T_s^E = 176 \text{ ms}$ and $R_s^E \sim 0.4 \text{ cm}$. The small increase of the electro-elastic free spiral meandering is consistent with the results shown and underlines the importance of the nonlinear mechanical feedback on the overall dynamics.

We also tested our results for different domain sizes, $L = 5, 6, 7 \text{ cm}$, in order to minimize the boundary effects and to make the unpinning band discussion independent of the pacing site. In Fig.3 we show the comparison between the unpinning as well as the spiraling rotation periods both for the rigid and the elastic cases and for three different sizes of the simulation domain. As shown by these curves, the spiraling rotation period, Fig.3(a), is not affected by a change of size of the simulation domain for both situations. In contrast, the unpinning bands, Fig.3(b)(c), behave differently. In fact, whereas the electro-elastic trend always seems to follow the same defibrillation points, the rigid case reduces the unpinning periods as the ratio between the obstacle radius and the domain size increases, specifically when $R_{ob}/L \geq 0.2$. This result is in agreement with the recent work of Cherry and Fenton [56] where no flux boundary conditions effects have been criticized for purely electric physiological models.

In Fig.4 we report a comprehensive sequence for defibrillation events, both rigid and elastic, for $R = 1.2 \text{ cm}$ and $L = 6 \text{ cm}$ with same pacing period, $T = 100 \text{ ms}$. The figure enhances the mechanical effects on the unpinning dynamics both in shape propagating waves and in timing. In fact, starting from the same initial conditions, the APs shape sequence is very similar, in accordance with the similar unpinning bands found, while the successful unpinning events occur for the elastic case before the rigid one, which is consistent with the separation of rotational periods shown before.

In Fig.5 we finally show the differences induced by both pacing site and elasticity. On the upper panel (a), a defibrillation sequence is reported in the case of the pacing electrode inside the tissue. The defibrillation dynamics is similar to the previous cases, reported in Fig.(4), suggesting that for the simplest scenario we modeled, differences in pacing sites seem not to affect the overall dynamics. On the lower panel three of Fig.(5), three domains ($L = 5, 6, 7 \text{ cm}$) with different obstacle sizes ($R_{ob} = 0.6, 1.2, 1.4 \text{ cm}$) are reported to show the different shapes induced on the obstacle geometry by propagating AP waves. The obstacle gets distorted from a circular towards a sort of ellipse, evidencing the strong nonlinearity introduced by finite elasticity.

IV. DISCUSSION

The study carried out in this article is relevant for the clinical necessity of obtaining the highest efficiency for low energy implantable defibrillation devices [20]. The problem to identify, both theoretically and experimentally, is the correct periods of the electrical stimuli necessary to detach and remove the electrical reentries [17] (a procedure here denoted as the *unpinning band* search), which should possibly take into account the electro-mechanical properties of a real pulsing heart. Concretely, lower pacing rates would save the tissue from a further induction of arrhythmia and, by using a smaller amount of delivered energy, would also save the mean life of the implantable device itself.

Here we have initiated such an analysis: in a first approximation, we have specifically limited our numerical study to a simple mechano-electric electro-physiological modeling; a two-dimensional heterogeneous, isotropic medium where a circular heterogeneity in the domain has been modeled as a non-excitabile area and capable of attaching action potential waves in a persisting manner (pinning); thus comparing the same stimulation protocol both for a purely electric (rigid) and electro-mechanic (elastic) modeling.

The associated feedback has been implemented by directly connecting the voltage conductivity tensor to the deformation, and not taking into account other more biologically accurate feedback mechanisms such as stretch activated currents (see Refs.[39, 40] and references therein for a discussion). The authors are well aware that this work has only touched the surface of an extremely complicated phenomenon. Even providing these simplifying assumptions however, the presence of an active stress tensor, coming from a multiplicative decomposition procedure, has made the modeling non trivial both from the theoretical and numerical points of view. Comparing the rigid and elastic models, in fact, we observed separating spiral rotational periods for increasing obstacle radii and similar unpinning bands shape. These results appear to be insensitive to the location of the pacing stimulus for both cases. We stress again that the mechanical coupling does not seem, for this specific situation studied at least, to play a major role in the pinning/unpinning dynamics. The nature of the equations involved both in the elastic and mechanical case however does not mean that in other different scenarios, like studies of free spiral dynamics on large domains, the role of the elastic coupling could be minor. We point out moreover that a more biologically accurate contractile heart modeling [50] could better reveal these differences in comparison with the non elastic case. For this purpose it will be necessary to extend in the near future the proposed model to a NMR imported three-dimensional cardiac domain with tissue heterogeneity and fiber anisotropy, possibly revealing more complex dynamics, in analogy with already existing purely electrical studies (see Ref. [67, 68] as an example).

The complex dynamics behavior of three-dimensional structures in excitable systems represent a current topic research in many related fields [62–66], where pinning, drifting and detaching effects are being explored. This aspect thus plays a key role to further increase the mentioned defibrillation efficiency, starting with simplified theoretical analysis [49, 57–61].

The final goal in any case will be to increase the existing data on defibrillation efficiency even more by reducing the energy dispersion in the tissue by taking into account the complete phenomenology of the tissue. In this spirit, the evidence of a remarkable electro-mechanic role in pinning phenomena, suggests the necessity to plan more advanced experiments, to be performed in order to fine-tune the electro-physiological and bio-mechanical experimental data of the nonlinear cardiac tissue dynamics.

Acknowledgements

Two of the authors (C.C. and S.F.) acknowledge ICRANet for partial support of this work.

-
- [1] A.T. Winfree, *When Time Breaks Down: The Three-Dimensional Dynamics of Electrochemical Waves and Cardiac Arrhythmias*, (Princeton University Press, 1987).
 - [2] A.T. Winfree, *The Geometry of Biological Time* 2nd edition, (Springer, 2001).
 - [3] M. C. Cross and P. C. Hohenberg, *Rev. Mod. Phys.* **65**, (1993).
 - [4] S. Sinha, A. Pande, and R. Pandit, *Phys. Rev. Lett.* **86**, 3678 (2001).
 - [5] S. Takagi, A. Pumir, D. Pazo, I. Efimov, V. Nikolski, and V. Krinsky, *Phys. Rev. Lett.* **93**, 058101 (2004).
 - [6] H. Zhang, Z. Cao, N.J. Wu, H.P. Ying, and G. Hu, *Phys. Rev. Lett.* **94**, 188301 (2005).
 - [7] G. Blatter, M.V. Feigel'man, V.B. Geshkenbein, A.I. Larkin, and V.M. Vinokur, *Rev. Mod. Phys.* **66**, 1125 (1994).
 - [8] J. M. Davidenko, A.V. Pertsov, R. Salomonsz, W. Baxter, and J. Jalife, *Nature (London)* **355**, 349 (1992).
 - [9] S. Alonso, F. Sagues, and A.S. Mikhailov, *Science* **299**, 1126 (2003).
 - [10] J. Keener and J. Sneyd, *Mathematical Physiology*, (Springer, 2001).
 - [11] V. Krinsky and K. Agladze, *Physica D* **8**, 50 (1983).

- [12] K. Agladze, M.W. Kay, V. Krinsky, and N. Sarvazyan, *Am. J. Physiol. Heart Circ. Physiol.* **293**, H503 (2007).
- [13] G. Gottwald, A. Pumir, and V. Krinsky, *Chaos* **11** 487 (2001).
- [14] V.I. Krinsky, V.N. Biktashev, A.M. Pertsov. *Ann. N. Y. Acad. Sci.* **591** 232 (1990).
- [15] L. Glass and M.E. Josephson, *Phys. Rev. Lett.* **75**, 2059 (1995).
- [16] A. Pumir, V. Nikolski, M. Horning, A. Isomura, K. Agladze, K. Yoshikawa, R. Gilmour, E. Bodenschatz, and V. Krinsky, *Phys. Rev. Lett.* **99**, 208101 (2007).
- [17] A. Pumir, S. Sinha, S. Sridhar, M. Argentina, M. Horning, S. Filippi, C. Cherubini, S. Luther, and V. Krinsky, *Phys. Rev. E* **81**, 010901(R) (2010).
- [18] A. M. Pertsov, E.A. Ermakova, and A.V. Panfilov, *Physica D* **14**, 117 (1984).
- [19] Z. Y. Lim, B. Maskara, F. Aguel, R.J. Emokpae, and I. Tung, *Circulation* **114**, 2113 (2006).
- [20] S. Luther, F.H. Fenton, B.G. Kornreich, A. Squires, P. Bittihn, D. Hornung, M. Zabel, J. Flanders, A. Gladuli, L. Campoy, E.M. Cherry, G. Luther, G. Hasenfuss, V.I. Krinsky, A. Pumir, R.F.J. Gilmour, and E. Bodenschatz, *Nature* **475**, 235 (2011).
- [21] V.V. Fedorov, I.T. Lozinsky, E.A. Sosunov, E.P. Anyukhovskiy, M.R. Rosen, C.W. Balke, I.R. Efimov, *Heart Rhythm* **4**, 619e26 (2007).
- [22] T.L. Riemer, E.A. Sobie, and L. Tung, *Am. J. Physiol.* **275**, H431 (1998).
- [23] T. Heimburg and A.D. Jackson, *Proc. Natl. Acad. Sci. USA* **102**, 9790 (2005).
- [24] D. Bini, C. Cherubini, and S. Filippi, *Phys. Rev. E* **72**, 041929 (2005).
- [25] L.L. Demer and F.C.P. Yin, *J. Physiol.* **339**, 615 (1990).
- [26] H.A. Spurgeon, M.D. Stern, G. Baartz, S. Raffaelli, R.G. Hansford, A. Talo, E.G. Lakatta, and M.C. Capogrossi, *Am. J. Physiol.* **258**, H574 (1990).
- [27] M.S. Sacks and C.J. Chuong, *J. Biomech. Eng.* **115**, 202 (1993).
- [28] G.C.J. Engelmayr, M. Cheng, C.J. Bettinger, J.T. Borenstein, R. Langer, and L.E. Freed, *Nature Materials* **7**, 1003 (2008).
- [29] S. Langeland, J.Dhooge, P.F. Wouters, H.A. Leather, P. Claus, B. Bijnens, and G.R. Sutherland, *Circulation* **112**, 2157 (2005).
- [30] T. Edvardsen, B.L. Gerber, J. Garot, D.A. Bluemke, J.A.C. Lima, and O.A. Smiseth, *Circulation* **106**, 50 (2002).
- [31] P. Kohl and F. Sachs, *Phil. Trans. R. Soc. Lond. A* **359**, 1173 (2001).
- [32] A. Kamkin and I. Kiseleva (Eds.), *Mechanosensitivity Ion Channels*, (Springer, Dordrecht, Netherlands, 2010).
- [33] R. Kaufmann and U. Theophile, *Pflugers. Arch. Gesamte. Physiol. Menschen. Tiere.* **297**, 174 (1967).
- [34] P. Kohl, C. Bollensdorff and A. Garny, *Exp. Physiol.* **91.2** 307 (2006).
- [35] P. Kohl and D. Noble, *Prog. Biophys. Mol. Biol.* **97**, 159 (2008).
- [36] M.R. Franz, R. Cima, D. Wang, D. Profitt, and R. Kurz *Circulation* **86**, 968 (1992) and erratum *Circulation* **86** 1663 (1992).
- [37] P. Nardinocchi and L. Teresi, *J. Elasticity* **88**, 27 (2007).
- [38] F.H. Fenton and A. Karma, *Chaos* **8**, 1054 (1998).
- [39] C. Cherubini, S. Filippi, P. Nardinocchi, and L. Teresi, *Prog. Biophys. Molec. Biol.* **97**, 562 (2008).
- [40] C. Cherubini, S. Filippi, P. Nardinocchi, and L. Teresi, *Kamkin A, Kiseleva I. (Eds.) Mechanosensitivity of the Heart, Mechanosensitivity in Cells and Tissues* **3** 12-449 (2009).
- [41] P.J. Hunter, A.D. McCulloch, and H.E.D.J. ter Keurs, *Prog. Biophys. Molec. Biol.* **69**, 289 (1998).
- [42] M.P. Nash and A.V. Panfilov, *Prog. Biophys. Molec. Biol.* **85**, 501-522 (2004).
- [43] A.V. Panfilov, R.H. Keldermann, and M.P. Nash, *Phys. Rev. Lett.* **95(25)**, 258104 (2005).
- [44] A.V. Panfilov, R.H. Keldermann, and M.P. Nash, *Proc. Natl. Acad. Sci. USA* **104** 7922 (2007) and erratum *Proc. Natl. Acad. Sci. USA* **104** 20142 (2007).
- [45] V.A. Lubarda. *Appl. Mech. Rev.* **57** 95 (2004).
- [46] A.L.M. Spencer, *Continuum Mechanics*, (Dover, 2004).
- [47] G.A. Holzapfel, *Nonlinear solid mechanics: a continuum approach for engineering*, (John Wiley and Sons, LTD, Chichester, 2000).
- [48] M.P. Nash and P. Hunter, *J. Elasticity* **61**, 113 (2000).
- [49] P. Pelce, J. Sun, and C. Langeveld, *Chaos, Sol. Frac.* **5**, 383 (1995).
- [50] A.J. Pullan, M.L. Buist and L.K. Cheng (Eds.), *Mathematically modelling the electrical activity of the heart: from cell to body surface and back again*, (World Scientific, Singapore, 2005).
- [51] <http://www.pardiso-project.org/>.
- [52] F.E. Curtis, O. Schenk and A. Wachter, *SIAM J. Sci. Comput.* **32**, 3447 (2010).
- [53] <http://www.comsol.com>
- [54] C. Fall, E. Marland, J. Wagner, J. Tyson (Eds.), *Computational Cell Biology*, (Springer, New York, 2002).
- [55] R.J. Atkin and N. Fox, *An introduction of the theory of elasticity*, (Dover, 2005).
- [56] E.M. Cherry and F.H. Fenton, *J. Theor. Biol.* **285**, 164 (2011).
- [57] R.R. Aliev and A.V. Panfilov, *Chaos, Sol. Frac.* **7**, 293 (1996).
- [58] V.N. Biktashev, A.V. Holden, M.A. Tsyganov, J. Brindley and N.A. Hill, *Phys. Rev. Lett.* **81**, 2815 (1998).
- [59] A.P. Munuzuri, C. Innocenti, J.M. Flesselles, J.M. Gilli, K.I. Agladze and V.I. Krinsky, *Phys. Rev. E* **50**, R667 (1994).
- [60] J.H.E. Cartwright, V.M. Eguiluz, E.H. Garcia and O. Piro, *Int. J. Bifurc. Chaos* **9**, 2197 (1999).
- [61] V.S. Zykov, G. Bordiougov, H. Brandtstadter, I. Gerdes, and H. Engel, *Phys. Rev. Lett.* **92**, 018304 (2004).
- [62] Z.A. Jimenez, B. Marts and O. Steinbock, *Phys. Rev. Lett.* **102**, 244101 (2009).
- [63] Z.A. Jimenez and O. Steinbock, *EPL* **91**, 50002 (2010).

- [64] S. Dutta and O. Steinbock, Phys. Rev. E **81**, 055202(R) (2010).
[65] S. Dutta and O. Steinbock, Phys. Rev. E **83**, 056213 (2011).
[66] S. Dutta and O. Steinbock, J. Phys. Chem. Lett. **2**, 945 (2011).
[67] A.V. Panfilov, Phys. Rev. E **59**, R6251 (1999).
[68] R.H. Keldermann, M.P. Nash, and A.V. Panfilov, Physica D. **238**, 1000 (2009).

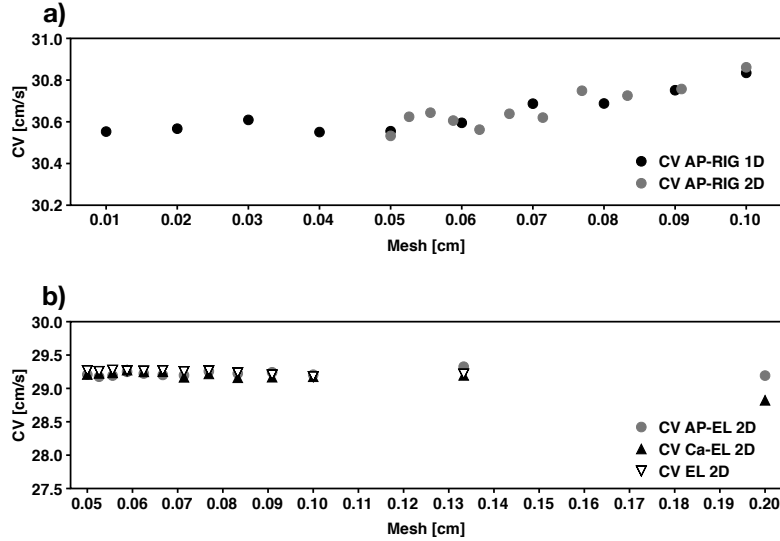


FIG. 1: Conduction velocity (CV) versus mesh size restitution graphs. Action potential (AP), elastic (EL) and calcium (Ca) (kinematic) waves are compared to set the right mesh size for numerical solution purposes. The plane wave travelling front timing has been taken at the 35% of its upstroke at two consecutive mesh positions nodes in order to evaluate the resulting velocity (several mesh nodes sequences have been tested). a) Purely electric AP conduction velocities are compared between 1D (black) and 2D (gray) simulation domains; b) AP (gray circle), Ca (black triangle) and EL (gray triangle) conduction velocities are compared for a 2D simulation domain where the electric mesh has been kept fixed at $dx = 0.5$ cm. Estimated velocities for mesh sizes lower than $dx = 0.1$ cm present similar values.

TABLE I: Adopted model parameters for the modified Beeler-Reuter electric setup [38] and finite elasticity [39], (M stands for mol/l).

$u_c = 0.13$	$u_v = 0.055$
$u_c^{s_i} = 0.85$	$\bar{g}_{f_i} = 4$
$\tau_r = 50$ ms	$\tau_{s_i} = 45$ ms
$\tau_o = 8.3$ ms	$\tau_v^+ = 3.33$ ms
$\tau_o = 8.3$ ms	$\tau_{v1}^- = 1000$ ms
$\tau_{v2}^- = 19.6$ ms	$\tau_w^+ = 667$ ms
$\tau_w^- = 11$ ms	$k = 8$
$d_o = 10^{-3}$ cm ² /ms	$V_o = -85$ mV
$V_{f_i} = 15$ mV	$V_{c_a} = 300$ mV
$c_o = 3.2 \cdot 10^{-7}$ M	$c^* = 10^{-7}$ M
$\gamma_o(c^*) = 1$	$\gamma_o^{max} = 0.8$
$\beta = 6$	$q_{c_a} = 2 \cdot 10^{-6}$
$k_{c_a} = 3256$ ms ⁻¹	$k^b = 0.1$

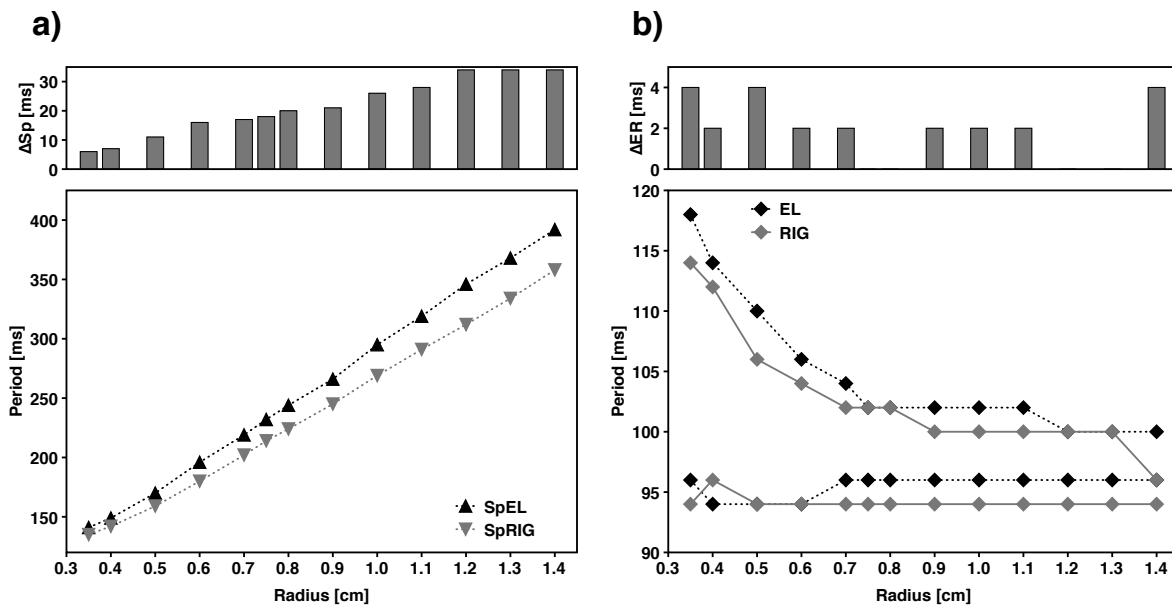


FIG. 2: (Color online) Overall results from the explored simulations set. a) Spiral rotational period compared for purely electric or rigid (RIG), gray, and electro-mechanic or elastic (EL), black, simulations versus obstacle radius. The superimposed histogram shows the difference between the two cases highlighting a divergence trend which reaches its maximum value of 34 ms for the higher radii analyzed. b) Comparison of the unpinning bands (upper and lower defibrillation limits) for the purely electric (gray) and the electro-mechanic (black) cases. The vertical axis reports the lowest and highest successful stimulation periods (ms), i.e. the ones for which the unpinning has been reached, having explored the range of periods $90 \div 120\text{ ms}$ with a finite time-step of 2 ms . The horizontal axis reports the discrete simulated obstacle radii ranging between 3.5 cm and 1.4 cm with a spatial step of 1 cm . The intermedium case, $R_{ob} = 0.75\text{ cm}$, has been tested in order to verify the resulting trend. The superimposed histogram shows the absolute difference of the band ranges between the two models. Both trends are highly nonlinear and reach their minimum range of frequencies for the larger obstacle radii analyzed.

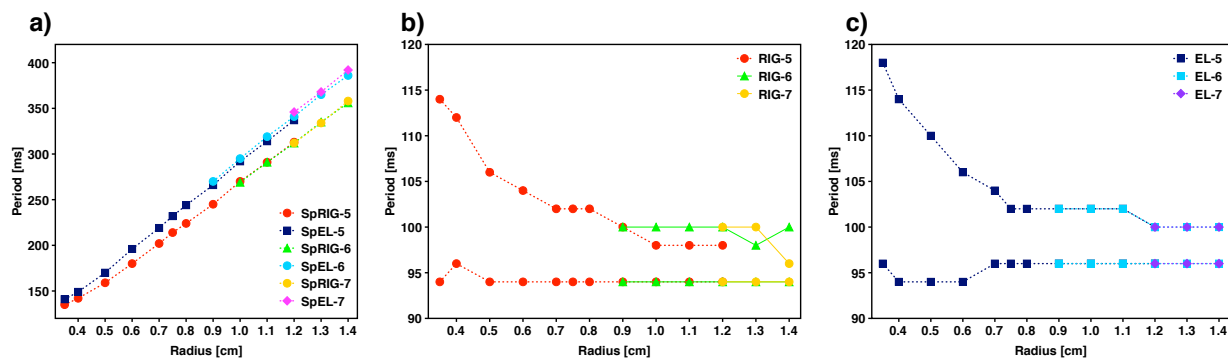


FIG. 3: (Color online) Comparison of the spiral rotation and successful defibrillation periods for three different domain sizes, $L = 5, 6, 7\text{ cm}$, for both rigid (RIG) and elastic (EL) modeling, versus obstacle radius. The spiral rotational periods a) seem to be unaffected by changing the domain size, following the same behavior as reported in the previous case. In the purely electric case b) the boundary effects induce a reduction of the unpinning band when the ratio $R_{ob}/L \geq 0.2$, while the electro-elastic model c) shows a better robustness to this effect.

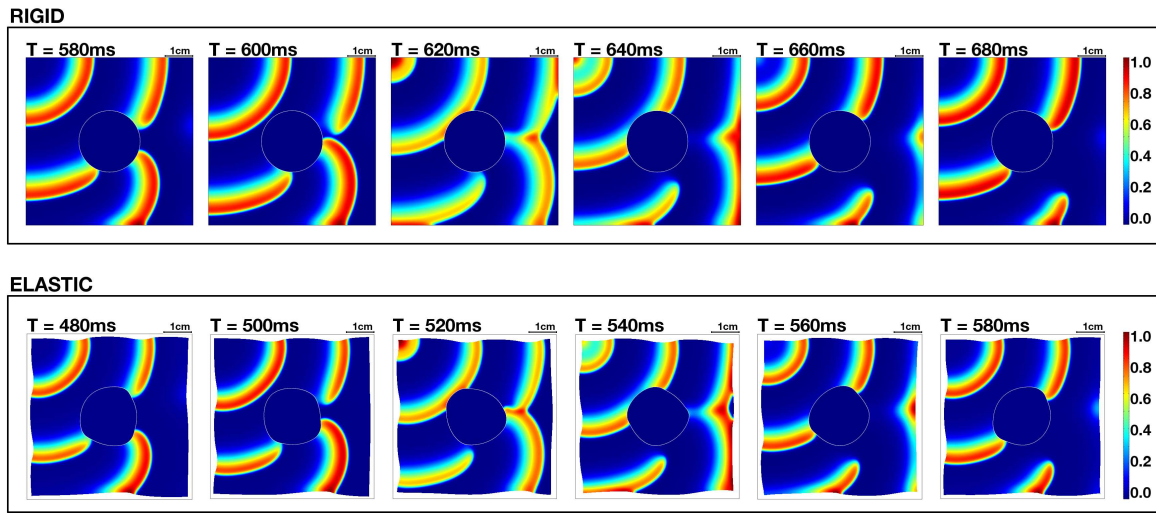


FIG. 4: (Color online) Sequences of defibrillation scenarios with no elasticity (upper, RIGID) and contraction activated (lower, ELASTIC). Both sequences refer to a domain size $L = 6\text{ cm}$, an obstacle radius $R_{ob} = 1.2\text{ cm}$ and a stimulation period $T = 100\text{ ms}$. The timing reported in the panels shows a shifting in the unpinning event between the two cases. The color map is referred to the normalized action potential of the Fenton-Karma model [38].

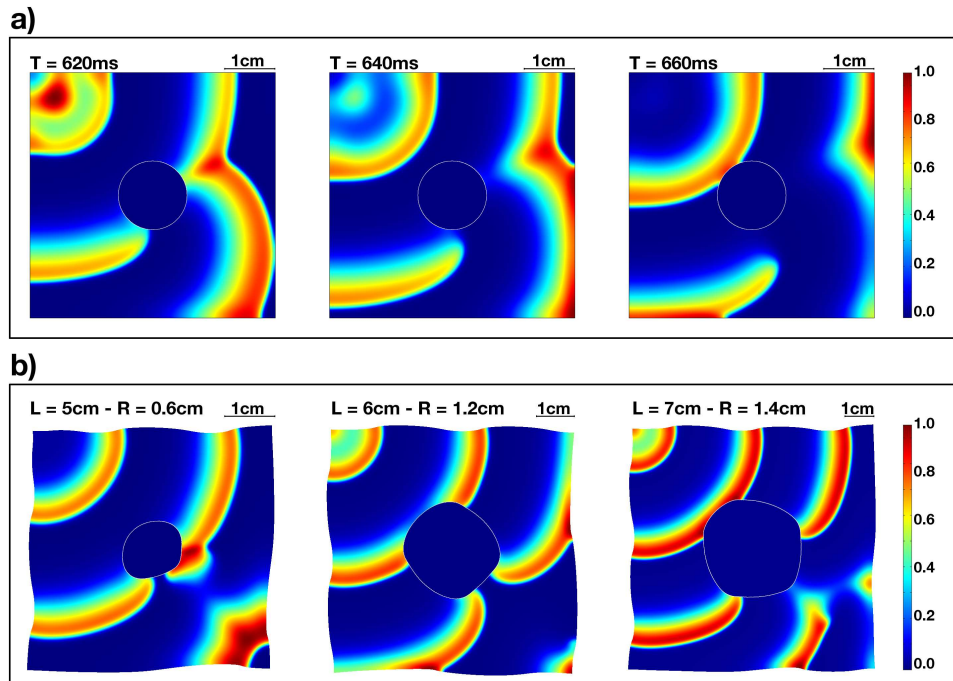


FIG. 5: (Color online) Differences induced by pacing site (upper) and elasticity (lower). a) Defibrillation sequence in the case of the pacing electrode inside the tissue (top left), confirming that the unpinning dynamics are similar to those observed with the pacing at the corner of the domain ($L = 5\text{ cm}$, $T = 98\text{ ms}$). b) Three different domain sizes ($L = 5, 6, 7\text{ cm}$) with different obstacle sizes ($R_{ob} = 0.6, 1.2, 1.4\text{ cm}$) reporting an example of the distorted obstacle shapes varying in time due to the presence of elastic effects. The color map referred to is the normalized action potential of the Fenton-Karma model [38].

Three-band decomposition analysis of wall shear stress in pulsatile flows

A. Gizzi,^{1,2} M. Bernaschi,³ D. Bini,^{3,4} C. Cherubini,^{1,4} S. Filippi,^{1,5} S. Melchionna,⁵ and S. Succi³

¹*Nonlinear Physics and Mathematical Modeling Lab, University Campus Bio-Medico, I-00128 Rome, Italy*

²*Alberto Sordi Foundation, Research Institute on Aging, Rome, Italy*

³*Istituto per le Applicazioni del Calcolo "M. Picone," CNR, I-00185 Rome, Italy*

⁴*ICRA, University of Rome "La Sapienza," I-00185 Rome, Italy*

⁵*CNR-IPCF, Istituto Processi Chimico-Fisici, CNR, I-00185, Rome, Italy*

(Received 23 September 2010; revised manuscript received 23 November 2010; published 4 March 2011)

Space-time patterns of wall shear stress (WSS) resulting from the numerical simulation of pulsating hemodynamic flows in semicoronal domains are analyzed, in the case of both regular semicoronal domains and semicoronal domains with bumpy insertions, mimicking aneurysm-like geometries. A new family of cardiovascular risk indicators, which we name three-band diagrams (TBDs), are introduced, as a sensible generalization of the two standard indicators, i.e., the time-averaged WSS and the oscillatory shear index. TBDs provide a handy access to additional information contained in the dynamic structure of the WSS signal as a function of the physiological risk threshold, thereby allowing a quick visual assessment of the risk sensitivity to individual fluctuations of the physiological risk thresholds. Due to its generality, TBD analysis is expected to prove useful for a wide host of applications in science, engineering, and medicine, where risk assessment plays a central role.

DOI: [10.1103/PhysRevE.83.031902](https://doi.org/10.1103/PhysRevE.83.031902)

PACS number(s): 87.80.-y, 87.90.+y

I. INTRODUCTION

The human cardiovascular system is a complex physiological network. It is in charge of pumping blood from the heart through the large arteries, to the smaller arterioles, then through capillaries, and, eventually, farther down to the venules, where the deoxygenated blood is passed through veins back to the heart, thereby imposing a circular pattern through the whole body. Such a complex network, providing on the order of a few hundred million heartbeats in a lifetime, is inevitably exposed to a number of risk factors. Among others, atherosclerosis is one of the most common cardiovascular diseases, primarily associated with a progressive malfunctioning of the arterial blood vessels due to the confluence of a variety of hemodynamic and chemico-physical factors. Although the development of atherosclerosis is highly sensitive to the presence of systemic risk factors, such as high cholesterol, diabetes, and high blood pressure, the clinical manifestations of the disease—heart attack, sudden coronary death, and angina pectoris—appear to be focal, resulting from the accumulation of lipid molecules and inflammatory cells at specific locations within the wall of the coronary arteries. Prior research, observational *in vitro* and *in vivo*, locates the seed of atherosclerosis mostly within regions of disturbed blood flow, where the local endothelial shear stress (ESS) is low (<0.5 Pa) or of alternating direction [1].

The ESS is the tangential stress stemming from the friction of the flowing blood on the endothelial surface of arterial walls, and a qualitative picture indicates that under low-ESS (LESS) conditions, endothelial cells present enhanced exposure to intramural penetration of micro- and nanoscale biological bodies, such as B cells and lipid molecules, whose subsequent accumulation in the underlying tissues may initiate serious atherosclerotic pathologies [1–5].

A fully quantitative assessment of the actual risk map for each individual is beyond the current modeling capabilities, mostly on account of the extreme complexity of the coupling

between biochemical mechanisms with their surrounding hemodynamic environment. Since geometry plays a driving role in establishing the local ESS patterns in human arteries, a growing body of computer simulations of relatively short biological timescales aimed at representing the global and local geometry in as much detail as affordable on the most powerful present-day supercomputers has been performed in the last decade [6–13]. Such leading-edge computational work is of primary importance to analyze the actual space-time configurations of hemodynamic flows to the highest possible degree of accuracy.

Even in relatively simple geometries, however, the ESS patterns can exhibit a very rich space-time structure, from which it is hard to extract synthetic indicators of clinical risk. At present, the most credited of such indicators are the LESS, as defined above, and the oscillatory shear index (OSI), a measure of time variability of the wall shear stress (WSS) signal [1]. Here we introduce a new set of indicators, which we name three-band diagrams (TBDs), which provide a more accurate, and still handy, access to the additional information contained in the dynamic structure of the WSS signal as a function of the physiological risk threshold. This allows a more quantitative and visually friendly assessment of the risk sensitivity to individual fluctuations of the physiological risk thresholds. The TBD analysis is here applied to a regular semicorona geometry, as well as a corona with a localized bump, mimicking an aneurysm-like deformation. For the case of the regular semicorona, the TBD indicators point to a low-risk situation all along the spatial extension of the corona. In contrast, the aneurysm-like geometry is found to exhibit a highly heterogeneous, low-WSS, distribution, eventually with sizable contrasts between nearby regions of the wall. The TBD analysis is also applied to an experimental WSS signal from a healthy patient and found to yield the same conclusions resulting from the simulations, namely, that healthy situations are associated with a substantial homogeneous permanence of the WSS signal above the physiological risk threshold.

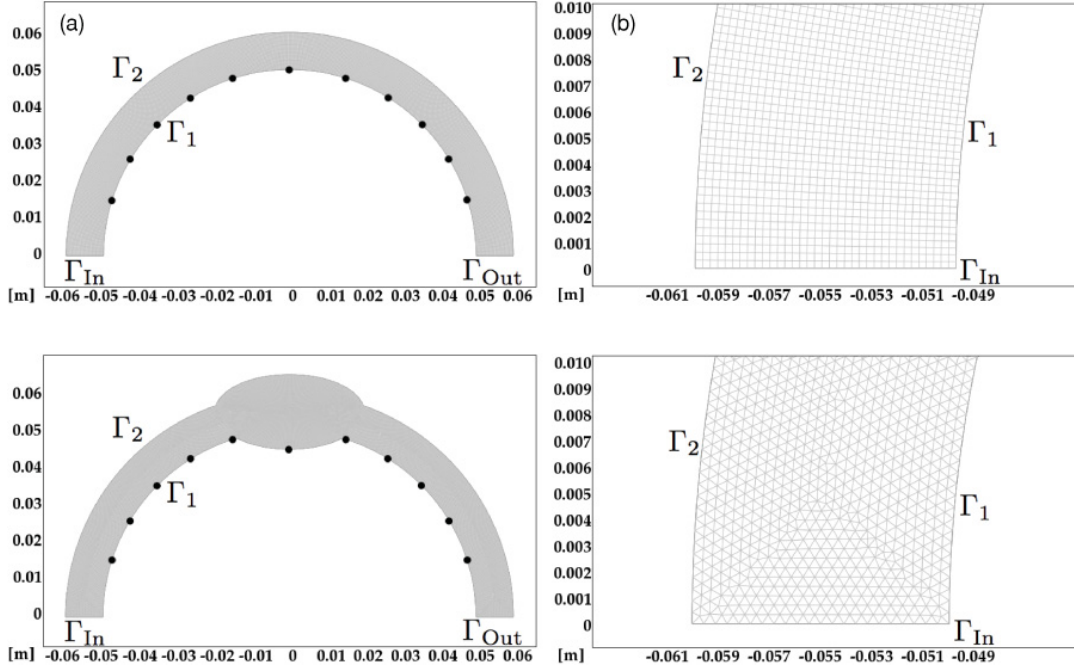


FIG. 1. (a) Geometrical simulation domain (units in meters) for regular (upper panel) and aneurysm (lower panel) domains. (b) Corresponding details of the mesh grid discretization for a numerical solution. The fluid flows within the domain with rigid boundaries (Γ_1 , Γ_2) from left (Γ_{In}) to right (Γ_{Out}). Bullets denote the points at which the velocity field is analyzed below in terms of a WSS map.

II. THE BASIC FLUID-DYNAMIC MODEL

Let us consider two-dimensional incompressible Navier-Stokes equations on the the semicoronal flat domain, defined by the following boundaries in Cartesian coordinates (see Fig. 1):

$$\begin{aligned} \Gamma_2 : & \quad x^2 + y^2 = R_2^2, \quad |x| \leq R_2 \quad y \geq 0, \\ \Gamma_1 : & \quad x^2 + y^2 = R_1^2, \quad |x| \leq R_1 \quad y \geq 0, \\ \Gamma_{In} : & \quad y = 0, \quad -R_2 \leq x \leq -R_1, \\ \Gamma_{Out} : & \quad y = 0, \quad R_1 \leq x \leq R_2. \end{aligned} \quad (1)$$

The relevant equations of motion read as follows:

$$\rho \frac{D\mathbf{u}}{dt} = -\nabla p + \mu \nabla^2 \mathbf{u}, \quad \text{div } \mathbf{u} = 0, \quad (2)$$

where ρ is the density of the fluid, p the pressure, μ the (constant) dynamic viscosity, and

$$\frac{D}{dt} = \partial_t + \mathbf{u} \cdot \nabla \quad (3)$$

denotes the Lagrangian derivative along the fluid flow. In Cartesian coordinates the components of the shear tensor are given by $S_{ij} = (\partial_i u_j + \partial_j u_i)/2$, namely,

$$\begin{aligned} S_{ij} &= \begin{pmatrix} \partial_x u & \frac{1}{2}(\partial_x v + \partial_y u) \\ \frac{1}{2}(\partial_x v + \partial_y u) & \partial_y v \end{pmatrix} \\ &\equiv \begin{pmatrix} -\partial_y v & \frac{1}{2}(\partial_x v + \partial_y u) \\ \frac{1}{2}(\partial_x v + \partial_y u) & \partial_y v \end{pmatrix}, \end{aligned} \quad (4)$$

where u and v are the Cartesian components of the velocity field, $\mathbf{u} = (u, v)$ and $\partial_x u = -\partial_y v$, due to the incompressibility of the fluid. In particular, we are interested in the components of the shear tensor along the vectors \mathbf{n} and $\boldsymbol{\tau}$, associated with the radial and tangential directions of a naturally associated polar coordinate system, respectively:

$$\begin{aligned} S_{\tau\tau} &= (\partial_x u) \frac{y^2}{r^2} + (\partial_y v) \frac{x^2}{r^2} - (\partial_y u + \partial_x v) \frac{xy}{r^2} = -S_{nn}, \\ S_{\tau n} &= (-\partial_x u + \partial_y v) \frac{xy}{r^2} + \frac{(\partial_y u + \partial_x v)(x^2 - y^2)}{2r^2}. \end{aligned} \quad (5)$$

Two scalar invariants are associated with the shear tensor. The first one, i.e., its trace $I_1 = \text{Tr } S = 0$, is trivially zero due to the fluid incompressibility, while the second one, i.e., the trace of its square, $I_2 = \frac{1}{2} \text{Tr } S^2 = -\det S$, contains important information on the local flow topology [14]. In this work, we shall focus on stress tensor $\boldsymbol{\sigma}$, measured in Pa, as given by the following constitutive relation:

$$\boldsymbol{\sigma} = \mu \mathbf{S}, \quad (6)$$

where the dynamic viscosity of the fluid μ is often re-expressed in terms of the kinematical viscosity $\nu = \mu/\rho$. Here and throughout, the fluid is regarded as Newtonian ($\mu = 3 \times 10^{-3}$ Pa s) with $\rho = 10^3$ kg/m³ (and then $\nu = 3 \times 10^{-6}$ m²/s), a plausible approximation for large arteries. Moreover, the component $\sigma_{\tau n}$ of the stress tensor will be also indicated simply as WSS hereafter.

Boundary conditions are chosen as follows: solid wall (no-slip) at Γ_1 and Γ_2 ; laminar inflow, with parabolic profile

pulsed in time, at Γ_{In} , (see Fig. 1); zero viscous stress, with pressure $p = 12.5$ kPa, at Γ_{Out} .

III. FLOW GEOMETRIES

Let us begin by addressing the current values of the physiological parameters that would meet the LESS criterion of a WSS < 0.5 Pa in simple geometries, where WSS would identify with the ESS in a physiological context. The idea is to appreciate, at least on qualitative grounds, to what extent an assessment for the above criterion in real-life geometries can be reached by composition of simple models.

A. Straight cylinder

For the simple case of laminar flow (Reynolds number approximately below 2000) in a straight cylinder the well-known Poiseuille solution in cylindrical coordinates reads as follows:

$$u_z(r) = U_0(1 - r^2/R^2), \quad (7)$$

where u_z is the axial velocity, R the cylinder radius, L the axial length, $\Delta P/L$ the driving pressure gradient, and $U_0 = \frac{R^2 \Delta P}{4\mu L}$ the resulting centerline speed. The corresponding nonvanishing shear-stress tensor components are $S_{rz} \equiv S_{zr} = -2U_0 r/R^2$, whose maximum $S_{(max)} = 2U_0/R$ is attained at the wall location $r = R$. For typical values of the aorta, $U_0 \sim 1$ m/s and $R \sim 0.005$ m, with a blood kinematic viscosity ν of about 3×10^{-6} m²/s, corresponding to a Reynolds number $Re = \frac{2U_0 R}{\nu} \sim 3300$, we obtain WSS ~ 1.2 Pa, which, as expected, lies above the risk threshold. The picture becomes less transparent in the presence of geometrical/topological complexities, such as curvature, bifurcations, etc. A general treatment of such complexities is beyond any analytical treatment. Nevertheless, the analysis of simplified and yet representative geometries may offer valuable insights into these complex problems.

B. Two-dimensional corona

One of the basic aspects affecting the shear-stress distribution in complex geometries is the competition between curvature and centrifugal effects. The latter tend to skew the velocity profile toward the outer side, while plain curvature favors higher shear on the higher-curvature side, i.e., the inner one. One then wonders which one of the two would prevail, and under what parametric conditions. For the case of two-dimensional simple geometry domains, the availability of a steady-state analytical solution can settle the question in a full generality, although for higher-dimensional and/or time-dependent flows, no closed analytical solutions are available in general, and one has to resort to numerical simulations.

In fact, it can be easily proved that [15]

$$u(r) = U_0 \left[C_1(1 + \beta x) + \frac{C_2}{(1 + \beta x)} + (1 + \beta x) \ln(1 + \beta x) \right], \quad (8)$$

$$x = \frac{1}{\beta} \left(\frac{r}{R_0} - 1 \right)$$

is a stationary solution to the incompressible Navier-Stokes equations (cylindrical coordinates) in a two-dimensional semicorona of radii satisfying $R_1 < R_2$. Here we have set $r = R_0(1 + \beta x)$, $x \in [-1, 1]$, with $R_0 = (R_1 + R_2)/2$ being the

centerline radius and $\beta = (R_2 - R_1)/(R_2 + R_1)$ the reduced diameter of the semicorona.

The values of C_1 and C_2 are given by

$$C_1 = \frac{1}{4\beta} [(1 - \beta)^2 \ln(1 - \beta) - (1 + \beta)^2 \ln(1 + \beta)], \quad (9)$$

$$C_2 = \frac{(1 - \beta)^2}{4\beta} \ln \frac{(1 + \beta)}{(1 - \beta)}.$$

The associated shear stress for small values of β , Taylor-expanding at the order $O(\beta^2)$, is given by

$$S = S_0 \left(\frac{\beta^2}{3} + \beta x - \beta^2 x^2 \right), \quad S_0 = \frac{U_0}{R_0}. \quad (10)$$

These expressions show that the inner WSS ($x = -1$) always exceeds the outer one ($x = +1$) by an amount of order β^2 . This is in line with the fact that the analytical solution of the velocity profile is always skewed toward the *inner* side of the corona, indicating that centrifugal effects are systematically outweighed by curvature effects of the boundaries. For this specific static solution, such a conclusion holds regardless of the values of the Reynolds and Dean numbers, $Re = 2\beta U_0 R_0/\nu$ and $De = \beta^{1/2} Re$.

It shall appear clear that although one should adopt three-dimensional study for accounting for physiological flows, a two-dimensional analysis already contains enough information to suggest the introduction of general proper tools that are also useful to deal with these more realistic situations.

For instance, the existence of this exact solution in a stationary regime should be complemented at least by a study of time-dependent regimes; to this end we proceed by implementing in the next section a numerical analysis either on the same semicoronal geometry discussed above or in a deformed one, i.e., a corona with a superimposed double cap, mimicking an expansive remodeling of the walls (aneurysm), inspired by Ref. [16].

IV. NUMERICAL EXPERIMENTS

We have considered a numerical analysis of incompressible fluid flow both in a regular semicoronal geometry as discussed above and in a deformed one by the presence of an aneurysm. In the following, we provide all the details concerning numerical solver, choice of geometry, and choice of grid.

The simulations have been performed with the finite-element multiphysics package COMSOL [17], running on a multiprocessor workstation. For the purpose of an accurate evaluation of the WSS, Lagrange quadratic elements with a square shape have been chosen for the semicircular corona while triangular-shaped elements have been chosen for the aneurysm case. Time marching proceeds through an adaptive algorithm linked to the PARDISO direct solver of the software.

A. Geometry and time load

In Fig. 1, a geometrical domain is shown, consisting of a two-dimensional circular corona with inner and outer radii (cm) $R_1 = 5$ and $R_2 = 6$, respectively, corresponding to a centerline radius $R_0 = 5.5$, a diameter $D = 1$, and $\beta \sim 0.09$, as appropriate for a human aorta. A detail of the computational grid is shown in the right panel of Fig. 1.

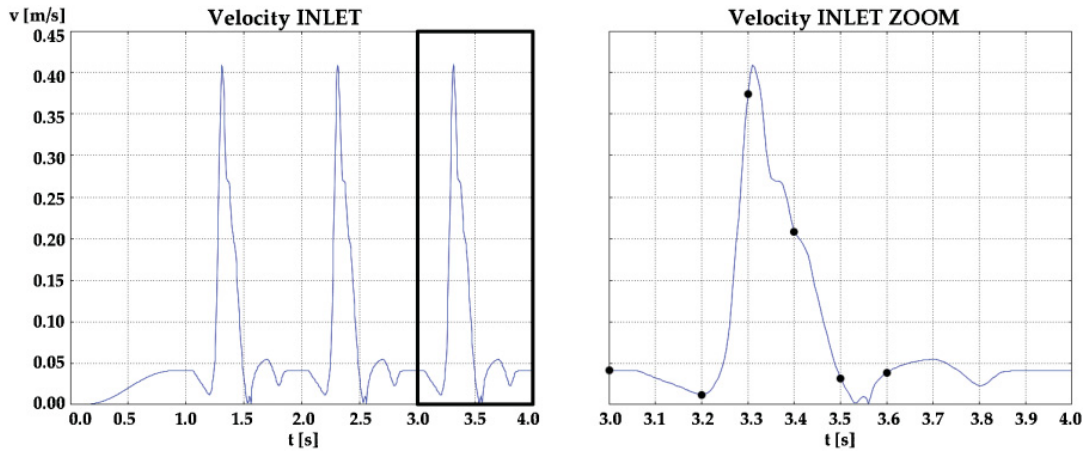


FIG. 2. (Color online) The pulsatile velocity field (centerline value) at the inlet (Γ_{in}). Right panel is the selected pulse in the regime state (third pulse) adopted for the present analysis. The bullets denote the sequence of time instants, $t = [3.0, 3.2, 3.3, 3.4, 3.5, 3.6]$ seconds selected to show snapshots of the velocity field in the Fig. 3.

In Fig. 2, we show the centerline value of the inlet velocity field as a function of time, as taken from Refs. [18,19]. The time history of this value averages at about 0.5 m/s with peaks at nearly 1 m/s. The simulation span covers three heartbeats, spaced about 1 second from each other.

B. Patterns of the velocity field

In Figs. 3 and 4, we show six representative snapshots of the magnitude of the velocity field at $t = 3.0, 3.2, 3.3, 3.4, 3.5, 3.6$ (time measured in seconds) for the regular and the aneurysm geometry, respectively. In the former case, we observe a series of localized patches of high velocity, around 0.4 m/s, downstream of the inlet region. As time unfolds, the above patches further increase their speed and coalesce under the effect of the mounting pressure. Reaching upon the flat top, a quasicontinuum coalescence takes place, at a speed of nearly 1 m/s around the centerline region. Finally, in the descending phase, the quasicontinuum breaks down again into a series of

coherent patches, preparing for the next pulse. Overall, the velocity field exhibits a rich dynamics, typical of moderately turbulent flows. The presence of the aneurysm, on the other hand, generates large-scale vortex-like structures, invading a big portion of the bumped domain, in stark contrast with the regular case described previously.

C. Space-time shear patterns

Having discussed the salient features of the flow velocity distribution, we next proceed to inspect the WSS. WSS distributions have made the object of intense investigations in computational hemodynamics, where they are usually presented as a discrete time sequence of spatial configurations. It is convenient to present this information in the suggestive form of *space-time* patterns, defined by the condition

$$\sigma_k(\phi; t) \equiv \sigma(r = R_k; \phi; t) = C, \quad k = 1, 2, \quad (11)$$

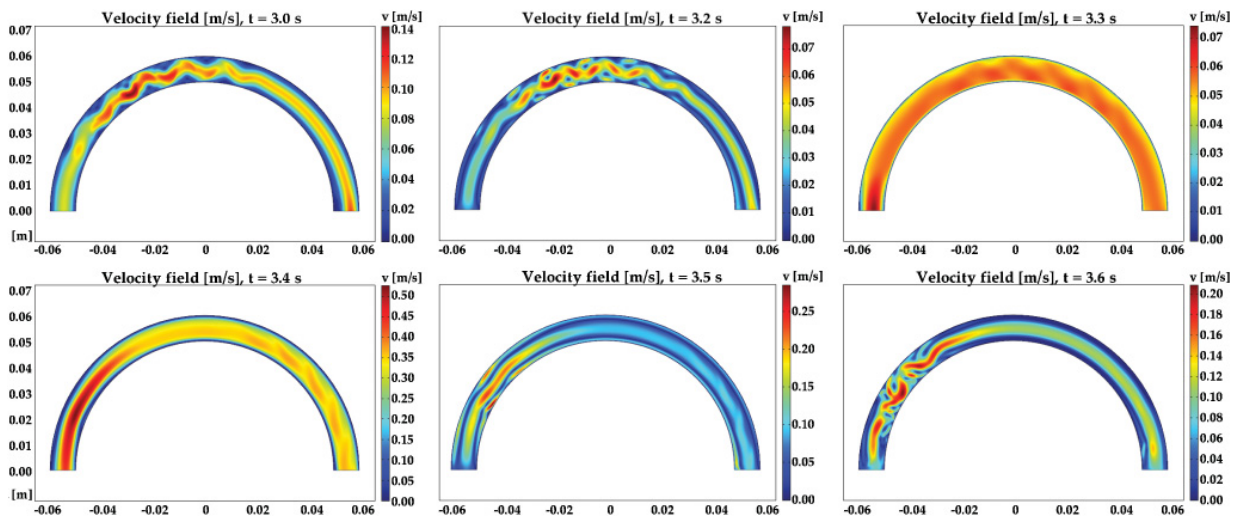


FIG. 3. (Color online) Maps of the velocity field magnitude at $t = [3.0, 3.2, 3.3, 3.4, 3.5, 3.6]$ seconds in the case of regular geometry. A series of turbulent patterns appears due to the irregular oscillation of the inlet pulse.

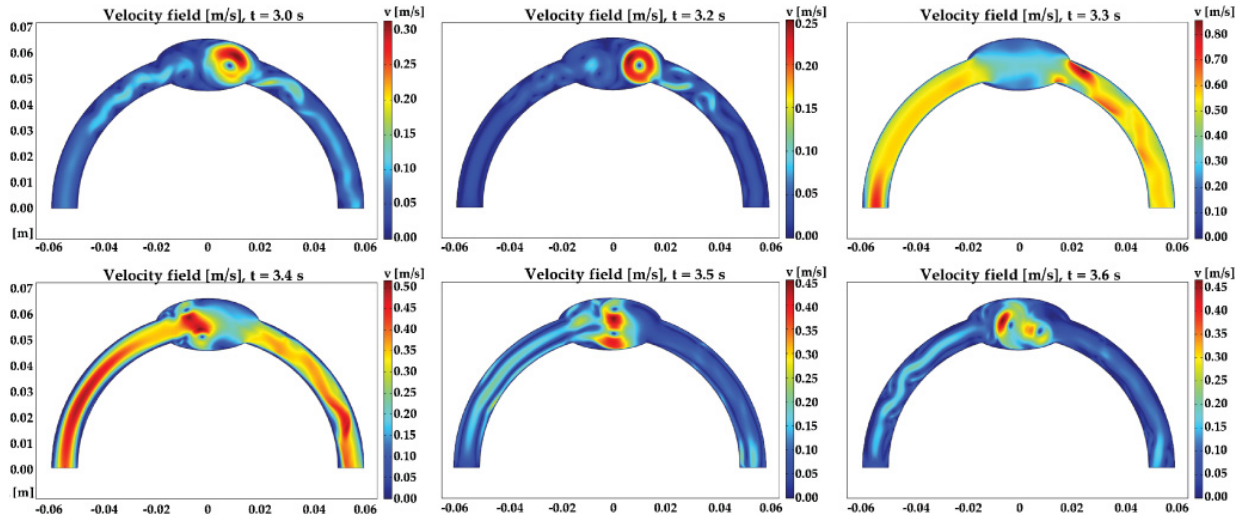


FIG. 4. (Color online) Maps of the velocity field magnitude at $t = [3.0, 3.2, 3.3, 3.4, 3.5, 3.6]$ seconds in the case of the aneurysm-like geometry. A series of turbulent patterns appears, due to the irregular oscillation of the inlet pulse, significantly enhanced by the presence of the aneurysm. Inside the aneurysm, the magnitude of the velocity field is suppressed with respect to the regular geometry case, thus inducing a corresponding decrease of the WSS.

at the inner and outer walls, $k = 1, 2$, respectively. Indeed, due to the existence of well-defined coherent patches in the velocity field, one is led to conjecture that the shear field should also organize in the form of dynamic coherent structures [20]. Formally, by inverting the relation (11), for each value of the constant C , one can define an associated “trajectory” $\phi = \phi(t; C)$. Indeed, by differentiating σ along a iso-shear space-time surface $\sigma(\phi; t) = C$, one obtains the equation of the “world lines” $\frac{d\phi}{dt} = -\frac{\partial\sigma/\partial t}{\partial\sigma/\partial\phi}$.

From this simple expression, it is seen that a purely time-dependent and uniform WSS, $\sigma = \sigma(t)$, would result in straight horizontal world lines. Conversely, a purely static nonuniform WSS distribution, $\sigma = \sigma(\phi)$, would result in straight vertical world lines. Within this representation, the existence of coherent structures visualizes as a bundle of nearby trajectories, which we term “shearlets.” Space-time patterns provide a visual appreciation of the characteristic propagation speed $\frac{d\phi}{dt}$ of the corresponding shearlets.

Figure 5 confirms the existence of a rich structure of the WSS, for cases of both regular and aneurysm geometries. In the first case, besides the thin red stripes, which correspond to the flat-top pulses, the WSS is seen to organize into a series of intermediate coherent structures, propagating along both directions (right- and leftward inclinations of the patches in the spacetime diagram). Similar considerations hold for the inner WSS. In the aneurysm geometry, the presence of the enlarged region influences such a phenomenology, leading to a traveling signal, here strongly localized.

V. THREE-BAND RUNNING THRESHOLD ANALYSIS

The best way to extract synthetic indicators of clinical risk out of the rich and heterogeneous space-time structure of the WSS is still an open question.

To date, the two main quantitative indicators of cardiovascular risk are the time average of the WSS over a period of time T and the oscillatory shear index (OSI), defined as follows:

$$\bar{S} = \frac{1}{T} \int_{\Omega} S(t) dt, \quad (12)$$

$$\tilde{S} = \frac{\int_{\Omega^-} |S(t)| dt}{\int_{\Omega^-} |S(t)| dt + \int_{\Omega^+} S(t) dt}, \quad (13)$$

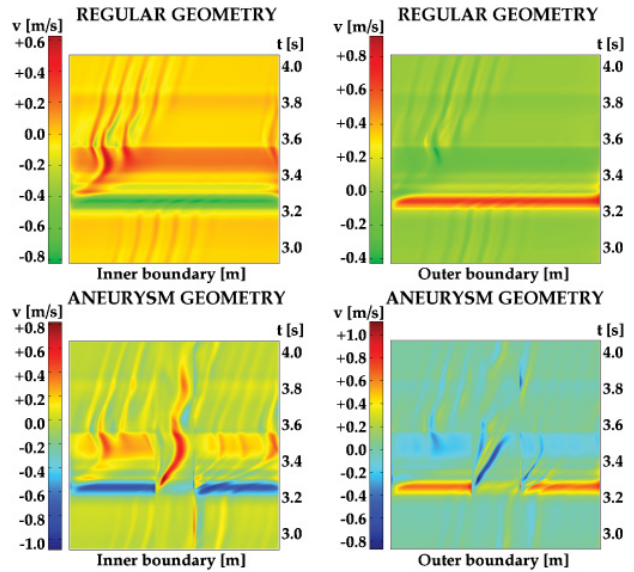


FIG. 5. (Color online) Space (horizontal axis)-time (vertical axis) pattern of the inner and outer WSS (units of 10^{-3} s^{-1} for a better visualization) on the regular (upper panel) and aneurysm-like geometry (lower panel). The aneurysm case shows strong inhomogeneities with respect to the regular case.

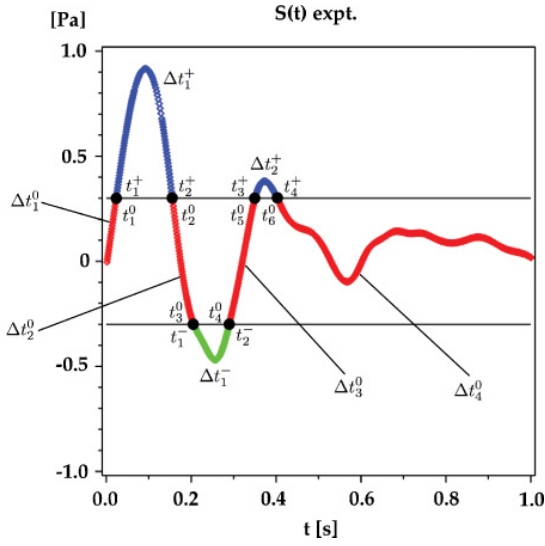


FIG. 6. (Color online) Three-band decomposition analysis of the signal $S(t)$ (reconstructed experimental signal; see Fig. 11 for details). The identification of the time sequence Ω^s associated with the three bands, $s = -, 0, +$ and the corresponding residency times Δt_j^s are explicitly shown. As is apparent from the figure, the residence intervals are defined as follows: $\Delta t_1^+ = t_2^+ - t_1^+$, $\Delta t_1^0 = t_1^0 - 0$, $\Delta t_2^0 = t_3^0 - t_2^0$, $\Delta t_1^- = t_2^- - t_1^-$, and so on. By definition, some endpoints of a given sequence coincide with the start points of another, for instance, $t_1^+ \equiv t_1^0$, $t_2^+ \equiv t_2^0$, $t_3^0 \equiv t_1^-$.

where $\Omega \equiv [0, T]$ is the full time interval, and Ω^\pm are the disjoint subsets where $S(t) > 0$ and $S(t) < 0$, respectively. The parameter \bar{S} gives the average strength of the signal

over the full period of oscillation, while \tilde{S} is a measure of its oscillatory content. It is commonly agreed [21] that “risky/unhealthy” signals are characterized by \tilde{S} below a given critical threshold and relatively high values of the OSI. Clearly, the specification of the pair (\bar{S}, \tilde{S}) cannot provide full information on the dynamical structure of the signal, so that different signals with different risk content may map into the same values of the pair (\bar{S}, \tilde{S}) . The information on the extra risk not contained in (\bar{S}, \tilde{S}) might be indeed of some value. For instance, short intervals carrying a negative signal might not bear much physiological relevance (physiological damage is often associated with sufficient persistence of the WSS below the critical threshold) and should therefore be discounted from the OSI value. Part of this information can be regained by the three-band decomposition analysis described in the following. Given a generic signed (both positive and negative) signal $S_{(\min)} \leq S(t) \leq S_{(\max)}$ and a control threshold $\sigma \geq 0$, we define the following triplet of “daughter” functions (three-band decomposition):

$$\begin{aligned} S^+(t) &\equiv S(t)H^+(\sigma), & S^-(t) &\equiv S(t)H^-(\sigma), \\ S^0(t) &\equiv S(t)H^0(\sigma), \end{aligned} \quad (14)$$

where $H^+(\sigma) = 1$ if $S > \sigma$ and 0 otherwise (the Heavyside $H(S - \sigma)$), $H^-(\sigma) = 1$ if $S < -\sigma$ and 0 otherwise, and finally $H^0(\sigma) = 1$ if $-\sigma \leq S \leq \sigma$ and 0 elsewhere. By definition $S^\pm(t)$ coincides with $S(t)$ where $S(t) > \sigma$, $(S(t) < -\sigma)$, while $S^0(t) \equiv S(t)$ in the intermediate band $-\sigma < S(t) < \sigma$.

The support of these three functions, $S^s(t) \equiv [S^-, S^0, S^+]$, in the time interval $\Omega = [0, T]$ is constituted by three series of discrete time intervals. The general formulas are not very illuminating. However, with respect to the signal shown in Fig. 6

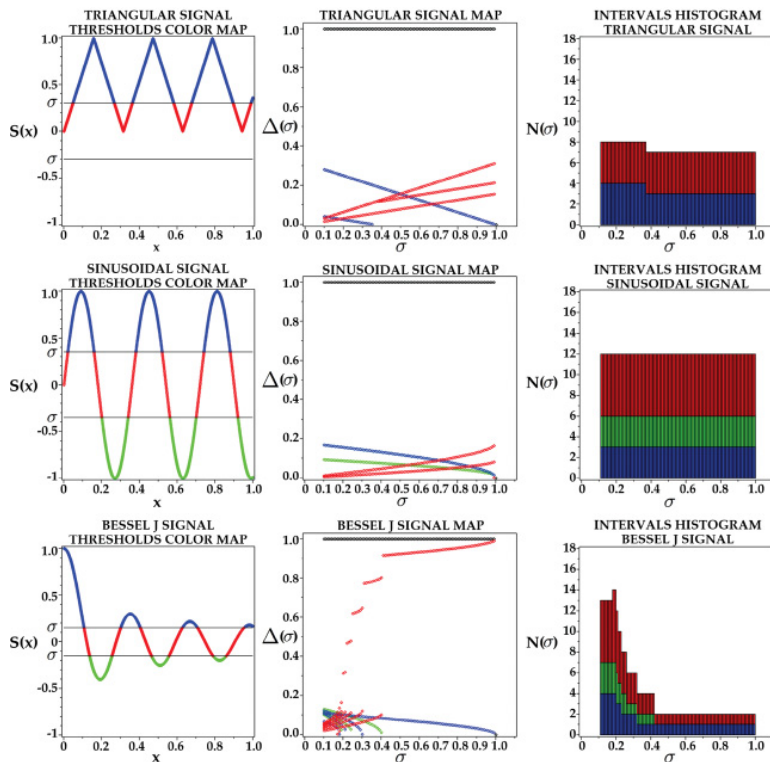


FIG. 7. (Color online) TBD representation of three analytical functions: sawtooth (top), sinusoidal (middle), and Bessel $J_0(20t)$, bottom. Left column: the original signal, with the three bands in color. Middle column: the corresponding “trajectories” $\Delta t_j(\sigma)$ (the dark line on the top of each graph indicates the verified sum of the unitary reference interval, the duration of the analyzed period). Right column: the TBD histograms. It can be appreciated that periodic signals give rise to very flat histograms and complementary (increasing/decreasing) trends, while the oscillating decay of the Bessel signal generates a peaked histogram profile and a series of jumps in the interval trajectories.

we have the following intervals:

$$\begin{aligned} \Omega^+ &= \cup_{j=1}^{N^+} [t_{2j}^+, t_{2j-1}^+], & \Omega^0 &= \cup_{j=0}^{N^0} [t_{2j+1}^0, t_{2j}^0], \\ \Omega^- &= \cup_{j=1}^{N^-} [t_{2j}^-, t_{2j-1}^-], \end{aligned} \quad (15)$$

where +, 0, and - label the three bands. Clearly $\cup_{s=0,\pm} \Omega^s = \Omega$, while, for instance,

$$T^+ = \sum_{j=1}^{N^+} (t_{2j}^+ - t_{2j-1}^+) \equiv \sum_{j=1}^{N^+} \Delta t_j^+ \quad (16)$$

(and similarly for T^- and T^0) measures the residency time of the signal in the corresponding band (see Fig. 6).

By construction, S^0 vanishes as $\sigma \rightarrow 0$, and so do S^\pm as $\sigma \rightarrow S_{(\text{sup})} = \text{Max}\{|S_{(\text{min})}|, S_{(\text{max})}\}$.

The idea of the three-band analysis is to inspect the number of intervals and their individual extent $\Delta t_j^s = (t_{2j}^s - t_{2j-1}^s)$, as a function of the running threshold σ . More specifically, any generic signal $S(t)$ induces a partition of the time interval $\Omega = [0, T]$ into three mutually disjoint sets Ω^s , each consisting of N^s time intervals. The family of sets generated by letting the threshold parameter σ scan the entire range of values $[0, S_{(\text{sup})}]$ defines an ensemble of N^s "trajectories" $\Delta t_j^s(\sigma)$ and a corresponding numerosity histogram $N^s(\sigma)$. This situation is described in detail in Fig. 6, where notation and conventions are also elucidated.

In passing, we note that t_j^\pm are the zeros of the up(down)-shifted signal $S_{\pm\sigma} \equiv S(t) \pm \sigma$, hence N^s is expected to be of the order of this number of these zeros. The statistical properties of the sequence of zeros of stochastic signals form a major subject of study in mathematics, statistical physics, and signal processing, and much is known about them in the case of Gaussian statistics. However, these results do not easily carry over to the interpretation of physiological WSS signals, which appear to be far from random Gaussian processes.

The standard risk indicators result from Eqs. (12) and (13), with $\tilde{S} \equiv \text{WSS}$ and $\tilde{S} \equiv \text{OSI}$, once the WSS signal is properly discretized.¹ For the sake of simplicity, we shall denote the set of trajectories and the corresponding histogram simply as the *three-band diagram* (TBD) of the signal.

Formally, TBDs are a family of *multi-functionals* mapping the signal $S(t)$ into a set of N intervals, for each value of the threshold σ :

$$\{S(t); \sigma\} \rightarrow \{\Delta t_j^s; N^s\}. \quad (17)$$

Note that, since t_j^\pm are the zeros of the shifted signal, the sum $N = \sum_s N^s$ is generally much smaller than the number \mathcal{N} of discrete time samples of the discrete signal, $S_i \equiv S(t_i)$, $i = 1, \mathcal{N}$. In other words, while the standard indicators WSS and OSI correspond to a strong $\mathcal{N}:2$ compression of the signal, the TBD representation corresponds to a milder $\mathcal{N}:N$ compression. A basic advantage of scanning the structure of the signal with a running threshold is that the risk indicators become available for any value of the threshold, thereby conveying an idea of the risk sensitivity to fluctuations of the physiological threshold, as they may occur from individual to individual.

¹The time-averaged WSS signal is denoted by $\overline{\text{WSS}}$.

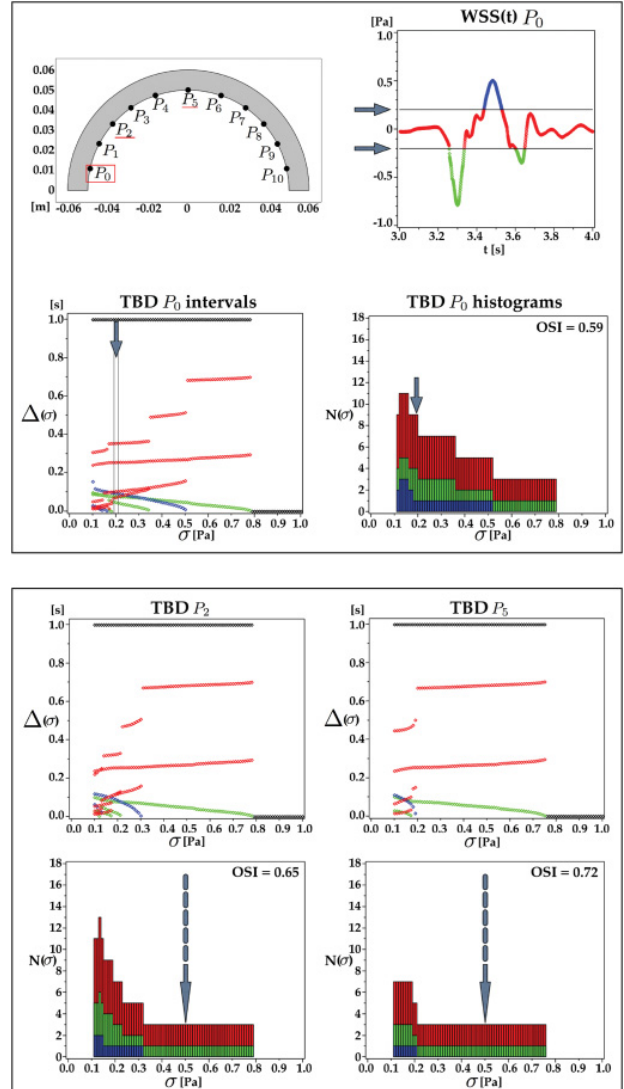


FIG. 8. (Color online) The three-band signal for the case of the regular corona at point P_0 (upper panel). As one can see, the signal and TBD data show a significant similarity to the analog data for the Bessel signal example. In the lower panel, shown are the TBD data at points P_2 and P_5 . The healthy nature of the signal at both locations P_2 and P_5 is evidenced by the broad nature of histograms, extending above the physiological threshold $\sigma = 0.5$ Pa, pointed to by the vertical arrow. This conclusion contrasts with the relatively high value of the OSI index, well above 0.5 Pa in both cases. Other locations, not shown for brevity, display the same qualitative behavior.

A. Pedagogical examples

As a pedagogical example, in Fig. 7 we show the TBDs associated with three toy functions: a sawtooth profile (top), a sinusoidal (middle), and a Bessel function $J_0(20t)$, (bottom). The left column shows the original signal, colored in red, green, and blue (RGB) for $S^0(t)$, $S^+(t)$, and $S^-(t)$, respectively. The middle column shows the trajectories $\Delta t_j(\sigma)$ as a function of the running threshold σ for the three RGB components.

The dark line at the top of the diagram verifies the sum of the intervals for each σ , which has to be equal to the duration of the considered signal (unitary). The number of trajectories (see right column) is a direct indicator of the variability of the signal around the given threshold σ , as best highlighted by the TBD of the Bessel function. Note that the TBD trajectories may eventually jump, bifurcate, or coalesce in correspondence with local extrema of the signal, where new intervals are suddenly generated or disappear. By definition, the blue and green components disappear as σ is increased; more precisely, green disappears when $\sigma > |S_{(\min)}|$ and blue when $\sigma > S_{(\max)}$. Also note that periodic signals generate a set of identical intervals, hence degenerate (superimposed) points along the trajectory. This degeneracy is reflected by the histograms reported in the third column, which show the number of RGB intervals as a function of σ . For strictly periodic signals, the histogram would be flat for all three components. The lower bound of the TBD histogram is discretionary, depending on the application, whereas the upper bound coincides with the maximum intensity of the signal. On a generic basis, healthy WSS signals should display all three RGB components above the absolute value of the critical threshold (0.5 Pa). For a direct test we also report the corresponding OSI value for each signal.

B. TBD analysis of the numerical versus experimental results

An example of a healthy situation is reported in Fig. 8, which shows the TBD associated with three probes P_0, P_2, P_5 in the inner boundary of the regular corona, as depicted in the upper left panel of the figure. The upper panel shows the RGB representation of the signal $S(t)$ as computed at point P_0 (the actual value of the threshold is indicated by the black lines). The time intervals and the corresponding numerosity histograms associated with a given threshold are also indicated by arrows. The same analysis, repeated at two spatial locations, P_2, P_5 , delivers the TBDs shown in the lower panel of Fig. 8. As can be clearly seen, at both spatial locations, the green component persists well beyond the critical threshold, which is a signature of a healthy situation. Incidentally, this is reminiscent of the Bessel function behavior previously discussed as a test bed. In addition, the TBD patterns are basically the same at the two locations, reflecting the quasihomogeneity of the flow commented on previously in this work. It is worth noting that in this case the OSI values are both high, implying a risky situation, which is not the simulated case. Other points show similar behaviors.

In Fig. 9, we contrast the TBDs for a healthy (denoted by H) and unhealthy (denoted by U) simulated signals, namely, the circular corona and the aneurysm-like geometry. As is

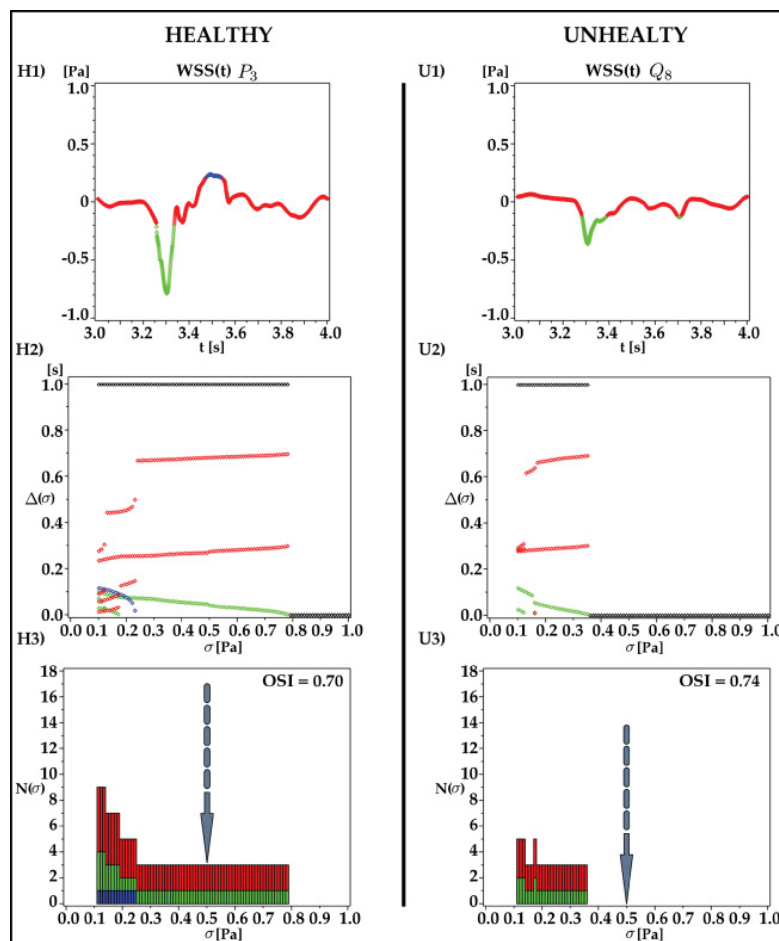


FIG. 9. (Color online) Three-band (top), trajectory (middle), and histogram (bottom) for a healthy (left) and unhealthy (right) signal. The healthy signal, at point P_3 in the circular corona, carries over the physiological threshold, while the unhealthy one, point Q_8 (for the zoomed geometry in the aneurysm in Fig. 10), does not. To be noted that the OSI index is very similar and pretty high in both cases, thus failing to highlight the absence of risk associated with the healthy signal.

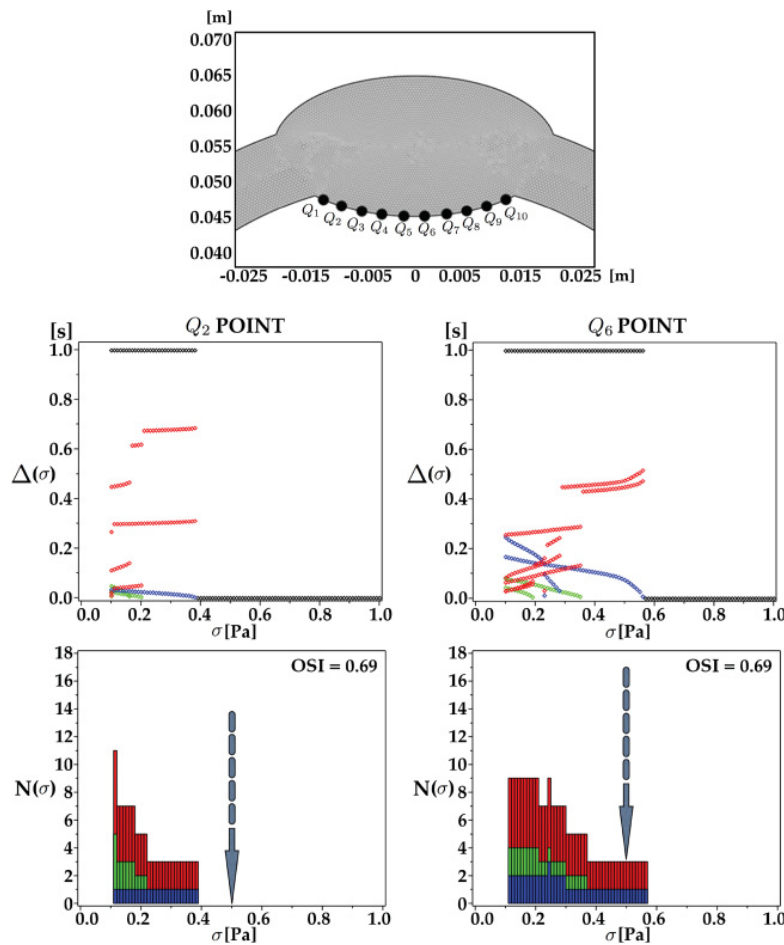


FIG. 10. (Color online) The three-band signals at points Q_2 and Q_6 within the aneurysm. Note that both locations provide the same OSI index, 0.69, even though the TBD histograms show a significant difference in the interval trajectories as well as in the histogram profiles, indicating a high risk in location Q_6 , which is not the case. The other points (not shown for space limitations) present an alternating TBD behavior between Q_2 and Q_6 . In particular, the outlet points Q_8 , Q_9 , Q_{10} behave quite similarly to the inlet ones Q_1 , Q_2 , Q_3 .

apparent from the original signals (H1, U1), the aneurysm signal is much flatter. The contrast between the two situations is further highlighted by the corresponding TBDs. Indeed, the unhealthy case displays very narrow TBDs (U2–U3), which do not extend above $\sigma \sim 0.35$ Pa, below the critical threshold $\sigma = 0.5$ Pa. Note that in the present case the OSI values are still high, implying for both signals a risky situation. However, only one of them (unhealthy) corresponds to a risky behavior.

In Fig. 10 we zoom into the aneurysm region (upper panel), and TBDs for point Q_2, Q_6 are given in the lower panels. The first observation is that TBD data show significant changes between the two locations, with the inlet point Q_2 (and similarly for point Q_8 , not shown) featuring the most hazardous histograms, below $\sigma = 0.4$ Pa. This heterogeneity shows that nearby regions of the inner aneurysm wall may be exposed to significantly different “physiological risk.” We

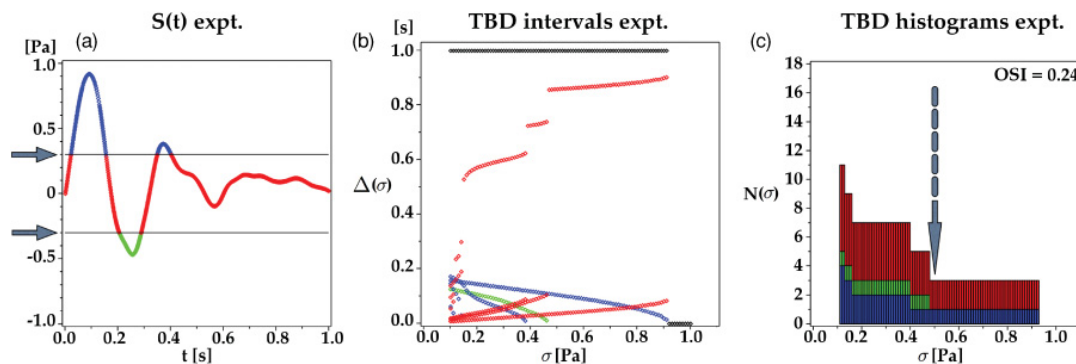


FIG. 11. (Color online) The three-banded (a) WSS signal from a healthy volunteer (see main text). The corresponding trajectories (b) and histogram (c) show a neat similarity with the healthy signals in Fig. 9. Note that here the OSI index as well as the TBD analysis confirms the healthy nature of the signal.

wish to emphasize a remarkable outcome of our analysis: two signals with essentially the same OSI value may correspond to “healthy” and “unhealthy” situations. On the other hand, such ambiguity is well resolved by the TBD histograms shown in panels (H3) and (U3) of Fig. 9.

As a further application, we present the TBD analysis of an experimental wall shear rate signal, taken from a healthy volunteer [see Ref. [22]; Fig. 11(a), and suitably interpolated for our analysis]. First, we note a striking similarity with the WSS signal simulated in the regular geometry (see Fig. 8, upper panel], which lends weight to the relevance of the numerical results. This similarity is faithfully reflected by the corresponding TBDs [see Figs. 11(c) and 11(d)], which show persistence of the blue component well beyond the critical threshold, as well as a remarkable similarity with the analog data for the case of the Bessel function previously discussed. In the present low-risk case, the OSI value is actually low and is compatible with the TBD analysis of the signal.

VI. CONCLUSIONS

Summarizing, we have investigated space-time patterns of wall shear stress (WSS) resulting from the numerical simulation of pulsating hemodynamic flows in semicoronal domains, both regular and with bumpy insertions, mimicking aneurysm-like geometries. To the purpose of extracting synthetic indicators of clinical risk from the space-time structure of the WSS, a new family of cardiovascular risk indicators, which we name three-band diagrams (TBDs), have been introduced.

As compared to standard \overline{WSS} and OSI, TBDs provide a handy access to additional risk information contained in the dynamic structure of the signal as a function of the physiological risk threshold. This allows a quick visual assessment of the risk sensitivity to individual fluctuations of the physiological risk thresholds. Also note that the TBDs described in this work are as easily computed as the \overline{WSS} and OSI and could therefore be automatized in connection with the analysis of any signal $S(t)$, be it of experimental or synthetic nature.

For the case of the regular semicorona, the TBD indicators point to a low-risk situation all along the spatial extension of the corona. In contrast, the aneurysm-like geometry is found to exhibit a highly heterogeneous, low-WSS distribution, eventually with sizable contrasts between nearby regions of the wall. Such heterogeneity adds to the complexity of predicting the long-term development of atherogenic pathologies.

The TBD analysis is also applied to an experimental WSS signal from a healthy patient and found to yield the same conclusions resulting from the simulations, namely, that healthy situations are associated with a substantial homogeneous permanence of the WSS signal above the physiological risk threshold.

We point out again that, in two numerically simulated scenarios, the standard OSI indicator does not seem to successfully discriminate between healthy and unhealthy situations, whereas TBDs appear to work more appropriately.

Finally, we wish to emphasize that the mathematical tools here introduced are not limited to hemodynamic studies, but readily extend to a broad class of applications dealing with risk-assessment analysis.

-
- [1] Y. S. Chatzizisis *et al.*, *Circulation* **117**, 993 (2008).
 - [2] C. Caro, J. Fitzgerald, and R. Schroter, *Nature (London)* **223**, 1159 (1969).
 - [3] A. M. Shaaban and A. J. Duerinckx, *Am. J. Roentgenol.* **174**, 1657 (2000).
 - [4] D. A. Vorp, D. A. Steinman, and C. R. Ethier, *Comput. Sci. Eng.* **51**, 64 (2001).
 - [5] Y. Wang and P. Dimitrakopoulos, *Phys. Rev. Lett.* **96**, 028106 (2006).
 - [6] C. A. Taylor and M. T. Draney, *Ann. Rev. Fluid Mech.* **36**, 197 (2004).
 - [7] L. Grinberg and G. Karniadakis, *Ann. Biomed. Eng.* **36**, 1496 (2008).
 - [8] M. D. Mazzeo and P. V. Coveney, *Comput. Phys. Comm.* **178**, 894 (2008).
 - [9] A. Artoli, A. Hoekstra, and P. Sloot, *J. Biomech.* **39**, 873 (2006).
 - [10] M. Fyta *et al.*, *Multiscale Model. Sim.* **5**, 1156 (2006).
 - [11] S. Melchionna *et al.*, *Comput. Phys. Comm.* **181**, 462 (2010).
 - [12] M. Bernaschi *et al.*, *Comput. Phys. Comm.* **180**, 1495 (2009).
 - [13] G. Amati *et al.*, *Int. J. Mod. Phys. C* **8**, 869 (1997).
 - [14] J. Soria and B. J. Cantwell, *Flow, Turbulence and Combustion* **53**, 375 (1994).
 - [15] T. J. Pedley, *The Fluid Mechanics of Large Blood Vessels* (Cambridge University Press, New York, 1980).
 - [16] M. Hirabayashi, M. Ohta, D. A. Rufenacht, and B. Chopard, *Phys. Rev. E* **68**, 021918 (2003).
 - [17] Comsol Multiphysics, Modeling and Simulation; see the Comsol website [www.comsol.com].
 - [18] L. Formaggia, A. Quarteroni, and A. Veneziani, *Cardiovascular Mathematics: Modelling and Simulation of the Circulatory System*, Vol. 1. (Springer, Milano, 2009).
 - [19] C. Egelhoff, R. Budwig, D. Elger, T. Khraishi, and K. Johansen, *J. Biomech.* **32**, 1319 (1999).
 - [20] S. C. Shadden and C. A. Taylor, *Ann. Biomed. Eng.* **36**, 1152 (2008).
 - [21] F. Chowicz *et al.*, *J. Magnetic Reson. Imag.* **30**, 77 (2009).
 - [22] J. R. Blake *et al.*, *Ultrasound in Medicine and Biology* **34**, 760 (2008).

A Bistable Field Model of Cancer Dynamics

C. Cherubini^{1,2,*}, A. Gizzi^{1,3}, M. Bertolaso⁴, V. Tambone⁴
and S. Filippi^{1,2}

¹ *Nonlinear Physics and Mathematical Modeling Lab, University Campus Bio-Medico, I-00128, Via A. del Portillo 21, Rome, Italy.*

² *International Center for Relativistic Astrophysics-I.C.R.A., University of Rome "La Sapienza", I-00185 Rome, Italy.*

³ *Alberto Sordi Foundation-Research Institute on Aging, I-00128 Rome, Italy.*

⁴ *Institute of Philosophy of Scientific and Technological Activity, University Campus Bio-Medico, I-00128, Via A. del Portillo 21, Rome, Italy.*

Received 27 July 2010; Accepted (in revised version) 22 February 2011

Communicated by Sauro Succi

Available online 5 September 2011

Abstract. Cancer spread is a dynamical process occurring not only in time but also in space which, for solid tumors at least, can be modeled quantitatively by reaction and diffusion equations with a bistable behavior: tumor cell colonization happens in a portion of tissue and propagates, but in some cases the process is stopped. Such a cancer proliferation/extinction dynamics is obtained in many mathematical models as a limit of complicated interacting biological fields. In this article we present a very basic model of cancer proliferation adopting the *bistable* equation for a single tumor cell dynamics. The reaction-diffusion theory is numerically and analytically studied and then extended in order to take into account dispersal effects in cancer progression in analogy with ecological models based on the porous medium equation. Possible implications of this approach for explanation and prediction of tumor development on the lines of existing studies on brain cancer progression are discussed. The potential role of continuum models in connecting the two predominant interpretative theories about cancer, once formalized in appropriate mathematical terms, is discussed.

AMS subject classifications: 92B05, 35K59

PACS: 87.19.xj, 87.23.Cc, 02.60.-x

Key words: Reaction-diffusion equations, cancer modeling, finite elements method.

*Corresponding author. *Email addresses:* c.cherubini@unicampus.it (C. Cherubini), a.gizzi@unicampus.it (A. Gizzi), m.bertolaso@unicampus.it (M. Bertolaso), v.tambone@unicampus.it (V. Tambone), s.filippi@unicampus.it (S. Filippi)

1 Introduction

The quantitative description of the form development in living beings is a central problem in Biology. The process of animal growth, or morphogenesis, occurs in Nature in a variety of shapes and patterns which seem to have typical regularities, as pointed out one century ago by Darcy Thompson in his classical work "On Growth and Form" [1]. Some biological populations of fungi and amoebae appear aggregated in complicated structures which often have a spiralling shape, but spirals of action potential are experimentally observed also in cardiac cell tissues and even in neural ones [2–5]. In plants complicated morphogenetic processes occur in the developmental process of *kinetic phyllotaxis* [6]. Finally it's worthwhile to notice that spiral waves appear not only in biological systems but also in unanimated ones as the chemical reactions of Zhabotinsky-Belousov type or the gaseous eddies in the atmosphere [4]. All of these different phenomenologies are seen as non-equilibrium thermodynamical processes which can be subject to complicated bifurcations in their dissipative dynamics [7–9] and which can be mathematically described, provided specific technical *caveats* regarding the validity of the continuum hypothesis, by systems of equations of Reaction-Diffusion (RD) class [4]. This type of partial differential equations have represented historically and still represents today a proper tool to deal with non-equilibrium chemical dynamics in fact (in particular when phenomena like oscillations, waves, pattern formation and turbulence occur). Alan Turing in the Fifties formulated an elegant theory for animal coats and morphogenesis using RD equations [10], so it appeared plausible to extend his successful theory to cancer growth processes whose understanding represents still today a major challenge for Biology [11]. Cancer is commonly believed to be a disease that begins at the cellular level. Its development is related with somatic mutations which are transferred from a cell to its progeny, bypassing controls of the immune system and being responsible then for the neoplastic phenotype. Therefore the initiation of cancer is mainly seen as a mutation that involves a set of regulatory genes [12], which either enhance or inhibit malignant properties.

On the other hand, tissues are relatively ordered complex structures which generate forces due to the adhesion between cells, the adhesion between cells and the extracellular matrix that surrounds them and the global property of the tissue itself. These interactions together with biochemical and electrical signals, contribute to the shape of the tissue and can even determine the cellular fate [3]. Cell-to-cell and/or tissue-to-tissue communication represent fundamental aspects which contribute to tissue organization then and their failure can generate cancer [13, 14]. Specific substances (morphostats) analogous to Turing morphogen fields drive this communication: their local concentrations in particular influence the phenotype of neighboring regions of tissue around the specific cell taken in considerations. Some substances which have the properties of the morphostats have been recently identified [15] but it is still unclear their hierarchy, and in particular the way in which they promote carcinogenic processes. One can interpret these results using the most diffused paradigm in cancer dynamics, the Somatic Mutation Theory (or SMT) which proposes that successive DNA mutations in a single cell cause cancer cell

proliferation placing carcinogenesis at the cellular and subcellular hierarchical levels of biological complexity [16] (a paradigm which in short sounds as "the cell is all"). In some sense this epistemological approach, transferred to the different scenario of Condensed Matter Physics (or Chemistry) could read as "single atoms are everything", which clearly is in contrast with the fact that matter is made by molecules which get organized in larger spatial ordered or disordered structures accounting for very different (and at a first glance unexpected) macroscopic properties. This analogy suggests that in cancer dynamics too spatial organization must be considered. This point of view is taken into account in another paradigm, the Tissue Organization Field Theory (or TOFT) of carcinogenesis and neoplasia. Here in particular carcinogens would act initially by disrupting the normal interactions that take place among cells in the parenchyma and stroma of an organ (the equivalent of the "morphogenetic fields" of developing organisms) [17]: perturbations in a morphostat gradient could initiate then carcinogenesis without any requirement for a mutation [18]. Nevertheless diffusive effects seem to be relevant, from a biological point of view, also at sub-cellular level as recent studies on the telomere dynamics performed in live human cancer cells have shown [19]. In this sense the reaction and diffusion mathematical point of view adopted in this article can be seen as a tool to deal with the same problem observed at different scales (a *multiscale* approach) for which a continuum mathematical theory remains valid. TOFTs main contribution has been to put the question about the right level of inquiry in experimental research and to have proposed one (tissue organization) for the neoplastic phenomenon that seems to be consistent with empirical data and evidences. In this scenario it is possible in any case the epistemological contribution of SMT admitting that a discrete component is also present and active in the dynamics of cancer spread, in this case cells.

We point out that such an idea of a field theory of cancer development is very appealing from the point of view of mathematical modeling. Solid tumor proliferation can be seen in fact as an abnormal morphogenetic process *a la Turing*, consequently it appears straightforward the idea of modeling this nonlinear diffusive biological phenomenon with the RD mathematical theory. On the other hand however SMT view is not absolutely ruled out by this choice when the challenge is to take into account the whole phenomenology of such a complex natural phenomena as cancer is.

As it will appear clear in the following, a reaction-diffusion equation shall account for both the diffusive gradients required by tissue organization previously discussed (clearly evidenced by TOFT) and local reactive cellular dynamics both of genetic (evidenced by SMT) and/or of environmental nature (again stressed by TOFT) performing an integration in this way of different existing theories on cancer [20]. In the simplest scenario a mathematical cancer model should manifest bistability. This is a critical behavior for the dynamics of a system which can choose in its evolution to settle down on one of two possible states. In an elementary picture justifying this choice, there is a threshold of cancer cells density (which should be patient dependent), which locally drives the normal tissue on a cancer cell regime or does not admit cancer to colonize the tissue so that this remains tumor-free (this is, mathematically speaking, a "reaction term"). A diffu-

sive contribution makes cancer cells move around leading to a not only time but also space dependent problem. While continuum models (ordinary, partial or integro-partial differential equations or delay equations) can describe very well this cancer dynamics, also discrete models (cellular automata) seem to lead to positive results towards a possible understanding of carcinogenesis [18]. This is not unexpected in fact because discrete models (as cellular automata are) and continuum diffusion processes share many common features in modeling nonlinear chemical and biological media [21,22]: in particular continuum field theory can be seen as continuum limit of collective discrete behaviors. Mathematical modeling of bistability in cancer dynamics dates back to Lefever and Horthemke work [23] although in the last thirty years many progresses have been done in this area (see as an example [24] for a recent review on mathematical models). In existing models bistability results as a consequence of complicated non-polynomial reactive terms.

In this article instead we shall introduce and discuss a very basic model of reaction-diffusion bistability based on a cubic nonlinear diffusion equation only. This is inspired by theoretical works calibrated on experimental data of brain tumor (see specifically [3, 25–30]) through a single linear or nonlinear diffusion equation for cancer cells. Assuming a relatively simple mathematical form, these pre-existing studies have shown a great relevance for surgery due to the unpleasant and dramatic recurrences of brain tumors. Given a certain volume of brain tissue resection in fact, it is possible to predict the amount of time required by the low density infiltrated tumor cells far afield from the gross tumor site to cause a large cancer again. In this way the surgeon can perform a balanced prediction optimizing the amount of tissue removed in union with the quality of life left to the patient. We shall frame our work on the lines of this type of studies then. To this aim however we shall need to introduce a short review of the mathematical aspects of RD processes first, as done in the next section.

2 Reaction-Diffusion systems

Reaction-Diffusion equations are mathematical models of parabolic type which describe the nonlinear concentration dynamics of one or more chemical substances. Differently as in standard global chemical kinetic problems, here the model allows the chemical species not only to locally react but also to spatially diffuse one through the others. In a biological context instead RD systems describe fields of activators and inhibitors (in the language introduced by Alan Turing in [10]) which compete to give peculiar patterns (the animal coat pattern theory) or even forms for the living beings (in Turing's original article the problem of gastrulation or of the form of an hydra). Here we present the prototype of reaction-diffusion equations which assumes two variables only together with homogeneous and isotropic diffusion. The equations in this case result in:

$$\frac{\partial u}{\partial t} = D_1 \nabla^2 u + f(u, v), \quad \frac{\partial v}{\partial t} = D_2 \nabla^2 v + h(u, v), \quad (2.1)$$

where f and h can have polynomial form in u and v , although more complicated functional dependencies (even on space and time) are allowed. Here D_1 and D_2 are the diffusion coefficients and ∇ is the gradient operator while ∇^2 represents the Laplacian one. In general, models with two species only represent a simplification of more realistic situations in which several diffusing and reacting species can interact. Moreover by coupling these models with temperature [31, 32] and mechanical deformations [33, 34] one can match even more the simulations with realistic biological problems. In the past, Turing showed that RD systems can be affected by the so called diffusion-driven instability (or Turing instability) which means that if the homogeneous state is stable against small perturbations in absence of diffusion, it may become unstable if the possibility of diffusion is introduced. This dynamical mechanism generates quasi-stationary spatial patterns although this type of equations can also lead to morphogenetic, chemical or electrophysiological waves [3]. Coming back to the model, an even simpler reaction-diffusion model can be obtained suppressing one of the two species in Eq. (2.1) (say field v) and assuming a simple cubic polynomial form for the function $f(u)$ which could be seen as a Taylor expansion of more complicated functional dependencies, in analogy with FitzHugh-Nagumo type models of electrophysiology and physical chemistry [3, 35]: this is the well-known bistable equation discussed in detail in the following.

3 A bistable model for cancer cell waves

The most generic one species reaction-diffusion equation is

$$\partial_t c = \underbrace{F(c)}_{\text{Reaction}} + \underbrace{\nabla \cdot (\hat{D} \nabla c)}_{\text{Diffusion}}, \quad (3.1)$$

where we identify for our purposes the field c with the tumor cell punctual concentration embedded in a pre-existing normal tissue and \hat{D} is the diffusion tensor which in the most general scenario can depend by time and space (anisotropic and inhomogeneous diffusion). In this article however we shall assume for the sake of simplicity homogeneous and isotropic time independent diffusion first so that we can rewrite

$$\nabla \cdot \hat{D} \nabla c \equiv D \nabla^2 c,$$

where D is the diffusion constant. The term $F(c)$ on the other hand takes into account the local dynamical properties of the system (reaction term) although one may extend the treatment assuming $F = F(c, t, \vec{x})$, which gives heterogeneities of different physical nature (chemical, biological, physical). Finally one may could have easily added on this reactive term of Eq. (3.1) an external time and space dependent stimulus which in our specific biological problem can account for possible external actions (chemotherapy as an example). We have under-braced explicitly in Eq. (3.1) the reactive and diffusive terms respectively. While the diffusive part can be seen as a typical TOFT quantity, the reactive

one, in the most general heterogeneous externally perturbed scenario, can contain both a genetically driven dynamics and an environmental factor: this modelization meets then both TOFT and SMT points of view about cancer origin. In mathematical terms, in absence of diffusion we have a dynamical system with one degree of freedom (an Ordinary Differential Equation), while the introduction of diffusion leads immediately to an infinite degrees of freedom problem (this is a Partial Differential Equation problem in fact) where the nonlinear parabolic character of the problem accounts for spatial communication and then possible global organization. We are ready now to specialize Eq. (3.1) to a particular case, i.e., the bistable one, which requires for this equation a functional form $F(c) = k(c - c_1)(c - c_2)(c_3 - c)$, where k is a model constant and c_1 , c_2 and c_3 are constant concentrations which may be genetically determined but also environmentally affected. We assume that a cancer-free tissue must have no cancer cells so we select $c_1 = 0$. Quantity c_2 instead represents the cancer generation threshold while c_3 is the maximum value of cancer cells which a tissue can support (possible necrosis effects lowering the tumor cell population are not taken into account here for the sake of simplicity). This equation must be cast now in non-dimensional form: this step is crucial because removes from the model the specifications of the particular tissue and cancer leading to a more general formulation. Following standard Literature [35], we introduce a typical length scale L of the process in consideration (working for the sake of simplicity in one spatial dimension first) and we define the non-dimensional quantities $T = tD/L^2$ and $X = x/L$. We use moreover the scaling $c_2 = \alpha c_3$ with $0 < \alpha < 1$, adopting a dimensionless concentration $C = c/c_3$ then and defining the quantity $a = c_3^2 L^2 k / D$. The resulting equation is:

$$\frac{\partial C}{\partial T} = \frac{\partial^2 C}{\partial X^2} + F(C), \quad (3.2)$$

with the functional form

$$F(C) = aC(1 - C)(C - \alpha) \quad (3.3)$$

with $C = 0$ and $C = 1$ being sinks and $C = \alpha$ being a source [36]. The process of adimensionalization performed has a great advantage that one can study now the dynamics of the problem forgetting about the physical context we started from. The result obtained with the new compact equations can be later re-converted then to dimensional quantities recovering the contact with experiments. This is a well known point of view adopted both in chemistry and in electrophysiology. In the latter case, as an example, the FitzHugh-Nagumo equation (which is an extension in a two dimensional phase-space of the bistable equation just described), once solved in a specific dimensionless case can be differently framed in the context of heart, nerves or even intestine dynamics [35] through specific dimensional mappings of space, time and action potential. We point out that, all of these examples have different time, space and action potential scales. For this reason, in this article we shall present mainly the general outcomes expected studying the non-dimensional theory, leaving to future studies the accurate analysis of mapping the

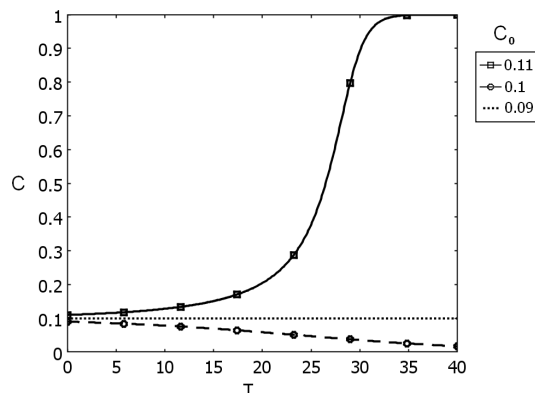


Figure 1: Bistable dynamics of the zero dimensional model with three different initial conditions: i) $C_0 \equiv C(0) = 0.11$ (above the threshold α which implies cancer development); ii) $C_0 = 0.1$ (on the threshold which implies a (metastable) constant in time dynamics) and finally iii) $C_0 = 0.09$ (below the threshold which implies cancer rejection by tissue).

parameters with specific tumor growth processes and for different tissues. Higher dimensional spatial cases require the addition to this equation of the second derivative terms with respect to Y and Z . We point out that our treatment is quite different with respect to the standard Verhulst logistic behavior commonly used to model cell growth [3,24,35,36]: here in fact we have a cubic behavior while in that case a quadratic one is adopted, missing completely the threshold effect. Locally, i.e., neglecting the spatial variations, we obtain the ordinary differential equation $dC/dT = F(C)$ which is, in the language of dynamical systems, a flow on a line. Such a type of equation cannot have periodic solutions (unless the domain is topologically bent to form a circle [36]) and once integrated (we assume here and in the rest of the paper $a = 1$ and $\alpha = 0.1$ which is a typical choice found in the literature of bistable equation simulations [35]) results in three type of possible solutions shown in Fig. 1: i) a solution which starting over the threshold α reaches asymptotically the maximum value $C = 1$, ii) a solution starting on the threshold which is stationary in time and iii) a solution starting below the threshold which asymptotically goes to zero.

Reintroducing diffusion we have a partial differential equation which as discussed before, has infinite degrees of freedom and can lead in fact to more involved situations in which diffusion plays a central role. Manipulations of the one-dimensional diffusing case in Eq. (3.2) lead to the analytical travelling wave solution for the bistable equation associated with specific initial data and boundary conditions (well known in the literature) [35]

$$C(T, X) = \frac{1}{2} + \frac{1}{2} \tanh \left[\frac{\sqrt{a}(X + VT)}{2\sqrt{2}} \right], \quad V = \frac{\sqrt{a}}{\sqrt{2}}(1 - 2\alpha). \quad (3.4)$$

It is clear the wave type behavior of this solution which travels at constant speed (de-

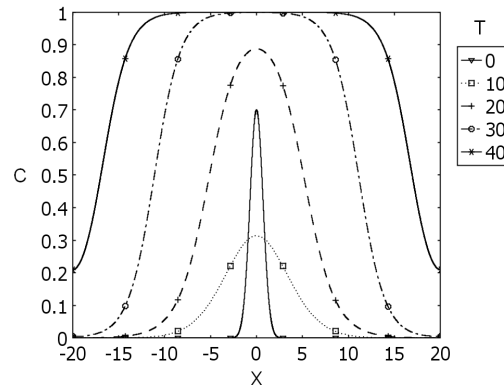


Figure 2: Spatial cancer progression in time on a linear tissue domain (dimensionless units). For the fixed threshold and initial data (see text) cancer front blows down but then recovers and colonizes the entire tissue.

pending by parameters a and α) transferring cancer to not invaded tissue regions. In more general situations associated with complicated initial data and boundary conditions however analytical solutions cannot be found anymore and the equations must be numerically integrated, leading to even more interesting scenarios. To this aim, we have performed an integration of the 1D bistable equation (3.2) on the domain $X \in [-20, 20]$ (dimensionless units) with Neuman zero flux boundary conditions, $\alpha=0.1$, $a=1$ together with initial data $C(0, X) = 0.7\exp(-x^2)$ first. In all the simulations performed we have adopted a finite element scheme using quadratic Lagrange elements with size $\delta x = 0.005$ together with a direct solver (UMFPACK) running on a parallelized Comsol Multiphysics engine with relative and absolute errors of 10^{-6} . Simulations have been tested also for finer spatial meshing in order to ensure convergence and stability.

In Fig. 2 we show superimposed at different times the behavior of the tumor cell concentration on the line of tissue. At $T = 10$ the concentration apparently gets lowered but at time $T = 20$ it starts to rise again. At $T = 30$ the central part reaches the maximum value of tumor cells and at late times the entire tissue domain gets invaded.

On the other hand starting with a lower initial cancer cell concentration, i.e., $C(0, X) = 0.3\exp(-x^2)$, the cancer colonization fails (see Fig. 3). It appears clear that such a diffusion driven mechanism is quite delicate in generating a tumor scenario or not, depending in fact on the total (non-dimensional) tumor mass amount $M = \int C dX$ evaluated on the whole tissue domain at the initial time. The initial conditions which can generate a full tumor outcome represent then a delicate problem to be addressed requiring advanced mathematical methods of dynamical systems (for a specific discussion of this point see [35] on pp. 275). In this article on the other hand we have preferred to study this point by performing selected *ad hoc* numerical simulations which can give us some hint on the role of cancer cells density peaks and in particular of their distance. To this aim we have extended our study to a two dimensional squared domain of 20×20 area (in dimensionless units). The code uses similar settings as the one dimensional case but

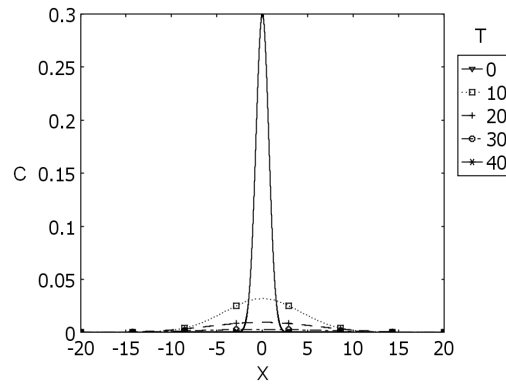


Figure 3: Spatial cancer no-progression in time on a linear tissue domain (dimensionless units). For the fixed threshold and initial data (see text) cancer front blows down and tissue remains cancer cell free.

regarding the meshing we have adopted squared sized (side length $\delta x = 0.25$) Lagrange cubic elements.

Results of the simulations are shown in Fig. 4. We have taken an initial data adding several distorted Gaussian functions centered at different points. In this approach, for a fixed choice of model constants α and a , there are clearly three critical parameters which can affect the entire dynamics: the Gaussian peak amplitudes, their widths and finally their distance. In our case we have chosen specifically:

$$C_0 = 0.8e^{-0.1(x-1)^2 - 0.3(y-3)^2} + 0.75e^{-0.25(x-10)^2 - 0.15(y+9)^2} + 0.6e^{-0.2(x+3)^2 - 0.5(y+4)^2} + 0.5e^{-0.25(x+5)^2 - 0.3(y-1)^2} \quad (3.5)$$

and left it free to evolve. The remaining panels of Fig. 4 show the cancer spread and finally a large scale invasion dynamics. We have performed also a more simplified study in order to understand if two over-threshold cell colonies of Gaussian form may lead to a tumor progression or extinction scenario depending on the distances of their peaks only. To this aim we have taken as initial data

$$C_0 = 0.61e^{-0.1(x-4)^2 - 0.3y^2} + 0.61e^{-0.1(x+4)^2 - 0.3y^2}, \quad (3.6)$$

which has lead to a final tumor progression as shown in Fig. 5.

On the other hand the initial data

$$C_0 = 0.61e^{-0.1(x-6)^2 - 0.3y^2} + 0.61e^{-0.1(x+6)^2 - 0.3y^2} \quad (3.7)$$

has not given any tumor progression as shown in Fig. 6. These results suggest that the nonlinear interaction of the two waves leads to a critical configuration which has cancer as an outcome, while if the two distorted Gaussian colonies are slightly more distant, the nonlinear mechanism is not sufficient to maintain the developmental process and the

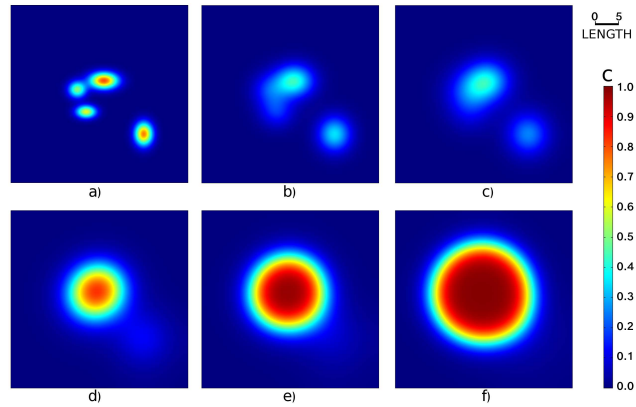


Figure 4: Spatial cancer progression at different times on a two-dimensional tissue domain (dimensionless units). Labels a) to f) stand for snapshot times of $T = (0, 2, 6, 15, 21, 27)$. Starting from a relatively irregular inhomogeneous initial data (see text), some cancer regions tend to blow down, but at the end one of the peaked populations is able to colonize the entire tissue.

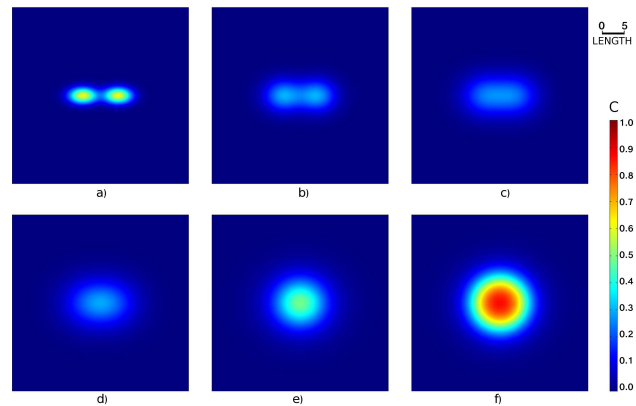


Figure 5: Spatial cancer progression at different times on a two-dimensional tissue domain (dimensionless units) for two distorted Gaussian populations with close peaks. Labels a) to f) stand for snapshot times of $T = (0, 3, 6, 11, 23, 30)$: in this scenario cancer cells are able to colonize the entire tissue due to their nonlinear interaction.

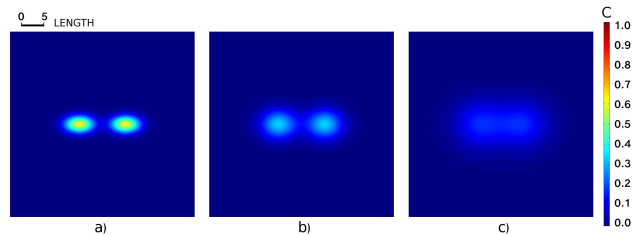


Figure 6: Spatial cancer progression at different times on a two-dimensional tissue domain (dimensionless units) for two distorted Gaussian initial populations with distant peaks. Labels a) to c) stand for snapshot times of $T = (0, 2, 8)$: in this scenario cancer colonization fails and the tumor cells decay very fast towards null concentration.

total cancer cells density vanishes in time. This model generalized in three dimensions (blocks of tissue) has to be calibrated on experiments, in order to estimate a realistic initial data, the diffusion coefficient and the physiological threshold α which could be patient dependent and possibly genetically and/or environmentally ruled [37].

Clearly stochastically induced mutations as well as instabilities driven by diffusion, angiogenesis and so on must play an important role in cancer development (see [24] and the more recent [38] for a discussion on the role of field theories in carcinogenesis). On the other hand, as anticipated already, an active field of research in tumor modeling adopts a *single* reaction-diffusion equation (see [3, 25–30] for details) to model solid cancer growth in anatomically correct 3D brain geometry (as already analyzed in [39] by some of the authors).

4 Bistable dynamics with ecological dispersal effects

We can now extend in a novel way the theory previously introduced, borrowing from the ecological models the possibility to have population dispersal. Discrete models [40] have been proposed to reproduce these properties. In this work we propose a continuum approach instead. The starting point of such a formulation is the experimental evidence that populations of animals in a territory diffuse with a certain (mean) speed depending by the density of animals in that region. Stated in a more straight way, if there are too many individuals in certain region, they tend to exhaust rapidly the local food supplies so that they should abandon the area as soon as possible. If their concentration is not so high on the other hand, they could spread around more slowly. Clearly such a point of view should work correctly also for bacteria, viruses and other microorganisms as well as for solid cancer cells, which in this simplified scenario would migrate because of the ecological pressure. Clearly this is a very basic starting point for more refined modelizations which should take into account also the role of chemotaxis and angiogenesis [3] together with advective effects for oxygen and nutrients and the importance of the immune system in these matters. Anyway this simplified point of view makes the formulation non-trivial because it requires mathematically to have a diffusion coefficient which depends by the local concentration of the diffusing field, i.e., in our case $\hat{D} = \hat{D}(c)$. Borrowing again from ecological models the theoretical formulation, we assume the isotropic power law functional dependence $\hat{D} = D \cdot [c(t, \vec{x}) / c_{ref}]^m \hat{I}$, where D is the diffusion constant, c_{ref} is a reference constant concentration, here introduced for dimensional analysis reasons, m is a non negative real number and \hat{I} is the identity matrix. Rewriting $c_{ref} = \sigma c_3$ with $\sigma > 0$, and adopting the same non-dimensional quantities previously discussed, we finally arrive to the dimensionless equation

$$\frac{\partial C}{\partial T} = \sigma^{-m} \nabla \cdot (C^m \nabla C) + F(C), \quad (4.1)$$

which in the limit $m \rightarrow 0$ reduces to the standard bistable equation previously discussed (in 1D Eq. (3.2)) while if $F(C) = 0$, becomes the porous media equation which has an-

analytical solutions in one dimensions [3]. Eq. (4.1) in 1D can be studied with the usual procedure adopted to find travelling wave solutions. Requiring $C = C(X + VT) \equiv C(\xi)$ (here V is the constant velocity of the pulse), it becomes

$$\sigma^{-m} \frac{d}{d\xi} \left(C^m \frac{d}{d\xi} C \right) - V \frac{dC}{d\xi} + F(C) = 0, \quad (4.2)$$

which could be possibly studied in search of analytical solutions or numerically as a boundary value problem for the allowed values of the constant V , again. Although this would lead to an interesting mathematical problem, from the physical point of view, such travelling waves of constant velocity V should be regarded in the best case as asymptotic states in time of more complicated solutions which already in the 1D case do not travel always at constant speed. The reason for this is that the dimensionless velocity of the standard bistable pulse in Eq. (3.4), once rewritten in dimensional variables, gives a velocity which grows linearly with the (constant) diffusion coefficient. The addition of dispersal implies a non constant diffusion coefficient (monotonically increasing with field concentration) so that, if one assumes a very slow growth of the density, the speed of the pulse too should change analogously and a constant speed travelling wave would not be possible. However, once the system reaches its highest asymptotic concentration value due to the bistable dynamics, practically a constant diffusion coefficient occurs so that constant speed travelling wave appears. In order to prove this scenario and have a complete view of the real dynamics of this extended model, we have studied Eq. (4.1) adopting the same codes for the numerical simulation previously discussed in the simple bistable case, requiring for the sake of simplicity $\sigma = 1$ and $m = 1$ (a linear growth for diffusion in function of concentration which is in agreement with the literature [3]).

In Fig. 7 (to be compared with Fig. 2) we show the evolution of the tumor at different times with initial data $C(0, x) = 0.7 \exp(-x^2)$ again. Notice the sharp interface of the cell front with the zero tumor region, which is totally absent in the simple diffusive case. The inclusion of the porous medium term in fact leads to a quasilinear partial differential equation, eliminating the unpleasant regularizing effect of the heat operator which generates a nonzero concentration in the entire domain (infinite propagation velocity).

In Fig. 8 (to be compared with Fig. 3) we can see that, differently than in the diffusive case, the smaller initial data $C(0, x) = 0.3 \exp(-x^2)$ leads in any case to tumor cell progression which has a different propagation velocity in time. In fact by focusing on the X -axis, one can see that at equidistant time intervals, the interface covers different spaces manifesting the expected concentration-dependent velocity of propagation which, once the upper concentration limit is reached, becomes approximately constant, confirming the physical scenario previously hypothesized.

A space-time diagram of the latter simulation shows this effect quantitatively as shown in Fig. 9 where there is a strong change in the slope (so in speed) due to the change of concentration. In Fig. 10 we present instead the space-time diagram for the interaction of the two initial data just discussed by assuming $C(0, X) = 0.7 \exp(-(x - 10)^2) + 0.3 \exp(-(x + 10)^2)$. We point out the change in slopes of the smaller distorted Gaussian in comparison

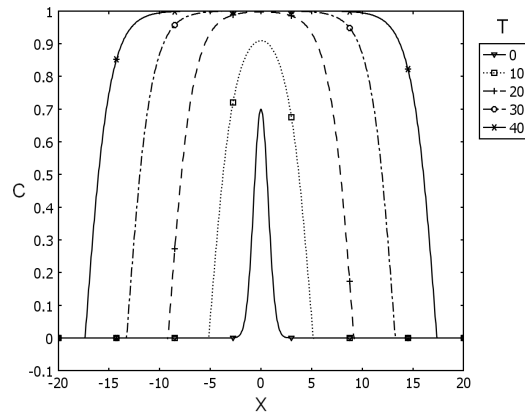


Figure 7: Spatial cancer progression in time on a linear tissue domain (dimensionless units) in the case of population dispersal for initial data $C(0,x) = 0.7\exp(-x^2)$.

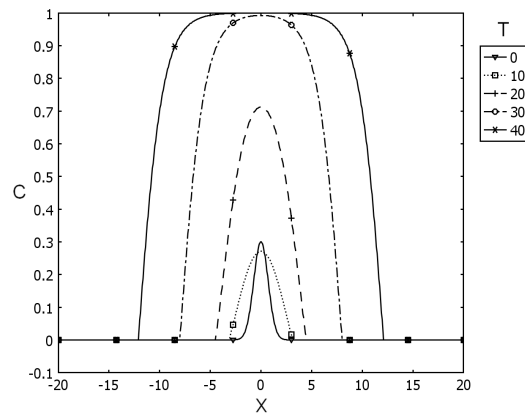


Figure 8: Spatial cancer progression in time on a linear tissue domain (dimensionless units) in the case of population dispersal for initial data $C(0,x) = 0.3\exp(-x^2)$. Differently as in the simpler reaction-diffusion theory, here even smaller initial data can lead to tumor progression.

with the higher one and the nonlinear interaction on the collision area.

We can now analyze the dynamics in higher dimensional cases. In three dimensions, assuming a purely radial dynamics, one starts from cartesian coordinates, adopts the same non-dimensional notations as in the one-dimensional case, and passing to dimensionless spherical coordinates (R, θ, ϕ) , finally obtains:

$$\frac{\partial C}{\partial T} = \frac{\sigma^{-m}}{R^2} \frac{d}{dR} \left(C^m R^2 \frac{d}{dR} C \right) + F(C). \quad (4.3)$$

This spherical scheme shall have relevance for realistic NMR imported 3D brain geometries, on the lines of precedent studies of some of the authors [39], performing a fine

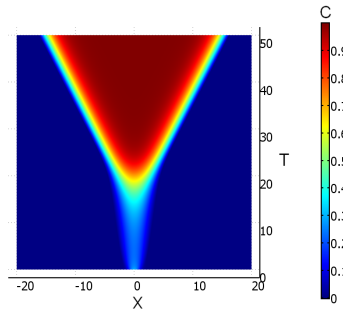


Figure 9: Space-time diagram of cancer progression in time on a linear tissue domain (dimensionless units) in the case of population dispersal for initial data $C(0,x) = 0.3\exp(-x^2)$. Notice the change of slope meaning a change of tumor progression speed.

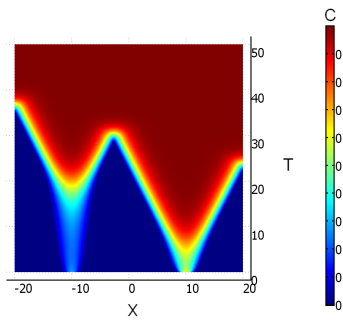


Figure 10: Space-time diagram of cancer interaction for the initial data $C(0,X) = 0.7\exp(-(x-10)^2) + 0.3\exp(-(x+10)^2)$. Due to the dispersal term the various populations interact nonlinearly with different speeds.

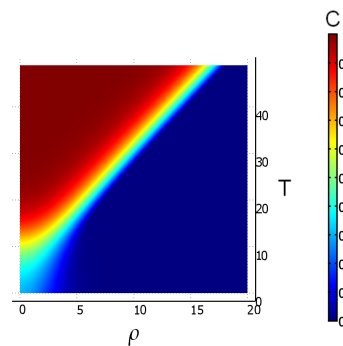


Figure 11: Space-time development of cancer growth in the cylindrical (planar radial) self-diffusing case for initial data $C(0,\rho) = 0.3e^{-0.1\rho^2}$.

tuning of the model parameters with radiological data taken at different times. Another possible field of application of this modelization is in the context of cancerous cell cultures. In circular dimensionless cylindrical coordinates (ρ, ϕ, Z) , assuming purely radial

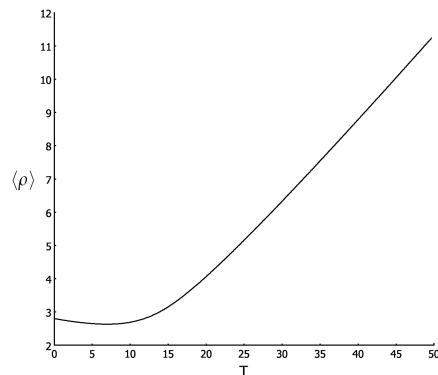


Figure 12: Mean value of tumor radius versus time in the case of Fig. 11.

diffusion (typical of cell cultures situations which are almost planar) we obtain instead

$$\frac{\partial C}{\partial T} = \frac{\sigma^{-m}}{\rho} \frac{d}{d\rho} \left(C^m \rho \frac{d}{d\rho} C \right) + F(C). \quad (4.4)$$

Taking as initial data $C(0, \rho) = 0.3e^{-0.1\rho^2}$ and zero flux again as boundary conditions [41], we obtain the spacetime diagram in Fig. 11.

In Fig. 12 we have plotted instead the mean radial distance of the cancer population from the origin versus time (see [3] pp. 553 for this definition), i.e.,

$$\langle \rho \rangle = \frac{\int_0^{\rho_0} \rho^2 C(\rho, T) d\rho}{\int_0^{\rho_0} \rho C(\rho, T) d\rho}, \quad (4.5)$$

where ρ_0 represent the outer boundary of the Petri dish which in our case has value twenty space dimensionless units. On page 555 of [3], based on experimental results by [42], an estimate, *in vitro*, of an (approximate) value of the mean radius versus time for an anaplastic astrocytoma, a mixed glioma and a glioblastoma multiforme cultures growing can be found. More in detail it is approximated by

$$\langle \rho \rangle \simeq \frac{\int_{\lambda}^{\rho_0} \rho(\rho - \lambda) C(\rho, T) d\rho}{\int_{\lambda}^{\rho_0} \rho C(\rho, T) d\rho}, \quad (4.6)$$

where λ^2 represents the uniform steady state of the cell distribution. Scaling the variables it is possible to obtain a growing trend for the tumor mean radius in qualitative agreement with some of these experiments, in particular in the case of the mixed glioma. The two other types of tumors on the other hand manifest a different regime so our model should be fine tuned also in the functional form of $D(c)$ in order to fit these data. A set of parametric simulations in which (m, σ, a, α) are varied shall improve the agreement of the model with experiments, especially for values of m close to zero (i.e., standard diffusion). We plan to perform all of these works in future studies in union with additional experimental data [37].

5 Conclusions

In this article we have introduced and discussed a very basic model of cancer spread which grasps the main feature of solid cancer progression in tissues, i.e., the possibility for the tumoral cell colonization to occur or the blocking action of this process due to different biological reactions of the organism. The model is based on the bistable equation, which can be seen as a polynomial approximation [36] for many different more complicated biological scenarios making the formulation very general. The inclusion of dispersal effects makes the formulation absolutely nontrivial but much more interesting because of the possibility to have different propagation speed in association with different cancer cells densities in the tissue. It is important to remark also that this modelization could play a central role not only in the field of cell growth modeling but also in the field of computational electrophysiology where reaction-diffusion theory with simple diffusion (and not with porous medium term) is commonly adopted to study electrochemical waves in biological media.

This article is a starting point for a field theoretical approach of cancer progression formulated in terms of very basic but at the same time very general equations aiming to extend in future the successful experimental and theoretical works regarding brain cancer [3, 25–30] with the techniques on real brain geometries developed by some of the authors in the past. The hope is to find, through mathematical modeling, some general behaviors which could be extrapolated from the patient dependent specific scenario, in analogy with other branches of Theoretical Physics in which apparently different systems simplify towards a common description once well expressed in mathematical terms. Such a formalization of cancer spread can bridge the requirements of the major existing interpretative theories. Nevertheless, any methodological approach needs a greater awareness of the complexity of the organism, which appears nowadays more and more evident, in order to develop consistent mathematical tools for modeling.

Acknowledgments

Two of the authors (C. Cherubini and S. Filippi) acknowledge ICRANet for partial financial support.

References

- [1] W. T. D'Arcy, *On Growth and Form*, Cambridge University Press, 1992.
- [2] D. Bini, C. Cherubini, S. Filippi, A. Gizzi and P. E. Ricci, On spiral waves arising in natural systems, *Commun. Comput. Phys.*, 8 (2010), 610–622.
- [3] J. D. Murray, *Mathematical Biology*, 3rd edition in 2 volumes, Springer, 2004.
- [4] A. T. Winfree, *The Geometry of Biological Time*, 2nd edition, Springer, 2001.
- [5] A. T. Winfree, *When Time Breaks Down: The Three-Dimensional Dynamics of Electrochemical Waves and Cardiac Arrhythmias*, Princeton University Press, 1987.

- [6] R. V. Jean, *Phyllotaxis: A Systemic Study in Plant Morphogenesis*, Cambridge University Press, 1994.
- [7] Y. Kuramoto, *Chemical Oscillations, Waves and Turbulence*, Dover, 2003.
- [8] D. Kondepudi and I. Prigogine, *Modern Thermodynamics: From Heat Engines to Dissipative Structures*, Wiley, 1998.
- [9] I. R. Epstein and J. A. Pojman, *An Introduction to Nonlinear Chemical Dynamics*, Oxford University Press, 1998.
- [10] A. M. Turing, The chemical basis of morphogenesis, *Phil. Trans. Roy. Soc. B*, 237 (1952), 37–72.
- [11] C. Panetta, M. A. J. Chaplain and J. Adam, The mathematical modelling of cancer: a review, *Proceedings of the MMMHS Conference* (eds. M. A. Horn, G. Simonett and G. Webb), Vanderbilt University Press, 1998.
- [12] E. R. Fearon and B. Vogelstein, A genetic model for colorectal tumorigenesis, *Cell*, 61 (1990), 759–767.
- [13] A. M. Soto and C. Sonnenschein, The somatic mutation theory of cancer: growing problems with the paradigm, *BioEssays*, 26 (2004), 1097–1107.
- [14] C. Sonnenschein and A. M. Soto AM, Theories of carcinogenesis: an emerging perspective, *Semin. Cancer Biol.*, 18 (2008), 372–377.
- [15] J. D. Potter, Morphostats, morphogens, microarchitecture and malignancy, *Nat. Rev. Cancer*, 7 (2007), 464–474.
- [16] R. A. Weinberg, *One Renegade Cell: How Cancer Begins*, New York, Basic Books, 1998.
- [17] C. Sonnenschein and A. M. Soto, Somatic mutation theory of carcinogenesis: why it should be dropped and replaced, *Mol. Carcinog.*, 29 (2000), 205–211.
- [18] S. G. Baker, A. M. Soto, C. Sonnenschein, A. Cappuccio, J. D. Potter and B. S. Kramer, Plausibility of stromal initiation of epithelial cancers without a mutation in the epithelium: a computer simulation of morphostats, *BMC Cancer*, 9 (2009), 89.
- [19] X. Wang, Z. Kam, P. M. Carlton, L. Xu, J. W. Sedat and E. H. Blackburn, Rapid telomere motions in live human cells analyzed by highly time-resolved microscopy, *Epigenetics & Chromatin*, 1 (2008), 4.
- [20] M. Bertolaso, Towards and integrated view of the neoplastic phenomena in cancer research, *Hist. Phil. Life Sci.*, 31 (2009), 79–98.
- [21] S. Wolfram, *A New Kind of Science*, Wolfram Media, 1st edition, 2002.
- [22] B. Chopard and M. Droz, *Cellular Automata Modeling of Physical Systems*, Cambridge University Press, 1998.
- [23] R. Lefever and W. Horsthemke, Bistability in fluctuating environments, implications in tumor immunology, *Bull. Math. Biol.*, 41 (1979), 269–290.
- [24] D. Wodarz and N. L. Komarova, *Computational Biology of Cancer: Lecture Notes and Mathematical Modeling*, World Scientific, 2005.
- [25] K. R. Swanson, E. C. Alvord and J. D. Murray, A quantitative model for differential motility of gliomas in grey and white matter, *Cell Proliferation*, 33(5) (2000), 317–330.
- [26] K. R. Swanson, E. C. Alvord Jr and J. D. Murray, Quantifying efficacy of chemotherapy of brain tumors (gliomas) with homogeneous and heterogeneous drug delivery, *Acta Biotheoretica*, 50(4) (2002), 223–237.
- [27] K. R. Swanson, E. C. Alvord Jr. and J. D. Murray, Virtual resection of gliomas: effects of location and extent of resection on recurrence, *Math. Comput. Model.*, 37 (2003), 1177–1190.
- [28] K. R. Swanson, C. Bridge, J. D. Murray and E. C. Alvord Jr, Virtual and real brain tumors: using mathematical modeling to quantify glioma growth and invasion, *J. Neurological Sci.*,

- 216(1) (2003), 1–10.
- [29] K. R. Swanson, E. C. Alvord, Jr. and J. D. Murray, Dynamics of a model for brain tumors reveals a small window for therapeutic intervention, *Disc. Cont. Dyn. Syst. B*, 4(1) (2004), 289–295.
- [30] H. L. P. Harpold, E. C. Alvord Jr. and K. R. Swanson, Visualizing beyond the tip of the iceberg: the evolution of mathematical modeling of glioma growth and invasion, *J. Neuropathol. Exp. Neurol.*, 66 (2007), 1–9.
- [31] D. Bini, C. Cherubini and S. Filippi, Heat transfer in FitzHugh-Nagumo model, *Phys. Rev. E*, 74 (2006), 041905.
- [32] C. Cherubini, S. Filippi, P. Nardinocchi and L. Teresi, An electromechanical model of cardiac tissue: constitutive issues and electrophysiological effects, *Prog. Biophys. Mol. Biol.*, 97 (2008), 562–573.
- [33] D. Bini, C. Cherubini and S. Filippi, Viscoelastic FitzHugh-Nagumo models, *Phys. Rev. E*, 72 (2005), 041929.
- [34] D. Bini, C. Cherubini and S. Filippi, On vortices heating biological excitable media, *Chaos, Solitons & Fractals*, 42 (2009), 2057–2066.
- [35] J. Keener and J. Sneyd, *Mathematical Physiology*, Springer, 2001.
- [36] S. H. Strogatz, *Nonlinear Dynamics and Chaos: with Applications to Physics, Biology, Chemistry and Engineering*, Westview Press, 2001.
- [37] C. Cherubini, A. Gizzi, M. Bertolaso, V. Tambone and S. Filippi, in preparation, 2010.
- [38] S. G. Baker, A. Cappuccio and J. D. Potter, Research on early-stage carcinogenesis: are we approaching paradigm instability?, *J. Clin. Oncol.*, 28 (2010), 3215–3218.
- [39] C. Cherubini, S. Filippi and A. Gizzi, Diffusion processes in human brain using COMSOL multiphysics, *Proceedings of COMSOL Users Conference of Milan, Italy*, 2006.
- [40] D. E. Marco, S. A. Cannas, M. A. Montemurro, B. Hu and S. Y. Cheng, Comparable ecological dynamics underlie early cancer invasion and species dispersal, involving self-organizing processes, *J. Theor. Biol.*, 256 (2009), 65–75.
- [41] K. W. Morton and D. F. Mayers, *Numerical Solutions of Partial Differential Equations*, Cambridge University Press, 1994.
- [42] M. R. Chicoine and D. L. Silbergeld, Assessment of brain tumor cell motility in vitro and in vivo, *J. Neurosurg.*, 82 (1995), 615–622.

On Spiral Waves Arising in Natural Systems

D. Bini^{1,2,*}, C. Cherubini^{2,3}, S. Filippi^{2,3}, A. Gizzi^{3,4} and P. E. Ricci⁵

¹ *Istituto per le Applicazioni del Calcolo "M. Picone", CNR I-00161 Rome, Italy.*

² *International Center for Relativistic Astrophysics -I.C.R.A., University of Rome "La Sapienza", I-00185 Rome, Italy.*

³ *Nonlinear Physics and Mathematical Modeling Lab, Faculty of Engineering, University Campus Bio-Medico, I-00128 Rome, Italy.*

⁴ *Alberto Sordi Foundation-Research Institute on Aging, I-00128 Rome, Italy.*

⁵ *Mathematics Department, University of Rome "La Sapienza", I-00185 Rome, Italy.*

Received 24 September 2009; Accepted (in revised version) 17 February 2010

Communicated by Sauro Succi

Available online 15 April 2010

Abstract. Spiral waves appear in many different natural contexts: excitable biological tissues, fungi and amoebae colonies, chemical reactions, growing crystals, fluids and gas eddies as well as in galaxies. While the existing theories explain the presence of spirals in terms of nonlinear parabolic equations, it is explored here the fact that self-sustained spiral wave regime is already present in the linear heat operator, in terms of integer Bessel functions of complex argument. Such solutions, even if commonly not discussed in the literature because diverging at spatial infinity, play a central role in the understanding of the universality of spiral process. In particular, we have studied how in nonlinear reaction-diffusion models the linear part of the equations determines the wave front appearance while nonlinearities are mandatory to cancel out the blowup of solutions. The spiral wave pattern still requires however at least two cross-reacting species to be physically realized. Biological implications of such a results are discussed.

AMS subject classifications: 92B25, 33E99, 65Z05

PACS: 05.45.-a, 87.10.-e, 51.20.+d, 98.62.Hr

Key words: Reaction-diffusion equations, biophysics, crystal growth, heat transfer.

1 Introduction

Regular geometrical patterns occur in Nature in many situations [1], a striking case being as an example the observation of practically perfect spherical objects, neutron stars, as

*Corresponding author. *Email addresses:* binid@icra.it (D. Bini), c.cherubini@unicampus.it (C. Cherubini), s.filippi@unicampus.it (S. Filippi), a.gizzi@unicampus.it (A. Gizzi), paoloemilio.ricci@uniroma1.it (P. E. Ricci)

a consequence of self-gravitational general relativistic effects [2]. Another pattern very common is the spiral. It is remarkable the fact that D'Arcy Thompson, around one century ago, devoted an entire chapter of his classical monograph "*On Growth and Form*" to the appearance of the spiral form in Nature discussing in particular animal horns and molluscan shells [3]. Nowadays spiral waves have been observed in many other different biological contexts: in the heart, for example, the motion of the spiral center seems to be associated with specific types of arrhythmias [4], while in neural tissues this motion can be related to epilepsy and to spreading depressions in the retina [5]. More in detail these centers specifically are known as phase singularities, i.e., points in physical or abstract spaces near which the full cycle of isochrons crowds together. It is possible then to have a line of singularities, as in the singular filament of organizing centers, or along the border of a "black hole", i.e., a region on "latency diagrams" on which timings are lost [6]. These filaments in heart and brain tissues are non static and their motion in severe pathological states usually appears to be turbulent (what is it known as "chemical turbulence" [7]). Some biological populations of fungi and amoebae, like the *Dictyostelium discoideum*, tend to organize themselves in spiralling structures while spiral waves appear spontaneously also in specific chemical reactions like the classical Zhabotinsky-Belousov one [4] and also in growing crystals [8]. Common patterns encountered in all these systems are also target patterns, i.e., circular expanding waves generated by oscillatory local behaviors or external stimulations. Even in plant morphogenesis processes both these patterns can occur (kinetic phyllotaxis) [9]. In Fig. 1, a picture taken by one of the authors as an example, the bark of a dead tree manifests a spiralling pattern. The spiral is constituted by outer bark layers, which are well known to be associated with the early stages of the tree, so the typical arboreal radially diffusive behavior (a sort of target one-wave pattern) in this very peculiar case has been replaced by a spiralling mode, probably in association with a "very singular" event (a lightning, an infection or similar).



Figure 1: This picture of spiraling bark was taken in Rome from one of the authors on February, 2009.

In all these systems just discussed, single armed spirals appear in various chiralities although many-armed spiral configurations have been found experimentally in chemical reactions [10]. Moreover, such phenomenologies develop in time with different time scales but they all manifest wave behaviors. Mathematically speaking, all these systems have a common root, i.e., they are properly modeled by nonlinear parabolic partial differential equations. A simple prototype for these equations are reaction-diffusion (RD) systems

$$\frac{\partial c_1}{\partial t} = D_1 \nabla^2 c_1 + f(c_1, c_2), \quad \frac{\partial c_2}{\partial t} = D_2 \nabla^2 c_2 + g(c_1, c_2), \quad (1.1)$$

(spatial homogeneity and isotropy are here assumed in the diffusion tensors for the sake of simplicity, so that D_1 and D_2 are single diffusion coefficients), where we have two possible nonlinearly interacting concentrations c_1 and c_2 . It is important to stress here that not only spiral waves but also multiform stationary pattern formation can occur in this system of PDEs as a consequence of the well known Turing diffusion-driven instability mechanism [10]. In the context of phyllotaxis kinetic in plants [9] as well as in cardiac dynamics [11,12], the evolution is described coupling reaction-diffusion equations to elasticity theory. We point out also that temperature effects can play an important role in many of these systems especially in biological [13,14] and chemical contexts. On the other hand, as anticipated, spirals appear also in vortices in ordinary liquids/gases (i.e., whirlpools) and in astrophysics in Galaxies [15]. These systems can be described by Navier-Stokes equations [15], which assuming for the sake of simplicity incompressibility, are given by

$$\frac{\partial \vec{v}}{\partial t} + (\vec{v} \cdot \nabla) \vec{v} - \mu \nabla^2 \vec{v} = -\frac{\nabla P}{\rho} + \frac{\vec{F}}{\rho}, \quad (1.2)$$

together with the constraint $\nabla \cdot \vec{v} = 0$. This is a generalized nonlinear parabolic system (nonlinearities being present in the convection term $(\vec{v} \cdot \nabla) \vec{v}$ only) for the velocity components, while ρ , P and \vec{F} are the density, the pressure and the body forces respectively. If gravitation is the only body-force present, \vec{F} can be written as $\vec{F} = -\rho \nabla \Phi$, where the gravitational potential Φ satisfies a Poisson's equation leading to the classical theory of self gravitating systems [16]. On the other hand neglecting the viscous term (i.e., $\mu = 0$ in Eq. (1.2)), one obtains perfect fluid which cannot physically support spirals, due to the lack of viscous dissipation [17,18], although not smooth solutions in weak form (i.e., generalized solutions as shock waves) have been found [19] while their physical realization is questionable on experimental grounds. Incidentally perfect fluids (described by Euler equation) can be directly connected by Madelung representation to quantum fluids described by Gross-Pitaevskii equation [20]. In these condensed systems, spiral radiation patterns have been observed in experiments, but they are a consequence of spiraling vortex line trajectories and not of a spiral geometry associated with the vortex itself [21]. Instead in the case of Complex Ginzburg-Landau equation

$$\frac{\partial A}{\partial t} = A + (1 + ib) \nabla^2 A - (1 + ic) A |A|^2, \quad (1.3)$$

for the complex function A (whose real and imaginary parts give two RD equations while b and c are real parameters), describing a vast variety of physical phenomena [22], dropping the nonlinear term and selecting $b=0$ one obtains a "complex diffusion equation" for the real and imaginary parts, so again spiral waves are expected, as it is effectively found in numerical experiments. It is then clear that nonlinear diffusion equations play a central role in the formation of this spiraling pattern, but a question arise naturally: can spiral waves belong to a linear regime?

In this article we discuss this question, showing that a spiral pattern comes specifically from the very simple linear diffusion equation for one specie only, so that the diffusion equations determine the shape of the wave. More impressively, associated with the appearance of a spiral a diffusive process is always occurring, a fact that has never received enough attention in the mathematical but especially physical Literature, although some analytical and numerical insights have shown spiral waves behaviors in linear "multispecies" reaction-diffusion systems [23,24], neglecting a discussion of physical implications. The main reason for this is the fact that spiral wave solutions of linear equations do not satisfy proper boundary conditions of the Sturm-Liouville problem. According to our point of view instead, the central point is to interpret the interplay between linearity and nonlinearity on physical grounds. Through analytical methods we find that when the frequency of these waves becomes zero (static solutions) the spiral pattern disappears, that is spirals must be waves, a fact widely confirmed by experiments. Nonlinearities, however result to be necessary in order to correct pathologies of the linear theory, i.e., eliminating blowups of the solution and leading to circular fronted waves (target patterns). Spiral and target patterns in fact can be approximated with linear regimes only close to the center. This requirement however is still not sufficient to physically realize spiral waves: for instance, the context of reaction-diffusion processes at least two cross-reacting species are needed. We can discuss now all these points in detail, giving a unique thread of many results scattered in the Literature by using quite simple mathematical arguments.

2 Spiral waves and the linear diffusion equation

Let's write the diffusion equation in Cartesian coordinates (x,y,z) , i.e., $\partial c/\partial t = D\Delta c$, where c is the concentration, D is the diffusion coefficient associated to a homogeneous and isotropic diffusion tensor, t is time and Δ is the Laplace operator. Using dimensionless parameters [25], i.e., $T = Dt/l^2$, and $X = x/l$ (l is an arbitrary length scale), similarly for y and z , with $c = \tilde{c}(C + C_0)$, where \tilde{c} is a constant (concentration), C represents the dimensionless concentration and C_0 is an arbitrary dimensionless shift, we make the diffusion coefficient disappear, i.e.,

$$\frac{\partial C}{\partial T} = \nabla^2 C, \quad (2.1)$$

where ∇^2 denotes here the Laplacian in dimensionless Cartesian coordinates.

It is convenient to write the diffusion equation above in dimensionless cylindrical coordinates (R, ϕ, Z) with R and ϕ defined so that

$$(X, Y) = R(\cos \phi, \sin \phi). \quad (2.2)$$

We use then the following separation of variables *ansatz*

$$C(R, \phi, Z, T) = P(R)e^{i\omega T + ikZ + im\phi}. \quad (2.3)$$

The linearity of the problem ensures us that the real and imaginary parts of this quantity both are solutions of Eq. (2.1). Moreover, m must be an integer in order to avoid problems of polidromy and cusps. We insert this functional form in Eq. (2.1), using in addition a rescaled dimensionless radius $R = q\zeta$, with

$$q^2 = \frac{(i\omega - k^2)}{(k^4 + \omega^2)}. \quad (2.4)$$

Such complex coordinate transformation brings the equation for P into the form

$$\zeta^2 \frac{d^2 P}{d\zeta^2} + \zeta \frac{dP}{d\zeta} + (\zeta^2 - m^2)P = 0, \quad (2.5)$$

which is a complex Bessel equation, whose solution is

$$P = a_1 J_m(\zeta) + a_2 Y_m(\zeta),$$

where a_1 and a_2 are generic constants. The Bessel functions Y_m must be disregarded being pathological on the origin of the complex plane (although nonlinear corrections, discussed in the following, may correct this pathology); hence we choose the values $a_1 = 1$ and $a_2 = 0$. The complex holomorphic function $J_m(\zeta)$ has a power series representation of the form [26, 27]

$$J_m(\zeta) = \sum_{h=0}^{+\infty} \frac{(-1)^h \left(\frac{\zeta}{2}\right)^{2h+m}}{h!(h+m)!}, \quad |\arg \zeta| < \pi, \quad m \geq 0, \quad (2.6)$$

whose convergence radius is infinite. In the case $m < 0$, the relation $J_{-m}(\zeta) = (-1)^m J_m(\zeta)$ is valid. The power series can be separated into real and imaginary parts by using Euler-De Moivre formulas, i.e., $\zeta = \rho e^{i\theta} = \rho [\cos(\theta) + i \sin(\theta)]$. In particular, $\rho = R/|q| \equiv R(k^4 + \omega^2)^{1/4}$ and $\theta = 1/2 \arctan(\omega k^{-2})$. The final result, after a little algebra, is

$$\operatorname{Re}[J_m(\zeta)] = \sum_{h=0}^{+\infty} \frac{(-1)^h \rho^{2h+m} \cos[(2h+m)\theta]}{2^{2h+m} h!(h+m)!}, \quad (2.7)$$

$$\operatorname{Im}[J_m(\zeta)] = \sum_{h=0}^{+\infty} \frac{(-1)^h \rho^{2h+m} \sin[(2h+m)\theta]}{2^{2h+m} h!(h+m)!}, \quad (2.8)$$

both quantities depending on k , ω and m . We can now easily recompose backwards our solution whose real and imaginary parts satisfy both separately the dimensionless real diffusion equation (2.3) in cylindrical coordinates

$$C = \left(\operatorname{Re}[J_m(\zeta)] + i\operatorname{Im}[J_m(\zeta)] \right) e^{i\omega T + ikZ + im\phi} \equiv \operatorname{Re}[C] + i\operatorname{Im}[C], \quad (2.9)$$

where

$$\operatorname{Re}[C] = \operatorname{Re}[J_m(\zeta)] \cos(\omega T + kZ + m\phi) - \operatorname{Im}[J_m(\zeta)] \sin(\omega T + kZ + m\phi), \quad (2.10a)$$

$$\operatorname{Im}[C] = \operatorname{Re}[J_m(\zeta)] \sin(\omega T + kZ + m\phi) - \operatorname{Im}[J_m(\zeta)] \cos(\omega T + kZ + m\phi). \quad (2.10b)$$

When $k = 0$, i.e., an infinite cylinder solution, the real and imaginary parts of C give moving target patterns and rotating spirals of various chiralities and numbers of arms as shown at a fixed time in Fig. 2. Fig. 3 instead shows the behavior when $k \neq 0$.

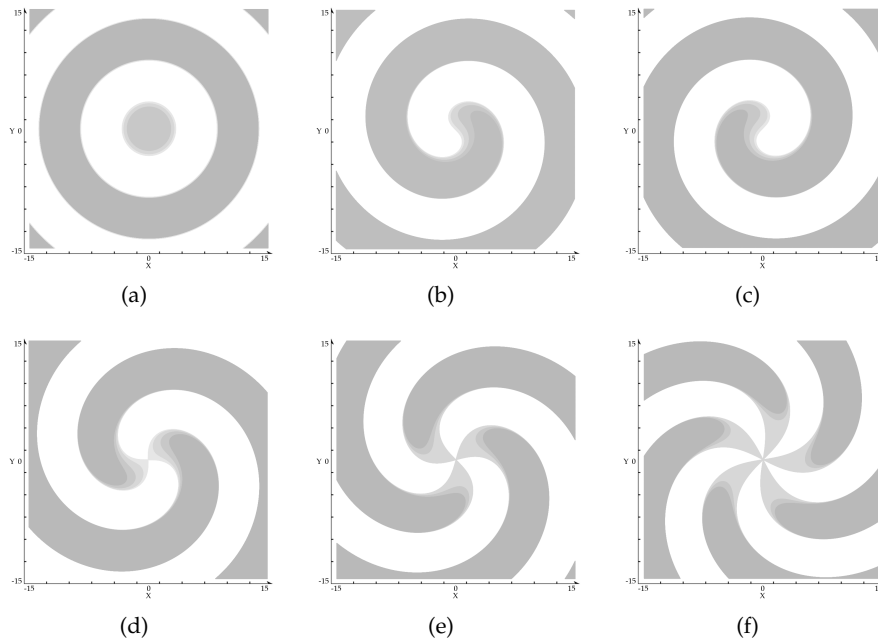


Figure 2: Real part of C (solution of the diffusion problem (2.1)), at $T=0$ assuming moreover $k=0$ (cylindrical symmetry). Surface levels $C=(0,0.15,0.5,1)$ are shown (grey color means high values while white is the opposite). For different m one obtains the following patterns: a) for $m=0$ which is reminiscent of target patterns, b) $m=1$ which is a spiral, c) $m=-1$ is a spiral with opposite chirality, d) $m=2$ a two armed spiral, e) $m=3$ a three armed spiral, f) $m=-5$ a five armed spiral with opposite chirality.

Except for selected values of θ , these real and imaginary parts of C diverge at infinity (while standard real Bessel functions J_m are well behaved everywhere). Such result is not unexpected: using the identity $J_m(i\xi) = iI_m(\xi)$, with $\xi \in \mathcal{R}$, connecting standard Bessel

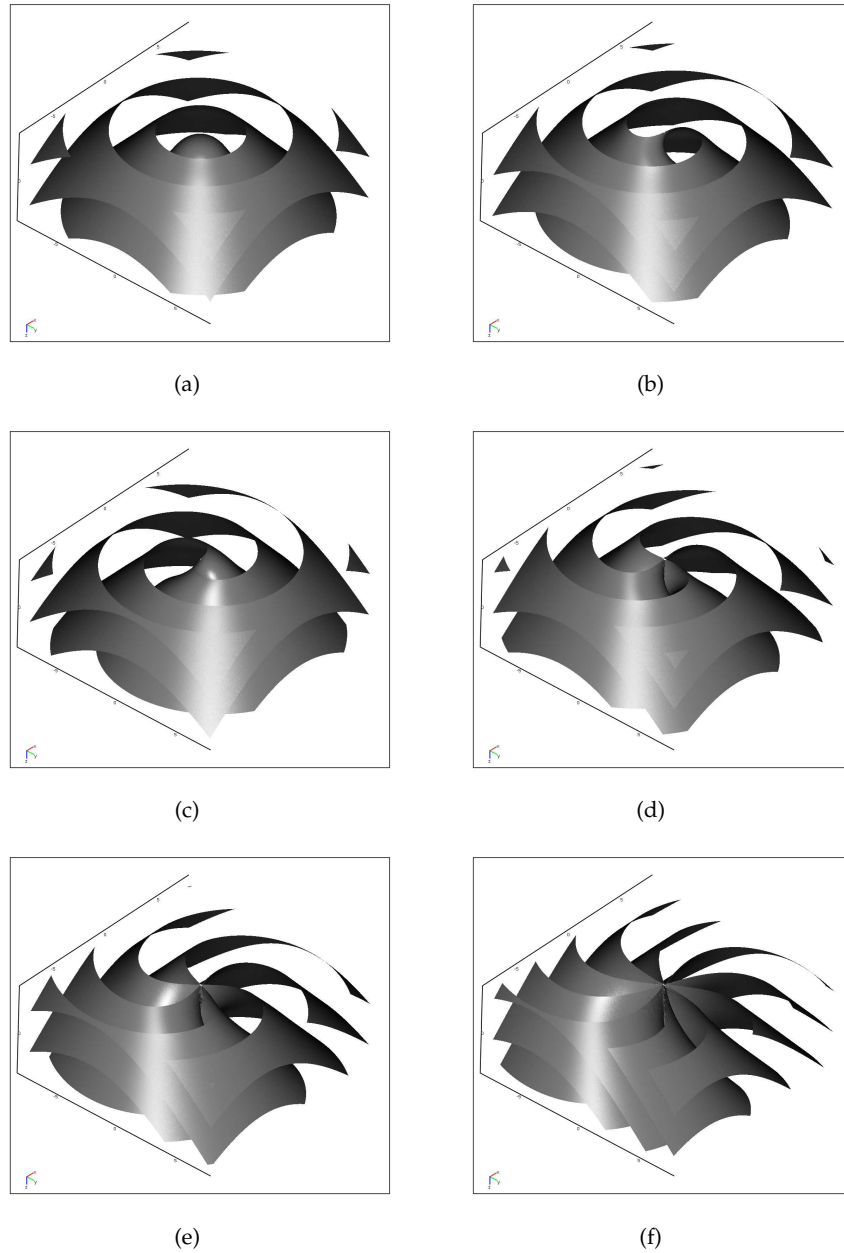


Figure 3: Real part of C (3D solution of the diffusion problem), at $T=1$ assuming $-\pi < z \leq \pi$. Surface gray level $C=0$. For different m one obtains these patterns: a) for $m=0$ which is reminiscent of target patterns, b) $m=1$ which is a spiral, c) $m=-1$ is a spiral with opposite chirality, d) $m=2$ a two armed spiral, e) $m=3$ a three armed spiral, f) $m=-5$ a five armed spiral with opposite chirality.

functions with their modified versions which diverge at large distances, we can easily see that our solutions must diverge too. We may have initially added to diffusion equation a linear term proportional to c but this step would have not changed the behavior of the divergence, i.e., we would have obtained again integer Bessel functions of complex argument.

When $\omega = 0$, coming back to the initial manipulations, we see that the Bessel functions have a real argument and spiral pattern is lost: hence, if spirals do exist they must be waves. We point out that the family of eigenfunctions found for the linear diffusion equation do not satisfy proper Sturm-Liouville problems with regularity both at the origin and at infinity. This is the main reason why we do not observe in nature in general, spirals which are described by linear parabolic equations. Such a particular pattern, belonging to the linear regime, in order to be physically realized needs nonlinear terms typical of reaction-diffusion systems in order to limit the blow up asymptotically. However in diffusion problems, when we have one diffusing species only, the mechanism above described would not produce rotating spiral waves or periodic target patterns, as discussed now.

3 The role of nonlinearity

Suppose to start from equation

$$\frac{\partial C}{\partial T} = \nabla^2 C + F(C). \quad (3.1)$$

Locally, i.e., neglecting the spatial variations, we obtain the ordinary differential equation $dC/dT = F(C)$, which represents the flow on a line, and cannot have periodic solutions (oscillations) unless the domain is topologically bent to form a circle [28]. Let's take as an example the Zeldovich's bistable equation, which has relevance both for gas dynamics and for nerve signal propagation [29,30], i.e., a normal form for many different dynamical systems with

$$F(C) = aC(1-C)(C-\alpha), \quad \text{with } 0 < \alpha < 1, \quad (3.2)$$

(we assume in the following $a = 1$ to simplify relations) with $C = 0$ and $C = 1$ being sinks and $C = \alpha$ being a source. The word *bistable* comes from the fact that this type of equation has two possible stable solutions which are asymptotically reached once one starts at right or left of value α . It's clear that periodic spirals cannot exist because such a dynamics is not "excitable", i.e., the system does not explore a large portion of phase-space (which here, due to the first order derivative in time is trivially one dimensional) before coming back to the stable point [29]. A nonlinear spiral should in fact repeatedly stimulate the various portion of the domain, which is not possible looking at Fig. 4. In fact as anticipated the system is bistable, which means that every point of the domain must be flow-dragged towards one of the two sinks. Once such a point arrives at value $C = 1$, a possible spiral front (having at maximum value $C \sim 1$, because bistable waves act as

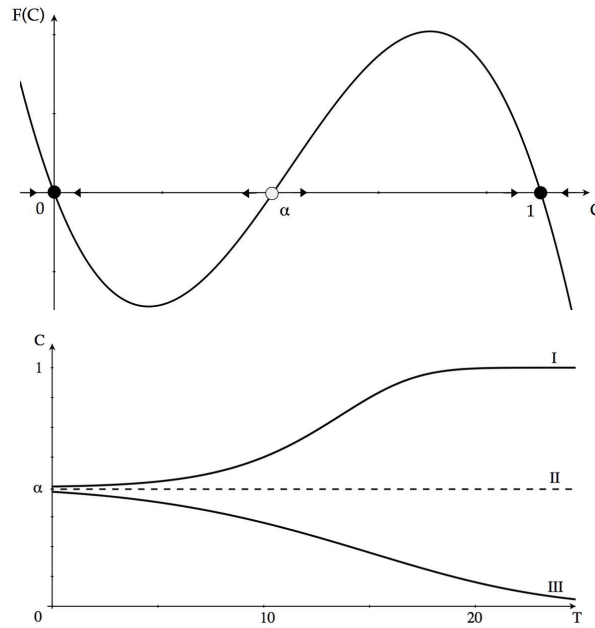


Figure 4: Upper panel: Phase space of the zero dimensional bistable equation (diffusion suppressed). There are two sinks and one repeller. Lower panel: Behavior of possible solutions of zeroth dimensional bistable equation with initial conditions over the repeller (curve I), on the repeller (curve II) and below the repeller (curve III).

a sort of shock waves connecting two asymptotic states) should move this point away from this stable fixed point. But this behavior is not possible because of the definition of stable point; so once the front arrives it extinguishes itself, as easily confirmed by simple numerical simulations. Manipulations in the one-dimensional case show that a traveling wave solution for bistable equation has analytical form [29]

$$C(T, X) = \frac{1}{2} + \frac{1}{2} \tanh \left[\frac{\sqrt{a}(X + VT)}{2\sqrt{2}} \right], \quad V = \frac{\sqrt{a}}{\sqrt{2}}(1 - 2\alpha), \quad (3.3)$$

which manifest the limitation of blowups at infinite distance due to the presence of nonlinearities. In the linear case

$$\frac{\partial C}{\partial T} = \frac{\partial^2 C}{\partial X^2}, \quad (3.4)$$

in fact the basic travelling wave solution is given by

$$C(T, X) = C_1 + C_2 \exp[v(X + vT)], \quad (3.5)$$

where C_1 and C_2 are arbitrary constants and v is the non dimensional velocity. This solution shows a divergence in space and time corrected in the nonlinear case previously discussed. In higher dimensions numerical solutions only are possible but the result is

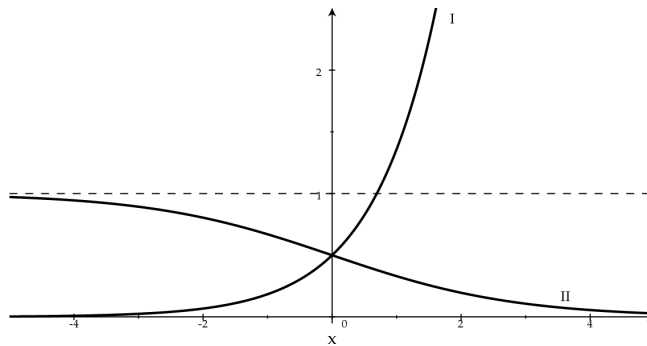


Figure 5: Graphics of the two solutions in space: *I*, linear case (3.5) with $C_1=0$ and $C_2=\frac{1}{2}$, *II*, nonlinear case (3.3).

not changed: a unique radial pattern evolving in time brings the entire domain at value $C=1$ asymptotically. More complicated functional forms $F(C)$ shall not modify such a behavior because the phase space will be a collection of fixed points on a line. Even a collection of semi-stable points described by the non-polynomial dynamics

$$F(C) = \frac{1}{2}(1 + \sin C)$$

has a trivial phase-space which cannot support repeated waves. A possible way out exists however: we may consider in fact for the nonlinear diffusion equation above an extension with a spatial dependent term, as in happens in crystal growth problems as an example [31], i.e., in cylindrical coordinates we may write

$$F(C) = \beta \sin(C - \gamma \phi) + \sigma,$$

with β , γ and σ real numbers. This choice produces rotating spiral waves but this non-linear term breaks the isotropy and homogeneity of space (external magnetic or gravitational fields may give similar effects). Here, on the other hand, we are interested in genuine self-sustained spiral behaviors embedded in homogeneous and isotropic domains. The examples discussed above show that in order to have spirals, a two-dimensional phase-space at least is needed.

Consequently, again, in order to have natural spiral waves and circular waves, we are forced to require at least two species nonlinearly reacting, i.e., a proper nonlinear reaction-diffusion system. As an example we show in Fig. 6 the typical patterns obtained numerically integrating a very simple two variables reaction diffusion system as in Eq. (1.1) of FitzHugh-Nagumo type (FHN) [4, 32], which implies

$$f(c_1, c_2) = c_1(1 - c_1)(c_1 - \alpha) - c_2, \quad \text{and} \quad g(c_1, c_2) = \epsilon(c_1 - \gamma c_2).$$

Here the variable c_1 could be associated with a dimensionless action potential while the quantity c_2 with a gating variable (an electrophysiological problem), but because of the

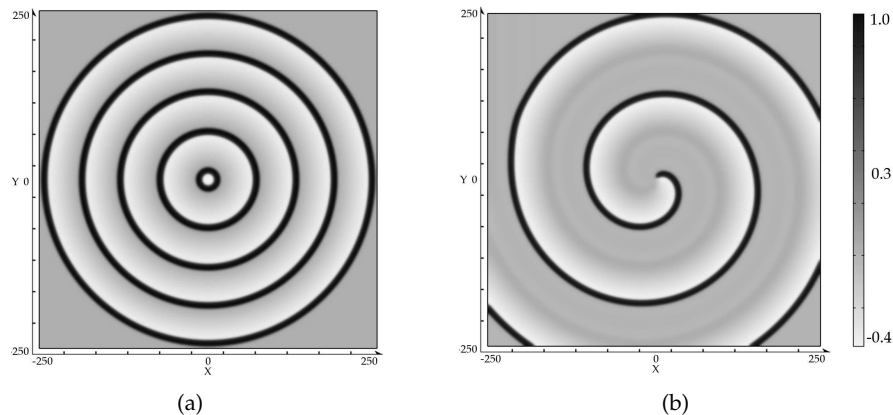


Figure 6: The model is a FitzHugh-Nagumo type with parameters $D_1 = 0.5$, $D_2 = 0.1$, $\alpha = 0.01$, $\epsilon = 0.01$ and $\gamma = 0.05$ and the value of variable c_1 is shown at a given time of the evolution for target patterns (a) and a spiral wave (b).

generality and simplicity of the FHN model, they could represent differently chemical quantities or other. While a negative parameter α leads to a self-oscillatory behavior, a positive one leads to excitable dynamics [29]. The numerical integrations of these equations have been performed using finite elements techniques, modifying an existing code described in [13]. The mesh is made of squared elements sufficiently small to ensure stability and convergence of the simulations. More in detail we have adopted several discretizations of the domain starting from 25 up to 100 equally spaced points per side and selected in the different simulations second, third and fourth order Lagrange elements in order to ensure convergence and stability. The numerical integrations have been performed adopting Comsol Multiphysics® software running on a 64 bit dual core Xeon® Hewlett-Packard workstation with 6Gb of RAM. Specifically we have adopted a direct solver (UMFPACK) while time steps have been optimally chosen by the software (although in order to have additional checks, the best meshed simulations have been performed also adopting user-constrained time steps with $\Delta t = 5 \cdot 10^{-4}$). Finally the relative and absolute errors thresholds have been selected at 10^{-7} . Our FHN model with $D_2 = 0$ can be easily obtained as a simplification of the Hodgkin-Huxley theory of the action potential in the giant squid axon, which is described by four variables, while the RD system here numerically studied is governed by c_1 and c_2 only, leading to a two dimensional phase-space (suppressing space variations) which simplifies noticeably the physics of excitability. We stress that it is well known the presence of spiral waves even if one of the two species does not diffuse (the case of the electrophysiological FHN just discussed) so that in order to have spirals it is necessary at least to have cross-reaction with one diffusing species and not necessarily cross-diffusion (both diffusion coefficients non-vanishing). The production of circular or spiral patterns in our simulations strongly depends on specific initial conditions and external actions (especially for the circular fronted

ones which here required external periodic stimuli). In fact if the cylindrical symmetry is maintained circular waves but not spirals occur. An external perturbation of non axisymmetric type on the other hand breaks the symmetry and drives the system towards more complicated regimes, possibly attractor configurations containing one-armed spiral waves only.

4 Concluding remarks

In this paper, we have explored the fact that self-sustained spirals patterns, commonly encountered in many natural systems, have their geometrical roots already in the single linear diffusion equation. Physically realized spirals however are determined by a nonlinearly corrected diffusion equation with two—at least—cross-reacting species are involved. In fact, while in linear diffusion problems spiral solutions are mostly associated with a blow up and non regularities, in nonlinear problems those solutions become mostly regular instead. Moreover, as soon as time dependence becomes negligible, diffusion equation predicts the disappearance of such a pattern, a fact observed in experiments. The diffusion process must be seen as a theoretical model of possible discrete complex systems (i.e., cells, molecules) whose dynamics can be described in a first approximation with a nonlinear continuum field theory, similarly to what happens to the Boltzmann equation for the statistical description of particles in a fluid, where the real molecular theory can be approximated with Euler and Navier-Stokes limits [33]. In any case, it is important to stress that diffusion processes and spiral waves in natural systems (biological or not) are associated phenomena, therefore, if there are more than one species cross-reacting and one of them at least diffuses, a spiral wave pattern may be expected to arise. This point of view can be an extremely important instrument in order to hypothesize on mathematical and physical grounds other biological or more general physical situations in which the ubiquitous spirals can appear as a byproduct of chemical reaction-diffusion processes, and perform then *ad hoc* experiments.

Acknowledgments

D. Bini, C. Cherubini and S. Filippi acknowledge ICRANet for partial supporting this work.

References

- [1] H. Weyl, *Symmetry*, Princeton University Press, 1952.
- [2] R. Belusevic, *Relativity, Astrophysics and Cosmology*, Wiley CH, 2008.
- [3] W. T. D'Arcy, *On Growth and Form*, Cambridge University Press, 1992.
- [4] A. T. Winfree, *The Geometry of Biological Time*, Springer, 2000.
- [5] M. A. Dahlem and S. C. Muller, Image processing techniques applied to excitation waves in chicken retina, *Methods.*, 21 (2000), 317–323.

- [6] A. T. Winfree, *When Time Breaks Down: The Three-Dimensional Dynamics of Electrochemical Waves and Cardiac Arrhythmias*, Princeton University Press, 1987.
- [7] Y. Kuramoto, *Chemical Oscillations, Waves, and Turbulence*, Dover, 2003.
- [8] C. Kittel, *Introduction to Solid State Physics*, 8th ed., John Wiley & Sons, 2004.
- [9] R. V. Jean, *Phyllotaxis: A Systemic Study in Plant Morphogenesis*, Cambridge University Press, 1994.
- [10] J. D. Murray, *Mathematical Biology* vol. II, 3rd ed., Springer, 2008.
- [11] C. Cherubini, S. Filippi, P. Nardinocchi and L. Teresi, An electromechanical model of cardiac tissue: constitutive issues and electrophysiological effects, *Prog. Biophys. Mol. Bio.*, 97 (2008), 562–573.
- [12] D. Bini, C. Cherubini and S. Filippi, Viscoelastic FitzHugh-Nagumo models, *Phys. Rev. E*, 72 (2005), 041929–1/041929–9.
- [13] D. Bini, C. Cherubini and S. Filippi, Heat transfer in FitzHugh-Nagumo models, *Phys. Rev. E*, 74 (2006), 041905–1/041905–12.
- [14] D. Bini, C. Cherubini and S. Filippi, On vortices heating biological excitable media, *Chaos. Soliton. Fract.*, 42 (2009), 2057–2066.
- [15] J. Binney and S. Tremaine, *Galactic Dynamics*, Princeton University Press, 1987.
- [16] S. Chandrasekhar, *Ellipsoidal Figures of Equilibrium*, New Haven Conn, Yale University Press, 1969.
- [17] J. Jeans, *Astronomy and Cosmogony*, Cambridge University Press, 2009.
- [18] R. A. Granger, *Fluid Mechanics*, Dover, 1995.
- [19] T. Chang, G. Q. Chen and S. Yang, *Nonlinear Problems in Engineering and Science-Numerical and Analytical Approach*, Science Press, Beijing, 1991.
- [20] T. Kambe, *Elementary Fluid Mechanics*, World Scientific, 2007.
- [21] N. G. Parker, N. P. Proukakis, C. F. Barenghi and C. S. Adams, Controlled vortex-sound interactions in atomic Bose-Einstein condensates, *Phys. Rev. Lett.*, 92 (2004), 160403–1/160403–4.
- [22] I. S. Aranson and L. Kramer, The world of the complex Ginzburg-Landau equation, *Rev. Mod. Phys.*, 74 (2002), 99–144.
- [23] J. Gomati, Pattern synthesis from singular solutions in the Debye limit: helical waves and twisted toroidal scroll structures, *J. Phys. A*, 15 (1982), 1463–1476.
- [24] M. Golubitsky and I. Stewart, *The Symmetry Perspective: From Equilibrium to Chaos in Phase Space and Physical Space*, Birkhäuser, Basel, 2004.
- [25] J. Crank, *The Mathematics of Diffusion*, 2nd ed., Oxford University Press, 1975.
- [26] M. Abramowitz and I. Stegun, *Handbook of Mathematical Functions*, Dover, 1964.
- [27] I. S. Gradshteyn and I. M. Ryzhik, *Table of Integrals, Series and Products*, 6th ed., Academic Press, 2000.
- [28] S. H. Strogatz, *Nonlinear Dynamics and Chaos: With Applications to Physics, Biology, Chemistry and Engineering*, Westview Press, 2001.
- [29] J. Keener and J. Sneyd, *Mathematical Physiology*, Springer, 2001.
- [30] Y. B. Zeldovich and D. A. Frank-Kamenetsky, A theory of thermal propagation of flame, *Acta. Physicochim.*, 9 (1938), 341–350.
- [31] T. Ogiwara and K. Nakamura, Spiral traveling wave solutions of nonlinear diffusion equations related to a model of spiral crystal growth, *Publ. Res. Inst. Math. Sci.*, 39 (2003), 767–783.
- [32] V. S. Zykov, A. S. Mikhailov and S. C. Muller, Wave instabilities in excitable media with fast inhibitor diffusion, *Phys. Rev. Lett.*, 81 (1998), 2811–2814.
- [33] K. Huang, *Statistical Mechanics*, 2nd ed., Wiley, 1987.

On the electrical intestine turbulence induced by temperature changes

A Gizzi^{1,2}, C Cherubini^{1,3}, S Migliori¹, R Alloni⁴, R Portuesi⁵ and S Filippi^{1,3}

¹ Nonlinear Physics and Mathematical Modeling Lab, Engineering Faculty, University Campus Bio-Medico, I-00128 Rome, Italy

² Alberto Sordi Foundation—Research Institute on Aging, I-00128 Rome, Italy

³ International Center for Relativistic Astrophysics (I.C.R.A.), University of Rome 'La Sapienza', I-00185 Rome, Italy

⁴ Department of Surgery, University Campus Bio-Medico of Rome, I-00128 Rome, Italy

⁵ Department of Endocrinology and Diabetes, University Campus Bio-Medico of Rome, Rome, Italy

E-mail: c.cherubini@unicampus.it

Received 7 July 2009

Accepted for publication 16 December 2009

Published 10 February 2010

Online at stacks.iop.org/PhysBio/7/016011

Abstract

Paralytic ileus is a temporary syndrome with impairment of peristalsis and no passage of food through the intestine. Although improvements in supportive measures have been achieved, no therapy useful to specifically reduce or eliminate the motility disorder underlying postoperative ileus has been developed yet. In this paper, we draw a plausible, physiologically fine-tuned scenario, which explains a possible cause of paralytic ileus. To this aim we extend the existing 1D intestinal electrophysiological Aliev–Richards–Wikswø ionic model based on a double-layered structure in two and three dimensions. Thermal coupling is introduced here to study the influence of temperature gradients on intestine tissue which is an important external factor during surgery. Numerical simulations present electrical spiral waves similar to those experimentally observed already in the heart, brain and many other excitable tissues. This fact seems to suggest that such peculiar patterns, here electrically and thermally induced, may play an important role in clinically experienced disorders of the intestine, then requiring future experimental analyses in the search for possible implications for medical and physiological practice and bioengineering.

Abbreviations

BHE	bio-heat equation
DL	double layered
DML	dimensionless
EB	external boundary
ECA	electrical control activity
EGG	electrogastrogram
ERA	electrical response activity
FEM	finite element method
FHN	FitzHugh–Nagumo model
GEA	gastric electrical activity
GI	gastrointestinal
IB	interior boundary
ICC	interstitial cells of Cajal

MENG	magnetoenterography
LM	longitudinal muscles
POI	postoperative ileus
PAF	postoperative atrial fibrillation
SB	sectional boundary
SM	smooth muscles

1. Introduction

Paralysis of the intestine, known as POI, is an inevitable consequence of major abdominal surgery [1–4], being the result of many interacting factors such as surgical trauma, local inflammatory reactions, electrolyte imbalances as well as hyperactivity of the sympathetic nervous system due to several autonomic, hormonal, behavioral responses to stressful

regional stimuli [5–15]. Drugs may also contribute to POI [16]. For the surgical team it is important to shorten the length of POI [17, 18] which causes bloating, nausea, abdominal distension and may lead to bacterial overgrowth in the intestinal lumen, with further complications. When peristalsis recovers, gastric content, bile and food, can flow through the bowel. Currently, no drugs are available to treat this condition. Some papers report that early feeding after surgical abdominal procedures seems to improve recovery from POI [19, 20] but little is known about the pathogenesis of this disorder as a consequence of the complexity of bowel activity regulation.

Cutaneous electrical and external magnetic fields recordings (EGG, GEA, MENG) of the normal and diseased functioning of the gastrointestinal (GI) tract [21–35] have shown many physiological and pathological similarities with the heart [36–38]. Anatomically, the intestine integrates the functions of many types of different cells and tissues [39]. It can be broadly divided into two different parts, the small and large intestine. Both share a general structure with the whole gut made up of several layers: starting from inside one has the lumen, going radially outward the mucosa (epithelium and muscularis), submucosa, muscularis externa (inner circular and outer longitudinal) and lastly serosa. Focusing on the first part of the small intestine (duodenum), the electrophysiological regime is governed by an excitable double-layered structure: longitudinal muscle (LM) and interstitial cells of Cajal (ICC). LM of the muscularis externa layer helps the continued peristaltic motion through an anisotropic spike propagation as shown by Lammers *et al* [40] and results correlated to the possible interaction between the ICC myenteric layer and both longitudinal and circular muscles. Many tissues which contain smooth and striatal muscles (SM) generate spontaneous electrical and mechanical activity: stretch-dependent and voltage-dependent calcium channels are well known to operate to this aim (see as an example [41] and references therein). In the GI tract electrical activity is generated by a separate group of cells, the ICC which are distributed, electrically connected and tightly coupled to neighboring SM cells which are selectively innervated by enteric nerve terminals [42]. In most regions of the GI tract, an interconnected network of ICC generates pacemaker potentials which conduct the signal passively to the adjacent longitudinal and circular muscle layers where they produce rhythmical waves of membrane depolarization and subsequent gut contraction. The importance of ICC role in gastric motility and neuronal control mechanisms as well as loss or reduced density of ICC in a variety of genetic, surgical, infectious and idiopathic motility disorders have been stressed by many authors [32, 43–45]. Although many types of SM tissues have now been shown to contain ICC, the specific function of these cells is not known and represents currently an area of active research.

In this paper we address specifically the understanding of one of the possible causes of POI, building up a mathematical model for the purely electrical activity and its relation to temperature effects. In a first approximation, we do not consider other important effects,

i.e. mechanical peristaltic motion (as usual in cardiac electrophysiology and computational cardiology [46]), in order to show how the thermal problem alone is able to induce significant perturbations to the physiological state. A complete comprehension of POI cannot obviously omit other multifactorial agents as well as further new experimental *in vivo* measurements that we hope to stimulate throughout this study. Here we adopt the approach by Bini *et al* [48, 49], i.e. we address the study of excitable intestinal tissue by modeling the electrophysiological activity through a set of nonlinear partial differential equations (PDE) [50] and the coupled thermal problem through the Pennes bio-heat equation (BHE) [51]. We recall that Nelsen and Becker [52] began the modeling of slow-wave propagation in the GI tract in the late 1960s. They suggested that a chain of *relaxation oscillators* could simulate the activity in the small intestine. Sarna *et al* [53] used a modified set of Van der Pol oscillators to simulate different aspects of GI tract activity. We adopt here the Aliev–Richards–Wikswow model [50] because their approach has shown qualitative agreement with experimental observations. It's worthwhile to mention that similar models for the GI tract were termed *core conduction* models [54] and have been used to simulate the electrical dynamics based on the underlying electrophysiology of intestine in the same manner that has been used successfully for many cardiac cell models (Pullan *et al* [26, 34], Lammers *et al* [36, 37] and the extensive work of the Vanderbilt University Group [28, 32, 33]).

The paper is organized as follows. After the introduction, in section 2 we present the adopted ionic model as well as the bio-heat transfer problem for intestinal tissue. We propose a two and three-dimensional extension of the one-dimensional scheme reported by Aliev *et al* [50] calibrated on animal experiments to simulate the electrical intestinal activity, addressing the first 240 cm of the GI tract. In a first approximation, in the absence of detailed human experiments, we make the ansatz that for humans similar behaviors occur. In this way we combine the advantages of core conduction and relaxation oscillator models [55] introducing higher dimensional spatial pattern observations. The electro-thermal system shall then consist of five coupled nonlinear PDEs. In section 3 we report the results of the two- and three-dimensional numerical simulations analyzing tissue response to different kinds of external stimuli. In particular, thermal coupling shows how external cooling could influence the physiological electrical activity of intestine leading to turbulent and spiraling patterns possibly related to motility disorder experienced by patients after abdomen surgery [1]. The spiral waves observed in silico suggest new electrophysiological experiments as done in [37]. They could follow the known procedure with voltage sensitive dyes [56] and superconducting quantum interference device (SQUID) gradiometers [57]. In section 4 we discuss clinical implications of the numerical results with special attention to similar problems in excitable tissues.

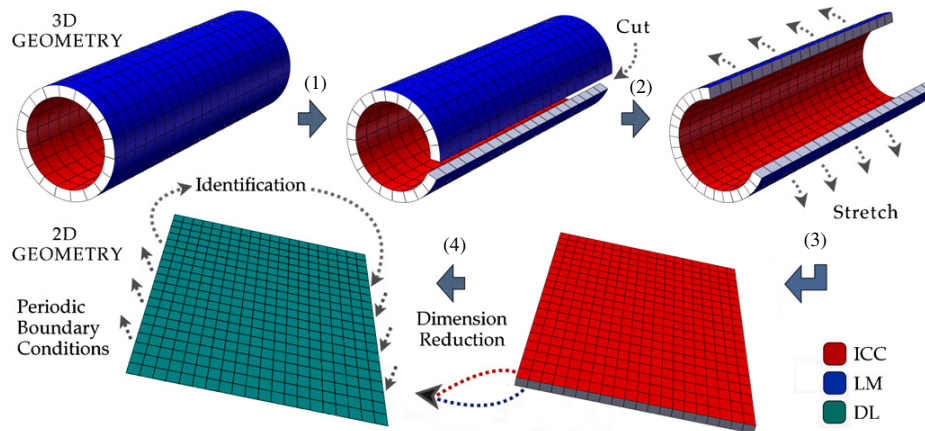


Figure 1. Schematic diagram of the transformation of the cylindrical three-dimensional domain into a two-dimensional plane. The method consists in (1) ‘cutting’ longitudinally the 3D geometry, (2–3) ‘stretching’ the domain transforming the tubular form in a parallelepiped one, (4) ‘reducing’ the 3D domain so obtained to a 2D plane adopting the DL structure of intestine tissue and imposing periodic boundary conditions to respect medium continuity. The blue and red surfaces in the 3D geometry represent the external LM and internal ICC layer, respectively, while the green final color of the 2D geometry represents the coincidence of the two transmembrane variables in the new reference grid.

2. Methods

The adopted ionic model [50] is based on a FitzHugh–Nagumo (FHN)-type structure [58] which represents the simplest model able to mimic Hodgkin–Huxley-type membrane dynamics [59] while maintaining the physical meaning of the Van der Pol oscillator [60]. The FHN model is widely used to simulate as a first step the dynamics of many different excitable biological systems, from microbial populations to heart action potential [61] coupling external agents as well as temperature [62, 63]. In this paper we approach the study of the intestine following the double-layered (DL) structure described in figure 1. The LM and ICC layers are considered physically distinct but mathematically coincident, identifying a single frame of reference. Differently from the 2D purely electric problem, the 3D multiphysics study needs a finite thickness (0.2 cm) to impose internal and external thermal boundary conditions as well as to represent physical gradients inside the tissue. A thin cylindrical distended tube is taken as the evolution domain. The geometric dimensions respect intestinal anatomy but for the purposes of our study we assume that lumen diameter and internal and external radii are constant neglecting villi and microvilli invaginations.

2.1. The intestine ionic model

The electrical activity of the small intestine in most mammalian species consists of two main components [64]: the slow waves or electrical control activity (ECA) and the electrical response activity (ERA). The ECA acts by changing the excitability of intestinal muscle in association with chemical and electrical stimuli which produce spikes and contractile responses [54]. In humans it consists of repetitive depolarizations of 5–15 mV in amplitude and about 6 s in duration which, at body temperature and healthy conditions (no disease, no operation), occur at a characteristic frequency depending on the level of intestine from which

they are recorded [65]. At the duodenum level the ICC frequency is about twelve times per minute and differs from the stomach, three times per minute, and the terminal ileum, eight times per minute [66]. The control activity is myogenic: it originates in the longitudinal muscle layer and spreads electrotonically to the circular muscle one. The occurrence of control potentials determines the development of response activity in time and space [67]. The ERA function consists of one or more spikes, which occur superimposed on the depolarization phase or plateau of the ECA potential in cells during mechanical activity. Electric dynamics in the intestine layers is here described by a pair of PDEs for layer: the first equation of each pair has a characteristic N -like nullcline [68], which is typical for excitable and oscillatory systems, and describes the dynamics of the transmembrane potential; the second equation describes slow transmembrane currents that ensure the repolarization of the membrane. Indicating with subscription ‘ l ’ and ‘ i ’ the LM and ICC layer, respectively, with ∇^2 the Laplacian operator in Cartesian coordinates [69] and considering an homogenous and isotropic tissue (quantities D_l , D_i , D_{li} , D_{il} are constant), we can write the following reaction–diffusion system:

$$\begin{aligned} \partial_t u_l &= f(u_l) + D_l \nabla^2 u_l - v_l + F_l(u_l, u_i) \\ \partial_t v_l &= \varepsilon_l [\gamma_l (u_l - \beta_l) - v_l] \\ \partial_t u_i &= g(u_i) + D_i \nabla^2 u_i - v_i + F_i(u_l, u_i) \\ \partial_t v_i &= \varepsilon_i (z) [\gamma_i (u_i - \beta_i) - v_i], \end{aligned} \quad (1)$$

where

$$\begin{aligned} f(u_l) &= k_l u_l (u_l - a_l) (1 - u_l) \\ F_l(u_l, u_i) &= \alpha_l D_{li} (u_l - u_i) \\ g(u_i) &= k_i u_i (u_i - a_i) (1 - u_i) \\ F_i(u_l, u_i) &= \alpha_i D_{il} (u_l - u_i). \end{aligned} \quad (2)$$

The variables u and v stand for non-dimensional transmembrane potentials and slow currents, respectively (time is measured in seconds and space in centimeters). It

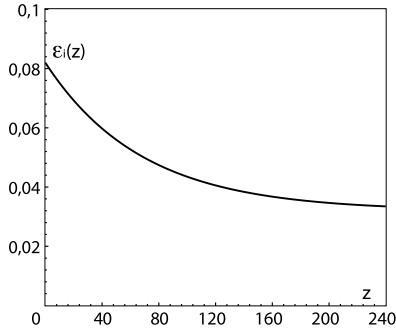


Figure 2. Plot of the analytical expression of the excitability parameter $\varepsilon_i(z)$ for the ICC layer as extracted from [50]. The spatial coordinate z represents the axial distance from pylorus.

is possible to obtain physical dimensions related to human or animal tissue adopting the following mapping:

$$u_l = \frac{V_l - V_{l,m}}{V_{l,M} - V_{l,m}}, \quad u_i = \frac{V_i - V_{i,m}}{V_{i,M} - V_{i,m}}, \quad (3)$$

where V_l is the dimensional transmembrane LM potential and $V_{l,m}$ and $V_{l,M}$ are its minimum and maximum physiological values, respectively. Analogous statements can be made for the other variables. The excitability parameter for the ICC layer is a function of the distance from pylorus, in agreement with the experimental interpolation plot reported in [50], so we extract the analytical form (4) reported in figure 2:

$$\varepsilon_i(z) = 0.032 + 0.05 \exp\left(-\frac{z}{68}\right). \quad (4)$$

In equations (1) and (2), β shifts the equilibrium point of the system from the stable branch of the nullcline, LM layer, to the unstable one, ICC layer. The two nonlinear functions $f(u_l)$ and $g(u_i)$ represent the cubic Zel'dovich's bistable term [70] that arises in many contexts for excitable tissues (a complete discussion is reported in [71]), while $F_l(u_l, u_i)$ and $F_i(u_l, u_i)$ terms complete the system coupling the four equations in the same but opposite manner. Here α describes the coupling between the two layers; ε is proportional to the frequency of oscillations in the ICC layer and is adjusted to mimic experimental observations in animals (in a first approximation, in the absence of human data, we shall assume that the values taken for animals will be plausibly valid for humans too); the coefficients D_{ll} and D_{ii} mimic a strong coupling inside the LM layer but a weaker coupling between the two layers and inside

Table 1. Aliev–Richards–Wikswø DML intestine ionic model parameters [50].

LM layer		ICC layer	
$k_l = 10$	$a_l = 0.06$	$k_i = 7$	$a_i = 0.5$
$\beta_l = 0$	$\gamma_l = 8$	$\beta_i = 0.5$	$\gamma_i = 8$
$\varepsilon_l = 0.15$	$\alpha_l = 1$	$\varepsilon_i = \varepsilon_i(x)$	$\alpha_i = -1$
$D_{ll} = 0.3$	$D_l = 0.4$	$D_{ii} = 0.3$	$D_i = 0.04$

the ICC layer. We stress the importance of conductance in the LM layer: unlike in cardiac myocytes only a relatively small number of gap junctions have been observed in cells of the LM layer. Thus, large values of D_{il} , D_l and relatively small value of D_i are necessary to fit well to the experimental data. Although α assumes the same absolute value for the two layers (see table 1), assuming therefore a symmetrical electrical coupling, we do not obtain such a behavior due to the nonlinearities of the ionic currents. In figure 3 we report the zero-dimensional time evolutions of the four ionic model variables (u_l , v_l , u_i , v_i) evaluated at the axial position $z = 120$ cm (spatial excitability – heterogeneity), that is $\varepsilon_i(z) = \varepsilon_i(120) \sim 0.04$. Parameters for the ionic model are calibrated for surgery when intestine frequency is lowered with respect to physiological conditions due to anesthetic drugs [72–76].

2.2. Bio-heat intestine problem

Heat transfer in biological systems is relevant in many diagnostic and therapeutic applications in which changes in temperature are involved [77]. Investigation of such diffusion equations requires the evaluation of temporal and spatial temperature distributions. This class of problems has been traditionally addressed using BHE [51], which accounts for the ability of tissues to remove heat both by passive conduction (diffusion) and blood perfusion. Heat conduction and perfusion contributions [78] are combined here in a generalized BHE [79] which, for a homogeneous and isotropic domain, assumes the form

$$\underbrace{C_l \partial_t T - k \nabla^2 T}_{\text{Diffusive evolution}} - \underbrace{\omega_m(T) C_b (T_a - T)}_{\text{Blood perfusion}} - \underbrace{q_m(T)}_{\text{Metabolic heat}} - \underbrace{p(\mathbf{x}, t)}_{\text{Stimulation}} = 0, \quad (5)$$

where equation terms and parameters values are reported and described in table 2. Although $\omega_m(T)$ and $q_m(T)$ include temperature dependence, considering the limited range of

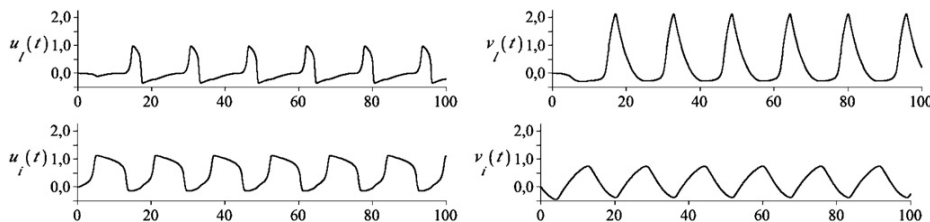


Figure 3. Numerical plots of the zero-dimensional (spatial dependences suppressed) time evolutions of the four ionic model variables, u_l , v_l , u_i and v_i , (without temperature dependence) evaluated for $\varepsilon_i(z) = \varepsilon_i(120) \sim 0.04$ (the mean duodenum length in our simulations). The horizontal axis represents time expressed in seconds while vertical axis assumes the non-dimensional values of the model variables.

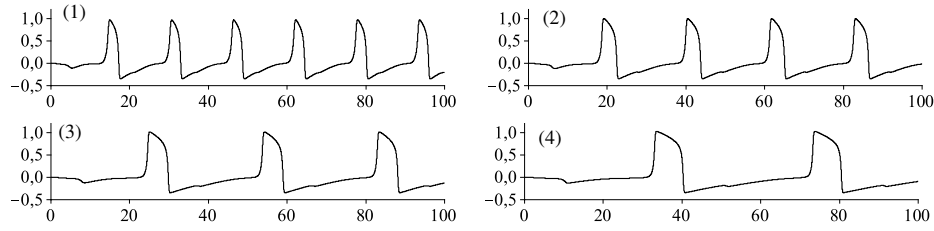


Figure 4. Numerical plot of the zero-dimensional time evolutions of the transmembrane potential u_t for $\varepsilon_i(z) \sim 0.04$ at four different temperatures: from panel (1) to panel (4) temperature assumes the values 37, 33, 29, 25 °C. The horizontal axis represents time expressed in seconds while vertical axis assumes the non-dimensional values of the model variables. We can note that thermal cooling leads the transmembrane potential to change its period as well as its duration and amplitude.

Table 2. Geometrical domain dimensions, model variables and model parameters referred to the human abdominal core and whole blood ($Hct = 40\%$) adopted to perform numerical simulations [93, 94].

Parameter	Description	Model value/range
L	Longitudinal length	240.0 cm
r_i	Internal radius	1.8 cm
r_e	External radius	2.0 cm
T	Local tissue temperature	[20–37] °C
C_t [93]	Specific tissue heat capacity	$3.89 \times 10^4 \text{ kg cm}^{-1} \text{ }^\circ\text{C}^{-1} \text{ s}^{-2}$
C_b [93]	Specific blood heat capacity	$3.82 \times 10^4 \text{ kg cm}^{-1} \text{ }^\circ\text{C}^{-1} \text{ s}^{-2}$
ρ_t [93]	Tissue density	$1050 \times 10^{-6} \text{ kg cm}^{-3}$
ρ_b [93]	Blood density	$1050 \times 10^{-6} \text{ kg cm}^{-3}$
k [93]	Tissue thermal conductivity	$54.4 \text{ kg cm }^\circ\text{C}^{-1} \text{ s}^{-3}$
ω_b [93]	Specific basal blood perfusion coefficient	$6.7 \text{ kg}^{-1} \text{ cm}^3 \text{ s}^{-1}$
q_0 [94]	Specific basal metabolic heat production	$6.32 \text{ kg cm}^{-1} \text{ s}^{-3}$

temperature variation in this study 20–37 °C and according to Rai and Rai [80] and Mitchell *et al* [81], we can assume $q_m = q_0$, $\omega_m = \omega_b \rho_t$ being equal to their constant basal values. This choice is motivated by the clinical setup we are considering: during abdominal surgery when the intestine is exposed to cold operating theatre's air and in the presence of anesthetic agents, metabolic intestine activity and blood perfusion rate reach their minimum value; thus, their thermal variation represents a little contribution as a heat source. The temperature gradients used in the model adopt a reasonable simplifying assumption: after sufficient time in operating theatre, the surface of the intestine thermalizes with the environment. These temperature gradients can relevantly influence the electrophysiological dynamics. A set of measurements during surgery however are planned by the authors in order to test and fine tune the model assumptions. In addition surgery causes inflammatory responses leading to loss of ICC pacemaker activity [2]; hence, in these conditions mechanical deformation caused by peristaltic motion can be neglected (deep anesthesia directly acts on calcium channels [82]). With these assumptions and with the definitions reported in table 3, we can rewrite equation (5) as

$$\partial_t T = \gamma \nabla^2 T + \omega^* (T_a - T) + q^* + P(\mathbf{x}, t). \quad (6)$$

In the following we do not directly use the $P(\mathbf{x}, t)$ term as external thermal stimulation (an electro-bistoury as an example) but we will adopt boundary geometry to impose temperature gradients. Electro-thermal coupling in biological media is introduced by the classical $Q_{10}(T)$ dimensionless

Table 3. Equivalent value parameters adopted in the BHE model (6).

Parameter	Description	Model value/range
$\gamma = k/C_t$	Thermal diffusivity coefficient	$1.4 \times 10^{-3} \text{ cm}^2 \text{ s}^{-1}$
$\omega^* = \omega_b \rho_b C_b / C_t$	Equivalent blood perfusion coefficient	$6.9 \times 10^{-3} \text{ s}^{-1}$
$q^* = q_m / C_t \equiv q_0 / C_t$	Equivalent metabolic heat production	$1.62 \times 10^{-4} \text{ }^\circ\text{C s}^{-1}$
$P(\mathbf{x}, t) = p(\mathbf{x}, t) / C_t$	Specific heating/cooling stimulus	$0 \text{ }^\circ\text{C s}^{-1}$

factor applied to transmembrane ionic currents. The quantity $Q_{10}(T) = (R_2/R_1) \exp[10/(T_2 - T_1)]$ represents the factor by which the rate R of a reaction, measured at T_1 and T_2 temperatures respectively, increases for every a 10 °C rise in temperature. The rate R may represent any measure of the progress of a process: action potential propagation along a nerve fiber in m s^{-1} , rate at which the products of a reaction are produced in mmol s^{-1} , current conducted through an ion channel, pump or transporter in pA , nA and μA , respectively, or rate at which the heart contracts per minute and many others. If the rate of the reaction is completely temperature independent, the resulting Q_{10} will be obviously 1. Although this factor is a convenient way to examine and report the temperature dependence of a process, it must be kept in mind that a thorough examination of such a dependence requires that the rate must be measured at more than two temperatures. Following the traditional formulation used in

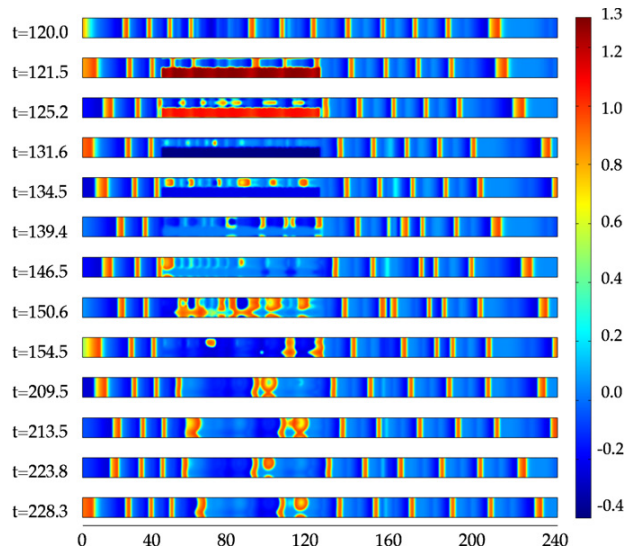


Figure 5. 2D simulations of the purely electrical intestine model (1) at constant temperature of 37 °C. Starting from constant initial data, at the regime state $t = 120$ s (the mathematical model needs some time to stabilize variable oscillations), an external step current stimulation is applied on a squared region of the tissue for about 10 s. The evolution figures are taken at different frames to show the turbulent pattern formation due to the destabilizing stimulus. The last two frames show that this electrical instability is persistent.

electrophysiological models [83], we adopt the exponential form $Q_{10}(T) = b \exp[(T - T_a)/10 \text{ } ^\circ\text{C}]$ where $T_a = 37 \text{ } ^\circ\text{C}$ is the physiological or reference tissue temperature. We note

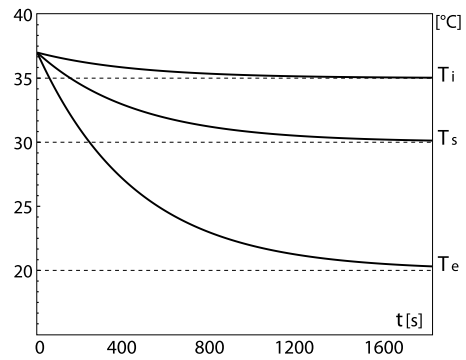


Figure 7. Example of time-dependent Dirichlet temperature boundary conditions adopted in the three-dimensional numerical simulations. T_i , T_s and T_e stand for internal, sectional and external boundary temperature, respectively (i.e. on all or part of the boundary of the 3D domain is imposed thermal cooling following the exponential laws reported in the figure).

that $b \sim 1$ for typical ion and molecule diffusion in bulk solutions while $b \sim 2$ for typical chemical reactions and for many biological processes. In this work, for intestine tissue we adopt $b = 2.6$ as reported in [64]. The resulting reaction–diffusion system (1) then becomes

$$\begin{aligned} \partial_t u_i &= f(u_i) + D_i \nabla^2 u_i - v_i + F_i(u_i, u_i) \\ \partial_t v_i &= Q_{10}(T)(10)\varepsilon_i[\gamma_i(u_i - \beta_i) - v_i] \\ \partial_t u_e &= g(u_e) + D_e \nabla^2 u_e - v_e + F_e(u_e, u_e) \\ \partial_t v_e &= Q_{10}(T)(10)\varepsilon_e[\gamma_e(u_e - \beta_e) - v_e]. \end{aligned} \quad (7)$$

Because of $T = T(t, \mathbf{x})$ (space and time dependences), then $Q_{10} = Q_{10}(T(t, \mathbf{x}))$ acts as an additional characteristic

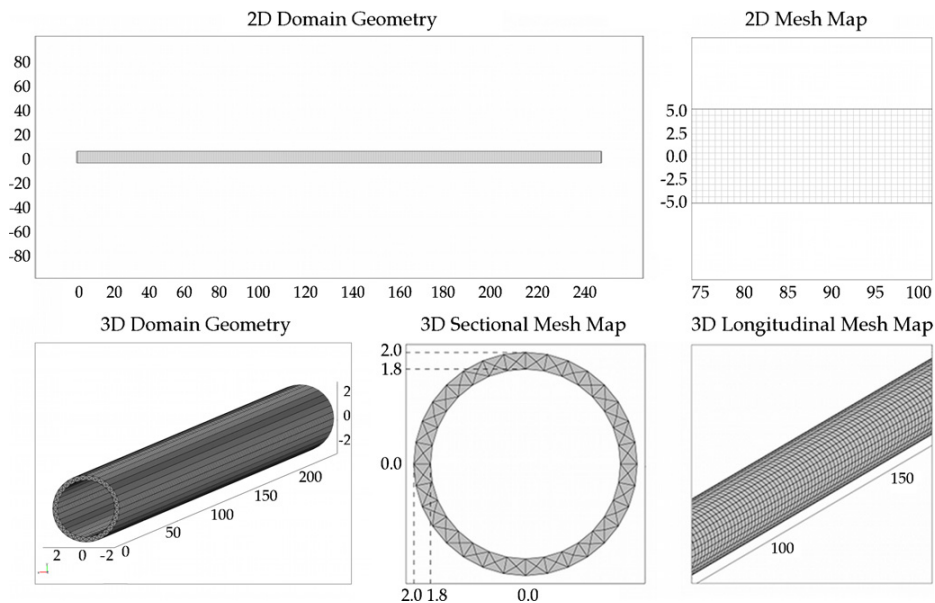


Figure 6. 2D and 3D adopted geometries, physical dimensions and meshes. The 2D domain geometry shows a rectangle $[240 \times 10]$ cm where the major dimension represents the duodenum length while the remaining one represents its mean circumference (in this case boundary identification gives the cylindrical closure as described in figure 1). The 2D discretization uses a quad mesh with element dimension $[0.67 \times 0.67]$ cm. 5400 nonlinear quadratic Lagrange elements lead to about 9×10^4 degrees of freedom. The 3D geometry assumes the same dimensions of the 2D one but introduces a finite constant thickness of 0.2 cm. In this case the discretization is made up of an adapted mesh method that leads to about 3×10^4 nonlinear quadratic elements and about 8×10^5 degrees of freedom.

heterogeneity of the tissue governed by thermal gradients. In figure 4 we report the zero-dimensional time evolutions of the transmembrane potential u_t , evaluated for $\varepsilon_i(z) = \varepsilon_i(120) \sim 0.04$ at four different temperatures 37, 33, 29, 25 °C. It is interesting to note that thermal cooling leads the transmembrane potential to change its period as well as its duration and shape similarly as it happens, as an example, in nerves [47–49, 84].

3. Results

3.1. Two-dimensional generalized study

We started our study analyzing a two-dimensional continuum, corresponding to an array of about 300×12 coupled cells (one cell is here roughly associated with a square of tissue of 8 mm length) of intestinal tissue. We assume periodic boundary conditions to simulate a two-dimensional cylindrical surface as described in figure 1. It is not necessary to write the Laplace operator in cylindrical polar coordinates (ρ, θ, z) because the cylinder is flat and results in a rectangle identifying longitudinal boundaries. Such a method permits us to reduce the computational requests and to examine different domain behaviors. In the simulations explored we have considered the tissue in its basal resting state, 37 °C with no heat transfer (starting with constant zero initial data for ionic variables the mathematical model generates and auto-stabilizes pacemaker oscillations), and we have introduced a current step-like external stimulation with non-dimensional

amplitude of 5, restricted in the rectangular space region $[0 \leq x \leq 40, y \leq 0]$ and applied for a specified time interval $\Delta t = 10$ s (the numerically simulated response is described in figure 5 at different times). The interesting result to be noted is the sustained turbulent electrical patterns arising because of the external stimulation. Such behavior may be experimentally associated with the destabilization of the physiological motility (peristaltic motion) following persisting external stimulations of different nature which could happen during abdominal surgery [1]. These results may be related to many other biological contexts in which spiraling wave behaviors arise [36, 37]. Numerical integrations of the equations have been obtained adopting the Comsol Multiphysics® software. The 2D FEM model consists of about 9×10^4 degrees of freedom with Lagrange quadratic squared mesh elements with space step $\Delta x = 0.67$ cm and time step $\Delta t = 0.05$ s. The solutions have been obtained using a UMFPAK FEM solver and a schematic representation of the adopted mesh and geometry model is reported in figure 6.

3.2. Three-dimensional simulations

Three-dimensional simulations have been carried out to reproduce the original results found in the previous section for the specific case of electro-thermal coupling (7). As a theoretical reasonable *ansatz*, in these simulations we have imposed thermal time-dependent Dirichlet boundary conditions, i.e. one of the different set-up imposed is

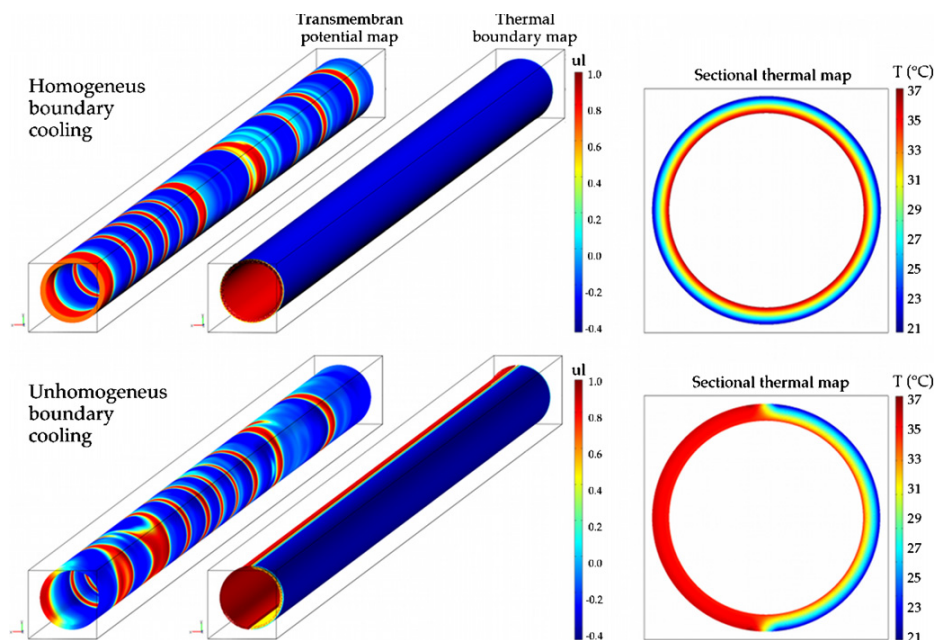


Figure 8. 3D model results obtained by FEM numerical integration of the complete thermo-ionic model (6) and (7). Two different boundary cooling setups imposed in the simulations, relative transmembrane potential u_t map, boundary and sectional thermal gradients are shown. In the upper figures we observe a uniform boundary cooling. In the lower figures two different cooling laws (see figure 7) are imposed on the external boundary modeling in this way the possibility that a part of the intestine is exposed to cold operating theater air while the remaining one is in contact with the body. In this case transmembrane potential patterns become definitively irregular and turbulent leading to spiral wave behaviors [71].

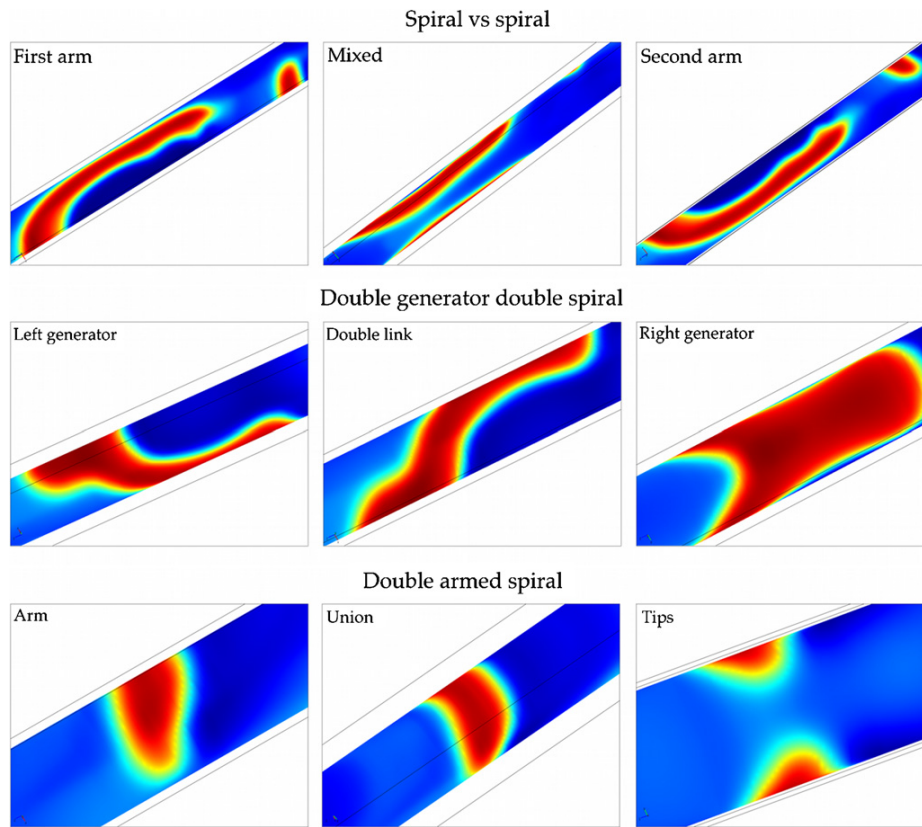


Figure 9. Particular of 3D simulations for a boundary set up subjected to inhomogeneous cooling described in figures 7 and 8. Transmembrane potential u_i map shows that turbulent and spiraling pattern behaviors arise in the region of excitability disorder caused by thermal gradients. In each sequence different orientations and zoom factors are chosen to better represent tissue behaviors.

$$\begin{aligned} \text{IB: } T_{\text{IB}} &= T_i + (T_a - T_i) \exp(-t/\tau) \\ \text{EB: } T_{\text{EB}} &= T_e + (T_a - T_e) \exp(-t/\tau) \\ \text{SB: } T_{\text{SB}} &= T_s + (T_a - T_s) \exp(-t/\tau) \end{aligned}$$

where IB, EB and SB stand for the internal, external and sectional boundary (the two ring-shaped surfaces which close the adopted 3D geometry), respectively; $\tau = 400$ s represents the time constant by which tissue temperature decreases towards the thermal regime; T_i , T_e and T_s are the asymptotic values reached after about 3τ time in the three subdomains (figure 7). In this case too, starting from a constant initial data, we consider a regime state for ionic variables and isothermal physiological conditions for temperature (T_a). In principle we should impose three different time constants describing three different decays for each boundary (i.e. for each tissue) but for the purposes of this work there is no need to perform such a high level of differentiation: in fact we are looking for global thermo-electrical duodenum response to external cooling.

The 3D FEM model consists of about 8×10^5 degrees of freedom with 3×10^4 Lagrange quadratic tetrahedral elements generated by a swept mesh method. Numerical solutions have been performed using a linear iterative system solver, Geometric Multigrid, optimized for parabolic problems. Numerical calculations have required about 5 Gb of RAM on an Intel Xeon dual core workstation and we were able to simulate about 60s of model dynamics

per day of computation. A picture of the adopted mesh and geometry model is reported in figure 6. 3D model simulation results are described in figures 8 and 9, and show how an inhomogeneous boundary cooling (see the captions) influences intestine electrical activity leading to turbulent patterns with spiral waves. These behaviors may be related to ileus disorder following abdominal surgery. Deep anesthesia, leading to blood perfusion reduction, is well known to decrease physiological body temperature (~ 37 °C) of about 2 °C [76, 82]. Cold operating theater air (~ 20 °C), as previously discussed, should cause an additional marked temperature reduction of exposed tissues (10–15 °C below the patient's temperature) in contrast with the remaining part in direct contact with the body. This condition influences the electrical dynamics of the model towards unstable behaviors, possibly associated with irregular bowel sounds, experimentally detected several hours after the surgery [1, 85].

4. Discussion

POI is a multifactorial disease: metabolic or electrical heterogeneities caused by regional mesenchymal ischemia, surgical trauma, or physical stress affect intestine tissue relevantly changing its electrical properties. Our numerical

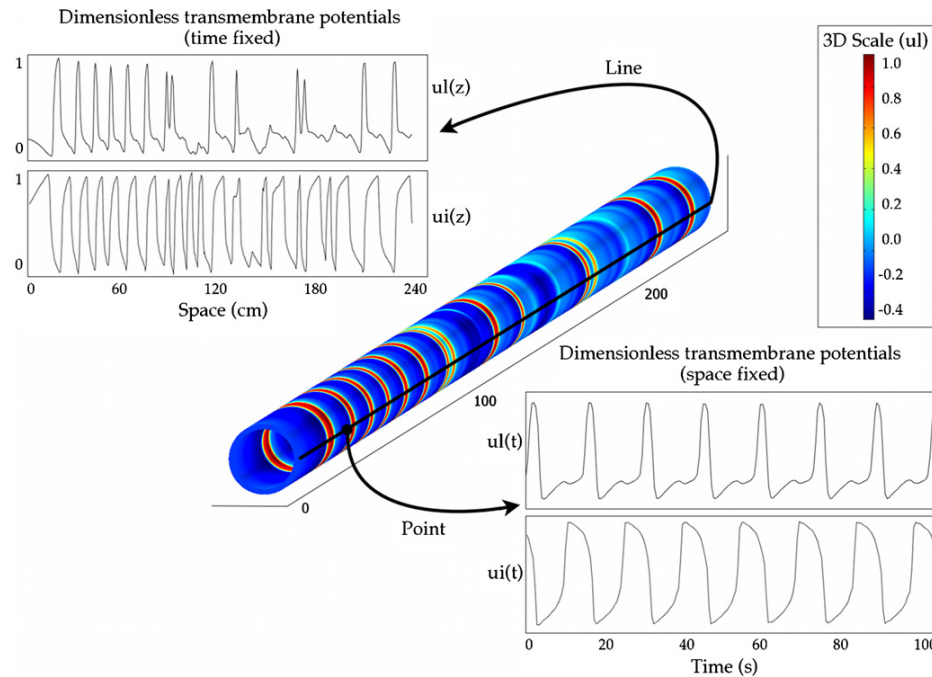


Figure 10. Schematic representation of the 3D FEM ionic model (1). The point-time evolution and the line-space distribution of the two transmembrane ionic potentials, u_t and u_i , are described. These are both referred to the three-dimensional regime state of intestine activity simulated in this work.

analysis has shown that spiral wave reentries due to temperature gradients could be an additional element of electrical instability possibly associated with patient disease. In detail, we have extended the 1D Aliev–Richards–Wiksw model adding isotropic heat transfer in order to simulate the GI tract electrical activity in two and three dimensions representing the first 240 cm of intestine. We correctly reproduced important experimentally observed phenomena of the intestinal activity: (i) synchronization along short distances and desynchronization for long distances, (ii) frequency change along the intestine, (iii) limited propagation length and time, (iv) decrease of propagation distance and propagation time along the intestine. All these characteristics can be seen from the space and time plots reported in figure 10. In this study however we obtained other interesting behaviors of transmembrane potential not observable in the 1D case. Particularly in two dimensions (figure 5), we observed that a steep tissue stimulation leads to turbulent intestinal activities giving rise to spiral wave behaviors which are a well-known phenomenon in many biological and clinical contexts [71, 86]. Analogous results have been obtained in three dimensions (figure 9) coupling the bio-heat equation to the adopted ionic model and imposing thermal inhomogeneous boundary cooling. In this case thermal cooling operates throughout $Q_{10}(T)$ ionic feedback, deforming and destabilizing the physiological electrical enteric activity in a persisting manner. The proposed thermo-ionic model may be widely generalized to any kind of excitable biological tissue subject to the operating theatre temperature (as well as to anesthetic agents and mechanical manipulations). These behaviors may then be in strict connection not only with postoperative ileus [1]

but also with the well-known problem of postoperative atrial fibrillation (PAF) [87, 88]. The GI tract system moreover has many pathologies similar to the heart, including arrhythmias and ischemia, that gives rise to intense pain, as reported in [26]. In the context of gastro-intestinal disease, methods based on SQUID and intragastric electrode techniques could be useful to detect the underlying electrophysiological disturbances (see [26, 30, 34] and references therein) and the model could be fine tuned on this ground. This work represents a first approach towards the modeling of tissues response following surgery and assumes the role of the integrative modeling framework of physiological, anatomical and medical knowledge of the GI tract system. The request of homogeneity and isotropy is a first approximation of a more general and realistic scenario of the intestine multilayered structure. Inhomogeneity and anisotropy are well known to induce complex spiralling behaviors in other biological contexts such as the heart [89] and brain [86]; therefore, a direct extension of this work should consist in analyzing thermo-ionic feedback on realistic reconstructed domains [33]. These anatomical complexities (i.e. anisotropic muscles layers studied in [40]) can affect the velocity propagation and the entire electrophysiological dynamics. Here we have not considered here moreover the mechanical counterpart of the problem which could be modeled as done in [41, 84] and [33]. The aim of this theoretical work has been to clarify the pathogenesis of POI in order to reduce the patients' postoperative discomfort, to improve recovery and shorten post-surgical hospital stay, with economic as well as patient benefits. We conclude by pointing out the possible role of temperature as one of the various external agents which may lead to POI, stressing the necessity

of experimental measurements in this direction for future works both *in vivo* and *in vitro* (i.e. following Roth and Barach [90–92]).

Acknowledgments

Two of the authors (CC and SF) acknowledge ICRANet for partially supporting this work.

References

- [1] Livingston E H and Passaro E P 1990 Postoperative ileus *Dig. Dis. Sci.* **35** 121–32
- [2] Yanagida H, Sanders K M and Ward S M 2007 Inactivation of inducible nitric oxide synthase protects intestinal pacemaker cells from postoperative damage *J. Physiol.* **582** 755–65
- [3] Stewart D and Waxman K 2007 Management of postoperative ileus *Am. J. Ther.* **14** 561–6
- [4] Liu Y-F, Chen K-B, Lin H-L, Ho C-H, Liu S-K, Liu Y-C and Wu R S-C 2009 Comparison of the effect of epidural and intravenous patient-controlled analgesia on bowel activity after cesarean section: a retrospective study of 726 Chinese patients *Acta Anaesthesiol. Taiwan.* **47** 22–7
- [5] Sajid M S, Mallick A S, Rimpel J, Bokari S A, Cheek E and Baig M K 2008 Effect of heated and humidified carbon dioxide on patients after laparoscopic procedures: a meta-analysis *Surg. Laparosc. Endosc. Percutan. Tech.* **18** 539–46
- [6] Sannour T, Kahokehr A and Hill A G 2008 Meta-analysis of the effect of warm humidified insufflation on pain after laparoscopy *Br. J. Surg.* **95** 950–6
- [7] Champin J K and Williams M 2006 Prospective randomized trial of heated humidified versus cold dry carbon dioxide insufflation during laparoscopic gastric bypass *Surg. Obes. Relat. Dis.* **2** 445–9
- [8] Farley D R, Greenlee S M, Larson D R and Harrington J R 2004 Double-blind, prospective, randomized study of warmed, humidified carbon dioxide insufflation versus standard carbon dioxide for patients undergoing laparoscopic cholecystectomy *Arch. Surg.* **139** 739–44
- [9] Danelli G, Berti M, Perotti V, Albertin A, Baccari P, Deni F, Fanelli G and Casati A 2002 Temperature control and recovery of bowel function after laparoscopic or laparotomic colorectal surgery in patients receiving combined epidural/general anesthesia and postoperative epidural analgesia *Anesth. Analg.* **95** 467–71
- [10] Luck A J, Moyes D, Maddern G and Hewett P J 1999 Core temperature changes during open and laparoscopic colorectal surgery *Surg. Endosc.* **13** 480–3
- [11] Cork R C, Vaughan R W and Humphrey L S 1983 Precision and accuracy of intraoperative temperature monitoring *Anesth. Analg.* **62** 211–4
- [12] Roe C F 1971 Effect of bowel exposure on body temperature during surgical operations *Am. J. Surg.* **122** 13–4
- [13] Stewart B T, Stitz R W, Tuch M M and Lumley J W 1999 Hypothermia in open and laparoscopic colorectal surgery *Dis. Colon. Rectum.* **42** 1292–5
- [14] Maron D J and Fry R D 2008 New therapies in the treatment of postoperative ileus after gastrointestinal surgery *Am. J. Ther.* **15** 59–65
- [15] Plourde V 1999 Stress-induced changes in the gastrointestinal motor system *Can. J. Gastroenterol.* **13** 26A–31A
- [16] So K Y, Kim S H, Sohn H M, Choi S J, Parajuli S P, Choi S, Yeum C H, Yoon P J and Jun J Y 2009 Carbachol regulates pacemaker activities in cultured interstitial cells of Cajal from the mouse small intestine *Mol. Cells* **27** 525–31
- [17] Nakayoshi T, Kawasaki N, Suzuki Y, Urashima M, Hanyu N and Yanaga K 2008 Epidural analgesia and gastrointestinal motility after open abdominal surgery—a review *J. Smooth Muscle Res.* **44** 57–64
- [18] Mochiki E, Asao T and Kuwano H 2007 Gastrointestinal motility after digestive surgery *Surg. Today.* **37** 1023–32
- [19] Bisgaard T and Kehlet H 2002 Early oral feeding after elective abdominal surgery—what are the issues? *Nutrition* **18** 944–8
- [20] Lewis S J, Egger M, Sylvester P A and Thomas S 2001 Early enteral feeding versus 'nil by mouth' after gastrointestinal surgery: a systematic review and meta-analysis of controlled trials *Br. Med. J.* **323** 773–6
- [21] Richards W O, Bradshaw L A, Staton D J, Garrard C L, Liu F, Buchanan S and Wiksw J P Jr 1996 Magnetoenterography (MENG) noninvasive measurement of bioelectric activity in human small intestine *Dig. Dis. Sci.* **41** 2293–301
- [22] Bradshaw L A, Ladipo J K, Staton D J, Wiksw J P and Richards W O 1999 The human vector magnetogram and magnetoenterogram *Biomed. Eng.* **46** 959–70
- [23] Seidel S A, Bradshaw L A, Ladipo J K, Wiksw J P and Richards W O 1999 Noninvasive detection of ischemic bowel *J. Vasc. Surg.* **30** 309–19
- [24] Bradshaw L A, Richards W O and Wiksw J P Jr 2001 Volume conductor effects on the spatial resolution of magnetic fields and electric potentials from gastrointestinal electrical activity *Med. Biol. Eng. Comput.* **39** 35–43
- [25] Bradshaw L A, Mayers A, Wiksw J P and Richards W O 2003 A spatio-temporal dipole simulation of gastrointestinal magnetic fields *Biomed. Eng.* **50** 836–47
- [26] Pullan A, Cheng L, Yassi R and Buist M 2004 Modelling gastrointestinal bioelectric activity *Prog. Biophys. Mol. Biol.* **85** 523–50
- [27] Bradshaw L A, Roy O P, O'Mahony G P, Mayers A G, McDowell J G, Wiksw J P and Richards W O 2005 Biomagnetic detection of injury currents in rabbit ischemic intestine *Dig. Dis. Sci.* **50** 1561–8
- [28] Lin A S-H, Buist M L, Smith N P and Pullan A J 2006 Modelling slow wave activity in the small intestine *J. Theor. Biol.* **242** 356–62
- [29] Irimia A, Richards W O and Bradshaw L A 2006 Magnetogastrographic detection of gastric electrical response activity in humans *Phys. Med. Biol.* **51** 1347–60
- [30] Bradshaw L A, Irimia A, Sims J A, Gallucci M R, Palmer R L and Richards W O 2006 Biomagnetic characterization of spatiotemporal parameters of the gastric slow wave *Neurogastroenterol. Motil.* **18** 619–31
- [31] Irimia A and Wiksw J P Jr 2008 Gastrointestinal arrhythmias are associated with statistically significant fluctuations in systemic information dimension *Physiol. Meas.* **28** N33–40
- [32] Faville R A, Pullan A J, Sanders K M and Smith N P 2008 A biophysically based mathematical model of unitary potential activity in interstitial cells of Cajal *Biophys. J.* **95** 88–104
- [33] Yassi R, Cheng L K, Rajagopal V, Nash M P, Windsor J A and Pullan A J 2009 Modeling of the mechanical function of the human gastroesophageal junction using an anatomically realistic three-dimensional model *J. Biomech.* **42** 1604–9
- [34] Bradshaw L A, Cheng L K, Richards W O and Pullan A J 2009 Surface current density mapping for identification of gastric slow wave propagation *Biomed. Eng.* **56** 2131–9
- [35] Erickson J C, Obioha C, Goodale A, Bradshaw L A and Richards W O 2009 Detection of small bowel slow-wave frequencies from noninvasive biomagnetic measurements *Biomed. Eng.* **56** 2181–9

- [36] Lammers W J E P, El-Kays A, Manefield G W, Arafat K and El-Sharkawy T Y 1997 Disturbances in the propagation of the slow wave during acute local ischemia in the feline small intestine *Eur. J. Gastroenterol. Hepatol.* **9** 381–8
- [37] Lammers W J E P, Donck L V, Stephen B, Smets D and Schuurkers J A J 2008 Focal activities and re-entrant propagations as mechanisms of gastric tachyarrhythmias *Gastroenterology* **135** 1601–11
- [38] Cysyk J and Tung L 2008 Electric field perturbations of spiral waves attached to millimeter-size obstacles *Biophys. J.* **94** 1533–41
- [39] Anthea M, Hopkins J, McLaughlin C W, Johnson S, Warner M Q, LaHart D and Wright J D 1993 *Human Biology and Health* (Englewood Cliffs, NJ: Prentice-Hall)
- [40] Lammers W J E P, Stephen B, Slack J R and Dhanasekaran S 2002 Anisotropic propagation in the small intestine *Neurogastroenterol. Motil.* **14** 357–64
- [41] Cherubini C, Filippi S, Nardinocchi P and Teresi L 2008 An electromechanical model of cardiac tissue: constitutive issues and electrophysiological effects *Prog. Biophys. Mol. Biol.* **97** 562–73
- [42] Hirst G D S and Hikaru S 2006 Involvement of interstitial cells of Cajal in the control of smooth muscle excitability *J. Physiol.* **576** 651–2
- [43] Komuro T 2006 Structure and organization of interstitial cells of Cajal in the gastrointestinal tract *J. Physiol.* **576** 653–8
- [44] Ward S M and Sanders K M 2006 Involvement of intramuscular ICC in neuroeffector transmission in the gastrointestinal tract *J. Physiol.* **576** 675–82
- [45] Zarate N, Mearin F, Wang X Y, Hewlett B, Huizinga J D and Malagelada J R 2003 Severe idiopathic gastroparesis due to neuronal and interstitial cells of Cajal degeneration: pathological findings and management *Gut* **52** 966–70
- [46] Pullan A J, Buist M L and Cheng L K 2005 *Mathematically Modelling the Electrical Activity of the Heart: From Cell to Body Surface and Back Again* (Singapore: World Scientific)
- [47] Hodgkin A L and Katz B 1949 The effect of temperature on the electrical activity of the giant axon of the squid *J. Physiol.* **109** 240–9
- [48] Bini D, Cherubini C and Filippi S 2006 Heat transfer in FitzHugh–Nagumo model *Phys. Rev. E* **74** 041905
- [49] Bini D, Cherubini C and Filippi S 2009 On vortices heating biological excitable media *Chaos Sol. Frac.* **42** 2057–66
- [50] Aliev R R, Richards W and Wikswo J P 2000 A simple nonlinear model of electrical activity in the intestine *J. Theor. Biol.* **204** 21–8
- [51] Pennes H H 1948 Analysis of tissue and arterial blood temperatures in the resting human forearm *J. Appl. Physiol.* **1** 93–122
- [52] Nelsen T S and Becker J C 1968 Simulation of the electrical and mechanical gradient of the small intestine *Am. J. Physiol.* **214** 749–57
- [53] Sarna S, Daniel E E and Kingma Y J 1971 Simulation of slow-wave electrical activity of small intestine *Am. J. Physiol.* **221** 166–75
- [54] Daniel E E, Bardakjian B L, Huizinga J D and Diamant N E 1994 Relaxation oscillator and core conductor models are needed for understanding of GI electrical activities *Am. J. Physiol.* **266** G339–49
- [55] Aliev R R and Vasiev B 1995 Phase breaks and chaos in a chain of diffusively coupled oscillators *Chaos Sol. Frac.* **5** 439–45
- [56] Zochowski M, Wachowiak M, Falk C X, Cohen L B, Lam Y W, Antic S and Zecevic D 2000 Imaging membrane potential with voltage-sensitive dyes *Biol. Bull.* **198** 1–21
- [57] Bradshaw L A, Allos S H, Wikswo J P Jr and Richards W O 1997 Correlation and comparison of magnetic and electric detection of small intestinal electric activity *Am. J. Physiol.* **272** G1159–67
- [58] FitzHugh R 1961 Impulses and physiological states in theoretical models of nerve membrane *Biophys. J.* **1** 445–66
- [59] Hodgkin A L and Huxley A F 1952 A quantitative description of membrane current and its application to conduction and excitation in nerve *J. Physiol.* **117** 500–44
- [60] Van der Pol B and van der Mark J 1927 Frequency demultiplication *Nature* **120** 363–4
- [61] Winfree A T 2000 *The Geometry of Biological Time* (Berlin: Springer)
- [62] FitzHugh R and Cole K S 1964 Theoretical potassium loss from squid axons as a function of temperature *Biophys. J.* **4** 257–65
- [63] FitzHugh R 1966 Theoretical effect of temperature on threshold in the Hodgkin–Huxley nerve model *J. Gen. Phys.* **49** 989–1005
- [64] El-Sharkawy T Y and Daniel E E 1975 Electrical activity of small intestinal smooth muscle and its temperature dependence *Am. J. Physiol.* **229** 1268–76
- [65] Guyton Arthur C and Hall Jhon E 2000 *Fisiologia Medica* (Napoli: EdiSES)
- [66] Nelsen T S and Becker J C 1968 Simulation of the electrical and mechanical gradient of the small intestine *Am. J. Physiol.* **214** 749–57
- [67] Daniel E E and Sarna S 1978 The generation and conduction of activity in smooth muscle *Ann. Rev. Pharmacol. Toxicol.* **18** 145–66
- [68] Keener J and Sneyd J 1988 *Mathematical Physiology* (Berlin: Springer)
- [69] Korn G A and Korn T M 2000 *Mathematical Handbook for Scientists and Engineers: Definitions, Theorems, and Formula for Reference and Review* (New York: Dover)
- [70] Zeldovich Y B and Frank-Kamenetsky D A 1938 Towards the theory of uniformly propagating flames *Acta Physicochim. CONT* **9** 341
- [71] Bini D, Cherubini C, Filippi S, Gizzi A and Ricci P E 2009 On spiral waves arising in natural systems *Commun. Comput. Phys.* submitted
- [72] Bueno L, Ferre J-P and Ruckebusch Y 1978 Effects of anesthesia and surgical procedures on intestinal myoelectric activity in rats *Dig. Dis. Sci.* **23** 690–5
- [73] Wright J W, Healy T E J, Balfour t W and Hardcastle J D 1982 Effects of inhalation anaesthetic agents on the electrical and mechanical activity of the rat duodenum *Br. J. Anaesth.* **54** 1223–30
- [74] Scheinin B, Lindgren L and Scheinin T M 1990 Perioperative nitrous oxide delays bowel function after colonic surgery *Br. J. Anaesth.* **64** 154–8
- [75] Lester G D, Bolton J R, Cullen L K and Thurgate S M 1992 Effects of general anesthesia on myoelectric activity of the intestine in horses *Am. J. Vet. Res.* **53** 1553–7
- [76] Vagts D A, Iber T, Szabo B, Haberstroh J, Reising K, Puccini M, Geiger K and Noldge-Schomburg G F E 2003 Effects of epidural anaesthesia on intestinal oxygenation in pigs *Br. J. Anaesth.* **90** 212–20
- [77] Gowrishankar TR, Stewart D A, Martin G T and Weaver J C 2004 Transport lattice models of heat transport in skin with spatially heterogeneous, temperature-dependent perfusion *Bio. Med. Eng. Online.* **3** 42
- [78] Scott E P, Robinson P S and Diller T E 1998 Development of methodologies for the estimation of blood perfusion using a minimally invasive thermal probe *Meas. Sci. Technol.* **9** 888–97
- [79] Lang J, Erdmann B and Seebass M 1999 Impact of nonlinear heat transfer on temperature control in regional hyperthermia *IEEE Trans. Biomed. Eng.* **46** 1129–38
- [80] Rai K N and Rai S K 1999 Effect of metabolic heat generation and blood perfusion on the heat transfer in the tissues with a blood vessel *Heat Mass Transfer* **35** 75–9

- [81] Mitchell J W, Galvez T L, Hengle J, Myers G E and Siebecker K L 1970 Thermal response of human legs during cooling *J. Appl. Physiol.* **29** 859–65
- [82] Kawasaki T, Ogata M, Kawasaki C, Okamoto K and Sata T 2007 Effects of epidural anaesthesia on surgical stress-induced immunosuppression during upper abdominal surgery *Br. J. Anaesth.* **98** 196–203
- [83] Moore J W 1958 Temperature and drug effects on squid axon membrane ion conductances *Fed. Proc.* **17** 113
- [84] Bini D, Cherubini C and Filippi S 2005 Viscoelastic FitzHugh–Nagumo models *Phys. Rev. E* **72** 041929
- [85] Luckey A, Livingston E and Tache' Y 2003 Mechanisms and treatment of postoperative ileus *Arch. Surg.* **138** 206–14
- [86] Murray J D 2001 *Mathematical Biology II: Spatial Models and Biomedical Applications* (Berlin: Springer)
- [87] Ashihara T, Yao T, Namba T, Kawase A, Ikeda T, Nakazawa K and Ito M 2002 After depolarizations promote the transition from ventricular tachycardia to fibrillation in a three-dimensional model of cardiac tissue *Circ. J.* **66** 505–10
- [88] Motsinger A A, Donahue B S, Brown N J, Roden D M and Ritchie M D 2006 Risk factor interactions and genetic effects associated with post-operative atrial fibrillation *Pac. Symp. Biocomput.* **11** 584–95
- [89] Fischer G, Tilg B, Modre R, Huiskamo G J M, Fetzer J, Rucker W and Wach P 2000 A bidomain model based BEM-FEM coupling formulation for anisotropic cardiac tissue *Ann. Biomed. Eng.* **28** 1229–43
- [90] Roth B J, Guo W-Q and Wikswo J P Jr 1988 The effects of spiral anisotropy on the electric potential and the magnetic field at the apex of the heart *Math. Biosci.* **88** 191–221
- [91] Barach J P 1996 Simulation calculations of cardiac virtual cathode effects *Comput. Biomed. Res.* **29** 77–84
- [92] Barach J P 1996 A two-dimensional simulation of the effects of late stimulation on a cardiac action potential *Comput. Biomed. Res.* **5** 373–81
- [93] Freitas R A 1999 *Nanomedicine vol. 1: Basic Capabilities* (Austin, TX: Landes Bioscience)
- [94] Cornelius T L 2002 *Computational Methods in Biophysics, Biomaterials, Biotechnology and Medical Systems: Algorithm Development, Mathematical Analysis and Diagnostics: Algorithm Techniques* vol 1 (Berlin: Springer)